Renormalization group approaches to strongly correlated electron systems

Fabian Bernd Kugler

SIGILL. UNIVERSITAT. LUDOVIC. MAXIM.

Munich 2019

Renormalization group approaches to strongly correlated electron systems

Fabian Bernd Kugler

A dissertation submitted
to the Faculty of Physics at the
Ludwig-Maximilians-Universität München
for the degree of
Doctor rerum naturalium

Munich, September 13, 2019

First referee: Prof. Dr. Jan von Delft
Second referee: Prof. Dr. Alessandro Toschi
Day of submission: September 13, 2019
Day of the oral examination: October 29, 2019

Zusammenfassung (Summary in German)

Stark korrelierte Elektronensysteme rufen eine Vielzahl faszinierender physikalischer Phänomene hervor und werfen erhebliche Herausforderungen in ihrer theoretischen Analyse auf. Die Herausforderungen sind begründet in der inhärenten Komplexität des Quanten-Vielteilchenproblems – kein klassischer Computer wird diese Systeme jemals vollständig simulieren können – und dem mangelnden effektiven Einteilchen-Bild, da die Elektronen aufgrund starker gegenseitiger Wechselwirkung nicht als unabhängig voneinander betrachtet werden können. Folglich können die meisten Systeme korrelierter Elektronen nur *näherungsweise* und *rechnergestützt* behandelt werden. In dieser Arbeit entwickeln wir einen Satz solcher numerischer Methoden für stark korrelierte Elektronen inspiriert durch die Renormierungsgruppen-(RG)-Idee der sukzessiven Hinzunahme von Freiheitsgraden von hohen zu niedrigen Energien. Dies ermöglicht eine effiziente Gliederung der verschiedenen Fluktuationen und ist essentiell für eine akkurate Beschreibung von wechselwirkenden Quantensystemen, bei welchen kollektives Verhalten und zusammengesetzte Objekte bei Energieskalen deutlich unerhalb jener der mikroskopischen Bestandteile entstehen.

In einem ersten Teil betrachten wir die funktionale Renormierungsgruppe (fRG), welche den Fluss von Korrelationsfunktionen unter Variation der zugrundeliegenden Wirkung beschreibt. Obgleich weit verbreitet fungiert fRG oftmals eher als qualitative denn als quantitative Methode wegen der intransparenten Näherung hervorgerufen durch die Trunkierung der Hierarchie von Flussgleichungen. Mittels eines iterativen “Multiloop”-fRG-Verfahrens können wir diese Näherung verbessern und viele bisherige Nachteile der fRG-Methode eliminieren. Insbesondere wird so die Unabhängig der Resultate von der Wahl des RG-Regulators wiederhergestellt und ein rigoroser Zusammenhang zum Parquet-Formalismus etabliert. Weiterhin zeigen wir, wie die Flussgleichungen direkt aus selbstkonsistenten Vielteilchen-Relationen hergeleitet werden können. Dies schafft eine Form der diagrammatischen Resummation auf dem Zweilteilchenlevel, welche singuläre, zweiteilchen-irreduzible Vertizes umgeht. Eine Anwendung auf das prototypische zwei-dimensionale Hubbard-Modell illustriert, wie unser Multiloop-Schema fRG-Behandlungen korrelierter Elektronensysteme zu *quantitativer* Aussagekraft verhilft.

Zweitens benutzen wir die numerische Renormierungsgruppe (NRG), basierend auf der iterativen Diagonalisierung von Störstellen-Hamilton-Operatoren, zusammen mit der dynamischen Molekularfeldtheorie (DMFT), um lokale Korrelationen in multi-orbitalen Systemen zu beschreiben. Der Zugang zu beliebig kleinen Temperaturen und Energien macht die NRG-Methode zu einem einzigartigen Realfrequenz-Störstellen-Solver für DMFT. Sie hat entscheidend zum Verständnis Hundscher Metalle, bei denen starke Korrelationen durch die Hundschen Regeln selbst bei moderater Coulomb-Abstoßung entstehen, beigetragen. Aufbauend auf jüngsten methodischen Fortschritten können wir den Anwendungsbereich von DMFT+NRG von orbital-entarteten Modellen zu *realistischeren* Problemstellungen erweitern: Zunächst undersuchen wir die orbitale Differenzierung in einem drei-orbitalen Modell für Hundsche Metalle und erklären Schlüsseleffekte des orbital-selektiven Mott-Übergangs. Im Zusammenhang realistischer Materialien nehmen wir dann die Bandstruktur aus der Dichtefunktionaltheorie (DFT) hinzu und analysieren ein urbildliches Material eines Hundschen Metalls, $\mathrm{Sr_2RuO_4}$. Dabei beschreiben wir insbesondere den RG-Fluss ins Fermiflüssigkeits-Regime bei zuvor unerreichbar niedrigen Temperaturen und präsentieren generell DFT+DMFT+NRG als neues Musterbeispiel zur rechnergestützten Analyse stark korrelierter Materialien.

Als Nebenprojekt unserer fRG-Studien entwickeln wir einen Algorithmus zum Abzählen von Feynman-Diagrammen ausgehend von einem geschlossenen Satz an Vielteilchen-Relationen, welcher überraschenderweise offenbart, dass total irreduzible Beiträge verantwortlich für den faktoriellen Anstieg der Anzahl an Diagrammen sind. Außerdem nutzen wir NRG zur Untersuchung von Transport durch Dreilevel-Quantenpunkt-Kontakte und stellen Vergleichsdaten für andere RG-Methoden, welche zusätzlich darauf abzielen, diese Systeme im Nichtgleichgewicht zu beschreiben, bereit.

Summary

(Summary in English)

Strongly correlated electron systems host a plethora of fascinating physical phenomena and pose formidable challenges in their theoretical analysis. The challenges originate from the inherent complexity of the quantum many-body problem—no classical computer will ever be able to fully simulate these systems—and the lack of an effective single-particle picture, as the strong mutual interactions make it impossible to regard the electrons as independent from each other. As a consequence, most systems of correlated electrons can only be tackled *approximately* and *numerically*. In this thesis, we develop a set of numerical methods for strongly correlated electrons, which are inspired by the renormalization group (RG) idea of including degrees of freedom successively from high to low energies. This enables an efficient organization of the diverse fluctuations and is key for an accurate treatment of interacting quantum systems, where collective behavior and composite objects emerge at energy scales far below those of the microscopic constituents.

In a first part, we consider the functional renormalization group (fRG), a versatile framework to study the flow of correlation functions upon modulating the underlying action. Though widely used, it has often acted more as a qualitative rather than quantitative method, due a nontransparent approximation induced by truncating the hierarchy of flow equations. We develop an iterative multiloop fRG (mfRG) scheme, which ameliorates this approximation and eliminates many of the drawbacks of fRG experienced hitherto. In particular, it restores the independence of results on the choice of RG regulator and establishes a rigorous relation to the parquet formalism. Furthermore, we show how to derive the flow equations directly from self-consistent many-body relations. This establishes a form of diagrammatic resummations at the two-particle level which circumvents ill-behaved two-particle-irreducible vertices. An application to the prototypical two-dimensional Hubbard model illustrates how our multiloop scheme elevates the fRG approach to correlated electron systems to a *quantitative* level.

Secondly, we employ the numerical renormalization group (NRG), based on the iterative diagonalization of impurity Hamiltonians, in conjunction with the dynamical mean-field theory (DMFT) to describe local correlations in multiorbital systems. Having access to arbitrarily low temperatures and energies, NRG is a unique, real-frequency impurity solver for DMFT. It has been pivotal to the understanding of Hund metals, where strong correlations arise from Hund's rules even at moderate Coulomb repulsion. Building on recent methodological advances, we extend the range of application of DMFT+NRG from orbital-degenerate models to more *realistic* setups: We first study orbital differentiation in a three-orbital Hund-metal model and unravel key effects of the orbital-selective Mott transition. In a real-materials setting, we then incorporate the bandstructure from density functional theory (DFT) and analyze the archetypal Hund-metal material $\mathrm{Sr_2RuO_4}$. We particularly follow its RG flow to the Fermi-liquid regime at previously inaccessible low temperatures and generally present DFT+DMFT+NRG as a new computational paradigm for strongly correlated materials.

As a side project of our fRG work, we develop an algorithm to count Feynman diagrams from closed many-body relations, which reveals the surprising outcome that totally irreducible contributions are responsible for the factorial growth in the number of diagrams. Additionally, we use NRG to study transport through three-level quantum dots and provide benchmark data for other RG methods, which aim at further describing these systems in nonequilibrium.

Publications

This dissertation is based on the following journal articles, ordered as they appear in this thesis.

P1 *Fermi-edge singularity and the functional renormalization group*
F. B. Kugler, J. von Delft
Sec. 3.2 / arXiv:1706.06872 J. Phys.: Condens. Matter **30**, 195501 (2018)

P2 *Multiloop functional renormalization group that sums up all parquet diagrams*
F. B. Kugler, J. von Delft
Sec. 3.3 / arXiv:1703.06505 Phys. Rev. Lett. **120**, 057403 (2018)

P3 *Multiloop functional renormalization group for general models*
F. B. Kugler, J. von Delft
Sec. 3.4 / arXiv:1707.04536 Phys. Rev. B **97**, 035162 (2018)

P4 *Multiloop functional renormalization group for the two-dimensional Hubbard model: Loop convergence of the response functions*
A. Tagliavini, C. Hille, **F. B. Kugler**, S. Andergassen, A. Toschi, C. Honerkamp
Sec. 3.5 / arXiv:1807.02697 SciPost Phys. **6**, 009 (2019)

P5 *Derivation of exact flow equations from the self-consistent parquet relations*
F. B. Kugler, J. von Delft
Sec. 3.6 / arXiv:1807.02898 New J. Phys. **20**, 123029 (2018)

P6 *Counting Feynman diagrams via many-body relations*
F. B. Kugler
Sec. 4.2 / arXiv:1808.01759 Phys. Rev. E **98**, 023303 (2018)

P7 *Flavor fluctuations in three-level quantum dots: Generic SU(3) Kondo fixed point in equilibrium and non-Kondo fixed points in nonequilibrium*
C. J. Lindner, **F. B. Kugler**, H. Schoeller, J. von Delft
Sec. 5.2 / arXiv:1802.09976 Phys. Rev. B **97**, 235450 (2018)

P8 *Renormalization group transport theory for open quantum systems: Charge fluctuations in multilevel quantum dots in and out of equilibrium*
C. J. Lindner, **F. B. Kugler**, V. Meden, H. Schoeller
Sec. 5.3 / arXiv:1810.12269 Phys. Rev. B **99**, 205142 (2019)

P9 *Orbital differentiation in Hund metals*
F. B. Kugler, S.-S. B. Lee, A. Weichselbaum, G. Kotliar, J. von Delft
Sec. 6.2 / arXiv:1904.10774 to appear in Physical Review B

P10 *Strongly correlated materials from a numerical renormalization group perspective: How the Fermi-liquid state of Sr_2RuO_4 emerges*
F. B. Kugler, M. Zingl, H. U. R. Strand, S.-S. B. Lee, J. von Delft, A. Georges
Sec. 6.3 / arXiv:1909.02389 submitted to Physical Review Letters

Acknowledgments

First of all, I would like to express my deep gratitude to Jan von Delft for his truly ideal supervision of my PhD studies. I profited from the many collaborations and contacts he initiated, from numerous research trips generously made possible, and his enormous support and trust in my work. In particular, I thank him for giving me the opportunity to present my results at the Exact Renormalization Group conference 2018 in Paris and as part of the condensed-matter field theory course at LMU. His unstoppable quest for improving the presentation and communication of scientific work and his leadership qualities are a genuine inspiration.

Second, I sincerely thank Alessandro Toschi not only for co-examining this thesis but also for a close scientific relationship since the early days of my PhD studies. I am grateful for his support, for insightful discussions, and for being introduced to many great colleagues. Moreover, I am honored to participate in collaborations with him, Sabine Andergassen, Patrick Chalupa, Cornelia Hille, Carsten Honerkamp, and Agnese Tagliavini.

I very much appreciate the opportunity of using Andreas Weichselbaum's QSpace tensor library and Seung-Sup Lee's routines built on top of it. Without these, the NRG results of the present thesis would not have been possible. A special thanks goes to Seung-Sup for long discussions on various topics and our intriguing joint work on NRG four-point correlators.

I am thankful to Gabriel Kotliar for inspiring discussions, our collaboration on orbital differentiation in Hund metals, and generally his encouragement and support.

Furthermore, my gratitude is due to the Simons foundation for hosting me at the Flatiron Institute during a research stay in the fall of 2018. I very much enjoyed the pleasant atmosphere at the Institute, many discussions with Yuan-Yao He, and an exciting collaboration with Antoine Georges, Hugo Strand, and Manuel Zingl.

I also thank Carsten Lindner, Volker Meden, and Herbert Schoeller for the collaboration on three-level quantum dots.

The research school IMPRS-QST provided a nice framework for my PhD studies. I thank Matthias Punk and Michael Knap for their help as members of my thesis advisory board and Sonya Gzyl for her friendly assistance in organizational aspects. Funding by IMPRS-QST is gratefully acknowledged.

Being part of the chair of theoretical solid-state physics was huge fun. I extend my thanks to all the great colleagues and friends I met in and around the office. In particular, I appreciate stimulating conversations about physics and beyond with Santiago Aguirre, Gianni del Bimbo, Maximilian Buser, Bin-Bin Chen, Andreas Gleis, Jonas Greitemann, Sebastian Huber, Claudius Hubig, Jheng-Wei Li, Dima Pimenov, Dennis Schimmel, Katharina Stadler, Andreas Swoboda, Julian Thönniß, Elias Walter, and Lukas Weidinger. A special thanks goes to Jonas Stapmanns and Elias Walter for proofreading this thesis.

Last but not least, I am grateful to Laura, my family, and my friends for their continuous support.

Contents

Zusammenfassung (Summary in German) **v**

Summary (Summary in English) **vi**

Publications **vii**

Acknowledgments **viii**

1 Introduction **1**
- 1.1 Motivation . . . 1
- 1.2 Scope . . . 2
- 1.3 Outline . . . 3

2 Methodological background **4**
- 2.1 Preliminaries on many-body theory . . . 4
- 2.2 Functional renormalization group from a Wilsonian perspective . . . 6
  - 2.2.1 Recap of Wilson's momentum-shell renormalization group . . . 6
  - 2.2.2 Functional renormalization . . . 8
- 2.3 Parquet theory . . . 9
  - 2.3.1 Derivation of the parquet equations . . . 10
    - 2.3.1.1 Schwinger–Dyson equation . . . 11
    - 2.3.1.2 Two-particle reducibility . . . 12
    - 2.3.1.3 Bethe–Salpeter equations for generalized susceptibilities . . . 13
    - 2.3.1.4 Remark on Φ-derivability . . . 15
    - 2.3.1.5 Bethe–Salpeter equations for two-particle-reducible vertices . . . 16
    - 2.3.1.6 Parquet equation . . . 17
    - 2.3.1.7 Parquet approximation . . . 18
- 2.4 Dynamical mean-field theory and the numerical renormalization group . . . 20
  - 2.4.1 Dynamical mean-field theory in a nutshell . . . 20
  - 2.4.2 Numerical renormalization group in a nutshell . . . 23
  - 2.4.3 Minimal models for Hund metals . . . 25
- 2.5 Diagrammatic extensions of dynamical mean-field theory . . . 26
  - 2.5.1 Nonlocal susceptibilities in dynamical mean-field theory . . . 27
  - 2.5.2 Ladder dynamical vertex approximation . . . 28
  - 2.5.3 Parquet dynamical vertex approximation . . . 29
  - 2.5.4 Dynamical mean-field functional renormalization group . . . 29
  - 2.5.5 Bare vertices in the dual fermion formalism . . . 30

3 Multiloop functional renormalization group **32**
- 3.1 Overview . . . 32
- 3.2 Publication: *Fermi-edge singularity and the functional renormalization group* . . . 34
- 3.3 Publication: *Multiloop functional renormalization group that sums up all parquet diagrams* . . . 50
- 3.4 Publication: *Multiloop functional renormalization group for general models* . . . 62
- 3.5 Publication: *Multiloop functional renormalization group for the two-dimensional Hubbard model: Loop convergence of the response functions* . . . 73
- 3.6 Publication: *Derivation of exact flow equations from the self-consistent parquet relations* 121

4 Counting of Feynman diagrams **140**
- 4.1 Overview . . . 140
- 4.2 Publication: *Counting Feynman diagrams via many-body relations* . . . 141

5 Transport through multilevel quantum dots 150
- 5.1 Overview . . . 150
- 5.2 Publication: *Flavor fluctuations in three-level quantum dots: Generic SU(3) Kondo fixed point in equilibrium and non-Kondo fixed points in nonequilibrium* . . . 151
- 5.3 Publication: *Renormalization-group transport theory for open quantum systems: Charge fluctuations in multilevel quantum dots in and out of equilibrium* . . . 172

6 Hund metals with nondegenerate orbitals 189
- 6.1 Overview . . . 189
- 6.2 Publication: *Orbital differentiation in Hund metals* . . . 190
- 6.3 Publication: *Strongly correlated materials from a numerical renormalization group perspective: How the Fermi-liquid state of Sr_2RuO_4 emerges* . . . 201

7 Summary and discussion 210
- 7.1 Multiloop functional renormalization group . . . 210
  - 7.1.1 Summary . . . 211
  - 7.1.2 Differential treatment of the parquet equations . . . 215
- 7.2 Counting of Feynman diagrams . . . 217
- 7.3 Transport through multilevel quantum dots . . . 218
- 7.4 Hund metals with nondegenerate orbitals . . . 219
  - 7.4.1 Summary . . . 219
  - 7.4.2 Interleaved numerical renormalization group for more than three orbitals . 221

8 Conclusion and outlook 223

9 Appendix 225
- 9.1 Schwinger–Dyson equation with reversed order . . . 225
- 9.2 Bethe–Salpeter equation in the parallel channel . . . 225
- 9.3 Bethe–Salpeter equation (parallel channel) with reversed order . . . 226

Bibliography 228

1 Introduction

1.1 Motivation

Strongly correlated electron systems are a continuous source of major scientific discovery in condensed-matter physics. Prominent examples are high-temperature superconductivity, metal–insulator transitions, colossal magnetoresistance, the fractional quantum Hall effect, or frustrated quantum magnetism. A recent case is the spectacular appearance of superconductivity upon twisting bilayers of graphene [CFD+18, CFF+18]. Some of these effects have already and others will likely find their way into technological applications.

The long list of fascinating experiments comes with a similarly long list of challenges for theoreticians. Still, numerous properties of strongly correlated materials remain elusive and cannot be reliably predicted. In fact, many of the above effects are not even understood on a qualitative level. The reason is that strongly correlated systems lack an intuitive, "single-particle" picture. Instead, the mutual interactions between an extremely large number of particles give rise to emergent phenomena that are not explainable by the individual constituents alone. Here, the inherent complexity of quantum physics is at full display; hardly any exact solutions are possible and meaningful approximations must be devised. This thesis follows the route of renormalization group approaches to strongly correlated electron systems.

What kind of electron systems?—A complete description of strongly correlated materials, including all electrons with all their types of interactions (and possibly the atomic nuclei) is an overwhelming—and often not even desired—task. In order to understand their characteristic properties and the key mechanisms, one should find an abstract, reductionist version of the problem. Strong correlations typically arise in materials which have partially filled d or f shells with narrow energy bands, where the magnitude of electron–electron interactions is comparable to their kinetic energy. Hence, one focuses on the electrons in those shells, considers their motion on the lattice set by the crystal structure and their interactions partially screened by all the remaining electrons. If we further approximate the crystal lattice and the screened electronic interactions in a simple, prototypical form, we arrive at *models* for strongly correlated electrons. Ideally, these are simple enough to have a (reasonably approximate) solution and yet complex enough to mimic a fair portion of the actual observation. An archetypal model for strongly correlated electrons is the single-orbital two-dimensional (2D) Hubbard model. Deceptively simple-looking, it has kept physicists busy for more than half a century [Edi13] and has inspired various theoretical techniques, most of which can only be pursued numerically. It has become a model of such prominent status that experiments, using setups of ultracold atoms in optical lattices, are even *designed*, as "quantum simulators", to probe the model as accurately as possible [GB17].

Two hallmark phenomena of correlated electrons, which can be described by Hubbard-like models and especially motivate the efforts of this thesis, are the Mott–Hubbard metal-to-insulator transition and unconventional superconductivity. The former is a phase transition between a metal and an insulator which cannot be explained by traditional band theory but is driven by the interactions between electrons. Understanding the Mott transition in one-band systems has been a breakthrough achievement in condensed-matter physics. However, the Mott transition in systems with multiple active orbitals remains a topic of current research. Even more so, the puzzle of high-temperature superconductivity remains unsolved in a decades-long quest. Again, one can distinguish systems whose electronic properties are dominated by a single orbital (cuprates) and those with multiple active orbitals (iron-based superconductors). The central question is: What is the precise pairing mechanism that makes electrons form Cooper pairs—and thereby enables them to conduct current without resistivity? To approach this problem, it is of paramount importance to understand these strongly correlated systems first in their *normal*, i.e., non-superconducting state. From there, one can tune external parameters, such as temperature and doping, to study the onset of superconductivity.

Why renormalization group approaches?—Direct approaches to interacting electron systems are impeded by the exponentially large Hilbert space of many-body systems or the fermionic sign problem in Monte Carlo samplings. Strong correlations make theoretical treatments particularly hard because one has to go beyond an effective single-particle description. In fact, one can *define* strong correlations as those arising beyond a Hartree–Fock description in the model context or the local-density approximation within the density functional theory (DFT) applied to materials. Another complication is that these systems exhibit their key effects at distinct energy scales, with, e.g., kinetic energy and Coulomb repulsion of a few electron volts (eV), magnetic exchange interactions below 1 eV, and transitions temperatures in the meV regime. In other words, collective behavior and composite objects emerge at energy scales far below those of the microscopic Hamiltonian.

A very powerful framework, designed to deal with diverse energy scales, is given by the renormalization group, invented from the 1950s to '70s. It has revolutionized the way we think about physics, introducing fundamental concepts such as running coupling constants in particle physics or universality in statistical physics. On top of that, it has influenced—and continues to influence—numerical approaches in condensed-matter physics. The latter aspect is the cornerstone of this thesis: We develop numerical approaches, inspired by the renormalization group idea, to provide the means to address the most challenging problems of strongly correlated electrons and use these methods to elucidate some of the intriguing effects listed above.

1.2 Scope

We focus on two different and almost complementary realizations of the renormalization group applied to correlated electron systems. The first is the *functional renormalization group* (fRG) [MSH$^+$12], a versatile action- or Green's function–based quantum field-theoretical approach. It can deal with general lattice or continuum systems, possibly treated directly in the thermodynamic limit; yet, it requires degrees of freedom that are in some sense weakly coupled. The second approach is the *numerical renormalization group* (NRG) [BCP08], which is a Hamiltonian- or state-based method. It is completely nonperturbative, such that the size of coupling and interaction parameters is almost irrelevant to its accuracy, but it can only be applied to the special class of impurity models. Statements about lattice systems are possible with the help of the dynamical mean-field theory (DMFT) [GKKR96], where the lattice problem is mapped onto a self-consistently determined impurity model, at the cost of neglecting nonlocal correlations.

The fRG method, having its origin in the high-energy community, is nowadays used widely also in condensed-matter physics. Adding to previous results of diagrammatic techniques, it has been instrumental in elucidating the formation of a superconducting instability by antiferromagnetic fluctuations [Sca12, MSH$^+$12]. There, an fRG flow, unbiased between all two-particle channels, compares to a similarly channel-unbiased, "parquet" resummation of Feynman diagrams [Bic04]. However, the fRG approach to strongly correlated electrons has throughout been used in a rather crude approximation. For 2D lattice systems, it has acted more as a qualitative rather than quantitative tool, and its relation to other techniques, like the parquet formalism, remained obscure.

The NRG method and its efficient implementation have been optimized in the von Delft group, pioneered by A. Weichselbaum [WvD07, Wei12a, Wei12b, SMvDW16, LW16]. For instance, the combination of DMFT and NRG was used for a highly accurate description of the single-orbital Hubbard model [LvDW17] as well as to unravel the key mechanisms in Hund metals [SYvD$^+$15, SKWvD19, DSK$^+$19]. However, the DMFT+NRG approach has so far only been applied in the model context and to three-orbital systems with full, SU(3) orbital symmetry. In Hund metals, the disparate (low-energy) behavior of different orbitals is an important aspect, and a realistic material description actually requires taking the bandstructure as input from DFT.

The guiding questions for this thesis are thus:

1. Can we use fRG as a *quantitative* tool? What is the precise relation between fRG flows and the more traditional, diagrammatic parquet theory?

2. Can we use DMFT+NRG for a *realistic* description of multiorbital systems?

A central result of this work is the invention of multiloop fRG (mfRG), which improves fRG algorithms, elevates fRG results to a quantitative level, and establishes a rigorous relation to the parquet theory. The main target for mfRG is the 2D Hubbard model, used to describe cuprates, for which a first test-bed analysis is presented. Another important result is that we are able to significantly extend the range of application of DMFT+NRG. We first study the effects of orbital differentiation in three-orbital models of Hund metals and drive the system close to an orbital-selective Mott transition, which is argued to be a key aspect of the iron-based superconductors [dMGC14]. Secondly, we shed light on the Fermi-liquid state of the unconventional, yet low-temperature superconductor $\mathrm{Sr_2RuO_4}$ [MRS01, MSHM17] in a novel DFT+DMFT+NRG approach.

1.3 Outline

The focus of this thesis is on the development of methods, used to tackle strongly correlated electron systems. In Chapter 2, we give the necessary methodological background to put the new developments into context. Specifically, we first introduce fRG as a computationally viable and advantageous realization of Wilson's successive mode elimination [Wil75, Sha94]. Then, we provide a compact derivation of the parquet equations and give special attention to properties of the so-called parquet approximation. Subsequently, we briefly review DMFT and NRG and recap the modeling of Hund metals from a DMFT+NRG point of view. Finally, we give a short overview of diagrammatic extensions of DMFT [RHT⁺18] targeted at long-range electronic correlations.

Chapter 3 deals with the development of mfRG and constitutes the main part of this thesis. We start by considering a toy model, the X-ray–edge singularity, and subsequently extend the formalism to the general fermionic many-body problem, while establishing a diagrammatic equivalence between mfRG and the parquet approximation. Next, we present a refined numerical study of the half-filled 2D Hubbard model. Ultimately, we generalize the whole framework and formulate it more abstractly by showing how to algebraically derive flow equations from the self-consistent parquet relations.

The following two chapters contain side projects conducted within the time frame of this thesis. First, the publication presented in Chapter 4 builds on the previous diagrammatic characterization of mfRG. It develops an algorithm to count Feynman diagrams from many-body relations, applicable to exact as well as approximate approaches. Second, the works of Chapter 5 can be understood as preparatory for the later application of DMFT+NRG to three-orbital systems. Numerically, they deal with the simplified setting of spinless three-level impurity systems; generally, they describe transport through multilevel quantum dots.

Chapter 6 is devoted to DMFT+NRG analyses of Hund metals. First, we consider a simplified model to study orbital differentiation and particularly the orbital-selective Mott transition. Then, we apply the method in the real-material context, characterizing the Fermi-liquid state of $\mathrm{Sr_2RuO_4}$ at arbitrarily low temperatures and energies.

In Chapter 7, we summarize the results of all publications and provide additional information on the interpretation or extension of the respective methods. The general conclusion of this thesis is found in Chapter 8. We close with an outlook on a possible combination of the rather different RG approaches of DMFT+NRG and mfRG, which could provide a unique handle on strong *and* long-range electronic correlations.

2 Methodological background

This chapter covers technical aspects of using fRG and NRG to treat strongly correlated electron systems and provides the necessary background to put the developments of the subsequent chapters into context. We start with preliminary aspects of the (fermionic) many-body problem, before introducing fRG from the traditional Wilsonian perspective. Next, we give a compact introduction to the parquet formalism, which allows us, as shown in publication [P5] and further elaborated in Sec. 7.1.2, to find the additional interpretation of (multiloop) fRG as differential form of the parquet equations. Then, we briefly discuss DMFT, NRG as impurity solver, and the DMFT+NRG perspective on Hund metals. Finally, we give an overview of various diagrammatic extensions of DMFT, which, in addition to the impurity-based description of DMFT, take correlations of arbitrarily long wavelength into account.

2.1 Preliminaries on many-body theory

Minimal models for strongly correlated electrons often describe electrons in partially filled atomic shells, moving on a lattice originating from the atomic crystal structure, with screened, or even purely local interactions. A compact formulation is possible through second-quantized Hamiltonians, $\hat{H}[\hat{c}^\dagger_x, \hat{c}_x]$, phrased in terms of operators, $\hat{c}^\dagger_x, \hat{c}_x$. These respectively create or annihilate fermionic degrees of freedom, whose quantum numbers are encoded in the index x. A prime example of this category is the single-orbital Hubbard model,

$$\hat{H}_1 = -t \sum_{\langle i,j\rangle,\sigma} \hat{c}^\dagger_{i,\sigma}\hat{c}_{j,\sigma} + U \sum_i \hat{n}_{i,\uparrow}\hat{n}_{i,\downarrow}. \tag{2.1}$$

Here, $\hat{c}^\dagger_{i,\sigma}$ creates an electron of spin σ on lattice site i, and $\hat{n}_{i,\sigma} = \hat{c}^\dagger_{i,\sigma}\hat{c}_{i,\sigma}$ counts the number of such electrons. The first term describes hopping of amplitude t between nearest-neighbor sites $\langle i, j\rangle$; the second one a local Coulomb repulsion of size U. Similarly, one can set up Hubbard models for electrons in multiple atomic orbitals, simply by adding an orbital index m to the collection of quantum numbers. Figure 2.1 gives two material-specific examples for orbital degrees of freedom. Considering a general tunneling matrix $\boldsymbol{t}_{ij}$ and a local interaction $\hat{H}_\mathrm{int}$, the Hamiltonian reads

$$\hat{H}_2 = -\sum_{i,j,m,m',\sigma} [\boldsymbol{t}_{ij}]_{mm'}\, \hat{c}^\dagger_{i,m,\sigma}\hat{c}_{j,m',\sigma} + \sum_i \hat{H}_\mathrm{int}[\hat{c}^\dagger_{i,m,\sigma}, \hat{c}_{i,m,\sigma}]. \tag{2.2}$$

The equilibrium properties of such systems are most easily described in the grand canonical ensemble at temperature T and chemical potential μ. The partition function Z can then be represented as a path integral over (anticommuting) Grassmann fields, $\bar{c}_x$, c_x, depending on imaginary time τ [NO98]:

$$Z = \int \mathcal{D}[\bar{c}, c]\, e^{-S[\bar{c},c]}, \qquad S[\bar{c}, c] = \int_0^\beta \mathrm{d}\tau \sum_x \big[\bar{c}_x(\tau)(\partial_\tau - \mu)c_x(\tau)\big] + H[\bar{c}_x(\tau), c_x(\tau)].$$

Here, we denote the measure of the functional integral, for fields antiperiodic in τ between 0 and β, by $\int \mathcal{D}[\bar{c}, c] = \int \mathcal{D}[\bar{c}] \int \mathcal{D}[c]$, the action by S, and $\beta = 1/T$ (setting $\hbar = 1 = k_B$).

In this framework, we formulate the general fermionic many-body problem more abstractly by the action

$$S[\bar{c}, c] = -\sum_{x',x} \bar{c}_{x'} \big[G_0^{-1}\big]_{x',x} c_x - \tfrac{1}{4} \sum_{x',x,y',y} \Gamma_{0;x',y';x,y}\bar{c}_{x'}\bar{c}_{y'}c_y c_x, \tag{2.3}$$

with bare propagator G_0 and bare four-point vertex Γ_0, which is antisymmetric in its first and last two arguments. The sums over indices x, x', etc. should be considered as generalized sums (either sums or integrals), properly normalized, with x additionally containing imaginary time, $\tau \in (0, \beta)$,

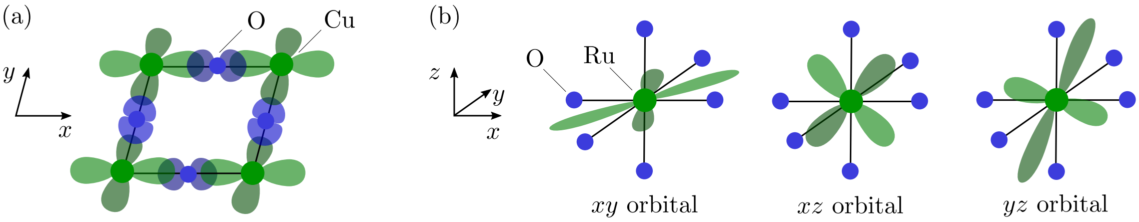

Figure 2.1 (a) The cuprates are often modeled by the single-orbital Hubbard model (2.1), as electrons mainly hop between the Cu-3$d_{x^2-y^2}$ orbitals (hybridized with O-2p states) in the two-dimensional copper-oxide planes [KKN$^+$15]. (b) In strontium ruthenate (Sr$_2$RuO$_4$), electronic properties are dominated by the three xy, xz, yz orbitals of Ru-4d and O-2p character [MRS01].

or (imaginary) Matsubara frequency, $i\nu \in (2\mathbb{Z}+1)i\pi T$ [NO98]. In fact, choosing a representation in terms of Matsubara frequency, momentum, and spin, with $x = (i\nu, \boldsymbol{k}, \sigma) \equiv (k, \sigma)$, the Hubbard model of Eq. (2.1) with dispersion $\epsilon_{\boldsymbol{k}}$ is recovered as

$$G_{0;x,x'} = \frac{\delta_{k',k}\delta_{\sigma',\sigma}}{i\nu+\mu-\epsilon_{\boldsymbol{k}}}, \qquad \Gamma_{0;x_1',x_2';x_1,x_2} = -U\delta_{\sigma_1,\bar{\sigma}_2}(\delta_{\sigma_1',\sigma_1}\delta_{\sigma_2',\sigma_2} - \delta_{\sigma_1',\sigma_2}\delta_{\sigma_2',\sigma_1})\,\delta_{k_1'+k_2',k_1+k_2}. \tag{2.4}$$

Using a representation adapted to the system (such as frequency and momentum in a system translationally invariant in time and space) eliminates some redundant arguments. However, we purposely keep the notation of general indices x, x', etc., so that the following derivations remain fully general and equally applicable to systems without such symmetries or even with more degrees of freedom.

The operators, $\hat{c}_x^\dagger$, $\hat{c}_x$, and Grassmann fields, $\bar{c}_x$, c_x, can be considered as auxiliary objects—what is measured experimentally are correlation functions. Correlation functions of fields, corresponding to time-ordered expectation values of operators, are given by [NO98]

$$\langle c_{x_1} \cdots \bar{c}_{x_n} \rangle = \frac{1}{Z} \int \mathcal{D}[\bar{c}, c]\, c_{x_1} \cdots \bar{c}_{x_n} e^{-S}. \tag{2.5}$$

Of particular relevance are correlations functions of two and four fields, describing single- and two-particle properties. On the one hand, their results can be directly compared to the parameters of the bare action (2.3) in terms of, e.g., an effective mass and an effective interaction. On the other hand, they are directly measurable in experiments, single-particle correlations through photoemission spectroscopy and two-particle correlations in the form of, say, optical or magnetic susceptibilities. Their analysis is simplified by introducing one-particle-irreducible (1PI) vertices [KBS10]. Firstly, the two-point correlation function is represented by the (full) propagator $G \equiv G^{(2)}$. Via Dyson's equation, G is expressed in terms of the bare propagator G_0 and the self-energy Σ (or 1PI two-point vertex, $\Sigma \equiv \Gamma^{(2)}$) according to

$$G_{x,x'} = -\langle c_x \bar{c}_{x'} \rangle, \qquad G_{x,x'} = G_{0;x,x'} + G_{0;x,y'}\Sigma_{y',y}G_{y,x'}. \tag{2.6}$$

This is illustrated diagrammatically in Fig. 2.2(a). In obvious matrix-product notation, we have

$$G = G_0 + G_0 \cdot \Sigma \cdot G \qquad \Leftrightarrow \qquad G^{-1} = G_0^{-1} - \Sigma.$$

Secondly, four-point correlation functions, denoted by $G^{(4)}$, can be expressed via the 1PI four-point vertex $\Gamma \equiv \Gamma^{(4)}$,

$$G^{(4)}_{x,y;x',y'} = \langle c_x c_y \bar{c}_{y'} \bar{c}_{x'} \rangle = G_{x,x'}G_{y,y'} - G_{x,y'}G_{y,x'} + G_{x,z'}G_{y,w'}\Gamma_{z',w';z,w}G_{z,x'}G_{w,y'}, \tag{2.7}$$

see Fig. 2.2(b). Similar to the bare vertex, Γ_0, $G^{(4)}$ and Γ are antisymmetric in their first and last two arguments, a property known as crossing symmetry [Bic04]. Higher-point correlation functions $G^{(n)}$ and vertices $\Gamma^{(n)}$ can be defined analogously.

Our discussion of fRG in later parts of this thesis and the derivation of the parquet equations will be mostly based on the general many-body problem (2.3). However, for the following, more traditional motivation of fRG via Wilson's RG, we temporarily consider a simple φ^4 theory. In

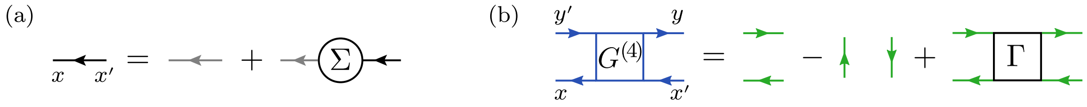

Figure 2.2 (a) Definition of the self-energy, Σ, through Dyson's equation (2.6). Dark and light lines denote the full (G) and bare (G_0) propagator, respectively. (b) Definition of the full four-point vertex, Γ, via the four-point correlation function, $G^{(4)}$, according to Eq. (2.7). The color coding indicates that the external legs are part of $G^{(4)}$, but they do not belong to Γ. Instead, Γ is obtained from $G^{(4)}$ by subtracting the disconnected parts and *amputating* the external legs.

the discussions related to DMFT and NRG, we come back to Hubbard models of the type (2.1), (2.2), which are also targeted by the diagrammatic extensions of DMFT discussed at the end of this chapter.

2.2 Functional renormalization group from a Wilsonian perspective

The fRG framework is a modern and very versatile quantum field-theoretical RG approach [KBS10, MSH$^+$12]. Its cornerstone is the exact, functional flow equation known as Wetterich equation [Wet93], which can be expanded into an infinite hierarchy of flow equations for the 1PI vertices [Mor94]. Moreover, fRG can be understood in the tradition of Wilson's RG [Wil75, Sha94], with the guiding principle to treat fluctuations successively from high energy (or short length scale) to low energy (or large length scale). In the following, we elaborate on this connection, and we show how the goal of using Wilsonian renormalization as a numerical tool in condensed-matter physics naturally leads to fRG.

2.2.1 Recap of Wilson's momentum-shell RG

Wilson's RG scheme has put the revolutionary RG ideas on solid footing. It is not only an essential tool to study critical phenomena, it has also shaped the way we think about physics, explaining, e.g., concepts such as universality [Wil75]. Here, we will be very brief in summarizing the key points of Wilson's momentum-shell RG, for the purpose of providing a natural transition towards fRG. To make the arguments most transparent, we employ a scalar, real φ^4 theory in D dimensions. It is compactly stated via the partition sum

$$Z = \int \mathcal{D}[\varphi]\, e^{-S[\varphi]}, \qquad S[\varphi] = -\int \mathrm{d}^D k\, \varphi(\boldsymbol{k}) G_0(\boldsymbol{k})^{-1} \varphi(-\boldsymbol{k}) \;+\; S_{\text{int}}[\varphi] \tag{2.8}$$

with field variable $\varphi : \mathbb{R}^D \to \mathbb{R}$. The bare propagator, G_0, and interaction, S_{int}, read

$$G_0(\boldsymbol{k})^{-1} = -(k^2 + r), \qquad S_{\text{int}}[\varphi] = u \int \mathrm{d}^D x\, \varphi(\boldsymbol{x})^4 .$$

We denote $k = |\boldsymbol{k}|$, use φ in the momentum ($\boldsymbol{k}$) and real-space ($\boldsymbol{x}$) representation, and have incorporated all potential prefactors into redefenitions of the mass and interaction parameters, r and u, respectively. Considering the plain, unbounded k^2 dependence of G_0, it is clear that, for any condensed-matter application, Eq. (2.8) is to be understood as an effective theory with an intrinsic ultraviolet (UV) cutoff Λ_0. Thus, all fields are implicitly understood to be restricted to momenta $k < \Lambda_0$, as is symbolized by $\varphi(\boldsymbol{k}) \equiv \varphi_{0 \le k < \Lambda_0}(\boldsymbol{k})$.

The (bare) action (2.8) describes properties at high energy scales, Λ_0, with bare parameters r and u. A central aspect of Wilson's RG is to look for an *effective* action that similarly describes properties at low energy scales. To this end, one starts by separating contributions to the functional integral between slow and fast degrees of freedom, using a variable scale parameter Λ and

$$\varphi_{0 \le k < \Lambda_0}(\boldsymbol{k}) = \underbrace{\Theta(\Lambda - k)\varphi(\boldsymbol{k})}_{\varphi_{0 \le k < \Lambda}(\boldsymbol{k})} + \underbrace{\Theta(k - \Lambda)\varphi(\boldsymbol{k})}_{\varphi_{\Lambda \le k < \Lambda_0}(\boldsymbol{k})} .$$

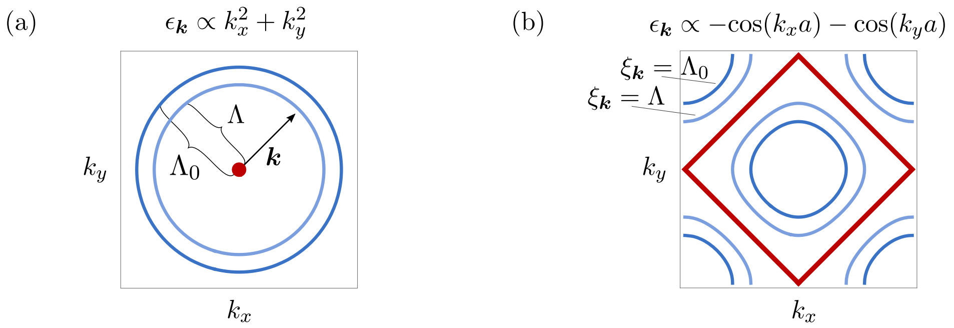
(a)
$\epsilon_{\boldsymbol{k}} \propto k_x^2 + k_y^2$
Λ
Λ_0
$\boldsymbol{k}$
k_y
k_x
(b)
$\epsilon_{\boldsymbol{k}} \propto -\cos(k_x a) - \cos(k_y a)$
$\xi_{\boldsymbol{k}} = \Lambda_0$
$\xi_{\boldsymbol{k}} = \Lambda$
k_y
k_x

Figure 2.3 Illustration of successive mode elimination in a momentum or energy shell from Λ_0 to Λ (dark and light blue lines) towards low energies (red region). (a) In φ^4 theory, low-energy properties are determined by $\boldsymbol{k} \to 0$ and the coupling constants $r(\boldsymbol{k}=0)$, $u(\boldsymbol{k}_i = 0)$ $(i = 1, \dots, 4)$. (b) In condensed-matter systems (with lattice spacing a), $\epsilon_{\boldsymbol{k}} = \mu$ defines the Fermi surface (here one-dimensional). Low-energy excitations have small $\xi_{\boldsymbol{k}} = \epsilon_{\boldsymbol{k}} - \mu$ and are subject to coupling *functions* defined on the Fermi surface.

The crucial idea is then to perform the functional integral over only the fast modes to obtain an effective action, S_{eff}, for the slow modes:

$$Z = \int \mathcal{D}[\varphi]\, e^{-S[\varphi]} = \int \mathcal{D}[\varphi_{0\le k<\Lambda}] \underbrace{\int \mathcal{D}[\varphi_{\Lambda\le k<\Lambda_0}]\, e^{-S[\varphi_{0\le k<\Lambda}+\varphi_{\Lambda\le k<\Lambda_0}]}}_{e^{-S_{\text{eff}}[\varphi_{0\le k<\Lambda}]}} .$$

Only this effective action and no bare parameters of the original theory are needed to continue the integration over lower energy scales. Moreover, knowledge of S_{eff} is sufficient to compute correlation functions of slow modes. For instance, the two-point correlator at momenta $p < \Lambda$ is obtained as

$$\langle \varphi(\boldsymbol{p})\varphi(-\boldsymbol{p})\rangle \propto \int \mathcal{D}[\varphi]\, \varphi(\boldsymbol{p})\varphi(-\boldsymbol{p}) e^{-S[\varphi]} \propto \int \mathcal{D}[\varphi_{0\le k<\Lambda}]\, \varphi(\boldsymbol{p})\varphi(-\boldsymbol{p}) e^{-S_{\text{eff}}[\varphi_{0\le k<\Lambda}]}.$$

So far, degrees of freedom in the momentum shell $[\Lambda, \Lambda_0]$ have been integrated out, where Λ_0 is the intrinsic UV cutoff. Clearly, this step can be repeated for any two scales taking the role of Λ and Λ_0. The calculation is simplified if we only include momenta within a *thin* shell, by using $\Lambda_0/\Lambda = e^l$ with small, or even infinitesimal l. We then have a flowing effective action as a function of a continuously decreasing scale parameter Λ. For analytic arguments in the spirit of [Wil75], it is beneficial to have an *autonomous* differential equation, which implies the notions of fixed points, stable and unstable manifolds, etc. The explicit dependence on Λ can be removed by rescaling momenta and fields,[1] $\boldsymbol{k}' = e^l \boldsymbol{k}$ and $\varphi'(\boldsymbol{k}') = e^{l\Delta_\varphi}\varphi(\boldsymbol{k}'/e^l) = e^{l\Delta_\varphi}\varphi(\boldsymbol{k})$ [Wil75, Sha94], to get

$$S_{\text{eff}}[\varphi_{0\le k<\Lambda}] = S'[\varphi'_{0\le k'<\Lambda_0}].$$

The new action S' has the original UV cutoff Λ_0, and the rescaling exponent Δ_φ is chosen such that the k^2 terms maps to k'^2 with no change in prefactor. Compared to S, S' is then composed of *running* coupling constants, r', u', and possibly infinitely many more. Due to the rescaling, $\mathrm{d}r/\mathrm{d}l = \lim_{l\to 0}(r'-r)/l$ depends only on the couplings $r, u, \dots$ and Λ_0. Hence, the momentum-shell integration needs to be performed only once, and one proceeds via a fixed-point analysis.

Whereas this type of an analytical RG approach has been instrumental in understanding critical phenomena [Wil75], it has a number of limitations when applied to condensed-matter systems:

- Working directly with the functional integral can only be done analytically. However, performing the momentum-shell integration accurately, say, by expanding the interaction to high "loop" orders, becomes increasingly involved. Hence, it is advisable to devise a numerical procedure that operates directly on the level of correlation functions.

- The technique of rescaling to reproduce the original action requires working, from the outset, with the effective low-energy theory, containing the intrinsic UV cutoff $\Lambda_0 \ll 1/a$, instead of the microscopic theory with $\Lambda_0 \sim 1/a$ (a being the lattice spacing). However, in many condensed-matter applications, the effective low-energy theory is not known a priori. Thus, the formalism should be set up more generally.

---

[1] An autonomous differential equation can also be obtained through a Λ-dependent rescaling of the coupling constants *after* their explicitly Λ-dependent flow equations have been obtained [KBS10].

- Furthermore, the effective action obtained upon iterative rescaling aims at the "ultimate" long-wavelength fluctuations: Consider n consecutive rescalings with $\Lambda^{(n)} = \Lambda_0/e^{nl}$, $\boldsymbol{k}^{(n)} = e^{nl}\boldsymbol{k}$, $\varphi^{(n)}(\boldsymbol{k}^{(n)}) = e^{nl\Delta_\varphi}\varphi(\boldsymbol{k})$, such that

$$\begin{aligned}
\langle \varphi(\boldsymbol{p})\varphi(-\boldsymbol{p})\rangle &\overset{p<\Lambda^{(1)}}{\propto} \int \mathcal{D}\big[\varphi_{0\le k<\Lambda^{(1)}}\big]\varphi(\boldsymbol{p})\varphi(-\boldsymbol{p})e^{-S_{\mathrm{eff}}[\varphi]} \\
&\propto \int \mathcal{D}\big[\varphi'_{0\le k'<\Lambda_0}\big]\varphi'\big(e^{l}\boldsymbol{p}\big)\varphi'\big(-e^{l}\boldsymbol{p}\big)e^{-S'[\varphi']} \\
&\overset{p<\Lambda^{(2)}}{\propto} \int \mathcal{D}\big[\varphi'_{0\le k'<\Lambda^{(1)}}\big]\varphi'\big(e^{l}\boldsymbol{p}\big)\varphi'\big(-e^{l}\boldsymbol{p}\big)e^{-S'_{\mathrm{eff}}[\varphi']} \\
&\propto \int \mathcal{D}\big[\varphi''_{0\le k'<\Lambda_0}\big]\varphi''\big(e^{2l}\boldsymbol{p}\big)\varphi''\big(-e^{2l}\boldsymbol{p}\big)e^{-S''[\varphi'']} \\
&\ \ \vdots \\
&\overset{p<\Lambda^{(n)}}{\propto} \int \mathcal{D}\big[\varphi^{(n)}_{0\le k^{(n)}<\Lambda_0}\big]\varphi^{(n)}\big(e^{nl}\boldsymbol{p}\big)\varphi^{(n)}\big(-e^{nl}\boldsymbol{p}\big)e^{-S^{(n)}[\varphi^{(n)}]}.
\end{aligned}$$

  After rescaling n times, the effective action $S^{(n)}$ describes fluctuations restricted to increasingly small momenta $\boldsymbol{p}$, requiring $p < \Lambda^{(n)} = \Lambda_0/e^{nl} \to 0$ as $n \to \infty$. Yet, one would like to also keep track of renormalized correlation functions at finite momenta.

- In Wilson's RG, one often restricts oneself to a few coupling constants r, u, arguing that $r(\boldsymbol{k} = 0)$ and $u(\boldsymbol{k}_i = 0)$ ($i = 1, \dots, 4$) are the most relevant for low-energy properties. Put simply, the iterative rescaling of momenta suppresses all arguments as $r^{(n)}(\boldsymbol{k}^{(n)}) = e^{nl\Delta_r} r(\boldsymbol{k}^{(n)}/e^{nl} \to 0)$. However, in condensed-matter physics, low-energy properties are determined by quasiparticle excitations, where $|\epsilon_{\boldsymbol{k}} - \mu|$ instead of $\epsilon_{\boldsymbol{k}} \sim k^2$ is small. Now, $\epsilon_{\boldsymbol{k}} = \mu$ defines the $(D-1)$-dimensional Fermi surface, and one must renormalize towards and expand $r(\boldsymbol{k})$, $u(\boldsymbol{k}_i)$ around the Fermi surface [Sha94], as illustrated in Fig. 2.3. Then, r and u become coupling functions instead of constants, and the whole procedure must be set up in a *functional* form.

2.2.2 Functional renormalization

In the preceding discussion, the successive renormalization was achieved by integrating out degrees of freedom in the momentum-shell $[\Lambda, \Lambda_0]$ within the functional integral expression,

$$e^{S_{\mathrm{eff}}[\varphi_{0\le k<\Lambda}]} = \int \mathcal{D}[\varphi_{\Lambda\le k<\Lambda_0}]\, e^{-S}.$$

However, the functional integral is numerically inaccessible. Loosely speaking, the functional integral contains an infinite load of information reflecting the exponentially large Hilbert space, but only correlation functions with a small number of arguments are experimentally relevant. One should therefore translate the mode separation from the functional integral into correlation functions. To this end, we denote the quadratic part of the action explicitly and rewrite the fast-mode integral as

$$\int \mathcal{D}[\varphi_{\Lambda\le k<\Lambda_0}]\, e^{\int \mathrm{d}^D k\, \varphi(\boldsymbol{k}) G_0(\boldsymbol{k})^{-1} \varphi(-\boldsymbol{k}) \,-\, S_{\mathrm{int}}} = \int \mathcal{D}[\varphi_{0\le k<\Lambda_0}]\, e^{\int \mathrm{d}^D k\, \varphi(\boldsymbol{k}) G_0^{\Lambda}(\boldsymbol{k})^{-1} \varphi(-\boldsymbol{k}) \,-\, S_{\mathrm{int}}}.$$

The separation of fast and slow modes is achieved through the scale-dependent (negative-definite) bare propagator,

$$G_0^{\Lambda}(\boldsymbol{k})^{-1}\big|_{k<\Lambda} = -\infty, \quad G_0^{\Lambda}(\boldsymbol{k})^{-1}\big|_{k\ge\Lambda} = G_0(k)^{-1} \qquad \Leftrightarrow \qquad G_0^{\Lambda}(\boldsymbol{k}) = \Theta(k-\Lambda)G_0(\boldsymbol{k}),$$

and the functional-integral measure reverts to its original form, $\int \mathcal{D}[\varphi_{0\le k<\Lambda_0}] = \int \mathcal{D}[\varphi]$.

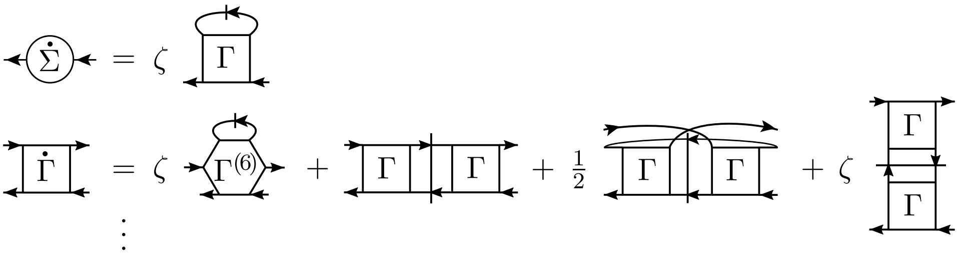

Figure 2.4 Diagrammatic representation of the fRG hierarchy of flow equations for n-point 1PI vertices, up to $n = 4$ (for complex or Grassmann fields). The flow of the self-energy, $\dot{\Sigma}^\Lambda = \partial_\Lambda \Sigma^\Lambda$, is determined by the four-point vertex, Γ^Λ; $\dot{\Gamma}^\Lambda = \partial_\Lambda \Gamma^\Lambda$ further involves the six-point vertex, $\Gamma^{(6),\Lambda}$. Lines with a vertical dash denote the single-scale propagator $S^\Lambda = \partial_\Lambda G^\Lambda|_{\Sigma^\Lambda=\text{const}}$; pairs of propagators with a vertical line denote the single-scale two-particle propagator $G^\Lambda S^\Lambda + S^\Lambda G^\Lambda$. Finally, we use $\zeta = \pm 1$ for bosons and fermions, respectively. For real (bosonic) fields, where the lines are not directed, one has identical prefactors for all pair combinations of vertices and conventionally uses a prefactor of $\frac{1}{2}$ for all terms on the r.h.s. [KBS10].

Scale-dependent n-point correlation functions in their full functional form follow from

$$\langle \varphi(\boldsymbol{p}_1) \cdots \varphi(\boldsymbol{p}_n) \rangle^\Lambda \propto \int \mathcal{D}[\varphi]\, \varphi(\boldsymbol{p}_1) \cdots \varphi(\boldsymbol{p}_n)\, e^{\int \mathrm{d}^D k\, \varphi(\boldsymbol{k}) G_0^\Lambda(\boldsymbol{k})^{-1} \varphi(-\boldsymbol{k}) - S_{\text{int}}}.$$

Finding the scale dependence of correlation functions, $G^{(n),\Lambda}$, or coupling functions (1PI vertices), $\Gamma^{(n),\Lambda}$, amounts to evaluating these objects using the scale-dependent bare propagator, G_0^Λ. The effect of eliminating modes in the shell $[\Lambda, \Lambda_0]$ is encoded in the evolution $\Gamma^{(n),\Lambda_0} \to \Gamma^{(n),\Lambda}$. The full renormalization, i.e., evaluating the full functional integral, corresponds to solving the flow equation

$$\partial_\Lambda \begin{pmatrix} \Gamma^{(2),\Lambda}(\boldsymbol{k}) \\ \Gamma^{(4),\Lambda}(\boldsymbol{k}_1, \boldsymbol{k}_2, \boldsymbol{k}_3) \\ \vdots \end{pmatrix} = \boldsymbol{f}\Big(\Gamma^{(2),\Lambda}(\boldsymbol{k}), \Gamma^{(4),\Lambda}(\boldsymbol{k}_1, \boldsymbol{k}_2, \boldsymbol{k}_3), \ldots, G_0^\Lambda(\boldsymbol{k}), \dot{G}_0^\Lambda(\boldsymbol{k})\Big), \tag{2.9}$$

where G_0^Λ and $\dot{G}_0^\Lambda = \partial_\Lambda G_0^\Lambda$ are known. As we work with general vertices $\Gamma^{(n)}$, we need not assume a specific form of the action—the initial point of the flow can be an effective or any microscopic theory. At $\Lambda_i = \infty$ and $G_0^{\Lambda_i} = 0$, one can read off $\Gamma^{(n),\Lambda_i}$ from the bare action, as follows, e.g., from a diagrammatic expansion. At the final point $\Lambda_f = 0$, the original theory with $G_0^{\Lambda_f} = G_0$ is recovered, and the vertices are fully renormalized.

It remains to find a suitable expression for the r.h.s., $\boldsymbol{f}$, of the flow equation (2.9). The most common choice in fRG is to exploit the Wetterich equation [Wet93], the exact flow equation for the generating functional of 1PI vertices, and expand this functional flow equation into an infinite hierarchy of flow equations for all $\Gamma^{(n)}$ [Mor94]. In this hierarchy, the flow of an n-point vertex, $\Gamma^{(n)}$, involves all other vertices up to the $(n+2)$-point level. The derivation of the Wetterich equation and its vertex expansion have been reprocessed at several instances [KBS10, MSH$^+$12, Kug16], and there is no need to repeat this here. For illustration, we show the diagrammatic representation of the fRG flow equations [for complex or Grassmann fields as in Eq. (2.3)] up to $n = 4$ in Fig. 2.4; the underlying structure will become more transparent once the parquet formalism is worked out. An important point is that the flow of the four-point vertex, $\Gamma^{(4)}$, depends on the six-point vertex $\Gamma^{(6)}$. However, a six-point vertex has at least five arguments and is almost impossible to treat numerically. This observation is one of our motivations to explore the parquet formalism, which contains at most four-point objects. Then, in publication [P5], we show how to derive the mfRG flow equations directly for the most interesting objects $\Sigma \equiv \Gamma^{(2)}$ and $\Gamma \equiv \Gamma^{(4)}$ from the self-consistent parquet equations, thus circumventing the reliance of standard fRG on higher-point vertices.

2.3 Parquet theory

The correlation functions $G^{(n)}$ are full, interacting, or *renormalized* correlation functions. In fact, one can imagine the perturbation series, obtained by separating the noninteracting part of the

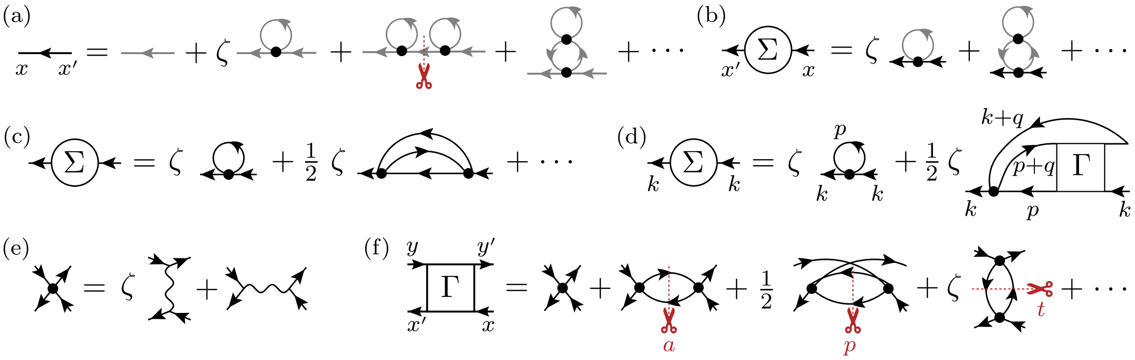

Figure 2.5 Illustrations of the diagrammatic expansion. (a) Low-order diagrams of the propagator, $G_{x,x'}$. The third diagram on the r.h.s. is one-particle reducible (1PR). (b) Corresponding diagrams of the (1PI) self-energy, $\Sigma_{x',x}$ (the external legs are amputated). Being built from G_0 lines, these are *bare* diagrams. (c) Instead, using full G lines (which themselves contain self-energy insertions) yields *bold* or *skeleton* diagrams. There are only two skeleton diagrams for Σ up to second order. If one of the bare vertices in the second diagram is replaced by a full one, the series actually terminates. This is (d) the Schwinger–Dyson equation for the self-energy. Labels exploit the energy-momentum representation $k = (i\nu, \boldsymbol{k})$ of a translationally invariant system. Given the vertex Γ, the double sum over p and q for each k can be performed at cost $O(N_k^3)$, see Sec. 2.3.1.7. (e) Throughout, we use Hugenholtz diagrams [NO98] in terms of the antisymmetric bare vertex Γ_0, simultaneously encoding direct and exchange interactions [cf. Eq. (2.4)]. (f) Skeleton expansion of Γ. The second-order diagrams can be separated into two parts by cutting two *a*ntiparllel, *p*arallel, or *t*ransverse antiparallel lines.

action, S_0, and expanding in the interaction, S_{int}, to renormalize the correlators. Accordingly, we write

$$\langle c_{x_1} \cdots \bar{c}_{x_n} \rangle = \frac{1}{Z} \int \mathcal{D}[\bar{c}, c]\, c_{x_1} \cdots \bar{c}_{x_n} e^{-(S_0 + S_{\text{int}})} = \frac{\langle c_{x_1} \cdots \bar{c}_{x_n} e^{-S_{\text{int}}} \rangle_0}{\langle e^{-S_{\text{int}}} \rangle_0},$$

employing the noninteracting averages $\langle \cdots \rangle_0 = \frac{1}{Z_0} \int \mathcal{D}[\bar{c}, c] \cdots e^{-S_0}$, with $\langle 1 \rangle_0 = 1$. The latter reduce to Gaussian integrals and can be evaluated using Wick's theorem [NO98]. The resulting perturbation series can then be organized w.r.t. irreducible parts and represented by (Feynman) diagrams. For instance, G and $G^{(4)}$ are fully determined by Σ and Γ through Eqs. (2.6) and (2.7). Exemplary diagrams for Σ and Γ are shown in Fig. 2.5. More details on the diagrammatic expansion can be found in [P6]. Here, we point out that going from the expansion of G in terms of *bare* G_0 lines in Fig. 2.5(a) to the *bold* or *skeleton* expansion of Σ (using full G lines) in Fig. 2.5(c) already renders the diagrammatic series much more compact. We also see that the self-energy diagrams are indeed 1PI—they cannot be separated into two valid diagrams by cutting one line (i.e., removing a line, leaving two more amputated legs). Regarding the series of bold vertex diagrams in Fig. 2.5(d), we detect already at second order another characteristic property, which will be of major importance for the discussion below: There are *two-particle-reducible* (2PR) diagrams, which can be separated into two valid diagrams by cutting two lines (i.e., removing two lines, leaving four more amputated legs). These lines can be either *a*ntiparallel, *p*arallel, or *t*ransverse antiparallel, giving rise to the definition of the three two-particle channels $r \in \{a, p, t\}$. Often, a and t are called particle-hole channels, while p is the particle-particle channel.

In principle, one could obtain the exact solution for the $G^{(n)}$ or $\Gamma^{(n)}$ by summing all diagrams. However, this is not only practically impossible, often the series does not even converge [NO98]. Hence, general relations between Σ and Γ, allowing for suitable, infinite resummations of subsets of diagrams, are needed. The parquet formalism provides such relations and enables particularly powerful diagrammatic resummations; their radius of convergence is further discussed in [P6]. The purpose of this section is to give a compact derivation of the parquet equations, which form the basis for the algebraic derivation of the mfRG flow equations in [P5].

2.3.1 Derivation of the parquet equations

The parquet formalism was developed in the 1950's by the Soviet school [LAK54] and in the 1960's by Western physicists [DDM64a, DDM64b]. Early on, it has been successfully used in analytical studies of meson–meson scattering [DSTM57], the Kondo problem [Abr65], and the X-ray–edge singularity [RGN69]. Later on, it was used as a basis for approximate numerical approaches by Bickers and coworkers [BSW89, BS89, BW91]. Recently, with increased numerical resources, the parquet equations have been applied in their full form, albeit only to finite-size (or impurity) systems (see e.g. [YFL⁺09, RVT12, TFY⁺13, VST⁺15, WLT⁺16, LWP⁺16, LKPH19, PTV⁺19, PKHL19]). For a reader unfamiliar with the parquet formalism, the derivations in the original articles may seem somewhat obscure. Conversely, a popular review article by Bickers [Bic04] gives a nice background of the parquet equations but refrains from deriving them.

In this section, we give a compact derivation of the parquet equations, proceeding in three steps: (i) By examining the partition function in the presence of sources coupling to the fields $\bar{c}$, c, we derive the Schwinger–Dyson equation relating the 1PI vertices Σ and Γ. (ii) A similar analysis in the presence of sources coupled to bilinears of the fields $\bar{c}$, c yields the Bethe–Salpeter equations involving two-particle-irreducible (2PI) vertices I_r in the three two-particle channels $r \in \{a, p, t\}$. (iii) Finally, the vertices from different two-particle channels are related to one another using diagrammatic arguments. When combing the 2PR vertices to the full vertex, Γ, through the central parquet equation, one is directly led to the most fundamental, diagrammatic building block of the parquet formalism: the totally irreducible vertex R. By making an approximation for R, the set of parquet equations closes, enabling the search for a solution self-consistent on the one- and two-particle level.

In the following parts, we use $\zeta \in \{\pm 1\}$ (as in Figs. 2.4, 2.5) to derive the parquet equations simultaneously for anticommuting ($\zeta = -1$) and commuting ($\zeta = 1$) fields. Moreover, we employ Einstein's convention, where a sum over repeated indices is understood.

2.3.1.1 Schwinger–Dyson equation

First, we derive the Schwinger–Dyson equation (SDE) for the self-energy, which is illustrated diagrammatically in Fig. 2.5(d). To this end, we consider the partition function in the presence of sources coupling to the fields $\bar{c}$, c,

$$Z[\bar{\jmath}, j] = \int \mathcal{D}[\bar{c}, c]\, e^{-S[\bar{c},c] + \bar{\jmath}_x c_x + \bar{c}_{x'} j_{x'}} .$$

Its logarithm, $\mathcal{G}[\bar{\jmath}, j] = \ln Z[\bar{\jmath}, j]$, is the generating functional for connected correlation functions [NO98]. Taking derivatives w.r.t. $\bar{\jmath}$, j, we first have

$$\frac{\delta^2 \mathcal{G}}{\delta j_{x'} \delta \bar{\jmath}_x} = \langle c_x \bar{c}_{x'} \rangle_{\bar{\jmath},j} - \langle c_x \rangle_{\bar{\jmath},j} \, \langle \bar{c}_{x'} \rangle_{\bar{\jmath},j} .$$

In the absence of sources, $\langle c_x \rangle = 0 = \langle \bar{c}_{x'} \rangle$, and we find that the two-point correlator is automatically connected (disconnected parts in $\langle c_x \bar{c}_{x'} \rangle$ are canceled by the denominator, Z [NO98]):

$$G_{c;x,x'} \equiv -\frac{\delta^2 \mathcal{G}}{\delta j_{x'} \delta \bar{\jmath}_x}\Big|_{\bar{\jmath},j=0} = -\langle c_x \bar{c}_{x'} \rangle \equiv G_{x,x'} .$$

In the particle-conserving phase where $\langle c_x c_y \rangle = 0 = \langle \bar{c}_{x'} \bar{c}_{y'} \rangle$, we further find, inserting Eq. (2.7),

$$\begin{aligned} G^{(4)}_{c;x,y;x',y'} &\equiv \frac{\delta^4 \mathcal{G}}{\delta j_{x'} \delta j_{y'} \delta \bar{\jmath}_y \delta \bar{\jmath}_x}\Big|_{\bar{\jmath},j=0} = \langle c_x c_y \bar{c}_{y'} \bar{c}_{x'} \rangle - \langle c_x \bar{c}_{x'} \rangle \langle c_y \bar{c}_{y'} \rangle - \zeta \langle c_x \bar{c}_{y'} \rangle \langle c_x \bar{c}_{y'} \rangle \\ &= G_{x,z'} G_{y,w'} \Gamma_{z',w';z,w} G_{z,x'} G_{w,y'} . \end{aligned} \tag{2.10}$$

Whereas the self-energy is specifically motivated as 1PI, this applies automatically to Γ, as follows from particle conservation: By cutting a line in Γ, the number of open ends increases from four to six. Since the external legs of Γ are amputated, it is not possible to split off a two-point, self-energy diagram in this way [Fig. 2.6(a)]. Accounting for the six open ends thus requires two three-point vertices [Fig. 2.6(b)], which do not exist in a purely fermionic system. However, higher-point vertices are not automatically 1PI, for cutting a line in, e.g., the six-point vertex can leave two four-point vertices [as indeed occurs below, see Fig. 2.16(b)].

The SDE is a model-dependent equation of motion and can be derived by shifting the field variables $\bar{c} \to \bar{c} + \bar{\Delta}$ in the functional integral [KBS10]. In the general many-body problem (2.3),

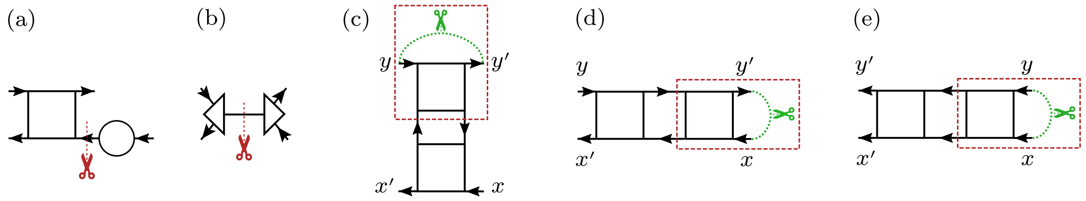

Figure 2.6 (a) The four-point vertex does not contain trivial 1PR contributions at its external legs since these are actually amputated. (b) Hence, a 1PR diagram of the four-point vertex would require two three-point vertices, which do not exist in a purely fermionic theory. (c)–(e) Illustrations of vertices obtained from functional derivatives of the self-energy, see Sec. 2.3.1.3. (c) The vertex $\delta\Sigma_{x',x}/\delta G_{y,y'}$ is obtained by removing $G_{y,y'}$ lines in $\Sigma_{x',x}$ diagrams. Assume the vertex were 2PR in the t channel [separable into two parts while the index pairs (x',x) and (y',y) remain connected]. Then, the original self-energy diagrams would have to contain self-energy insertions (dashed box) on internal lines. However, these are absent in the skeleton expansion $\Sigma[G,\Gamma_0]$. (d) Similarly, vertex diagrams $\delta\Sigma_{x',y}/\delta G_{x,y'}$ which are 2PR in the a channel [separable with index pairs (x',y) and (x,y') connected] would require self-energy insertions on internal lines. (e) The analogous argument in the p channel with $\delta\Sigma_{x',y'}/\delta G_{x,y}$ requires anomalous diagrams with two in- or two out-going legs. Only here, we change the position of the labels y' and y for better readability.

we assume only a bare four-point interaction. To linear order in $\bar\Delta$, we then need

$$S[\bar c,c] = -\bar c_{x'}(G_0^{-1})_{x',x}c_x - \tfrac{1}{4}\Gamma_{0;x',y';x,y}\bar c_{x'}\bar c_{y'}c_y c_x, \tag{2.11a}$$

$$\frac{\delta S}{\delta \bar c_{x'}} = -(G_0^{-1})_{x',x}c_x - \tfrac{1}{2}\Gamma_{0;x',y';x,y}\bar c_{y'}c_y c_x. \tag{2.11b}$$

The invariance of $Z[\bar j, j]$ upon shifting $\bar c$ is reflected in

$$Z[\bar j, j] = \int \mathcal{D}[\bar c,c]\, e^{-S[\bar c,c]+\bar j_x c_x+\bar c_{x'}j_{x'}} = \int \mathcal{D}[\bar c,c]\, e^{-S[\bar c+\bar\Delta,c]+\bar j_x c_x+(\bar c+\bar\Delta)_{x'}j_{x'}}.$$

For infinitesimal $\bar\Delta$ (i.e., to linear order in $\bar\Delta$), this implies

$$0 = \int \mathcal{D}[\bar c,c]\,\Big(j_{x'} - \frac{\delta S}{\delta \bar c_{x'}}\Big)e^{-S[\bar c,c]+\bar j_x c_x+\bar c_{x'}j_{x'}}.$$

Differentiating w.r.t. $j_{v'}$, setting the sources to zero, and inserting Eq. (2.11b) gives

$$0 = \int \mathcal{D}[\bar c,c]\,\Big(\delta_{x',v'} + (G_0^{-1})_{x',y}c_y\bar c_{v'} + \tfrac{1}{2}\Gamma_{0;x',y';z,w}\bar c_{y'}c_w c_z\bar c_{v'}\Big)e^{-S}.$$

Multiplying by $1/Z$, inserting Eq. (2.7), and using the (anti)symmetry of Γ_0 yields

$$\begin{aligned} 0 &= \delta_{x',v'} - (G_0^{-1})_{x',y}G_{y,v'} + \zeta\tfrac{1}{2}\Gamma_{0;x',y';z,w}\,\langle c_z c_w \bar c_{y'}\bar c_{v'}\rangle \\ &= \delta_{x',v'} - (G_0^{-1})_{x',y}G_{y,v'} + \zeta\tfrac{1}{2}\Gamma_{0;x',y';z,w}\,\big(2G_{z,v'}G_{w,y'} + G_{z,z'}G_{w,w'}\Gamma_{z',w';v,y}G_{v,v'}G_{y,y'}\big). \end{aligned}$$

Finally, we multiply by $(G^{-1})_{v',x}$ to get the algebraic form of the SDE,

$$\Sigma_{x',x} = (G^{-1})_{x',x} - (G_0^{-1})_{x',x} = \zeta\Gamma_{0;x',y';x,y}G_{y,y'} + \tfrac{1}{2}\zeta\Gamma_{0;x',y';z,w}G_{y,y'}G_{w,w'}G_{z,z'}\Gamma_{z',w';x,y}. \tag{2.12}$$

As characteristic for an SDE, the expression (2.12) combines bare (Γ_0) and renormalized (Γ) vertices. Moreover, Γ_0 and Γ appear in a specific order (Γ_0 attached to x' and Γ to x). Since variations of this order are exploited in [P5], we further show in App. 9.1 that Eq. (2.12) can be analogously derived with the reversed order of Γ_0 and Γ when c instead of $\bar c$ is varied.

2.3.1.2 Two-particle reducibility

In Fig. 2.5, we have already seen vertex diagrams which are 2PR in a two-particle channel $r \in \{a,p,t\}$. There are precisely three two-particle channels since cutting two *a*ntiparallel, *p*arallel, or *t*ransverse antiparallel lines leaves as connected pairs of external legs either (x',y)-(x,y'), (x',y')-(x,y), or (x',x)-(y',y), respectively, see Fig. 2.7. Generally, any 2PR diagram must have the form of two

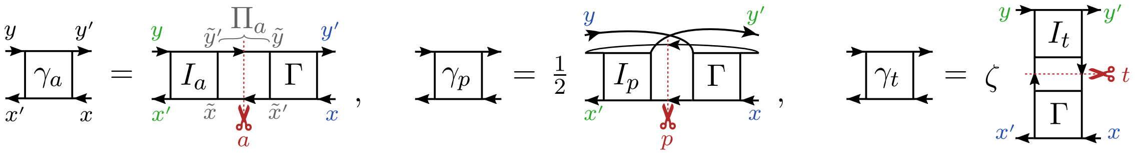

Figure 2.7 The general form of 2PR diagrams in one of the three two-particle channels $r \in \{a, p, t\}$. As one removes two lines in a vertex diagram, there are three possibilities for pairs of external legs to remain connected: Cutting two *a*ntiparallel, *p*arallel, or *t*ransverse antiparallel lines leaves as connected pairs (x', y)-(x, y'), (x', y')-(x, y), or (x', x)-(y', y), respectively. Combining the 2PI (I_r) and full (Γ) vertices with the appropriate prefactors, the above relations are the Bethe–Salpeter equations for the 2PR vertices γ_r.

four-point objects connected by two lines. The connecting pair of propagators for channel r is called two-particle propagator Π_r (Π_a is shown explicitly in Fig. 2.7). For the discussion below, we define

$$\Pi_{a;\tilde{x},\tilde{y};\tilde{x}',\tilde{y}'} = G_{\tilde{x},\tilde{x}'} G_{\tilde{y},\tilde{y}'}, \qquad \Pi_{p;\tilde{x},\tilde{y};\tilde{x}',\tilde{y}'} = \tfrac{1}{2} G_{\tilde{x},\tilde{x}'} G_{\tilde{y},\tilde{y}'}, \qquad \Pi_{t;\tilde{x},\tilde{y};\tilde{x}',\tilde{y}'} = \zeta G_{\tilde{x},\tilde{y}'} G_{\tilde{y},\tilde{x}'}. \tag{2.13}$$

The equations shown in Fig. 2.7 anticipate the Bethe–Salpeter equations (BSEs) in their most compact representation. We will derive below that the 2PR vertex γ_r, comprising all 2PR diagrams of the r channel, is obtained by combining the 2PI vertex I_r and the full vertex, Γ, with the appropriate prefactors (like $\frac{1}{2}$ and ζ). Further, $\Gamma = I_r + \gamma_r$ for each channel r. It can be intuitively understood that, in Fig. 2.7, one has to exclude 2PR contributions in channel r in one of the vertices (i.e., use I_r instead of Γ) to avoid overcounting of diagrams.

The BSEs can be derived for generalized susceptibilities χ_r as well as for vertices [RHT+18]. We will first consider the χ_r and generate 2PI vertices by functional derivatives of the self-energy. Then, the BSEs on the vertex level directly follow from those of the χ_r by amputating external legs.

2.3.1.3 Bethe–Salpeter equations for generalized susceptibilities

We begin by deriving the BSE for the generalized susceptibility in the *transverse* or t channel, χ_t. This will be done by examining the partition function, Z, in the presence of a source J coupled to $\bar{c}$ and c [RJM15],

$$Z[J] = \int \mathcal{D}[\bar{c}, c]\, e^{-S[\bar{c},c] + J_{x',x} \bar{c}_{x'} c_x}. \tag{2.14}$$

Taking derivatives of $\mathcal{G}[J] = \ln Z[J]$ yields the propagator G and generalized susceptibility χ_t,

$$G^J_{x,x'} \equiv -\zeta \frac{\delta \mathcal{G}}{\delta J_{x',x}} = -\langle c_x \bar{c}_{x'} \rangle_J, \qquad G^J_{x,x'}\big|_{J=0} = G_{x,x'}, \tag{2.15a}$$

$$\chi_{t;x,y;x',y'} \equiv \frac{\delta^2 \mathcal{G}}{\delta J_{y',y} \delta J_{x',x}}\Big|_{J=0} = \langle c_x c_y \bar{c}_{y'} \bar{c}_{x'} \rangle - \langle c_x \bar{c}_{x'} \rangle \langle c_y \bar{c}_{y'} \rangle. \tag{2.15b}$$

Compared to $G^{(4)}_c$ in Eq. (2.10), only one disconnected contribution is subtracted in χ_t. Evidently, we have

$$\chi_{t;x,y;x',y'} = -\zeta \frac{\delta G^J_{x,x'}}{\delta J_{y',y}}\Big|_{J=0}. \tag{2.16}$$

This simple relation is in fact the origin of the BSE. Our goal is to get rid of the explicit appearance of J, such that we can directly set $J = 0$. For this reason, we will express G through the self-energy and find another instance of $\delta G / \delta J$, ultimately giving rise to a self-consistent equation for χ_t.

In order to rephrase Eq. (2.16) in terms of Σ, we use the trivial identity

$$G^J_{x,z'} (G^{-1})^J_{z',z} = \delta_{x,z} \qquad \Rightarrow \qquad \frac{\delta G^J_{x,z'}}{\delta J_{y',y}} (G^{-1})^J_{z',z} + G^J_{x,z'} \frac{\delta (G^{-1})^J_{z',z}}{\delta J_{y',y}} = 0. \tag{2.17}$$

Upon multiplying by $G_{z,x'}$ and summing over z, this is rephrased as

$$\frac{\delta G^J_{x,x'}}{\delta J_{y',y}}\Big|_{J=0} = -G_{x,z'} G_{z,x'} \frac{\delta (G^{-1})^J_{z',z}}{\delta J_{y',y}}\Big|_{J=0}. \tag{2.18}$$

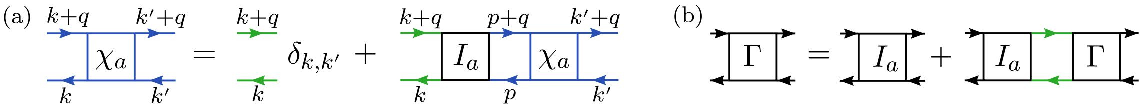

Figure 2.8 Bethe–Salpeter equation in the a channel for (a) the generalized susceptibility, Eq. (2.28), and (b) the vertex, Eq. (2.32). As in Fig. 2.2, the color coding indicates that χ_a contains the external legs, whereas they are amputated for the vertices I_a and Γ. Green lines denote the two-particle propagator Π_a [Eq. (2.13)]. Using the energy-momentum representation $k = (i\nu, \boldsymbol{k})$ in translationally invariant systems, the index contractions of Eq. (2.28) reduce to simple matrix multiplications for each transfer argument q, which can thus be computed at numerical cost $O(N_k^4)$, see Sec. 2.3.1.7.

Now, Dyson's equation allows us to incorporate the self-energy via

$$(G^{-1})^J = (G_0^{-1})^J - \Sigma^J = G_0^{-1} + J - \Sigma^J. \tag{2.19}$$

Moreover, Σ has a bold perturbation series in terms of only G (and the bare vertex) [LW60]:

$$\Sigma^J = \Sigma[G^J, \Gamma_0] \qquad \Rightarrow \qquad \frac{\delta \Sigma^J_{x',x}}{\delta J_{z',z}} = \frac{\delta \Sigma^J_{x',x}}{\delta G^J_{y,y'}} \frac{\delta G^J_{y,y'}}{\delta J_{z',z}}. \tag{2.20}$$

This relation will later introduce $\chi_t \propto \delta G/\delta J$ on the r.h.s. of Eq. (2.16). For the time being, we observe that $\delta\Sigma^J_{x',x}/\delta G^J_{y,y'}$ yields a four-point vertex: The functional derivative of Σ w.r.t. G amounts to cutting one line in all self-energy diagrams at all positions. This produces two more legs and thus a total of four amputated external legs. The index pairs attached to Σ and G, (x', x) and (y', y), are the same index pairs that remain connected when separating a diagram which is 2PR in the t channel (cf. Fig. 2.7). Indeed, it turns out that the vertex $\delta\Sigma^J_{x',x}/\delta G^J_{y,y'}$ is 2PI in the t channel: As illustrated in Fig. 2.6(c), a diagram obtained from $\delta\Sigma^J_{x',x}/\delta G^J_{y,y'}$ that is 2PR in the t channel could arise only if diagrams of Σ^J contained self-energy insertions. These are, however, absent in the skeleton expansion $\Sigma[G^J, \Gamma_0]$ [cf. Fig. 2.5(c)]. We thus obtain a particle-hole 2PI vertex as [BK61]

$$I_{t;x',y';x,y} = \zeta \frac{\delta \Sigma^J_{x',x}}{\delta G^J_{y,y'}}\Big|_{J=0} = \zeta \frac{\delta \Sigma_{x',x}}{\delta G_{y,y'}}. \tag{2.21}$$

Here, we can set $J = 0$ even before taking the functional derivative, since J does not lead to any symmetry breaking in Eq. (2.14). This is different for the *parallel* or p channel treated in App. 9.2.

By combining Eqs. (2.20) and (2.21) with Eq. (2.19), we find

$$\frac{\delta (G^{-1})^J_{z',z}}{\delta J_{y',y}}\Big|_{J=0} = \delta_{z',y'}\delta_{z,y} - \frac{\delta \Sigma^J_{z',z}}{\delta J_{y',y}}\Big|_{J=0} = \delta_{z',y'}\delta_{z,y} - \zeta I_{t;z',w';z,w} \frac{\delta G^J_{w',w}}{\delta J_{y',y}}\Big|_{J=0}. \tag{2.22}$$

Next, inserting Eq. (2.22) into (2.18) as well as Eq. (2.18) into (2.16), we eventually get the BSE for the generalized susceptibility,

$$\chi_{t;x,y;x',y'} = \zeta G_{x,y'} G_{y,x'} + \zeta G_{x,z'} G_{z,x'}\, I_{t;z',w';z,w}\, \chi_{t;w,y;w',y'}. \tag{2.23}$$

Using the two-particle propagator Π_t from Eq. (2.13), it is intuitive (and explicitly shown in [P3, P5]) that the index contractions are (generalized) matrix multiplications. We can thus state Eq. (2.23) compactly as

$$\chi_t = \Pi_t + \Pi_t \circ I_t \circ \chi_t \qquad \Leftrightarrow \qquad I_t = \Pi_t^{-1} - \chi_t^{-1}. \tag{2.24}$$

The generalized susceptibility in the *antiparallel* or a channel is defined as

$$\chi_{a;x,y;x',y'} \equiv \zeta \frac{\delta^2 \mathcal{G}}{\delta J_{y',x} \delta J_{x',y}}\Big|_{J=0} = -\frac{\delta G^J_{y,x'}}{\delta J_{y',x}}\Big|_{J=0}, \tag{2.25}$$

analogous to Eq. (2.15b) for χ_t with a change of indices $x \leftrightarrow y$. This direct connection can be understood in the context of crossing symmetry: Diagrams of χ_t and χ_a are translated into one

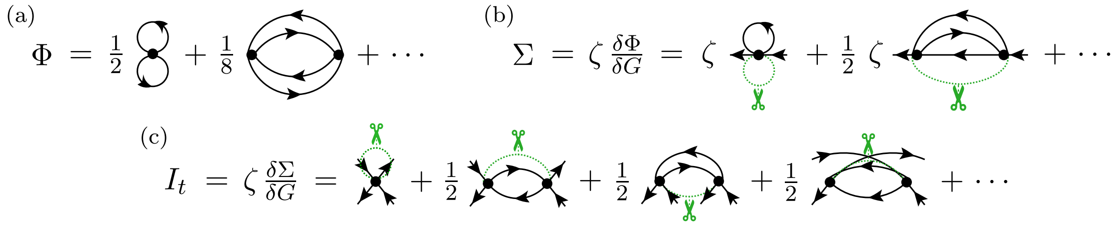
(a)
Φ = ½ + ⅛ + ···
(b)
Σ = ζ δΦ/δG = ζ + ½ ζ + ···
(c)
I_t = ζ δΣ/δG = + ½ + ½ + ½ + ···

Figure 2.9 Illustration of Φ-derivability at the first two orders in the bare vertex Γ_0. The functional derivative is performed by cutting a full line, leaving two more amputated legs. From the (particle-conserving) diagrammatic series of (a) the LW functional $\Phi[G, \Gamma_0]$ follow the skeleton expansion of (b) the self-energy [cf. Fig. 2.5(c)] and (c) the 2PI vertex I_t. At the first two orders of $\delta\Phi/\delta G$, cutting any line in one of the diagrams yields the same contribution due to the (anti)symmetry of the bare vertex. Similarly, the second and third vertex diagrams are equivalent by (anti)symmetry of Γ_0, such that the expansion of I_t indeed reproduces the vertex diagrams from Fig. 2.5(f) without the last contribution, which is reducible in the t channel. In panel (c), the external legs of the self-energy were used as legs (x', x) of the vertex. By exchanging two external legs, which amounts to using the external self-energy legs as vertex legs (x', y) or (y', x), we get ζI_a, as required by crossing symmetry.

another by exchanging two in- or two out-going legs. The same applies to Π_r, γ_r, I_r. Indeed, next to the simple relation $\Pi_{a;x,y;x',y'} = \zeta \Pi_{t;y,x;x',y'}$ in Eq. (2.13), we have

$$\chi_{a;x,y;x',y'} = \zeta \chi_{t;y,x;x',y'} = \langle c_x c_y \bar{c}_{y'} \bar{c}_{x'} \rangle - \zeta \langle c_x \bar{c}_{y'} \rangle \langle c_x \bar{c}_{y'} \rangle, \tag{2.26a}$$

$$I_{a;x',y';x,y} = \zeta I_{t;x',y';y,x} = \frac{\delta \Sigma_{x',y}}{\delta G_{x,y'}}. \tag{2.26b}$$

The vertex $\delta\Sigma_{x',y}/\delta G_{x,y'}$, with index pairs (x', y) and (x, y'), is indeed 2PI in the a channel, as verified in Fig. 2.6(d). Inserting Eq. (2.26) into (2.23), we obtain the BSE in the a channel as

$$\chi_{a;x,y;x',y'} = G_{x,x'} G_{y,y'} + G_{y,z'} G_{z,x'} \, I_{a;z',w';z,w} \, \chi_{a;x,w;w',y'}. \tag{2.27}$$

The a channel is also chosen for the diagrammatic representation of the BSE in Fig. 2.8(a). Finally, by using a generalized matrix multiplication adapted to the a channel, Eq. (2.27) is stated compactly [and perfectly analogous to Eq. (2.24)] as

$$\chi_a = \Pi_a + \Pi_a \circ I_a \circ \chi_a \qquad \Leftrightarrow \qquad I_a = \Pi_a^{-1} - \chi_a^{-1}. \tag{2.28}$$

Note that the order of I_r and χ_r on the r.h.s. of Eqs. (2.24) and (2.28) can be reversed by interchanging the order of the J derivatives in Eqs. (2.15b) and (2.25). For the derivation of the BSE in the p channel in App. 9.2 and 9.3, we must introduce sources that couple to two c and two $\bar{c}$ fields. Accordingly, I_p can be obtained by a functional derivative of Σ only when allowing for variations in the extended space of anomalous, non-particle-conserving propagators [see also Fig. 2.6(e)]. However, when the functional differentiation is performed in an analytical, Feynman-diagrammatic context (as in [P6]), one typically cuts lines connecting in- and out-going legs of vertices in the standard, particle-conserving diagrams, thus yielding I_t or I_a.

Before translating the BSEs from the generalized susceptibilities to the vertices, we use the present context for an intermezzo on Φ-derivability.

2.3.1.4 Remark on Φ-derivability

According to Eq. (2.26b), the 2PI vertices I_t and I_a do not have the full (anti)symmetry of Γ but are mapped onto each other by permuting two indices (crossing symmetry). Still, they are symmetric upon exchanging both the in- and out-going legs, $I_{t;x,y;x',y'} = I_{t;y,x;y',x'}$. As pointed out by Baym [Bay62], the combination of this symmetry with the functional derivative (2.21) implies a "vanishing curl condition",

$$\frac{\delta \Sigma_{x',x}}{\delta G_{y,y'}} = \frac{\delta \Sigma_{y',y}}{\delta G_{x,x'}},$$

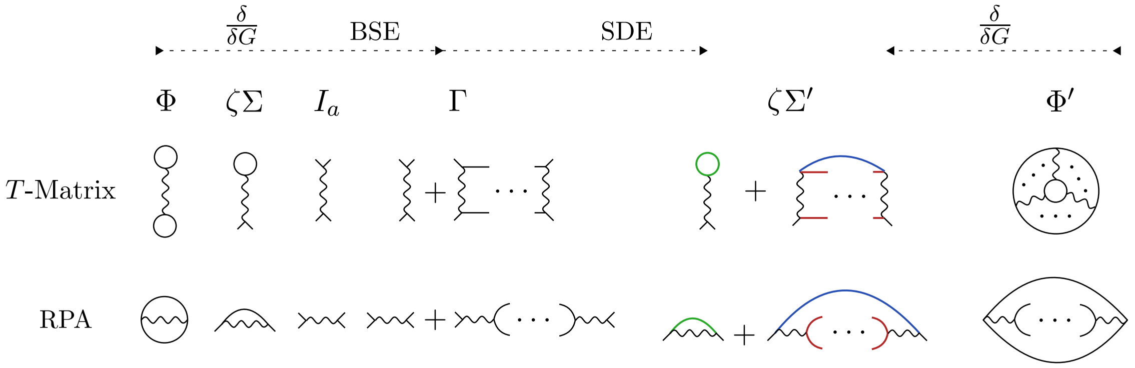

Figure 2.10 Illustrations for the T-matrix and RPA approaches, both breaking crossing symmetry by including only direct or exchange interactions (wiggly lines), respectively. They can be understood by starting from a first-order LW functional Φ, taking functional derivatives to get skeleton expansions of Σ and I_a, and using the BSE to get Γ. The actual T-matrix or RPA self-energy Σ', related to another functional Φ', is then obtained by inserting Γ into the SDE. Note that the factor 1/2 in Fig. 2.5(d) does not occur if only the direct or exchange part of Γ_0 is kept. If we cut the green line in Σ', we recover the original 2PI vertex I_a. If we also cut the blue line, we actually get the full vertex, Γ. However, further cutting red lines yields a vertex much more complicated than any of the original ones.

and thus the existence of a functional $\Phi[G, \Gamma_0]$ from which the self-energy follows by functional differentiation,

$$\Sigma_{x',x}[G, \Gamma_0] = \frac{\delta \Phi}{\delta G_{x,x'}}. \tag{2.29}$$

Here, $\Phi[G, \Gamma_0]$ is the Luttinger–Ward (LW) functional [LW60]. Accordingly, “Φ-derivable” solutions are those where a diagrammatic approximation is made for Φ, and the skeleton expansions of Σ and I_t are deduced by functional derivatives. Figure 2.9 illustrates this strategy at low orders. The physical propagator, G, at which the functionals Σ and I_t are to be evaluated, is found from Dyson’s equation; susceptibilities like χ_t follow from BSEs. The advantage of Φ-derivable (also called *conserving*) approaches is that they ensure (i) that macroscopic observables, like particle number, momentum, energy, as computed from the correlation functions, fulfill conservation laws (continuity equations) and (ii) that thermodynamic expectation values, like particle number, energy, pressure, can be equivalently computed from the correlation functions or the partition function, Z (related to Φ) [BK61, Bay62].

The Φ-derivable procedure starts from the abstract Φ and uses functional derivatives to first get Σ and then I_t. Sometimes, however, one proceeds the other way round: One uses an auxiliary vertex, different from $\delta\Sigma/\delta G$, and the SDE to *practically* construct a self-energy, which is *conceptually* related to an LW functional. Two examples are the T-matrix and RPA self-energy, illustrated in Fig. 2.10: The auxiliary 2PI vertex (we choose I_a for better illustration) is the bare interaction. It relates to the first-order Φ and (skeleton) Σ. Through the BSE, one builds from I_a a ladder-type vertex Γ. Now, inserting Γ into the SDE yields a much more refined self-energy Σ' than the first-order Σ. Further, Σ' is conceptually related to another, infinite-order LW functional Φ'. In this combination of vertex and self-energy, conservation laws are *only* fulfilled on the one-particle level. As shown in [P5], the same applies to the parquet approximation, albeit, in this case, the 2PI vertex is not derivable from any LW functional (but the self-energy likely is). These examples illustrate a practical dilemma of approaches aiming to be Φ-derivable for both one- and two-particle correlation functions: The structure of the vertex is inherited from that of the self-energy. If one can easily construct the vertex, the approximation for the self-energy is too crude. For a refined self-energy, the functional derivative, yielding the vertex, is very challenging. Moreover, simultaneous fulfillment of both the SDE and the functional derivative $I_t = \zeta\delta\Sigma/\delta G$ can only be achieved in the exact solution of the problem [Smi92, P5].

2.3.1.5 Bethe–Salpeter equations for two-particle-reducible vertices

Since a functional derivative is numerically inaccessible, the BSEs for the generalized susceptibilities, χ_r, do not provide a useful connection between the one- and two-particle level. They rather

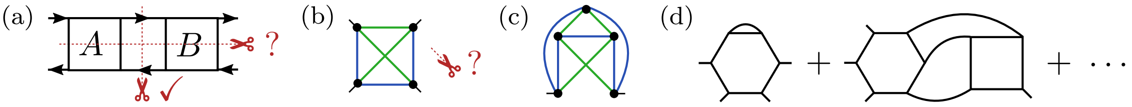

Figure 2.11 (a) Consider a diagram reducible in, e.g., the a channel, which can thus be expressed via two vertices A and B connected by antiparallel lines. If the diagram were also reducible in the t channel, the upper and lower two external legs could be separated. However, this would require A and B to be 1PR, which is impossible due to particle conservation [see Fig. 2.6(a,b)]. (b) The fourth-order, envelope vertex diagram is irreducible in all three two-particle channels. Thus, it is not included in the PA, see Sec. 2.3.1.7. To evaluate it in k representation, one can associate three independent integration variables with the blue lines while the remaining variables on the green lines are fixed by energy-momentum conservation. This amounts to a numerical cost $O(N_k^6)$. (c) Self-energy diagrams missing in the PA start at fifth order and similarly are at least of complexity $O(N_k^6)$. (d) Four-point diagrams built from a bare six-point vertex, which are irreducible in all two-particle channels.

introduce the 2PI vertices, I_r, for a refined computation of susceptibilities. In fact, even though the χ_r differ from each other only by trivial disconnected contributions, approximations in the vertices I_r result in very different four-point correlators $G^{(4)}$. The crucial benefit of the BSEs comes into play when *combining* all three of them to find a two-particle self-consistent, channel-unbiased vertex Γ. To realize this, we first translate the BSEs from the generalized susceptibilities to vertices.

Comparing the definition of χ_t [Eq. (2.15b)] to $G_c^{(4)}$ [Eq. (2.10)], we obtain its relation to Γ:

$$\chi_{t;x,y;x',y'} = \zeta G_{x,y'} G_{y,x'} + G^{(4)}_{c;x,y;x',y'} = \zeta G_{x,y'} G_{y,x'} + G_{x,z'} G_{y,v'} \Gamma_{v',z';v,z} G_{z,x'} G_{v,y'}.$$

If we now insert the BSE (2.23) for χ_t, we get

$$\begin{aligned} G_{x,z'} G_{y,v'} \Gamma_{z',v';z,v} G_{z,x'} G_{v,y'} = {}& G_{x,z'} G_{z,x'} I_{t;z',w';z,w} \\ & \times \big(G_{w,y'} G_{y,w'} + \zeta G_{w,u'} G_{y,v'} \Gamma_{v',u';v,u} G_{u,w'} G_{v,y'} \big). \end{aligned} \tag{2.30}$$

We remove the external legs, i.e., multiply by $(G^{-1})_{\tilde{x}',x} (G^{-1})_{x',\tilde{x}} (G^{-1})_{\tilde{y}',y} (G^{-1})_{y',\tilde{y}}$, to find the vertex BSE in the t channel,

$$\Gamma_{\tilde{x}',\tilde{y}';\tilde{x},\tilde{y}} = I_{t;\tilde{x}',\tilde{y}';\tilde{x},\tilde{y}} + \zeta I_{t;\tilde{x}',v';\tilde{x},v} G_{v,u'} G_{u,v'} \Gamma_{\tilde{y}',u';\tilde{y},u} \equiv I_{t;\tilde{x}',\tilde{y}';\tilde{x},\tilde{y}} + \gamma_{t;\tilde{x}',\tilde{y}';\tilde{x},\tilde{y}}. \tag{2.31}$$

For a given I_t, this is a self-consistent equation in Γ. Furthermore, we introduced the 2PR vertex γ_t, precisely in the form anticipated in Fig. 2.7: The full vertex Γ can be divided into 2PI (I_t) and 2PR (γ_r) contributions of the t channel, and the 2PR part can be fully expressed by combining I_t and Γ. By permuting indices, we find the analogous equation in the a channel,

$$\Gamma_{x',y';x,y} = I_{a;x',y';x,y} + I_{a;x',z';z,y} G_{z,v'} G_{v,z'} \Gamma_{v',y';x,v} \equiv I_{a;x',y';x,y} + \gamma_{a;x',y';x,y},$$

which is illustrated in Fig. 2.8(b). As shown in App. 9.2, the p channel fulfills

$$\Gamma_{x',y';x,y} = I_{p;x',y';x,y} + \tfrac{1}{2} I_{p;x',y';z,v} G_{z,z'} G_{v,v'} \Gamma_{z',v';x,y} \equiv I_{p;x',y';x,y} + \gamma_{p;x',y';x,y}.$$

In the compact notation of channel-dependent generalized matrix multiplications, we can simultaneously write for all channels

$$\Gamma = I_r + \underbrace{I_r \circ \Pi_r \circ \Gamma}_{\gamma_r} \qquad \Leftrightarrow \qquad \Gamma^{-1} = I_r^{-1} - \Pi_r. \tag{2.32}$$

2.3.1.6 Parquet equation

The parquet formalism combines the SDE and all three BSEs. The relation between the different 2PR vertices is made via diagrammatic arguments [Bic04]: As illustrated in Fig. 2.11(a) (similar to [RVT12]), a diagram cannot be simultaneously reducible in more than one channel [DDM64b, RGN69, RVT12]. Having established that the γ_r contain disjunct classes of diagrams, it is natural to add all reducible vertices to get the full vertex. What is missing are diagrams irreducible in all

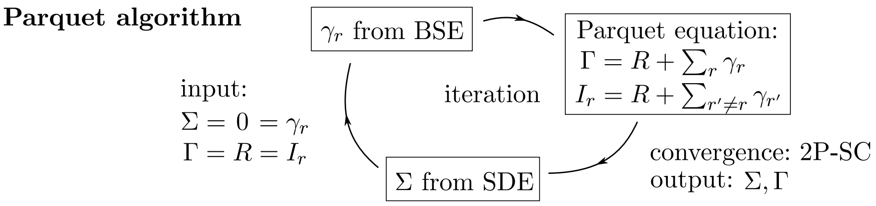

Figure 2.12 Illustration of the parquet algorithm, which takes as input the totally irreducible vertex, R. A two-particle self-consistent (2P-SC) solution of the vertex, Γ, and self-energy, Σ, is found by iteratively solving the Bethe–Salpeter equations (BSEs) and the Schwinger–Dyson equation (SDE).

three channels. Next to the bare vertex, totally irreducible contributions start at fourth order in the interaction with the "envelope" diagram, see Fig. 2.11(b). By collecting diagrams of this type in the totally irreducible vertex, R, the parquet equation can be understood as a classification of diagrams w.r.t. two-particle reducibility:

$$\Gamma = R + \sum_r \gamma_r. \tag{2.33}$$

Altogether, the parquet formalism gives us a unique handle on approximations on the two-particle level: One approximates the most fundamental diagrammatic object R and solves the BSEs (2.32) for the three vertices γ_r self-consistently. This can be understood in a skeleton (functional) sense and practically done for any fixed G. At the same time, the self-energy in G is related to Γ through the SDE (2.12), rendering the parquet formalism *self-consistent on the one- and two-particle level.* The solution is typically obtained by iteration, as illustrated in Fig. 2.12.

In contrast to the SDE, the derivation of the BSEs was completely general and did not assume a specific form of the action (i.e., whether it also contains six- or even higher-point vertices). The parquet equation itself is also general; one basically defines $R = \Gamma - \sum_r \gamma_r$. However, the diagrammatic expansion of R becomes more complicated for models with higher-order bare vertices, see Fig. 2.11(d). The simplest approximation for the totally irreducible vertex is $R = \Gamma_0$. This is the famous parquet approximation, which we discuss next.

2.3.1.7 Parquet approximation

The parquet approximation (PA) is the simplest possible solution of the full set of parquet equations, defined by the approximation $R = \Gamma_0$. Its original motivation is to sum up all leading contributions in logarithmically divergent perturbation series, as found, e.g., in the Kondo [Abr65] or X-ray–edge [RGN69] problem. It can be understood as an iterative replacement of bare vertices by the singular particle-hole and particle-particle bubbles in two-particle diagrams. On top of this essential low-energy feature, the PA also fulfills a variety of properties spanning all energy scales. For instance, the structure of the BSEs entails certain diagrammatic identities, such that, in Hubbard-like models, response functions like susceptibilities, χ_r, and three-point vertices, $\Gamma^{(3)}_r$, are encoded in high-frequency asymptotics of the vertex [WLT$^+$16, P2]: $\chi_{r;q} = \lim_{|\nu|,|\nu'|\to\infty} \gamma_{r;q,k,k'}/U^2$, $\Gamma^{(3)}_{r;q,k} = 1 + \lim_{|\nu'|\to\infty} \gamma_{r;q,k,k'}/U$. Moreover, ongoing work shows numerical evidence that the PA fulfills sum rules of susceptibilities [Cha19]. For instance, in the Hubbard model, such a sum rule reads $\sum_q \chi_{\sigma\sigma;q} = n_\sigma(1-n_\sigma)$ for the local, equal-spin susceptibility [RHT$^+$18]. Via the SDE, this ensures the correct high-frequency tail of the self-energy [RHT$^+$18], $\Sigma_{\bar\sigma} \sim U n_\sigma + U^2 n_\sigma(1-n_\sigma)/(i\nu)$ as $\nu \to \infty$. The fact that only the single-particle quantity n_σ appears in a sum rule of the two-particle object $\chi_{\sigma\sigma}$ is fundamentally related to the Pauli principle, dictating that each mode be occupied at most once, as seen through the operator identity $\hat n_\sigma^2 = \hat n_\sigma$ and $\sum_q \chi_{\sigma\sigma;q} = \langle \hat n_\sigma^2 \rangle - \langle \hat n_\sigma \rangle^2$.

In the field-theoretical language, the Pauli principle translates into the anticommutativity of Grassmann fields, which implies the crossing symmetry of correlators $G^{(n)}$ or vertices $\Gamma^{(n)}$ upon exchanging two in- or out-going legs. Through the parquet equations, crossing symmetry is fulfilled by construction. Vilk and Tremblay [VT97] relate this to the fulfillment of the fundamental Mermin–Wagner theorem [MW66], which forbids, e.g., antiferromagnetic order in the 2D Hubbard model at finite temperature. Furthermore, Bickers and Scalapino [BS92] have shown that the PA fulfills the Mermin–Wagner theorem by comparing the necessary diagrams in the effective bosonic and in the original fermionic theory, finding that the latter are indeed the two-particle-reducible diagrams of the PA.

The PA can also be characterized from the perspective of diagrammatic complexity. In the common case of translationally invariant systems, it comprises *all* diagrams of complexity $O(N_k^4)$, where $N_k = N_\nu N_{\boldsymbol{k}} = N_\nu N_{k_1} \cdots N_{k_D}$ denotes the number of grid points for each argument $k = (i\nu, \boldsymbol{k})$. This is in fact the maximal complexity feasible for numerical approaches. Diagrams more complex than this start at $O(N_k^6)$, see Fig. 2.11(b) and (c), and have only been computed for certain slices of the external arguments [RVT12]. On the two-particle level, where each vertex already has three arguments, diagrams of complexity $O(N_k^4)$ are iterative two-vertex combinations, as obtained by iterating the BSEs (Fig. 2.8). On the one-particle level, where Σ has only one external argument, nested integrations are possible, as they already occur in the SDE [Fig. 2.5(d)]. Consequently, if one compares the PA to perturbation theory, one finds discrepancies from the exact (ex) expressions starting at rather high orders: $\Gamma^{\mathrm{ex}} = \Gamma^{\mathrm{PA}} + O(U^4)$, $\Sigma^{\mathrm{ex}} = \Sigma^{\mathrm{PA}} + O(U^5)$. This holds not only in terms of bare propagators, G_0, and bare interactions, Γ_0 or U, but also in terms full propagators, G, and even full interaction vertices, Γ, underlining the fully self-consistent structure.

Indeed, the SDE relates the one- and two-particle level self-consistently and encodes the effect of collective fluctuations on single-particle excitations. Their back reaction is incorporated through self-energy dressing of the propagators connecting the vertices in the BSEs. The coupling of all BSEs together with the parquet equation provides self-consistency on the two-particle level, as required for an unbiased treatment of competing instabilities. This implies crossing symmetry but is a stronger statement, since crossing symmetry would remain intact if one, e.g., fully neglected a vertex like γ_p, which is crossing symmetric itself.

Finally, our recent results [P5] show that the PA fulfills conservation laws on the one- but not on the two-particle level. If, e.g., the nonequilibrium current is computed from the one-particle propagator, it fulfills the continuity equation, but if, say, the equilibrium linear conductance is to be inferred from the vertex, particle conservation may be violated. Correspondingly, Ward identities in the PA exhibit deviations at $O(U^4)$, where the self-energy is still exact but envelope vertices have already been neglected. Since the simultaneous fulfillment of the functional Ward identity, $I_t = \zeta \delta\Sigma/\delta G$, and the SDE requires the exact solution [Smi92, P5], evaluating Ward identities can be used to check the accuracy of the PA. This, in turn, can be used to gauge the influence of higher-order contributions to R, within the parquet formalism itself, i.e., even if benchmark results from other methods are not available.

In summary, the PA fulfills a list of important properties:

1. It contains all leading logarithmic contributions in logarithmically divergent perturbation series.
2. It obeys various diagrammatic identities (relating, e.g., susceptibilities to high-frequency asymptotics of the vertex) and is numerically found to fulfill sum rules of susceptibilities and thus the exact high-frequency asymptote of the self-energy.
3. It is crossing-symmetric by construction and fulfills the Mermin–Wagner theorem.
4. It contains *all* diagrams of numerical complexity $O(N_k^4)$, where N_k is the number of energy-momentum grid points for translationally invariant systems. Thus, discrepancies from perturbation theory start at $O(U^4)$ for vertices and $O(U^5)$ for the self-energy, each expressed through renormalized propagators and interactions.
5. It self-consistently relates the one- and two-particle level through the SDE and all two-particle channels through the coupled BSEs.
6. It fulfills conservation laws on the one- but not on the two-particle level. However, Ward identities can be used to gauge the accuracy of the PA within the formalism itself.

Generally, a solution to the self-consistent parquet relations is obtained by iteration (Fig. 2.12). As typical in the context of iterating self-consistent equations, it is unclear whether a unique solution exists, and a suitable choice of the initial condition and update rule in the self-consistency cycle is crucial to its success. From this point of view, a reformulation of the self-consistent equations as, e.g., differential equations is highly desirable. This goal was achieved in [P5] and is further discussed in Sec. 7.1.2. It constitutes a major improvement of the formalism and promises to ensure unique, physical solutions, found by following an RG flow on a two-particle self-consistent trajectory.

2.4 Dynamical mean-field theory and the numerical renormalization group

In this section, we give a very brief overview over dynamical mean-field theory (DMFT) and the numerical renormalization group (NRG). The DMFT method has acquired a central role in condensed-matter physics, with the outstanding successes of explaining the Mott–Hubbard metal-to-insulator transition and of bridging the gap from model studies to material science [GKKR96, KSH$^+$06]. It is used by a huge number of groups, and there is no need to provide a detailed description here. In our short synopsis, we write the most important (single-particle) relations, directly in terms of retarded, real-frequency correlation functions, $G(\omega) = G(i\nu \to \omega + i0^+)$, but revert to the imaginary-time formalism when evoking an underlying action or the diagrammatic origin through the LW functional. Using NRG as impurity solver has been optimized in the von Delft group, pioneered by A. Weichselbaum, for a long time and was already discussed in a number of theses. Hence, we are again brief in the description and mostly list technical aspects, relevant to the code used in [P9, P10]. Finally, we introduce Hund metals from a DMFT+NRG perspective and deduce the necessary ingredients for a minimal model of Hund metals.

2.4.1 Dynamical mean-field theory in a nutshell

The guiding principle of DMFT [GKKR96], originating from the study of perturbation theory in large dimensions [MV89, GK92], is to neglect spatial fluctuations but take full account of local, temporal (or *quantum*) fluctuations. Its approximation becomes exact in the limit of infinite dimension, and one can imagine it to be a good approximation for lattices of large coordination number, where the large number of neighbors of a given site can be treated as a bath without spatial structure [GKKR96]. The neglect of spatial fluctuations is reflected in the central DMFT approximation of a local, momentum-independent self-energy:

$$\Sigma_{ij}(\omega) = \delta_{ij}\Sigma(\omega) \qquad \Leftrightarrow \qquad \Sigma_{\boldsymbol{k}}(\omega) = \Sigma(\omega). \tag{2.34}$$

Crucial to the success of DMFT is not only the fact that it is exact in infinite dimensions, but also that it becomes exact in the two opposite cases of the noninteracting limit, $U = 0$, where the self-energy vanishes completely, and the atomic limit, $t_{ij} = 0$, where the collection of independent, identical atoms clearly fulfills Eq. (2.34). Therefore, DMFT is able to tune through the whole range of interactions and is a powerful tool to study metal–insulator transitions [GKKR96].

Since DMFT focuses on a single site on a lattice and approximates the effect of its neighbors through a bath of electrons, there is an immediate connection to impurity physics. Using Grassmann fields $\bar{d}_\sigma$, d_σ, corresponding to operators that create or annihilate an electron on the impurity, an impurity problem can be defined through the imaginary-time action

$$S_{\mathrm{imp}} = -\int_0^\beta \mathrm{d}\tau \int_0^\beta \mathrm{d}\tau' \sum_\sigma \bar{d}_\sigma(\tau)\, G_{0,\mathrm{imp}}^{-1}(\tau - \tau')\, d_\sigma(\tau') + \int_0^\beta \mathrm{d}\tau\, H_{\mathrm{imp}}[\bar{d}_\sigma(\tau), d_\sigma(\tau)].$$

The bare propagator, $G_{0,\mathrm{imp}}$, henceforth written as retarded correlation function,

$$G_{0,\mathrm{imp}}^{-1}(\omega) = \omega + \mu - \epsilon_d - \Delta(\omega),$$

contains the hybridization function Δ. In the present context, it characterizes the *dynamical mean field.* A Hamiltonian formulation is provided by Anderson-type impurity models [And61]

$$H = H_{\mathrm{imp}} + H_{\mathrm{hyb}} + H_{\mathrm{bath}},$$

where the hybridization is realized by an explicit account of bath degrees of freedom. For instance, these can be conduction electrons with dispersion $\epsilon_{\boldsymbol{k}}$, coupled to the impurity via matrix elements $V_{\boldsymbol{k}}$, such that

$$H_{\mathrm{hyb}} = \sum_{\sigma,\boldsymbol{k}} \big(V_{\boldsymbol{k}} d_\sigma^\dagger c_{\sigma,\boldsymbol{k}} + V_{\boldsymbol{k}}^* c_{\sigma,\boldsymbol{k}}^\dagger d_\sigma \big), \qquad H_{\mathrm{bath}} = \sum_{\sigma,\boldsymbol{k}} \epsilon_{\boldsymbol{k}} c_{\sigma,\boldsymbol{k}}^\dagger c_{\sigma,\boldsymbol{k}}. \tag{2.35}$$

The hybridization, fully specified by its imaginary part due to Kramers–Kronig relations, then reads[2]

$$\mathcal{A}_\Delta(\omega) = -\tfrac{1}{\pi}\mathrm{Im}\Delta(\omega) = \sum_{\boldsymbol{k}} |V_{\boldsymbol{k}}|^2 \delta(\omega + \mu - \epsilon_{\boldsymbol{k}}). \tag{2.36}$$

It is a priori unclear how to choose a bath that properly mimics the neighbors of a given lattice site. As typical in mean-field approaches, one demands that the degrees of freedom represented by the bath have the same properties as the site singled out. Hence, the impurity propagator

$$G_{\mathrm{imp}}(\omega) = \frac{1}{\omega + \mu - \epsilon_d - \Delta(\omega) - \Sigma(\omega)} \tag{2.37}$$

should equal the local propagator on the lattice, computed within the approximation (2.34),

$$G_{\mathrm{loc}}(\omega) = \sum_{\boldsymbol{k}} G_{\boldsymbol{k}}(\omega) \overset{\mathrm{(DMFT)}}{=} \sum_{\boldsymbol{k}} \frac{1}{\omega + \mu - \epsilon_{\boldsymbol{k}} - \Sigma(\omega)}. \tag{2.38}$$

Thus, one arrives at the DMFT self-consistency condition $G_{\mathrm{imp}}(\omega) \overset{!}{=} G_{\mathrm{loc}}(\omega)$, implying

$$\Delta(\omega) = \omega + \mu - \epsilon_d - \Sigma(\omega) - G_{\mathrm{loc}}^{-1}(\omega) \qquad \Leftrightarrow \qquad \mathcal{A}_\Delta(\omega) = \tfrac{1}{\pi}\mathrm{Im}\big[G_{\mathrm{loc}}^{-1}(\omega) + \Sigma(\omega)\big]. \tag{2.39}$$

A conceptually useful, yet more abstract definition of DMFT is possible through the LW functional Φ, introduced in Sec. 2.3.1.4. The DMFT approximation, again exact in the respective limits $D = \infty$, $U = 0$, $t = 0$, is stated as

$$\Phi^{\mathrm{DMFT}}[G, \Gamma_0] = \sum_i \phi[G_{ii}, \Gamma_{0;iiii}]. \tag{2.40}$$

Here, Φ^{DMFT} is the DMFT LW functional with the full propagator, G, and the Hubbard-like, *local* bare vertex, Γ_0; ϕ is the *exact* LW functional of an impurity model in terms of the local propagator and vertex *at a given lattice site*.

To elaborate on this, we consider again the LW functional up to second order from Fig. 2.9(a). Its general expression (Einstein's summation convention used) is given by

$$\Phi[G, \Gamma_0] = \tfrac{1}{2}\Gamma_{0;x',y';x,y} G_{x,x'} G_{y,y'} + \tfrac{1}{8}\Gamma_{0;x_1',y_1';x_1,y_1} G_{x_1,x_2'} G_{x_2,x_1'} G_{y_1,y_2'} G_{y_2,y_1'} \Gamma_{0;x_2',y_2';x_2,y_2} + \cdots .$$

Hubbard-like models have a local interaction: Γ_0 is only nonzero if all legs are at the same site. If we suppress spin indices for clarity (though they are needed for the antisymmetry of Γ_0) and resolve lattice-site and frequency arguments, we get

$$\begin{aligned}\Phi[G, \Gamma_{0,\mathrm{loc}}] = \tfrac{1}{2} &\sum_{i,\nu,\nu'} \Gamma_{0;iiii} G_{ii}(i\nu) G_{ii}(i\nu') \\ &+ \tfrac{1}{8} \sum_{i,j,\nu,\nu',\omega} \Gamma_{0;iiii} G_{ij}(i\nu) G_{ij}(i\nu') G_{ji}(i\nu + i\omega) G_{ji}(i\nu' + i\omega) \Gamma_{0;jjjj} + \cdots ,\end{aligned}$$

with (normalized) lattice-site and frequency summations. By contrast, the impurity LW functional involves only frequency (and spin) variables. Its frequency-dependent propagators and its vertices can be taken as those from a given lattice site i, such that

$$\begin{aligned}\phi[G_{ii}, \Gamma_{0;iiii}] = \tfrac{1}{2} &\sum_{\nu,\nu'} \Gamma_{0;iiii} G_{ii}(i\nu) G_{ii}(i\nu') \\ &+ \tfrac{1}{8} \sum_{\nu,\nu',\omega} \Gamma_{0;iiii} G_{ii}(i\nu) G_{ii}(i\nu') G_{ii}(i\nu + i\omega) G_{ii}(i\nu' + i\omega) \Gamma_{0;iiii} + \cdots .\end{aligned}$$

Clearly, $\Phi[G, \Gamma_{0,\mathrm{loc}}]$ and $\sum_i \phi[G_{ii}, \Gamma_{0;iiii}]$ differ already at second order. Hence, although ϕ in Eq. (2.40) is the exact LW functional on each lattice site, the approximation comes in through the arguments.

---

[2] Sums yielding local quantities should be considered normalized by the number of $\boldsymbol{k}$ points in the Brillouin zone.

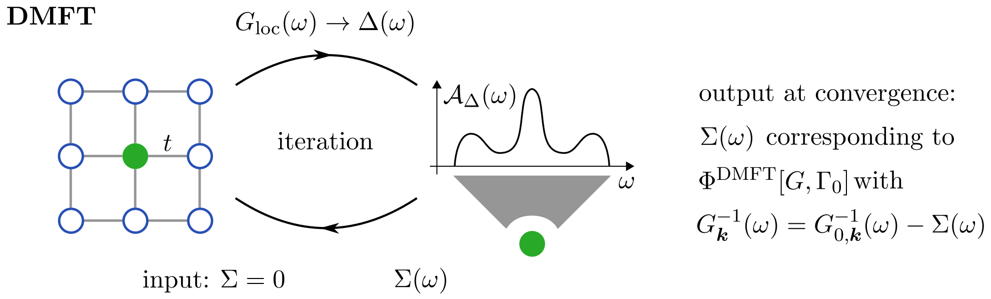
DMFT
$G_{\mathrm{loc}}(\omega) \to \Delta(\omega)$
t
iteration
$\mathcal{A}_\Delta(\omega)$
ω
output at convergence:
$\Sigma(\omega)$ corresponding to
$\Phi^{\mathrm{DMFT}}[G,\Gamma_0]$ with
$G_{\boldsymbol{k}}^{-1}(\omega) = G_{0,\boldsymbol{k}}^{-1}(\omega) - \Sigma(\omega)$
input: $\Sigma = 0$
$\Sigma(\omega)$

Figure 2.13 Illustration of the DMFT algorithm. The lattice model (with hopping amplitude t) is mapped onto an impurity model with a hybridization function Δ [Eq. (2.36)], self-consistently determined from G_{loc} and Σ through Eq. (2.39). An impurity solver is used to find the (frequency-dependent) self-energy of this Anderson-type impurity model. Convergence is achieved by iteration, starting, e.g., from the uncorrelated problem with $\Sigma = 0$. The resulting self-energy of the self-consistent impurity model corresponds to the functional derivative of the (lattice) LW functional $\Phi^{\mathrm{DMFT}}[G,\Gamma_0] = \sum_i \phi[G_{ii},\Gamma_0]$, evaluated at G_{ii}, the local part of the physical propagator fulfilling Dyson's equation on the lattice.

If we deduce the self-energy from the LW functional according to $\Sigma[G,\Gamma_0] = \delta\Phi/\delta G$ [Eq. (2.29)] and denote the skeleton self-energy as $\Sigma^{\mathrm{sk}} = \Sigma[G,\Gamma_0]$, the DMFT approximation (2.34) immediately follows:

$$\Sigma^{\mathrm{sk}}_{ij}(i\nu) = \frac{\delta\Phi}{\delta G_{ij}(i\nu)} \overset{(\mathrm{DMFT})}{=} \delta_{ij} \frac{\delta\phi}{\delta G_{ii}(i\nu)} = \delta_{ij}\Sigma^{\mathrm{sk}}(i\nu).$$

An important consequence is that DMFT is a conserving approximation in the sense of Baym and Kadanoff [BK61, Bay62] (which is summarized very briefly in Sec. 2.3.1.4). From this perspective, the impurity model is a *tool* for summing all (local) diagrams of the functional $\Sigma[G_{ii},U]$, evaluated as $\Sigma(\omega)$ for a propagator $G_{ii}(\omega)$ realized by $G_{\mathrm{imp}}(\omega)$. The space of local propagators is explored by iteratively varying the hybridization function of the auxiliary impurity model. All intermediate solutions fulfill Dyson's equation on the impurity. However, the solution to the lattice problem is the one that fulfills Dyson's equation on the lattice,

$$G_{\boldsymbol{k}}^{-1}(\omega) = G_{0,\boldsymbol{k}}^{-1}(\omega) - \Sigma(\omega) \qquad \Rightarrow \qquad G_{\mathrm{loc}}(\omega) = \sum_{\boldsymbol{k}} \left[G_{0,\boldsymbol{k}}^{-1}(\omega) - \Sigma(\omega)\right]^{-1}.$$

Since the local propagator ($G_{\mathrm{loc}} = G_{ii}$) under consideration is the one of the impurity model, this means

$$G_{\mathrm{imp}}(\omega) = \sum_{\boldsymbol{k}} \frac{1}{\omega + \mu - \epsilon_{\boldsymbol{k}} - \Sigma(\omega)},$$

which is precisely the DMFT self-consistency condition of Eqs. (2.37)–(2.39). We illustrate the DMFT algorithm in Fig. 2.13.

Finally, the above relations can be directly generalized to the multiorbital context. If the hopping matrix $\boldsymbol{t}_{ij}$ in Eq. (2.2) is diagonal in orbital space (as in [P9]), so are G and Σ. The local propagator can be obtained using the lattice density of states $D_m(\epsilon)$ of orbital m as

$$G_{\mathrm{loc},m}(\omega) = \sum_{\boldsymbol{k}} \frac{1}{\omega + \mu - \epsilon_{\boldsymbol{k},m} - \Sigma_m(\omega)} = \int \mathrm{d}\epsilon \, \frac{D_m(\epsilon)}{\omega + \mu - \epsilon - \Sigma_m(\omega)}.$$

The impurity energy levels are $\epsilon_{d,m} = \int \mathrm{d}\epsilon \, D_m(\epsilon)\epsilon$. However, if the dispersion $\boldsymbol{\epsilon}_{\boldsymbol{k}}$ has offdiagonal components, as typically arises in material calculations (like [P10]), the momentum sum has to be performed explicitly,

$$\boldsymbol{G}_{\mathrm{loc}}(\omega) = \sum_{\boldsymbol{k}} \left[\omega + \mu - \boldsymbol{\epsilon}_{\boldsymbol{k}} - \boldsymbol{\Sigma}(\omega)\right]^{-1}, \qquad \boldsymbol{\epsilon}_d = \sum_{\boldsymbol{k}} \boldsymbol{\epsilon}_{\boldsymbol{k}}.$$

This applies even if the crystal symmetry implies that the local quantities $\boldsymbol{G}$, $\boldsymbol{\Sigma}$, $\boldsymbol{\Delta}$, and $\boldsymbol{\epsilon}_d$ are orbital diagonal [P10].

2.4.2 Numerical renormalization group in a nutshell

The numerical renormalization group (NRG) was invented by K. Wilson to solve the Kondo problem [Wil75]. Remarkably, it constitutes a fully nonperturbative RG transformation, and is still unique as a real-frequency impurity solver at arbitrarily low temperatures and energies [BCP08]. The renormalization group flow is realized by successively including bath degrees of freedom at decreasing energy scales. It is not characterized by renormalized couplings (for any restriction to a finite set of couplings would violate the fully nonperturbative character) but by the (low-energy) spectrum of the Hamiltonian. Rescaling of the Hamiltonian after each inclusion of another bath degree of freedom allows for a transparent flow diagram with various types of fixed points. However, the rescaling is conceptually not needed for the impurity solver to work; it rather brings numerical benefits and facilitates the interpretation.

As mentioned before, an impurity problem is fully characterized by the (imaginary part of the) hybridization function. Even if $\mathcal{A}_\Delta(\omega)$ originates (in the thermodynamic limit) from a continuum of bath states [Eq. (2.36)], a diagonalization-based approach like NRG has to represent this hybridization (for the whole range of energies within the bandwidth) by a finite number of states [BCP08],

$$\mathcal{A}_\Delta(\omega) \approx \mathcal{A}_\Delta^{\mathrm{disc}}(\omega) = \sum_{n,\pm} (\gamma_n^\pm)^2 \delta(\omega - \xi_n^\pm), \qquad \xi_n^+ > 0, \quad \xi_n^- < 0.$$

In interacting quantum systems, the relevant energy scales often span several orders of magnitude [BCP08]. Hence, full diagonalization of the system with a linear discretization of the bath is impossible, as the required number of bath sites exceeds all numerical resources. However, a *logarithmic* discretization of the bath ensures an exponential decay of the hopping amplitudes in a semi-infinite one-dimensional representation of the bath (Wilson chain, see below). This has two important consequences: (i) exponentially small energy scales become accessible with only linear increase of the chain length; (ii) to find the low-energy spectrum, an *iterative diagonalization* with an intermediate truncation of high-energy states is possible.

The semi-infinite Wilson chain of the bath is obtained through a tridiagonalization of the discretized bath Hamiltonian, transforming Eq. (2.35) into

$$H_{\mathrm{hyb}}^{\mathrm{disc}} = \sum_{\sigma,n} \big(t_n c_{\sigma,n-1}^\dagger c_{\sigma,n} + t_n^* c_{\sigma,n}^\dagger c_{\sigma,n-1} \big), \qquad H_{\mathrm{bath}}^{\mathrm{disc}} = \sum_{\sigma,n} \tilde{\epsilon}_n c_{\sigma,n}^\dagger c_{\sigma,n}, \tag{2.41}$$

where $n = 1 \dots N$ and $c_{\sigma,0} = d_\sigma$. This corresponds to a continued fraction expansion of the hybridization function:

$$\Delta^{\mathrm{disc}}(\omega) = \cfrac{t_1^2}{\omega^+ - \epsilon_1 - \cfrac{t_2^2}{\omega^+ - \epsilon_2 - \cfrac{t_3^2}{\ddots \; \omega^+ - \epsilon_N}}}, \qquad \omega^+ = \omega + i0^+, \quad \epsilon_n = \tilde{\epsilon}_n - \mu. \tag{2.42}$$

The first hopping amplitude encodes the overall hybridization strength, $t_1^2 = \sum_{n,\pm} (\gamma_n^\pm)^2 = \int \mathrm{d}\omega \, \mathcal{A}_\Delta(\omega)$. The logarithmic spacing (using a discretization parameter $\Lambda > 1$) of the representative energies, $\xi_n^\pm \sim \Lambda^{-n}$, implies the same asymptotic behavior for the spectral weights, $(\gamma_n^\pm)^2 \sim \Lambda^{-n}$, as well as an exponential decay of the Wilson-chain parameters, $t_n, \epsilon_n \sim \Lambda^{-n/2}$. The important property $t_{n+1} \ll t_n$ (and similarly for ϵ_n) is called energy-scale separation and makes the iterative diagonalization possible: Successively adding sites of the Wilson chain changes the system on lower and lower energy scales. Upon adding site $n+1$ of the Wilson chain, only those states of the n-site chain with energies comparably small to t_{n+1} and ϵ_{n+1} contribute to the low-energy spectrum of the longer chain. Hence, to find the low-energy spectrum of the $(n+1)$-site chain, high-lying states from the previous iteration can be discarded, such that the size of the Hamiltonian matrix to be diagonalized remains bounded from above. This procedure is illustrated in Fig. 2.14.

In the full-density-matrix NRG [WvD07], one combines the states discarded at each iteration (more precisely, not further resolved in energy) with "environmental" contributions for the remainder of the chain, to construct a *complete* many-body basis of *approximate* eigenstates [AS05]. Then, static expectation values and dynamic correlation functions are computed from the density matrix

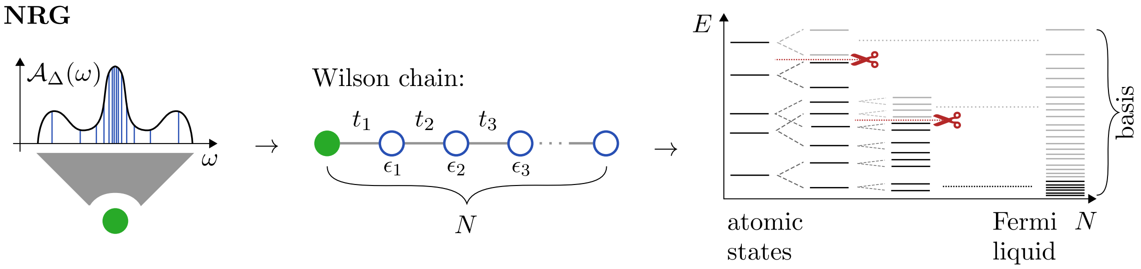

Figure 2.14 Illustration of the iterative diagonalization in NRG. The hybridization function $\mathcal{A}_\Delta$ of an impurity model is discretized on a logarithmic grid centered around the Fermi energy, and the resulting Hamiltonian is tridiagonalized. Consequently, the hopping amplitudes t_n along the semi-infinite Wilson chain decay exponentially. This allows for an iterative diagonalization, successively discarding energetically high-lying states, to find the low-energy spectrum. Combining the discarded states with their “environmental” contributions yields a complete many-body basis of approximate eigenstates [AS05, WvD07].

and the Lehmann representation at any temperature in an accurate and unambiguous fashion [WvD07]. Moreover, the one-dimensional geometry of the Wilson chain is perfectly suited for an efficient representation in terms of matrix product states (MPS) [Wei12b]. For the NRG results presented within this thesis, we use the QSpace tensor library developed by A. Weichselbaum, which provides such an MPS representation [Wei12b] with a general implementation of Abelian and non-Abelian symmetries [Wei12a]. Use of these symmetries enables a tremendous gain in efficiency of NRG by factorizing the matrix diagonalizations and tensor contractions into the symmetry-multiplet and the Clebsch–Gordan-coefficient space, exploiting the Wigner–Eckhardt theorem [Wei12a]. For models with reduced symmetry, an interleaved geometry of the Wilson chain, which shifts the discretization grids among different flavors, was proposed [MGWF$^+$14, SMvDW16]. This provides an additional energy-scale separation between different degrees of freedom of a single Wilson-chain site, such that high-lying states can be truncated even after adding a *subset* of degrees of freedom. If this subset is only a single spinful fermionic degree of freedom, the Hilbert space grows by a constant factor of 4 w.r.t. to the states that have been kept from the previous diagonalization. This interleaved NRG (iNRG) procedure is crucial to make multiorbital models with reduced orbital symmetry tractable [P9, P10].

The shifted discretization grids in iNRG are inspired from the z-averaging trick, already employed for the single-orbital model [SMvDW16]. At high energies, the logarithmic discretization in Eq. (2.41) or (2.42) is rather crude: Choosing slightly different representative states at high energies would yield an appreciable change in the results. The idea of z averaging is to use several shifted logarithmic grids [OO94, BCP08], with $\xi_n^\pm, (\gamma_n^\pm)^2 \sim \Lambda^{-n-z}$ parametrized by $z \in (0, 1]$ under the constraint

$$\mathcal{A}_\Delta(\omega) = \int_0^1 \mathrm{d}z\, \mathcal{A}_\Delta^{\mathrm{disc},z}(\omega) \approx \frac{1}{n_z} \sum_{l=1}^{n_z} \mathcal{A}_\Delta^{\mathrm{disc},z_l}(\omega). \tag{2.43}$$

The NRG algorithm clearly is a highly nonlinear process, and one cannot expect the z-averaged NRG results to truly represent the continuum limit of the continuous hybridization $\mathcal{A}_\Delta$, despite the requirement (2.43). However, z averaging does help to significantly improve the resolution at high energies and removes discretization artifacts (such as spurious oscillations with period $\propto \ln \Lambda$).

Finally, NRG spectral functions obtained from the Lehmann representation are at first only a collection of discrete δ peaks. Since these are spaced on the logarithmic grid of energy differences $E_n - E_m$, one employs a log-Gaussian broadening kernel [WvD07]. Recently, Lee and Weichselbaum [LW16] developed an adaptive broadening scheme, where the effect of an infinitesimal z shift to the final spectrum is tracked efficiently (using the Hellmann–Feynman theorem) in order to find a suitable broadening width at the respective energies: Only if the resulting eigenenergies depend strongly on the discretization (i.e., the z-dependent representative energy levels of the bath), the corresponding spectral features should be strongly broadened; otherwise, a finer broadening width can be used. For the NRG results presented in this thesis, we use Žitko’s and Pruschke’s version of z averaging [ZP09] (in the numerically stable procedure developed by K. M. Stadler, see Sec. 2.2.3 in [Sta19]), the adaptive broadening scheme [LW16], and an iNRG routine, as implemented by S.-S. B. Lee, on top of the QSpace tensor library, developed by A. Weichselbaum.

2.4.3 Minimal models for Hund metals

The DMFT framework combines the local, atomic description (exact in the limit of $t = 0$) with the coherent metallic state (as trivially obtained for $U = 0$). Generally, in strongly correlated metals, both the atomic and the coherent aspects are present, yet at distinct energy scales: The degenerate spectrum of fluctuating spin and orbital moments is visible at high temperatures and energies, and the nondegenerate Fermi-liquid state with coherent quasiparticle excitations is found at low temperatures and energies. From this point of view, NRG is an ideal tool for revealing this crossover as an RG flow from atomic constituents to a collective Fermi-liquid state, which can be understood as a self-consistent (multistage) Kondo screening process [SYvD$^+$15, DSK$^+$19] of charge, possibly orbital, and spin degrees of freedom.

From the DMFT+NRG perspective, the single-orbital Hubbard model exhibits charge fluctuations at high energies and spin fluctuations at low energies. The former manifest themselves in the Hubbard (side) bands; the latter in the quasiparticle peak of the local spectral function. Once the charge fluctuations are screened, the system can be described by an effective Kondo model. If the spin fluctuations of the local moments are screened as well, the Kondo singlet, corresponding to the electronic Fermi-liquid state, is formed. This process occurs below the energy scale of the (spin) Kondo temperature T_{sp}, which decreases with increasing U. In the correlated-metal regime at large U, T_{sp} is strongly suppressed and the Fermi liquid only found at very small energy scales.

In multiorbital Hubbard models, the situation is more complex. After the charge fluctuations have been screened, there remains an effective Kondo model with spin *and* orbital degrees of freedom [AK15, HZM16]. In the Hund-metal phase, the orbital fluctuations are screened at much higher energies than spin fluctuations—a phenomenon called spin–orbital scale separation and expressed in terms of Kondo scales as $T_{\mathrm{orb}} \gg T_{\mathrm{sp}}$ [GdMM13, SYvD$^+$15]. As thoroughly explained in [SKWvD19], upon increasing Hund's coupling J (see below) at a fixed size of the bare gap (i.e., the spectral gap in the atomic limit as a measure of Mott physics, which reduces to U in the single-orbital case), T_{sp} decreases while T_{orb} remains of similar magnitude. Thus, J can induce strong correlations through a reduced spin coherence scale. Hund metals [YHK11] are then multiorbital systems with strong correlations primarily arising from the Hund's coupling J, even at moderate Coulomb repulsion U [GdMM13]. In fact, for a long time, Hubbard U or the proximity to a Mott insulator, well known from the single-orbital Hubbard model, was considered the main source of electronic correlations. However, recently, it has become clear that, in Hund metals, J is the key player [SKWvD19].

What is needed for a minimal model of Hund metals? Generally, in Hubbard models, the interaction is approximated to be local. In Eq. (2.1) and (2.4), we have already seen the local Coulomb repulsion for the single-orbital model, with Hubbard U as its single parameter,

$$\hat{H}_{\mathrm{int},1} = U \hat{n}_{\uparrow} \hat{n}_{\downarrow} = \tfrac{1}{2} U \sum_{\sigma\sigma'} \hat{d}^{\dagger}_{\sigma} \hat{d}^{\dagger}_{\sigma'} \hat{d}_{\sigma'} \hat{d}_{\sigma}. \tag{2.44}$$

In multiorbital systems, the antisymmetric interaction vertex Γ_0 can be much more complex. We can immediately write down an interaction with an additional coefficient J,

$$\hat{H}_{\mathrm{int},2} = \tfrac{1}{2} U \sum_{mm'\sigma\sigma'} \hat{d}^{\dagger}_{m\sigma} \hat{d}^{\dagger}_{m'\sigma'} \hat{d}_{m'\sigma'} \hat{d}_{m\sigma} + \tfrac{1}{2} J \sum_{mm'\sigma\sigma'} \hat{d}^{\dagger}_{m\sigma} \hat{d}^{\dagger}_{m'\sigma'} \hat{d}_{m\sigma'} \hat{d}_{m'\sigma}, \tag{2.45}$$

fulfilling SU(2) spin symmetry and SU(M) orbital symmetry (where M is the number of orbitals). The first term in Eq. (2.45), proportional to Hubbard U, looks very similar to Eq. (2.44) and encodes density–density terms, as the creation and annihilation operators are labeled in the same way by orbital and spin indices. By contrast, the second term in Eq. (2.45), proportional to Hund J, includes exchange processes that are only possible with more than one orbital.

To understand the effect of J, we rewrite Eq. (2.45) with as many number operators $\hat{n}_{m\sigma} = \hat{d}^{\dagger}_{m\sigma} \hat{d}_{m\sigma}$ as possible,

$$\hat{H}_{\mathrm{int},2} = U \sum_{m} \hat{n}_{m\uparrow} \hat{n}_{m\downarrow} + U' \sum_{m \neq m'} \hat{n}_{m\uparrow} \hat{n}_{m'\downarrow} + (U' - J) \sum_{m<m',\sigma} \hat{n}_{m\sigma} \hat{n}_{m'\sigma} - J \sum_{m \neq m'} \hat{d}^{\dagger}_{m\uparrow} \hat{d}_{m\downarrow} \hat{d}^{\dagger}_{m'\downarrow} \hat{d}_{m'\uparrow}, \tag{2.46}$$

where $U' = U - J$. We find that J reduces the density–density interaction between electrons in different orbitals, most strongly for electrons with aligned spin. Further, it introduces a spin-flip term, as seen in the last summand in Eq. (2.46). An even more transparent expression is obtained by using the total charge and spin operators, $\hat{N} = \sum_{m\sigma} \hat{n}_{m\sigma}$ and $\hat{\boldsymbol{S}} = \frac{1}{2} \sum_{m\sigma\sigma'} \hat{d}^\dagger_{m\sigma} \boldsymbol{\tau}_{\sigma\sigma'} \hat{d}_{m\sigma'}$, where $\boldsymbol{\tau}$ are the Pauli matrices. Then, the Hamiltonian reads

$$\hat{H}_{\text{int},2} = \tfrac{3}{4} J \hat{N} + \tfrac{1}{2}\big(U - \tfrac{3}{2}J\big) \hat{N}\big(\hat{N} - 1\big) - J \hat{\boldsymbol{S}}^2 . \tag{2.47}$$

Here, the first summand is merely a shift of the chemical potential; the second penalizes large occupation due to the mutual repulsion of each of the N electrons from its $N-1$ partners. The last term, $-J\hat{\boldsymbol{S}}^2$, favors a large, local spin. It induces long-lived spin fluctuations and thus a reduced spin coherence scale T_{sp}. The energetically favorable maximization of the total spin is known as the *first* rule due to F. Hund [Hun25].

From Eq. (2.46), it is obvious that Hund-metal physics can only be observed in multiorbital systems. Further, the spin operator $\hat{\boldsymbol{S}}$, used in Eq. (2.47), distinguishes different ground-state sectors only if their average occupation N exceeds unity and different combinations of spins can be formed. Finally, by using either the particle or hole representation (such that $N \leq M$), it is clear that the Coulomb repulsion $\frac{1}{2}\hat{N}\big(\hat{N}-1\big)$ acts most prominently at half filling, with the maximal number of either particles or holes—a configuration inducing Mott physics of localized charges. We thus conclude that a minimal setting for Hund metals (multiple orbitals with $1 < N < M$) at the experimentally most relevant *integer filling* requires three orbitals at a filling of $N = 2$ (particles or holes). This is indeed the case for the ruthenates, with four electrons distributed among the three t_{2g} orbitals [GdMM13]. The Fe-SCs have five correlated (t_{2g} and e_g) orbitals occupied by four electrons, similarly enabling a strong effect of J [dM14].

The minimalist interaction (2.47) already describes the dominant effect of spin alignment in Hund metals. In total, there are three Hund rules, the second of which dictates the maximization of the total angular momentum at the given, maximized total spin. For the three-orbital case of t_{2g} physics, the angular-momentum operator has components $\hat{L}_m = i \sum_{\sigma m m'} \epsilon_{mm'm''} \hat{d}^\dagger_{m'\sigma} \hat{d}_{m''\sigma'}$, with the Levi-Civita symbol $\epsilon_{mm'm''}$ [GdMM13]. To incorporate $\hat{\boldsymbol{L}}$, the orbital SU(3) symmetry of the interaction (2.45)–(2.47) (with $M = 3$) must be reduced to SO(3)-symmetric form [GdMM13],

$$\begin{aligned} \hat{H}_{\text{int},3} = U \sum_{m} \hat{n}_{m\uparrow}\hat{n}_{m\downarrow} + U' \sum_{m \neq m'} \hat{n}_{m\uparrow}\hat{n}_{m'\downarrow} + (U' - J) \sum_{m < m', \sigma} \hat{n}_{m\sigma}\hat{n}_{m'\sigma} \\ - J \sum_{m \neq m'} \hat{d}^\dagger_{m\uparrow}\hat{d}_{m\downarrow}\hat{d}^\dagger_{m'\downarrow}\hat{d}_{m'\uparrow} + J_P \sum_{m \neq m'} \hat{d}^\dagger_{m\uparrow}\hat{d}^\dagger_{m\downarrow}\hat{d}_{m'\downarrow}\hat{d}_{m'\uparrow}, \end{aligned} \tag{2.48}$$

including an additional pair-hopping term with prefactor $J_P = U - U' - J$. In the physically relevant setting, $J_P = J$ and thus $U' = U - 2J$ [GdMM13]. Then, from the equivalent expression

$$\hat{H}_{\text{int},3} = \tfrac{5}{2} J \hat{N} + \tfrac{1}{2}\big(U - 3J\big) \hat{N}\big(\hat{N} - 1\big) - 2J \hat{\boldsymbol{S}}^2 - \tfrac{1}{2} J \hat{\boldsymbol{L}}^2, \tag{2.49}$$

the hierarchy in the first two Hund rules (first maximize total spin and then total angular momentum) can be directly understood from the respective coefficients, $2J > \frac{1}{2}J$. Finally, the third rule requires the inclusion of spin-orbit coupling via a term proportional to $\hat{\boldsymbol{L}} \cdot \hat{\boldsymbol{S}}$. Regarding DMFT treatments, this drastically increases the numerical effort in Monte Carlo solvers due to the sign problem, and appears challenging but feasible with NRG [Lee19] (see [LZH+19] for a recent work using matrix product states). However, a discussion of spin-orbit coupling exceeds the scope of this work.

2.5 Diagrammatic extensions of dynamical mean-field theory

The DMFT framework has enabled a breakthrough in the understanding of strongly correlated electron systems, including phenomena such as quasiparticle renormalization and metal–insulator transitions. Yet, it only describes local correlations, whereas many fascinating effects, like high-temperature superconductivity or quantum criticality, crucially depend on nonlocal correlations. To treat those, while building on the success of DMFT and its power as nonperturbative method exact in both opposite limits $U = 0$ and $t = 0$, nonlocal extensions of DMFT have to be explored.

For that purpose, a natural and important approach is to extend the exact treatment from a single site to a cluster of a few sites. These cluster extensions of DMFT [MJPH05] have the advantage that they possess a clear control parameter: the cluster size. However, due to the exponential growth of the Hilbert space with system size, numerical results are limited to clusters of about 10 × 10 sites, and correlations remain more or less short-ranged [RHT+18]. For the same reason, inclusion of multiple orbitals in cluster DMFT appears very challenging. Additionally, using Quantum Monte Carlo as cluster solver in the presence of complicated interactions or lattice geometries (such as frustrated lattices) soon becomes impossible due to the sign problem.

An alternative approach, which we focus on in this section, is given by diagrammatic extensions of DMFT [RHT+18]. There, nonlocal correlations are computed via Feynman diagrams, often directly in the thermodynamic limit, allowing for truly long-ranged correlations. The inclusion of multiple orbitals comes with additional arguments of vertex functions—a significant but feasible complication. Nevertheless, diagrammatic extensions of DMFT are harder to control than their cluster counterparts. One has to make a selection in the classes of diagrams to include, based on physical or heuristic arguments.

In our view, the most promising candidates for diagrammatic extensions of DMFT, for models with competing instabilities originating from local interactions, are the dynamical vertex approximation (DΓA) [TKH07, HKT08], a functional RG flow starting from DMFT (DMF^{2}RG) [TAB+14], and the dual fermion (DF) formalism [RKL08]. Below, we give a short and strongly simplified overview of these approaches, using a chain of arguments from nonlocal susceptibilities in DMFT via ladder and parquet DΓA [RHT+18] towards DMF^{2}RG and briefly anticipate multiloop DMF^{2}RG (introduced in Chapter 3). Furthermore, we argue that the DF formalism, albeit conceptually appealing, may not be optimal from a computational point of view. We here mention only briefly that methods with auxiliary bosonic degrees of freedom, such as the dual boson [RKL12] or TRILEX [AP15] approach, are useful for models with nonlocal interactions or a single, known instability. However, in the presence of competing instabilities, one still needs to accurately resolve the fermionic four-point vertex [P1], and the locality approximation of the three-point vertex in TRILEX seems too severe of an approximation.

2.5.1 Nonlocal susceptibilities in DMFT

In DMFT, correlations are approximated as local, but one can still compute nonlocal propagators and (generalized) susceptibilities [GKKR96]. Technically, the locality approximation is

$$\Phi^{\mathrm{DMFT}}[G, \Gamma_0] = \sum_i \phi[G_{ii}, \Gamma_{0;iiii}], \qquad \Sigma_k^{\mathrm{DMFT}} = \Sigma_\nu, \qquad I^{\mathrm{DMFT}}_{a;k,k',q} = I_{a;\nu,\nu',\omega}.$$

Here, we use a representation in terms of Matsubara frequencies and momenta (suppressing spin and possible orbital indices for clarity) via fermionic and bosonic energy-momenta $k = (i\nu, \boldsymbol{k})$ and $q = (i\omega, \boldsymbol{q})$, respectively. We consider the particle-hole vertex in the a channel for concreteness. The nonlocal propagator follows from the local (1PI) self-energy [cf. Fig. 2.2(a)],

$$G^{-1} = G_0^{-1} - \Sigma \qquad \Leftrightarrow \qquad G_k = G_{0,k} + G_{0,k}\Sigma_\nu G_k.$$

The nonlocal generalized susceptibility is obtained from the local 2PI vertex I_a,

$$\chi_a^{-1} = \Pi_a^{-1} - I_a \qquad \Leftrightarrow \qquad \chi_{a;k,k',q} = \Pi_{a;k,k',q} + \sum_{k_1,k_2} \Pi_{a;k,k_1,q} I_{a;\nu_1,\nu_2,\omega} \chi_{a;k_2,k',q}, \tag{2.50}$$

where $\Pi_{a;k,k',q} = G_k G_{k+q} \delta_{k,k'}$ [cf. Fig. 2.8(a)], and the sums are considered normalized. The (nonperturbative) Σ and I_a, used in these relations, are computed from the self-consistent ($\sum_{\boldsymbol{k}} G_k = G_\nu^{\mathrm{imp}}$) impurity model either directly or through inversion,

$$\Sigma = G_0^{\mathrm{imp},-1} - G^{\mathrm{imp},-1}, \qquad I_a = \Pi_a^{\mathrm{imp},-1} - \chi_a^{\mathrm{imp},-1}.$$

The inversion related to the single-particle self-energy can easily be done. However, the inversion of the two-particle generalized susceptibility (usually performed in a spin-resolved representation) is much harder and gave rise to a fundamental observation [SRG+13, SCW+16, GRS+17, CGS+18, TGCR18]: For certain (infinitely many) parameters, the nonperturbative $\chi^{\mathrm{imp}}_{a;\nu,\nu',\omega}$, viewed as matrix in ν and ν' for fixed transfer frequency ω, has vanishing eigenvalues. This implies *divergences* of the 2PI vertex I_a, even in the absence of a (physical) phase transition. These divergences only occur for the auxiliary object I_a and not for the full vertex, Γ: Only I_a involves a matrix inverse while Γ is simply obtained by amputating legs ("reg." denotes regular terms):

$$I_a \propto \chi_a^{-1} + \text{reg.}, \qquad \Gamma^{\text{imp}}_{\nu,\nu',\omega} \propto \chi_{a;\nu,\nu',\omega}/(G^{\text{imp}}_{\nu} G^{\text{imp}}_{\nu+\omega} G^{\text{imp}}_{\nu'} G^{\text{imp}}_{\nu'+\omega}) + \text{reg.}$$

In the decomposition $\Gamma = I_r + \gamma_r$, divergences of I_r and γ_r thus cancel. This indicates an intrinsic barrier for many-body frameworks that employ 2PI vertices taken from a nonperturbative solution.

For the ladder-type construction in Eq. (2.50), one can circumvent the potentially divergent 2PI vertex by using the BSE not for the generalized susceptibility but on the vertex level [Eq. (2.32)]. To explain this trick, known from ladder DΓA applications [RHT+18], we isolate the 2PI vertex,

$$\Gamma^{-1} + \Pi_a = I_a^{-1} = \Gamma^{\text{imp},-1} + \Pi_a^{\text{imp}},$$

and then define $\delta\Pi_a = \Pi_a - \Pi_a^{\text{imp}}$ to get

$$\Gamma^{-1} = \Gamma^{\text{imp},-1} - \delta\Pi_a \qquad \Leftrightarrow \qquad \Gamma = \Gamma^{\text{imp}} + \Gamma^{\text{imp}} \circ \delta\Pi_a \circ \Gamma. \tag{2.51}$$

Hence, we can use Γ^{imp} as "irreducible building block" in the vertex BSE if the corresponding two-particle propagator is adjusted to $\delta\Pi_a$. Finally, Eq. (2.51) can also be written via purely nonlocal propagators, $\tilde{G}_k = G_k - G^{\text{imp}}_{\nu}$, and thus $\tilde{\Pi}_{a;k,k',q} = \tilde{G}_k \tilde{G}_{k+q} \delta_{k,k'}$. Since the vertex Γ depends only on the transfer momentum $\boldsymbol{q}$, one finds at DMFT self-consistency ($\sum_{\boldsymbol{k}} G_k = G^{\text{imp}}_{\nu}$) that

$$\begin{aligned}
\Gamma_{\nu,\nu',q} &= \Gamma^{\text{imp}}_{\nu,\nu',\omega} + \sum_{\tilde{k}} \Gamma^{\text{imp}}_{\nu,\tilde{\nu},\omega} (G_{\tilde{k}} G_{\tilde{k}+q} - G^{\text{imp}}_{\tilde{\nu}} G^{\text{imp}}_{\tilde{\nu}+\omega}) \Gamma_{\tilde{\nu},\nu',q} \\
&= \Gamma^{\text{imp}}_{\nu,\nu',\omega} + \sum_{\tilde{k}} \Gamma^{\text{imp}}_{\nu,\tilde{\nu},\omega} (G_{\tilde{k}} G_{\tilde{k}+q} - G_{\tilde{k}} G^{\text{imp}}_{\tilde{\nu}+\omega} - G^{\text{imp}}_{\tilde{\nu}} G_{\tilde{k}+q} + G^{\text{imp}}_{\tilde{\nu}} G^{\text{imp}}_{\tilde{\nu}+\omega}) \Gamma_{\tilde{\nu},\nu',q} \\
&= \Gamma^{\text{imp}}_{\nu,\nu',\omega} + \sum_{\tilde{k}} \Gamma^{\text{imp}}_{\nu,\tilde{\nu},\omega} \tilde{G}_{\tilde{k}} \tilde{G}_{\tilde{k}+q} \Gamma_{\tilde{\nu},\nu',q}.
\end{aligned} \tag{2.52}$$

2.5.2 Ladder DΓA

Having a momentum-dependent ladder vertex $\Gamma_{\nu,\nu',q}$ available, it is an intuitive step of ladder DΓA [TKH07, HKT08] to compute a momentum-dependent self-energy through the self-consistent SDE (2.12),

$$\Sigma_k = \Sigma_{\text{H}} + U \sum_{k',q} G_{k'} G_{k'+q} G_{k+q} \Gamma^{\uparrow\downarrow}_{\nu',\nu,q}. \tag{2.53}$$

Here, $\Sigma_{\text{H}} = U n_\sigma$ is the Hartree part at density n, and spin symmetry was assumed. The resulting G_k can be used for a modified self-consistency condition of the impurity model, $\sum_{\boldsymbol{k}} G_k \overset{!}{=} G^{\text{imp}}_{\nu}$.

Local susceptibilities, e.g., $\chi_{\sigma\sigma}(\tau) = \langle T_\tau \hat{n}_\sigma(\tau) \hat{n}_\sigma(0) \rangle - n_\sigma^2$, with time-ordering operator T, can be computed both from the impurity model and on the lattice. Their results (even at self-consistency) can generally be different,

$$\begin{aligned}
\chi_{a;\omega} = \sum_{k,k',\boldsymbol{q}} \chi_{a;k,k',q} &= \sum_{k,\boldsymbol{q}} G_k G_{k+q} + \sum_{k,k',\boldsymbol{q}} G_k G_{k+q} \Gamma_{\nu,\nu',q} G_{k'} G_{k'+q} \\
&= \sum_{\nu} G^{\text{imp}}_{\nu} G^{\text{imp}}_{\nu+\omega} + \sum_{k,k',\boldsymbol{q}} G_k G_{k+q} \Gamma_{\nu,\nu',q} G_{k'} G_{k'+q} \\
&\neq \sum_{\nu} G^{\text{imp}}_{\nu} G^{\text{imp}}_{\nu+\omega} + \sum_{\nu,\nu'} G^{\text{imp}}_{\nu} G^{\text{imp}}_{\nu+\omega} \Gamma^{\text{imp}}_{\nu,\nu',\omega} G^{\text{imp}}_{\nu'} G^{\text{imp}}_{k'+q} = \chi^{\text{imp}}_{a;\omega}.
\end{aligned}$$

Indeed, due to the crude approximation in the vertex $\Gamma_{\nu,\nu',q}$, they often differ considerably. What is more, sum rules of local susceptibilities are determined by local equal time correlators, such as the previously mentioned $\sum_\omega \chi_{\sigma\sigma,\omega} = n_\sigma(1 - n_\sigma)$. In ladder D$\Gamma$A, one introduces auxiliary parameters—the "Moriyaesque λ correction"—in the susceptibility for each channel r through the transformation $\chi^{-1}_{r;q} \to \chi^{-1}_{r;q} + \lambda_r$ and tunes the λ_r to fulfill such sum rules [RHT+18]. The SDE (2.53) can be rewritten to incorporate the transformation as well [RHT+18]. This heuristic correction is responsible for a number of helpful properties in ladder DΓA; particularly, it reduces the susceptibility and ensures the absence of a finite-temperature phase transition in the 2D Hubbard model [RHT+18]. However, it is surely not fully satisfying from a conceptual point of view and might serve as a motivation to further refine the nonlocal vertex.

2.5.3 Parquet DΓA

The parquet formalism provides a recipe for a channel-unbiased treatment of self-energy and vertex. It combines *all* diagrammatic contributions of the maximally feasible numerical complexity $O(N_k^4)$, while assuming as input a given totally irreducible vertex, R. Previously, we discussed the purely diagrammatic PA with $R = \Gamma_0$. Parquet DΓA [TKH07, HKT08] goes much beyond this by merely approximating R to be local, i.e., by taking the fully nonperturbative R^{imp} from the exact solution of a self-consistently chosen impurity model.[3] Compared to DMFT, parquet DΓA thus reduces the locality approximation from Σ and I_a to the most fundamental diagrammatic building block on the two-particle level, R. By solving the parquet equations with R^{imp} on the lattice, one obtains nonlocal correlation functions on the one- and two-particle level, subject to the parquet self-consistency. Often the impurity model from DMFT is used, but one can also impose self-consistency between lattice and impurity on G_k resulting from the parquet iteration. The QUADRILEX formalism [AP16] (derived from a functional point of view) additionally provides a self-consistency condition for a retarded interaction on the impurity.

The numerical challenge of parquet DΓA consists of the following aspects: (i) multiple solutions of an impurity model, which also provide the full vertex, Γ^{imp}, at self-consistency; (ii) inversions of the parquet equations on the impurity to deduce the totally irreducible vertex, R^{imp}, from Γ^{imp}; and (iii) solutions of the parquet equations on the lattice using $R = R^{\mathrm{imp}}$. Given the enormous advance of impurity solvers over the last decades [GKKR96, RHT+18], the hardest step is (iii), solving the parquet equations with fully frequency- and momentum-dependent vertices. In principle, such costly objects are already present for any solution of the lattice parquet equations, including the PA with $R = \Gamma_0$. However, additional difficulties for the parquet solver arise due to the complicated starting point taken from DMFT. On the one hand, at strong coupling, R^{imp} is expected to be large, making it hard to converge a solution of the parquet equations. On the other hand, the divergences of 2PI vertices inherent in a nonperturbative solution—although hidden in the physical and regular 1PI vertex Γ—are at full display in R^{imp}. If the system parameters are close to such divergences, the parquet algorithm then starts from ill-defined diagrammatic objects.

2.5.4 DMF^{2}RG

Instead of disassembling the nonperturbative vertex Γ^{imp} from DMFT into a possibly ill-defined diagrammatic object R^{imp} in order to reassemble lattice correlators, a more elegant approach is to continuously evolve the solution from the self-consistently determined impurity model towards the lattice problem. In 2014, the method of DMF^{2}RG was introduced [TAB+14], where a functional RG flow is used for that purpose. The RG parameter Λ in the bare propagator G_0^Λ, normally used to distinguish energy scales, is now used to interpolate between the impurity and lattice problem. A simple realization of an fRG flow, going from the DMFT solution with self-consistent Δ at Λ_i to the lattice model with dispersion $\epsilon_{\boldsymbol{k}}$ at Λ_f, is given by [TAB+14]

$$G_{0;k}^{\Lambda} = \frac{1}{i\nu + \mu - (1-\Lambda)\epsilon_{\boldsymbol{k}} - \Lambda\Delta_\nu}, \qquad \Lambda_i = 1, \qquad \Lambda_f = 0. \tag{2.54}$$

The evolution of Σ^Λ and Γ^Λ from the impurity to the lattice is governed by the fRG flow equations.

In the original article [TAB+14], promising results were obtained despite a coarse parametrization of the vertex. Since then, much progress has been achieved in this regard, most notably by adapting the parametrization to each two-particle channel individually. This allows one to (i) single out the high-frequency asymptotics [WLT+16], as illustrated in Fig. 2.15, and (ii) expand the weak dependence on “fermionic” momenta in form factors [LSdlPR+17]. Moreover, Vilardi et al. [VTM19] proposed a refined interpolation scheme, which employs a function g_ν^Λ, numerically determined for

---

[3] Pioneering computations indeed suggest a weak momentum dependence of R in the Hubbard model [MJS06].

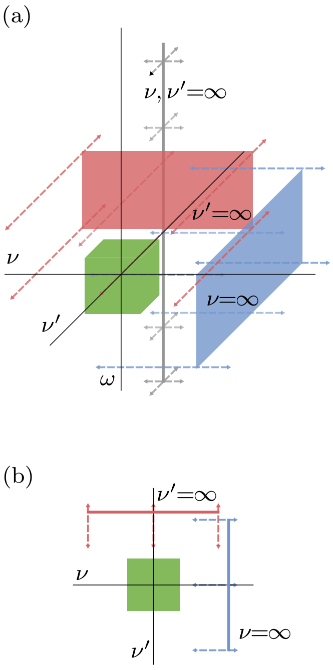

Figure 2.15 (a) Illustration of an efficient frequency parametrization of the vertex by including high-frequency asymptotics [WLT$^+$16]. The totally irreducible vertex, R, decays in all frequency arguments. By contrast, the 2PR vertices, γ_r, only vanish when their respective bosonic transfer frequency ω is taken to infinity. In the parametrization of [WLT$^+$16], we write (suppressing indices r and using $\Theta_{|\nu|<\Omega} = \Theta(\Omega - |\nu|)$ for brevity, cf. supplement of [P2]) $\gamma_{r;\omega,\nu,\nu'} = K_{1;\omega}\Theta_{|\omega|<\Omega_1} + K_{2;\omega,\nu}\Theta_{|\omega|<\Omega_2^b}\Theta_{|\nu|<\Omega_2^f} + K_{2';\omega,\nu'}\Theta_{|\omega|<\Omega_2^b}\Theta_{|\nu'|<\Omega_2^f} + K_{3;\omega,\nu,\nu'}\Theta_{|\omega|<\Omega_3^b}\Theta_{|\nu|<\Omega_3^f}\Theta_{|\nu'|<\Omega_3^f}$, with $\Omega_1 > \Omega_2^{b,f} > \Omega_3^{b,f}$. This implies an overarching $K_{1;\omega} = \lim_{|\nu|,|\nu'|\to\infty} \gamma_{r;\omega,\nu,\nu'}$ dependence (gray line), extending through the whole three-dimensional space. Rectangles of $K_{2^{(\prime)},\omega,\nu^{(\prime)}} = \lim_{|\nu^{(\prime)}|\to\infty} \gamma_{r;\omega,\nu,\nu'} - K_{1;\omega}$, (red and blue) take the dominant two-dimensional frequency dependence into account, and the actual three-dimensional K_3 dependence is restricted to a small (green) box. (b) For each slice at fixed ω, K_1 gives a background value, $K_{2^{(\prime)}}$ lines describe the one-dimensional dependence, and K_3 contributions are confined to a small rectangle. Importantly, the channel-dependent high-frequency asymptotes $K_{1,r}$ and $K_{2^{(\prime)},r}$ can also be determined from the full vertex, Γ [WLT$^+$16]. The intricate $K_{3,r}$ decays in all frequency directions; it need not be channel-resolved but can be gathered as $K_3 = R + \sum_r K_{3,r}$ after subtracting the asymptotics from Γ. Hence, the parametrization is well suited for DMF^{2}RG, too, where one wants to avoid dividing the DMFT vertex into two-particle channels.

all Λ before the flow, such that

$$G_\nu^{\mathrm{imp}} \overset{!}{=} \sum_{\boldsymbol{k}} \frac{1}{i\nu + \mu - (1-\Lambda)\epsilon_{\boldsymbol{k}} - g_\nu^\Lambda \Delta_\nu - \Sigma_\nu^{\mathrm{imp}}}, \qquad \Lambda \in [\Lambda_f, \Lambda_i]. \tag{2.55}$$

With this choice, the single-scale propagator $S_k^\Lambda = \partial_\Lambda G_k^\Lambda|_{\Sigma^\Lambda=\mathrm{const}}$ is purely nonlocal at the initial scale Λ_i, i.e., $\sum_{\boldsymbol{k}} S_k^{\Lambda_i} = 0$. Then, the flow actually starts with $\dot{\Sigma}^{\Lambda_i} = 0$ and $\dot{\Gamma}^{\Lambda_i} = 0$ before G_0 incorporates the $\boldsymbol{k}$ dependence at $\Lambda < \Lambda_i$. Likewise, the initial contribution of the six-point vertex to the flow of the four-point vertex, $\sum_{\boldsymbol{k}} \Gamma^{(6),\Lambda_i}_{\nu_1,\nu_2,\nu_3,\nu,\nu} S_{\boldsymbol{k}}$, vanishes.

Nevertheless, the six-point vertex acquires nonlocal contributions during the flow, and $\sum_{\boldsymbol{k}} S_k^\Lambda = 0$ does not hold at $\Lambda < \Lambda_i$ because of the self-energy contribution. The neglect of $\Gamma^{(6)}$ is thus the crucial approximation which limits the accuracy of the DMF^{2}RG flow. In Chapter 3, we present a *multiloop* fRG (mfRG) flow, which incorporates all contributions of the contracted six-point vertex at the complexity $O(N_k^4)$ of the parquet algorithm, using iterative combinations of differentiated four-point vertices. We expect this to significantly improve the DMF^{2}RG flow and achieve the same accuracy as parquet DΓA, while the approach retains the numerically efficient structure of a differential equation and avoids any appearance of 2PI vertices.

Finally, since part of the 1PI six-point vertex appearing in the fRG hierarchy of flow equations can be replaced by four-point objects in the mfRG reformulation of the parquet equations, we draw the important conclusion that *the influence of three-particle (and higher) interactions is formalism dependent.* In the following, we discuss how the dependence on the six-point vertex (even involving 1PR contributions) is responsible for computational challenges of the DF formalism.

2.5.5 Bare vertices in the DF formalism

The dual fermions [RKL08] are auxiliary degrees of freedom introduced by a Hubbard–Stratonovich decoupling of the quadratic (instead of the usual quartic) part of the action into a local and nonlocal part. The local part can be integrated out, giving rise to the DMFT solution; the nonlocal part is carried by the dual fermions. However, the bare action of the dual fermions is highly nontrivial and consists of all local DMFT vertices [RHT$^+$18]. The bare dual propagator (purely nonlocal at DMFT self-consistency) is given by

$$\tilde{G}_{0;k} = \frac{1}{i\nu + \mu - \epsilon_{\boldsymbol{k}} - \Sigma_\nu^{\mathrm{imp}}} - G_\nu^{\mathrm{imp}}, \qquad \sum_{\boldsymbol{k}} \tilde{G}_{0;k} \overset{\text{(DMFT)}}{=} 0. \tag{2.56}$$

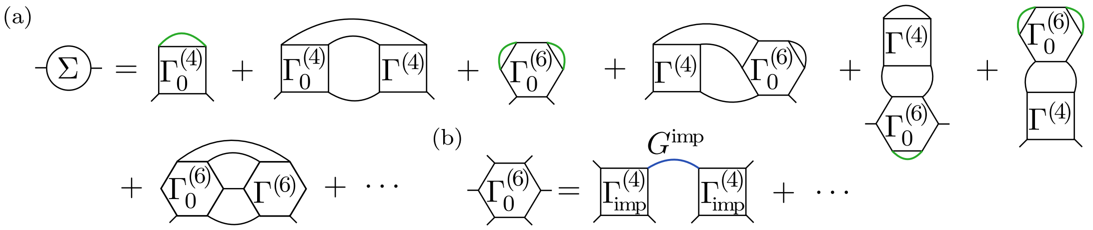

Figure 2.16 (a) Illustration of the SDE for the self-energy including bare six-point vertices, as it occurs for dual fermions. In fact, the infinite number of bare vertices in the dual action implies infinitely many more terms. By using a modified self-consistency condition, $\sum_{\boldsymbol{k}} \tilde{G}_k = 0$, the terms with green lines contracting local, bare vertices can be forced to vanish. (b) Contributions to the bare dual (i.e. renormalized impurity) six-point vertex start with this second-order diagram, 1PR in the impurity (i.e. DMFT local) propagator.

The bare vertices are given by $\tilde{\Gamma}_0^{(n\geq 4)} = \Gamma_{\text{1PI+1PR}}^{\text{imp},(n\geq 4)}$. Importantly, these include 1PR contributions (except for the four-point vertex). The translation from the dual to the actual self-energy reads

$$\Sigma_k = \Sigma_\nu^{\text{imp}} + \frac{\tilde{\Sigma}_k}{1 + G_\nu^{\text{imp}} \tilde{\Sigma}_k}. \tag{2.57}$$

While $\tilde{\Sigma}$ is 1PI w.r.t. $\tilde{G}$ lines, it does contain contributions that are 1PR in G^{imp} lines. These are then canceled by the denominator to yield a 1PI self-energy of the original fermions [RHT+18].

The DF formalism provides a conceptually appealing perturbation theory around DMFT, using nonlocal (dual) degrees of freedom and without reference to bare parameters of the system. By contrast, the SDE in DΓA retains the bare interaction, U. However, since the dual action contains bare n-point vertices of arbitrarily high n, it is computationally very challenging. In other words, the clean formulation of DF comes at the price of a profound influence of high-point vertices.

For instance, recalling the derivations in Sec. 2.3, one understands that an infinite-order bare action yields an SDE for the self-energy that includes an infinite number of terms. Already the six-point vertex gives rise to a number of additional terms, as illustrated in Fig. 2.16(a). While some of them can be forced to vanish by imposing a modified self-consistency condition in terms of the *full* dual propagator, $\sum_{\boldsymbol{k}} \tilde{G}_k = 0$ [cf. Eq. (2.56)], other terms contribute in the same way as those parts involving four-point vertices only. As the 1PR six-point vertex starts already at second-order in the (effective) interaction [see Fig. 2.16(b)], its first contribution to $\tilde{\Sigma}$ then starts at third order. Hence, if we briefly consider the *bare* perturbation theory of the self-energy, the DF formalism requires the six-point vertex already at order U^3, whereas DΓA (and even the PA) yields the exact self-energy up to corrections of order U^5, using only four-point vertices.

An infinite resummation of dual diagrams has so far only been obtained in ladder form [RHT+18]. The simplest self-energy diagram involving the six-point vertex has been considered for testing purposes, showing that it actually yields significant contributions in some parameter regimes [RRH17, RGI+17]. Furthermore, it has been argued that the denominator in Eq. (2) should be neglected when six- and higher-point vertices are not included in the perturbative series, since it otherwise introduces rather cancels spurious 1PR contributions [Kat13]. Yet, numerical results show that this actually deteriorates agreement of DF results with benchmark data [GKH17]. One might interpret this as evidence that the diagrammatic treatment of the dual problem has not yet matured sufficiently. Finally, in the presence of competing instabilities, any ladder approximation breaks down, and a dual parquet approach is needed. However, the bare six- and higher-point vertices also complicate the vertex part of the parquet algorithm, as they produce contributions to R starting already at lower orders than the envelope diagram [cf. Fig. 2.11(d)]. This might be related to the tentative observation that the parquet equations are harder to converge in the dual theory (neglecting six- and higher-point vertices) than for the original fermions (in DΓA) [Rib18].

In summary, we have provided a list of arguments that advocate *multiloop* DMF^{2}RG as an advantageous diagrammatic extension of DMFT. This approach promises the accuracy of parquet DΓA in a numerically more efficient setting and, particularly, circumvents potentially divergent 2PI vertices (see Chapter 3). The DF formalism, a conceptually appealing alternative, does not require 2PI vertices either, but poses a number of computational challenges for accurate solutions in the dual theory.

3 Multiloop functional renormalization group

3.1 Overview

Strongly correlated electron systems pose formidable challenges for computational methods: Strong correlations require treatments beyond the mean-field level, and nonlocal correlations even those beyond DMFT. Finite-size approaches reach their limitations to resolve long-range fluctuations, and the specialized tools of one dimension [e.g. Bethe Ansatz and the density-matrix renormalization group (DMRG)] fail to work in the physically most relevant case of two and three dimensions. A class of methods suitable to deal with these systems is given by quantum field-theoretical techniques. From the diagrammatic perspective, strong correlations demand going beyond finite-order perturbation theory, and competing instabilities beyond simple, single-channel resummations. Proper diagrammatic resummations are formulated in terms of the self-consistent parquet equations, which are, however, numerically very challenging.[1] From the RG point of view, fRG flows are a viable tool for a channel-unbiased description reaching beyond the weak-coupling regime. However, fRG has been plagued by a limited predictive power due to the nontransparent approximation in the truncation of the infinite hierarchy of flow equations, which is responsible for results depending on the choice of regulator, ambiguous ways to compute response functions, and spurious vertex divergences.

This raises major conceptual questions: Can we eliminate these flaws of fRG while keeping its versatile and efficient structure? Can we find a rigorous relation between the parquet and fRG frameworks? Can we make the self-consistent parquet algorithm numerically more robust and fRG flows *quantitative*?

The following series of papers documents the development of the multiloop functional renormalization group (mfRG), which achieves precisely that. In the first article [P1], we investigate whether a simple truncation of an fRG flow following a multichannel Hubbard–Stratonovich (HS) transformation, as proposed by [LDSK15], can provide a resummation of the parquet diagrams—finding that this is not the case. Instead, we show that the HS transformation does not save one from having to calculate the fermionic four-point vertex. On top of that, with or without the HS transformation, the parquet diagrams include 1PI n-point vertices of arbitrarily high n in the standard, *one-loop* fRG hierarchy of flow equations. In the subsequent publications, we diagrammatically construct the mfRG flow, which does sum up all parquet diagrams, using an iterative *multiloop* construction of differentiated vertices. In [P2], we provide a transparent derivation of the mfRG vertex flow for the prototypical X-ray–edge singularity, demonstrate numerically the improvement over the truncated one-loop fRG, and prove the equivalence of mfRG and the PA by an analytical enumeration of all involved diagrams. In [P3], we extend the mfRG construction to the general fermionic many-body problem. There, the—in principle—exact fRG self-energy flow has to be amended, too, when working with the vertex in the PA, in order to reproduce all diagrams of the parquet equations in conjunction with the SDE for the self-energy. The following article[2] [P4] first presents the diagrammatic derivation of mfRG flow equations for response function, and then applies the formalism to the 2D Hubbard model. Next to the multiloop extension, it combines several methodological advances in the numerical implementation and demonstrates how fRG results can be brought under quantitative control, even for models as challenging as the 2D Hubbard model. Finally, publication [P5] presents an algebraic derivation of flow equations from self-consistent many-body relations. It develops a clear framework for constructing (multiloop functional) RG flows in diverse settings, particularly for nonlocal extensions of DMFT. It also shows how two-particle diagrammatic resummations can be performed without potentially divergent 2PI vertices and resolves long-standing questions on the fulfillment of conservation laws in the PA.

---

[1] As explained in Sec. 2.5, the parquet equations with input from DMFT suffer from parameter regimes that constitute an ill-defined diagrammatic starting point, where nonperturbative 2PI vertices diverge. Intriguingly, this is directly related [GRS+17] to the multivaluedness of the LW functional [KFG15, VWFP18], hampering bold diagrammatic Monte Carlo approaches.

[2] The implementation of the mfRG code for the 2D Hubbard model and the analysis of the results are mainly due to A. Tagliavini and C. Hille. The author of this thesis played an important role in deriving the multiloop flow equations for the response functions and contributed to writing the manuscript.

P1 *Fermi-edge singularity and the functional renormalization group*
F. B. Kugler, J. von Delft
J. Phys.: Condens. Matter **30**, 195501 (2018)
DOI: 10.1088/1361-648X/aaba2e
© 2018 IOP Publishing Ltd
Preprint reproduced on pages 34–49.

P2 *Multiloop functional renormalization group that sums up all parquet diagrams*
F. B. Kugler, J. von Delft
Phys. Rev. Lett. **120**, 057403 (2018)
DOI: 10.1103/PhysRevLett.120.057403
© 2018 American Physical Society
reprinted on pages 50–55.
Supplemental Material reproduced on pages 56–61.

P3 *Multiloop functional renormalization group for general models*
F. B. Kugler, J. von Delft
Phys. Rev. B **97**, 035162 (2018)
DOI: 10.1103/PhysRevB.97.035162
© 2018 American Physical Society
reprinted on pages 62–72.

P4 *Multiloop functional renormalization group for the two-dimensional Hubbard model: Loop convergence of the response functions*
A. Tagliavini, C. Hille, **F. B. Kugler**, S. Andergassen, A. Toschi, C. Honerkamp
SciPost Phys. **6**, 009 (2019)
DOI: 10.21468/SciPostPhys.6.1.009
© 2019 The Authors
reprinted on pages 73–120.

P5 *Derivation of exact flow equations from the self-consistent parquet relations*
F. B. Kugler, J. von Delft
New J. Phys. **20**, 123029 (2018)
DOI: 10.1088/1367-2630/aaf65f
© 2018, 2019 The Authors
reprinted on pages 121–139.

arXiv:1706.06872v2 [cond-mat.str-el] 13 May 2018

Fermi-edge singularity and the functional renormalization group

Fabian B. Kugler and Jan von Delft
Physics Department, Arnold Sommerfeld Center for Theoretical Physics, and Center for NanoScience,
Ludwig-Maximilians-Universität München, Theresienstr. 37, 80333 Munich, Germany

(Dated: May 15, 2018)

We study the Fermi-edge singularity, describing the response of a degenerate electron system to optical excitation, in the framework of the functional renormalization group (fRG). Results for the (interband) particle-hole susceptibility from various implementations of fRG (one- and two-particle-irreducible, multi-channel Hubbard-Stratonovich, flowing susceptibility) are compared to the summation of all leading logarithmic (log) diagrams, achieved by a (first-order) solution of the parquet equations. For the (zero-dimensional) special case of the X-ray-edge singularity, we show that the leading log formula can be analytically reproduced in a consistent way from a truncated, one-loop fRG flow. However, reviewing the underlying diagrammatic structure, we show that this derivation relies on fortuitous partial cancellations special to the form of and accuracy applied to the X-ray-edge singularity and does not generalize.

I. INTRODUCTION

Fermi-edge singularities describe infrared divergences in optical spectra arising from the discontinuity of the electronic distribution. The advance in the experimental techniques of cavity quantum electrodynamics [1–3] has renewed the need for a precise understanding of such response functions of degenerate Fermi systems to optical excitation. From a theoretical perspective, the study of the X-ray-edge singularity serves as a prototypical fermionic problem which exhibits a logarithmically divergent perturbation theory [4]. Whereas a solution of the (interband) particle-hole susceptibility via parquet equations [5, 6] amounts to rather involved computational effort, Lange et al. [7] have recently suggested to perform this resummation via simple approximations in a functional renormalization group (fRG) scheme. Here, we confirm that it is, indeed, possible to reproduce the (first-order) parquet result from a truncated, one-loop fRG flow without further approximations. However, a detailed analysis of the underlying diagrammatic structure shows that this conclusion relies on fortuitous partial cancellations special to the X-ray-edge singularity.

In more detail, experimentally, X-ray absorption in metals has been a topic of interest for a long time. Similar measurements with infrared light can be performed using heavily doped semiconductors. Whereas photon absorption in metals typically excites a localized deep core electron, effects due to the mobility of valence-band electrons in semiconductors can significantly alter the absorption spectrum [2]. When a quasi-two-dimensional layer of such a semiconducting material is placed inside an optical cavity, the reversible light-matter coupling leads to the formation of half-light, half-matter excitations, attributed to the so-called polariton [8]. Properties of the microcavity system are deduced from the polariton, i.e., from the photon dressed by light-matter interaction, bringing its self-energy into focus [9–11]. To leading order in the coupling, this self-energy is proportional to the particle-hole susceptibility, well-known from the standard literature on the Fermi-edge singularity [5, 6, 12–15]. The effect of light-matter interaction on the photon is thus governed by a correlation function of the fermionic system.

The basic theoretical formulation of the X-ray-edge singularity involves a localized scattering impurity, corresponding to a deep core level of a metal. In this form, the problem is exactly solvable in a one-body approach, as performed by Nozières and De Dominicis [12]. This approach is, however, limited to the special case that the scattering impurity is structureless. If the problem is tackled in a many-body treatment, the solution can be generalized to more complicated situations and has relevance for other problems involving logarithmic divergences. This includes the Kondo problem [16, 17] as well as the generalization to scattering processes involving a finite-mass valence-band hole, as necessary for the description of optical absorption in semiconductors [13, 14].

In a diagrammatic treatment of the Fermi-edge singularity, logarithmic divergences appear at all orders, demanding resummation procedures. A suitable resummation, containing all leading logarithmic (log) diagrams, can be phrased in terms of parquet equations. These consist of coupled Bethe-Salpeter equations in two-particle channels; here, distinguished by antiparallel or parallel conduction-valence-band lines [5]. Parquet equations can be used in a variety of theoretical applications [18], and it is worthwile to explore whether results comparable or even equivalent to solving those can be obtained by alternative resummation techniques, such as fRG.

The functional renormalization group is a versatile many-body framework, which has proven to give accurate results for low-dimensional fermionic systems [19, 20]. Different realizations and approximations of an exact hierarchy of differential equations for vertex functions allow for rich resummations in the calculation of correlation functions. Inspired by Lange et al. [7], we study the Fermi-edge singularity and show that, for the (zero-dimensional) special case of the X-ray-edge singularity, it actually is possible to analytically derive the (first-order) parquet result from a one-loop fRG scheme. However, this derivation relies on fortuitous partial cancellations of diagrams and cannot be applied to more general situations. We further show that various truncated fRG flows (see below) do not provide a full summation of parquet diagrams. Though this conclusion may seem disappointing, we believe that the analysis by which it was arrived at is very instructive and motivates the extension of *one-loop* fRG by *multiloop* corrections. Indeed, in two follow-up publications [21, 22], we present a multiloop fRG flow that does succeed in summing all parquet diagrams for generic many-body systems.

The paper is organized as follows. In Sec. II, we give the standard formulation of the Fermi-edge and X-ray-edge singularity. The basics of the parquet solution are briefly reviewed in Sec. III, before, in Sec. IV, we introduce the fRG framework in its one-particle- and two-particle-irreducible form. In Sec. V, we apply the fRG flow to the fermionic four-point vertex and construct the particle-hole susceptibility at the end of the flow. Furthermore, we briefly consider the potential of computing this susceptibility using a Hubbard-Stratonovich transformation. In Sec. VI, we rephrase the particle-hole susceptibility as a photonic self-energy to obtain a "flowing susceptibility"; we compare results from using a dynamic and static four-point vertex and use the latter approach to analytically reproduce the parquet formula. We also relate our findings to the work by Lange et al. [7] and show how their treatment can be simplified. Finally, we present our conclusions in Sec. VII.

II. FERMI-EDGE SINGULARITY

In this section, we review the standard formulation of the Fermi-edge singularity for a two-band electron system. We are interested in the (interband) particle-hole susceptibility, describing the response to optical excitation. A typical absorption process, where a photon lifts an electron from the lower to the upper band, is shown in Fig. 1(a). There, we anticipate the simplification to the X-ray-edge singularity, ignoring kinetic energy in the lower band, thereby considering a static, photo-excited scattering impurity.

Before going into detail, let us state more generally the Hamiltonian of the Fermi-edge singularity,

$$H' = \sum_{\boldsymbol{k}} \epsilon_{\boldsymbol{k}} c^\dagger_{\boldsymbol{k}} c_{\boldsymbol{k}} + \sum_{\boldsymbol{k}} E_{\boldsymbol{k}} d^\dagger_{\boldsymbol{k}} d_{\boldsymbol{k}} + \frac{U}{V} \sum_{\boldsymbol{kpq}} c^\dagger_{\boldsymbol{k+q}} c_{\boldsymbol{k}} d^\dagger_{\boldsymbol{p-q}} d_{\boldsymbol{p}}, \tag{1}$$

describing a two-band electron system with interband (screened) Coulomb interaction of the contact type ($U_{\boldsymbol{q}} = U > 0$). The operator $c_{\boldsymbol{k}}$ ($d_{\boldsymbol{k}}$) annihilates an electron in the conduction (valence) band, V is the volume, and the dispersion relations $\epsilon_{\boldsymbol{k}}$, $E_{\boldsymbol{k}}$, account for any intraband interaction in a Fermi-liquid picture. This is supposed to work well when electronic energies close to the Fermi level μ, which we take to be on the order of the conduction-band width, dominate. Using the effective electron and hole masses, m and m_h, one has ($\hbar = 1$)

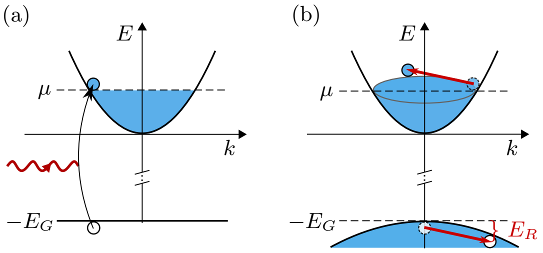

FIG. 1. (Color online) Bandstructure illustrations for two-band electron systems with chemical potential μ and band gap E_G. (a) X-ray absorption in metals typically excites a localized, deep core level to the conduction band. The flat band acts as a two-level scattering impurity for conduction electrons. (b) A similar process occurs with infrared light in (direct-gap) heavily doped semiconductors. Only in the limit of infinite valence-band (hole) mass, one reverts to the situation of (a). Accounting for the mobility of the hole, scattering processes of conduction electrons on top of the Fermi surface cost a finite amount of energy, the recoil energy E_R.

$$\epsilon_{\boldsymbol{k}} = \frac{\boldsymbol{k}^2}{2m}, \qquad E_{\boldsymbol{k}} = -E_G - \frac{\boldsymbol{k}^2}{2m_h}, \qquad E_G > 0. \tag{2}$$

Note that we further ignore Auger-type interactions containing three c or d operators, since such transitions are suppressed by the size of the band gap E_G. This allows us to treat electrons from both bands as different fermion species, each with conserved particle number. With the targeted (leading log) accuracy (cf. Sec. III), including spin degeneracy (while keeping the density-density interaction) only results in a doubled density of states ρ [12]. In two space dimensions, the free density of states is $m/(2\pi)$; in other cases, one approximates ρ by its value at the Fermi level [cf. Eq. (11)].

The particle-hole susceptibility is a two-particle correlation function, given by

$$i\Pi'(\boldsymbol{q}, t) = \frac{1}{V} \sum_{\boldsymbol{k},\boldsymbol{p}} \langle \mathcal{T} d^\dagger_{\boldsymbol{k}}(t) c_{\boldsymbol{k+q}}(t) c^\dagger_{\boldsymbol{p+q}}(0) d_{\boldsymbol{p}}(0) \rangle, \tag{3}$$

with time-ordering operator $\mathcal{T}$. It exhibits an infrared divergence—the Fermi-edge singularity—which is cut by the (valence-band) recoil energy [11, 13] at Fermi momentum, equal to $\mu \cdot m/m_h$ [cf. Fig. 1(b)].

For the case of a polariton experiment using, e.g., a GaAs semiconductor [2], one has a ratio of effective masses between the conduction and heavy-hole-valence band [11] of $m/m_h \sim 0.14$. Considering X-ray absorption in metals, one usually encounters the excitation of a localized, deep core level to the conduction band [cf. Fig. 1(a)]. This motivates the severe simplification of an infinite valence-band (hole) mass, corresponding to a two-level scattering impurity, resulting in the Hamiltonian known from the X-ray-edge singularity, ($\epsilon_d = -E_G < 0$)

$$H = \sum_{\boldsymbol{k}} \epsilon_{\boldsymbol{k}} c^\dagger_{\boldsymbol{k}} c_{\boldsymbol{k}} + \epsilon_d d^\dagger d + \frac{U}{V} \sum_{\boldsymbol{kp}} c^\dagger_{\boldsymbol{k}} c_{\boldsymbol{p}} d^\dagger d. \tag{4}$$

Momentum dependencies in interband quantities are completely absorbed by the infinitely heavy hole, and only the local conduction-band operators play a role:

$$i\Pi(t) = \langle \mathcal{T} d^\dagger(t) c(t) c^\dagger(0) d(0)\rangle, \quad c = \frac{1}{\sqrt{V}}\sum_{\boldsymbol{k}} c_{\boldsymbol{k}}. \qquad (5)$$

Without the intrinsic infrared cutoff of the recoil energy, the (infinite-mass) particle-hole susceptibility shows a true divergence. In a zero-temperature calculation and for small interaction, this takes the form [5, 6, 12]

$$\Pi(\omega) = \frac{\rho}{2u}\Big[1 - \Big(\frac{\omega + \xi_d + i0^+}{-\xi_0}\Big)^{-2u}\Big], \quad u = \rho U. \qquad (6)$$

Here, $-\xi_d = \mu - \epsilon_d = \mu + E_G$ is the threshold frequency and $\xi_0 \sim \mu$ an intrinsic ultraviolet cutoff of the order of the conduction-band width [cf. Eq. (11)]. Note that, for absorption processes, one has an initially fully occupied valence band ($E_G \gg k_B T$), such that $\Pi(t)$ is automatically retarded. Analogously, the valence-band propagator $iG^d(t) = \langle \mathcal{T} d(t) d^\dagger\rangle$ is purely advanced. Although our calculations will proceed in a finite-temperature formalism, we aim to reproduce the result (6). Hence, we numerically consider very low temperatures and perform the zero-temperature limit in analytic calculations. As we attribute the constant Hartree part of a fermionic self-energy to the renormalized band gap E_G, a diagrammatic expansion using $G^d(t) \propto \Theta(-t)$ (with the Heaviside step function) directly shows that conduction-band propagators are not further renormalized by interband interaction.

As already mentioned, the particle-hole susceptibility can also be viewed as the leading contribution (in the light-matter coupling $\rho|M|^2$, M being the dipole matrix element) to a photon self-energy. In the regime under consideration, electronic processes happen on a timescale $1/\mu$ much shorter than typical times of absorption and emission of a photon $1/(\rho|M|^2)$ [11]. For $\mu \gg \rho|M|^2$, one can thus approximate the photon self-energy by an interacting particle-hole bubble, given the standard coupling

$$H'_{\text{cpl}} = \frac{1}{\sqrt{V}}\sum_{\boldsymbol{pq}}\big(M c^\dagger_{\boldsymbol{p}+\boldsymbol{q}} d_{\boldsymbol{p}} a_{\boldsymbol{q}} + M^* d^\dagger_{\boldsymbol{p}} c_{\boldsymbol{p}+\boldsymbol{q}} a^\dagger_{\boldsymbol{q}}\big), \qquad (7)$$

where $a_{\boldsymbol{q}}$ annihilates a photon. For infinite hole mass, the momentum dependence of the photon absorption can no longer be resolved, and we use the simplified coupling

$$H_{\text{cpl}} = M c^\dagger d a + M^* d^\dagger c a^\dagger, \quad \sum_{\boldsymbol{q}} a_{\boldsymbol{q}} = a. \qquad (8)$$

Having defined the system under consideration [Eq. (4)] and the quantity of interest [Eq. (5)], our analysis will proceed in an imaginary-time action formalism. We transform the Grassmann fields for both bands $(c, \bar{c}, d, \bar{d})$ to Matsubara frequencies according to $c_\omega = \int_0^\beta \mathrm{d}\tau\ c(\tau) e^{i\omega\tau}/\sqrt{\beta}$, etc., where $\beta = 1/(k_B T)$. For the X-ray-edge singularity, a change to the position basis immediately shows that conduction-band fields other than the local ones [cf. Eq. (5)] can be integrated out, leading to the action

$$S = -\int_\omega G^{c,-1}_{0,\omega} \bar{c}_\omega c_\omega - \int_\omega G^{d,-1}_{0,\omega} \bar{d}_\omega d_\omega + U \int'_{\omega\nu\bar{\omega}} \bar{d}_\omega d_\nu \bar{c}_{\bar{\omega}+\nu} c_{\bar{\omega}+\omega}. \qquad (9)$$

Here, we have introduced a notation where $\int_\omega$ is a sum over Matsubara frequencies, bosonic Matsubara frequencies are denoted by a bar, and each prime on an integral sign represents a prefactor of $1/\beta$. The zero-temperature limit is then conveniently obtained as

$$\lim_{\beta\to\infty} \int'_\omega f_\omega = \int \frac{\mathrm{d}\omega}{2\pi} f(\omega). \qquad (10)$$

It is worth noting that the action of the more general Fermi-edge singularity, defined by the Hamiltonian (1), is perfectly analogous to the one of the X-ray-edge singularity [Eq. (9)]. One merely has to identify each Matsubara frequency with a double index for frequency and momentum $(\omega, \boldsymbol{k})$ and Matsubara summations with a double sum over frequencies and momenta, the prefactor being $1/(\beta V)$ instead of $1/\beta$. Hence, all diagrammatic and fRG arguments apply simultaneously to the case of finite and infinite hole mass. Only for numerical as well as analytic computations, we restrict ourselves to the (zero-dimensional) special case of the X-ray-edge singularity, such that we can readily ignore any momentum dependence.

Whereas for finite hole mass, the propagator of valence (conduction) electrons is given by $1/(i\omega + \mu - E_{\boldsymbol{k}})$ $[1/(i\omega + \mu - \epsilon_{\boldsymbol{k}})]$, for infinite mass, the valence-band propagator simply reads $G^d_{0,\omega} = 1/(i\omega - \xi_d)$. As we use a parabolic dispersion in the conduction band, we introduce an ultraviolet cutoff $\epsilon_{\boldsymbol{k}} \le \mu + \xi_0$ in momentum space. The choice of a half-filled conduction band, i.e., $\xi_0 = \mu$, yields the particularly simple local propagator

$$G^c_{0,\omega} = \frac{1}{V}\sum_{\boldsymbol{k}} \frac{1}{i\omega - \epsilon_{\boldsymbol{k}} + \mu} = \rho \int_{-\xi_0}^{\xi_0} \mathrm{d}\xi\, \frac{1}{i\omega - \xi} = -2i\rho \arctan(\xi_0/\omega) \approx -i\pi\rho\, \mathrm{sgn}(\omega) \Theta(\xi_0 - |\omega|). \qquad (11)$$

In the last step, we have ignored any details of the ultraviolet cutoff, which are of no physical relevance. Note that different leading log diagrams typically contain the energy range of occupied (μ) or unoccupied conduction band states (ξ_0) in the argument of the logarithm. Minor deviations from half-filling, still in the regime of $|\mu - \xi_0| \ll \xi_0$, have only subleading effects.

Including photon fields $(a, \bar{a})$ into the theory, one might perform a simple transformation for dimensional reasons of the type $\gamma = Ma$, $\bar{\gamma} = M^*\bar{a}$, resulting in a rescaled coupling term

$$S_{\text{cpl}} = \frac{1}{\sqrt{\beta}} \int_{\bar{\omega}\omega} (\bar{c}_{\bar{\omega}+\omega} d_\omega \gamma_{\bar{\omega}} + \bar{d}_\omega c_{\bar{\omega}+\omega} \bar{\gamma}_{\bar{\omega}}). \qquad (12)$$

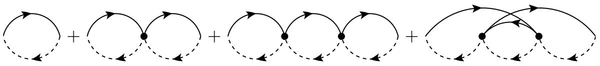

FIG. 2. Particle-hole susceptibility Π [Eq. (13)] up to second order in the interaction, consisting of the first three ladder diagrams [L(0), L(1), L(2)] and the crossed diagram [C(2)]. Full (dashed) lines denote propagators of conduction (valence) electrons. Dots represent bare vertices with a factor $-U$.

Then, in the limit of $M \to 0$, i.e., $G_0^\gamma \propto |M|^2 \to 0$, one obtains the leading contribution to the photon self-energy Π^γ as precisely the particle-hole susceptibility

$$\lim_{M\to 0} \Pi^\gamma_{\bar\omega} = \Pi_{\bar\omega} = \int'_{\omega\nu} \langle \bar d_\omega d_\nu \bar c_{\bar\omega+\nu} c_{\bar\omega+\omega}\rangle. \tag{13}$$

Again, the formula is similarly applicable for the more general Fermi-edge singularity, where $\bar\omega$ denotes frequency and momentum $(\bar\omega, \boldsymbol{q})$. According to the rules of analytic continuation, $i\bar\omega \to \omega + i0^+$, the X-ray-edge singularity written in terms of Matsubara frequencies can directly be inferred from Eq. (6):

$$\Pi_{\bar\omega} = \frac{\rho}{2u}\Big[1 - \Big(\frac{i\bar\omega + \xi_d}{-\xi_0}\Big)^{-2u}\Big]. \tag{14}$$

It is our goal to reproduce this result, originating from a (first-order) solution of the parquet equations, using an fRG scheme. Before getting into the details of fRG, let us briefly review the basics of the parquet solution leading to Eq. (14).

III. FIRST-ORDER PARQUET SOLUTION

We already mentioned that the X-ray-edge singularity has been exactly solved in a one-body approach [12] containing the parquet result (6) in the weak-coupling limit. For the sake of generalizability to actual fermionic many-body problems, one is interested in other (approximate) solutions obtained from a many-body treatment. Roulet et al. [5] have achieved such a solution of the X-ray-edge singularity in leading order of the logarithmic singularity. This *first-order* parquet solution sums up all perturbative terms of the type $u^{n+p} \ln^{n+1} |\xi_0/(\omega + \xi_d)|$, where $p = 0$. These correspond to the leading log (or parquet) diagrams; subleading terms with $p > 0$ are neglected. Such an approximation is applicable for small interaction, $u \ll 1$, and frequencies not too close to the threshold $-\xi_d$. Yet, a subsequent work [6] as well as the exact solution [12] show that, for small coupling, the result actually holds for frequencies arbitrarily close to the threshold.

The lowest-order diagrams for the particle-hole susceptibility, corresponding to the first terms of an expansion of Eq. (14) in u, are shown in Fig. 2. Full lines denote conduction-band (c) and dashed lines valence-band (d) propagators. Self-energy corrections, affecting the d propagator, can be ignored, as discussed later. A bare vertex, symbolized by a solid circle, demands energy(-momentum) conservation and multiplication by $-U$. Apart from that, there are no combinatorial or sign factors attached to diagrams. Free variables are to be integrated over with dimension-full integrals [cf. Eq. (10)].

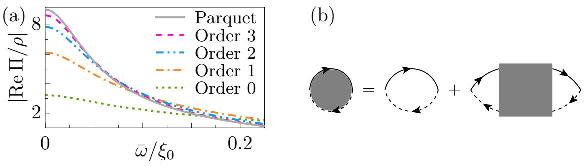

FIG. 3. (a) (Color online) Leading log formula in terms of Matsubara frequencies [Eq. (14)] at increasing orders in the coupling u. Numerical parameters are $u = 0.28$, $|\xi_d/\xi_0| = 1/25$, and the grid for Matsubara frequencies is set by $\beta\xi_0 = 500$. (The same parameters are used throughout this work.) Here, we show (connected) lines for clarity. (b) The particle-hole susceptibility Π (full circle) can be expressed via the bare bubble and the 1PI four-point vertex $\Gamma^{(4)}$, denoted by a full square, according to Eq. (16).

The first three diagrams in Fig. 2 are called ladder diagrams. It is easy to see that taking into account only ladder diagrams leads to the false prediction of a bound state [14]. Crossed diagrams, such as the last diagram in Fig. 2, are crucial for an accurate description and encode screening effects (conduction-band holes) of the Fermi sea. Figure 3(a) shows how the leading log result is built up in an expansion of Eq. (14), exemplified by the real part. Numerical results in Sec. V and Sec. VI aim to reproduce this form. Note that, written in terms of Matsubara frequencies, the particle-hole susceptibility (14) is no longer singular. The seemingly quick convergence of the perturbative curves to the full solution at an interaction parameter $u = 0.28$ in Fig. 3(a) is also due to a rapid decay of the expansion coefficients.

Though, for real frequencies, ξ_d acts as a frequency shift, it is a property of the analytic continuation that, in imaginary-frequency space, different values for ξ_d stretch/flatten the curve. Since we have incorporated the physical effect of the size of the band gap already in the choice of the interaction in the Hamiltonian (1), we can choose any value for ξ_d in our calculations. In order to have a pronounced peak in the Matsubara curve, we take $|\xi_d/\xi_0| = 1/25$, implying $u \ln |\xi_0/\xi_d| \approx 0.9$. Note that, as can be seen from the simple computation of the particle-hole bubble, zero-temperature calculations are discontinuous w.r.t. to ξ_d at $\xi_d = 0$. Choosing $\xi_d = 0$, one loses analytic properties and only obtains the real part of the logarithmic factors depending on $|\bar\omega|$ (cf. App.).

The four-point correlation function in the particle-hole susceptibility can be rephrased by cutting external legs (in general, as dressed propagators G^d, G^c) in the connected part according to [cf., e.g., Eq. (6.92) of Ref. 20]

$$\begin{aligned}\langle \bar d_\omega d_\nu \bar c_{\bar\omega+\nu} c_{\bar\omega+\omega}\rangle &= G^d_\omega G^c_{\bar\omega+\omega} \delta_{\omega,\nu} + G^d_\omega G^d_\nu \\ &\times G^c_{\bar\omega+\omega} G^c_{\bar\omega+\nu} \Gamma^{\bar d c \bar c d}_{\omega,\bar\omega+\omega,\bar\omega+\nu,\nu}/\beta. \end{aligned} \tag{15}$$

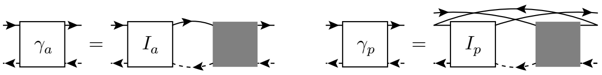

FIG. 4. Bethe-Salpeter equations for both two-particle channels, where γ_a and γ_p are reducible while I_a and I_p are irreducible vertices in antiparallel and parallel conduction-valence-band lines, respectively. The vertices are further related via Eq. (17a).

This introduces the one-particle-irreducible (1PI) four-point vertex $\Gamma^{\bar{d}c\bar{c}d}$. Consequently, the particle-hole susceptibility is fully determined by $\Gamma^{(4)} = \Gamma^{\bar{d}c\bar{c}d}$ via

$$\Pi_{\bar{\omega}} = \int_{\omega}^{\prime} G^d_{\omega} G^c_{\bar{\omega}+\omega} + \int_{\omega\nu}^{\prime\prime} G^d_{\omega} G^d_{\nu} G^c_{\bar{\omega}+\omega} G^c_{\bar{\omega}+\nu} \Gamma^{(4)}_{\omega,\bar{\omega}+\omega,\bar{\omega}+\nu,\nu}, \tag{16}$$

the graphical representation of which is shown in Fig. 3(b).

The parquet equations are then focused on the four-point vertex and use a diagrammatic decomposition in two-particle channels. For the Fermi-edge singularity, the leading log divergence is determined by the two channels characterized by parallel and antiparallel conduction-valence-band lines:

$$\Gamma^{(4)} = R + \gamma_p + \gamma_a, \quad I_p = R + \gamma_a, \quad I_a = R + \gamma_p, \tag{17a}$$

$$\gamma_{a;\,\omega,\bar{\omega}+\omega,\bar{\omega}+\nu,\nu} = \int_{\omega'}^{\prime} I_{a;\,\omega,\bar{\omega}+\omega,\bar{\omega}+\omega',\omega'} G^d_{\omega'} G^c_{\bar{\omega}+\omega'} \times \Gamma^{(4)}_{\omega',\bar{\omega}+\omega',\bar{\omega}+\nu,\nu}, \tag{17b}$$

$$\gamma_{p;\,\omega,\bar{\nu}-\nu,\bar{\nu}-\omega,\nu} = \int_{\omega'}^{\prime} I_{p;\,\omega,\bar{\nu}-\omega',\bar{\nu}-\omega,\omega'} G^d_{\omega'} G^c_{\bar{\nu}-\omega'} \times \Gamma^{(4)}_{\omega',\bar{\nu}-\nu,\bar{\nu}-\omega',\nu}. \tag{17c}$$

Here, R is the totally (two-particle-) irreducible vertex; γ_a and γ_p are reducible while I_a and I_p are irreducible vertices in the antiparallel and parallel channel, respectively. Note that a $\Gamma^{(4)}$ diagram can be reducible in exclusively one of the two channels [5]; diagrams irreducible in both channels belong to R. The Bethe-Salpeter equations for γ_a (17b) and γ_p (17c), which are the crucial components of the parquet equations, are illustrated in Fig. 4.

The parquet equations (17) as such are exact and merely represent a classification of diagrams. In the first-order solution [5] (also referred to as parquet approximation [18]), one approximates the totally irreducible vertex by its bare part, i.e., $R = -U$. To be consistent with the leading log summation (of the X-ray-edge singularity), one further neglects any fermionic self-energies [5, 6]. In fact, it is easily shown that the lowest (non-constant) contribution to Σ^d involves the subleading term $u^2 \ln|\xi_0/(\omega+\xi_d)|$. Similarly, higher-order corrections to R are subleadingly divergent. From the exact solution [12], it is known that extensions of the first-order parquet scheme just lead to the replacement of u by more complicated functions of u in the characteristic form of the particle-hole susceptibility [Eq. (6)]. For weak coupling, it is thus justified to focus on the leading-order result. We will henceforth ignore all fermionic self-energies and omit the index 0 on fermionic propagators when referring to the X-ray-edge singularity. (It should be noted that these arguments do not directly apply to *any* Fermi-edge singularity. In particular, considering a finite-mass valence-band hole, it was shown that Σ^d has a crucial effect on the particle-hole susceptibility and encodes the influence of indirect transitions [11, 13].)

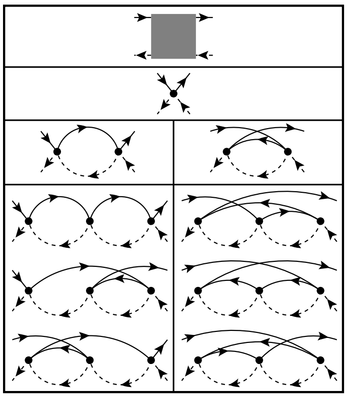

FIG. 5. Parquet graphs for the four-point vertex $\Gamma^{(4)}$, consisting of diagrams reducible in (left) antiparallel lines and (right) parallel lines, up to third order in the interaction. Note that all diagrams are obtained by successively replacing bare vertices by antiparallel and parallel bubbles.

From the parquet equations (17), one can also extract the diagrammatic content of the emergent four-point vertex $\Gamma^{(4)}$. All leading log diagrams (parquet graphs) are obtained by successively replacing bare vertices (starting from the first-order, bare vertex) by parallel and antiparallel bubbles (cf. Fig. 5). Note that such a parquet resummation is the natural extension to two channels of what the ladder summation is to one channel. Having gained insight into the structure of the parquet equations and the leading log diagrams, let us move on to the formalism used in the remainder of this paper.

IV. FUNCTIONAL RENORMALIZATION GROUP

The functional renormalization group (fRG) is a many-body framework, which in principle allows one to examine the renormalization group flow of all coupling constants in their full functional dependence and to obtain diagrammatic resummations of vertex and correlation functions. Its basic idea is to consider the change of a many-body generating functional upon the variation of an artificially introduced scale parameter, which can act as an effective infrared cutoff and allows to successively integrate out high-energy degrees of freedom. This procedure of "zooming out" from microscopic to many-body physics, i.e., the evolution of physical quantities upon lowering the scale

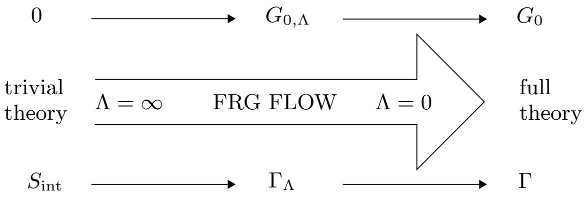

FIG. 6. 1PI fRG flow: The flow parameter Λ, introduced in the quadratic part of the action, makes the theory evolve from a trivial to the original, full one. At the initial scale, the (quantum) effective action Γ can directly be read off from the interacting part of the action S_{int}. Finally, the desired generating functional for 1PI vertices Γ is obtained.

parameter Λ, modulating from a trivial to the full theory (cf. Fig. 6), is described by an exact functional differential equation.

Most commonly, one incorporates the scale parameter in the bare propagator of the theory. Since we are interested in interband quantities such as the particle-hole susceptibility, it is sufficient to modify the propagator of one band alone. As $G^d_{0,\omega}$ follows the typical $1/(i\omega - \xi_d)$ behavior (cf. Sec. II), it is convenient to choose the lower band. The appropriate boundary conditions, to initially ($\Lambda_i = \infty$) extinguish all interband diagrams and finally ($\Lambda_f = 0$) revert to the original theory, are $G^d_{0,\Lambda_i} = 0$, $G^d_{0,\Lambda_f} = G^d_0$.

We will use two alternative realizations with particularly useful computational properties, namely the δ regulator,

$$\begin{aligned} G^d_{0,\Lambda,\,\omega} &= \Theta(|\omega| - \Lambda) G^d_{0,\,\omega} = \frac{\Theta(|\omega| - \Lambda)}{i\omega - \xi_d}, \\ \partial_\Lambda G^d_{0,\Lambda,\,\omega} &= -\delta(|\omega| - \Lambda) G^d_{0,\,\omega} = \frac{-\delta(|\omega| - \Lambda)}{i\omega - \xi_d}, \end{aligned} \tag{18}$$

and the Litim [23] regulator,

$$\begin{aligned} G^d_{0,\Lambda,\,\omega} &= \frac{1}{i\,\mathrm{sgn}(\omega)\max(|\omega|, \Lambda) - \xi_d}, \\ \partial_\Lambda G^d_{0,\Lambda,\,\omega} &= \frac{-i\,\mathrm{sgn}(\omega)\Theta(\Lambda - |\omega|)}{[i\,\mathrm{sgn}(\omega)\Lambda - \xi_d]^2}. \end{aligned} \tag{19}$$

In an exact solution of the flow, all regulators give identical results since, at the end of the flow ($\Lambda_f = 0$), the original theory is restored. However, once approximations are made, the outcomes might differ significantly. In particular, this will happen once the flow of certain quantities does not form a total derivative of diagrams, e.g., due to truncation.

One can consider different functionals paraphrasing the many-body problem under the fRG flow. Two common choices are the (quantum) effective action and the Luttinger-Ward functional serving as generating functionals for one-particle-irreducible (1PI) and two-particle-irreducible (2PI) vertices, respectively. Our study is focused on 1PI fRG flows. We will only briefly mention the 2PI formulation to show that this provides no benefit for our treatment.

A. One-particle-irreducible formulation

The (quantum) effective action Γ is obtained from the (log of the) partition function—in the presence of sources coupled directly to the fields ($S_{\mathrm{src}} = \int_\alpha j_\alpha \varphi_\alpha$)—by a Legendre transformation. Its behavior under the flow is given by the (so-called) Wetterich equation [24]. In the notation of Ref. 20, particularly useful for mixed (fermionic and bosonic) theories, it is stated as

$$\begin{aligned} \partial_\Lambda \Gamma_\Lambda[\bar\varphi] = -\frac{1}{2}\mathrm{STr}\bigg\{ &\Big(\partial_\Lambda G^{-1}_{0,\Lambda}\Big) \\ &\times \bigg(\bigg[\bigg(\frac{\delta^2 \Gamma_\Lambda[\bar\varphi]}{\delta\bar\varphi\,\delta\bar\varphi}\bigg)^{\mathrm{T}} - G^{-1}_{0,\Lambda} \bigg]^{-1} + G_{0,\Lambda} \bigg) \bigg\}. \end{aligned} \tag{20}$$

Here, the super trace runs over multi-indices α, which specify field as well as conjugation indices and all further quantum numbers, and contains a minus sign when summing over fermionic degrees of freedom. If the propagator of all fields is set to zero at the beginning of the flow, the initial condition for Γ is given by the interacting part of the action [20], $\Gamma_{\Lambda_i} = S_{\mathrm{int}}$ (no renormalization of vertices by propagating degrees of freedom is possible). Although we choose only the bare valence-band propagator to be Λ-dependent, all interband quantities are still given by the bare interactions of S_{int}.

In order to tackle the fundamental and in general unsolvable flow equation (20), Γ can be expanded in terms of 1PI n-point vertices $\Gamma^{(n)}$, where we set

$$\Gamma^{(n)}_{\alpha_1 \dots \alpha_n} = \beta^{\frac{n}{2}-1} \frac{\delta^n \Gamma[\bar\varphi]}{\delta\bar\varphi_{\alpha_1} \dots \delta\bar\varphi_{\alpha_n}}\bigg|_{\bar\varphi = 0}. \tag{21}$$

The functional differential equation (20) is transformed into a hierarchy of infinitely many coupled ordinary differential equations with an interesting structure [20]: $\partial_\Lambda \Gamma^{(n)}$ depends on other vertices only up to $\Gamma^{(n+2)}$ and, then, always via $\mathrm{STr}\{\Gamma^{(n+2)} S\}$. Here, S is the (so-called) single-scale propagator $S = -G(\partial_\Lambda G_0^{-1})G$, adding self-energy corrections to a differentiated bare line. Since, with logarithmic accuracy (cf. Sec. III), we can neglect fermionic self-energies, we have the notable simplification $S = \partial_\Lambda G_0$.

The most common truncation of the still unsolvable hierarchy of flow equations is to leave higher-order vertices constant ($\Gamma^{n>n_0}_\Lambda = \Gamma^{n>n_0}_{\Lambda_i}$) yielding a finite set of differential equations. This has a weak coupling motivation, as higher-order vertices typically are of increasing order in the interaction. Furthermore, for a four-point interaction as in our fermionic theory, the only non-zero initial condition of a 1PI interband vertex is $\Gamma^{\bar d c \bar c d} = -U$. Note that, when specifying a vertex, we usually omit the superscript

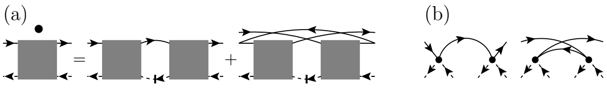

FIG. 7. (a) Diagrammatic representation of the flow equation (22) for $\Gamma^{\bar{d}c\bar{c}d}$ upon neglecting the six-point vertex. The dot denotes the differentiated vertex; lines with a vertical dash symbolize the single-scale propagator. (b) Three-particle vertices $\Phi^{\bar{d}\bar{c}dcd\bar{d}}$ and $\Phi^{\bar{d}c\bar{c}dd\bar{d}}$, responsible for the 2PI fRG flow of I_p and I_a, respectively, at second order in U.

(n) and, instead, write field indices as superscripts and quantum numbers as indices. With the photon included in the theory, we have the additional non-trivial initial condition $\Gamma^{\bar{c}d\gamma}_{\Lambda_i,\,\omega,\omega-\bar{\omega},\bar{\omega}} = 1 = \Gamma^{\bar{d}c\bar{\gamma}}_{\Lambda_i,\,\omega-\bar{\omega},\omega,\bar{\omega}}$ for the mixed three-point vertex.

The flow equations of the individual vertices are obtained by performing the vertex expansion (21) on both sides of the Wetterich equation (20). Given a certain truncation and the above mentioned initial conditions, the set of differential equations can be solved by standard methods, possibly requiring further approximations. Solutions for the self-energy [$\Gamma^{(2)}$] or higher-order vertex functions [$\Gamma^{(n>2)}$] can be used to compute correlation functions, such as the particle-hole susceptibility [cf. Eq. (16)].

For future reference, let us already state the 1PI fRG flow equation for the four-point vertex in the purely fermionic theory [in the matrix notation of Eq. (20), we omit the second index for one-particle quantities: $G^{c\bar{c}}_{\omega,\omega} = G^{c}_{\omega}$, etc.]. To describe the leading logarithmic divergence of the Fermi-edge singularity, we only consider interband combinations of four-point vertices and obtain

$$\begin{aligned}
\partial_\Lambda \Gamma^{\bar{d}c\bar{c}d}_{\Lambda,\,\omega,\bar{\omega}+\omega,\bar{\omega}+\nu,\nu} &= \int_{\omega'}^{\prime} S^{d}_{\Lambda,\,\omega'} \\
&\times \Big(\Gamma^{\bar{d}c\bar{c}d}_{\Lambda,\,\omega,\bar{\omega}+\omega,\bar{\omega}+\omega',\omega'} G^{c}_{\bar{\omega}+\omega'} \Gamma^{\bar{d}c\bar{c}d}_{\Lambda,\,\omega',\bar{\omega}+\omega',\bar{\omega}+\nu,\nu} \\
&\quad + \Gamma^{\bar{d}c\bar{c}d}_{\Lambda,\,\omega,\bar{\nu}-\omega',\bar{\nu}-\omega,\omega'} G^{c}_{\bar{\nu}-\omega'} \Gamma^{\bar{d}c\bar{c}d}_{\Lambda,\,\omega',\bar{\nu}-\nu,\bar{\nu}-\omega',\nu} \\
&\quad + \Gamma^{\bar{d}c\bar{c}d\bar{d}d}_{\Lambda,\,\omega,\bar{\omega}+\omega,\bar{\omega}+\nu,\nu,\omega',\omega'} \Big), \quad \bar{\nu} = \bar{\omega} + \omega + \nu. \qquad (22)
\end{aligned}$$

Without fermionic self-energies, the propagators G^c, G^d, and S^d are known functions. If the fRG hierarchy is further truncated by discarding the six-point vertex, $\Gamma^{(6)}_{\Lambda} = \Gamma^{(6)}_{\Lambda_i} = 0$, the resulting flow equation is closed in itself and can be solved as such. Figure 7(a) illustrates this flow equation, where we denote a single-scale propagator, i.e., a differentiated d line, by a vertical dash next to the arrow. Evidently, the 1PI fRG scheme does not yield separate flow equations for four-point vertices distinguished in two-particle channels, in contrast to the parquet equations (17). However, one immediately sees in Fig. 7(a) that contributions from the first summand are reducible in antiparallel lines, whereas contributions from the second one are reducible in parallel lines. Totally irreducible diagrams are still present in Eq. (22) as initial condition (the bare vertex) and encoded in $\Gamma^{(6)}$, but, importantly, contributions from $\mathrm{STr}\{\Gamma^{(6)}S\}$ are also relevant for higher-order parquet diagrams in both channels (cf. Sec. V). To explore the possibility of treating the two-particle channels separately from the outset, let us sketch the applicability of 2PI fRG to the Fermi-edge singularity.

B. Two-particle-irreducible formulation

The 2PI formulation of fRG is based on the Luttinger-Ward functional Φ, obtained by a Legendre transformation from the (log of the) partition function with sources coupled to two fields ($S_{\mathrm{src}} = \int_{\alpha\alpha'} \varphi_\alpha J_{\alpha\alpha'} \varphi_{\alpha'}$). It can be shown [25] and is intuitive from its diagrammatic expansion that, contrary to Γ, Φ does not explicitly depend on the bare propagator of the theory. The scale dependence is only given by its argument $\mathcal{G}$, representing the full propagator. Therefore, one immediately derives the flow equations

$$\partial_\Lambda \Phi[\mathcal{G}] = \frac{1}{2}\mathrm{STr}\Big\{\frac{\delta\Phi}{\delta\mathcal{G}}\partial_\Lambda\mathcal{G}\Big\}, \qquad (23a)$$

$$\partial_\Lambda \Phi^{(2n)}_{\Lambda,\alpha_1\alpha_1'\ldots\alpha_n\alpha_n'} = \frac{1}{2\beta}\sum_{\tilde{\alpha},\tilde{\alpha}'} \Phi^{(2n+2)}_{\Lambda,\alpha_1\alpha_1'\ldots\alpha_n\alpha_n'\tilde{\alpha}\tilde{\alpha}'} \partial_\Lambda G_{\tilde{\alpha}\tilde{\alpha}'}, \qquad (23b)$$

where G is the physical propagator $\mathcal{G}|_{J=0}$. Equation (23a) has a much simpler structure compared to the Wetterich equation (20). The 2PI n-particle vertices, as coefficients of Φ when expanded around the physical propagator,

$$\Phi^{(2n)}_{\alpha_1\alpha_1'\ldots\alpha_n\alpha_n'} = \beta^{n-1} \frac{\delta^n\Phi}{\delta\mathcal{G}_{\alpha_1\alpha_1'}\ldots\delta\mathcal{G}_{\alpha_n\alpha_n'}}\bigg|_{\mathcal{G}=G}, \qquad (24)$$

are primarily suited (to compute correlation functions) for a purely fermionic theory, where vertices only connect an even number of fields.

Unlike the totally antisymmetric 1PI four-point vertex (where particularly $\Gamma^{\bar{d}c\bar{c}d} = \Gamma^{\bar{d}\bar{c}dc}$), we have $\Phi^{\bar{d}\bar{c}dc} = I_p$ and $\Phi^{\bar{d}c\bar{c}d} = I_a$, implying the desired distinction between the two-particle channels. (Note that the parquet approximation, which considers only the bare vertex as the totally irreducible contribution in I_p and I_a has not yet been made.) In contrast to the parquet equations, the 2PI flow, however, does not interrelate these two-particle vertices; instead, it demands the computation of corresponding three-particle vertices. Moreover, since the 2PI vertices $\Phi^{(2n)}$ are not necessarily 1PI, their initial conditions are more complex than those of $\Gamma^{(n)}$: We have $\Phi^{(2n)}_{\Lambda_i} \neq 0$ for infinitely many n, namely for all $\Phi^{(2n)}$ which contain diagrams without internal valence-band lines [cf. Fig. 7(b)]. Therefore, truncation schemes need to be devised more carefully in the 2PI formulation.

The flow equations for I_p and I_a, deduced from

Eq. (23b),

$$\partial_\Lambda I_{p;\,\omega_1,\omega_2,\omega_3,\omega_4} = \int_\omega' \Phi^{\bar{d}\bar{c}dcd\bar{d}}_{\omega_1,\omega_2,\omega_3,\omega_4,\omega,\omega} \partial_\Lambda G^d_\omega, \tag{25a}$$

$$\partial_\Lambda I_{a;\,\omega_1,\omega_2,\omega_3,\omega_4} = \int_\omega' \Phi^{\bar{d}c\bar{c}dd\bar{d}}_{\omega_1,\omega_2,\omega_3,\omega_4,\omega,\omega} \partial_\Lambda G^d_\omega, \tag{25b}$$

require knowledge about six-point vertices, for which an exact consideration is numerically out of reach (similar to $\Gamma^{(6)}$). The lowest-order diagrams of $\Phi^{\bar{d}\bar{c}dcd\bar{d}}$ and $\Phi^{\bar{d}c\bar{c}dd\bar{d}}$ are depicted in Fig. 7(b). The simplest way of generating a non-perturbative flow is to replace bare vertices with interacting four-point vertices, which are then part of the flow. As opposed to previous proposals, namely to replace the bare interaction $U_{\alpha_1\alpha_2\alpha_3\alpha_4}$ by $\Phi^{(4)}_{\alpha_1\alpha_2\alpha_3\alpha_4}$ [26] or by an average over $\Phi^{(4)}$ with different index permutations [25], we suggest that the diagrammatically most sensible choice is the 1PI four-point vertex. Here, this amounts to replacing $-U$ by $\Gamma^{\bar{d}c\bar{c}d} = \Phi^{\bar{d}\bar{c}dc} + \Phi^{\bar{d}c\bar{c}d} - R$ [cf. Eq. (17a)]. The 1PI four-point vertex $\Gamma^{\bar{d}c\bar{c}d}$ incorporates all possible diagrams; since both 2PI vertices contain the totally irreducible vertex R, it must be subtracted. $\Gamma^{\bar{d}c\bar{c}d}$ also has the full crossing (index-permutation) symmetry as the bare interaction. Overcounting does not occur since both vertices are separated by an open d line and connecting $\partial_\Lambda G$ to this approximation of $\Phi^{\bar{d}\bar{c}dcd\bar{d}}$ and $\Phi^{\bar{d}c\bar{c}dd\bar{d}}$ induces diagrams reducible in antiparallel and parallel lines, respectively. Since no further totally irreducible diagram for the 2PI vertices on top of the initial condition will be generated, it is consistent to use $R = -U$ in the relation for $\Gamma^{\bar{d}c\bar{c}d}$ [Eq. (17a)].

It is possible to evolve I_p and I_a separately, using the above described approximations in Eq. (25), and check the consistence with the parquet equations (17), interrelating both of them, during the flow. However, in the ultimately interesting combination [cf. Eq. (16) and (17)], one has the flow $\partial_\Lambda \Gamma^{\bar{d}c\bar{c}d} = \partial_\Lambda I_p + \partial_\Lambda I_a$. Combining the diagrams of Fig. 7(b) with full vertices and attaching the scale-derived propagator (here, equal to the single-scale propagator), we find exactly the same flow equation for the four-point vertex as given in the truncated 1PI system [Fig. 7(a)]. The replacement of S_Λ by $\partial_\Lambda G$ in the flow of the four-point vertex when neglecting the six-point vertex, which is very natural in the above prescription, is a well known correction [19] that has been found to lead to smaller errors in Ward identities [27]. Finally, we conclude that the above simple 2PI fRG flow does not enrich the possibilities for an fRG treatment of the Fermi-edge singularity compared to the 1PI framework.

V. CORRELATOR FROM EVOLVED VERTICES

In this section, we start to present the results of our fRG treatment of the X-ray-edge singularity. First, we perform the fRG flow of vertices and construct the particle-hole susceptibility at the end of the flow. More precisely, we examine the flow equation (22) in more detail and compare the resulting form of the particle-hole susceptibility, obtained from the relation (16), with the leading log result (14). We briefly check whether it is useful to perform a (multi-channel) Hubbard-Stratonovich transformation to generate parquet diagrams in the particle-hole susceptibility from combining several 1PI vertices, finding that this is not the case.

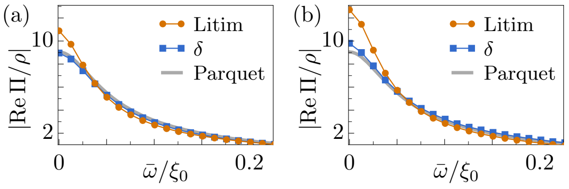

FIG. 8. (Color online) (a) Particle-hole susceptibility Π computed via $\Gamma^{(4)}$ [Eq. (16)], which is obtained from a numerical solution of the truncated flow [cf. Fig. 7(a)]. Different results are generated using a Litim or δ regulator [cf. Eqs. (18), (19)] and compared to the leading log formula (14). (b) Π obtained from a numerical solution of the flow in the light-matter system [Figs. 7(a), 12]. Stronger deviations (for both regulators) from the parquet curve compared to (a) occur since the truncated photon flow neglects derivatives of parallel bubbles.

A. Fermionic four-point vertex

According to Eq. (16), the fermionic four-point vertex is sufficient to compute the particle-hole susceptibility. In Eq. (22), we have already given its flow equation. Since a vertex with more than four arguments (and a meaningful resolution in frequency space) is numerically intractable, we neglect the six-point vertex by truncation and obtain the simplified flow for $\Gamma^{(4)}$ illustrated in Fig. 7(a).

Solving this flow equation numerically with the initial condition $\Gamma^{(4)}_{\Lambda_i} = -U$, the final form of the particle-hole susceptibility [using Eq. (16)] is shown in Fig. 8(a). We find overall qualitative agreement between both the numerical and the analytic curve. Quantitatively, there are disagreements to the leading log result depending on the choice of regulator, which originate from neglecting $\Gamma^{(6)}$ in the flow of Fig. 7(a). The reason why the δ regulator yields much better results than the Litim regulator has recently been clarified in Ref. 21: The former gives less weight to multiloop corrections that are neglected in the present approach.

Let us briefly indicate which types of differentiated diagrams are missing in the flow equation when neglecting $\Gamma^{(6)}$: One can easily check, by inserting the second-order diagrams of $\Gamma^{(4)}$ (cf. Fig. 5) on the l.h.s. and the bare vertex on the r.h.s., that the truncated flow equation [Fig. 7(a)] is satisfied at second order in the interaction. Note that (without fermionic self-energies) a diagram is simply differentiated by summing up all copies of this

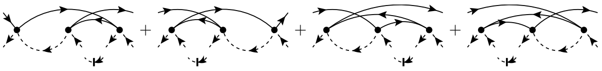

FIG. 9. Third-order contributions from the six-point vertex to the flow of $\Gamma^{(4)}$ via $\mathrm{STr}\{\Gamma^{(6)}S\}$, neglected by the truncated flow in Fig. 7(a). (S is graphically separated for clarity.)

diagram in which one d line is replaced by a single-scale propagator $S = \partial_\Lambda G_0$ at any position (product rule). At third order, however, the simplified flow equation is no longer fulfilled since the six-point vertex [neglected in Fig. 7(a)] starts contributing. Indeed, the four terms coming from $\mathrm{STr}\{\Gamma^{(6)}S\}$, depicted in Fig. 9 (but neglected in the present scheme), generate the remaining derivatives of third-order parquet diagrams (cf. Fig. 5).

We emphasize that all (differentiated) diagrams generated by the truncated flow [Fig. 7(a)] are of the parquet type. Indeed, totally (two-particle-) irreducible diagrams of $\Gamma^{(4)}$ exceeding the bare vertex [corresponding to higher-order contributions of R in the parquet equations (17)] require proper inclusion of the six-point vertex (and intraband four-point vertices). Similar to the recipe given in Sec. III, the truncated flow builds on the bare vertex by incorporating antiparallel and parallel bubbles and therefore only generates parquet graphs. Within the class of leading log diagrams, the six-point vertex is needed to provide *all* derivatives of diagrams of $\Gamma^{(4)}$, starting at third order in U (cf. Fig. 9). In fact, it is easy to see that, in the fRG hierarchy, the parquet graphs comprise (1PI as well as 2PI) n-point vertices of arbitrarily large n: Cutting a valence-band line (without leaving a single conduction-band line in the case of a 1PI description) generates a vertex of order two higher without leaving the class of parquet graphs. The corresponding higher-point vertices are required in the flow via the universal contribution $\mathrm{STr}\{\Gamma_\Lambda^{(n+2)}S_\Lambda\}$ or $\mathrm{STr}\{\Phi_\Lambda^{(n+2)}\partial_\Lambda G_\Lambda\}$ [cf. Eqs. (20), (23b)]. Simply truncating the (purely fermionic) fRG hierarchy of flow equations will thus always dismiss contributions to parquet graphs.

The question of how to sum up all parquet diagrams in the fermionic four-point vertex via fRG is beyond the scope of the present work and is addressed in Ref. 21 using a multiloop flow. Here, instead, we explore various other ways of computing $\Pi_{\bar\omega}$ by using one-loop fRG, proceeding with auxiliary bosonic fields.

B. Hubbard-Stratonovich fields

Hubbard-Stratonovich (HS) transformations are used in the context of several approximation techniques in many-body problems. Such an exact transformation reformulates the fermionic two-particle interaction in terms of propagating auxiliary particles. For instance, the lowest-order contribution to a bosonic self-energy already encodes a ladder summation in the corresponding susceptibility. For a parquet resummation, it seems therefore sensible

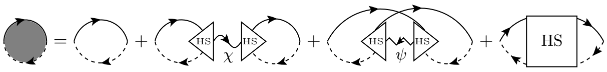

FIG. 10. Particle-hole susceptibility after a HS transformation, determined by HS three-point vertices and the four-point vertex $\Gamma^{(4)}_{\mathrm{HS}}$ (white square). Wavy and zig-zag lines denote dressed bosonic propagators. Both three-point vertices $\Gamma^{\bar c d\chi}$ and $\Gamma^{\bar c\bar d\psi}/i$ are depicted by a triangle and can be distinguished by the attached bosonic line.

to perform a multi-channel HS transformation [7]. With bosonic fields for the exchange (χ) and pairing (ψ) channels, one has the identification

$$
\begin{aligned}
S_{\mathrm{HS}} &= \int_{\bar\omega} U_\chi^{-1}\bar\chi_{\bar\omega}\chi_{\bar\omega} + \frac{1}{\sqrt{\beta}}\int_{\bar\omega\omega}\left(\bar c_{\bar\omega+\omega}d_\omega\chi_{\bar\omega} + \bar d_\omega c_{\bar\omega+\omega}\bar\chi_{\bar\omega}\right) \\
&\quad + \int_{\bar\omega} U_\psi^{-1}\bar\psi_{\bar\omega}\psi_{\bar\omega} + \frac{i}{\sqrt{\beta}}\int_{\bar\omega\omega}\left(\bar c_{\bar\omega+\omega}\bar d_\omega\psi_{\bar\omega} - d_\omega c_{\bar\omega+\omega}\bar\psi_{\bar\omega}\right), \\
S_{\mathrm{int}} &= U\int'_{\omega\nu\bar\omega}\bar d_\omega d_\nu\bar c_{\bar\omega+\nu}c_{\bar\omega+\omega} \to S_{\mathrm{HS}}, \quad U_\chi + U_\psi = U.
\end{aligned}
\tag{26}
$$

Note that one can also set U_χ or U_ψ to zero, such that one HS field effectively decouples from the system.

The more general relation between the particle-hole susceptibility and 1PI vertices in the presence of bosonic fields [cf. Eq. (6.92) of Ref. 20] is illustrated in Fig. 10. Three-point vertices (denoted by triangles) and full bosonic propagators (wavy and zig-zag line) contribute to the correlation function. This proves beneficial in terms of computational effort as, next to the bosonic self-energies, the three-point vertices $\Gamma^{\bar c d\chi}_{\omega,\omega-\bar\omega,\bar\omega}$ and $\Gamma^{\bar c\bar d\psi}_{\omega,\bar\omega-\omega,\bar\omega}/i$ (with initial condition unity) contain less arguments compared to the four-point vertex. However, in Fig. 10, we see that the particle-hole susceptibility is still directly affected by the fermionic four-point vertex (which is one-particle-irreducible in fermionic as well as bosonic lines). The second and third summand on the r.h.s. take the role of a four-point vertex reducible χ and ψ lines, respectively, and the actual four-point vertex still covers all contributions irreducible in these lines. Although the HS transformation by construction ensures that the four-point vertex does not contribute to first order, it does comprise indispensable diagrams starting at second order in the interaction.

In Fig. 11(a), we show the simplest diagrams of $\Gamma^{(4)}_{\mathrm{HS}}$ after the transformation, which now start at second order in U. The lowest-order contributions to these diagrams, obtained by using bare bosonic propagators, represent the second-order ladder [with weight $U_\psi^2 = (G_0^\psi)^2$] and second-order crossed diagram [with weight $U_\chi^2 = (G_0^\chi)^2$], known from Fig. 2 [cf. Figs. 3(b) and 5]. The main contributions of the exchange (χ) and pairing (ψ) boson in Fig. 10 are reducible in the antiparallel and parallel (two-particle) channels, respectively. Correspondingly, the lowest-order diagrams of $\Gamma^{(4)}_{\mathrm{HS}}$ in Fig. 11(a) built from χ and ψ lines are reducible in the complementary channels, i.e., in parallel

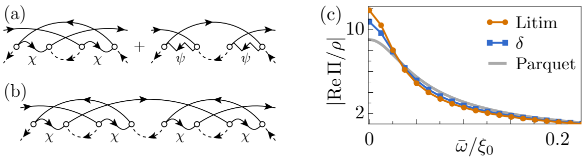

FIG. 11. (Color online) (a) After a HS transformation, $\Gamma^{(4)}_{\text{HS}}$ contributes with the above diagrams, starting at second order, where white circles denote the bare three-point vertices, equal to unity. It is therefore needed to produce all parquet graphs in the correlator. (b) Whereas diagrams of the four-point vertex in (a) that are built from χ lines are irreducible in the (corresponding) antiparallel channel, starting at fourth order, diagrams with χ lines that are reducible in antiparallel (fermionic) lines occur, too. (c) Particle-hole susceptibility Π computed via the relation in Fig. 10 without $\Gamma^{(4)}_{\text{HS}}$, where bosonic self-energies and three-point vertices are obtained from the truncated fRG flow (27), (28), and the interaction strength is divided equally between both channels, $U_\chi = U/2 = U_\psi$.

and antiparallel (fermionic) lines, respectively. However, starting at fourth order in the interaction, also four-point-vertex diagrams with χ lines reducible in the antiparallel channel exist, as is demonstrated in Fig. 11(b) and analogously occurs with ψ lines in the parallel channel. In fact, the diagrams in Fig. 11(a) can be used as building blocks that replace the bare interaction in the original parquet diagrams [cf. Fig. 5] to construct diagrams of $\Gamma^{(4)}_{\text{HS}}$. Yet, this still covers only a fraction of the possible diagrams. We conclude that obtaining the full weight for higher-order parquet contributions to Π via the relation in Fig. 10 requires a complicated, parquet-like resummation of diagrams containing fermionic and bosonic lines in the four-point vertex.

The flow equations for the HS self-energies and three-point vertices can be deduced from the fundamental flow equation (20). When neglecting four-point and higher vertices, they take a form which has already been given in Eqs. (44), (45) of Ref. 7. We repeat them here for the sake of completeness and later purposes. The flow of the self-energies is given by

$$\partial_\Lambda \Pi^{\chi}_{\Lambda,\,\bar{\omega}} = \int_{\omega}' S^{d}_{\Lambda,\,\omega} G^{c}_{\bar{\omega}+\omega} \big(\Gamma^{\bar{c}d\chi}_{\Lambda,\,\bar{\omega}+\omega,\omega,\bar{\omega}}\big)^2, \tag{27a}$$

$$\partial_\Lambda \Pi^{\psi}_{\Lambda,\,\bar{\omega}} = \int_{\omega}' S^{d}_{\Lambda,\,\omega} G^{c}_{\bar{\omega}-\omega} \big(\Gamma^{\bar{c}d\psi}_{\Lambda,\,\bar{\omega}-\omega,\omega,\bar{\omega}}/i\big)^2. \tag{27b}$$

For the three-point vertices, one obtains

$$\begin{aligned}\partial_\Lambda \Gamma^{\bar{c}d\chi}_{\Lambda,\,\omega,\omega-\bar{\omega},\bar{\omega}} = \int_{\omega'}' S^{d}_{\Lambda,\,\omega'} \Gamma^{\bar{c}d\chi}_{\Lambda,\,\bar{\omega}+\omega',\omega',\bar{\omega}} G^{c}_{\bar{\omega}+\omega'} \\ \times \Gamma^{\bar{c}\bar{d}\psi}_{\Lambda,\,\bar{\omega}+\omega',\omega-\bar{\omega},\omega+\omega'}/i\, G^{\psi}_{\Lambda,\,\omega+\omega'} \Gamma^{\bar{c}\bar{d}\psi}_{\Lambda,\,\omega,\omega',\omega+\omega'}/i,\end{aligned} \tag{28a}$$

$$\begin{aligned}\partial_\Lambda \Gamma^{\bar{c}\bar{d}\psi}_{\Lambda,\,\omega,\bar{\omega}-\omega,\bar{\omega}}/i = \int_{\omega'}' S^{d}_{\Lambda,\,\omega'} \Gamma^{\bar{c}\bar{d}\psi}_{\Lambda,\,\bar{\omega}-\omega',\omega',\bar{\omega}}/i\, G^{c}_{\bar{\omega}-\omega'} \\ \times \Gamma^{\bar{c}d\chi}_{\Lambda,\,\bar{\omega}-\omega',\bar{\omega}-\omega,\omega-\omega'} G^{\chi}_{\Lambda,\,\omega-\omega'} \Gamma^{\bar{c}d\chi}_{\Lambda,\,\omega,\omega',\omega-\omega'}.\end{aligned} \tag{28b}$$

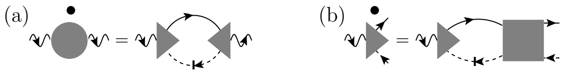

FIG. 12. Truncated flow equations for (a) the photon self-energy Π (depicted as circle) and (b) the photon three-point vertex $\Gamma^{\bar{c}d\gamma}$ (depicted as triangle), where the contributions of $\Gamma^{\bar{d}d\gamma\bar{\gamma}}$ [Eq. (29a)] and $\Gamma^{\bar{c}d\gamma\bar{d}d}$ [Eq. (29b)] are neglected. External (rapidly oscillating) wavy lines denote amputated photon legs. Note that the truncated flow of the four-point vertex $\Gamma^{\bar{d}c\bar{c}d}$ is still given by Fig. 7(a).

To gauge the importance of the HS four-point vertex, we have numerically solved the fRG flow in the HS-transformed system [Eqs. (27), (28)]. The resulting particle-hole susceptibility shown in Fig. 11(c), which is computed using the relation of Fig. 10 without $\Gamma^{(4)}_{\text{HS}}$, shows much stronger deviations from the leading log result than Fig. 8(a), which was obtained using only $\Gamma^{(4)}$. This provides additional, numerical evidence that a HS transformation does not save us from having to calculate the fermionic four-point vertex.

VI. FLOWING SUSCEPTIBILITY

An alternative approach to calculating the particle-hole susceptibility from renormalized 1PI vertices is based on the identification of Π as a bosonic self-energy. In Eq. (13), we have shown how Π is obtained from the self-energy of a rescaled photon field in the limit of its propagator (containing the dipole matrix element) going to zero. Flow equations for the photon self-energy without internal photon propagation thus describe the flow of the particle-hole susceptibility. It should be noted that this appears natural given the interpretation of polariton physics, but can also be seen as a mere computational trick in order to directly include a susceptibility in the fRG flow. In this section, we consider the flow of the photon self-energy in different levels of truncation and comment on the related publication by Lange et al. [7].

A. Dynamic four-point vertex – numerical solution

In the extended theory of the light-matter (photon and fermion) system, we derive from the fundamental flow equation (20) the flow of the photon self-energy and three-point vertex:

$$\partial_\Lambda \Pi_{\Lambda,\,\bar{\omega}} = \int_{\omega}' S^{d}_{\Lambda,\,\omega} \big[G^{c}_{\bar{\omega}+\omega} \big(\Gamma^{\bar{c}d\gamma}_{\Lambda,\,\bar{\omega}+\omega,\omega,\bar{\omega}}\big)^2 + \Gamma^{\gamma\bar{\gamma}\bar{d}d}_{\Lambda,\,\bar{\omega},\bar{\omega},\omega,\omega}\big], \tag{29a}$$

$$\begin{aligned}\partial_\Lambda \Gamma^{\bar{c}d\gamma}_{\Lambda,\,\omega,\omega-\bar{\omega},\bar{\omega}} = \int_{\omega'}' S^{d}_{\Lambda,\,\omega'} \big(\Gamma^{\bar{c}d\gamma}_{\Lambda,\,\bar{\omega}+\omega',\omega',\bar{\omega}} G^{c}_{\bar{\omega}+\omega'} \\ \times \Gamma^{\bar{d}c\bar{c}d}_{\Lambda,\,\omega',\bar{\omega}+\omega',\omega,\omega-\bar{\omega}} + \Gamma^{\bar{c}d\gamma\bar{d}d}_{\Lambda,\,\omega,\omega-\bar{\omega},\bar{\omega},\omega',\omega'}\big).\end{aligned} \tag{29b}$$

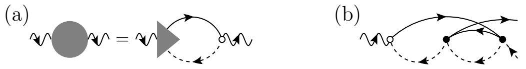

FIG. 13. (a) Schwinger-Dyson equation between photon self-energy and three-point vertex, where the small white circle denotes a bare photon three-point vertex, equal to unity. (b) Second-order diagram of the three-point vertex, which [according to (a)] is responsible for the crossed diagram in the photon self-energy, viz., the particle-hole susceptibility (cf. Fig. 2).

The flow of $\Gamma^{\bar d c \bar c d}$, relevant for the second differential equation (29b), is still given by Eq. (22). In general, three-point vertices connecting bosons and fermions would alter the flow of $\Gamma^{\bar d c \bar c d}$, but in the limit $G_0^\gamma \to 0$ these terms drop out. Similarly, in the absence of propagating photons, one finds that the (interband) flow of $\Gamma^{\gamma\bar\gamma\bar d d}$ is only determined by five- and six-point vertices. At our level of truncation $\Gamma^{(n>4)}_\Lambda = \Gamma^{(n>4)}_{\Lambda_i} = 0$, it is therefore consistent to set $\Gamma^{\gamma\bar\gamma\bar d d}_\Lambda = \Gamma^{\gamma\bar\gamma\bar d d}_{\Lambda_i} = 0$ alongside $\Gamma^{\bar c d\gamma\bar d d}_\Lambda = \Gamma^{\bar c d\gamma\bar d d}_{\Lambda_i} = 0$. The resulting simplified flow is illustrated in Fig. 12.

Note that the diagrammatic expansion of the three-point vertex $\Gamma^{\bar c d\gamma}$ is immediately deduced from the Schwinger-Dyson equation [cf., e.g., Fig. 11.6(b) of Ref. 20] shown in Fig. 13(a). As a consequence of truncation, the connection between Π and $\Gamma^{\bar d c\bar c d}$ generated by the flow (via $\Gamma^{\bar c d\gamma}$, cf. Fig. 12) violates the basic relation between susceptibility and four-point vertex that was given in Eq. (16). This is, however, intended in order to obtain new resummations, given an approximate four-point vertex, from the explicit photon flow.

The numerical solution of the triple set of flow equations for Π, $\Gamma^{\bar c d\gamma}$ (Fig. 12) and $\Gamma^{\bar d c\bar c d}$ [Fig. 7(a)] results in the particle-hole susceptibility shown in Fig. 8(b). The agreement between the numerical solution and the parquet formula is worse compared to Fig. 8(a), where only $\Gamma^{(4)}$ was used to compute Π. The reason is that the additional flow equations in Fig. 12 exclusively contain antiparallel S^d-G^c lines. They therefore induce an imbalance between the two-particle channels and neglect important contributions of diagrams with parallel lines. This begins with the crossed diagram at second order (cf. Fig. 2), which is known [15] to give a positive contribution to the particle-hole susceptibility and thus reduce the infrared divergence.

So far, the more complicated way to generate the particle-hole susceptibility from the four-point vertex, namely the additional photon flow [Eq. (29), Fig. 12] instead of the direct relation [Eq. (16), Fig. 3(b)], has led to worse agreement with the leading log formula. It is an underlying expectation of (vertex-expanded) fRG that, by incorporating more vertices in the flow, one improves the results, coming closer to the exact, infinite hierarchy of flow equations and having agreement with higher orders in perturbation theory. By contrast, in the next section, we show that if we approximate $\Gamma^{\bar d c\bar c d}$ in the simplest fashion possible—namely by the bare vertex—we actually reproduce the precise leading log result.

B. Static four-point vertex – analytic solution

The enormous simplification of using the bare four-point vertex throughout the flow has hardly any justification. Yet, we will show that, with this simplification, the flow equations can be solved analytically to yield the parquet result without further approximations. This demonstrates that one cannot judge about the content of the diagrammatic resummation solely based on the final result for a specific quantity. We will first present a purely algebraic derivation of the leading log formula for the particle-hole susceptibility and then illustrate the steps to diagrammatically understand the underlying structure.

Let us adopt a harsh but concise truncation of the flow equations: we keep all 1PI vertices starting from the four-point vertex at their initial value. The only (interband) contribution with a non-vanishing value at Λ_i is the fermionic four-point vertex $\Gamma^{\bar d c\bar c d}_\Lambda$, which thus remains equal to $-U$ throughout the flow. The simplified flow equations [cf. Eq. (29)] then read

$$\partial_\Lambda \Pi_{\Lambda,\bar\omega} = \int'_\omega S^d_{\Lambda,\omega} G^c_{\bar\omega+\omega} \big(\Gamma^{\bar c d\gamma}_{\Lambda,\bar\omega+\omega,\omega,\bar\omega}\big)^2, \tag{30a}$$

$$\partial_\Lambda \Gamma^{\bar c d\gamma}_{\Lambda,\omega,\omega-\bar\omega,\bar\omega} = -U \int'_{\omega'} S^d_{\Lambda,\omega'} G^c_{\bar\omega+\omega'} \Gamma^{\bar c d\gamma}_{\Lambda,\bar\omega+\omega',\omega',\bar\omega}. \tag{30b}$$

The important observation is that the first derivative (and consequently any higher derivative) of $\Gamma^{\bar c d\gamma}_\Lambda$ is independent of ω, i.e., completely independent of the first argument. (The second argument is fixed by conservation, anyway.) Since also the initial condition is independent of the first argument, the vertex only depends on $\bar\omega$, but not on ω, for all scales. (This is a consequence of our truncation as diagrams of $\Gamma^{\bar c d\gamma}_\Lambda$ such as the one in Fig. 13(b), corresponding to the crossed diagram in the particle-hole susceptibility, do depend on the fermionic frequencies.)

Since $\Gamma^{\bar c d\gamma}_\Lambda$ is independent of ω, the differential equations (30) can be dramatically simplified: Using the definition $g_{\Lambda,\bar\omega} = \big(\Gamma^{\bar c d\gamma}_{\Lambda,\cdot,\cdot,\bar\omega}\big)^2$, we get

$$\partial_\Lambda g_{\Lambda,\bar\omega} = -2U g_{\Lambda,\bar\omega} \int'_\omega S^d_{\Lambda,\omega} G^c_{\bar\omega+\omega}, \tag{31a}$$

$$\partial_\Lambda \Pi_{\Lambda,\bar\omega} = g_{\Lambda,\bar\omega} \int'_\omega S^d_{\Lambda,\omega} G^c_{\bar\omega+\omega} = -\frac{1}{2U}\partial_\Lambda g_{\Lambda,\bar\omega}. \tag{31b}$$

Evidently, $g_{\Lambda,\bar\omega}$ is given by an exponential of an auxiliary function $f_{\Lambda,\bar\omega}$,

$$g_{\Lambda,\bar\omega} = g_{\Lambda_i,\bar\omega} e^{-2uf_{\Lambda,\bar\omega}}, \;\; f_{\Lambda,\bar\omega} = \int_{\Lambda_i}^{\Lambda} \mathrm{d}\Lambda' \int'_\omega S^d_{\Lambda',\omega} G^c_{\bar\omega+\omega}/\rho, \tag{32}$$

and the self-energy becomes

$$\Pi_{\Lambda,\bar\omega} = \Pi_{\Lambda_i,\bar\omega} - \frac{g_{\Lambda_i,\bar\omega}}{2U}\big[e^{-2uf_{\Lambda,\bar\omega}} - 1\big]. \tag{33}$$

Inserting the boundary conditions $\Pi_{\Lambda_i} = 0$ and $g_{\Lambda_i} = 1$,

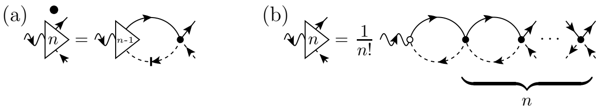

FIG. 14. (a) Flow equation for an approximate $\Gamma^{\bar{c}d\gamma}$ (at order n) when $\Gamma^{\bar{d}c\bar{c}d}$ is reduced to its bare part [cf. Fig. 12(b)]. (b) Its solution, given by sequence of bubbles with a prefactor $1/n!$, a bare photon three-point vertex (equal to unity) and n bare electronic interaction vertices.

when Λ flows from ∞ to 0, we get

$$\Pi_{\bar{\omega}} = \frac{1}{2U}\left[1 - e^{-2uf_{\bar{\omega}}}\right], \quad f_{\bar{\omega}} = \int_{\infty}^{0} \mathrm{d}\Lambda \int'_{\omega} S^d_{\Lambda,\omega} G^c_{\bar{\omega}+\omega}/\rho. \tag{34}$$

So far, fermionic self-energies have not been neglected, yet. However, for the X-ray-edge singularity, we can use $S^d_\Lambda = \partial_\Lambda G^d_\Lambda$ and the Λ-integration becomes trivial. Using the bare bubble, computed in App., Eq. (A.3), we arrive at the remarkable conclusion that our harsh truncation directly yields the leading log result:

$$f_{\bar{\omega}} = \int'_{\omega} G^d_{\omega} G^c_{\bar{\omega}+\omega}/\rho = \ln\left(\frac{i\bar{\omega}+\xi_d}{-\xi_0}\right), \tag{35a}$$

$$\Pi_{\bar{\omega}} = \frac{\rho}{2u}\left[1 - \left(\frac{i\bar{\omega}+\xi_d}{-\xi_0}\right)^{-2u}\right]. \tag{35b}$$

How is this possible? We have argued above that, in the combined, truncated system of flow equations for $\Gamma^{\bar{d}c\bar{c}d}$ and photon quantities, a large class of parquet contributions is missed by the approximate flow due to a mistreatment of parallel bubbles. We will now show diagrammatically why the parquet result could nevertheless be obtained and will find that this is only possible for the X-ray-edge singularity.

The diagrammatic solution of the simplified flow makes extensive use of the property that ladder diagrams factorize into a sequence of (particle-hole) bubbles and that, with leading log accuracy, we can ignore fermionic self-energies and use $S^d = \partial_\Lambda G^d_0$. If we use the bare four-point vertex in the flow of the three-point vertex [Fig. 12(b)], we obtain the flow equation shown in Fig. 14(a), which interrelates contributions to $\Gamma^{\bar{c}d\gamma}$ from subsequent orders. Due to factorization, the solution to this flow equation can be expressed diagrammatically as a three-point vertex which, at order n, consists of n consecutive particle-hole bubbles multiplied by a prefactor $1/n!$ [Fig. 14(b)]. The simple ladder structure is directly related to the fact that $\Gamma^{\bar{c}d\gamma}_{\Lambda,\omega,\omega-\bar{\omega},\bar{\omega}}$ is independent of ω.

Inserting this three-point vertex in the flow equation of the photon self-energy [Fig. 12(a)], we get, at order n, a sequence of $n+1$ bubbles with one single-scale propagator (cf. Fig. 15). Again using factorization, this is a fraction $[1/(n+1)]$ of the derivative of the whole ladder diagram. By computing the sum $\sum_{m=0}^{n} 1/[m!(n-m)!] = 2^n/n!$ in Fig. 15, one ends up with a proportionality relation (at arbitrary order n) between the derivative of the self-energy, $\partial_\Lambda \Pi^{(n)}$, and the derivative of a ladder-diagram, $\partial_\Lambda \Pi^{\mathrm{L}(n)}$. As these quantities also agree at the initial scale (both vanish when $G^d = 0$), we extract an equality at all scales. Using the bare bubble as in Eq. (35a), we get

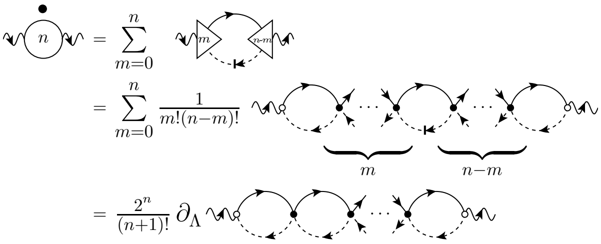

FIG. 15. Inserting the approximate $\Gamma^{\bar{c}d\gamma}$ from Fig. 14(b) in the simplified flow of Π [Fig. 12(a)], we obtain a proportionality relation between ladder diagrams and the particle-hole susceptibility at arbitrary order n, in exact agreement with the leading log result [cf. Eq. (37)].

$$\Pi^{(n)}_{\bar{\omega}} = \frac{2^n}{(n+1)!}\Pi^{\mathrm{L}(n)}_{\bar{\omega}}, \quad \Pi^{\mathrm{L}(n)}_{\bar{\omega}} = (-U)^n (\rho f_{\bar{\omega}})^{n+1}. \tag{36}$$

It remains to sum all orders $\Pi^{(n)}_{\bar{\omega}}$, i.e., sum all ladder diagrams with the appropriate prefactor [cf. Eq. (36)]. Indeed, we precisely reproduce the leading log result

$$\begin{aligned} \Pi_{\bar{\omega}} &= \sum_{n=0}^{\infty} \Pi^{(n)}_{\bar{\omega}} = -\frac{1}{2U}\sum_{n=0}^{\infty} \frac{(-2uf_{\bar{\omega}})^{n+1}}{(n+1)!} \\ &= -\frac{\rho}{2u}\left(e^{-2uf_{\bar{\omega}}} - 1\right) = \frac{\rho}{2u}\left[1 - \left(\frac{i\bar{\omega}+\xi_d}{-\xi_0}\right)^{-2u}\right]. \end{aligned} \tag{37}$$

We observe that *only* ladder diagrams are generated by the flow while crossed diagrams do not contribute at all. However, the ladder diagrams come with prefactors, such as $1/n!$ in Fig. 14(b) and $2^n/(n+1)!$ in Eq. (36). That the correct form of the particle-hole susceptibility is obtained at every order is then possible due to proportionality relations present in the X-ray-edge singularity, such as $\Pi^{\mathrm{L}(2)} = -3\Pi^{\mathrm{C}(2)}$ [cf. Fig. 2], as already shown by Mahan [15] fifty years ago. Yet, these relations only hold with logarithmic accuracy, and in the more general Fermi-edge singularity, where the assumption of an infinite hole mass is lifted, they hold only in a very narrow parametric regime (namely for m/m_h being exponentially small in the coupling u) [11, 13]. For other problems, surely such relations will only hold, if at all, subject to further assumptions. We therefore conclude that obtaining the exact first-order parquet result from a truncated fRG flow with a static four-point vertex is only possible due to a fortuitous partial cancellation of diagrams, specific to the X-ray-edge singularity.

C. Comparison to a work by Lange et al.

In a recent publication, Lange, Drukier, Sharma, and Kopietz [7] (LDSK) have addressed the question of using

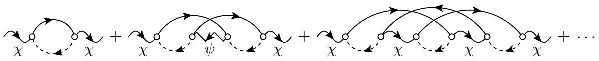

FIG. 16. Diagrams for the χ self-energy Π^χ, expressed with bare three-point vertices (small white circles), equal to unity. At zeroth order in U, Π^χ is given by a bare particle-hole bubble; the only first-order contribution arises from the second diagram using $G_0^\psi = -U_\psi$. Starting at second order in the interaction, Π^χ contains diagrams with internal χ lines, as in the third diagram above.

fRG to tackle the X-ray-edge singularity. In fact, it is their paper which has drawn our attention to the problem at hand and deeply inspired our approach. LDSK, too, obtain the (first-order) parquet formula for the particle-hole susceptibility [our Eq. (14) and their Eq. (54)] and from this draw conclusions about the relation between parquet summations and fRG. We hope that our analysis has further elucidated the derivation of the analytic result and added valuable arguments to the discussion about fRG and parquet graphs. Let us comment on some interesting points from LDSK's treatment in detail.

LDSK extract the particle-hole susceptibility from a bosonic self-energy (Π^χ) arising from a multi-channel Hubbard-Stratonovich (HS) transformation in the exchange (χ, U_χ) and pairing (ψ, U_ψ) channel. They choose (i) equal weights in both channels, $U_\chi = U_\psi$, while we will argue that only the choice $U_\chi = 0$ allows the particle-hole susceptibility to be extracted correctly from the χ self-energy. We will (ii) further show that, with the choice $U_\chi = 0$, one can avoid one of the approximations made by LDSK, namely to take $u \ln(\xi_0/|\bar\omega|) \ll 1$. We will (iii) comment on the similarity between our approximate flow in the light-matter system and LDSK's flow in the HS-transformed system and demonstrate numerically that including the HS-bosonic self-energies weakens the agreement with the parquet result. Furthermore, LDSK use an approximation scheme where all frequency dependencies are initially neglected and finally restored by stopping the RG flow at a final value of $\Lambda_f = \bar\omega$. We will (iv) give an argument, using the δ regulator, for why this scheme successfully leads to the parquet result.

(i) From the actions in Eqs. (12) and (26), it is clear that the HS field in the exchange channel, χ, couples similarly to fermions as the photon field γ. However, just as for the photon [cf. Eq. (13)], it is crucial that the particle-hole susceptibility Π be fully represented by only the *leading* part of the χ self-energy Π^χ, i.e., the part without internal χ propagation. This is easily seen in terms of diagrams (Fig. 16): Π^χ at zeroth order is given by a conduction-valence-band particle-hole bubble, representing the zeroth-order contribution to Π. At first order in the interaction, Π^χ is affected solely by ψ propagation, for an intermediate χ line would result in a reducible diagram. Hence, for Π^χ to fully account for the first-order ladder diagram of Π, the bare ψ propagator must have full weight, $U_\psi = U$. On the other hand, at second and higher orders, Π^χ contains irreducible diagrams with internal χ lines. If one chose $U_\chi > 0$, one would overcount these contributions and not properly generate the second-order order contribution to Π. Hence, the exact parquet graphs for Π can only be reproduced from Π^χ by using $U_\psi = U$ and $U_\chi = 0$.

(ii) Interestingly enough, with the latter choice, the approximate analytic approach of LDSK can be simplified. LDSK use $U_\chi = U_\psi = U$ and arrive at an integration of the frequency-independent, squared χ three-point vertex g_l from a logarithmic scale parameter $l = 0$ up to $l^* = \ln(\xi_0/|\bar\omega|)$. There, they approximate $\cosh(2ul)$ by unity [their Eq. (52)], although $ul \ll 1$ holds no longer when l reaches the upper integration limit, since in the first-order parquet regime $ul^* = u\ln(\xi_0/|\bar\omega|) \lesssim 1$. If one avoids this approximation and instead uses the actual $g_l = e^{2ul}/\cosh(2ul)$ for the integral in LDSK's Eq. (52), one obtains

$$\begin{aligned}\Pi^\chi_{\bar\omega} &= -\rho \int_0^{l^*} \mathrm{d}l\, \frac{e^{2ul}}{\cosh(2ul)} = -\frac{\rho}{2u} \ln\left(\frac{e^{4ul^*}+1}{2}\right) \\ &= -\rho l^* - \rho u l^{*2} + \mathcal{O}(u^3),\end{aligned} \tag{38}$$

This contains no second-order term and thus deviates already at second order in U from the parquet result (14). Note that, with $\xi_d = 0$ (as chosen by LDSK), one can only obtain the real part of the particle-hole susceptibility, solely depending on $|\bar\omega|$ (cf. App.). In this case, an expansion of Eq. (14) yields

$$\begin{aligned}\mathrm{Re}\, \Pi_{\bar\omega}\Big|_{\xi_d=0} &= \frac{\rho}{2u}\left[1 - \left(\frac{|\bar\omega|}{\xi_0}\right)^{-2u}\right] = \frac{\rho}{2u}\left(1 - e^{2ul^*}\right) \\ &= -\rho l^* - \rho u l^{*2} - \tfrac{2}{3}\rho u^2 l^{*3} + \mathcal{O}(u^3).\end{aligned} \tag{39}$$

The reason why performing the integral more accurately leads to an incorrect result is that the expression $g_l = e^{2ul}/\cosh(2ul)$ is inaccurate at second order, since it was obtained using $U_\chi \neq 0$. (Consequently, Π^χ deviates from Π starting at second order, consistent with our diagrammatic argument above.) If, instead, one uses $U_\chi = 0$ and $U_\psi = U$, then Eq. (49a) of LDSK naturally yields $g_l = e^{2ul}$ instead of $g_l = e^{2ul}/\cosh(2ul)$, so that the integration in their Eq. (52) reads

$$\Pi^\chi_{\bar\omega} = -\rho \int_0^{l^*} \mathrm{d}l\; e^{2ul} = \frac{\rho}{2u}\left(1 - e^{2ul^*}\right) \tag{40}$$

and precisely reproduces the result of Eq. (39).

(iii) If one sets $U_\chi = 0$ in LDSK's flow equations (44), (45) [our Eqs. (27), (28)], the three-point vertex $\Gamma^{\bar c d \psi}/i$ remains equal to unity, since $G^\chi = 0$ implies $\partial_\Lambda \Gamma^{\bar c \bar d \psi} = 0$. If one further omits bosonic self-energy reinsertions (as done by LDSK), one has $G^\psi = -U_\psi = -U$. Hence, the resulting flow equations for Π^χ and $\Gamma^{\bar c d \chi}$ reduce to exactly the form of our Eq. (30) (replacing γ by χ). As we have shown, this flow yields the leading log result for the particle-hole susceptibility without further approximations. Actual effects of the multi-channel HS transformation become noticeable only if one actually includes bosonic self-energies

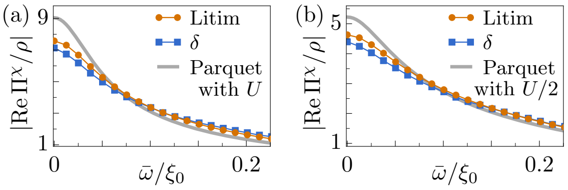

FIG. 17. (Color online) Self-energy of χ, Π^χ, as obtained from the flow in the HS-transformed system (neglecting $\Gamma^{(n>3)}$) [cf. Eqs. (27), (28)]. The interaction strength is divided according to (a) $U_\chi = 0$, $U_\psi = U$ and (b) $U_\chi = U/2 = U_\psi$. Since χ propagation affects Π^χ only starting at second order (cf. Fig. 16), the result in (b) is more similar to the leading log formula with $U/2$.

on the r.h.s. of the HS flow [Eqs. (27), (28)]. Figure 17 shows (a) that, in the case of $U_\chi = 0$, $U_\psi = U$, this spoils the agreement with the leading log result and (b) the strikingly different outcome when using $U_\chi = U_\psi = U/2$. In the latter case, $\Gamma^{\bar{c}\bar{d}\psi}$ contributes non-trivially, and the result is more similar to that of the leading log formula with $U/2$, since the effect of using $U_\chi > 0$ enters only at second and higher orders (cf. Fig. 16). We conclude that a (multi-channel) HS transformation has no advantage over the version advocated in Sec. VI of this work, based on a flowing susceptibility in the fermionic system.

(iv) In their analytic solution of the flow, LDSK use an approximation scheme where frequency dependencies in all 1PI vertices were omitted initially. Viewing this as a low-energy approximation, they let Λ flow from ξ_0 to $\bar{\omega}$ instead of the expected range ∞ to 0. From another perspective, this integration range for Λ can be obtained by computing the "single-scale" bubble [Eq. (41)] with the δ regulator. As explained above, LDSK's system of flow equations with $U_\chi = 0$ and $G^\psi = -U$ can be directly related to our photon flow in Eq. (30). We have shown that the $\bar{\omega}$-dependence enters only in the (integrated) single-scale bubble [$f_{\bar{\omega}}$ in Eq. (34)], which can also be integrated *first* w.r.t. frequency and *then* w.r.t. Λ. Making use of the δ regulator, $\xi_d = 0$ (such that $|\bar{\omega}| \ll \xi_0$), and the (simplified) local c propagator [Eq. (11)], one readily obtains

$$\begin{aligned}
\int_\omega' S^d_{\Lambda,\omega} G^c_{\bar{\omega}+\omega}/\rho &= \int_{-\xi_0-\bar{\omega}}^{\xi_0-\bar{\omega}} \mathrm{d}\omega\ \mathrm{sgn}(\bar{\omega}+\omega)\frac{\delta\big(|\omega|-\Lambda\big)}{2\omega} \\
&\approx \int_{-\xi_0}^{\xi_0} \mathrm{d}\omega\ \mathrm{sgn}(\bar{\omega}+\omega)\frac{\delta\big(|\omega|-\Lambda\big)}{2\omega} \\
&= \Theta\big(\xi_0-\Lambda\big)\sum_{\omega=\pm\Lambda}\frac{\mathrm{sgn}(\bar{\omega}+\omega)}{2\omega} \\
&= \frac{\Theta\big(\xi_0-\Lambda\big)\Theta\big(\Lambda-|\bar{\omega}|\big)}{\Lambda}. \qquad (41)
\end{aligned}$$

Using this as a factor in the relevant flow equations, similarly as in Eq. (31), naturally restricts the integration range for Λ precisely in the way chosen by LDSK.

VII. CONCLUSIONS

We have analyzed the X-ray-edge (zero-dimensional Fermi-edge) singularity—an instructive fermionic problem with simplified diagrammatics focused on two-particle quantities, an analytic parquet and exact one-body solution. Our goal was to use the functional renormalization group to achieve a partial resummation of diagrams, to be compared to the (first-order) solution of the parquet equations. We compared results for the particle-hole susceptibility with the leading log formula in terms of Matsubara frequencies and examined the diagrammatic structure of the flow equations. We found that different realizations of a truncated, one-loop fRG flow do not fully generate the leading log diagrams.

Focusing on the flow of the fermionic four-point vertex $\Gamma^{(4)}$ first, we argued that, in the fRG hierarchy, the parquet diagrams comprise (1PI and 2PI) vertices of any order, and that these higher-order vertices, obtained by cutting appropriate scale-dependent lines, universally contribute to the flow. Hence, simply truncating the fRG hierarchy of flow equations will always miss contributions to parquet graphs. We further showed that a (multichannel) Hubbard-Stratonovich transformation does not remedy this problem: Although the transformation ensures that $\Gamma^{(4)}_{\mathrm{HS}}$ does not contribute to the particle-hole susceptibility Π at first order, it does contribute important, parquet diagrams to Π starting at second order in the interaction, which are lost when the four-point vertex is neglected.

As a different approach, we included Π in the fRG flow as a (leading contribution to a) photon self-energy (i.e., as a flowing susceptibility). We showed that the relation between $\Gamma^{(4)}$ and Π generated by truncated flow equations systematically misses contributions from parallel bubbles. However, in contrast to the underlying philosophy of fRG, we found an *improved* result for Π when treating the four-point vertex *less* accurately. In fact, we analytically reproduced the leading log formula using a truncated fRG flow that keeps four-point and higher vertices *constant*. We showed that, in this way, one effectively *only* sums up ladder diagrams, but with a set of prefactors that fortuitously turns out to precisely yield the correct form of Π. This is possible thanks to proportionality relations of ladder and crossed diagrams, which, however, only hold with logarithmic accuracy and are violated when extending the theory, e.g., to a finite-mass valence-band description. Our derivation of the (first-order) parquet result from a truncated fRG flow using a static four-point vertex is thus only possible due to a fortuitous partial cancellation of diagrams specific to the X-ray-edge singularity.

In related publications [21, 22], we show how the truncated flow equations *can* actually be extended to capture all parquet graphs. This *multiloop* fRG flow simulates the effect of the six-point vertex on parquet contributions and iteratively completes the derivative of diagrams in the flow equations of both four-point vertex and self-energy.

ACKNOWLEDGMENTS

We thank D. Pimenov, D. Schimmel, and L. Weidinger for useful discussions and P. Kopietz for a helpful correspondence. We acknowledge support by the Cluster of Excellence Nanosystems Initiative Munich; F.B.K. acknowledges funding from the research school IMPRS-QST.

Appendix: Particle-hole bubble

In this section, we explicitly compute the bare (interband) particle-hole bubble, needed in Sec. VI, Eq. (35). We also show that this bubble is discontinous w.r.t. the bandgap $-\xi_d$ at $\xi_d = 0$. Thus, we choose ξ_d suitably small (cf. Sec. III) but nonzero in our numerical calculations.

The bare bubble is given by the integral

$$\begin{aligned} \Pi_{0,\bar\omega} &= \int_\omega' G_0^c(\bar\omega+\omega) G_0^d(\omega) \\ &= -i\pi\rho \int_\omega' \frac{\mathrm{sgn}(\bar\omega+\omega)\Theta(\xi_0 - |\bar\omega+\omega|)}{i\omega - \xi_d} \\ &= \Pi^*_{0,-\bar\omega}, \end{aligned} \tag{A.1}$$

which we divide into three parts: $\Pi_{0,\bar\omega} = I_1 + I_2 + I_3$. We first consider $\bar\omega > 0$, revert to frequency integrals in the zero-temperature limit [cf. Eq. (10)], and obtain

$$I_1 = \frac{\rho}{2i}\int_{\bar\omega}^{\xi_0-\bar\omega} \frac{\mathrm{d}\omega}{i\omega-\xi_d} = \frac{\rho}{2}\ln\left(\frac{i\bar\omega-\xi_d}{i\xi_0 - i\bar\omega - \xi_d}\right), \tag{A.2a}$$

$$I_2 = \frac{\rho}{2i}\int_{-\bar\omega}^{\bar\omega} \frac{\mathrm{d}\omega}{i\omega-\xi_d} = \frac{\rho}{2}\ln\left(\frac{-i\bar\omega-\xi_d}{i\bar\omega-\xi_d}\right), \tag{A.2b}$$

$$I_2 = i\rho\int_0^{\bar\omega} \mathrm{d}\omega\, \frac{\xi_d}{(\xi_d)^2+(\bar\omega)^2} = i\rho\arctan\left(\frac{\bar\omega}{\xi_d}\right), \tag{A.2c}$$

$$I_3 = \frac{i\rho}{2}\int_{-\xi_0-\bar\omega}^{-\bar\omega} \frac{\mathrm{d}\omega}{i\omega-\xi_d} = \frac{\rho}{2}\ln\left(\frac{i\bar\omega+\xi_d}{i\xi_0 + i\bar\omega + \xi_d}\right). \tag{A.2d}$$

In the form of Eq. (A.2c), one can directly see that the integral I_2 is discontinuous w.r.t. ξ_d at $\xi_d = 0$. Essentially, the contribution from I_2 is needed to produce the correct phase in the susceptibility, when summing I_1, I_2, and I_3. Using the fact that, upon analytic continuation to real frequencies, one has $|i\bar\omega + \xi_d| \to |\omega + \xi_d + i0^+| \ll \xi_0$, we obtain the approximate form

$$\begin{aligned} \Pi_{0,\bar\omega} &= \frac{1}{2}\ln\left(\frac{i\bar\omega+\xi_d}{i\bar\omega+\xi_d-i\xi_0}\right) + \frac{1}{2}\ln\left(\frac{i\bar\omega+\xi_d}{i\bar\omega+\xi_d+i\xi_0}\right) \\ &\approx \frac{1}{2}\ln\left(\frac{i\bar\omega+\xi_d}{-i\xi_0}\right) + \frac{1}{2}\ln\left(\frac{i\bar\omega+\xi_d}{i\xi_0}\right) \\ &= \ln\left(\frac{i\bar\omega+\xi_d}{-\xi_0}\right), \end{aligned} \tag{A.3}$$

which also holds for negative frequencies according to the symmetry relation $\Pi_{0,\bar\omega} = \Pi^*_{0,-\bar\omega}$.

If, instead, one sets $\xi_d = 0$ in the first place, one in effect omits the contribution from I_2 [cf. Eq. (A.2c)]. With the approximation $|i\bar\omega| \ll \xi_0$, one then obtains from $I_1 + I_3$:

$$\begin{aligned} \Pi_{0,\bar\omega}\Big|_{\xi_d=0,\,\bar\omega>0} &= \frac{1}{2}\ln\left(\frac{i\bar\omega}{i\xi_0 - i\bar\omega}\right) + \frac{1}{2}\ln\left(\frac{i\bar\omega}{i\xi_0+i\bar\omega}\right) \\ &\approx \ln\left(\frac{\bar\omega}{\xi_0}\right). \end{aligned} \tag{A.4}$$

Reverting to positive and negative frequencies via Eq. (A.1) again, we finally get

$$\Pi_{0,\bar\omega}\Big|_{\xi_d=0} = \ln\left(\frac{|\bar\omega|}{\xi_0}\right). \tag{A.5}$$

Having set $\xi_d = 0$, one only obtains the real part of the particle-hole bubble, solely depending on $|\bar\omega|$. Moreover, in contrast to the real-frequency calculations of Roulet et. al [5], who focus on the real part and argue that the imaginary part can be reconstructed by Kramers-Kronig relations, this is not possible in the Matsubara framework, where one does *not* have such relations between Re Π and Im Π. We conclude that one should therefore refrain from setting $\xi_d = 0$.

[1] A. Gabbay, Y. Preezant, E. Cohen, B. M. Ashkinadze, and L. N. Pfeiffer, Phys. Rev. Lett. **99**, 157402 (2007).

[2] S. Smolka, W. Wuester, F. Haupt, S. Faelt, W. Wegscheider, and A. Imamoglu, Science **346**, 332 (2014).

[3] M. Sidler, P. Back, O. Cotlet, A. Srivastava, T. Fink, M. Kroner, E. Demler, and A. Imamoglu, Nat. Phys. **13**, 255 (2016).

[4] T. Giamarchi, *Quantum Physics in One Dimension* (Clarendon Press, 2004) p. 347.

[5] B. Roulet, J. Gavoret, and P. Nozières, Phys. Rev. **178**, 1072 (1969).

[6] P. Nozières, J. Gavoret, and B. Roulet, Phys. Rev. **178**, 1084 (1969).

[7] P. Lange, C. Drukier, A. Sharma, and P. Kopietz, J. Phys. A **48**, 395001 (2015).

[8] I. Carusotto and C. Ciuti, Rev. Mod. Phys. **85**, 299 (2013).

[9] N. S. Averkiev and M. M. Glazov, Phys. Rev. B **76**, 045320 (2007).

[10] M. Baeten and M. Wouters, Phys. Rev. B **89**, 245301 (2014); Eur. Phys. J. D **69**, 243 (2015).

[11] D. Pimenov, *Fermi-edge polaritons with finite hole mass*, Master's thesis, Ludwig-Maximilians-Universität München (2015); D. Pimenov, J. von Delft, L. Glazman, and M. Goldstein, Phys. Rev. B **96**, 155310 (2017).

[12] P. Nozières and C. T. De Dominicis, Phys. Rev. **178**, 1097 (1969).

[13] J. Gavoret, P. Nozières, B. Roulet, and M. Combescot, J. Phys. France **30**, 987 (1969).

[14] G. D. Mahan, Phys. Rev. **153**, 882 (1967).

[15] G. D. Mahan, Phys. Rev. **163**, 612 (1967).

[16] A. A. Abrikosov, Physics **2**, 5 (1965).

[17] K. Fukushima, Prog. Theor. Phys. **46**, 1307 (1971).

[18] N. Bickers, in *Theoretical Methods for Strongly Correlated Electrons*, CRM Series in Mathematical Physics, edited by D. Sénéchal, A.-M. Tremblay, and C. Bourbonnais (Springer New York, 2004) pp. 237–296.

[19] W. Metzner, M. Salmhofer, C. Honerkamp, V. Meden, and K. Schönhammer, Rev. Mod. Phys. **84**, 299 (2012).

[20] P. Kopietz, L. Bartosch, and F. Schütz, *Introduction to the Functional Renormalization Group (Lecture Notes in Physics)* (Springer, Berlin, 2010).

[21] F. B. Kugler and J. von Delft, Phys. Rev. Lett. **120**, 057403 (2018).

[22] F. B. Kugler and J. von Delft, Phys. Rev. B **97**, 035162 (2018).

[23] D. F. Litim, Phys. Rev. D **64**, 105007 (2001).

[24] C. Wetterich, Phys. Lett. B **301**, 90 (1993).

[25] J. F. Rentrop, S. G. Jakobs, and V. Meden, J. Phys. A **48**, 145002 (2015).

[26] N. Dupuis, Eur. Phys. J. B **48**, 319 (2005).

[27] A. A. Katanin, Phys. Rev. B **70**, 115109 (2004).

Multiloop Functional Renormalization Group That Sums Up All Parquet Diagrams

Fabian B. Kugler and Jan von Delft
Physics Department, Arnold Sommerfeld Center for Theoretical Physics, and Center for NanoScience, Ludwig-Maximilians-Universität München, Theresienstrasse 37, 80333 Munich, Germany

(Received 9 August 2017; published 31 January 2018)

We present a multiloop flow equation for the four-point vertex in the functional renormalization group (FRG) framework. The multiloop flow consists of successive one-loop calculations and sums up all parquet diagrams to arbitrary order. This provides substantial improvement of FRG computations for the four-point vertex and, consequently, the self-energy. Using the x-ray–edge singularity as an example, we show that solving the multiloop FRG flow is equivalent to solving the (first-order) parquet equations and illustrate this with numerical results.

DOI: 10.1103/PhysRevLett.120.057403

Introduction.—Two-particle correlations play a fundamental role in the theory of strongly correlated electron systems. Most response functions measured in condensed-matter experiments are two-particle quantities such as optical or magnetic susceptibilities. The behavior of the two-particle (or four-point) vertex has even been used to distinguish "weakly" and "strongly" correlated regions in the phase diagram of the Hubbard model [1]. Moreover, the four-point vertex is a crucial ingredient for a large number of theoretical methods to study strongly correlated electron systems, such as nonlocal extensions of the dynamical mean-field theory [2]—particularly, via dual fermions [3], the 1PI [4], and QUADRILEX [5] approach, or the dynamical vertex approximation [6]—the multiscale approach [7], the functional renormalization group [8,9], and the parquet formalism [10,11].

The parquet equations provide an exact set of self-consistent equations for vertex functions at the two-particle level and are thus able to treat particle and collective excitations on equal footing. In the first-order [10] (or so-called *parquet* [11]) approximation, they constitute a viable many-body tool [11–13] and, in logarithmically divergent perturbation theories, allow for an exact summation of all leading logarithmic diagrams of the four-point vertex (*parquet* diagrams [10]). It is a common belief [14] that results of the parquet approximation are equivalent to those of the one-loop renormalization group (RG). However, there is hardly any evidence of this statement going beyond the level of (static) flowing coupling constants [15].

Recently, the question was raised [16] whether it is possible to sum up all parquet diagrams using the functional renormalization group (FRG), a widely used realization of a quantum field-theoretical RG framework [8,9]. The parquet result for the x-ray–edge singularity (XES) [10,17–19] was indeed obtained [16], but using arguments that work only for this specific problem and do not apply generally [20]. In fact, the common truncation of the vertex-expanded FRG flow completely neglects contributions from the six-point vertex, which start at third order in the interaction. Schemes have been proposed for including some contributions from the six-point vertex [21–23]; however, until now it was not known how to do this in a way that captures all parquet diagrams.

In this work, we present a multiloop FRG (MFRG) scheme, which sums up all parquet diagrams to arbitrary order in the interaction. We apply it to the XES, a prototypical fermionic problem with a logarithmically divergent perturbation theory [24]; in a related publication [25], we develop the MFRG framework for general models. The XES allows us to focus on two-particle quantities, as these are solely responsible for the leading logarithmic divergence [10,17], and exhibits greatly simplified diagrammatics. In fact, it contains the minimal structure required to study the complicated interplay between different two-particle channels. We demonstrate how increasing the number of loops in the MFRG improves the numerical results with respect to the known solution of the parquet equations [10,17,18]. We establish the equivalence of the MFRG flow to the parquet approximation by showing that both schemes generate the same number of diagrams order for order in the interaction [26].

Model.—The minimal model for the XES is defined by the Hamiltonian

$$H = \sum_{\epsilon} \epsilon c_{\epsilon}^{\dagger} c_{\epsilon} + \epsilon_d d^{\dagger} d + U c^{\dagger} c d^{\dagger} d, \qquad U > 0. \qquad (1)$$

Here, d and c_{ϵ}, respectively, annihilate an electron from a localized, deep core level ($\epsilon_d < 0$) or a half-filled conduction band with constant density of states ρ, half-bandwidth ξ_0, and chemical potential $\mu = 0$, while $c = \sum_{\epsilon} c_{\epsilon}$ annihilates a band electron at the core-level site. In order to describe optical properties of the system, one examines the particle-hole susceptibility $i\Pi(t) = \langle \mathcal{T} d^{\dagger}(t) c(t) c^{\dagger}(0) d(0) \rangle$. It exhibits a power-law divergence for frequencies close

© 2018 American Physical Society

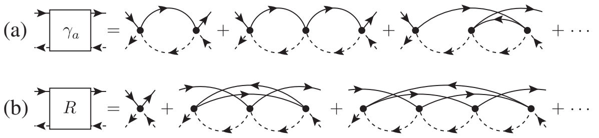

FIG. 1. Low-order diagrams for (a) the vertex reducible in antiparallel lines, γ_a, and (b) the totally irreducible vertex R. Solid (dashed) lines denote G^c (G^d), and a dot the bare vertex $-U$. The first-order or so-called parquet approximation only retains the bare vertex for R.

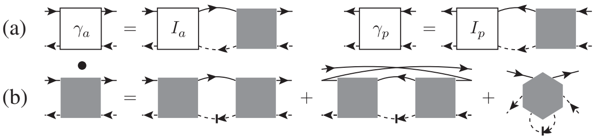

FIG. 2. (a) Bethe-Salpeter equations in the antiparallel (a) and parallel (p) channels. A full square denotes the full vertex $\Gamma^{(4)}$. (b) FRG flow equation for both channels relating $\partial_\Lambda \Gamma^{(4)}$ to $\Gamma^{(4)}$ and $\Gamma^{(6)}$. The conventional approximation is to set $\Gamma^{(6)} = 0$.

to the absorption threshold, as found both by the solution of parquet equations [10,17] and by an exact one-body approach [18].

In the Matsubara formalism, the bare level propagator reads $G^d_\omega = 1/(i\omega - \epsilon_d)$, and, focusing on infrared properties, we approximate the local band propagator as $G^c_\omega = -i\pi\rho\,\mathrm{sgn}(\omega)\Theta(\xi_0 - |\omega|)$. The particle-hole susceptibility takes the form (at a temperature $1/\beta \ll |\epsilon_d|$)

$$\Pi_{\bar\omega} = \frac{\rho}{\alpha(u)}\left[1 - \left(\frac{i\bar\omega + \epsilon_d}{-\xi_0}\right)^{-\alpha(u)}\right], \qquad u = \rho U, \tag{2}$$

where $\alpha(u) = 2u + O(u^2)$ and ϵ_d is considered as a renormalized threshold. The corresponding retarded correlation function is obtained by analytic continuation $i\bar\omega \to w + i0^+$, in which case the summands leading to the power law are logarithmically divergent as $u^n \ln^{n+1}(\xi_0/|w + \epsilon_d|)$. For imaginary frequencies, however, the perturbative parameter is finite, with a maximal value of $u\ln(\xi_0/|\epsilon_d|) \approx 0.9$, for our choice of parameters. Our goal will be to reproduce Eq. (2) using the FRG.

Parquet formalism.—The particle-hole susceptibility is fully determined by the one-particle-irreducible (1PI) four-point vertex via the following relation (using the shorthand notation $\Gamma^{(4)}_{\omega,\nu,\bar\omega} = \Gamma^{\bar d c \bar c d}_{\omega,\bar\omega+\omega,\bar\omega+\nu,\nu}$ [20]):

$$\Pi_{\bar\omega} = \frac{1}{\beta}\sum_{\omega} G^d_\omega G^c_{\bar\omega+\omega} + \frac{1}{\beta^2}\sum_{\omega,\nu} G^d_\omega G^c_{\bar\omega+\omega} \Gamma^{(4)}_{\omega,\nu,\bar\omega} G^d_\nu G^c_{\bar\omega+\nu}. \tag{3}$$

In principle, G^c and G^d are full propagators. However, for the XES, electronic self-energies do not contribute to the leading logarithmic divergence [10,17], and we can restrict ourselves to bare propagators.

Diagrams for the four-point vertex are exactly classified by the central parquet equation

$$\Gamma^{(4)} = R + \gamma_a + \gamma_p, \qquad I_a = R + \gamma_p, \qquad I_p = R + \gamma_a. \tag{4}$$

The leading divergence of the XES is determined by only two two-particle channels [10,17]: γ_a (cf. Fig. 1(a) [29]) and γ_p contain diagrams reducible by cutting two antiparallel or parallel lines, respectively, whereas I_a and I_p contain diagrams irreducible in the respective channel. The totally irreducible vertex R [cf. Fig. 1(b)] is the only input into the parquet equations, as the reducible vertices are determined self-consistently via Bethe-Salpeter equations [cf. Fig. 2(a)]. Similarly as for the self-energy, terms of R beyond the bare interaction only contribute subleadingly to the XES and can hence be neglected [10,17].

In this (parquet) approximation, Eq. (4) together with the Bethe-Salpeter equations for reducible vertices [Fig. 2(a)] form a closed set and can be solved. The analytic solution, employing logarithmic accuracy, provides the leading term of the exponent in Eq. (2). Our numerical solution, to which we compare all following results, is both consistent with the power-law-like behavior of Eq. (2) for small frequencies [cf. Fig. 4(c)] and with the corresponding exponent $\alpha(u)$ [cf. Fig. 4(d)].

Multiloop FRG flow.—The functional renormalization group provides an exact flow equation for the four-point vertex as a function of a RG scale parameter Λ, serving as infrared cutoff. Introducing Λ only in the bare d propagator, the flow encompassing both channels [26] is illustrated in Fig. 2(b), where the dashed arrow symbolizes the single-scale propagator S^d_Λ. Neglecting self-energies, we have $S^d_\Lambda = \partial_\Lambda G^d_\Lambda$, and $\partial_\Lambda \Gamma^{(4)}$ only depends on $\Gamma^{(4)}$ and $\Gamma^{(6)}$. The boundary conditions $G^d_{\Lambda_i} = 0$ and $G^d_{\Lambda_f} = G^d$ imply $\Gamma^{(4)}_{\Lambda_i} = -U$ and $\Gamma^{(6)}_{\Lambda_i} = 0$.

For almost all purposes, it is unfeasible to treat the six-point vertex exactly. Approximations of $\Gamma^{(6)}$ thus render the FRG flow approximate. The conventional approximation is to set $\Gamma^{(6)}$ and all higher-point vertices to zero, arguing that they are at least of third order in the interaction. This affects the resulting four-point vertex starting at third order and neglects terms that contribute to parquet diagrams [20]. Since, however, the parquet approximation involves *only* four-point vertices, it should be possible to encode the influence of six- and higher-point vertices during the RG flow by four-point contributions and, still, *fully* capture all parquet graphs.

In the following, we show how this can be accomplished using the MFRG. The first observation is that all the diagrammatic content of the truncated FRG (i.e., without $\Gamma^{(6)}$) is two-particle reducible, due to the bubble structure in the flow equation [first two summands of Fig. 2(b)], very similar to the Bethe-Salpeter equations [Fig. 2(a)]. The only irreducible contribution is the initial condition of the vertex, $\Gamma^{(4)}_{\Lambda_i} = -U$. Hence, diagrams generated by the flow are always of the parquet type. It is then natural to express $\Gamma^{(4)}$ as follows, using the channel classification of the parquet equations:

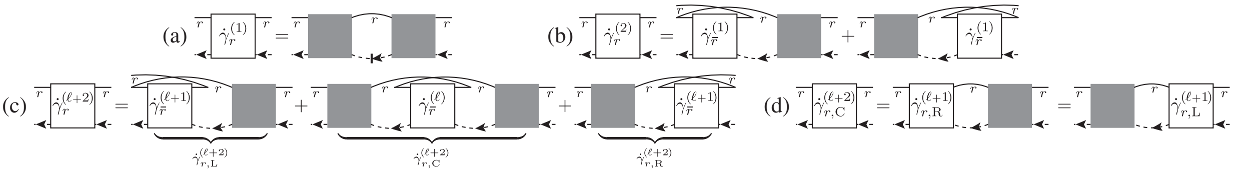
(a)
$\dot{\gamma}_r^{(1)}$
(b)
$\dot{\gamma}_r^{(2)}$
$\dot{\gamma}_{\bar{r}}^{(1)}$
(c)
$\dot{\gamma}_r^{(\ell+2)}$
$\dot{\gamma}_{\bar{r}}^{(\ell+1)}$
$\dot{\gamma}_{\bar{r}}^{(\ell)}$
$\dot{\gamma}_{r,\mathrm{L}}^{(\ell+2)}$
$\dot{\gamma}_{r,\mathrm{C}}^{(\ell+2)}$
$\dot{\gamma}_{r,\mathrm{R}}^{(\ell+2)}$
(d)
$\dot{\gamma}_{r,\mathrm{C}}^{(\ell+2)}$
$\dot{\gamma}_{r,\mathrm{R}}^{(\ell+1)}$
$\dot{\gamma}_{r,\mathrm{L}}^{(\ell+1)}$
r
$\bar{r}$

FIG. 3. Multiloop FRG flow equations, $\partial_\Lambda \gamma_r = \sum_{\ell \geq 1} \dot{\gamma}_r^{(\ell)}$, for the four-point vertex reducible in channel r, with $r = a$ or p, and $\bar{r} = p$ or a. The subscript r in the diagrams further symbolizes antiparallel or parallel c-d lines, respectively. (a) One-loop, (b) two-loop, (c) three- and higher-loop flows. (d) One-loop calculation of $\dot{\gamma}_{r,\mathrm{C}}^{(\ell+2)}$, using the previously computed $\dot{\gamma}_{r,\mathrm{R}}^{(\ell+1)}$ or $\dot{\gamma}_{r,\mathrm{L}}^{(\ell+1)}$.

$$\Gamma^{(4)} = -U + \gamma_a + \gamma_p, \qquad \partial_\Lambda \gamma_r = \sum_{\ell \geq 1} \dot{\gamma}_r^{(\ell)}. \qquad (5)$$

Here, r stands for a or p and $\dot{\gamma}_r^{(\ell)}$ for diagrams involving ℓ loops connecting full vertices. We will show that $\dot{\gamma}_r^{(\ell)}$ can be constructed iteratively from lower-loop contributions.

The conventional (or *one-loop*) FRG flow in channel r is formulated in Fig. 3(a), where full vertices are connected by an r "single-scale" bubble, i.e., either antiparallel or parallel G^c-S^d lines. [Detailed diagrams with all arrows and their mathematical translations are given in Ref. [26], Fig. S2, Eq. (S2).] If one inserts the bare vertex for $\Gamma^{(4)}$ on the rhs of such a one-loop flow equation [Fig. 3(a)], one fully obtains the differentiated second-order vertex. However, inserting first- and second-order vertices on the rhs will miss some diagrams of the differentiated third-order vertex, because these invoke an $\bar{r}$ single-scale bubble that is not generated by $\dot{\gamma}_r^{(1)}$ (an overbar denotes the complementary channel: $\bar{a} = p$, $\bar{p} = a$). An example of such a missing third-order diagram is that obtained by differentiating the rightmost d propagator of the third diagram in Fig. 1(a) (cf. Fig. S1 of Ref. [26]). All such neglected contributions can be added to the rhs of the flow equation by hand (replacing bare by full vertices), resulting in the construction in Fig. 3(b). It uses an r "standard" bubble [(anti)parallel G^c-G^d lines] to connect the one-loop contribution from the complementary channel, $\dot{\gamma}_{\bar{r}}^{(1)}$, with the full vertex, thus generating *two*-loop contributions. These corrections have already been suggested from slightly different approaches [21,23].

The resulting third-order corrected flow will still miss derivatives of parquet graphs starting at fourth order in the interaction. These can be included via two further additions to the flow, which have the same form for all higher loop orders, $\dot{\gamma}_r^{(\ell+2)}$ with $\ell \geq 1$ [cf. Fig. 3(c)]. First, for the flow of $\dot{\gamma}_r^{(\ell+2)}$, an r bubble is used to attach the previously computed $(\ell+1)$-loop contribution from the complementary channel, $\dot{\gamma}_{\bar{r}}^{(\ell+1)}$, to either side of the full vertex, just as in the two-loop case. Second, by using two r bubbles, we include the differentiated ℓ-loop vertex from the complementary channel, $\dot{\gamma}_{\bar{r}}^{(\ell)}$, to the flow of $\dot{\gamma}_r^{(\ell+2)}$. Double counting of diagrams in all these contributions does not occur due to the unique position of the single-scale propagator [26]. Note that the central term in Fig. 3(c) can be computed by a one-loop integral, too, using the previous computations from the same channel, as shown in Fig. 3(d). Consequently, the numerical effort in the multiloop corrections scales linearly in ℓ.

By its diagrammatic construction, organized by the number of loops connecting full vertices, the MFRG flow incorporates *all* differentiated diagrams of a vertex reducible in channel r, built up from the bare interaction, and thus captures *all* parquet graphs of the full four-point vertex. Indeed, in Ref. [26], we prove algebraically for the XES that the number of differentiated diagrams in the MFRG matches precisely the number of differentiated parquet graphs. An ℓ-loop FRG flow generates *all* parquet diagrams up to order $n = \ell + 1$ in the interaction and, naturally, generates an increasing number of parquet contributions at arbitrarily large orders in U.

Numerical results.—In Fig. 5, we show numerical results for the XES particle-hole susceptibility. Using four different regulators (see below), we compare the susceptibility obtained from an ℓ-loop FRG flow to the numerical solution of the parquet equations. We find that the one-loop curves differ among each other and deviate strongly from the parquet result. With increasing loop order ℓ, the multiloop results from all regulators oscillate around and approach the parquet result, with very good agreement already for $\ell = 4$. For $\ell \geq 7$, the oscillations in the relative deviation (at $\bar{\omega} = 0$) are damped to $\lesssim 2\%$ (insets, solid line). A similar behavior is observed for the identity [30] $\Pi_{\bar{\omega}} = \lim_{|\omega|,|\nu| \to \infty} \gamma_{a;\omega,\nu,\bar{\omega}} / U^2$ ($\bar{\omega}$ is the exchange frequency, and ω, ν are two fermionic frequencies), which the parquet solution is guaranteed to fulfill (cf. Ref. [26], Eq. (S4) and following) (insets, dashed line).

As regulators, we choose the Litim regulator [31], and propagators of the type $G_\Lambda^d(\omega) = \theta(\omega/\Lambda - 1) G^d(\omega)$, where $\theta(x)$ is either a sharp, smooth, or oscillating step function (cf. Figs. 4(a) and 4(b); Eq. (S8) of Ref. [26]). The fact that different regulators give the same result in the MFRG flow is a strong indication for an exact resummation of diagrams.

Let us note that the MFRG flow also increases the stability of the solution towards larger interaction. Whereas, in the one-loop scheme, the four-point vertex diverges for $u > 0.4$, higher-loop schemes converge up to larger values of u. The reason is that the one-loop scheme contains the *full* ladder series of diagrams (in any channel), but only

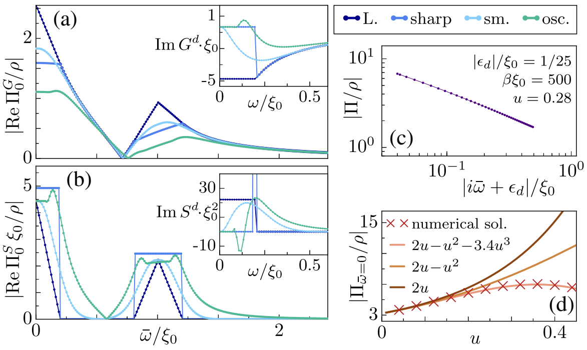

FIG. 4. (a) Noninteracting "standard" particle-hole bubble Π_0^G and propagator G^d (inset) for different regulators (cf. Eq. (S8) of Ref. [26]) and $\Lambda/\xi_0 = 0.2$. (b) Same as (a) for the "single-scale" bubble Π_0^S and propagator S^d. (c) Double-logarithmic plot for the particle-hole susceptibility Π, obtained from solving the parquet equations. (d) $\Pi_{\bar\omega=0}(u)$ computed via the parquet equations [ϵ_d, β as in (c)] and according to Eq. (2) with different choices for $\alpha(u)$. The comparison between these guide-to-the-eye lines and the numerical solution confirms that $\alpha(u) \approx 2u$, but also shows that subleading contributions become sizable for larger u. These are present since internal numerical calculations go beyond logarithmic accuracy.

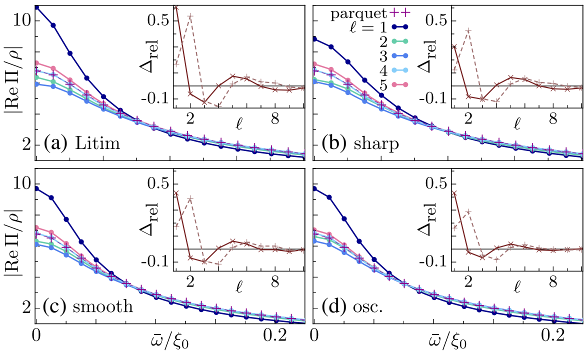

FIG. 5. (a)–(d) Numerical solutions for the particle-hole susceptibility Π, obtained from the parquet equations and from MFRG with different regulators [cf. Figs. 4(a) and 4(b)], using the parameters of Fig. 4(c). Insets: Relative deviation between parquet and MFRG results for Π (solid line) and between Π and $\lim_{|\omega|,|\nu|\to\infty}\gamma_a/U^2$ (dashed line), all evaluated at $\bar\omega = 0$.

parts of nonladder diagrams. Whereas the (imaginary-frequency) pure particle-hole ladder already diverges at $u \sim 0.3$, higher-loop extensions approaching the parquet summation are needed for the full feedback between both channels to eliminate the divergence.

The equivalence between the MFRG flow and parquet summation allows us to explain how the quality of FRG results depends on the choice of regulator. Whereas the one-loop scheme only involves a single-scale bubble $\Pi_0^S = \sum G^c S^d$, all extensions invoke successive standard bubbles $\Pi_0^G = \sum G^c G^d$. By minimizing the weight of Π_0^G compared to Π_0^S, one minimizes the effect of the multiloop corrections and thus the difference between low-level MFRG and parquet. Indeed, from Figs. 4(a) and 4(b) we see that a regulator with small (large) weight in Π_0^G and large (small) weight in Π_0^S, such as the oscillating-step (Litim) regulator, gives comparatively good (bad) agreement with parquet for low ℓ. Accordingly, the sharp-step regulator performs slightly better than its smooth counterpart.

Generalizations.—The MFRG flow can be readily extended to more general models, where one normally does not treat two particle species separately, as done here for c and d electrons. If three two-particle channels (antiparallel, parallel, and transverse) are involved, the higher-loop flow must incorporate feedback from both complementary channels via $\dot\gamma_{\bar r}^{\ell} = \sum_{r'\neq r}\dot\gamma_{r'}^{\ell}$ [25]. The self-energy Σ enters the $\Gamma^{(4)}$ flow via full propagators, and, in the one-loop flow of the four-point vertex [Fig. 3(a)], one should follow the usual practice [8,21] of using the derivative of the full propagator ($\partial_\Lambda G_\Lambda$) instead of the single-scale propagator ($S_\Lambda = \partial_\Lambda G_\Lambda|_{\Sigma=\mathrm{const}}$) which excludes any differentiated self-energy contributions. The reason is that, in the exact FRG flow equation [Fig. 2(b)], those diagrams of $\partial_\Lambda\Gamma^{(4)}$ that involve $\partial_\Lambda\Sigma$ are encoded in the six-point vertex.

Evidently, an improved flow for $\Gamma^{(4)}$ also improves FRG calculations of the self-energy. In the parquet formalism, Σ is constructed from the four-point vertex by an exact, self-consistent Schwinger-Dyson equation [11]. In order to obtain the same self-energy diagrams from the (in principle) *exact* FRG flow equation for Σ, with only the vertex in the parquet *approximation* at one's disposal, multiloop extensions to the self-energy flow, similar to those introduced here, can be performed [25]. Given the self-energy, all arguments about capturing parquet diagrams (which now consist of dressed lines) with the multiloop FRG flow remain valid since they only involve generic, model-independent statements about the structure of two-particle diagrams.

The MFRG flow is applicable for any initial condition $\Gamma^{(4)}_{\Lambda_i}$. An example where one would not start from $G_{\Lambda_i} = 0$, as done here, arises in the context of dynamical mean-field theory (DMFT) [2]. There, the goal of adding nonlocal correlations, with the local vertex from DMFT ($\Gamma^{(4)}_{\mathrm{DMFT}}$) as input, can be pursued using the FRG [32]. Alternatively, this goal is also being addressed by using the parquet equations in the dynamical vertex approximation (DΓA) [6]. However, the latter approach requires the *diagrammatic* decomposition of the *nonperturbative* vertex [33] $\Gamma^{(4)}_{\mathrm{DMFT}} = R + \sum_r \gamma_r$, which yields diverging results close to a quantum phase transition [1,35]. In contrast, the MFRG flow is built from the *full* vertex $\Gamma^{(4)}_{\mathrm{DMFT}}$ and could thus be used to scan a larger region of the phase diagram.

Conclusion.—Using the x-ray–edge singularity as an example, we have presented multiloop FRG flow equations, which sum up all parquet diagrams to arbitrary order, so that solving the MFRG flow is equivalent to solving the (first-order) parquet equations. Our numerical results demonstrate that solutions of an ℓ-loop flow quickly approach the parquet result with increasing ℓ. This applies for a variety of regulators, confirming an exact resummation of diagrams. The MFRG construction is generic and can be readily generalized to more complex models.

The MFRG-parquet equivalence established here shows that one-loop FRG calculations generate only a subset of (differentiated) parquet diagrams and that a multiloop FRG flow is needed to reproduce parquet results. From a practical point of view, the MFRG appears advantageous over solving the parquet equations since solving a first-order ordinary differential equation is numerically more stable than solving a self-consistent equation. Moreover, one can choose a suitable regulator and flow from any initial action. Altogether, the MFRG scheme achieves, in effect, a solution of the (first-order) parquet equations while retaining all treasured FRG advantages: no need to solve self-consistent equations, purely one-loop costs, and freedom of choice for regulators.

We thank A. Eberlein, C. Honerkamp, S. Jakobs, V. Meden, W. Metzner, and A. Toschi for useful discussions and acknowledge support by the Cluster of Excellence Nanosystems Initiative Munich. F. B. K. acknowledges funding from the research school IMPRS-QST.

---

[1] T. Schäfer, G. Rohringer, O. Gunnarsson, S. Ciuchi, G. Sangiovanni, and A. Toschi, Phys. Rev. Lett. **110**, 246405 (2013).

[2] A. Georges, G. Kotliar, W. Krauth, and M. J. Rozenberg, Rev. Mod. Phys. **68**, 13 (1996).

[3] A. N. Rubtsov, M. I. Katsnelson, and A. I. Lichtenstein, Phys. Rev. B **77**, 033101 (2008); S. Brener, H. Hafermann, A. N. Rubtsov, M. I. Katsnelson, and A. I. Lichtenstein, Phys. Rev. B **77**, 195105 (2008); H. Hafermann, G. Li, A. N. Rubtsov, M. I. Katsnelson, A. I. Lichtenstein, and H. Monien, Phys. Rev. Lett. **102**, 206401 (2009).

[4] G. Rohringer, A. Toschi, H. Hafermann, K. Held, V. I. Anisimov, and A. A. Katanin, Phys. Rev. B **88**, 115112 (2013).

[5] T. Ayral and O. Parcollet, Phys. Rev. B **94**, 075159 (2016).

[6] A. Toschi, A. A. Katanin, and K. Held, Phys. Rev. B **75**, 045118 (2007); K. Held, A. A. Katanin, and A. Toschi, Prog. Theor. Phys. Suppl. **176**, 117 (2008); A. Valli, G. Sangiovanni, O. Gunnarsson, A. Toschi, and K. Held, Phys. Rev. Lett. **104**, 246402 (2010).

[7] C. Slezak, M. Jarrell, T. Maier, and J. Deisz, J. Phys. Condens. Matter **21**, 435604 (2009).

[8] W. Metzner, M. Salmhofer, C. Honerkamp, V. Meden, and K. Schönhammer, Rev. Mod. Phys. **84**, 299 (2012).

[9] P. Kopietz, L. Bartosch, and F. Schütz, *Introduction to the Functional Renormalization Group*, Lecture Notes in Physics (Springer, Berlin, 2010).

[10] B. Roulet, J. Gavoret, and P. Nozières, Phys. Rev. **178**, 1072 (1969).

[11] N. Bickers, in *Theoretical Methods for Strongly Correlated Electrons*, edited by D. Sénéchal, A.-M. Tremblay, and C. Bourbonnais, CRM Series in Mathematical Physics (Springer, New York, 2004), pp. 237–296.

[12] A. Valli, T. Schäfer, P. Thunström, G. Rohringer, S. Andergassen, G. Sangiovanni, K. Held, and A. Toschi, Phys. Rev. B **91**, 115115 (2015).

[13] G. Li, N. Wentzell, P. Pudleiner, P. Thunström, and K. Held, Phys. Rev. B **93**, 165103 (2016).

[14] A. Gogolin, A. Nersesyan, and A. Tsvelik, *Bosonization and Strongly Correlated Systems* (Cambridge University Press, Cambridge, England, 2004), p. 332.

[15] D. Zanchi and H. J. Schulz, Phys. Rev. B **61**, 13609 (2000); R.-Q. Xing, L. Classen, M. Khodas, and A. V. Chubukov, Phys. Rev. B **95**, 085108 (2017); C. Bourbonnais, in *Strongly Interacting Fermions and High-Tc Superconductivity*, edited by B. Douçout and J. Zinn-Justin (Elsevier Sience, Amsterdam, 1995), pp. 307–369.

[16] P. Lange, C. Drukier, A. Sharma, and P. Kopietz, J. Phys. A **48**, 395001 (2015).

[17] P. Nozières, J. Gavoret, and B. Roulet, Phys. Rev. **178**, 1084 (1969).

[18] P. Nozières and C. T. De Dominicis, Phys. Rev. **178**, 1097 (1969).

[19] G. D. Mahan, Phys. Rev. **163**, 612 (1967).

[20] F. B. Kugler and J. von Delft, arXiv:1706.06872.

[21] A. A. Katanin, Phys. Rev. B **70**, 115109 (2004).

[22] M. Salmhofer, C. Honerkamp, W. Metzner, and O. Lauscher, Prog. Theor. Phys. **112**, 943 (2004).

[23] A. Eberlein, Phys. Rev. B **90**, 115125 (2014).

[24] T. Giamarchi, *Quantum Physics in One Dimension* (Clarendon Press, Oxford, 2004), p. 347.

[25] F. B. Kugler and J. von Delft, Phys. Rev. B **97**, 035162 (2018).

[26] See Supplemental Material at http://link.aps.org/supplemental/10.1103/PhysRevLett.120.057403 for the technical details used in our calculations, which includes Refs. [27,28].

[27] I. Gradshteyn and I. Ryzhik, *Table of Integrals, Series, and Products*, edited by A. Jeffrey and D. Zwillinger (Academic Press, Boston, 2007), 7th ed., p. 990.

[28] N. J. A. Sloane, The On-Line Encyclopedia of Integer Sequences (Mar. 2017), published electronically at https://oeis.org.

[29] Since, in a zero-temperature real-frequency treatment [10] of x-ray absorption, G^d is purely advanced, we draw diagrams such that all G^d lines are oriented to the left.

[30] N. Wentzell, G. Li, A. Tagliavini, C. Taranto, G. Rohringer, K. Held, A. Toschi, and S. Andergassen, arXiv:1610.06520.

[31] D. F. Litim, Phys. Rev. D **64**, 105007 (2001).

[32] C. Taranto, S. Andergassen, J. Bauer, K. Held, A. Katanin, W. Metzner, G. Rohringer, and A. Toschi, Phys. Rev. Lett. **112**, 196402 (2014).

[33] Alternatives to DΓA which do not require the totally irreducible vertex are the dual fermion [3] and the related 1PI approach [4]. However, upon transformation to the dual variables, the bare action contains n-particle vertices for all n. Recent studies [34] show that the corresponding six-point

vertex yields sizable contributions for the (physical) self-energy, and it remains unclear how a truncation in the (dual) bare action can be justified.

[34] T. Ribic, G. Rohringer, and K. Held, Phys. Rev. B **95**, 155130 (2017); T. Ribic, P. Gunacker, S. Iskakov, M. Wallerberger, G. Rohringer, A. N. Rubtsov, E. Gull, and K. Held, Phys. Rev. B **96**, 235127 (2017).

[35] T. Schäfer, S. Ciuchi, M. Wallerberger, P. Thunström, O. Gunnarsson, G. Sangiovanni, G. Rohringer, and A. Toschi, Phys. Rev. B **94**, 235108 (2016); O. Gunnarsson, G. Rohringer, T. Schäfer, G. Sangiovanni, and A. Toschi, Phys. Rev. Lett. **119**, 056402 (2017).

Supplemental Material for
"Multiloop Functional Renormalization Group That Sums Up All Parquet Diagrams"

Fabian B. Kugler and Jan von Delft
Physics Department, Arnold Sommerfeld Center for Theoretical Physics, and Center for NanoScience,
Ludwig-Maximilians-Universität München, Theresienstrasse 37, 80333 Munich, Germany

This supplement consists of four parts. First, we show detailed equations for the mfRG flow, the identity between susceptibility and reducible vertex, and the regulators we used. Second, we provide the numerical details of our computations. Third, we prove algebraically for the XES that the mfRG flow generates all parquet diagrams at arbitrary order, based on expanding the parquet and flow equations in the interaction and counting diagrams. Last, we briefly mention that many quantities appearing in this proof happen to have an interpretation as giving the number of special paths on a triangular grid.

In this supplement, citations and references without the extra label "S" refer to those given in the main text.

S-I. DETAILED EQUATIONS

Figure S1 illustrates how the two-loop corrections of mfRG cure the flow of the vertex γ_a at third order in the interaction. Figure S2 shows the detailed form of the mfRG flow equations from Fig. 3. In principle [25], the flow equations also contain contributions from a third (transversal) channel, where the *interband* vertex $\Gamma^{\bar{d}c\bar{c}d}$ is connected to an *intraband* vertex $\Gamma^{\bar{d}d\bar{d}d}$ by valence band lines G^d and S^d. However, one can easily see that, for the XES, all such terms contribute subleadingly and belong to higher-order diagrams of R in the parquet treatment [10]. Hence, they are neglected throughout this work.

The mathematical translation of our flow equations only requires the formula for an r bubble connecting two vertices (where $r = a, p$). This is most compactly written in a notation adapted to the respective channel: The three independent frequencies necessary to describe a full vertex can be chosen to include two fermionic frequencies combined with either the bosonic *exchange* frequency $\bar{\omega}_a$, suited for the antiparallel channel, or the bosonic *pairing* frequency $\bar{\omega}_p$, suited for the parallel channel. This is, however, merely a choice of parametrization and does not require any properties of the vertex itself. We choose the parametrization according to

$$\mathcal{V}_{\omega,\nu,\bar{\omega}_a} = \mathcal{V}^{\bar{d}c\bar{c}d}_{\omega,\bar{\omega}_a+\omega,\bar{\omega}_a+\nu,\nu}, \quad \text{(S1a)}$$

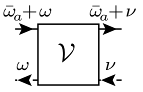

$$\mathcal{V}_{\omega,\nu,\bar{\omega}_p} = \mathcal{V}^{\bar{d}c\bar{c}d}_{\omega,\bar{\omega}_p-\nu,\bar{\omega}_p-\omega,\nu}, \quad \text{(S1b)}$$

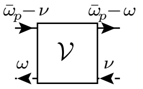

where the bosonic frequencies are related via $\bar{\omega}_p = \bar{\omega}_a + \omega + \nu$.

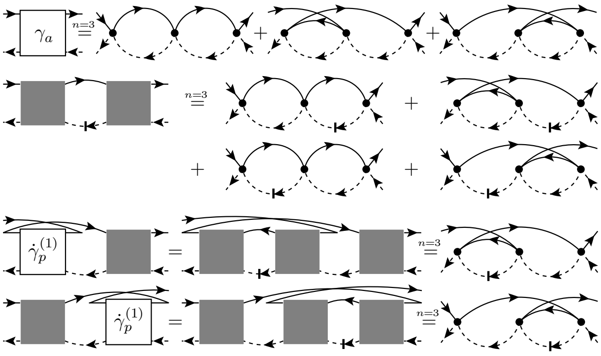

FIG. S1. First row: All third-order contributions to γ_a. Its flow is described by the six diagrams obtained by differentiating each dashed line once. In the mfRG scheme, these six diagrams are encoded in $\dot{\gamma}_a^{(1)}$ (second and third rows) and $\dot{\gamma}_a^{(2)}$ (last two rows), the one- and two-loop flow equations [cf. Fig. S2] for γ_a, respectively. The third-order contributions are obtained by inserting first- and second-order diagrams for the full vertex.

In this notation, an r bubble $\mathcal{V}_r$ connecting the vertices $\mathcal{V}'$ and $\mathcal{V}''$ can be computed as follows:

$$\mathcal{V}_{r;\omega,\nu,\bar{\omega}_r} = \frac{1}{\beta}\sum_{\omega'} \mathcal{V}'_{\omega,\omega',\bar{\omega}_r} G^d_{\omega'} G^c_{\bar{\omega}_r+\sigma_r\omega'} \mathcal{V}''_{\omega',\nu,\bar{\omega}_r}, \quad \text{(S2)}$$

with $\sigma_a = 1$ and $\sigma_p = -1$.

The channel notation (S1) is also used in the identity between particle-hole susceptibility Π and reducible vertex γ_a considered in Fig. 5. If we, more generally, denote the susceptibility in the antiparallel channel by $\Pi_a = \Pi$ and the one in the parallel channel by Π_p, the relation between susceptibility and 1PI vertex, already used in Eq. (3), reads

$$\Pi_{r;\bar{\omega}_r} = \frac{1}{\beta}\sum_{\omega} G^d_{\omega} G^c_{\bar{\omega}_r+\sigma_r\omega}\Big(1+\frac{1}{\beta}\sum_{\nu}\Gamma^{(4)}_{\omega,\nu,\bar{\omega}_r} G^d_{\nu} G^c_{\bar{\omega}_r+\sigma_r\nu}\Big). \quad \text{(S3)}$$

The identity between susceptibility and reducible vertex [30] is given by

$$\lim_{|\omega|,|\nu|\to\infty} \gamma_{r;\omega,\nu,\bar{\omega}_r} = U^2 \Pi_{r;\bar{\omega}_r}. \quad \text{(S4)}$$

To see that a solution of the parquet equations with any approximation for the totally irreducible vertex R is

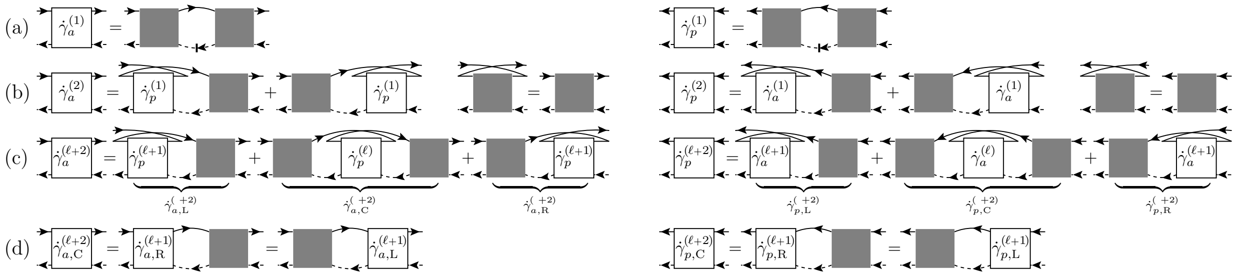
(a)
(b)
(c)
(d)
$\dot\gamma_a^{(1)}$
$\dot\gamma_p^{(1)}$
$\dot\gamma_a^{(2)}$
$\dot\gamma_p^{(2)}$
$\dot\gamma_a^{(\ell+2)}$
$\dot\gamma_p^{(\ell+2)}$
$\dot\gamma_p^{(\ell+1)}$
$\dot\gamma_p^{(\ell)}$
$\dot\gamma_a^{(\ell+1)}$
$\dot\gamma_a^{(\ell)}$
$\dot\gamma_{a,\mathrm{L}}^{(\ +2)}$
$\dot\gamma_{a,\mathrm{C}}^{(\ +2)}$
$\dot\gamma_{a,\mathrm{R}}^{(\ +2)}$
$\dot\gamma_{p,\mathrm{L}}^{(\ +2)}$
$\dot\gamma_{p,\mathrm{C}}^{(\ +2)}$
$\dot\gamma_{p,\mathrm{R}}^{(\ +2)}$
$\dot\gamma_{a,\mathrm{C}}^{(\ell+2)}$
$\dot\gamma_{a,\mathrm{R}}^{(\ell+1)}$
$\dot\gamma_{a,\mathrm{L}}^{(\ell+1)}$
$\dot\gamma_{p,\mathrm{C}}^{(\ell+2)}$
$\dot\gamma_{p,\mathrm{R}}^{(\ell+1)}$
$\dot\gamma_{p,\mathrm{L}}^{(\ell+1)}$

FIG. S2. Multiloop flow equations in the (left) antiparallel and (right) parallel channels, corresponding to Fig. 3.

guaranteed to fulfill Eq. (S4), we note first that, by the very fact that R is totally irreducible, we have

$$\lim_{|\omega|\to\infty} R_{\omega,\nu,\bar\omega_r} = -U. \tag{S5}$$

Regarding the reducible vertices, we can perform the limit in the Bethe-Salpeter equations [Fig. 2(a)] and obtain

$$\lim_{|\omega|\to\infty} \gamma_{\bar r;\omega,\nu,\bar\omega_r} = 0, \quad \Rightarrow \lim_{|\omega|\to\infty} I_{r;\omega,\nu,\bar\omega_r} = -U, \tag{S6a}$$

$$\lim_{|\omega|\to\infty} \gamma_{r;\omega,\nu,\bar\omega_r} = -\frac{U}{\beta}\sum_{\omega'} G^d_{\omega'} G^c_{\bar\omega_r+\sigma_r\omega'} \Gamma^{(4)}_{\omega',\nu,\bar\omega_r}. \tag{S6b}$$

By symmetry [cf. Eq. (S11)], Eqs. (S5), (S6) also hold for $\omega \leftrightarrow \nu$, and we further deduce

$$\begin{aligned}\lim_{|\nu|\to\infty}\Gamma^{(4)}_{\omega',\nu,\bar\omega_r} &= \lim_{|\nu|\to\infty} R_{\omega',\nu,\bar\omega_r} + \lim_{|\nu|\to\infty} \gamma_{r;\omega',\nu,\bar\omega_r} \\ &= -U - \frac{U}{\beta}\sum_{\omega''}\Gamma^{(4)}_{\omega',\omega'',\bar\omega_r} G^d_{\omega''} G^c_{\bar\omega_r+\sigma_r\omega''}.\end{aligned} \tag{S7}$$

Adding the limit $\lim_{|\nu|\to\infty}$ to Eq. (S6b) and using Eqs. (S3) and (S7) yields the identity (S4).

Next, we give the mathematical definition of the regulators, which we have used in the numerical calculations (Fig. 5) and already illustrated in Figs. 4(a) and 4(b):

$$G^{d,\mathrm{L}}_{\omega,\Lambda} = \frac{1}{i\,\mathrm{sgn}(\omega)\max(|\omega|,\Lambda) - \epsilon_d}, \tag{S8a}$$

$$G^{d,\mathrm{sharp}}_{\omega,\Lambda} = \Theta(|\omega|-\Lambda)\frac{1}{i\omega-\epsilon_d}, \tag{S8b}$$

$$G^{d,\mathrm{smooth}}_{\omega,\Lambda} = \left[1 - \mathrm{e}^{-\left(\frac{|\omega|}{\Lambda}\right)^a}\right]\frac{1}{i\omega-\epsilon_d}, \quad a=2, \tag{S8c}$$

$$G^{d,\mathrm{osc.}}_{\omega,\Lambda} = \mathrm{e}^{-\left(\frac{\Lambda}{|\omega|}\right)^a\left[1-ib\,\mathrm{sgn}(w)\right]}\frac{1}{i\omega-\epsilon_d}, \quad a=2,\ b=1. \tag{S8d}$$

The regulator in Eq. (S8a) is known as Litim regulator [31]. Note that the parameters in Eqs. (S8c) and (S8d), $a>0$ and b, can also be chosen differently, keeping the boundary conditions $G^d_{\Lambda_i=\infty}=0$ and $G^d_{\Lambda_f=0}=G^d$ fulfilled.

Finally, we remark that, in principle, the band gap is the largest energy scale in the XES. This would require $|\epsilon_d| \gg \xi_0$. However, in the choice of the Hamiltonian [Eq. (1)], we have already restricted ourselves to an inter-band density-density interaction, which implies individual particle-number conservation. As a consequence, we are free to choose *any* numerical value for ϵ_d, the only exception being $\epsilon_d = 0$, which violates analytic properties of the (bare) susceptibility [20]. In fact, we find small values for $|\epsilon_d|$ most suitable to visualize the power-law divergence in the particle-hole susceptibility for imaginary frequencies [cf. Eq. (2)].

S-II. NUMERICAL DETAILS

We have solved the self-consistent parquet equations [Eq. (4), Fig. 2(a)] by an iterative algorithm. For that, we use the initial values $\gamma_r = 0$ and an update rule that combines the previous value and the predicted value from the Bethe-Salpeter equations according to

$$\gamma_r^{\mathrm{new}} = z\gamma_r^{\mathrm{pred.}} + (1-z)\gamma_r^{\mathrm{prev.}}, \quad z \lesssim 0.2. \tag{S9}$$

The mfRG flow equations are solved by an adaptive-step Runge-Kutta algorithm. The numerical costs of the mfRG flow and the parquet algorithm are similar: In both scenarios, one computes bubbles of vertices multiple times—either to evaluate the flow equations during the mfRG flow or to evaluate the Bethe-Salpeter equations during a self-consistency loop in the parquet algorithm.

In either case, we use a parametrization of four-point vertices which accounts for the important high-frequency asymptotics [13,30]. This parametrization [30] is adapted to the channel in which a vertex is reducible: We approximate the frequency dependence of a vertex reducible in channel r, using the respective channel notation from Eq. (S1), by

$$\begin{aligned}\gamma_{r;\omega,\nu,\bar\omega_r} = {} & \Theta(\Omega_1 - |\bar\omega|)K^1_{\bar\omega_r} \\ & + \Theta(\Omega_2 - |\bar\omega_r|)\Theta(\Omega_2 - |\omega|)K^2_{\bar\omega_r,\omega} \\ & + \Theta(\Omega_2 - |\bar\omega_r|)\Theta(\Omega_2 - |\nu|)\bar K^2_{\bar\omega_r,\nu} \\ & + \Theta(\Omega_3 - |\bar\omega_r|)\Theta(\Omega_3 - |\omega|)\Theta(\Omega_3 - |\nu|)K^3_{\bar\omega_r,\omega,\nu}.\end{aligned} \tag{S10}$$

Note that the first summand in this parametrization already incorporates the limit used in Eq. (S4). We have chosen the cutoffs Ω_i in Eq. (S10) such that we keep 1000, 500, and 100 positive frequencies on each axis for K^1, K^2 and $\bar{K}^2$, and K^3, respectively. Using the symmetries for vertices [30],

$$(\mathcal{V}_{\omega,\nu,\bar{\omega}_r})^* = \mathcal{V}_{-\omega,-\nu,-\bar{\omega}_r}, \quad \mathcal{V}_{\omega,\nu,\bar{\omega}_r} = \mathcal{V}_{\nu,\omega,\bar{\omega}_r}, \tag{S11}$$

further reduces the computational effort. Note that, while the latter symmetry holds for $\gamma_r^{(\ell)}$ and $\gamma_{r,\mathrm{C}}^{(\ell)}$, it does not hold for $\gamma_{r,\mathrm{L}}^{(\ell)}$ and $\gamma_{r,\mathrm{R}}^{(\ell)}$ individually. Instead, one has $\gamma_{r,\mathrm{L};\omega,\nu,\bar{\omega}_r}^{(\ell)} = \gamma_{r,\mathrm{R};\nu,\omega,\bar{\omega}_r}^{(\ell)}$.

The Matsubara summations in all our calculations are naturally restricted to a finite frequency interval, since we approximate the c propagator using a sharp cutoff:

$$\begin{aligned} G_\omega^c &= \rho \int_{-\xi_0}^{\xi_0} \mathrm{d}\epsilon \frac{1}{i\omega - \epsilon} = -2i\rho \arctan\left(\frac{\xi_0}{\omega}\right) \\ &= -i\pi\rho\, \mathrm{sgn}(w)\Theta(\xi_0 - |\omega|) + O\Big(\frac{\omega}{\xi_0}\Big). \end{aligned} \tag{S12}$$

At an inverse temperature of $\beta\xi_0 = 500$, this yields about 160 summands.

S-III. PROOF OF EQUIVALENCE

We prove below for the XES that solving the full mfRG flow is equivalent to solving the (first-order) parquet equations. We also show that a solution of an ℓ-loop fRG flow fully contains all parquet graphs up to order $n = \ell + 1$. In order to check that the parquet vertex is a solution of the mfRG flow equation (viz., an ordinary differential equation), one has to verify that the initial condition is fulfilled and that the differential equation is fulfilled (during the whole flow). At the initial scale ($\Lambda_i = \infty$, $G_{\Lambda_i}^d = 0$, $\Gamma_{\Lambda_i}^{(4)} = -U$) the parquet vertex is trivially given by the bare vertex; thus the initial condition is fulfilled. At an arbitrary scale parameter Λ during the flow, inserting all parquet diagrams for the vertex into, e.g., the one-loop flow equation generates only a subset of all differentiated parquet diagrams (cf. Fig. S1), i.e., the differential equation is not fulfilled. However, inserting all parquet diagrams into the full mfRG flow equation yields all differentiated parquet diagrams, i.e., the differential equation is fulfilled.

To show that, indeed, all differentiated parquet diagrams are generated in mfRG, we proceeds in two steps: First, we argue that, by the structure of the mfRG flow, the differentiated diagrams are of the parquet type without any double counting. Second, we show (without caring about the specific form of a diagram) that the number of differentiated diagrams in mfRG exactly matches the number of differentiated parquet graphs order for order in the interaction.

No double counting in mfRG

The only totally irreducible contribution to the four-point vertex contained in the multiloop (or conventionally truncated) fRG flow is the bare interaction stemming from the initial condition of the vertex. All further diagrams on the r.h.s. of the flow equations are obtained by iteratively combining two vertices with parallel or antiparallel propagators. Hence, they correspond to differentiated *parquet* diagrams in the respective channel.

The fact that there is no double counting in mfRG is easily seen employing arguments of diagrammatic reducibility and the unique position of the single-scale propagator in differentiated diagrams. To be specific, let us consider here the channel reducible in antiparallel lines (cf. left side of Fig. S2); the arguments for the other channel are completely analogous.

First, we note that diagrams in the one-loop term always differ from higher-loop ones. The reason is that, in higher-loop terms, the single-scale propagator appears in the vertex coming from $\partial_\Lambda \gamma_p$. This can never contain vertices connected by an antiparallel G^c-S^d bubble, since such terms only originate upon differentiating γ_a.

Second, diagrams in the left, center, or right part of an ℓ-loop contribution always differ. This is because the vertex $\gamma_p^{(\ell)}$ is irreducible in antiparallel lines. The left part is then reducible in antiparallel lines *only after* the single-scale propagator appeared, the right part *only before*, and the center part is reducible in this channel *before and after* S^d.

Third, the same parts (say, the left parts) of different loop contributions ($\ell \neq \ell'$) are always different. Assume they agreed: As the antiparallel bubble induces the first (leftmost) reducibility in this channel, already $\gamma_p^{(\ell)}$ and $\gamma_p^{(\ell')}$ would have to agree. For these, only the same parts can agree, as mentioned before. The argument then proceeds iteratively until one compares the one-loop part to a higher-loop ($|\ell - \ell'| + 1$) one. These are, however, distinct according to the first point.

To summarize: All mfRG diagrams belong to the parquet class and are included at most once. To show that *all* differentiated parquet diagrams are included, it remains to compare their number to the number of diagrams in mfRG.

Counting the number of diagrams

To count the number of diagrams generated by the parquet equations and mfRG, we expand the parquet (Bethe-Salpeter) and flow equations in the interaction. As we need not consider the specific form of a diagram, the calculation is identical for both channels.

Let us denote the number of parquet diagrams of $\Gamma^{(4)}$ at order n by $P_0(n)$ (mnemonic: P for parquet). A

$\Gamma^{(4)}$ diagram of order n contains $n-1$ scale-dependent d lines. Differentiating an n-th order diagram by Λ thus produces $n-1$ differentiated diagrams, and, in total, we have $P_0(n)(n-1)$ differentiated diagrams. Let us further denote the number of differentiated diagrams at order n in one channel, generated by mfRG at loop order ℓ, by $F_\ell(n)$ (mnemonic: F for flow). The ℓ-loop contributions start at order $n = \ell + 1$ in the interaction, i.e., $F_\ell(n) = 0$ for $n \leq \ell$. To show that all parquet diagrams are generated by the (full) mfRG flow, we thus have to establish the following equality:

$$P_0(n)(n-1) = 2\sum_{\ell=1}^{\infty} F_\ell(n) = 2\sum_{\ell=1}^{n-1} F_\ell(n). \tag{S13}$$

In order to sum the parquet graphs up to order n, it suffices to solve the multiloop fRG flow up to loop order $\ell = n-1$.

First, let us count the number of parquet diagrams. From the Bethe-Salpeter equations [cf. Fig.2(a)], one can directly deduce the number of diagrams at order n inherent in γ (of any channel), $P_\gamma(n)$, given the number of diagrams in I, P_I, and in $\Gamma^{(4)}$, P_0:

$$P_\gamma(n) = \sum_{m=1}^{n-1} P_I(m) P_0(n-m). \tag{S14}$$

As both I and Γ start at order 1, the order on the l.h.s. exceeds the maximal order of a diagram on the r.h.s. From the parquet equations, we further know

$$P_0(1) = 1 = P_I(1); \quad P_0(n) = 2P_\gamma(n) = 2P_I(n),\ n \geq 2. \tag{S15}$$

Inserting this, we obtain a closed relation for P_0:

$$P_0(n) = \sum_{m=1}^{n-1} P_0(m) P_0(n-m) + P_0(n-1), \quad n \geq 2. \tag{S16}$$

Let us solve this recursion by the method of generating functions. We define the generating function $p_0(x)$ for the sequence $P_0(n)$ by

$$p_0(x) = \sum_{n=1}^{\infty} P_0(n) x^{n-1} \tag{S17}$$

and calculate

$$\begin{aligned} x p_0(x)^2 &= x \sum_{n,m=1}^{\infty} P_0(n) P_0(m) x^{n+m-2} \\ &= \sum_{n=2}^{\infty} x^{n-1} \sum_{m=1}^{n-1} P_0(m) P_0(n-m) \\ &= \sum_{n=2}^{\infty} P_0(n) x^{n-1} - \sum_{n=2}^{\infty} P_0(n-1) x^{n-1} \\ &= \sum_{n=1}^{\infty} P_0(n) x^{n-1} - 1 - x \sum_{n=1}^{\infty} P_0(n) x^{n-1}. \end{aligned} \tag{S18}$$

From this, we find the defining equation for the generating function,

$$x p_0(x)^2 + (x-1) p_0(x) + 1 = 0, \tag{S19}$$

to which the solution with positive Taylor coefficients is

$$p_0(x) = \frac{1 - x - \sqrt{1 - 6x + x^2}}{2x}. \tag{S20}$$

Recognizing that $(1 - 2tx + x^2)^{-\lambda}$ is the generating function for Gegenbauer polynomials $C_{n-1}^{\lambda}(t)$ [27], we find

$$P_0(n) = -\frac{1}{2} C_n^{-1/2}(3), \quad n \geq 2 \tag{S21}$$

and can read off $P_0(n)$ from a tabulated sequence:

$$P_0 : 1,\ 2,\ 6,\ 22,\ 90,\ 394,\ 1806,\ 8558, \ldots \tag{S22}$$

Note that $P_0(n)$ grows exponentially for large n. This is much less than the number of all, i.e., parquet and nonparquet diagrams of $\Gamma^{(4)}$, which grows faster than $n!$.

The defining equation for the generating function (S19) can be used to find the generating function $q(x)$ of the related sequence $P_0(n)(n-1)$:

$$q(x) = \sum_{n=1}^{\infty} P_0(n)(n-1) x^{n-1} = x p_0'(x). \tag{S23}$$

Differentiating Eq. (S19), we find the expression

$$\begin{aligned} 0 &= p_0(x)^2 + p_0(x) + [1 - x + 2x p_0(x)] p_0'(x), \\ \Rightarrow\ q(x) &= x p_0(x) \frac{p_0(x) + 1}{1 - x - 2x p_0(x)}. \end{aligned} \tag{S24}$$

Next, we count the number of differentiated diagrams generated by mfRG. For this purpose, we consider the auxiliary vertices in Fig. S3, which can be seen as the building blocks of the multiloop flow equations (Fig. S2). Denoting the number of diagrams of $\dot{\mathcal{V}}_\ell$ at order n by $P_\ell(n)$, we find, given all parquet diagrams in the full vertex $\Gamma^{(4)}$, similar to Eq. (S14) the relation

$$P_{\ell+1}(n) = \sum_{m=1}^{n-1} P_\ell(m) P_0(n-m). \tag{S25}$$

This convolution of two sequences can be expressed in terms of the product of their generating functions, defined by $p_\ell(x) = \sum_{n=1}^{\infty} P_\ell(n) x^{n-1}$:

$$\begin{aligned} x p_\ell(x) p_0(x) &= x \sum_{n,m=1}^{\infty} P_\ell(n) P_0(m) x^{n+m-2} \\ &= \sum_{n=2}^{\infty} x^{n-1} \sum_{m=1}^{n-1} P_\ell(m) P_0(n-m) \\ &= \sum_{n=2}^{\infty} P_{\ell+1}(n) x^{n-1} = p_{\ell+1}(x). \end{aligned} \tag{S26}$$

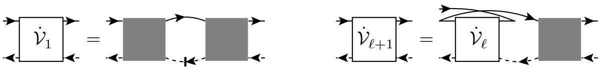

FIG. S3. One-loop equations for auxiliary vertices, which can be seen as building blocks for the multiloop flow equations (Fig. S2).

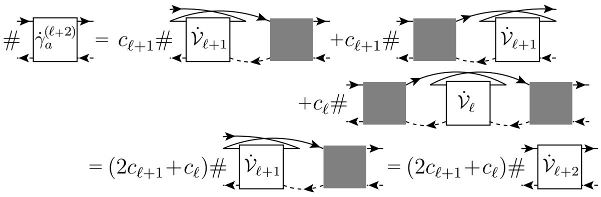
$\#\ \dot{\gamma}_a^{(\ell+2)}$
$= c_{\ell+1}\#$
$\dot{\mathcal{V}}_{\ell+1}$
$+c_{\ell+1}\#$
$\dot{\mathcal{V}}_{\ell+1}$
$+c_\ell\#$
$\dot{\mathcal{V}}_\ell$
$=(2c_{\ell+1}+c_\ell)\#$
$\dot{\mathcal{V}}_{\ell+1}$
$=(2c_{\ell+1}+c_\ell)\#$
$\dot{\mathcal{V}}_{\ell+2}$

FIG. S4. Relation between the number of diagrams contained in $\dot{\gamma}_a^{(\ell+2)}$ in $\dot{\mathcal{V}}_{\ell+2}$, where # symbolizes that we count the number of diagrams of the subsequent vertex.

As a direct consequence, we have

$$p_\ell(x) = x^\ell p_0^{\ell+1}(x); \qquad P_\ell(n) = 0, \quad \ell \geq n. \tag{S27}$$

To relate this to mfRG, note that the flow of n-th order diagrams is only determined by lower-order diagrams, and that the equivalence (S13) as well as our arguments using generating functions hold for all orders individually. Building the series from the bare interaction, we can therefore assume the parquet diagrams of the vertex on the r.h.s. to be given.

At the one-loop level [Fig. 3(a)], the definitions for $\dot{\gamma}_a^{(1)}$ and $\dot{\mathcal{V}}_1$ are identical, hence we also have $F_1(n) = P_1(n)$. For $\dot{\gamma}_a^{(2)}$ [Fig. 3(b)], the one-loop contribution from the complementary channel, $\dot{\gamma}_{\bar{p}}^{(1)}$, is inserted on the left and right side of the full vertex. Both of these parts have the same number of diagrams, which is precisely the number of diagrams in $\dot{\mathcal{V}}_2$ (cf. Fig. S3). Hence, we get $F_2(n) = 2P_2(n)$. For all higher loops, $\dot{\gamma}_a^{(\ell+2)}$ [Fig. 3(c)], the previous term is similarly inserted on both sides of the full vertex, however the center part is constructed with $\dot{\gamma}_{\bar{p}}^{(\ell)}$ from loop order ℓ, and the proportionality relation becomes more complicated. We use an inductive argument, starting at $\ell = 3$, and that the number of diagrams contributing to the lower-loop vertices, $\dot{\gamma}_{\bar{p}}^{(1)}$ and $\dot{\gamma}_{\bar{p}}^{(2)}$, is obtained by multiplying the number of diagrams of the auxiliary vertices by a counting constant (which keeps track of the different ways to combine vertices at fixed loop order):

$$F_1(n) = c_1 P_1(n),\ c_1 = 1; \quad F_2(n) = c_2 P_2(n),\ c_2 = 2. \tag{S28}$$

Using further the equation illustrated in Fig. S4, we similarly obtain for all higher loops:

$$F_{\ell+2}(n) = c_{\ell+2} P_{\ell+2}(n), \quad c_{\ell+2} = 2c_{\ell+1} + c_\ell, \quad \ell \geq 1. \tag{S29}$$

The recursion relation for c_ℓ with the initial conditions c_1 and c_2 is known to define the so-called Pell numbers [28, A000129], which are explicitly given by

$$c_\ell = \frac{(1+\sqrt{2})^\ell - (1-\sqrt{2})^\ell}{2\sqrt{2}}. \tag{S30}$$

To summarize, the number of diagrams at order n of the full vertex, generated by mfRG at loop order ℓ, is given by $2F_\ell(n)$, where $F_\ell(n) = c_\ell P_\ell(n)$, with generating functions $f_\ell(x) = c_\ell p_\ell(x)$. Summing all loops, we find by using Eqs. (S27) and (S30):

$$\begin{aligned} 2\sum_{\ell=1}^{\infty} f_\ell(x) &= \frac{1}{\sqrt{2}} p_0(x) \sum_{\sigma=\pm1} \sigma \sum_{\ell=1}^{\infty} \left[x p_0(x)(1+\sigma\sqrt{2})\right]^\ell \\ &= \frac{1}{\sqrt{2}} p_0(x) \sum_{\sigma=\pm1} \frac{\sigma}{1 - x p_0(x)(1+\sigma\sqrt{2})} \\ &= \frac{2x p_0(x)^2}{1 - 2x p_0(x) - x^2 p_0(x)^2} = q(x), \end{aligned} \tag{S31}$$

where the last equality follows by repeated use of Eq. (S19). Consequently, the sequences corresponding to $q(x)$ and $2\sum_{\ell\geq1} f_\ell(x)$ are also equal. Using $F_\ell(n) = 0$ for $\ell \geq n$ [cf. Eq. (S27)], this means

$$P_0(n)(n-1) = 2\sum_{\ell=1}^{\infty} F_\ell(n) = 2\sum_{\ell=1}^{n-1} F_\ell(n). \tag{S32}$$

We thus have shown that the number of differentiated diagrams produced by mfRG at any order n matches the number of differentiated parquet diagrams at this order, and that an ℓ-loop fRG flow includes all parquet graphs up to order $n = \ell + 1$. The details of the proof rely on properties of the XES. However, generalizing the above strategy to more general models should be straightforward.

S-IV. RELATION TO PATHS ON A TRIANGULAR GRID

As a mathematical curiosity, we mention that the sequences appearing in the previous section have a certain meaning when counting paths on a triangular grid. We are not aware of an underlying connection which goes beyond coincidental properties of the recursion relations of the sequences $P_\ell(n)$. Nevertheless, the details are sufficiently intriguing that we present them here.

The sequence $P_0(n)$ of Eq. (S22), giving the number of parquet graphs at order n, happens to be known in the mathematical literature by the name of the (large) Schröder numbers. These denote the number of paths on

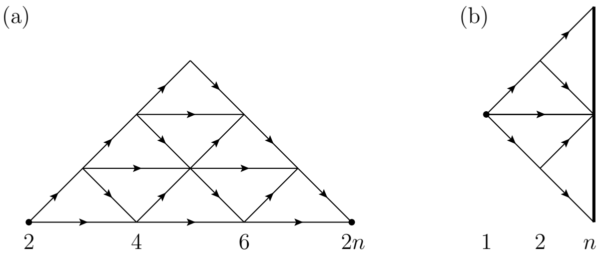

FIG. S5. (a) The (large) Schröder numbers count the number of paths on a triangular grid (in the half-plane) between two points on a line. For $n = 4$, these are 22. 16 of these have a peak at the first level, 6 at the second, and only 1 at the third level [cf. Eq. (S38)]. (b) The Pell numbers count the number of paths on a triangular grid (not restricted to the half-plane) from a point to a vertical line. For $n = 3$, these are 5.

a half-triangular grid beginning and ending on the horizontal axis [28, A006318][cf. Fig. S5(a)]. The sequences $P_\ell(n)$ give the number of these paths with a peak at level ℓ [28, A006318-A006321], or the number of paths starting from the left corner and ending at level ℓ on the right triangle leg (see below). The Pell numbers [cf. Eq. (S30)] count the number of paths on a triangular grid (not restricted to a half-plane) from a point to a vertical line [28, A000129][cf. Fig. S5(b)].

The interpretation for $P_\ell(n)$, $\ell \geq 0$, as paths ending on the right triangle leg can be understood from a recursion relation between $P_\ell(n)$ with neighboring ℓ and n [cf. Eq. (S35)]. For this purpose, let us first derive the relation and construct $P_\ell(n)$ as a matrix. By using Eq. (S25) twice and reordering summation indices, we obtain for $\ell, n \geq 1$:

$$\begin{aligned}
P_{\ell+1}(n+1) &= \sum_{m=1}^{n} P_\ell(m) P_0(n+1-m) \\
&= \sum_{m=1}^{n} \sum_{k=1}^{m-1} P_{\ell-1}(k) P_0(m-k) P_0(n+1-m) \\
&= \sum_{m=1}^{n-1} P_{\ell-1}(m) \sum_{k=1}^{n-m} P_0(k) P_0(n+1-m-k).
\end{aligned} \tag{S33}$$

Via Eqs. (S22) and (S25), this yields

$$\begin{aligned}
P_{\ell+1}(n+1) &= \sum_{m=1}^{n-1} P_{\ell-1}(m)[P_0(n+1-m) - P_0(n-m)] \\
&= \sum_{m=1}^{n-1} P_{\ell-1}(m) P_0(n+1-m) - P_\ell(n) \\
&= \sum_{m=1}^{n} P_{\ell-1}(m) P_0(n+1-m) - P_{\ell-1}(n) - P_\ell(n) \\
&= P_\ell(n+1) - P_{\ell-1}(n) - P_\ell(n).
\end{aligned} \tag{S34}$$

We can combine this recursion

$$P_\ell(n+1) = P_{\ell-1}(n) + P_\ell(n) + P_{\ell+1}(n+1) \tag{S35}$$

with the relation known from Eq. (S16),

$$P_0(n+1) = P_0(n) + P_1(n+1), \tag{S36}$$

and Eq. (S27), which implies

$$P_n(n) = 1; \qquad P_\ell(n) = 0, \quad \ell \geq n. \tag{S37}$$

These equations suffice to build the following matrix, defined as $A_{n,\ell} = P_\ell(n)$, with $n \geq 1$ and $\ell \geq 0$:

$$\begin{array}{r c}
 & \begin{array}{ccccccc} \ell=0, & 1, & 2, & 3, & 4, & 5, & \dots \end{array} \\
\begin{array}{r} n=1 \\ 2 \\ 3 \\ 4 \\ 5 \\ \vdots \end{array} &
\left(\begin{array}{ccccccc}
1 & 0 & \dots & & & & \\
2 & 1 & 0 & \dots & & & \\
6 & 4 & 1 & 0 & \dots & & \\
22 & 16 & 6 & 1 & 0 & \dots & \\
90 & 68 & 30 & 8 & 1 & 0 & \dots \\
\vdots & & & & & \ddots & \ddots
\end{array} \right) \\
 & c_\ell = 1, \quad 2, \quad 5, \quad 12, \quad 29
\end{array} \tag{S38}$$

If one distorts the matrix slightly, e.g. by raising the ℓ-th column by ℓ times half the width between subsequent rows and ignores all vanishing entries, one obtains a triangle structure as in Fig. S5. We might consider the entry $A_{0,1}$ as the starting point of paths, for which the steps

$$\begin{aligned}
&n \to n+1, && \ell \to \ell, \\
&n \to n+1, && \ell \to \ell+1, \\
&n \to n, && \ell+1 \to \ell
\end{aligned} \tag{S39}$$

are allowed. Then, the entry $A_{n,\ell}$ indeed gives the number of such paths ending at the corresponding point on the triangular grid.

The equality between the number of differentiated parquet and mfRG diagrams shown in Sec. S-III, Eq. (S32), translates into

$$(n-1) A_{n,0} = 2 \sum_{\ell=1}^{n-1} c_\ell A_{n,\ell}. \tag{S40}$$

While many relations for the matrix A [Eq. (S38)] are known [28, A033877], we have not found a proof of Eq. (S40) in the literature.

PHYSICAL REVIEW B **97**, 035162 (2018)

Multiloop functional renormalization group for general models

Fabian B. Kugler and Jan von Delft
Physics Department, Arnold Sommerfeld Center for Theoretical Physics, and Center for NanoScience,
Ludwig-Maximilians-Universität München, Theresienstrasse 37, 80333 Munich, Germany

(Received 9 August 2017; revised manuscript received 1 December 2017; published 31 January 2018)

We present multiloop flow equations in the functional renormalization group (fRG) framework for the four-point vertex and self-energy, formulated for a general fermionic many-body problem. This generalizes the previously introduced vertex flow [F. B. Kugler and J. von Delft, Phys. Rev. Lett. **120**, 057403 (2018)] and provides the necessary corrections to the self-energy flow in order to complete the derivative of all diagrams involved in the truncated fRG flow. Due to its iterative one-loop structure, the multiloop flow is well suited for numerical algorithms, enabling improvement of many fRG computations. We demonstrate its equivalence to a solution of the (first-order) parquet equations in conjunction with the Schwinger-Dyson equation for the self-energy.

DOI: 10.1103/PhysRevB.97.035162

I. INTRODUCTION

Two of the most powerful generic methods in the study of large or open many-body systems at intermediate coupling strength are the parquet formalism [1,2] and the functional renormalization group (fRG) [3,4]. As is commonly known, these frameworks are intimately related. However, their equivalence has only recently been established via multiloop fRG (mfRG) flow equations, introduced in a case study of the x-ray-edge singularity [5]. In this paper, we consolidate this equivalence and formulate the mfRG flow for the general many-body problem. For this, we generalize the multiloop vertex flow from Ref. [5], and, to ensure full inclusion of the self-energy, we present two multiloop corrections to the self-energy flow. Altogether, the mfRG flow is shown to fully generate all parquet diagrams for the vertex and self-energy; it is thus equivalent to solving the (first-order) parquet equations in conjunction with the Schwinger-Dyson equation (SDE) for the self-energy.

The parquet equations (together with the SDE) provide exact, self-consistent equations for the four-point vertex and self-energy, allowing one to describe one-particle and two-particle correlations [1]. The only input is the totally irreducible (four-point) vertex. Approximating it by the bare interaction yields the first-order parquet equations [2] (or parquet approximation [1]), a solution of which generates the so-called parquet diagrams for the four-point vertex and self-energy.

The functional renormalization group provides an infinite hierarchy of exact flow equations for vertex functions, depending on an RG scale parameter Λ. During the flow, high-energy ($\gtrsim \Lambda$) modes are successively integrated out, and the full solution is obtained at $\Lambda = 0$, such that one is free in the specific way the Λ dependence (regulator) is chosen [3,4]. If one restricts the fRG flow equations to the four-point vertex and self-energy, one is left with the six-point vertex as input. In the typical approximation, the six-point vertex is neglected, implying that all diagrams contributing to the flow are of the parquet type [5,6]. However, due to this truncation, the flow equations (for both self-energy and four-point vertex) no longer form a total derivative of diagrams with respect to the flow parameter Λ. This limits the predictive power of fRG and yields results that actually depend on the choice of regulator.

The mfRG corrections to the fRG flow simulate the effect of six-point vertex contributions on parquet diagrams, by means of an iterative multiloop construction. They complete the derivative of diagrams in the flow equations of both self-energy and four-point vertex, which are otherwise only partially contained. As it achieves a full resummation of all parquet diagrams in a numerically efficient way, the mfRG flow allows for significant improvement of fRG computations and overcomes weaknesses of the formalism experienced hitherto.

The paper is organized as follows. In Sec. II, we give the setup with all notations, before we recall the basics of the parquet formalism in Sec. III. In Sec. IV, we present the mfRG flow equations for the four-point vertex and self-energy. We show that they fully generate all parquet diagrams to arbitrary order in the interaction and comment on computational and general properties of the flow equations. Finally, we present our conclusions in Sec. V.

II. SETUP

We consider a general theory of interacting fermions, defined by the action

$$S = -\sum_{x',x} \bar{c}_{x'} \big[(G^0)^{-1} \big]_{x',x} c_x - \frac{1}{4} \sum_{x',x,y',y} \Gamma^0_{x',y';x,y} \bar{c}_{x'} \bar{c}_{y'} c_y c_x , \tag{1}$$

with a bare propagator G^0 and a bare four-point vertex Γ^0, which is antisymmetric in its first and last two arguments. The index x denotes all quantum numbers of the Grassmann field c_x. If we choose, e.g., Matsubara frequency, momentum, and spin, with $x = (i\omega, \boldsymbol{k}, \sigma) = (k, \sigma)$, and consider a translationally invariant system with interaction $U_{|\boldsymbol{k}|}$, the bare quantities read

$$G^0_{x',x} \overset{\text{e.g.}}{=} G^0_{k,\sigma} \delta_{k',k} \, \delta_{\sigma',\sigma} \, , \tag{2a}$$

$$-\Gamma^0_{x_1',x_2';x_1,x_2} \overset{\text{e.g.}}{=} \big(U_{|\boldsymbol{k}_1' - \boldsymbol{k}_1|} \delta_{\sigma_1',\sigma_1} \delta_{\sigma_2',\sigma_2} - U_{|\boldsymbol{k}_1' - \boldsymbol{k}_2|} \delta_{\sigma_1',\sigma_2} \delta_{\sigma_2',\sigma_1} \big) \, \delta_{k_1'+k_2',k_1+k_2} . \tag{2b}$$

Correlation functions of fields, corresponding to time-ordered expectation values of operators, are given by the path

©2018 American Physical Society

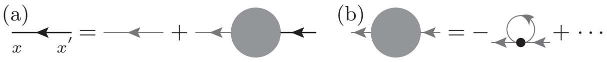

FIG. 1. (a) Dyson's equation relating the full propagator $G_{x,x'}$ (black, thick line) to the bare propagator G^0 (gray, thin line) and the self-energy Σ (circle). (b) First-order diagram for the self-energy using the bare vertex Γ^0 (solid dot).

integral

$$\left\langle c_{x_1} \cdots \bar{c}_{x_n} \right\rangle = \frac{1}{Z} \int \mathcal{D}[\bar{c}]\mathcal{D}[c]\, c_{x_1} \cdots \bar{c}_{x_n} e^{-S}, \tag{3}$$

where Z ensures normalization, such that $\langle 1 \rangle = 1$. Two-point correlation functions are represented by the full propagator G. Via Dyson's equation, G is expressed in terms of the bare propagator G^0 and the self-energy Σ [cf. Fig. 1(a)], according to

$$G_{x,x'} = -\langle c_x \bar{c}_{x'} \rangle, \quad G = G^0 + G^0 \cdot \Sigma \cdot G, \tag{4}$$

using the matrix product $(A \cdot B)_{x,x'} = \sum_y A_{x,y} B_{y,x'}$.

In a diagrammatic expansion, the lowest-order contribution to the self-energy is given by the diagram in Fig. 1(b), making use of the bare objects G^0, Γ^0. For later purposes, we define a *self-energy loop* (L) as

$$L(\Gamma,G)_{x',x} = -\sum_{y',y} \Gamma_{x',y';x,y} G_{y,y'}. \tag{5}$$

With this, we can write the first-order contribution from Fig. 1(b) generally and in the above example as

$$\Sigma^{1\text{st}}_{x',x} = L(\Gamma^0,G^0)_{x',x} \tag{6a}$$

$$\overset{\text{e.g.}}{=} \Bigg(U_0 \sum_{\tilde{k},\tilde{\sigma}} G^0_{\tilde{k},\tilde{\sigma}} - \sum_{\tilde{k}} U_{|\boldsymbol{k}-\tilde{\boldsymbol{k}}|} G^0_{\tilde{k},\sigma} \Bigg) \delta_{k',k} \delta_{\sigma',\sigma}. \tag{6b}$$

Four-point correlation functions can be expressed via the full (one-particle-irreducible) four-point vertex Γ:

$$\begin{aligned} \left\langle c_{x_1} c_{x_2} \bar{c}_{x'_2} \bar{c}_{x'_1} \right\rangle = {} & G_{x_1 x'_1} G_{x_2 x'_2} - G_{x_1 x'_2} G_{x_2 x'_1} \\ & + G_{x_1 y'_1} G_{x_2 y'_2} \Gamma_{y'_1,y'_2;y_1,y_2} G_{y_1 x'_1} G_{y_2 x'_2}. \end{aligned} \tag{7}$$

Note that we omit the superscript compared to the usual notation ($\Gamma^{(4)}$) [3–6] and often refer to the four-point vertex simply as the vertex. Our definition of Γ [7] agrees with that of Ref. [4] and therefore contains a relative minus sign compared to Ref. [3].

The diagrammatic expansion of Γ up to second order in the interaction is shown in Fig. 2. In such diagrams, the position of the external legs will always be fixed and labeled in correspondence to the four arguments of a vertex. Let us define *bubble functions* (B), distinguished between the three two-particle channels $r \in \{a,p,t\}$, as

$$\begin{aligned} & B_a(\Gamma,\Gamma')_{x'_1,x'_2;x_1,x_2} \\ & \quad = \sum_{y'_1,y_1,y'_2,y_2} \Gamma_{x'_1,y'_2;y_1,x_2} G_{y_1,y'_1} G_{y_2,y'_2} \Gamma'_{y'_1,x'_2;x_1,y_2}, \end{aligned} \tag{8a}$$

$$\begin{aligned} & B_p(\Gamma,\Gamma')_{x'_1,x'_2;x_1,x_2} \\ & \quad = \frac{1}{2} \sum_{y'_1,y_1,y'_2,y_2} \Gamma_{x'_1,x'_2;y_1,y_2} G_{y_1,y'_1} G_{y_2,y'_2} \Gamma'_{y'_1,y'_2;x_1,x_2}, \end{aligned} \tag{8b}$$

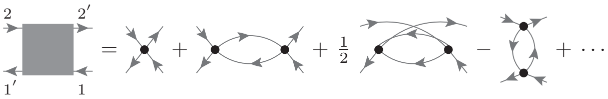

FIG. 2. Diagrammatic expansion of the four-point vertex Γ (square) up to second order in the interaction (i.e., these diagrams define $\Gamma^{2\text{nd}}$). The positions of the external (amputated) legs refer to the arguments of $\Gamma_{x'_1,x'_2;x_1,x_2}$.

$$\begin{aligned} & B_t(\Gamma,\Gamma')_{x'_1,x'_2;x_1,x_2} \\ & \quad = -\sum_{y'_1,y_1,y'_2,y_2} \Gamma_{y'_1,x'_2;y_1,x_2} G_{y_2,y'_1} G_{y_1,y'_2} \Gamma'_{x'_1,y'_2;x_1,y_2}. \end{aligned} \tag{8c}$$

The translation of Fig. 2 is then simply given by

$$\Gamma^{2\text{nd}} = \Gamma^0 + \textstyle\sum_r B_r(\Gamma^0,\Gamma^0). \tag{9}$$

Following the conventions of Bickers [1], the factor of 1/2 in Eq. (8b) (Fig. 2) makes sure that, when summing over all internal indices, one does not overcount the effect of the two indistinguishable (parallel) lines. The minus sign in Eq. (8c) (Fig. 2) stems from the fact that the antiparallel bubbles (8a) and (8c) are related by exchange of fermionic legs. Indeed, using the antisymmetry of Γ and Γ' in their arguments (crossing symmetry), we find that

$$B_a(\Gamma,\Gamma')_{x'_1,x'_2;x_1,x_2} = -B_t(\Gamma,\Gamma')_{x'_2,x'_1;x_1,x_2}. \tag{10}$$

The channel label $r \in \{a,p,t\}$ refers to the fact that the individual diagrams are reducible—i.e., they fall apart into disconnected diagrams—by cutting two *antiparallel* lines, two *parallel* lines, or two *transverse* (antiparallel) lines, respectively. (The term transverse itself refers to a horizontal spacetime axis.) In using the terms antiparallel and parallel, we adopt the nomenclature used in the seminal application of the parquet equations to the x-ray-edge singularity by Roulet *et al.* [2]. Equivalently, a common notation [8,9] for the channels a,p,t is $ph,pp,\overline{ph}$, referring to the (longitudinal) particle-hole, the particle-particle, and the transverse (or vertical) particle-hole channel, respectively. One also finds the labels x,p,d in the literature [10], referring to the so-called exchange, pairing, and direct channel, respectively.

In the context of fRG (cf. Sec. IV), functions such as G, Σ, Γ develop a scale (Λ) dependence (which will be suppressed in the notation). If we write the bubble functions also symbolically as

$$B_r(\Gamma,\Gamma') = [\Gamma \circ G \circ G \circ \Gamma']_r, \tag{11}$$

we can immediately define bubbles with differentiated propagators (but undifferentiated vertices) according to

$$\dot{B}_r(\Gamma,\Gamma') = [\Gamma \circ (\partial_\Lambda (G \circ G)) \circ \Gamma']_r. \tag{12}$$

In the fRG flow equations, we will further need the (so-called) single-scale propagator, defined by ($\mathbb{1}_{x,y} = \delta_{x,y}$)

$$S = \partial_\Lambda G|_{\Sigma=\text{const.}} = (\mathbb{1} + G \cdot \Sigma) \cdot (\partial_\Lambda G^0) \cdot (\Sigma \cdot G + \mathbb{1}). \tag{13}$$

Before moving on to the mfRG flow, let us next review the basics of the parquet formalism.

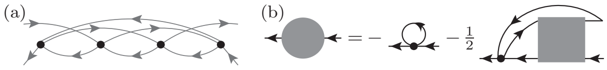

FIG. 3. (a) Vertex diagram irreducible in all two-particle channels (i.e., it belongs to R) and thus not part of Γ in the parquet approximation. (b) Schwinger-Dyson equation, relating the self-energy to the four-point vertex self-consistently.

III. PARQUET FORMALISM

The parquet formalism [1,2] provides exact, self-consistent equations for both four-point vertex and self-energy. Focusing on the vertex first, the central parquet equation represents a classification of diagrams distinguished by reducibility in the three two-particle channels:

$$\Gamma = R + \sum_r \gamma_r, \quad I_r = R + \sum_{r' \neq r} \gamma_{r'}. \tag{14}$$

Diagrams of Γ are either reducible in one of the three channels (i.e., part of γ_r for $r \in \{a,p,t\}$; cf. Fig. 2), or they belong to the class of totally irreducible diagrams R [cf. Fig. 3(a)]. (The notation again refers to Ref. [2].) As a diagram cannot simultaneously be reducible in more than one channel [2], one collects diagrams that are not reducible in r lines into the irreducible vertex I_r of that channel. Reducible and irreducible vertices are further related by the self-consistent Bethe-Salpeter equations (BSEs)

$$\gamma_r = B_r(I_r,\Gamma), \tag{15}$$

the graphical representations of which are given in Fig. 4.

The BSEs (15) are computed with full propagators G. Thus, they require knowledge of the self-energy, which itself can be determined by the self-consistent SDE depending on the four-point vertex [cf. Fig. 3(b)]:

$$\begin{aligned}\Sigma &= L(\Gamma^0,G) + L\big[B_p(\Gamma^0,\Gamma),G\big] \\ &= L(\Gamma^0,G) + \frac{1}{2}L\big[B_a(\Gamma^0,\Gamma),G\big].\end{aligned} \tag{16}$$

The only input required for solving the parquet equations is the totally irreducible vertex R. All remaining contributions to the vertex and self-energy are determined self-consistently. The simplest way to solve the parquet equations is to approximate R by the bare vertex Γ^0. This is called the first-order parquet solution [2], or parquet approximation [1], and corresponds to a summation of the leading logarithmic diagrams in logarithmically divergent perturbation theories.

The diagrams generated by the first-order parquet solution are called parquet diagrams. For Γ, these can be obtained by successively replacing bare vertices by one of the three bubbles from Eq. (8) (connected by full lines), starting from the bare vertex. For Σ, the parquet diagrams are obtained by inserting the parquet vertex into the SDE. They can also be characterized by the property that one needs to cut at most one bare line to obtain a *parquet* vertex with possible dressing at the external legs. By this, we mean that, instead of an ingoing or outgoing amputated leg, the external line is of the type $\mathbb{1} + \Sigma \cdot G$ or $\mathbb{1} + G \cdot \Sigma$, respectively, using again a parquet self-energy.

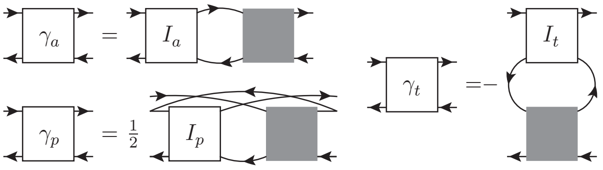

FIG. 4. Bethe-Salpeter equations in the three two-particle channels, relating the reducible (γ_r) and irreducible (I_r) vertices self-consistently in the parquet formalism.

IV. MULTILOOP FRG FLOW

The functional renormalization group [3,4] provides a hierarchy of exact flow equations for vertex functions, depending on an RG parameter Λ, serving as infrared cutoff in the bare propagator. A typical choice for the Λ dependence, in order to flow from the trivially uncorrelated to the full theory, is characterized by the boundary conditions $G_{\Lambda_i} = 0$ and $G_{\Lambda_f} = G$, implying $\Gamma_{\Lambda_i} = \Gamma^0$. Restring the flow to Σ and Γ, the six-point vertex remains as input and is neglected in the standard approximation.

Here, we view fRG as a tool to resum diagrams which does not necessarily rely on the original fRG hierarchy deduced from the flow of the (quantum) effective action. In previous works [5,6], we have used the x-ray-edge singularity as an example to show that the standard truncation of fRG restricts the flow to parquet diagrams of the vertex, and that the derivatives of those diagrams are only partially contained. Using the same model, we have introduced multiloop fRG flow equations for the vertex which complete the derivative of parquet diagrams in an iterative manner, as organized by the number of loops connecting full vertices, and thus do achieve a full summation of all parquet diagrams [5]. The x-ray-edge singularity facilitates diagrammatic arguments as it allows one to consider only two two-particle channels and to neglect self-energies. Here, we give the details of how the mfRG flow of the vertex is generalized to all three two-particle channels with indistinguishable particles (as already indicated in Ref. [5]) and formulate the mfRG corrections to the self-energy flow (not discussed in Ref. [5]).

We first pose the mfRG flow equations and motivate them by showing examples of diagrams, which are otherwise only partially contained. Then, we justify the extensions of the truncated fRG flow by arguing that all diagrams are of the appropriate type without any overcounting. Subsequently, we give a recipe for counting the number of diagrams generated by the parquet and mfRG flow equations. This allows one to check that the mfRG flow fully captures all parquet diagrams order for order in the interaction. Finally, we discuss computational and general properties of the flow equations.

A. Flow equations for the vertex

The mfRG flow of the vertex proposed in Ref. [5] makes use of the channel classification known from the parquet equations and is organized by the *loop order* ℓ. We write

$$\partial_\Lambda \Gamma = \sum_r \partial_\Lambda \gamma_r, \quad \partial_\Lambda \gamma_r = \sum_{\ell \geqslant 1} \dot{\gamma}_r^{(\ell)}, \quad \dot{\gamma}_{\bar{r}}^{(\ell)} = \sum_{r' \neq r} \dot{\gamma}_{r'}^{(\ell)}, \tag{17}$$

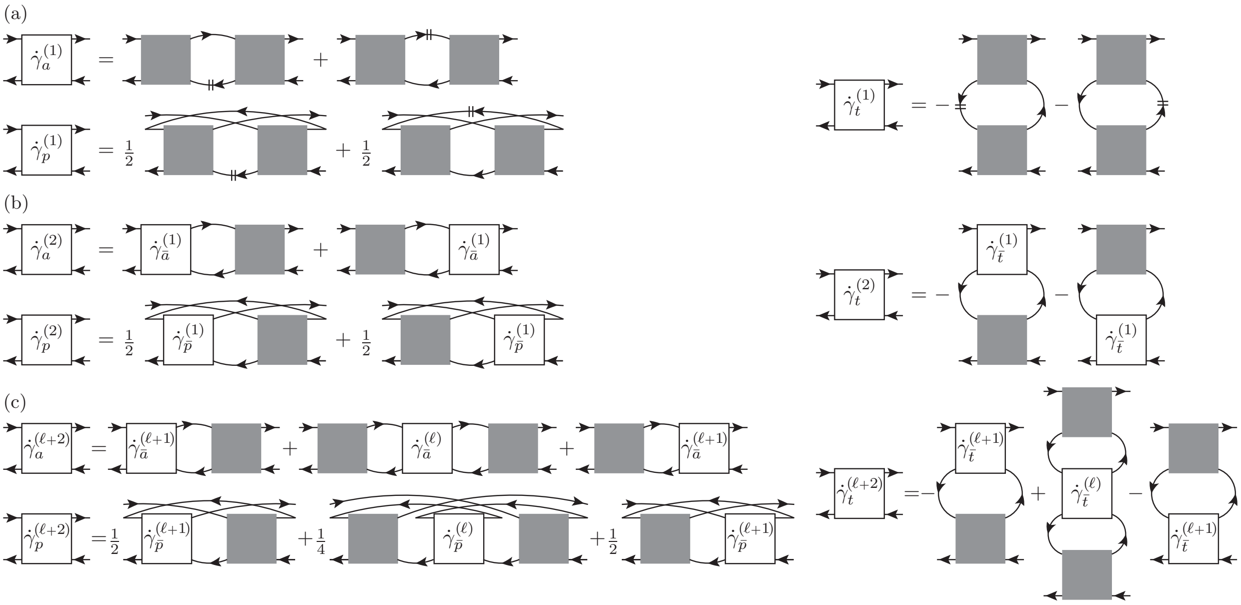
(a)
$\dot\gamma_a^{(1)}$ = +
$\dot\gamma_p^{(1)}$ = $\frac{1}{2}$ + $\frac{1}{2}$
$\dot\gamma_t^{(1)}$ = − −
(b)
$\dot\gamma_a^{(2)}$ = $\dot\gamma_{\bar a}^{(1)}$ + $\dot\gamma_{\bar a}^{(1)}$
$\dot\gamma_p^{(2)}$ = $\frac{1}{2}$ $\dot\gamma_{\bar p}^{(1)}$ + $\frac{1}{2}$ $\dot\gamma_{\bar p}^{(1)}$
$\dot\gamma_t^{(2)}$ = − $\dot\gamma_{\bar t}^{(1)}$ − $\dot\gamma_{\bar t}^{(1)}$
(c)
$\dot\gamma_a^{(\ell+2)}$ = $\dot\gamma_{\bar a}^{(\ell+1)}$ + $\dot\gamma_{\bar a}^{(\ell)}$ + $\dot\gamma_{\bar a}^{(\ell+1)}$
$\dot\gamma_p^{(\ell+2)}$ = $\frac{1}{2}$ $\dot\gamma_{\bar p}^{(\ell+1)}$ + $\frac{1}{4}$ $\dot\gamma_{\bar p}^{(\ell)}$ + $\frac{1}{2}$ $\dot\gamma_{\bar p}^{(\ell+1)}$
$\dot\gamma_t^{(\ell+2)}$ =− $\dot\gamma_{\bar t}^{(\ell+1)}$ + $\dot\gamma_{\bar t}^{(\ell)}$ − $\dot\gamma_{\bar t}^{(\ell+1)}$

FIG. 5. Multiloop flow equations for the four-point vertex in a general fermionic model. (a) Standard truncated, one-loop flow, where a line with double dashes denotes $\partial_\Lambda G$. (b) Two-loop correction (upon inserting the one-loop contributions, one obtains two loops connecting full vertices). (c) Higher-loop corrections starting from $\ell + 2 = 3$, which contain the additional contribution (center part) where vertices from the complementary channels are connected by two bubbles.

where $\dot\gamma_r^{(\ell)}$ contains differentiated diagrams reducible in channel r with ℓ loops connecting full vertices and will be constructed iteratively; $\bar r$ represents the complementary channels to channel r. Using the bubble functions (8) and the channel decomposition, the multiloop flow for Γ is compactly stated as ($\ell \geqslant 1$)

$$\dot\gamma_r^{(1)} = \dot B_r(\Gamma,\Gamma), \tag{18a}$$

$$\dot\gamma_r^{(2)} = B_r\big(\dot\gamma_{\bar r}^{(1)},\Gamma\big) + B_r\big(\Gamma,\dot\gamma_{\bar r}^{(1)}\big), \tag{18b}$$

$$\dot\gamma_r^{(\ell+2)} = B_r\big(\dot\gamma_{\bar r}^{(\ell+1)},\Gamma\big) + \dot\gamma_{r,\mathrm{C}}^{(\ell+2)} + B_r\big(\Gamma,\dot\gamma_{\bar r}^{(\ell+1)}\big), \tag{18c}$$

$$\dot\gamma_{r,\mathrm{C}}^{(\ell+2)} = B_r\big[\Gamma,B_r\big(\dot\gamma_{\bar r}^{(\ell)},\Gamma\big)\big] = B_r\big[B_r\big(\Gamma,\dot\gamma_{\bar r}^{(\ell)}\big),\Gamma\big] \tag{18d}$$

and illustrated in Fig. 5.

The standard truncated, one-loop flow of Γ is simply given by Eq. (18a) [Fig. 5(a)]. A simplified version of this equation, in which one uses the single-scale propagator S (13) instead of $\partial_\Lambda G$ in the differentiated bubble (12), corresponds to the result obtained from the exact flow equation upon neglecting the six-point vertex [11]. The form given here, with $\partial_\Lambda G$ instead of S (also known as Katanin substitution [3,12]), already includes corrections to this originating from vertex diagrams containing differentiated self-energy contributions. In the exact flow equation, these contributions are contained in the six-point vertex $\Gamma^{(6)}$ and excluded in S; omitting $\Gamma^{(6)}$, they are incorporated again by $\partial_\Lambda G = S + G \cdot (\partial_\Lambda \Sigma) \cdot G$.

Comparing Eqs. (9), (11), (12) with Eq. (18a) [or Fig. 2 with Fig. 5(a)], it is clear that the one-loop flow is correct up to second order, for which only bare vertices are involved. Indeed, all differentiated diagrams of $\Gamma^{2\mathrm{nd}}$, which are obtained by summing all copies of diagrams in which one G^0 line is replaced by $\partial_\Lambda G^0$, are contained in $\sum_r \dot\gamma_r^{(1)}$. However, starting at third order, the one-loop flow (18a) does not fully generate all (parquet) diagrams, since, in the exact flow, the six-point vertex starts contributing. In mfRG, the two-loop flow [Eq. (18b), Fig. 5(b)] completes the derivative of third-order diagrams of Γ (i.e., it contains all diagrams needed to ensure that $\dot\gamma_r^{(1)} + \dot\gamma_r^{(2)}$ fully represent $\partial_\Lambda \gamma_r^{3\mathrm{rd}}$). An example is given in Fig. 6(a), which shows a parquet diagram reducible in channel a. The differentiated diagram in Fig. 6(d), as part of the derivative of Fig. 6(a), is not included in the one-loop flow. The reason is that $\dot\gamma_a^{(1)}$ only contains vertices connected by antiparallel G^0-$\partial_\Lambda G^0$ lines, and not parallel ones, as would be necessary for this differentiated diagram. It is, however, included in the two-loop correction to the flow, as can be seen by inserting the lowest-order contributions for all vertices into the first summand on the right-hand side of $\dot\gamma_a^{(2)}$ (using $\dot\gamma_p^{(1)}$) in Fig. 5(b).

At all higher loop orders ($\ell + 2 \geqslant 3$) [Eq. (18c), Fig. 5(c)], we iterate this scheme and further add the *center part* (18d) of the vertex flow. This connects the ℓ-loop flow from the complementary ($\bar r$) channels by r bubbles on both sides, and is needed to complete the derivative of parquet diagrams starting at fourth order. Since $\dot\gamma_{r,\mathrm{C}}^{(\ell+2)}$ raises the loop order by two, it was still absent in the two-loop flow. The three summands in $\dot\gamma_r^{(\ell+2)}$, including $\dot\gamma_{r,\mathrm{C}}^{(\ell+2)}$, exhaust all possibilities to obtain differentiated vertex diagrams in channel r at loop order $\ell + 2$ in an iterative one-loop procedure. The mfRG vertex flow up to loop order ℓ therefore fully captures all parquet diagrams up to order $n = \ell + 1$ in the interaction (cf. Sec. IV D).

B. Flow equation for the self-energy

The self-energy has an *exact* fRG flow equation, which simply connects the four-point vertex with the single-scale

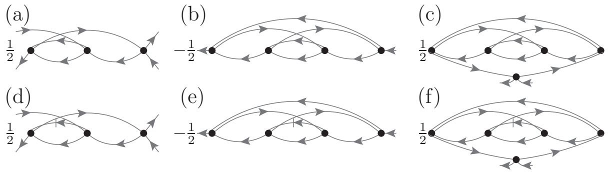

FIG. 6. (a)–(c) Some diagrams that are included in the parquet approximation and only partially contained in one-loop fRG. (d)–(f) One particular differentiated diagram for each of the diagrams (a)–(c) [the (gray, thin) line with a dash stands for $\partial_\Lambda G^0$] that is not part of the standard truncated flow, but included in mfRG.

propagator (cf. Fig. 7). However, if a vertex obtained from the truncated vertex flow is inserted into this standard self-energy flow equation, it generates diagrams that are only partially differentiated. In fact, even after correcting the vertex flow via mfRG to obtain all parquet diagrams of Γ, $\dot\Sigma_{\mathrm{std}}$ does not yet form a total derivative. Although $\dot\Sigma_{\mathrm{std}}$ is in principle exact [as is the SDE (16)], using the *parquet* vertex in this flow gives a less accurate result than inserting it into the SDE: All diagrams obtained from $\dot\Sigma_{\mathrm{std}}$ are of the parquet type, but their derivatives are not fully generated by the standard flow equation.

This problem can be remedied by adding multiloop corrections to the self-energy flow, which complete the derivative of all involved diagrams. The corrections consist of two additions that build on the center parts (18d) of the vertex flow in the a and p channels,

$$\dot\gamma_{\bar t,\mathrm{C}} = \sum_{\ell\geqslant 1}\big(\dot\gamma^{(\ell)}_{a,\mathrm{C}} + \dot\gamma^{(\ell)}_{p,\mathrm{C}}\big). \tag{19}$$

Using the self-energy loop (5), the mfRG flow equation for Σ is then given by (cf. Fig. 7)

$$\partial_\Lambda\Sigma = \dot\Sigma_{\mathrm{std}} + \dot\Sigma_{\bar t} + \dot\Sigma_t, \quad \dot\Sigma_{\mathrm{std}} = L(\Gamma,S), \tag{20a}$$

$$\dot\Sigma_{\bar t} = L(\dot\gamma_{\bar t,\mathrm{C}},G), \qquad \dot\Sigma_t = L(\Gamma,G\cdot\dot\Sigma_{\bar t}\cdot G). \tag{20b}$$

Note that self-energy diagrams in $\dot\Sigma_t$ and $\dot\Sigma_{\bar t}$ are reducible and irreducible in the t channel, respectively. However, here, this property is not exclusive; $\dot\Sigma_{\mathrm{std}}$, too, contains diagrams that are reducible and irreducible in the t channel, as is directly seen by inserting the second-order vertex from Fig. 2 into the first summand of Fig. 7.

To motivate the addition of $\dot\Sigma_{\bar t}$ and $\dot\Sigma_t$, let us consider the first examples where multiloop corrections are needed to complete the derivative of diagrams, which occur at fourth and fifth order, respectively. The diagram in Fig. 6(b) is obtained by inserting the γ_a diagram from Fig. 6(a) (and the symmetry-related γ_t diagram) into the SDE [Fig. 3(b)]. The differentiated diagram in Fig. 6(e) is part of the derivative of Fig. 6(b), but not contained in the standard flow. In fact, the vertex needed for this diagram to be part of $\dot\Sigma_{\mathrm{std}}$ [i.e., the vertex obtained by cutting the differentiated line in Fig. 6(e)] is a so-called envelope vertex, the lowest-order realization of a nonparquet vertex [cf. Fig. 3(b)] [13]. The diagram from Fig. 6(e) is, however, included in the first correction $\dot\Sigma_{\bar t}$, as can be seen by inserting the lowest-order contributions of all vertices in the center part of $\dot\gamma^{(3)}_a$ (using again $\dot\gamma^{(1)}_p$) in Fig. 5(c) and connecting the top lines.

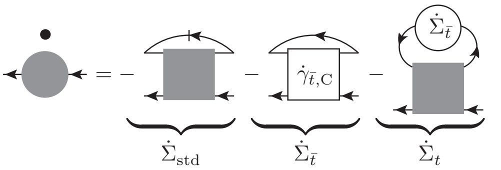

FIG. 7. Multiloop flow equation for the self-energy, adding two corrections ($\dot\Sigma_{\bar t}$, $\dot\Sigma_t$) to the standard fRG flow, $\dot\Sigma_{\mathrm{std}}$. The (black, thick) line with a dash denotes the single-scale propagator S.

Inserting the self-energy diagram from Fig. 6(b) into the full propagator of the first summand in the SDE [Fig. 3(b)] yields the diagram in Fig. 6(c). Similar to the previous discussion, one finds that the differentiated diagram in Fig. 6(f), needed for the full derivative of Fig. 6(c), is neither contained in $\dot\Sigma_{\mathrm{std}}$ nor $\dot\Sigma_{\bar t}$. It is, however, included in the second mfRG correction, $\dot\Sigma_t$, as one of the lowest-order realizations of the last summand in Fig. 7.

The two extra terms of the mfRG self-energy flow, $\dot\Sigma_{\bar t}$ and $\dot\Sigma_t$, incorporate the whole multiloop hierarchy of differentiated vertex diagrams via $\dot\gamma_{\bar t,\mathrm{C}}$ [Eq. (19)]. As is discussed in the following subsections, they suffice to generate all parquet diagrams of Σ and, therefore, provide the full dressing of the parquet vertex in return.

C. Justification

We will now justify our claim that the mfRG flow fully generates all parquet diagrams for Γ and Σ. We will first show that all differentiated diagrams in mfRG are of the parquet type and that there is no overcounting of diagrams. Concerning the vertex, this has already been done for the two-channel case of the x-ray-edge singularity [5]. The arguments for the general case are in fact completely analogous and repeated here for the sake of completeness. The self-energy is discussed thereafter.

The only totally irreducible contribution to the four-point vertex in the mfRG flow is the bare interaction stemming from the initial condition of the vertex, $\Gamma_{\Lambda_i} = \Gamma^0$. All further diagrams on the right-hand side of the flow equations are obtained by iteratively combining two vertices by one of the three bubbles from Eq. (8). Hence, they correspond to differentiated *parquet* diagrams in the respective channel.

The fact that there is no overcounting in mfRG, i.e., that each diagram occurs at most once, can be seen by employing arguments of diagrammatic reducibility and the unique position of the differentiated line in the diagrams. To be specific, let us consider here the a channel; the arguments for the other channels are completely analogous.

First, we note that diagrams in the one-loop term always differ from higher-loop ones. The reason is that in higher-loop terms, the differentiated line appears in the vertex coming from $\partial_\Lambda\gamma_{\bar a}$. This can never contain two vertices connected by an a G-$\partial_\Lambda G$ bubble, since such terms only originate upon differentiating γ_a, the vertex reducible in a lines.

Second, diagrams in the left, center, or right part [first, second, and third summand in Fig. 5(c), respectively] of an ℓ-loop contribution always differ. This is because the vertex $\gamma^{(\ell)}_{\bar a}$ is irreducible in a lines. The left part is then reducible in a lines *only after* the differentiated line appeared, the right part

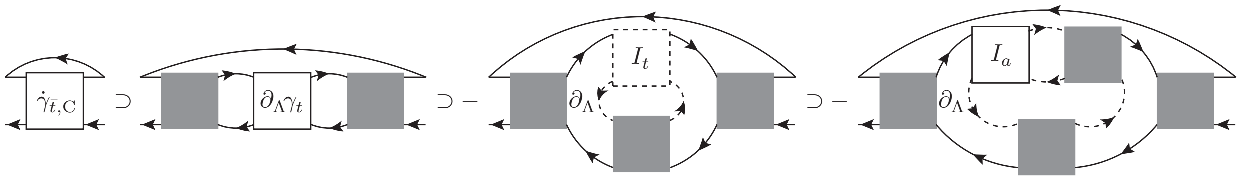

FIG. 8. Special diagrams contributing to $\dot{\Sigma}_{\bar{t}}$. In the last two diagrams, we consider a scenario where the differentiated line is contained in one of the dashed contributions.

only before, and the center part is reducible in this channel *before and after* $\partial_\Lambda G$.

Third, the same parts (say, the left parts) of different-order loop contributions ($\ell \neq \ell'$) are always different. Assume they agreed: As the a bubble induces the first reducibility in this channel, already $\gamma_{\bar{a}}^{(\ell)}$ and $\gamma_{\bar{a}}^{(\ell')}$ would have to agree. For these, only the same parts can agree, as mentioned before. The argument then proceeds iteratively until one compares the one-loop part to a higher-loop ($|\ell - \ell'| + 1$) one. These are, however, distinct according to the first point.

Concerning the self-energy, all diagrams of the flow belong to the parquet type, since they are constructed from (differentiated) parquet vertices by closing loops of external legs in an iterative one-loop procedure. By cutting one G^0 or the $\partial_\Lambda G^0$ line in such a self-energy diagram, one can always obtain a (differentiated) parquet vertex with possibly dressed amputated legs.

First, there is no overcounting between $\dot{\Sigma}_{\mathrm{std}}$ and $\dot{\Sigma}_{\bar{t}}$ because cutting the differentiated line in $\dot{\Sigma}_{\mathrm{std}}$ generates a parquet vertex (with possibly dressed amputated legs coming from the single-scale propagator; cf. Fig. 7), whereas this is not the case for $\dot{\Sigma}_{\bar{t}}$. To illustrate this statement, we consider in Fig. 8 a typical case of a $\dot{\Sigma}_{\bar{t}}$ correction, where we take the a part of $\dot{\gamma}_{\bar{t},\mathrm{C}}$ [cf. Eq. (19)] with $\partial_\Lambda\gamma_t$ in the center. We can insert the BSE $\gamma_t = B_t(I_t,\Gamma)$ (Fig. 4) and consider simultaneously all scenarios where the differentiated line, originating from $\partial_\Lambda\gamma_t$, is contained in any of the dashed parts. To be even more specific, we take a specific part of $I_t = R + \gamma_a + \gamma_p$, namely $\gamma_a = B_a(I_a,\Gamma)$ (Fig. 4), and consider the cases where the differentiated line, if contained in I_t, is contained in the corresponding bubble. If one now cuts any of the dashed lines, as candidates for the differentiated line, one finds that the remaining vertex is *not* of the parquet type, as it is not reducible in any of the two-particle channels. The same irreducibility in three lines, when starting to cut the differentiated line in $\dot{\gamma}_{\bar{t},\mathrm{C}}$, occurs in all diagrammatic realizations of $\dot{\Sigma}_{\bar{t}}$.

Since the standard flow $\dot{\Sigma}_{\mathrm{std}}$ with the *full* instead of the *parquet* vertex is exact, it follows that the $\dot{\Sigma}_{\bar{t}}$ part can be written similarly as $\dot{\Sigma}_{\mathrm{std}}$, but using a *nonparquet* (np) vertex [Fig. 9(a)]. As a consequence, $\dot{\Sigma}_t$, obtained by connecting $\dot{\Sigma}_{\bar{t}}$ and Γ by a t bubble, can similarly be written with a nonparquet vertex [Fig. 9(b)]. Thus, there cannot be any overcounting between $\dot{\Sigma}_{\mathrm{std}}$ and $\dot{\Sigma}_t$, either. Finally, there is likewise no overcounting between $\dot{\Sigma}_{\bar{t}}$ and $\dot{\Sigma}_t$: After removing the differentiated line in $\dot{\Sigma}_{\bar{t}}$, the remaining nonparquet vertex Γ_{np} is in particular irreducible in the t channel (as was discussed above). However, removing the differentiated line in $\dot{\Sigma}_t$ after expressing $\dot{\Sigma}_{\bar{t}}$ via Γ_{np} [cf. Fig. 9(b)], the remaining vertex Γ'_{np} is by construction reducible in t lines (although not a parquet vertex).

In summary, all diagrams of the four-point vertex and self-energy generated by the mfRG flow belong to the parquet class and are included at most once. To show that the mfRG flow generates *all* differentiated parquet diagrams, we will demonstrate next that, at any given order in the interaction, their number is equal to the number of diagrams generated by the mfRG flow.

D. Counting of diagrams

In order to count the number of diagrams in all involved functions, we make use of either exact, self-consistent equations or the mfRG flow equations. As a first example, we count the number of diagrams in the full propagator G at order n in the interaction, $\mathcal{N}_G(n)$, given the number of diagrams in the self-energy, $\mathcal{N}_\Sigma(n)$. Concerning the bare propagator and self-energy, we know $\mathcal{N}_{G^0}(n) = \delta_{n,0}$ and $\mathcal{N}_\Sigma(0) = 0$. From Dyson's equation (4), we then get

$$\mathcal{N}_G(n) = \delta_{n,0} + \sum_{m=1}^{n} \mathcal{N}_\Sigma(m)\mathcal{N}_G(n-m). \tag{21}$$

Defining a convolution of sequences, according to

$$\mathcal{N}_1 = \mathcal{N}_2 * \mathcal{N}_3 \Leftrightarrow \mathcal{N}_1(n) = \sum_{m=0}^{n} \mathcal{N}_2(m)\mathcal{N}_3(n-m) \quad \forall n, \tag{22}$$

we can write Eq. (21) in direct analogy to the original equation (4) as

$$\mathcal{N}_G = \mathcal{N}_{G^0} + \mathcal{N}_{G^0} * \mathcal{N}_\Sigma * \mathcal{N}_G. \tag{23}$$

Similar relations for the self-energy and vertex can be obtained from the SDE (16), the parquet equation (14), and the BSEs (15). The number of diagrams in the bare vertex is $\mathcal{N}_{\Gamma^0} = \delta_{n,1}$ (one can also take any $\mathcal{N}_{\Gamma^0} \propto \delta_{n,1}$). From the SDE

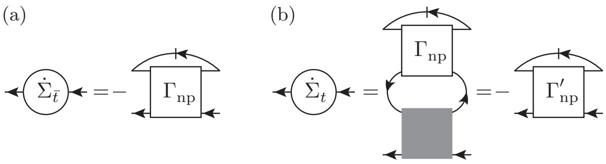

FIG. 9. Rewriting of the corrections to the self-energy flow: (a) $\dot{\Sigma}_{\bar{t}}$ can be expressed by a nonparquet vertex Γ_{np} contracted with the single-scale propagator S. (b) $\dot{\Sigma}_t$, obtained by connecting $\dot{\Sigma}_{\bar{t}}$ and Γ by a t bubble, then involves a bubble connecting a nonparquet and parquet vertex, which yields another nonparquet vertex Γ'_{np}, contracted with S.

TABLE I. Number of (bare) parquet diagrams, differentiated parquet diagrams, and diagrams generated by mfRG up to interaction order 6 and loop order 5. Fractional parts originate from multiple factors of 1/2, used to avoid double counting of the antisymmetric vertex [1]. As we use $\mathcal{N}_{\Gamma^0} = \delta_{n,1}$, we count Hugenholtz diagrams [15] [where, e.g., $\mathcal{N}_\Sigma(1) = 1$, cf. Fig. 1]. The choice $\mathcal{N}_{\Gamma^0} = 2\delta_{n,1}$ [cf. Eq. (2b)] would give an extra factor 2^n for all numbers of diagrams at order n, resulting in the (integer) numbers of Feynman diagrams [where, e.g., $\mathcal{N}_\Sigma(1) = 2$].

n	1	2	3	4	5	6
$\mathcal{N}_\Gamma$	1	$2\frac{1}{2}$	$15\frac{1}{4}$	$108\frac{1}{8}$	$832\frac{1}{16}$	$6753\frac{21}{32}$
$\mathcal{N}_\Sigma$	1	$1\frac{1}{2}$	$5\frac{1}{4}$	$25\frac{7}{8}$	$156\frac{1}{16}$	$1073\frac{3}{32}$
$\mathcal{N}_{\dot{\Gamma}}$	0	5	61	$648\frac{3}{4}$	$6656\frac{1}{2}$	$67536\frac{9}{16}$
$\mathcal{N}_{\dot{\Gamma}^{(1\ell)}}$	0	5	45	$373\frac{3}{4}$	$3117\frac{1}{2}$	$26519\frac{1}{16}$
$\mathcal{N}_{\dot{\Gamma}^{(2\ell)}}$	0	0	16	216	2264	21972
$\mathcal{N}_{\dot{\Gamma}^{(3\ell)}}$	0	0	0	59	1062	$13481\frac{1}{2}$
$\mathcal{N}_{\dot{\Gamma}^{(4\ell)}}$	0	0	0	0	213	$4792\frac{1}{2}$
$\mathcal{N}_{\dot{\Gamma}^{(5\ell)}}$	0	0	0	0	0	$771\frac{1}{2}$
$\mathcal{N}_{\dot{\Sigma}}$	1	$4\frac{1}{2}$	$26\frac{1}{4}$	$181\frac{1}{8}$	$1404\frac{9}{16}$	$11804\frac{1}{32}$
$\mathcal{N}_{\dot{\Sigma}_{\mathrm{std}}}$	1	$4\frac{1}{2}$	$26\frac{1}{4}$	$177\frac{1}{8}$	$1311\frac{9}{16}$	$10348\frac{1}{32}$
$\mathcal{N}_{\dot{\Sigma}_{\bar{t}}}$	0	0	0	4	89	1349
$\mathcal{N}_{\dot{\Sigma}_t}$	0	0	0	0	4	107

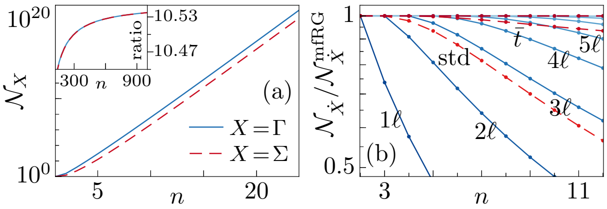

FIG. 10. Logarithmic plots for the number of diagrams at interaction order n for both vertex and self-energy. (a) $\mathcal{N}_\Gamma$, $\mathcal{N}_\Sigma$ grow exponentially for large n (inset: the ratio of subsequent elements approaches a constant). (b) The cumulative low-loop vertex flows (1ℓ up to 5ℓ) and the self-energy flows $\dot{\Sigma}_{\mathrm{std}}$ (labeled std) and $\dot{\Sigma}_{\mathrm{std}} + \dot{\Sigma}_{\bar{t}}$ (labeled $\bar{t}$) miss differentiated parquet diagrams. However, the full multiloop flow for vertex and self-energy generates all differentiated parquet diagrams to arbitrary order in the interaction.

(16), we get for the self-energy

$$\mathcal{N}_\Sigma = \mathcal{N}_{\Gamma^0} * \mathcal{N}_G + \tfrac{1}{2} \mathcal{N}_{\Gamma^0} * \mathcal{N}_G * \mathcal{N}_G * \mathcal{N}_G * \mathcal{N}_\Gamma. \tag{24}$$

Note that, when counting diagrams, we can ignore the extra minus signs but must keep track of prefactors of magnitude not equal to unity. These prefactors avoid double counting of the antisymmetric vertex [1] and originate from the way the diagrams are constructed [14].

Concerning the full vertex, we can use that the symmetry relation between the a and t bubble given in Eq. (10) holds for the full reducible vertices γ_a and γ_t [1], such that $\mathcal{N}_{\gamma_a} = \mathcal{N}_{\gamma_t}$. In the parquet approximation $R = \Gamma^0$, and the parquet equation (14) and the BSEs (15) yield

$$\mathcal{N}_\Gamma = \mathcal{N}_R + 2\mathcal{N}_{\gamma_a} + \mathcal{N}_{\gamma_p}, \tag{25a}$$

$$\mathcal{N}_{\gamma_a} = (\mathcal{N}_\Gamma - \mathcal{N}_{\gamma_a}) * \mathcal{N}_G * \mathcal{N}_G * \mathcal{N}_\Gamma, \tag{25b}$$

$$\mathcal{N}_{\gamma_p} = \tfrac{1}{2}(\mathcal{N}_\Gamma - \mathcal{N}_{\gamma_p}) * \mathcal{N}_G * \mathcal{N}_G * \mathcal{N}_\Gamma. \tag{25c}$$

Since $\mathcal{N}_{\Gamma^0}(0) = 0$, these equations, just like the original equations, can be solved iteratively. Knowing the number of diagrams in all quantities up to order $n-1$ allows one to calculate them at order n. This can also be done numerically. Table I (first two lines) shows the number of parquet diagrams up to order 6. For large interaction order n, we find that the number of diagrams in the parquet vertex and self-energy grows exponentially in n [cf. Fig. 10(a)].

To prove our claim that the mfRG flow generates all parquet diagrams, we must count the number of diagrams, $\mathcal{N}_{\dot{\Sigma}}(n)$ and $\mathcal{N}_{\dot{\gamma}_r}(n)$, obtained by differentiating the set of all corresponding parquet graphs. Then, we check that these numbers are exactly reproduced by the number of diagrams contained on the right-hand side of the mfRG flow equations. A diagram of the full propagator at order n has $2n+1$ internal lines, a self-energy diagram $2n-1$, and vertex diagram $2n-2$. According to the product rule, the number of differentiated diagrams is thus

$$\mathcal{N}_{\dot{G}}(n) = \mathcal{N}_G(n)(2n+1), \tag{26a}$$

$$\mathcal{N}_{\dot{\Sigma}}(n) = \mathcal{N}_\Sigma(n)(2n-1), \tag{26b}$$

$$\mathcal{N}_{\dot{\gamma}_r}(n) = \mathcal{N}_{\gamma_r}(n)(2n-2). \tag{26c}$$

From the mfRG flow of the vertex [Eq. (18)], we deduce

$$\mathcal{N}_{\dot{\gamma}_a^{(1)}} = 2\mathcal{N}_\Gamma * \mathcal{N}_{\dot{G}} * \mathcal{N}_G * \mathcal{N}_\Gamma, \tag{27a}$$

$$\mathcal{N}_{\dot{\gamma}_p^{(1)}} = \mathcal{N}_\Gamma * \mathcal{N}_{\dot{G}} * \mathcal{N}_G * \mathcal{N}_\Gamma, \tag{27b}$$

$$\mathcal{N}_{\dot{\gamma}_a^{(2)}} = 2\left(\mathcal{N}_{\dot{\gamma}_a^{(1)}} + \mathcal{N}_{\dot{\gamma}_p^{(1)}}\right) * \mathcal{N}_\Pi * \mathcal{N}_\Gamma, \tag{27c}$$

$$\mathcal{N}_{\dot{\gamma}_p^{(2)}} = 2\mathcal{N}_{\dot{\gamma}_a^{(1)}} * \mathcal{N}_\Pi * \mathcal{N}_\Gamma, \tag{27d}$$

where $\mathcal{N}_\Pi = \mathcal{N}_G * \mathcal{N}_G$ denotes the number of diagrams in a bubble. For $\ell + 2 \geqslant 3$, we have

$$\begin{aligned} \mathcal{N}_{\dot{\gamma}_a^{(\ell+2)}} = {} & 2\left(\mathcal{N}_{\dot{\gamma}_a^{(\ell+1)}} + \mathcal{N}_{\dot{\gamma}_p^{(\ell+1)}}\right) * \mathcal{N}_\Pi * \mathcal{N}_\Gamma \\ & + \mathcal{N}_\Gamma * \mathcal{N}_\Pi * \left(\mathcal{N}_{\dot{\gamma}_a^{(\ell)}} + \mathcal{N}_{\dot{\gamma}_p^{(\ell)}}\right) * \mathcal{N}_\Pi * \mathcal{N}_\Gamma, \end{aligned} \tag{28a}$$

$$\begin{aligned} \mathcal{N}_{\dot{\gamma}_p^{(\ell+2)}} = {} & 2\mathcal{N}_{\dot{\gamma}_a^{(\ell+1)}} * \mathcal{N}_\Pi * \mathcal{N}_\Gamma \\ & + \tfrac{1}{2} \mathcal{N}_\Gamma * \mathcal{N}_\Pi * \mathcal{N}_{\dot{\gamma}_a^{(\ell)}} * \mathcal{N}_\Pi * \mathcal{N}_\Gamma. \end{aligned} \tag{28b}$$

Summing all loop contributions yields

$$\mathcal{N}_{\dot{\gamma}_a}^{\mathrm{mfRG}} = \textstyle\sum_{\ell \geqslant 1} \mathcal{N}_{\dot{\gamma}_a^{(\ell)}}, \quad \mathcal{N}_{\dot{\gamma}_p}^{\mathrm{mfRG}} = \textstyle\sum_{\ell \geqslant 1} \mathcal{N}_{\dot{\gamma}_p^{(\ell)}}. \tag{29}$$

For the flow of the self-energy (20), we need the center part of the vertex flow in the a and p channel, for which the number of diagrams sums up to

$$\mathcal{N}_{\dot{\gamma}_{\bar{t},\mathrm{C}}} = \mathcal{N}_\Gamma * \mathcal{N}_\Pi * \left(\tfrac{3}{2} \mathcal{N}_{\dot{\gamma}_a}^{\mathrm{mfRG}} + \mathcal{N}_{\dot{\gamma}_p}^{\mathrm{mfRG}}\right) * \mathcal{N}_\Pi * \mathcal{N}_\Gamma. \tag{30}$$

The number of diagrams in the single-scale propagator S (13) can be obtained from two equivalent relations

$$\begin{aligned} \mathcal{N}_S &= \mathcal{N}_{\dot{G}} - \mathcal{N}_G * \mathcal{N}_{\dot{\Sigma}} * \mathcal{N}_G & \text{(31a)} \\ &= (\mathcal{N}_{\mathbb{1}} + \mathcal{N}_G * \mathcal{N}_\Sigma) * \mathcal{N}_{\dot{G}^0} * (\mathcal{N}_{\mathbb{1}} + \mathcal{N}_\Sigma * \mathcal{N}_G), & \text{(31b)} \end{aligned}$$

with $\mathcal{N}_{\dot{G}^0}(n) = \delta_{n,0} = \mathcal{N}_{\mathbb{1}}(n)$. From Eq. (20), we then get

$$\mathcal{N}_{\dot{\Sigma}}^{\mathrm{mfRG}} = \mathcal{N}_{\dot{\Sigma}_{\mathrm{std}}} + \mathcal{N}_{\dot{\Sigma}_{\bar{t}}} + \mathcal{N}_{\dot{\Sigma}_{t}}, \quad \mathcal{N}_{\dot{\Sigma}_{\mathrm{std}}} = \mathcal{N}_{\Gamma} * \mathcal{N}_{S},$$
$$\mathcal{N}_{\dot{\Sigma}_{\bar{t}}} = \mathcal{N}_{\dot{\gamma}_{\bar{t},\mathrm{C}}} * \mathcal{N}_{G}, \qquad \mathcal{N}_{\dot{\Sigma}_{t}} = \mathcal{N}_{\Gamma} * \mathcal{N}_{\Pi} * \mathcal{N}_{\dot{\Sigma}_{\bar{t}}}. \tag{32}$$

Numerically, one can check order for order in the interaction [cf. Table I and Fig. 10(b)] that, indeed, the mfRG flow generates exactly the same number of diagrams as obtained by differentiating all parquet diagrams, i.e.,

$$\mathcal{N}_{\dot{\gamma}_r}(n) = \mathcal{N}_{\dot{\gamma}_r}^{\mathrm{mfRG}}(n), \quad \mathcal{N}_{\dot{\Sigma}}(n) = \mathcal{N}_{\dot{\Sigma}}^{\mathrm{mfRG}}(n) \quad \forall n. \tag{33}$$

This demonstrates the equivalence between solving the multiloop fRG flow and solving the (first-order) parquet equations for a general model.

E. Computational aspects

All contributions to the mfRG flow—for the vertex as well as for the self-energy—are of an iterative one-loop structure and hence well suited for numerical algorithms. In fact, by keeping track of the left (L) and right (R) summands in the higher-loop vertex flow (18c)

$$\dot{\gamma}_{r,\mathrm{L}}^{(\ell+2)} = B_r\big(\gamma_{\bar{r}}^{(\ell+1)},\Gamma\big), \quad \dot{\gamma}_{r,\mathrm{R}}^{(\ell+2)} = B_r\big(\Gamma,\gamma_{\bar{r}}^{(\ell+1)}\big), \tag{34}$$

the center part (18d) can be efficiently computed as

$$\dot{\gamma}_{r,\mathrm{C}}^{(\ell+2)} = B_r\big(\Gamma,\gamma_{r,\mathrm{L}}^{(\ell+1)}\big) = B\big(\gamma_{r,\mathrm{R}}^{(\ell+1)},\Gamma\big). \tag{35}$$

Consequently, the numerical effort in the multiloop corrections of the vertex flow scales linearly in ℓ. The self-energy flow (20) is already stated with one integration only.

The (standard) fRG hierarchy of flow equations constitutes a (first-order) ordinary differential equation. Neglecting the six-point vertex, it can be written as

$$\partial_\Lambda \Sigma = f_{\Sigma}^{\mathrm{std}}(\Lambda,\Sigma,\Gamma), \quad \partial_\Lambda \Gamma = f_{\Gamma}^{\mathrm{std}}(\Lambda,\Sigma,\Gamma), \tag{36}$$

where, here and henceforth, f denotes the part of the right-hand side of the flow equation corresponding to its indices. Improving this approximation by adding differentiated self-energy contributions in the vertex flow (as is also done in mfRG), $f_{\Gamma}^{\mathrm{std}}$ is replaced by another function $\tilde{f}_{\Gamma}^{\mathrm{std}}(\Lambda,\Sigma,\Gamma,\partial_\Lambda\Sigma)$, which further depends on the Λ derivative of the self-energy. Such a differential equation is still feasible for many algorithms as one can simply compute $\partial_\Lambda\Sigma$ first and use it in the calculation of $\partial_\Lambda\Gamma$. However, the full mfRG flow for the vertex and self-energy has the form

$$\partial_\Lambda \Sigma = f_{\Sigma}(\Lambda,\Sigma,\Gamma,\partial_\Lambda\Gamma), \quad \partial_\Lambda \Gamma = f_{\Gamma}(\Lambda,\Sigma,\Gamma,\partial_\Lambda\Sigma), \tag{37}$$

in which derivatives occur on all parts of the right-hand side, yielding an algebraic (as opposed to ordinary) differential equation.

Techniques to solve algebraic differential equations exist, but a discussion of them exceeds the scope of this paper. Let us merely suggest an approximate solution strategy that reduces the mfRG flow to an ordinary differential equation, has no computational overhead, and deviates from the exact flow starting at sixth order in the interaction, summarized as follows:

$$\dot{\Sigma}_{\mathrm{std}} = f_{\dot{\Sigma}_{\mathrm{std}}}(\Lambda,\Sigma,\Gamma), \tag{38a}$$
$$\partial_\Lambda \Gamma \approx \dot{\Gamma}_{\mathrm{approx}} = f_{\Gamma}(\Lambda,\Sigma,\Gamma,\partial_\Lambda\Sigma = \dot{\Sigma}_{\mathrm{std}}), \tag{38b}$$
$$\partial_\Lambda \Sigma \approx \dot{\Sigma}_{\mathrm{std}} + f_{\dot{\Sigma}_{\bar{t}}}(\Lambda,\Sigma,\partial_\Lambda\Gamma = \dot{\Gamma}_{\mathrm{approx}}) + f_{\dot{\Sigma}_{t}}(\Lambda,\Sigma,\partial_\Lambda\Gamma = \dot{\Gamma}_{\mathrm{approx}}). \tag{38c}$$

According to this scheme, one computes first the standard flow of the self-energy, which deviates from the full Σ flow at interaction order U^4. Inserting this into the vertex flow yields an approximate vertex derivative, $\dot{\Gamma}_{\mathrm{approx}}$, where deviations from the full flow, induced by the approximate form of $\partial_\Lambda\Sigma$, start at order U^6. The center part of the vertex flow involves at least four vertices, such that deviations, induced by the self-energy, start at order U^8. The resulting, approximate $\dot{\gamma}_{\bar{t},\mathrm{C}}$ can then be used to complete $\partial_\Lambda\Sigma$, adding the terms $\dot{\Sigma}_{\bar{t}}$ and $\dot{\Sigma}_t$, such that the self-energy flow is correctly computed up to errors of order U^8. Evidently, this scheme can also be iterated [using Eqs. (38b) and (38c)], increasing the accuracy by four orders with each step. We have attached a pseudocode for such a solution strategy of the mfRG flow in Appendix A.

F. General aspects

Since the standard fRG flow for the self-energy and four-point vertex—*including* the six-point vertex—is exact, all mfRG corrections can be understood as fully simulating the effect of the six-point vertex on parquet diagrams of Σ and Γ. For instance, the two-loop corrections to the vertex flow and the Katanin substitution in the improved one-loop flow equation contain all third-order contributions of the six-point vertex [6,12,16]. Nevertheless, in the standard fRG hierarchy of flow equations, the parquet graphs comprise n-point vertices of arbitrary order (n) [6], such that a non-diagrammatic derivation of mfRG based on this hierarchy appears rather difficult. Conversely, the derivation of the mfRG flow does not rely on the fRG hierarchy or properties of the (quantum) effective action; it can thus be understood independently and without prior knowledge of fRG.

The mfRG flow at the two- or higher-loop level is exact up to third order in the interaction and therefore naturally fulfills Ward identities with accuracy $O(\Gamma^4)$, compared to $O(\Gamma^3)$ in the case of one-loop fRG [12]. Yet, since the parquet self-energy is exact up to *fourth* order but the parquet vertex only up to *third* order, such identities are typically violated starting at fourth order. One can think of schemes to extend mfRG beyond the parquet approximation. However, we find those rather impracticable and only briefly mention them in Appendix B.

Furthermore, the mfRG flow is applicable for any initial condition of the vertex functions. Whereas the choice $G_{\Lambda_i} = 0$ used here leads to a summation of all parquet diagrams, starting the mfRG flow from the local quantities of dynamical mean-field theory (DMFT) [17,18] allows one to add nonlocal correlations, similarly to solving the parquet equations in the dynamical vertex approximation (DΓA) [19–21]. However, contrary to DΓA, the mfRG flow is built on the full vertex

$\Gamma^{(4)}_{\mathrm{DMFT}}$ and does not require the *diagrammatic* decomposition of the *nonperturbative* vertex [22] $\Gamma^{(4)}_{\mathrm{DMFT}} = R + \sum_r \gamma_r$ that leads to diverging results close to a quantum phase transition [29–31].

Inspecting the one-loop flow equations of the vertex once more, we observe that diagrams on the right-hand side contain the differentiated propagator *only* in the two-particle lines that induce the reducibility. Propagators which appear in two-particle lines which do not induce the reducibility are not differentiated. Therefore, only those diagrams that are reducible in *all* positions of two-particle lines—the so-called ladder diagrams—are fully included. It follows that the standard truncated, one-loop fRG flow is biased towards *ladder* constructions of the four-point vertex.

For a constant interaction U and a transfer energy-momentum Ω, ladder diagrams of a certain channel can easily be summed to $\Gamma^{\mathrm{ladder}}_{\Omega} = U(1 - U\Pi_{\Omega})^{-1}$, where Π_{Ω} is the corresponding bubble. Ladder diagrams are therefore particularly prone to divergences with increasing U or increasing values of Π_{Ω} (as can occur upon lowering the cutoff scale Λ) and can thus be responsible for premature vertex divergences in fRG. Indeed, so far, fRG computations have often suffered from such vertex divergences, and the flow had be stopped at finite RG scale Λ_c [3,32]. In this context, the two-loop corrections have already been found to significantly reduce the critical scale of vertex divergences Λ_c [16,33]. This suggests that it would be worthwhile to study the effect of higher-loop mfRG corrections—we expect that they reduce Λ_c even further.

Throughout this paper, we have taken a perspective that views fRG as a tool to resum diagrams (say, *physical* diagrams) by integrating a collection of *differentiated* (and thus Λ-dependent) diagrams. In this regard, the mfRG corrections do not add new *physical* diagrams to the flow, they only add *differentiated* diagrams to complete those derivatives of physical diagrams that are only partially contained by one-loop fRG. In other words, for any physical diagram to which a differentiated diagram of mfRG contributes, there also exists a differentiated diagram in one-loop fRG. The differentiated diagrams of the higher-loop corrections *and* the one-loop flow all contribute the *same* set of physical diagrams—the parquet diagrams.

Whereas the *one-loop* flow of the vertex contains differentiated propagators at the two-particle-reducible positions, the *multiloop* flow iteratively adds those parts for which the differentiated line is increasingly nested. Such nonladder contributions are crucial to suppress vertex divergences originating from the summation of ladder diagrams [5]. Similarly, the *standard* self-energy flow does not form a total derivative any more if one has only the parquet vertex at one's disposal. All diagrams of the standard flow are of the parquet type, but differentiated lines in heavily nested positions are omitted (cf. Fig. 6). The mfRG corrections incorporate all remaining contributions by two additions that build up on the multiloop vertex flow. Altogether, the mfRG flow achieves a full summation of all parquet diagrams of the vertex and self-energy. Consequently, mfRG solutions are no longer dependent on the specific way the Λ dependence (regulator) was introduced [5] and thus fully implement the meaning of the original fRG idea.

V. CONCLUSION

We have presented multiloop fRG flow equations for the four-point vertex and self-energy, formulated for the general fermionic many-body problem. The mfRG corrections fully simulate the effect of the six-point vertex on parquet diagrams, completing the derivatives of diagrams that are only partially contained in the standard truncated fRG flow. Whereas one-loop fRG contains differentiated propagators only at the two-particle-reducible positions and the standard self-energy flow does not suffice to form a total derivative when having only the parquet vertex at one's disposal, the multiloop iteration adds all remaining parts, where the differentiated line appears at increasingly nested positions. We have motivated the multiloop corrections at low orders and ruled out any overcounting of diagrams. Moreover, we have put forward a simple recipe to count diagrams and numerically check that the mfRG flow generates all differentiated parquet diagrams for the vertex and self-energy, order for order in the interaction.

Due to its iterative one-loop structure, the mfRG flow is well suited for efficient numerical computations. We have given a simple approximation, which renders the algebraic differential equation accessible to standard solvers for ordinary differential equations and exhibits only minor deviations from the full mfRG flow. Given the general formulation, the benefits of mfRG on physical problems can be exploited in a large number of fRG applications. The full resummation of parquet diagrams via mfRG eliminates the bias of fRG computations towards divergent ladder constructions of the vertex and restores the independence on the choice of regulator. We expect that this will generically enhance the usefulness of the truncated fRG framework and increase the robustness of the physical conclusions drawn from fRG results.

ACKNOWLEDGMENTS

We thank S. Jakobs for pointing out the need for multiloop corrections to the self-energy flow and W. Metzner and A. Toschi for useful discussions. We acknowledge support by the Cluster of Excellence Nanosystems Initiative Munich; F.B.K. acknowledges funding from the research school IMPRS-QST.

APPENDIX A: PSEUDOCODE IMPLEMENTATION

In this section, we present a pseudocode for the approximate solution strategy of the mfRG flow explained in Sec. IV E. Generally, an ordinary differential equation (ODE) is of the form $\partial_{\Lambda}\Psi(\Lambda) = f(\Lambda,\Psi)$, and numerous numerical ODE solvers are available. The only input required for such an ODE solver, apart from stating the initial condition $\Psi(\Lambda_i) = \Psi_i$ and the extremal points Λ_i, Λ_f, is an implementation of the function $f(\Lambda,\Psi)$.

In the case of mfRG, Ψ—describing the state of the physical system at a specified value of the flow parameter Λ—is a vector that contains the self-energy (say, $\Psi.\Sigma$) and the vertex (say, $\Psi.\Gamma$) for all configurations of quantum numbers (e.g., Matsubara frequency, momenta, and spin). In order to use an ODE solver to compute the mfRG flow, we only need to specify a way to compute $f(\Lambda,\Psi)$. This is provided by Algorithm 1, written in pseudocode.

ALGORITHM 1. Pseudocode for computing the right-hand side of the mfRG flow for a given state of the system Ψ (containing $\Psi.\Sigma$ and $\Psi.\Gamma$) and a scale parameter Λ.

```
Function $f(\Lambda,\Psi)$:
1:  $S = S(\Lambda,\Psi.\Sigma)$
2:  $G = G(\Lambda,\Psi.\Sigma)$
3:  $d\Sigma_{std} = L(\Psi.\Gamma,S)$
4:  $d\Psi.\Sigma = d\Sigma_{std}$
5:  for $it = 1 \ldots it_f$ do
6:    $dG = S + G \cdot d\Psi.\Sigma \cdot G$
7:    for $r = a,p,t$ do
8:      $d\gamma_r = \dot{B}_r(\Psi.\Gamma,\Psi.\Gamma,G,dG)$
9:    end for
    /* jump to line 41 for one-loop fRG */
10:   for $r = a,p,t$ do
11:     $d\gamma_r^L = B_r\big(\sum_{r' \neq r} d\gamma_{r'},\Psi.\Gamma,G\big)$
12:     $d\gamma_r^R = B_r\big(\Psi.\Gamma,\sum_{r' \neq r} d\gamma_{r'},G\big)$
13:   end for
14:   for $r = a,p,t$ do
15:     $d\gamma_r^T = d\gamma_r^L + d\gamma_r^R$
16:     $d\gamma_r \leftarrow d\gamma_r + d\gamma_r^T$
17:   end for
    /* jump to line 41 for two-loop fRG */
18:   $d\gamma_{\bar{t}}^C = 0$
19:   for $\ell = 3 \ldots \ell_f$ do
20:     for $r = a,p,t$ do
21:       $d\gamma_r^C = B_r(\Psi.\Gamma,d\gamma_r^L,G)$
22:       $d\gamma_r^L = B_r\big(\sum_{r' \neq r} d\gamma_{r'}^T,\Psi.\Gamma,G\big)$
23:       $d\gamma_r^R = B_r\big(\Psi.\Gamma,\sum_{r' \neq r} d\gamma_{r'}^T,G\big)$
24:     end for
25:     for $r = a,p,t$ do
26:       $d\gamma_r^T = d\gamma_r^L + d\gamma_r^C + d\gamma_r^R$
27:       $d\gamma_r \leftarrow d\gamma_r + d\gamma_r^T$
28:     end for
29:     $d\gamma_{\bar{t}}^C \leftarrow d\gamma_{\bar{t}}^C + d\gamma_a^C + d\gamma_p^C$
30:     if $\max_r\{||d\gamma_r^T||/||d\gamma_r||\} < \epsilon$ then
31:       break
32:     end if
33:   end for
    /* jump to line 41 for $\ell_f$-loop fRG without corrections to
    the self-energy flow */
34:   $d\Sigma_{\bar{t}} = L(d\gamma_{\bar{t}}^C,G)$
35:   $d\Sigma_t = L(\Psi.\Gamma,G \cdot d\Sigma_{\bar{t}} \cdot G)$
36:   $d\Psi.\Sigma = d\Sigma_{std} + d\Sigma_{\bar{t}} + d\Sigma_t$
37:   if $||S + G \cdot d\Psi.\Sigma \cdot G - dG||/||dG|| < \epsilon$ then
38:     break
39:   end if
40: end for
41: $d\Psi.\Gamma = \sum_r d\gamma_r$
42: return $d\Psi$
```

Algorithm 1 makes use of functions outlined in the main text, for which we also include dependencies that have been suppressed earlier. This applies to the single-scale propagator S [Eq. (13)] in line 1, the Dyson equation for G [Eq. (4)] in line 2, the differentiated bubble $\dot{B}$ [Eq. (12)] in line 8, and the bubble B [Eq. (8)], which is used several times. For a good numerical performance, an efficient implementation of the bubble functions appearing in Algorithm 1 using vertex symmetries and high-frequency asymptotics is crucial [9,34].

The algorithm has a few external parameters: ℓ_f (line 19) denotes the maximal loop order, and it_f (line 5) the number of iterations that improve the accuracy of the flow by four orders of the interaction with each step (cf. Sec. IV E). These parameters can also be used dynamically via the break conditions of the loops depending on the tolerance ϵ (lines 30, 37). Note that typically, one also specifies a tolerance for the numerical ODE solver, say ϵ_{ODE}. If ϵ is chosen in accordance with ϵ_{ODE} and the number of loops (ℓ_f) or iterations (it_f) is not fixed *a priori*, this algorithm yields a solution of the *full* mfRG flow and thus a full summation of *all* parquet diagrams—to the specified numerical accuracy.

The straightforward implementation as given by the pseudocode in Algorithm 1 demonstrates the feasibility of the mfRG flow for almost any fRG application.

APPENDIX B: MULTILOOP FLOW BEYOND THE PARQUET APPROXIMATION

The mfRG flow as described so far achieves a full summation of all parquet diagrams of the vertex and self-energy. The first deviations from the exact quantities, i.e., the first nonparquet diagrams, occur at fourth order for the vertex—these are the envelope vertices, such as the one shown in Fig. 3(a)—and, as follows by use of the SDE (16), at fifth order for the self-energy.

One can in principle add terms to the mfRG flow equations that go beyond the parquet approximation. The flow equation of Γ then also needs to generate differentiated diagrams of envelope vertices. This is achieved by adding the differentiated envelope vertices, i.e., all envelope diagrams of Γ with one G line replaced by $\partial_\Lambda G$ at all possible positions, to the flow equation. Subsequently, one performs the replacement $\Gamma^0 \to \Gamma$ to generate contributions at all interaction orders. (Note that the mfRG corrections of the self-energy flow have to be changed accordingly.) However, such contributions to the vertex flow are—by the very fact that they are of nonparquet type—not of an iterative one-loop structure anymore [i.e., their evaluation requires the computation of two or more (nested) integrals] and are thus computationally unfavorable.

Another possibility to obtain nonparquet diagrams from mfRG is to keep the flow equations unchanged and modify the initial condition. One can then add scale-independent envelope vertices, i.e., envelope vertices computed in the final theory (at Λ_f) with some approximation of the self-energy, to the initial condition of the vertex: $\Gamma_{\Lambda_i} = \Gamma^0 + \Gamma^{\mathrm{envelope}}_{\Lambda_f}$. (Hence, $\Gamma^{\mathrm{envelope}}$ must be computed only once.) This yields contributions to the flow that are not actually differentiated diagrams at a given scale Λ. Nevertheless, the initial vertex Γ_{Λ_i} constitutes a new totally irreducible building block in the mfRG flow. After completion of the flow, one obtains a summation of all "parquet" diagrams with the totally irreducible vertex $R = \Gamma_{\Lambda_i}$ instead of $R = \Gamma^0$; i.e., one obtains vertex and self-energy at one level beyond the parquet approximation [cf. Eq. (14)]. Such results deviate from the exact quantities starting at fifth and sixth order for Γ and Σ, respectively. This scheme of adding nonparquet contributions can also be iterated and used with expressions for $R = \Gamma_{\Lambda_i}$ of even higher order. However, it appears rather tedious and is more in the spirit of an iterative solution of the parquet equations than of an actual fRG flow.

---

[1] N. Bickers, in *Theoretical Methods for Strongly Correlated Electrons*, CRM Series in Mathematical Physics, edited by D. Sénéchal, A.-M. Tremblay, and C. Bourbonnais (Springer, New York, 2004), pp. 237–296.

[2] B. Roulet, J. Gavoret, and P. Nozières, Phys. Rev. **178**, 1072 (1969).

[3] W. Metzner, M. Salmhofer, C. Honerkamp, V. Meden, and K. Schönhammer, Rev. Mod. Phys. **84**, 299 (2012).

[4] P. Kopietz, L. Bartosch, and F. Schütz, *Introduction to the Functional Renormalization Group*, Lecture Notes in Physics (Springer, Berlin, 2010).

[5] F. B. Kugler and J. von Delft, Phys. Rev. Lett. **120**, 057403 (2018).

[6] F. B. Kugler and J. von Delft, arXiv:1706.06872.

[7] Defining the four-point vertex as an expansion coefficient of the (quantum) effective action $\mathbf{\Gamma}$, we use $\Gamma_{x',y';x,y} = \delta^4\mathbf{\Gamma}/(\delta\bar{c}_{x'}\delta\bar{c}_{y'}\delta c_x\delta c_y)$ at zero fields. Via antisymmetry, we have $\Gamma_{x',y';x,y} = -\Gamma_{x',y';y,x}$, and all of the standard relations in our paper agree precisely with those of Ref. [4].

[8] G. Rohringer, H. Hafermann, A. Toschi, A. A. Katanin, A. E. Antipov, M. I. Katsnelson, A. I. Lichtenstein, A. N. Rubtsov, and K. Held, arXiv:1705.00024.

[9] N. Wentzell, G. Li, A. Tagliavini, C. Taranto, G. Rohringer, K. Held, A. Toschi, and S. Andergassen, arXiv:1610.06520.

[10] S. G. Jakobs, M. Pletyukhov, and H. Schoeller, Phys. Rev. B **81**, 195109 (2010).

[11] Note that in the flow equation of the vertex in Ref. [3], Eq. (52), a minus sign in the first line on the right-hand side is missing.

[12] A. A. Katanin, Phys. Rev. B **70**, 115109 (2004).

[13] The third-order diagram of R in Fig. 1(b) of Ref. [5] is of nonparquet type only in the x-ray-edge singularity, where reducibility is required in interband two-particle lines. The corresponding diagram with identical lines belongs to the t channel.

[14] In the SDE (16), e.g., the self-energy is constructed in a way that involves two parallel lines connected to the same vertex, requiring a factor of $1/2$ to avoid double counting. In the standard flow equation (20a) for Σ, no such lines exist and hence no extra factor either.

[15] J. W. Negele and H. Orland, *Quantum Many-Particle Systems*, Advanced Books Classics (Perseus Books, New York, 1998).

[16] A. Eberlein, Phys. Rev. B **90**, 115125 (2014).

[17] A. Georges, G. Kotliar, W. Krauth, and M. J. Rozenberg, Rev. Mod. Phys. **68**, 13 (1996).

[18] C. Taranto, S. Andergassen, J. Bauer, K. Held, A. Katanin, W. Metzner, G. Rohringer, and A. Toschi, Phys. Rev. Lett. **112**, 196402 (2014).

[19] A. Toschi, A. A. Katanin, and K. Held, Phys. Rev. B **75**, 045118 (2007).

[20] K. Held, A. A. Katanin, and A. Toschi, Prog. Theor. Phys. Suppl. **176**, 117 (2008).

[21] A. Valli, G. Sangiovanni, O. Gunnarsson, A. Toschi, and K. Held, Phys. Rev. Lett. **104**, 246402 (2010).

[22] Alternatives to DΓA which do not require the totally irreducible vertex are the dual fermion [23–25] and the related 1PI approach [26]. However, upon transformation to the dual variables, the bare action contains n-particle vertices for all n. Recent studies [27] show that the corresponding six-point vertex yields sizable contributions for the (physical) self-energy, and it remains unclear how a truncation in the (dual) bare action can be justified.

[23] A. N. Rubtsov, M. I. Katsnelson, and A. I. Lichtenstein, Phys. Rev. B **77**, 033101 (2008).

[24] S. Brener, H. Hafermann, A. N. Rubtsov, M. I. Katsnelson, and A. I. Lichtenstein, Phys. Rev. B **77**, 195105 (2008).

[25] H. Hafermann, G. Li, A. N. Rubtsov, M. I. Katsnelson, A. I. Lichtenstein, and H. Monien, Phys. Rev. Lett. **102**, 206401 (2009).

[26] G. Rohringer, A. Toschi, H. Hafermann, K. Held, V. I. Anisimov, and A. A. Katanin, Phys. Rev. B **88**, 115112 (2013).

[27] T. Ribic, G. Rohringer, and K. Held, Phys. Rev. B **95**, 155130 (2017).

[28] T. Ribic, P. Gunacker, S. Iskakov, M. Wallerberger, G. Rohringer, A. N. Rubtsov, E. Gull, and K. Held, Phys. Rev. B **96**, 235127 (2017).

[29] T. Schäfer, G. Rohringer, O. Gunnarsson, S. Ciuchi, G. Sangiovanni, and A. Toschi, Phys. Rev. Lett. **110**, 246405 (2013).

[30] T. Schäfer, S. Ciuchi, M. Wallerberger, P. Thunström, O. Gunnarsson, G. Sangiovanni, G. Rohringer, and A. Toschi, Phys. Rev. B **94**, 235108 (2016).

[31] O. Gunnarsson, G. Rohringer, T. Schäfer, G. Sangiovanni, and A. Toschi, Phys. Rev. Lett. **119**, 056402 (2017).

[32] A. Eberlein and W. Metzner, Phys. Rev. B **89**, 035126 (2014).

[33] M. Rueck and J. Reuther, arXiv:1712.02535.

[34] See Supplemental Material of Ref. [5].

SciPost Phys. 6, 009 (2019)

Multiloop functional renormalization group for the two-dimensional Hubbard model: Loop convergence of the response functions

Agnese Tagliavini[1,2], Cornelia Hille[1⋆], Fabian B. Kugler[3], Sabine Andergassen[1], Alessandro Toschi[2] and Carsten Honerkamp[4,5]

1 Institut für Theoretische Physik and Center for Quantum Science, Universität Tübingen,
Auf der Morgenstelle 14, 72076 Tübingen, Germany
2 Institute for Solid State Physics, Vienna University of Technology, 1040 Vienna, Austria
3 Physics Department, Arnold Sommerfeld Center for Theoretical Physics,
and Center for NanoScience, Ludwig-Maximilians-Universität München,
Theresienstrasse 37, 80333 Munich, Germany
4 Institute for Theoretical Solid State Physics,
RWTH Aachen University, D-52056 Aachen, Germany
5 JARA - Fundamentals of Future Information Technology

⋆ cornelia.hille@uni-tuebingen.de

Abstract

We present a functional renormalization group (fRG) study of the two dimensional Hubbard model, performed with an algorithmic implementation which lifts some of the common approximations made in fRG calculations. In particular, in our fRG flow; (i) we take explicitly into account the momentum and the frequency dependence of the vertex functions; (ii) we include the feedback effect of the self-energy; (iii) we implement the recently introduced multiloop extension which allows us to sum up *all* the diagrams of the parquet approximation with their exact weight. Due to its iterative structure based on successive one-loop computations, the loop convergence of the fRG results can be obtained with an affordable numerical effort. In particular, focusing on the analysis of the physical response functions, we show that the results become *independent* from the chosen cutoff scheme and from the way the fRG susceptibilities are computed, i.e., either through flowing couplings to external fields, or through a "post-processing" contraction of the interaction vertex at the end of the flow. The presented substantial refinement of fRG-based computation schemes paves a promising route towards future quantitative fRG analyses of more challenging systems and/or parameter regimes.

Copyright A. Tagliavini *et al*.
This work is licensed under the Creative Commons
Attribution 4.0 International License.
Published by the SciPost Foundation.

Received 10-08-2018
Accepted 19-12-2018
Published 18-01-2019
doi:10.21468/SciPostPhys.6.1.009

Contents

1 Introduction 2

2 Theory and formalism 4

2.1 Definitions and formalism 4
2.2 Flow equations for the response functions 6

3 Numerical implementation 11
3.1 Full frequency and momentum parametrization 11
3.1.1 Truncated Unity fRG 12
3.1.2 Dynamical fRG 12
3.1.3 Flow equations for the TU-dynamical fRG 13
3.1.4 Calculation of the fermionic particle-hole and particle-particle excitation 14
3.1.5 Diagrammatic and lattice related symmetries 15
3.2 The mfRG implementation 15

4 Numerical results 17
4.1 2D Hubbard model at half filling as test system 17
4.2 Convergence and stability study on the TUfRG-implementation 18
4.3 Effects of different approximations 19
4.4 Computation of the self-energy 21
4.5 Effect of the multiloop implementation 23

5 Conclusions 28

A Symmetries and symmetrized notation 30
A.1 Lattice related symmetries 31
A.2 Diagrammatic symmetries 32
A.3 Connection between $\mathcal{K}_2$ and $\bar{\mathcal{K}}_2$ 33

B Formal derivation of the fRG flow equations for χ and γ_3 33

C Connection between the vertex asymptotics and the response functions 35

D "Post-processed" flow equations for γ_3 and χ 36

E Two-loop approximation for γ_3's flow equation 38

F Implementation details 40

G Performance of the code 41

References 42

1 Introduction

Over the last two decades, functional renormalization group (fRG) methods have been broadly used for analyzing two-dimensional (2D) lattice electron systems (for reviews, see Refs. [1,2]). The main advantage of the fRG lies in the exploration of the leading low-energy correlations and instabilities towards long-range ordered states, similar to what has been investigated earlier for one-dimensional systems [3–5]. However, in one dimension, other methods like Bethe-Ansatz, bosonization [6,7] and DMRG [8] exist, which are for certain aspects more controlled. Hence, assessing the precision of RG methods in one-dimensional systems was not really in the foreground. The situation evidently changes for two- and three-dimensional systems, where the specific simplifications associated to the peculiar one-dimensional geometry are not applicable. At the same time, spatial correlations in 2D are strong enough to induce qualitative corrections [9,10] with respect to another class of rigorous many-body approaches, such as the Dynamical Mean-Field Theory (DMFT) [11–13] which allows one to include all purely local dynamical correlations.

In fact, due to the intrinsic complexity of the many-electron problem in 2D, the development of unbiased quantitative methods applicable to a wide energy range from electronic structures on the scale of a few eV down to, e.g., ground state ordering in the (sub-)meV region is still on the wishlist. This goal has motivated, in the last decade, the development of several algorithmic schemes for treating electronic correlations in 2D from different perspectives [1, 14, 15]. In this context, the fRG has already unveiled quite promising features: The fRG has the potential of resolving band structures and Fermi surface details *and* to treat competing orders on low energy scales in a rather unbiased way, since it does not require preliminary assumptions about dominating scattering channels. Recent applications range from studies of cuprate high-T_c superconductors [16–19] over iron superconductors [2, 20] to few-layer graphene systems [21, 22], to cite a few.

We also note that, while the current applicability of the fRG is generally restricted to the weak to intermediate coupling regimes, its combination [23, 24] with the DMFT might allow one, in the future, to access much more strongly correlated parameter regions, including the ones in proximity of the Mott-Hubbard metal-insulator transition. This is achieved by constructing a fRG flow starting from the DMFT solution of the considered lattice problem to the exact solution, i.e., in practice, using the DMFT to determine the initial conditions for the fRG flow [23]. Similarly to other diagrammatic extensions [15] of DMFT, such as the Dynamical Vertex Approximation (DΓA) [25] or the Dual Fermion [26] approach, one might work either with the physical degrees of freedom (as in the so-called DMF^{2}RG [23]) or in the space of auxiliary (dual) fermions [27], introduced by means of a suitable [15, 26] Hubbard-Stratonovich transformation.

Yet, what is hitherto missing is a thorough analysis of the *quantitative* reliability of the fRG for a well-defined test case. More precisely this would require to clarify how much the fRG results, going beyond the correct estimation of general physical trends, depend on the approximations inherent in the used fRG scheme. This study within the fRG would then also provide a solid basis for future comparisons with other numerical techniques.

The mentioned approximations can be grouped in three categories:
(i) *Momentum/frequency discretization*: As the fRG algorithm typically exploits the flow of vertex functions that depend continuously on multiple momenta and frequencies, various approximations are performed to mitigate numerical and memory costs. Early on, N-patch discretizations of the momentum dependencies through the Brillouin zone were used. Later, it was noticed that channel-decompositions in conjunction with form factor expansions [28–30] lead to physically appealing approximations featuring advantageous momentum resolution and numerical performance [31]. Clever prescriptions for the treatment of the high-frequency tails of the vertex function have been devised [32–34] which are also used in this work.

(ii) *Self-energy feedback*: In many applications of the fRG the self-energy and its feedback on the flow of the n-particle ($n > 1$) vertex functions has *not* been accounted for. While there are arguments that the self-energy may be important mainly when the interactions are close to a flow to strong coupling (see Appendix in Ref. [35]), more quantitative results should overcome this deficit. In fact, neglecting the self-energy feedback was mainly motivated by the disregarded frequency dependence of the interactions in earlier fRG studies: Within a static treatment the self-energy lacks the effects of quasiparticle degradation, so that its inclusion became less important. Within the current frequency-dependent fRG treatments, the self-energy feedback can be included in a meaningful way. A number of works have already investigated the self-energy effects in the flows to strong coupling in Hubbard-type models [29, 36–44], mainly exploring the quantitative effects, besides signatures of pseudogap openings [39, 40] and non-Fermi liquid behavior [29] in particular cases.

(iii) *Truncation of the flow equation hierarchy*: Finally, one should also consider the truncation of the hierarchy of flow equations for the n-point one-particle irreducible (1PI) vertex functions. This is usually done at "level-II" as defined in Ref. [1], also referred to as one-loop (1ℓ) approximation, i.e., the 1PI six-point vertex is set to zero. Due to this truncation, the final result of an fRG flow might depend – to a certain degree – on the cutoff scheme adopted for the calculation.

In this perspective, it was noticed by Katanin [45] that replacing the so-called single-scale propagator in the loops on the r.h.s. of the flow equation for the four-point vertex by a scale-derivative of the full Green's function allows this scheme to become equivalent to one-particle self-consistent (a.k.a. mean-field) theories in reduced models, and then to go beyond such self-consistent approximations in more general models. Another significant comparison can be made with the parquet-based approaches [46, 47], such as the parquet approximation (PA) [33, 34, 48–50]. The latter represents the "lowest order" solution of the parquet equations, where the two-particle irreducible vertex is approximated by the bare interaction. In fact, although the diagrams summed in the 1ℓ truncation of the fRG are topologically the same as in the PA, the way the single contributions are generated during the flow leads in general to differences with respect to the PA [34, 51]. This is due to some internal-line combinations, e.g., in particle-hole corrections to the particle-particle channel, which are suppressed by the cutoff functions attached to the propagators and not fully reconstructed during the flow because of the truncation. A quantitative analysis of this effect has been performed for the single impurity Anderson model in Ref. [34]. These differences are absent for single-channel summations (e.g. RPA), but could lead to more pronounced quantitative errors in presence of channel coupling, e.g., in the generation of superconducting pairing through spin fluctuations. Furthermore, while the Mermin-Wagner theorem is fulfilled within the PA [52], it is typically violated by 1ℓ fRG calculations. First steps to remedy this shortcoming were undertaken in various works [43, 53, 54], but only recently a comprehensive path of how the PA contributions can be recovered in full extent was presented within the multiloop extension of the fRG (mfRG) [55–57]. The mfRG flow equations incorporate all contributions of the six-point vertex that complement the derivative of diagrams already part of the 1ℓ flow, as organized by their loop structure. A key insight in this approach is that the higher-loop contributions can be generated by computing 1ℓ flows for scale-differentiated vertices, with an effort growing only linearly with the loop order that is fully kept. The multiloop corrections stabilize the flow by enabling full screening of competing two-particle channels, ultimately recovering the self-consistent structure of the PA. As the PA corresponds to a well-defined subset of diagrams, a converged mfRG flow able to reproduce the PA is by construction independent of the adopted cutoff.

In this paper, we present a fRG study of the 2D Hubbard model performed with an algorithm combining the most recent progress on all three approximation levels. We use (i) the so-called "truncated unity" fRG [31] (TUfRG) formalism to describe the momentum dependence of the vertex and, in addition, keep the full frequency dependence as a function of three independent frequencies. Differently from the approach adopted in Ref. [44], we employ a refined scheme to treat the high-frequency asymptotics [34] that allows us to reduce the numerical effort considerably. Within this scheme, we can consistently include (ii) the (frequency-dependent) self-energy feedback in our fRG flow equations. Finally, we present (iii) first data for the 2D Hubbard model computed with the multiloop extension proposed by Kugler and von Delft [55]. In this context, we have also generalized the multiloop formalism to compute the flow of the response functions, and illustrated the loop convergence of the fRG results for the 2D Hubbard model. In particular, we show that including up to 8 loops in the fRG flow yields a clear convergence of the data with the loop order and the final results are independent of the cutoff. This represents an important check and illustrates that fRG flows can be brought in quantitative control for 2D problems. Finally, our multiloop analysis of the response functions demonstrates that the two different ways to compute susceptibilities in the fRG, either by tracking the renormalization group flow of the couplings to external fields [1] or by contracting the final interaction vertex (see, e.g., Ref. 23), converge to the same value with increasing loop order. This confirms that the output of this improved fRG scheme can indeed be trusted on a quantitative level.

The paper is organized as follows: The formalism and theory of the linear response functions and their computation by mfRG flow equations are introduced in Section 2. In Section 3 we present the actual implementation scheme for the full momentum- and frequency-dependent fRG. In Section 4 we show the results for the 2D Hubbard model, with a detailed analysis of the effects of the different approximation levels and in particular of the convergence with the loop order. A conclusion and outlook is provided in Section 5.

2 Theory and formalism

2.1 Definitions and formalism

In this section we provide the definitions of the linear response functions to an external field, before describing their computation with the fRG. We focus on correlation functions of fermionic bilinears. In particular, in a time-space translational-invariant system, we consider the charge (density) and spin (magnetic) bilinears, both charge invariant,

$$\rho^n_{\mathrm{d}}(q) = \sum_\sigma \int dp\, \bar\psi_\sigma(p) f_n(p,q) \psi_\sigma(p+q)\,, \tag{1a}$$

$$\rho^n_{\mathrm{m}}(q) = \sum_\sigma (-1)^\sigma \int dp\, \bar\psi_\sigma(p) f_n(p,q) \psi_\sigma(p+q)\,, \tag{1b}$$

and the non-charge invariant pairing (superconducting) bilinears

$$\rho^n_{\mathrm{sc}}(q) = \int dp\, \psi_\downarrow(q-p) f^*_n(p,q) \psi_\uparrow(p)\,, \tag{2a}$$

$$\rho^{n*}_{\mathrm{sc}}(q) = \int dp\, \bar\psi_\uparrow(p) f_n(p,q) \bar\psi_\downarrow(q-p)\,, \tag{2b}$$

where ψ and $\bar\psi$ represent the Grassman variables and p (q) a fermionic (bosonic) quadri-momentum $p = \{i\nu_o, \mathbf{p}\}$ ($q = \{i\omega_l, \mathbf{q}\}$). The integral includes a summation over the Matsubara frequencies ($i\nu_o$), normalized by the inverse temperature β, and an integral over the first Brillouine Zone normalized by its volume $\mathcal{V}_{\mathrm{BZ}}$. The function $f_n(p,q)$ determines the momentum and frequency structure of the bilinears in the different physical channels. In the present case we restrict ourselves to a static external source field, such that the function $f_n(p,q) = f_n(\mathbf{p})$ acquires only a momentum dependence, whose structure is specified by the subscript n and explicitly shown in Table 1 (in the present work we will mostly focus on the s- as well as d-wave momentum structure). Note that, when using a different frequency-momentum notation, centered in the center of mass of the scattering process (see “symmetrized” notation in Appendix A), one should account for an additional shift of the momentum dependence $\mathbf{p}$ by means of the momentum transfer $\mathbf{q}$.

After a reshift of the operators in Eq. (1) with respect to their average value $\rho^n_{\mathrm{d/m}} \to \rho^n_{\mathrm{d/m}} - \langle \rho^n_{\mathrm{d/m}} \rangle$, we can now define the correlation functions of these bilinears in the three channels

$$\chi^{nn'}_{\mathrm{d/m}}(q) = \frac{1}{2} \langle \rho^n_{\mathrm{d/m}}(q) \rho^{n'*}_{\mathrm{d/m}}(q) \rangle \tag{3a}$$

$$\chi^{nn'}_{\mathrm{sc}}(q) = \langle \rho^n_{\mathrm{sc}}(q) \rho^{n'*}_{\mathrm{sc}}(q) \rangle \, . \tag{3b}$$

In linear response theory, these correlation functions correspond to the physical susceptibilities in the corresponding channels. Divergences in $\chi^{nn'}_\eta(q)$, with $\eta = \{\mathrm{d}, \mathrm{m}, \mathrm{sc}\}$, indicate spontaneous ordering tendencies or instabilities of the system. The above definition encodes not only the real-space pattern or wavevector for which the system starts ordering, but also the symmetry of the order parameter associated to the instability. In the 2D Hubbard model study presented here (see Section 4) we detect various response functions growing considerably towards low T, such as the spin-density wave (SDW) response, characterized by the isotropic s-wave magnetic susceptibility at $\mathbf{q} = (\pi, \pi)$, as well as s- and d-wave pairing response functions at $\mathbf{q} = (0, 0)$ and Pomeranchuk instabilities [58]. Inserting Eq. (1) or Eq. (2) into Eq. (3), the susceptibilities appear as two-particle Green's functions. In particular, they can be determined from the two-particle vertex γ_4 by

$$\begin{aligned}\chi^{nn'}_{\mathrm{d/m}}(q) =& \frac{1}{2} \sum_{\sigma\sigma'} \int dp dp' f_n(\mathbf{p}) f^*_{n'}(\mathbf{p}') \boldsymbol{\sigma}^{0/3}_{\sigma\sigma} \boldsymbol{\sigma}^{0/3}_{\sigma'\sigma'} \big[\Pi_{\mathrm{d/m};\sigma,\sigma'}(q,p,p') + \\ & \Pi_{\mathrm{d/m};\sigma\sigma}(q,p,p) \gamma_{4;\sigma\sigma\sigma'\sigma'}(p, p+q, p'+q, p') \Pi_{\mathrm{d/m};\sigma'\sigma'}(q,p',p') \big]\end{aligned} \tag{4a}$$

$$\begin{aligned}\chi^{nn'}_{\mathrm{sc}}(q) =& \int dp dp' f_n(\mathbf{p}) f^*_{n'}(\mathbf{p}') \big[\Pi_{\mathrm{sc};\uparrow\downarrow}(q,p,p') + \\ & \Pi_{\mathrm{sc};\uparrow\downarrow}(q,p,p) \gamma_{4;\uparrow\uparrow\downarrow\downarrow}(p, p', q-p, q-p') \Pi_{\mathrm{sc};\uparrow\downarrow}(q,p',p') \big] \, ,\end{aligned} \tag{4b}$$

where $\boldsymbol{\sigma}^{0/3}$ represent the Pauli matrices ($\boldsymbol{\sigma}^0 = \mathbb{1}$) and we made use of the spin conservation. Eqs. (4) can be considerably simplified by making use of the SU(2) symmetry. The "bare bubbles" Π_η appearing in (4) read

$$\Pi_{\mathrm{d/m};\sigma\sigma'}(q,p,p') = -\beta \mathcal{V}_{\mathrm{BZ}} \delta_{\sigma,\sigma'} \delta_{p,p'} G_\sigma(p) G_\sigma(p+q) \, , \tag{5a}$$

$$\Pi_{\mathrm{sc};\uparrow\downarrow}(q,p,p') = \beta \mathcal{V}_{\mathrm{BZ}} \delta_{p,p'} G_\uparrow(p) G_\downarrow(q-p) \, . \tag{5b}$$

By exploiting the SU(2) symmetry,

$$G_\sigma(p) = G_{\bar{\sigma}}(p) = G(p) \, , \tag{6}$$

we can drop the spin dependencies for the bare bubbles. In presence of the above symmetries, we can introduce the following definitions for (spin-independent) channels of the two-particle vertex

$$\gamma_{4,\mathrm{d}}(q,p,p') = \frac{1}{2} \sum_{\sigma,\sigma'} \gamma_{4;\sigma\sigma\sigma'\sigma'}(p, p+q, p'+q, p') \tag{7a}$$

$$\gamma_{4,\mathrm{m}}(q,p,p') = \frac{1}{2} \sum_{\sigma,\sigma'} (-1)^{\epsilon_{\sigma\sigma'}} \gamma_{4;\sigma\sigma\sigma'\sigma'}(p, p+q, p'+q, p') \tag{7b}$$

$$\gamma_{4,\mathrm{sc}}(q,p,p') = \gamma_{4;\uparrow\uparrow\downarrow\downarrow}(p, p', q-p, q-p') \, , \tag{7c}$$

with ϵ the Levi-Civita symbol. The resulting spin-independent expression of the physical susceptibilities reads

$$\chi^{nn'}_\eta(q) = \int dp dp' f_n(\mathbf{p}) f^*_{n'}(\mathbf{p}') \big[\Pi_\eta(q,p,p') + \Pi_\eta(q,p,p) \gamma_{4,\eta}(q,p,p') \Pi_\eta(q,p',p') \big] \, . \tag{8}$$

We conclude this section by recalling the definition of the so-called fermion-boson vertex [59], which, for the considered symmetries, reads

$$\gamma^{n}_{3,\mathrm{d/m};\sigma\sigma}(q,p) = \Pi^{-1}_{\mathrm{d/m}}(q,p,p)\boldsymbol{\sigma}^{0/3}_{\sigma\sigma}\langle\bar{\psi}_{\sigma}(p)\psi_{\sigma}(p+q)\rho^{n*}_{\mathrm{d/m}}(q)\rangle \tag{9a}$$

$$\gamma^{n}_{3,\mathrm{sc};\downarrow\uparrow}(q,p) = \Pi^{-1}_{\mathrm{sc}}(q,p,p)\langle\psi_{\downarrow}(p)\psi_{\uparrow}(q-p)\rho^{n*}_{\mathrm{sc}}(q)\rangle\,. \tag{9b}$$

Similarly to the susceptibility, one can rewrite Eqs. (9a) and (9b) in a form where the two-particle vertex $\gamma_{4,\eta}$ appears explicitly

$$\gamma^{n}_{3,\eta}(q,p) = f_n(\mathbf{p}) + \int dp' f_n(\mathbf{p}')\gamma_{4,\eta}(q,p,p')\Pi_{\eta}(q,p',p')\,, \tag{10}$$

where, because of the SU(2) symmetry, we dropped the spin dependence of the fermion-boson vertices

$$\gamma^{n}_{3,\mathrm{d/m};\sigma\sigma} = \gamma^{n}_{3,\mathrm{d/m};\bar{\sigma}\bar{\sigma}} = \gamma^{n}_{3,\mathrm{d/m}} \tag{11a}$$

$$\gamma^{n}_{3,\mathrm{sc};\downarrow\uparrow} = \gamma^{n}_{3,\mathrm{sc};\uparrow\downarrow} = \gamma^{n}_{3,\mathrm{sc}}\,. \tag{11b}$$

2.2 Flow equations for the response functions

In this section we derive the mfRG [55] flow equations of the response functions and discuss the improvement with respect to the 1ℓ version [1]. Note that one can also provide a formal analytical derivation of these flow equations [57]. In the following we provide the main steps of the derivation in the 1PI formulation [1,60] (see also Ref. [58] for the Wick-ordered formulation), for the details we refer to Appendix B. Following the review of Metzner et al. [1], we introduce the coupling of the density operators in Eqs. (1) and (2), shifted with respect to their average values, i.e. $\rho^n_\eta \to \rho^n_\eta - \langle\rho^n_\eta\rangle$, to the external field J_η by defining the following scalar product

$$(J^{n}_{\mathrm{d/m}},\rho^{n}_{\mathrm{d/m}}) = \int dq J^{n}_{\mathrm{d/m}}(q)\rho^{n}_{\mathrm{d/m}}(q)\,, \tag{12a}$$

$$(J^{n}_{\mathrm{sc}},\rho^{n*}_{\mathrm{sc}}) + (J^{n\,*}_{\mathrm{sc}},\rho^{n}_{\mathrm{sc}}) = \int dq\big[J^{n}_{\mathrm{sc}}(q)\rho^{n*}_{\mathrm{sc}}(q) + J^{n\,*}_{\mathrm{sc}}(q)\rho^{n}_{\mathrm{sc}}(q)\big]\,. \tag{12b}$$

We note that, although J^n_η appears as a functional dependence in our derivation, it is not an integration variable since our system is fully fermionic (for an fRG formulation of coupled fermion-boson systems, see Refs. [1,61–63]).

By expanding the scale-dependent effective action Γ^Λ in powers of the fermionic fields, as well as of the external bosonic source field, we obtain

$$\begin{aligned}\Gamma^{\Lambda}[J_\eta,\bar{\psi},\psi] = \Gamma^{\Lambda}[\bar{\psi},\psi] + \sum_{\eta}\sum_{y_1,y_2}\frac{\partial^{(2)}\Gamma^{\Lambda}[J_\eta,\bar{\psi},\psi]}{\partial J_\eta(y_1)\partial J^{*}_{\eta}(y_2)}\bigg|_{\substack{\psi=\bar{\psi}=0\\ J=0}} J_\eta(y_1)J^{*}_{\eta}(y_2) - \\ \sum_{\eta'=\,\mathrm{d,m}}\sum_{y,x,x'}\frac{\partial^{(3)}\Gamma^{\Lambda}[J_\eta,\bar{\psi},\psi]}{\partial J_{\eta'}(y)\partial\bar{\psi}(x')\psi(x)}\bigg|_{\substack{\psi=\bar{\psi}=0\\ J=0}} J_{\eta'}(y)\bar{\psi}(x')\psi(x) - \\ \sum_{y,x,x'}\frac{\partial^{(3)}\Gamma^{\Lambda}[J_\eta,\bar{\psi},\psi]}{\partial J_{\mathrm{sc}}(y)\partial\bar{\psi}(x')\partial\bar{\psi}(x)}\bigg|_{\substack{\psi=\bar{\psi}=0\\ J=0}} J_{\mathrm{sc}}(y)\bar{\psi}(x')\bar{\psi}(x) + \ldots\end{aligned} \tag{13}$$

Note that the index $x = \{\sigma, k\}$ combines the spin index σ and the fermionic quadrivector $k = (i\nu_l, \mathbf{k})$ (here we disregard additional quantum dependencies, e.g., orbital), while

$y = \{n, q\}$ refers to the momentum structure of the coupling to the bilinears, n, and to the bosonic quadrivector $q = \{i\omega_l, \mathbf{q}\}$. In Eq. (13) the first term on the r.h.s. represents the expansion of the effective action in absence of external field (see Section 3), while the functional derivatives in the following terms represent the Λ-dependent susceptibility and the fermion-boson vertex in the different channels. Taking the derivative with respect to the scale parameter Λ (see Appendix B) yields the following flow equations for the susceptibility and fermion-boson vertex (assuming SU(2) symmetry and momentum-frequency as well as spin conservation)

$$\begin{aligned}\partial_\Lambda \chi^{nn',\Lambda}_{\text{d/m}}(q) = \int dk\, \big[-S^\Lambda(k)\tilde{\gamma}^{nn',\Lambda}_{4,\text{d/m}}(q,k) - \\ \gamma^{n,\Lambda}_{3,\text{d/m}}(q,k)[G^\Lambda(k)S^\Lambda(q+k)\ +(S \leftrightarrow G)]\gamma^{n',\Lambda,\dagger}_{3,\text{d/m}}(q,k)\big] \qquad \text{(14a)}\\ \partial_\Lambda \chi^{nn',\Lambda}_{\text{sc}}(q) = \int dk\, \big[-S^\Lambda(k)\tilde{\gamma}^{nn',\Lambda}_{4,\text{sc}}(q,k) + \\ \gamma^{n,\Lambda}_{3,\text{sc}}(q,k)[G^\Lambda(k)S^\Lambda(q-k) + (S \leftrightarrow G)]\gamma^{n',\Lambda,\dagger}_{3,\text{sc}}(q,k)\big], \qquad \text{(14b)}\end{aligned}$$

and respectively

$$\begin{aligned}\partial_\Lambda \gamma^{n,\Lambda}_{3,\text{d/m}}(q,k) = \int dk'\, \big[-S^\Lambda(k)\gamma^{n,\Lambda}_{5,\text{d/m}}(q,k,k') \\ \gamma^{n,\Lambda}_{3,\text{d/m}}(q,k')[G^\Lambda(k')S^\Lambda(q+k')\ +(S \leftrightarrow G)]\gamma^{\Lambda}_{4,\text{d/m}}(q,k',k)\big] \qquad \text{(15a)}\\ \partial_\Lambda \gamma^{n,\Lambda}_{3,\text{sc}}(q,k) = \int dk'\, \big[-S^\Lambda(k)\gamma^{n,\Lambda}_{5,\text{sc}}(q,k,k') + \\ \gamma^{n,\Lambda}_{3,\text{sc}}(q,k')[G^\Lambda(k')S^\Lambda(q-k')\ +(S \leftrightarrow G)]\gamma^{\Lambda}_{4,\text{sc}}(q,k',k)\big], \qquad \text{(15b)}\end{aligned}$$

where

$$S^\Lambda = \partial_\Lambda G^\Lambda|_{\Sigma=\text{const}} \qquad (16)$$

represents the single-scale propagator. The function $\tilde{\gamma}_4$, differently from the (fermionic) two-particle vertex γ_4, represents a mixed bosonic-fermionic vertex, i.e., with two bosonic and two fermionic legs where we summed over its spin dependences

$$\tilde{\gamma}^{nn',\Lambda}_{4,\eta}(q,k) = \sum_\sigma \tilde{\gamma}^{nn',\Lambda}_{4,\eta;\sigma\sigma}(q,k)\,, \qquad (17)$$

while the spin-independent form for γ_5 used in Eqs. (15) reads

$$\begin{aligned}\gamma^{n,\Lambda}_{5,\text{d/m}}(q,k,k') = \sum_{\sigma'} \boldsymbol{\sigma}^{0/3}_{\sigma\sigma}\gamma^{n,\Lambda}_{5,\text{d/m};\sigma\sigma\sigma'\sigma'}(q,k,k') \qquad \text{(18a)}\\ \gamma^{n,\Lambda}_{5,\text{sc}}(q,k,k') = \sum_{\sigma'} \gamma^{n,\Lambda}_{5,\text{sc};\sigma\bar{\sigma}\sigma'\sigma'}(q,k,k')\,. \qquad \text{(18b)}\end{aligned}$$

The conventional approximations [1, 58, 60] disregard the first terms on the r.h.s. of Eqs. (14) and (15). This 1ℓ approximation is consistent with the corresponding approximation of γ^Λ_4 (see Appendix C) and justified in the weak-coupling regime. Using the notation of Refs. [45, 55], one can rewrite the 1ℓ approximation of Eqs. (14) and (15) in a more concise tensor-form

$$\begin{aligned}\dot{\boldsymbol{\chi}}^{\Lambda(1)}_\eta = \boldsymbol{\gamma}^\Lambda_{3,\eta} \circ \dot{\boldsymbol{\Pi}}^\Lambda_{S,\eta} \circ \boldsymbol{\gamma}^{\Lambda,\dagger}_{3,\eta} \qquad \text{(19a)}\\ \dot{\boldsymbol{\gamma}}^{\Lambda(1)}_{3,\eta} = \boldsymbol{\gamma}^\Lambda_{3,\eta} \circ \dot{\boldsymbol{\Pi}}^\Lambda_{S,\eta} \circ \boldsymbol{\gamma}^{\Lambda}_{4,\eta}\,. \qquad \text{(19b)}\end{aligned}$$

where

$$\dot{\Pi}^{\Lambda}_{S,\mathrm{d/m}(ph)}(q,k) = -\,G^{\Lambda}(k)S^{\Lambda}(q+k) + (S \leftrightarrow G) \tag{20a}$$

$$\dot{\Pi}^{\Lambda}_{S,\mathrm{sc}(pp)}(q,k) = G^{\Lambda}(k)S^{\Lambda}(q-k) + (S \leftrightarrow G)\,. \tag{20b}$$

We here introduced also the subscript *ph* and *pp* indicating the diagrammatic channels that will be referred to in Sec. 3.

So far we pinpointed two possible ways to compute the susceptibility and fermion-boson vertex from an fRG calculation: (i) Solving Eqs. (14) and (15) alongside the ones for Σ and γ_4 (at the same level of approximation), and (ii) by means of Eqs. (8) and (10) at the end of the fRG flow, using $\Sigma^{\Lambda_{\mathrm{final}}}$ and $\gamma_4^{\Lambda_{\mathrm{final}}}$, later referred to as "post-processing". These two procedures are non-equivalent in the presence of approximations, e.g., if one restricts oneself to the 1ℓ level. This leads to an ambiguity in practical implementations of the fRG. In fact, as shown in Appendix D, the two results deviate at $\mathcal{O}((\gamma_4^{\Lambda})^2)$ for the 1ℓ case (for a larger number of loops the deviations occur at higher orders in the effective interaction γ_4^{Λ}). In order to solve this ambiguity we note that the exact relations (8) and (10) are fulfilled in the PA. At the same time, the recently introduced multiloop extension allows one to sum up all parquet diagrams. Hence, generalizing the multiloop flow to the computation of the response functions recovers the equivalence of the two procedures.

In order to derive the mfRG equations for the response functions, we first recall the channel-decomposition of the two-particle vertex as known from the parquet formalism. The latter divides γ_4 in the two-particle reducible vertex ϕ (all diagrams that can be divided into two separate ones by removing two internal fermionic propagators) and the two-particle irreducible vertex I (which can be not be divided). Depending on the direction of the propagation lines the diagrams are reducible in either parallel, longitudinal antiparallel or transverse antiparallel, corresponding to the particle-particle, particle-hole, and particle-hole crossed channel, respectively. Besides this diagrammatic channel decomposition, there is also a distinct physical channel decomposition that identifies the components $\eta = \{\mathrm{d}, \mathrm{m}, \mathrm{sc}\}$ and which we will use in the following. Inserting this decomposition into the flow equation for the two-particle vertex, we obtain

$$\partial_{\Lambda}\gamma^{\Lambda}_{4,\eta} = \partial_{\Lambda}I^{\Lambda}_{\eta} + \partial_{\Lambda}\phi^{\Lambda}_{\eta}\,. \tag{21}$$

While the usual diagrammatic channel decomposition [64] leads to simple expressions for the two-particle irreducible vertex I^{Λ}_{η}, the latter assumes a more complicated form in the physical channels

$$\begin{aligned} I^{\Lambda}_{\mathrm{d}}(q,k,k') = {}& -U - \frac{1}{2}\phi^{\Lambda}_{\mathrm{d}}(k'-k,k,k+q) - \frac{3}{2}\phi^{\Lambda}_{\mathrm{m}}(k'-k,k,k+q) + \\ & + 2\phi^{\Lambda}_{\mathrm{sc}}(q+k+k',k,k') - \phi^{\Lambda}_{\mathrm{sc}}(q+k+k',k,q+k) \end{aligned} \tag{22a}$$

$$\begin{aligned} I^{\Lambda}_{\mathrm{m}}(q,k,k') = {}& U - \frac{1}{2}\phi^{\Lambda}_{\mathrm{d}}(k'-k,k,k+q) + \frac{1}{2}\phi^{\Lambda}_{\mathrm{m}}(k'-k,k,k+q) - \\ & + \phi^{\Lambda}_{\mathrm{sc}}(q+k+k',k,k+q) \end{aligned} \tag{22b}$$

$$\begin{aligned} I^{\Lambda}_{\mathrm{sc}}(q,k,k') = {}& -U - \phi^{\Lambda}_{\mathrm{m}}(k'-k,k,q-k') + \frac{1}{2}\phi^{\Lambda}_{\mathrm{d}}(q-k-k',k,k') - \\ & - \frac{1}{2}\phi^{\Lambda}_{\mathrm{m}}(q-k-k',k,k')\,, \end{aligned} \tag{22c}$$

where we approximated the fully two-particle irreducible vertex by its first-order contribution in the interaction $\sim U$, which is known as PA.

We now derive the mfRG flow equations for the response functions, which mimic the effect of the mixed fermion-boson vertices $\tilde{\gamma}^{\Lambda}_4$ and γ^{Λ}_5 in the exact flow Eqs. (14) and (15). First, one performs the so-called Katanin substitution [45] $S^{\Lambda} \to \partial_{\Lambda}G^{\Lambda}$, which implies $\dot{\mathbf{\Pi}}^{\Lambda}_{S,\eta} \to \dot{\mathbf{\Pi}}^{\Lambda}_{\eta}$ in

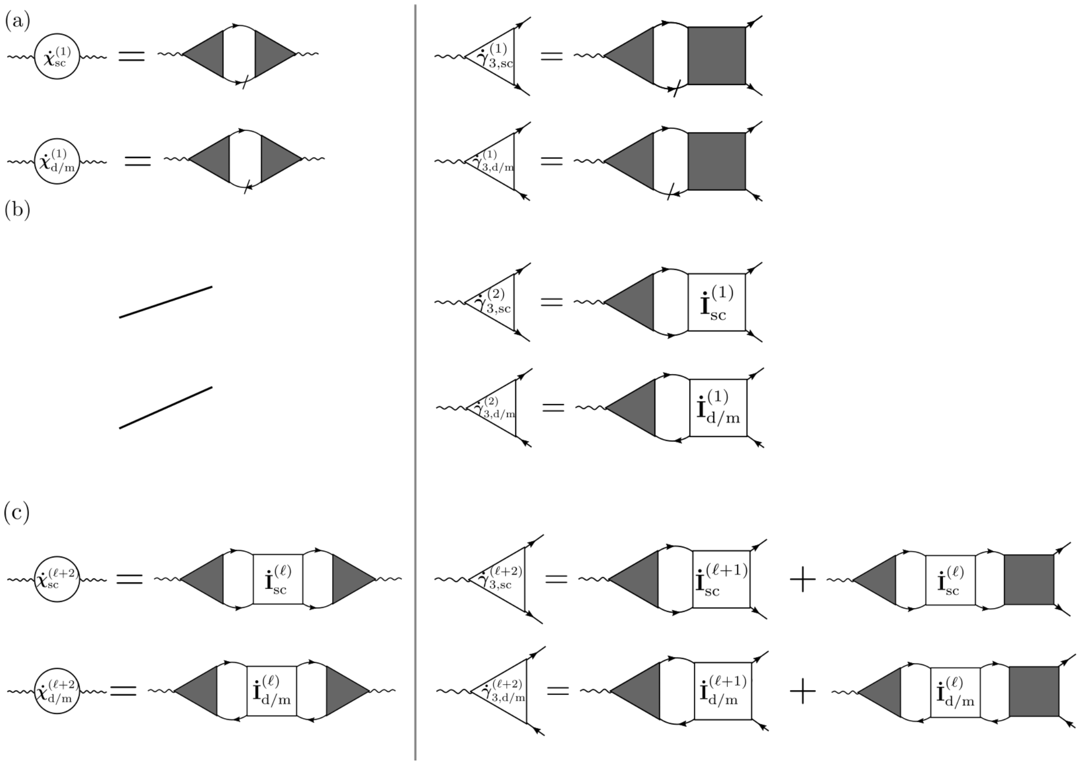
(a)
$\dot{\chi}^{(1)}_{\rm sc}$
$\dot{\chi}^{(1)}_{\rm d/m}$
(b)
(c)
$\dot{\chi}^{(\ell+2)}_{\rm sc}$
$\dot{\chi}^{(\ell+2)}_{\rm d/m}$
$\dot{\mathbf{I}}^{(\ell)}_{\rm sc}$
$\dot{\mathbf{I}}^{(\ell)}_{\rm d/m}$
$\dot{\gamma}^{(1)}_{3,\rm sc}$
$\dot{\gamma}^{(1)}_{3,\rm d/m}$
$\dot{\gamma}^{(2)}_{3,\rm sc}$
$\dot{\gamma}^{(2)}_{3,\rm d/m}$
$\dot{\mathbf{I}}^{(1)}_{\rm sc}$
$\dot{\mathbf{I}}^{(1)}_{\rm d/m}$
$\dot{\gamma}^{(\ell+2)}_{3,\rm sc}$
$\dot{\gamma}^{(\ell+2)}_{3,\rm d/m}$
$\dot{\mathbf{I}}^{(\ell+1)}_{\rm sc}$
$\dot{\mathbf{I}}^{(\ell+1)}_{\rm d/m}$
$\dot{\mathbf{I}}^{(\ell)}_{\rm sc}$
$\dot{\mathbf{I}}^{(\ell)}_{\rm d/m}$

Figure 1: Multiloop flow equations for the susceptibility (left column) and the fermion-boson vertex (right column) for all physical channels $\eta = \{\mathrm{sc}, \mathrm{m}, \mathrm{d}\}$. Whereas the filled boxes and triangles represent the vertex $\gamma^{\Lambda}_{4,\eta}$ and $\gamma^{\Lambda}_{3,\eta}$, respectively, the empty ones contain the scale-parameter derivative of the two-particle irreducible vertex $\dot{\mathbf{I}}^{\Lambda}_{\eta}$ in the respective channel (see Eq. (22)). (a) Standard one-loop truncated flow equations as in Eq. (19). (b) Two loop corrections for the fermion-boson vertex as in Eq. (24). As argued in the text, because of the fermionic leg contractions, no two-loop correction terms appear in the susceptibility flow equation. (c) Higher loop corrections starting from the third loop order for both susceptibility and fermion-boson vertex as reported in Eqs. (26) and (25), respectively.

the 1ℓ flow equations (19). One observes that all differentiated lines in these flow equations come from $\dot{\mathbf{\Pi}}^{\Lambda}_{\eta}$. Secondly, differentiated lines from the other channels are contained in the higher-loop terms of the expansion

$$\partial_\Lambda \boldsymbol{\chi}^{\Lambda}_{\eta} = \sum_{\ell \geqslant 1} \dot{\boldsymbol{\chi}}^{\Lambda(\ell)}_{\eta} \tag{23a}$$

$$\partial_\Lambda \boldsymbol{\gamma}^{\Lambda}_{3,\eta} = \sum_{\ell \geqslant 1} \dot{\boldsymbol{\gamma}}^{\Lambda(\ell)}_{3,\eta}\,. \tag{23b}$$

Using the channel decomposition (21), we can directly write down the 2ℓ correction to the flow of the fermion-boson vertex, which accounts for the leading-order diagrams of the effective interaction and stem from γ^{Λ}_{5} in Eq. (15) (see Appendix E)

$$\dot{\boldsymbol{\gamma}}^{\Lambda(2)}_{3,\eta} = \boldsymbol{\gamma}^{\Lambda}_{3,\eta} \circ \mathbf{\Pi}^{\Lambda}_{\eta} \circ \dot{\mathbf{I}}^{\Lambda(1)}_{\eta}\,. \tag{24}$$

On the three- and higher-loop level, we can now use $\dot{\mathbf{I}}^{\Lambda(\ell)}_{\eta}$ in an analogous way. In addition,

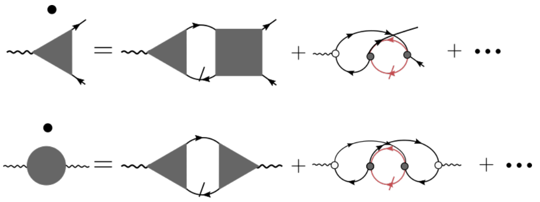

Figure 2: Multiloop corrections (beyond 1ℓ) for $\gamma^{\Lambda}_{3,\mathrm{d/m}}$ (top) and $\chi^{\Lambda}_{\mathrm{d/m}}$ (bottom) at the leading order in the bare interaction (filled black dot). The empty dot represents the bare fermion-boson vertex $\gamma^{n}_{3,\eta,0}(q,k) = f_n(\mathbf{k})$.

we have to consider the vertex corrections to the right of the differentiated lines, yielding

$$\dot{\boldsymbol{\gamma}}^{\Lambda(\ell+2)}_{3,\eta} = \boldsymbol{\gamma}^{\Lambda}_{3,\eta} \circ \boldsymbol{\Pi}^{\Lambda}_{\eta} \circ \dot{\mathbf{I}}^{\Lambda(\ell+1)}_{\eta} + \boldsymbol{\gamma}^{\Lambda}_{3,\eta} \circ \boldsymbol{\Pi}^{\Lambda}_{\eta} \circ \dot{\mathbf{I}}^{\Lambda(\ell)}_{\eta} \circ \boldsymbol{\Pi}^{\Lambda}_{\eta} \circ \boldsymbol{\gamma}^{\Lambda}_{4,\eta} \,. \tag{25}$$

Considering the 1ℓ flow equation of the susceptibility (19a), we see that the fermion-boson vertices provide vertex corrections on both sides of the differentiated lines in $\dot{\boldsymbol{\Pi}}^{\Lambda}_{\eta}$. Hence, for all higher-loop corrections we can simply connect $\dot{\mathbf{I}}^{\Lambda(\ell)}_{\eta}$ to both fermion-boson vertices, thereby raising the loop order by two. We obtain $\dot{\boldsymbol{\chi}}^{\Lambda(2)}_{\eta} = 0$, as well as

$$\dot{\boldsymbol{\chi}}^{\Lambda(\ell+2)}_{\eta} = \boldsymbol{\gamma}^{\Lambda}_{3,\eta} \circ \boldsymbol{\Pi}^{\Lambda}_{\eta} \circ \dot{\mathbf{I}}^{\Lambda(\ell)}_{\eta} \circ \boldsymbol{\Pi}^{\Lambda}_{\eta} \circ \boldsymbol{\gamma}^{\Lambda,\dagger}_{3,\eta} \,. \tag{26}$$

For a schematic representation of the multiloop flow equations for χ_η and $\gamma_{3,\eta}$ see Fig. 1, while an example of the multiloop corrections at the leading order in the bare interaction is illustrated in Fig. 2. The above equations, together with the multiloop flow of the fermionic two-particle vertex (see Section 3.2) allow us to sum up all differentiated parquet diagrams of $\boldsymbol{\gamma}^{\Lambda}_{3}$ and $\boldsymbol{\chi}^{\Lambda}$. As a consequence, the aforementioned two ways of computing the response functions within the fRG become equivalent. We finally note that for a consistent fRG scheme, it is important to adopt the same level of approximation (truncating the sums in Eq. (23a) to a certain finite ℓ-loop level) for all flowing quantities.

3 Numerical implementation

3.1 Full frequency and momentum parametrization

In order to illustrate the fRG algorithm adopted in the present work, let us start from the flow equations for the 1PI fermionic vertex in the 1ℓ fRG approximation. In the following, the SU(2) spin conserving symmetry will be always assumed. Exploiting this symmetry, the self-energy and two-particle fermionic vertices can be written as

$$\Sigma_{\sigma\sigma'}(k) = \delta_{\sigma,\sigma'}\Sigma_{\sigma}(k) = \delta_{\sigma,\sigma'}\Sigma(k) \tag{27}$$

$$\gamma_{4,\sigma_1\sigma_2\sigma_3\sigma_4}(k_1,k_2,k_3) = \left[-\delta_{\sigma_1,\sigma_4}\delta_{\sigma_2,\sigma_3}\gamma_4(k_1,k_4,k_3) + \delta_{\sigma_1,\sigma_2}\delta_{\sigma_3,\sigma_4}\gamma_4(k_1,k_2,k_3)\right], \tag{28}$$

where the fourth argument of γ_4 is determined by $k_4 = k_1 + k_3 - k_2$ in a momentum and energy conserving system. The spin-independent flow equation for the self-energy reads

$$\dot{\Sigma}^{\Lambda}(k) = -\int dp S^{\Lambda}(p) \left[2\,\gamma^{\Lambda}_4(k,k,p) - \gamma^{\Lambda}_4(p,k,k)\right], \tag{29}$$

where $S^{\Lambda}(p)$ represents the single-scale propagator specified in Eq. (16). We formulate the flow equation for γ_4 in the channel decomposed form suggested by Husemann and Salmhofer

[28]

$$\dot{\gamma}_4^\Lambda(k_1,k_2,k_3) = \mathcal{T}^\Lambda_{pp}(k_1+k_3,k_1,k_4) + \mathcal{T}^\Lambda_{ph}(k_2-k_1,k_1,k_4) + \mathcal{T}^\Lambda_{\overline{ph}}(k_3-k_2,k_1,k_2)\,, \tag{30}$$

where the diagrammatic channel index $r = \{pp, ph, \overline{ph}\}$ distinguishes between particle-particle, particle-hole and particle-hole exchange diagrams, and the first dependence of the functions $\mathcal{T}^\Lambda_r$ refers to the bosonic four-momentum transfer in the internal loop of their corresponding equations

$$\begin{aligned}\mathcal{T}^\Lambda_{pp}(k_1+k_3,k_1,k_4) = &\int dp\, \gamma_4^\Lambda(k_1,k_1+k_3-p,k_3)\gamma_4^\Lambda(p,k_2,k_1+k_3-p)\times \\ &\Big[S^\Lambda(p)G^\Lambda(k_1+k_3-p)+(S\leftrightarrow G)\Big]\,,\end{aligned} \tag{31a}$$

$$\begin{aligned}\mathcal{T}^\Lambda_{ph}(k_2-k_1,k_1,k_4) = -&\int dp \Big[2\,\gamma_4^\Lambda(k_1,k_2,k_2-k_1+p)\;\gamma_4^\Lambda(p,k_2-k_1+p,k_3) - \\ &\gamma_4^\Lambda(k_1,p,k_2-k_1+p)\;\gamma_4^\Lambda(p,k_2-k_1+p,k_3) - \\ &\gamma_4^\Lambda(k_1,k_2,k_2-k_1+p)\;\gamma_4^\Lambda(p,k_2,k_3)\Big]\times \\ &\Big[S^\Lambda(p)G^\Lambda(k_2-k_1+p)+(S\leftrightarrow G)\Big]\,,\end{aligned} \tag{31b}$$

$$\begin{aligned}\mathcal{T}^\Lambda_{\overline{ph}}(k_3-k_2,k_1,k_2) = &\int dp\, \gamma_4^\Lambda(k_1,p,k_3-k_2+p)\gamma_4^\Lambda(p,k_2,k_3)\times \\ &\Big[S^\Lambda(p)G^\Lambda(k_3-k_2+p)+(S\leftrightarrow G)\Big]\,.\end{aligned} \tag{31c}$$

Note that the assignment of the various terms on the right hand side of the flow equation to the three channels is not unique. The version we use here corresponds to the choice by Wang et al. in their singular-mode fRG [31, 65]. Each of the above equations depends, besides the aforementioned bosonic transfer dependence (k_1+k_3, k_2-k_1 and k_3-k_2), on two fermionic dependencies. Such mixed 'bosonic-fermonic' notation, referred to as 'non-symmetrized' notation, has been substituted in some work (e.g., in Ref. [31]) by a different notation where the dependencies of the four fermionic propagators involved in the scattering process have been chosen symmetrically with respect to the bosonic four-momentum transfer. This symmetrized notation simplifies the implementation of the symmetries exploited in the fRG code (see Appendix F and Ref. [31]) but leads to less compact flow equations. The equation (31) generates the two-particle reducible vertices $\mathcal{T}_r = \dot{\phi}_r$ of the diagrammatic parquet decomposition

$$\gamma_4(k_1,k_2,k_3) \approx U + \phi_{pp}(k_1+k_3,k_1,k_4) + \phi_{ph}(k_2-k_1,k_1,k_4) + \phi_{\overline{ph}}(k_3-k_2,k_1,k_2)\,. \tag{32}$$

The two-particle fermionic vertex can be reconstructed by using Eq. (32). The use of a mixed 'bosonic-fermonic' notation allows us to identify the bosonic transfer four-momentum as the strongest dependence, while the two fermionic dependencies can be treated with controllable approximations. In the following we illustrated two efficient ways to simplify the treatment of both momentum and frequency dependencies.

3.1.1 Truncated Unity fRG

The approximation for the fermionic momentum dependencies in TUfRG [31] is done by the expansion of the fermionic momentum dependencies in form factors, illustrated here for the pp channel

$$\phi_{pp}(\mathbf{q},\mathbf{k},\mathbf{k}') = \sum_{n,n'} f_n(\mathbf{k}) f^*_{n'}(\mathbf{k}') P_{n,n'}(\mathbf{q})\,, \tag{33}$$

while the expansion of the ϕ_{ph} and $\phi_{\overline{ph}}$ analogously defines $D_{n,n'}(\mathbf{q})$ and $C_{n,n'}(\mathbf{q})$. Following the conventions introduced in previous works [28, 29, 31, 41, 66, 67], we choose the form factors such that they correspond to a specific shell of neighbors in the real space lattice. The unity inserted in the flow equations contains a complete basis set of form factors

$$\mathbb{1} = \int d\mathbf{p}' \sum_n f_n^*(\mathbf{p}') f_n(\mathbf{p}) \,. \tag{34}$$

Converged results can be obtained already with a small set of form factors [31], i.e. the unity (34) can be approximated by a truncated unity, giving rise to the name "truncated-unity fRG". For a fast convergence it is convenient to include one shell after another, starting from the constant local form factor and increasing the distance of neighbors taken into account. The form factors used in this paper are listed in Table 1.

A major difficulty in this approach is the feedback of the different channels into each other. In addition to the dressing of the objects by the form factors, the translation of the notation in momentum and frequency from one to another channel has to be considered. Computationally time consuming integrations in momentum space can be avoided by Fourier transformation and evaluation in real space [31, 65]. Furthermore the expression of the projection in terms of a matrix multiplication allows for the precalculation of the projection matrices which can be found in the Appendix F.

3.1.2 Dynamical fRG

In frequency space, we adopt the simplifications proposed in Refs. [33,34]. For all systems with an instantaneous microscopic interaction one can use diagrammatic arguments to prove that, in the high-frequency regime, the fermionic two-particle vertex exhibits a simplified asymptotic structure. In this region one can reduce the three-dimensional frequency dependence of γ_4 using functions with a simplified parametric dependence. It is straightforward to see that, sending all three frequencies to infinity, γ_4 reduces to the instantaneous microscopic interaction, which in the present case is represented by the Hubbard on-site U. The contribution of the reducible vertices ϕ_r to γ_4 becomes non-negligible if the bosonic frequency transfer is kept finite, while sending the two secondary fermionic frequencies to infinity. This contribution, depending on a single bosonic frequency transfer in a given channel r, is denoted by $\mathcal{K}_{1,r}(i\omega_l, q)$. For models with an instantaneous and local microscopic interaction, one observes that the momentum dependencies disappear alongside the frequency dependencies when performing such limits. In the limit where just one fermionic frequency is sent to infinity, the vertex ϕ_r can be parametrized by the function $\mathcal{K}_{2,r}(i\omega_l, i\nu_o, q, k) + \mathcal{K}_{1,r}(i\omega_l, q)$. By subtracting the asymptotic functions from the full object ϕ_r we obtain the so-called [34]"rest-function" $\mathcal{R}(i\omega_l, i\nu_o, i\nu_{o'}, q, k, k')$ which decays to zero within a small frequency box. The parametrization in terms of $\mathcal{K}_{1/2}$ allows us to reduce the numerical cost of computing and storing the fermionic two-particle vertices. In fact, for any of the three channels, we calculate the fRG flow of the three-frequency dependent function $\mathcal{R}$ on a small low-frequency region and add the information on the high frequencies by computing the flow of the functions $\mathcal{K}_1$ and $\mathcal{K}_2$ which are numerically less demanding. The full two-particle reducible vertex ϕ_r is then recovered by

$$\begin{aligned}\phi_r(i\omega_l, i\nu_o, i\nu_{o'}, \mathbf{q}, \mathbf{k}, \mathbf{k}') = \mathcal{R}_r(i\omega_l, i\nu_o, i\nu_{o'}, \mathbf{q}, \mathbf{k}, \mathbf{k}') + \\ \mathcal{K}_{2,r}(i\omega_l, i\nu_o, \mathbf{q}, \mathbf{k}) + \bar{\mathcal{K}}_{2,r}(i\omega, i\nu_{o'}, \mathbf{q}, \mathbf{k}') + \mathcal{K}_{1,r}(i\omega_l, \mathbf{q}),\end{aligned} \tag{35}$$

where $\bar{\mathcal{K}}_{2,r}$ can be obtained from $\mathcal{K}_{2,r}$ by exploiting the time reversal symmetry (see Appendix A.3).

3.1.3 Flow equations for the TU-dynamical fRG

Finally, applying the aforementioned projection on the form-factor basis we can write matrix-like 1ℓ fRG flow equations for the self-energy, the two-particle vertex, the fermion-boson vertex and the susceptibility:

$$\dot{\Sigma}^{\Lambda}(k) = -\int dp\, S^{\Lambda}(p)\Big[2\,\gamma_4^{\Lambda}(k,k,p) - \gamma_4^{\Lambda}(p,k,k)\Big] \tag{36a}$$

$$\dot{\mathbf{P}}^{\Lambda}(q,i\nu_o,i\nu_{o'}) = \frac{1}{\beta}\sum_{i\nu_{n''}} \boldsymbol{\gamma}^{\Lambda}_{4,P}(q,i\nu_o,i\nu_{n''})\dot{\mathbf{\Pi}}^{\Lambda}_{S,pp}(q,i\nu_{n''})\boldsymbol{\gamma}^{\Lambda}_{4,P}(q,i\nu_{n''},i\nu_{o'}) \tag{36b}$$

$$\begin{aligned}\dot{\mathbf{D}}^{\Lambda}(q,i\nu_o,i\nu_{o'}) = \frac{1}{\beta}\sum_{i\nu_{n''}} \dot{\mathbf{\Pi}}^{\Lambda}_{S,ph}(q,i\nu_{n''})\Big[&2\boldsymbol{\gamma}^{\Lambda}_{4,D}(q,i\nu_o,i\nu_{n''})\boldsymbol{\gamma}^{\Lambda}_{4,D}(q,i\nu_{n''},i\nu_{o'}) - \\ &-\boldsymbol{\gamma}^{\Lambda}_{4,C}(q,i\nu_o,i\nu_{n''})\boldsymbol{\gamma}^{\Lambda}_{4,D}(q,i\nu_{n''},i\nu_{o'}) - \\ &-\boldsymbol{\gamma}^{\Lambda}_{4,D}(q,i\nu_o,i\nu_{n''})\boldsymbol{\gamma}^{\Lambda}_{4,C}(q,i\nu_{n''},i\nu_{o'})\Big]\end{aligned} \tag{36c}$$

$$\dot{\mathbf{C}}^{\Lambda}(q,i\nu_o,i\nu_{o'}) = -\frac{1}{\beta}\sum_{i\nu_{n''}} \boldsymbol{\gamma}^{\Lambda}_{4,C}(q,i\nu_o,i\nu_{n''})\dot{\mathbf{\Pi}}^{\Lambda}_{S,ph}(q,i\nu_{n''})\boldsymbol{\gamma}^{\Lambda}_{4,C}(q,i\nu_{n''},i\nu_{o'}) \tag{36d}$$

$$\dot{\boldsymbol{\gamma}}^{\Lambda}_{3,\eta}(q,i\nu_o) = \frac{1}{\beta}\sum_{i\nu_{n'}} \boldsymbol{\gamma}^{\Lambda}_{3,\eta}(q,i\nu_{n'})\dot{\mathbf{\Pi}}^{\Lambda}_{S,\eta}(q,i\nu_{n'})\boldsymbol{\gamma}^{\Lambda}_{4,\eta}(q,i\nu_{n'},i\nu_o) \tag{36e}$$

$$\dot{\boldsymbol{\chi}}^{\Lambda}_{\eta}(q) = \frac{1}{\beta}\sum_{i\nu_{n}} \boldsymbol{\gamma}^{\Lambda}_{3,\eta}(q,i\nu_{n})\dot{\mathbf{\Pi}}^{\Lambda}_{S,\eta}(q,i\nu_{n})\boldsymbol{\gamma}^{\Lambda}_{3,\eta}(q,i\nu_{n})\,, \tag{36f}$$

where the multiplication of bold symbols has here to be understood as matrix multiplications with respect to the form factors. For a schematic visualization of the practical implementation of these equations, see Fig. 3. We note that, in order to derive Eqs. (36), we inserted the unity (34), truncated to a finite number of form factors, in Eqs. (19) as well as in (31). The full vertex $\gamma_{4,r}$, with $r = \{P, D, C\}$ represents the fermionic two-particle vertex in the channel-specific mixed 'bosonic-fermionic' notations, while $\gamma_{4,\eta}$ with $\eta = \{\mathrm{sc}, \mathrm{d}, \mathrm{m}\}$ is given by

$$\boldsymbol{\gamma}_{4,\mathrm{d}} = 2\boldsymbol{\gamma}_{4,D} - \boldsymbol{\gamma}_{4,C} \tag{37a}$$

$$\boldsymbol{\gamma}_{4,\mathrm{m}} = -\boldsymbol{\gamma}_{4,D} \tag{37b}$$

$$\boldsymbol{\gamma}_{4,\mathrm{sc}} = \boldsymbol{\gamma}_{4,P}\,. \tag{37c}$$

Note that the TUfRG equations for the channel couplings $\mathbf{P}^{\Lambda}(q,i\nu_o,i\nu_{o'})$, $\mathbf{D}^{\Lambda}(q,i\nu_o,i\nu_{o'})$, and $\mathbf{C}^{\Lambda}(q,i\nu_o,i\nu_{o'})$ are equivalent to the singular-mode fRG equations derived earlier in a different way by Wang et al. [65], as also discussed in [31]. The new point here is the dynamical implementation also taking into account the frequency dependence.

The 1ℓ-fRG flow consists in integrating the coupled differential equations in (36) with the following initial conditions:

$$\Sigma^{\Lambda_{\mathrm{init}}} = 0 \tag{38a}$$

$$\boldsymbol{\gamma}^{\Lambda_{\mathrm{init}}}_{4,P} = \boldsymbol{\gamma}^{\Lambda_{\mathrm{init}}}_{4,D} = \boldsymbol{\gamma}^{\Lambda_{\mathrm{init}}}_{4,C} = U\delta_{n,0}\delta_{n',0} \tag{38b}$$

$$\boldsymbol{\chi}^{\Lambda_{\mathrm{init}}}_{\eta} = 0 \tag{38c}$$

$$\boldsymbol{\gamma}^{\Lambda_{\mathrm{init}}}_{3,\eta} = \delta_{n,n'}\,. \tag{38d}$$

Finally, $\dot{\mathbf{\Pi}}_{S,\eta}$ relative to the particle-hole $\eta = \{\mathrm{d}/\mathrm{m}(ph)\}$ and to the particle-particle channels

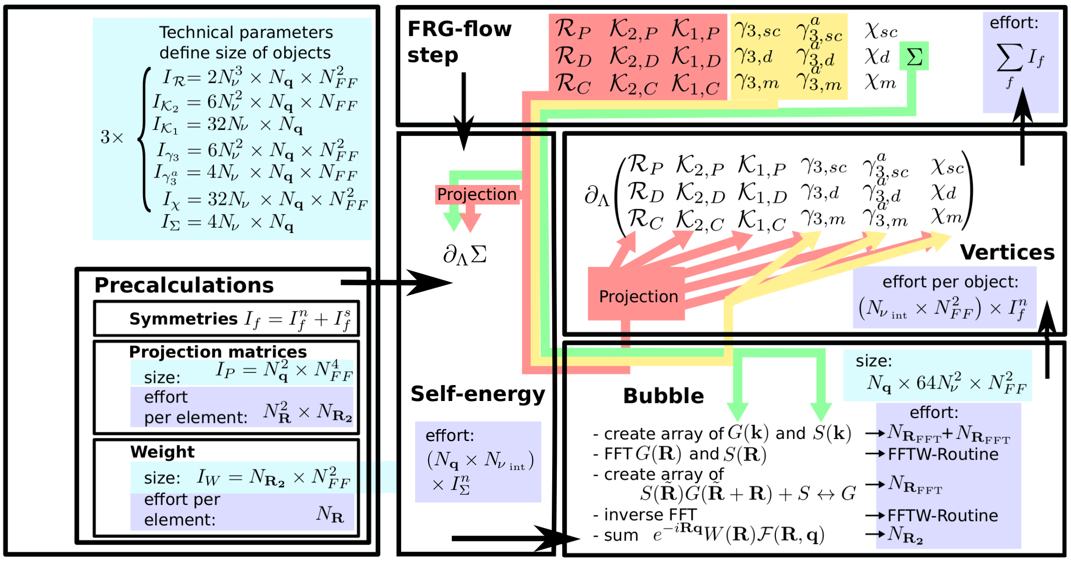
Technical parameters define size of objects
3×
$I_{\mathcal{R}} = 2N_\nu^3 \times N_{\mathbf{q}} \times N_{FF}^2$
$I_{\mathcal{K}_2} = 6N_\nu^2 \times N_{\mathbf{q}} \times N_{FF}$
$I_{\mathcal{K}_1} = 32N_\nu \times N_{\mathbf{q}}$
$I_{\gamma_3} = 6N_\nu^2 \times N_{\mathbf{q}} \times N_{FF}^2$
$I_{\gamma_3^a} = 4N_\nu \times N_{\mathbf{q}} \times N_{FF}$
$I_\chi = 32N_\nu \times N_{\mathbf{q}} \times N_{FF}^2$
$I_\Sigma = 4N_\nu \times N_{\mathbf{q}}$
Precalculations
Symmetries $I_f = I_f^n + I_f^s$
Projection matrices
size: $I_P = N_{\mathbf{q}}^2 \times N_{FF}^4$
effort per element: $N_{\mathbf{R}}^2 \times N_{\mathbf{R_2}}$
Weight
size: $I_W = N_{\mathbf{R_2}} \times N_{FF}^2$
effort per element: $N_{\mathbf{R}}$
FRG-flow step
$\mathcal{R}_P$ $\mathcal{K}_{2,P}$ $\mathcal{K}_{1,P}$ $\gamma_{3,sc}$ $\gamma_{3,sc}^a$ χ_{sc}
$\mathcal{R}_D$ $\mathcal{K}_{2,D}$ $\mathcal{K}_{1,D}$ $\gamma_{3,d}$ $\gamma_{3,d}^a$ χ_d Σ
$\mathcal{R}_C$ $\mathcal{K}_{2,C}$ $\mathcal{K}_{1,C}$ $\gamma_{3,m}$ $\gamma_{3,m}^a$ χ_m
effort: $\sum_f I_f$
Projection
$\partial_\Lambda \Sigma$
Self-energy
effort: $(N_{\mathbf{q}} \times N_{\nu\,\mathrm{int}}) \times I_\Sigma^n$
$\partial_\Lambda \begin{pmatrix} \mathcal{R}_P & \mathcal{K}_{2,P} & \mathcal{K}_{1,P} & \gamma_{3,sc} & \gamma_{3,sc}^a & \chi_{sc} \\ \mathcal{R}_D & \mathcal{K}_{2,D} & \mathcal{K}_{1,D} & \gamma_{3,d} & \gamma_{3,d}^a & \chi_d \\ \mathcal{R}_C & \mathcal{K}_{2,C} & \mathcal{K}_{1,C} & \gamma_{3,m} & \gamma_{3,m}^a & \chi_m \end{pmatrix}$
Vertices
Projection
effort per object: $(N_{\nu\,\mathrm{int}} \times N_{FF}^2) \times I_f^n$
Bubble
size: $N_{\mathbf{q}} \times 64N_\nu^2 \times N_{FF}^2$
effort:
- create array of $G(\mathbf{k})$ and $S(\mathbf{k})$ → $N_{\mathbf{R}_{\mathrm{FFT}}} + N_{\mathbf{R}_{\mathrm{FFT}}}$
- FFT $G(\mathbf{R})$ and $S(\mathbf{R})$ → FFTW-Routine
- create array of $S(\mathbf{R})G(\mathbf{R}+\mathbf{R}) + S \leftrightarrow G$ → $N_{\mathbf{R}_{\mathrm{FFT}}}$
- inverse FFT → FFTW-Routine
- sum $e^{-i\mathbf{R}\mathbf{q}} W(\mathbf{R})\mathcal{F}(\mathbf{R},\mathbf{q})$ → $N_{\mathbf{R_2}}$

Figure 3: Schematic code structure specifying the array sizes and the numerical effort of the single steps. I_f denotes the number of elements of the object f. N_ν is the number of fermionic frequencies of the rest function, $N_{\mathbf{q}}$ the number of bosonic momentum patches, N_{FF} the number of form factors, $N_{\mathbf{R}_{\mathrm{FFT}}}$ and $N_{\nu_{\mathrm{int}}}$ the number of frequencies over which the internal fermionic bubble is integrated. The symmetries reduce the total number of elements I_f to I_f^n independent elements which have to be calculated and to I_f^s which can be obtained by using symmetry relations. The arrows indicate the feedback of the different parts, namely the two-particle fermionic vertices (red), fermion-boson vertex (yellow), and the self-energy (green). In the multiloop-extended version of the fRG program, the numerical effort scales linearly in the number of loops ℓ accounted. Here, $\gamma_{3,\eta}^a$ is the asymptotic function of $\gamma_{3,\eta}$, obtained by sending the fermionic frequency to infinity.

$\eta = \{\mathrm{sc}(pp)\}$, are defined as

$$\dot{\Pi}^\Lambda_{S,\mathrm{d/m}(ph)}(i\omega_l, i\nu_o, \mathbf{q})_{n,n'} = -\int d\mathbf{p} f_n^*(\mathbf{p}) f_{n'}(\mathbf{p})\, \dot{\Pi}^\Lambda_{S,\mathrm{d/m}(ph)}(i\omega_l, i\nu_o, \mathbf{q}, \mathbf{p})\,, \tag{39a}$$

$$\dot{\Pi}^\Lambda_{S,\mathrm{sc}(pp)}(i\omega_l, i\nu_o, \mathbf{q})_{n,n'} = \int d\mathbf{p} f_n^*(\mathbf{p}) f_{n'}(\mathbf{p})\, \dot{\Pi}^\Lambda_{S,\mathrm{sc}(pp)}(i\omega_l, i\nu_o, \mathbf{q}, \mathbf{p})\,, \tag{39b}$$

where $\dot{\Pi}^\Lambda_{S,\eta}(q,k)$ is defined in Eq. (20). In order to perform the momentum integration in Eqs. (39) we adopt a strategy which, exploiting the convolution theorem, represents a numerically convenient alternative to the use of adaptive integration algorithms. The latter is described in the following section.

3.1.4 Calculation of the fermionic particle-hole and particle-particle excitation

We here present a numerically convenient way of calculating the fermionic particle-hole and particle-particle bubbles in the flow equations of the vertex (36), defined in Eqs. (39). Since the integral over momenta is very sensitive on the momentum mesh resolution near the Fermi surface and a refined adaptive integration is computationally time consuming, we rewrote the integrals in such a way to use the convolution theorem. The Green's function can then be transformed via the Fast-Fourier-Transform (FFT) to real space, where the real-space expression of the form factors is provided in Table 1. After some algebraic steps, we find an expression without momentum integration

$$\begin{aligned}\dot{\Pi}_{S,ph}(i\omega_l, i\nu_o, \mathbf{q})]_{n,n'} &= -\sum_{\mathbf{R}} e^{i\mathbf{R}\mathbf{q}} W_{n,n'}(\mathbf{R}) \times \\ &\mathcal{F}\Big[S(i\nu_o, -\tilde{\mathbf{R}})G(i\omega_l + i\nu_o, \tilde{\mathbf{R}} - \mathbf{R}) + (S \longleftrightarrow G)\Big](\mathbf{q})\,, \qquad (40a)\\ \dot{\Pi}_{S,pp}(i\omega_l, i\nu_o, \mathbf{q})]_{n,n'} &= \sum_{\mathbf{R}} e^{-i\mathbf{R}\mathbf{q}} W_{n,n'}(\mathbf{R}) \times \\ &\mathcal{F}\Big[S(i\nu_o, \tilde{\mathbf{R}})G(i\omega_l - i\nu_o, \tilde{\mathbf{R}} + \mathbf{R}) + (S \longleftrightarrow G)\Big](\mathbf{q})\,, \qquad (40b)\end{aligned}$$

where $\mathcal{F}\Big[f(\tilde{R})\Big](\mathbf{k})$ is the Fourier transform which can be determined by using FFT-methods and the weight $W_{n,n'}(R)$ is defined as

$$W_{n,n'}(\mathbf{R}) = \sum_{\mathbf{R}'} f_n^*(\mathbf{R}') f_{n'}(\mathbf{R} + \mathbf{R}')\,. \qquad (41)$$

The infinite sum of the lattice points in Eqs. (40b), (40a), and (41) is restricted by the finite range of the form factors for a specific truncation. For instance the sum in Eq. (41) is limited to the maximal shell taken into account by the form factors. Hence, the weight has a nonzero contribution only inside a shell twice as large the maximal shell of the form factors and therefore the sum in Eq. (40a) can be constrained to twice the distance of the maximal form factor shell.

The momentum and real space grid for the Fourier transformations needed in the bubbles has to be chosen fine enough, especially at low temperatures. The convergence in terms of FFT-grid points $N_{\mathbf{R}_{\mathrm{FFT}}}$ has to be checked separately from the bosonic momentum grid of the vertex. Recent works using the TUfRG [31, 67] have demonstrated that, if needed, both low temperatures and high wavevector resolutions can be achieved by means of an adaptive integration scheme.

3.1.5 Diagrammatic and lattice related symmetries

Further numerical simplifications come from the extensive use of symmetries related to diagrammatic arguments and lattice-specific properties, which can be found in Appendix A.

3.2 The mfRG implementation

The mfRG flow introduced in Ref. [55] ameliorates the approximation induced by the truncation of the fRG hierarchy of flow equations as it incorporates all contributions from the six-point vertex γ_6 that can be computed at the same cost as the 1ℓ flow considered so far. In fact, it includes all contributions coming from γ_6 that can be computed in an iterative 1ℓ construction of four-point objects; hence, the numerical effort grows only linearly in the number of loops retained. It has been shown [55] that the multiloop prescription fully sums up all parquet diagrams. This gives rise to a number of advantageous properties, the most important of which are (i) that the multiloop corrections restore the independence on the choice of regulator, and (ii) that the multiloop flow fully accounts for the interplay between different two-particle channels and thus hampers spurious vertex divergences coming from ladder diagrams in the individual channels.

Let us briefly recall the multiloop vertex flow employing the same line of arguments as used for the flow of the response functions in Section 2.2. We consider the reducible vertices in the physical channels $\boldsymbol{\phi}_{\eta=\{\mathrm{sc,d,m}\}}$. At first, one performs the Katanin substitution [45] $S^\Lambda \to \partial_\Lambda G^\Lambda$ ($\dot{\Pi}_{S,\eta} \to \dot{\Pi}_\eta$) in the 1ℓ flow equation

$$\dot{\boldsymbol{\phi}}_\eta^{\Lambda,(1)} = \boldsymbol{\gamma}_{4,\eta}^\Lambda \circ \dot{\boldsymbol{\Pi}}_\eta^\Lambda \circ \boldsymbol{\gamma}_{4,\eta}^\Lambda\,, \qquad (42)$$

and finds that, for every channel $\boldsymbol{\phi}_\eta^\Lambda$, all differentiated lines come from $\dot{\boldsymbol{\Pi}}_\eta^\Lambda$. Differentiated lines from the other channels are contained in higher-order terms of the loop expansion

$$\partial_\Lambda \boldsymbol{\phi}_\eta^\Lambda = \sum_{\ell\geq 1} \dot{\boldsymbol{\phi}}_\eta^{\Lambda,(\ell)} \,. \tag{43}$$

Using the channel decomposition (21), one has the two-loop correction

$$\dot{\boldsymbol{\phi}}_\eta^{\Lambda,(2)} = \boldsymbol{\gamma}_{4,\eta}^\Lambda \circ \boldsymbol{\Pi}_\eta^\Lambda \circ \dot{\mathbf{I}}_\eta^{\Lambda,(1)} + \dot{\mathbf{I}}_\eta^{\Lambda,(1)} \circ \boldsymbol{\Pi}_\eta^\Lambda \circ \boldsymbol{\gamma}_{4,\eta}^\Lambda \,, \tag{44}$$

where, according to Eq. (22), $\dot{\mathbf{I}}_\eta^{\Lambda,(\ell)}$ can be determined from the $\dot{\boldsymbol{\phi}}_{\eta'}^{\Lambda,(\ell)}$ of the complementary channels $\eta' \neq \eta$. All higher-loop terms are obtained in a similar fashion where one additionally accounts for vertex corrections to both sides of $\dot{\mathbf{I}}_\eta^{\Lambda,(\ell)}$

$$\begin{aligned}\dot{\boldsymbol{\phi}}_\eta^{\Lambda,(\ell+2)} &= \boldsymbol{\gamma}_{4,\eta}^\Lambda \circ \boldsymbol{\Pi}_\eta^\Lambda \circ \dot{\mathbf{I}}_\eta^{\Lambda,(\ell+1)} + \dot{\mathbf{I}}_\eta^{\Lambda,(\ell+1)} \circ \boldsymbol{\Pi}_\eta^\Lambda \circ \boldsymbol{\gamma}_{4,\eta}^\Lambda + \boldsymbol{\gamma}_{4,\eta}^\Lambda \circ \boldsymbol{\Pi}_\eta^\Lambda \circ \dot{\mathbf{I}}_\eta^{\Lambda,(\ell)} \circ \boldsymbol{\Pi}_\eta^\Lambda \circ \boldsymbol{\gamma}_{4,\eta}^\Lambda \\ &= \big(\dot{\boldsymbol{\phi}}_\eta^{\Lambda,(\ell+2)}\big)_{\mathrm{R}} + \big(\dot{\boldsymbol{\phi}}_\eta^{\Lambda,(\ell+2)}\big)_{\mathrm{L}} + \big(\dot{\boldsymbol{\phi}}_\eta^{\Lambda,(\ell+2)}\big)_{\mathrm{C}} \,,\end{aligned} \tag{45}$$

where in the last line the subscripts $\{\mathrm{R},\mathrm{L},\mathrm{C}\}$ refer to the diagrammatic position of $\dot{\mathbf{I}}^\Lambda$, i.e., right, left and central, respectively. Using Eq. (21) one can easily deduce the multiloop flow of the vertices $\boldsymbol{\gamma}_{4,\eta}$

$$\partial_\Lambda \boldsymbol{\gamma}_{4,\eta}^\Lambda = \sum_{\ell\geq 1} \dot{\boldsymbol{\gamma}}_{4,\eta}^{\Lambda,(\ell)} = \sum_{\ell\geq 1} \big(\dot{\boldsymbol{\phi}}_\eta^{\Lambda,(\ell)} + \dot{\mathbf{I}}_\eta^{\Lambda,(\ell)}\big) \,. \tag{46}$$

In Ref. [55], it has further been pointed out that corrections to the self-energy flow (29) are necessary in order to generate all differentiated diagrams of the parquet self-energy. These corrections are included in the central part of the vertex flow $\boldsymbol{\gamma}_{4,\eta} \circ \boldsymbol{\Pi}_\eta \circ \dot{\mathbf{I}}_\eta \circ \boldsymbol{\Pi}_\eta \circ \boldsymbol{\gamma}_{4,\eta}$ and read

$$\partial_\Lambda \Sigma^\Lambda = \dot{\Sigma}^\Lambda + \delta\dot{\Sigma}_1^\Lambda + \delta\dot{\Sigma}_2^\Lambda \,, \tag{47}$$

with $\dot{\Sigma}$ given by Eq. (36a) and

$$\delta\dot{\Sigma}_1^\Lambda(k) = -\int dp\, G^\Lambda(p) \Big[2\big(\dot{\phi}_{\bar{D}}^\Lambda\big)_{\mathrm{C}}(k,p,k) - \big(\dot{\phi}_{\bar{D}}^\Lambda\big)_{\mathrm{C}}(p,k,k) \Big] \tag{48a}$$

$$\delta\dot{\Sigma}_2^\Lambda(k) = -\int dp\, \delta S^\Lambda(p) \Big[2\gamma_4^\Lambda(k,p,k) - \gamma_4^\Lambda(p,k,k) \Big] \,, \tag{48b}$$

where the central part (see Eq. (45)) for the differentiated reducible vertices $\dot{\boldsymbol{\phi}}_{r=\{P,C,D\}} = \{\dot{\mathbf{P}}, \dot{\mathbf{D}}, \dot{\mathbf{C}}\}$ is defined by

$$\begin{aligned}\big(\dot{\phi}_{\bar{D}}^\Lambda\big)_{\mathrm{C}}(k_1,k_2,k_3) = \sum_{\ell\geq 1}\sum_{n,n'} \Big[& f_n(\mathbf{k}_1) f_{n'}^*(\mathbf{k}_4) \big(\dot{\boldsymbol{\phi}}_P^{\Lambda,(\ell)}\big)_{\mathrm{C}}^{n,n'}(\nu_1+\nu_3, \nu_1, \nu_4, \mathbf{k}_1+\mathbf{k}_3) + \\ & f_n(\mathbf{k}_1) f_{n'}^*(\mathbf{k}_3-\mathbf{k}_2+\mathbf{k}_1) \big(\dot{\boldsymbol{\phi}}_C^{\Lambda,(\ell)}\big)_{\mathrm{C}}^{n,n'}(\nu_3-\nu_2, \nu_1, \nu_3-\nu_2+\nu_1, \mathbf{k}_3-\mathbf{k}_2) \Big] \,,\end{aligned} \tag{49}$$

and $\delta S^\Lambda(p) = G^\Lambda(p) \delta\dot{\Sigma}_1^\Lambda(p) G^\Lambda(p)$.

4 Numerical results

In this section we show fRG numerical results obtained with the formalism and code described in the previous sections. After introducing our test system, namely the 2D Hubbard model at half filling, we will test our full momentum-frequency resolved fRG implementation, together

Table 1: Local and first nearest-neighbor form factors both in momentum and real space presentation. For each calculation we specify which form factors are used. A pure s-wave calculation restricts to the first line corresponding to the local form factor, the d-wave accounts for the first two nearest neighbors form factors, and a calculation with all nearest neighbors form factors includes all five form factors shown here.

	n	$f_n(\mathbf{k})$	$f_n(r_i, r_j)$
loc	0	$\frac{1}{2\pi}$	$\delta_{j,i}$
1NN	1	$\frac{1}{\sqrt{2}\pi}\cos(k_x)$	$\frac{1}{\sqrt{2}}(\delta_{j,i+x} + \delta_{j,i-x})$
	2	$\frac{1}{\sqrt{2}\pi}\cos(k_y)$	$\frac{1}{\sqrt{2}}(\delta_{j,i+y} + \delta_{j,i-y})$
	3	$\frac{1}{\sqrt{2}\pi}\sin(k_x)$	$\frac{i}{\sqrt{2}}(\delta_{j,i+x} - \delta_{j,i-x})$
	4	$\frac{1}{\sqrt{2}\pi}\sin(k_y)$	$\frac{i}{\sqrt{2}}(\delta_{j,i+y} - \delta_{j,i-y})$

with the inclusion of the self-energy feedback, and study the effect of including multiloop corrections to the 1ℓ approximated flow equations. If not specified differently, we will make use of a “smooth” frequency-dependent regulator throughout this work:

$$G_0^{\Lambda}(k) = \frac{\nu^2}{\nu^2 + \Lambda^2} G_0(k)\,, \tag{50}$$

where G_0 specifies the non-interacting Green’s function of the 2D Hubbard model. The fRG scheme associated to such a regulator is referred to as Ω-flow [29]. For details on the numerical effort, we refer to the Appendix G.

4.1 2D Hubbard model at half filling as test system

As test model we consider the single-band two-dimensional (2D) Hubbard model on the square lattice. Its Hamiltonian reads

$$\hat{\mathcal{H}} = -t \sum_{\langle ij\rangle,\sigma} \hat{c}^{\dagger}_{i\sigma}\hat{c}_{j\sigma} + U \sum_i \hat{n}_{i\uparrow}\hat{n}_{i\downarrow} - \mu \sum_{i,\sigma} \hat{n}_{i\sigma}\,, \tag{51}$$

where $\hat{c}^{(\dagger)}_{i\sigma}$ annihilates (creates) an electron with spin σ at the lattice site $\mathbf{R}_i$ ($\hat{n}_{i\sigma} = \hat{c}^{\dagger}_{i\sigma}\hat{c}_{i\sigma}$), t is the hopping amplitude for electrons between neighboring sites, μ the chemical potential and $U > 0$ the repulsive on-site Coulomb interaction. In the present study, we consider $U = 2t$, $\mu = U/2$, and different temperature regimes. Since the present model has been extensively studied in the theoretical literature (see, e.g., Refs. [11, 14, 15, 46, 68–71]) as well as in fRG (for a review, see Ref. [1]), it constitutes a reference system to test our novel fRG implementation. Furthermore, the 2D Hubbard model constitutes a delicate case in the context of the Mermin-Wagner theorem [72], which prevents the onset of the antiferromagnetic ordering at finite temperature. Whereas the 1ℓ fRG results exhibit a pseudocritical Néel temperature T_{pc}, the inclusion of the multiloop corrections to the standard fRG flow should, from a theoretical perspective, recover the parquet solution, which is known to fulfill the Mermin-Wagner theorem [73]. Therefore, we expect T_{pc} to be suppressed down to 0 in the (converged) multiloop fRG scheme. Despite the rich phase diagram of the 2D Hubbard model out of particle-hole symmetry, we restrict this study to the half-filled particle-hole symmetric case, in order to reduce the numerical efforts.

Let us stress that the bosonic momentum discretization of the first Brillouin zone (BZ) has been chosen such that one obtains a uniform grid along the x- and y- directions. This represents, though, not the unique choice of resolving the reciprocal space and one could adopt

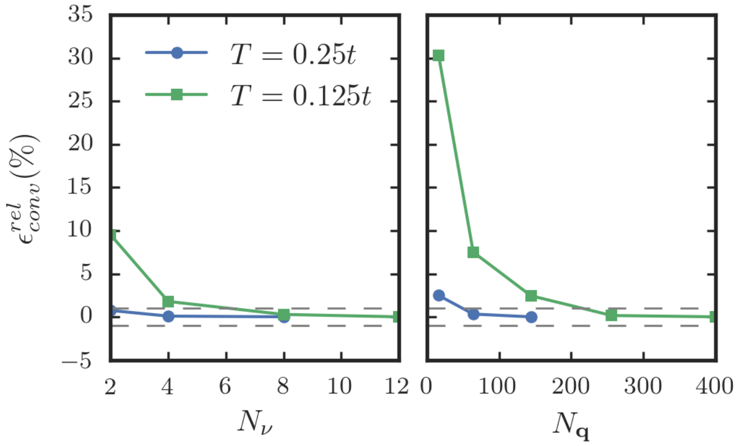

Figure 4: Relative error $\epsilon^{rel}_{conv} = -(\chi - \chi_{conv})/\chi_{conv}$ of the (1ℓ) AF susceptibilities as a function of the number of fermionic frequencies N_ν (left) and the number of bosonic momentum patching points $N_{\mathbf{q}}$ (right), for $U = 2t$ and different values of T. All calculations are performed with only local (s-wave) form factors. In the left panel, $N_{\mathbf{q}}$=144 and $N_{\text{FFT}} = 24 \times 24 = 576$ momentum patching points for the fast Fourier transform. In the right panel, $N_{\mathbf{R}_{\text{FFT}}} = \max(576, 4 \times N_{\mathbf{q}})$ and $N_\nu = 4$ for $T = 0.25$ and $N_\nu = 8$ for $T = 0.125$ respectively. The dashed line corresponds to our tolerance limit of 1%.

some sophisticated "patching" schemes [44], which should be accounted in future optimization of our code.

4.2 Convergence and stability study on the TUfRG-implementation

In the previous section 3.1, we presented an efficient parameterization of the vertex which combines the TUfRG scheme [31] for treating momenta with the dynamical fRG implementation proposed in Ref. [34]. In order to illustrate its efficiency of such merge, we have performed a convergence study of the (dominant) antiferromagnetic (AF) susceptibility $\chi_{\text{AF}} = \chi^{00}_m(i\omega_l = 0, \mathbf{q} = (\pi,\pi))$ by means of Eq. (36f), as a function of the number of Matsubara frequencies, momenta and form factors, used in our algorithm. The convergence tests have been performed at temperatures $T = 0.25t \gg T_{\text{pc}}$ and $T = 0.125t \sim T_{\text{pc}}$.

Let us first consider the convergence in the number of fermionic frequencies N_ν at which the low-frequency structure of the rest-function $\mathcal{R}$ is captured. For $T = 0.25t$ in Fig. 4 (left panel) one observes that the susceptibility does not exhibit significant changes as a function of N_ν. In fact, it is known that, in weakly correlated electron systems, the frequency dependence of the vertex is less important because of power counting arguments [58, 74] and as shown by numerics for small numbers of fermionic Matsubara frequencies, e.g., in Ref. [42]. At $T = 0.125t$ the convergence with respect to N_ν is slower. According to our tolerance of 1% we obtain convergence at $N_\nu = 8$. In the right panel, we analyze the dependence of the AF susceptibility on the number of bosonic patching points, $N_{\mathbf{q}}$, as shown in Fig. 4. The data for $T = 0.25t$ are already converged at $N_{\mathbf{q}} = 64$, while for $T = 0.125t$ we need $N_{\mathbf{q}} = 256$. In the latter case, one sees that the convergence is more sensitive to $N_{\mathbf{q}}$ than to N_ν. This can be ascribed to the presence of a finite pseudocritical temperature since for $T \to T_{\text{pc}}$ the AF fluctuations become long-ranged, requiring an increasingly finer momentum resolution. At the same time, the size of the objects to handle grows only linearly with $N_{\mathbf{q}}$ while it is expected

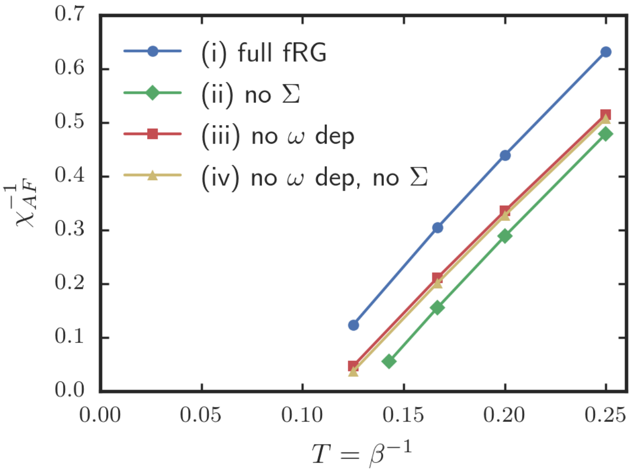

Figure 5: Inverse (1ℓ) AF susceptibility at $\mathbf{q} = (\pi, \pi)$ as a function of temperature, for $U = 2t$. Only local (s-wave) form factors are used, but including the nearest-neighbor form factors does not change the results within the accuracy. Besides the curve obtained using the full TU dynamical fRG scheme (i) (blue dots, "full fRG"), different approximations are shown: approximation (ii) (green diamonds, "no Σ"), (iii) (red squares, "no ω dep") and (iv) (yellow triangles, "no ω dep, no Σ").

to scale with the third power in N_ν, depending on the quantity considered (see Fig. 3). Moreover, the number of independent momentum patching points can be substantially reduced by exploiting point-group symmetries of the lattice.

Last but not least, we have also verified that, for all values of T considered, the AF response function is fully converged with respect to the number of form factors (not shown).

4.3 Effects of different approximations

In our fRG scheme, we can choose different approximation levels regarding the treatment of the frequency dependence of the interactions and the self-energy. This allows us to gain a better understanding of the interplay of the different interaction channels and the role of the self-energy.

Here we define four approximation levels (i) to (iv) with decreasing rigor. Approximation (i) represents the fRG treatment described in Sec. (3) which merges the TUfRG scheme with an efficient inclusion of the vertex dynamics; (ii) denotes the flow with a frequency-dependent effective interaction but without the flow and feedback of the self-energy; (iii) is the frequency-independent (static) approximation for the effective interaction and the self-energy, in which the fermion-fermion, fermion-boson and boson-boson vertices are approximated by their value at zero frequency; and (iv) combines the neglect of the self-energy feedback with a static approximation for the vertices.

Approximation (iv) has been the standard one adopted in many previous works, as those reviewed in Ref. [1]. Various other fRG works have already explored the changes occurring by using better approximations like (i) to (iii) introduced above. Earlier studies of the self-energy without explicit frequency dependence of the effective interaction pointed to the possibility of non-Fermi liquid behavior [39, 75]. Later, channel-decomposed fRG [29, 41] and N-patch fRG [42] were used to explore the effects of a frequency-dependent effective interaction and of the self-energy feedback. In the following, we rediscover some of their findings, with a more refined momentum- and frequency-dependent self-energy. Eberlein [43] used a channel-decomposed description of the interaction where each exchange propagator was allowed to depend on one bosonic frequency. He found that in the presence of antiferromagnetic hot spots on the Fermi surface, antiferromagnetic fluctuations lead to a flattening of the Fermi surface and increase the critical scales. Most recently, Vilardi et al. [44] presented a refined 1ℓ study of the role of the various frequency structures in the interaction, parametrized by three frequencies, albeit with a reduced set of form factors. They argued that a one-frequency parametrization can in some cases lead to spurious instabilities. Our study differs from this work by the ability of taking into account more form factors, using a more economic description of the higher frequencies, and by implementing the multiloop corrections.

In Fig. 5 we show how differently the approximations affect the results for the AF susceptibility. More precisely, we plot the inverse AF susceptibility which decreases quite linearly, i.e., Curie-Weiss-like, upon lowering T. The intersection of the curve with the abscissa marks the pseudocritical temperature which, violating the Mermin-Wagner theorem, assumes a finite value in the 1ℓ fRG scheme. One can observe that the full TU-dynamic fRG approach (i) leads to larger inverse AF susceptibilities, or smaller χ_{AF}, than the other three approximations, shifting T_{pc} to a smaller value.

Let us first compare the full calculation (i) with the calculation without self-energy but frequency-dependent interactions (ii). It is to be expected that the self-energy renormalizes the leading vertices and therefore also susceptibilities, as has also been observed in fRG studies [29,44]. This explains why the calculations without self-energy flow diverge at higher T_{pc} with respect to scheme (i).

The flow variants with static interactions (iii) and (iv) differ only slightly. Compared to the fRG flow using scheme (ii), the AF tendencies in these static flows are somewhat weaker as their suppression by particle-particle processes increases when the pairing channel is approximated by its static part, for which it assumes the maximum value. The downward-shift in the inverse AF susceptibility from (iii) and (iv) to (ii) with the inclusion of the frequency dependence of the couplings is however overcompensated by the inclusion of the dynamical self-energy in (i).

Finally, we consider the pseudocritical temperature and the AF susceptibility for the combined approximation of no self-energy and no frequency dependence (iv). Without the screening effect of the self-energy, the pseudocritical temperature increases a little bit more with respect to the static approximation (iii). This has been already observed in Ref. [42]. The small difference may come from the real part of the self-energy that can be understood as upward-renormalization of the hopping parameter, or equivalently a downward-renormalization of the density of states. This is consistent with the self-energy shown below in Fig. 7. For a detailed discussion on the pseudocritical temperatures on a wider range of parameters, we refer the reader to Ref. [41].

4.4 Computation of the self-energy

As already implied above, the implementation presented in Sec. 3.1 allows one to compute a frequency and momentum dependence of self-energy during the flow according to Eq. (36a). In Figs. 6 and 7, we present the results for the frequency- and momentum-dependence of the self-energy for different temperatures and momentum points. For the fermionic momentum patching we use the same momentum grid as for the bosonic transfer momentum of the vertex. In the results shown in Fig. 7 (left panel), we subtracted the Hartree contribution, which represents a rigid $U/2$ energy shift at half filling. By looking at Fig. 6, we notice that the frequency dependence of the imaginary part of the self-energy is consistent with a Fermi-liquid, yet without any remarkable difference at different temperatures. As the slope of these curves determines the quasiparticle weight Z, we arrive at the conclusion that Z does not decrease

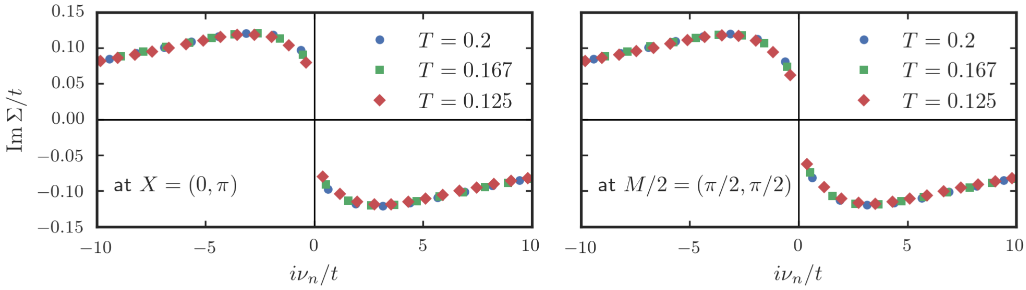

Figure 6: Imaginary part of the self-energy as a function of the Matsubara frequency, at X=$(0,\pi)$ and M/2=$(\pi/2,\pi/2)$, for $U = 2t$ and different temperatures $T = 0.2t$ (blue dots), $T = 0.167t$ (green squares) and $T = 0.125t$ (red diamonds).

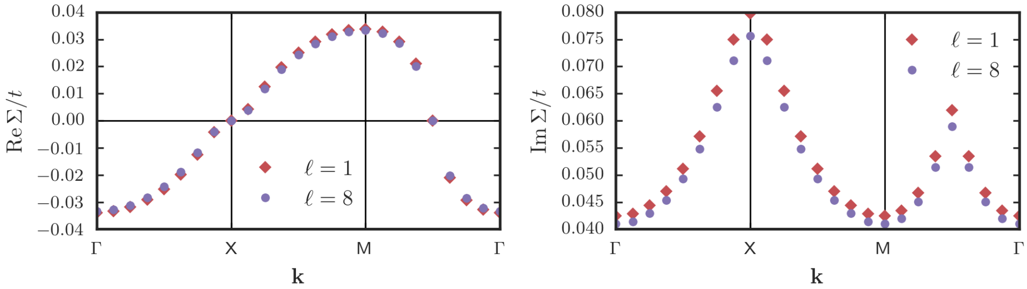

Figure 7: Real (right) and imaginary (left) part of the self-energy $\Sigma(-i\pi T)$ as a function of the bosonic transfer momentum in the 1ℓ and 8ℓ truncation of the flow equations, for $U = 2t$ and $T = 0.125t$.

steeply when we lower T towards the AF pseudocritical temperature, as already observed in Refs. [42, 43]. Figure 7 shows the momentum dependence of the real and imaginary part of the self-energy along a path in the first BZ defined by $\Gamma = (0,0)$, $X = (0,\pi)$ and $M = (\pi,\pi)$. The fermionic frequency is set to the first fermionic Matsubara frequency. The real part is positive at M and negative at Γ, while at X and Y it is zero. At lowest order, this momentum structure can be approximated by a positive nearest-neighbor hopping renormalization, which increases the bandwidth. The vanishing of the Fermi surface shift is caused by the particle-hole symmetry of the model at half filling. As for the 2D Hubbard model at half filling, the particle-hole symmetry manifests itself through

$$\Sigma(i\nu, \mathbf{k})^* = -\Sigma(i\nu, (\pi,\pi) - \mathbf{k}) , \tag{52}$$

the real part of the self-energy vanishes always at the Fermi surface and the perfect nesting remains intact. This symmetry is not violated by any of the perturbative corrections and also not by the numerical implementation (e.g. the choice of k-points in the BZ). Besides this, there is a substantial bandwidth renormalization that however also reflects the symmetries of the system, i.e. it has opposite sign at Γ and at M. The 8ℓ results in Fig. 7 will be discussd in Sec. 4.5.

The imaginary part of the self-energy shows two peaks around X and M/2= $(\pi/2,\pi/2)$. This corresponds to a maximal scattering on the nested Fermi surface and minimal on the points Γ and M, which are at maximal distance from the Fermi surface. Note that this refers to the self-energy at small fixed imaginary frequency and not at real frequency equal to the

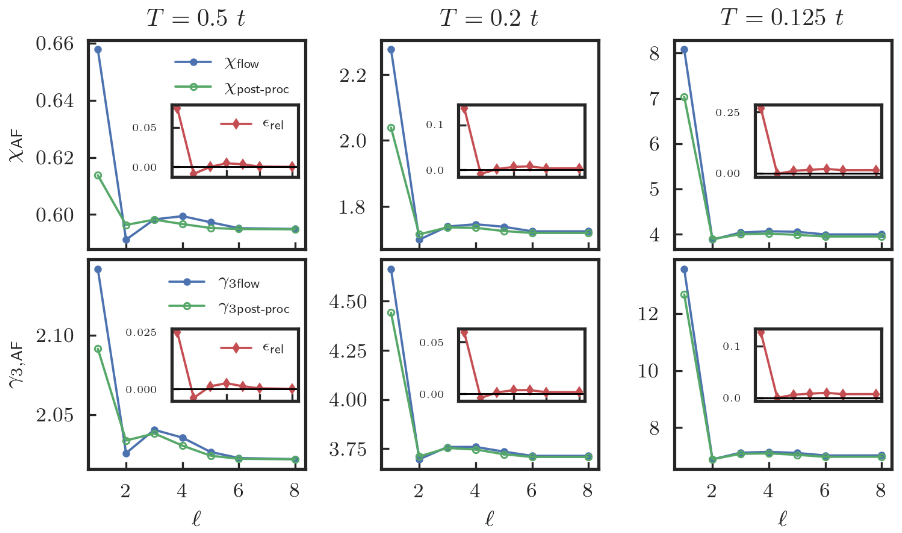

Figure 8: AF susceptibility (upper panels) and fermion-boson vertex (lower panel) at $\mathbf{q} = (\pi, \pi)$ as a function of the number of loops, for $U = 2t$ and $T = 0.5t, 0.2t, 0.125t$ (from left to right). The susceptibility is evaluated at $\omega = 0$ and the fermion-boson vertex at $\omega = 0$ and $\nu = \pi/\beta$. The blue line shows the behavior of the integrated Eq. (23a) up to $\ell = 8$, while the green line the one obtained from the post-processed calculation by means of Eq. (8) for χ and of (10) for γ_3. The insets show the relative difference between the blue and the green lines, defined for the susceptibility as $\epsilon_{\text{rel}} = (\chi^{\ell}_{\text{flow}} - \chi^{\ell}_{\text{post-proc}})/\chi^{\ell=8}_{\text{post-proc}}$.

excitation energy, i.e., this behavior does not contradict the typical behavior that the scattering rates for quasiparticles rise with distance from the Fermi surface.

4.5 Effect of the multiloop implementation

Let us now investigate the effect of including multiloop corrections to the flow equations of the susceptibility and the fermion-boson vertex as in Eq. (23a). As previously discussed, the inclusion of the multiloop corrections should allow us to recover the full derivative of Eq. (8) and (10) with respect to the scale parameter Λ. This means that the integration of the multiloop fRG flow equations should converge, by increasing the number of loops, to Eq. (8) and (10), as well as to the parquet equations for γ_4 and Σ as discussed in Ref. [55].

Although, in the half-filled case, the numerical effort is already reduced compared to the non-particle-hole symmetric situation, calculations for $T < 0.5t$ are already quite demanding if a multiloop cycle is included. Therefore, the only calculations involving more than one form factor (i.e., s-wave) that will be presented here were performed at a rather high temperature of $T = 0.5t$. Despite this restriction, since the physics of the single band Hubbard model at half filling is dominated by the AF fluctuations, the fRG results are already converged in the number of form factors. Nevertheless, a meaningful part of the d-wave susceptibilities is still accessible, as it will be shown in the following, via the s-wave two-particle vertex.

In Fig. 8 we show the s-wave susceptibility χ (fermion-boson vertex γ_3) in the upper (lower) panels in the magnetic channel for $i\omega_l = 0$ ($i\omega_l = 0$ and $i\nu_o = \pi/\beta$ for γ_3) and $\mathbf{q} = (\pi, \pi)$ as a function of the number of loops considered in the mfRG calculation, for three

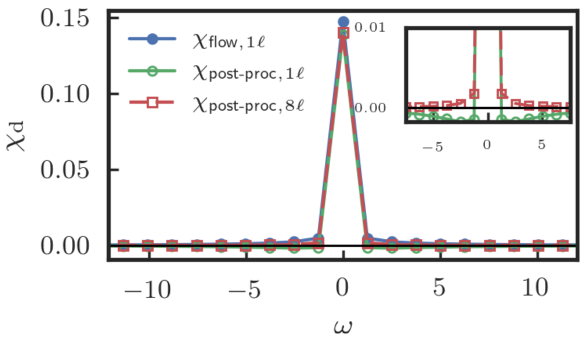

Figure 9: S-wave density susceptibility evaluated at $\mathbf{q} = (0,0)$ as a function of bosonic Matsubara frequencies, for $U = 2t$ and $T = 0.2t$. The blue and green lines represent the flow and post-processed values for 1ℓ, while the red dashed line corresponds to the post-processed mfRG result for 8ℓ. The zoom in the inset shows that the post-processed 1ℓ data assume unphysical negative values at finite frequencies.

selected temperatures $T = \{0.5t, 0.2t, 0.125t\}$ (left to right). The blue lines show the value of χ and γ_3 calculated by the integration of Eq. (23a). On the other hand, the green lines show χ (γ_3) acquired at the end of the ℓ-loop fRG flow ($\Lambda = \Lambda_{\text{fin}}$) by means of Eq. (8) ((10)), where we inserted on the r.h.s $\gamma_4^{\Lambda_{\text{fin}}}$ and $G^{\Lambda_{\text{fin}}}$, referred to in Section 2.2 as “post-processed” method. In the present case, one sees how the convergence of the two lines is achieved after 8ℓ for all temperatures presented. Thus, we have a dual convergence: as a function of the loop number and between two ways of computing the same quantity. Clearly, by decreasing the temperature and approaching the 1ℓ fRG pseudocritical temperature (see Fig. 11), the antiferromagnetic (AF) susceptibility and $\gamma_{3,\text{m}}^{00}(\omega = 0, \nu = \pi/\beta, \mathbf{q} = (\pi,\pi)) = \gamma_{3,\text{AF}}$ increase and the green and blue lines for the two ways to compute the susceptibility exhibit the largest relative difference at $\ell = 1$ of $\sim 25\%$. This difference decreases by increasing the loop number down to less then 1% for $\ell = 8$.

It is interesting to see the main effect of the multiloop corrections occurs already at the 2ℓ level, where the 1ℓ results experience the strongest screening effect. Furthermore, as explicitly argued in Ref. [34] the inclusion of the two-loop corrections to the flow of the interaction allows to substantially enrich the virtual excitation content of the fRG equations. By looking at Fig. 8 one could deduce that, performing a post-processed evaluation of the susceptibility, as well as of the fermion-boson vertex, brings them closer to the converged values than the corresponding results coming from the fRG flow (blue curves). However, it has to be stressed that the convergence trend observed in the magnetic channel for the post-processed χ and γ_3 does not apply in general. Counterexamples can be observed, for instance, in the s-wave secondary channels (i.e., charge and superconducting), where the post-processed evaluation of the 1ℓ susceptibility not only leads to an overscreening (i.e., an underestimation with respect to the converged result), but, e.g., in the charge channel, to even unphysical results, as can be observed in Fig. 9. Here, the s-wave susceptibility in the density channel is plotted at $\mathbf{q} = (0,0)$ as a function of the bosonic Matsubara frequencies. One observes negative values of the post-processed susceptibility (green line) at finite bosonic frequencies, which are restored to positive values by the multiloop corrections (red line). An attempt to explain this different trend between the dominant (magnetic) and the secondary channels (density and superconducting) is extensively discussed in Appendix D and summarized in the following observations.

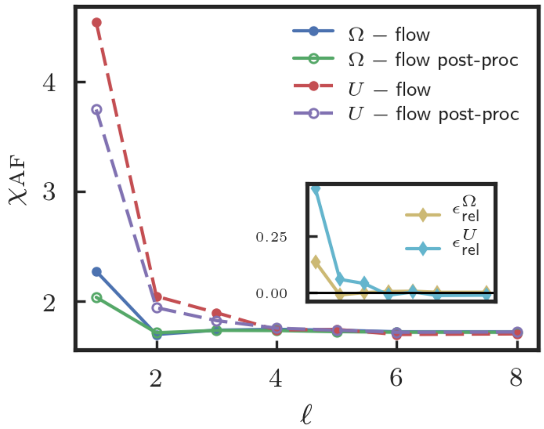

Figure 10: Comparison of two cutoff schemes, the U-flow and the Ω-flow, for the AF susceptibility as a function of the number of loops, for $U = 2t$ and $T = 0.2t$. *Inset*: Relative difference with respect to the converged value $(\chi^{\ell}_{\text{AF}} - \chi^{\text{post-proc},\ell}_{\text{AF}})/\chi^{8\ell}_{\text{AF}}$.

As explicitly derived in Appendix D, the Λ-derivative of the formal definition for the susceptibility reported in Eq. (8) (as well as Eq. (10) for γ_3), after substituting the derivative of γ_4 and Σ by their 1ℓ fRG flow equations, leads to additional terms with respect to the standard 1ℓ flow equations for χ in Eq. (19a) (for γ_3 in Eq. (19b)). These terms, besides self-energy derivative corrections (which are generally introduced starting from the second loop-order under the name of *Katanin* corrections [53]), have a 3ℓ-like topological diagrammatic form (see Eq. (26)). The internal loops of $\dot{\mathbf{I}}^{\Lambda,(1)}_{\eta}$ (marked in red in Fig. 16) contained in such terms act as a screening effect provided by the complementary channels (η') to the one considered ($\eta \neq \eta'$). Because of the imbalance between the 1ℓ approximation for the two-particle vertex γ_4 and Σ, and the 3ℓ diagrams included in the modified "post-processed flow equation" for the susceptibility (see Appendix D), this screening effect ends up being overestimated. Nonetheless, it represents a minor effect on the dominant (magnetic) channel, where the imbalance effect is still governed by the large 1ℓ antiferromagnetic contribution. It could however lead to major changes in the secondary channels, which are affected by the strong screening effect of the magnetic channel appearing on the 3ℓ-like terms. The overscreening affects all frequencies, because of the internally summed diagrams. Therefore, it is particularly severe at nonzero frequencies where the susceptibility assumes small values. This explains the unphysical negative values of the density susceptibility in Fig. 9.

By applying different fRG cutoff schemes, we obtain further tests of the reconstruction of the full derivative of Eq. (8) provided by the multiloop approach. In Fig. 10 we compare the results shown already in Fig. 8 (central upper panel) for $T = 0.2t$ using a frequency-dependent regulator (Ω-flow) with the results for χ at the same temperature obtained by a trivial or flat regulator, also known as interaction or U-cutoff [76]. Differently from the Ω-flow, the U-flow just multiplies the bare propagator with a scale factor that is increased from 0 to 1. Hence, it does not provide any cutoff in energy during the fRG flow so that all energy scales are treated on an equal footing. The insertion of the multiloop corrections into the fRG flow equations, as already observed in a different system in Ref. [56], makes the mfRG calculation almost independent, at high enough loop-order, from the specific regulator considered. A more detailed analysis of our results revealed a persisting small discrepancy even for higher loops. Since it vanishes in absence of self-energy corrections, we attribute it to the truncation of the form factor basis in the vertex flow which prevents the reconstruction of the full derivative of the self-energy.

The substantial reduction of the pseudocritical temperature (T_{pc}) provided by the multiloop corrections can be easily inferred from the data in Fig. 11. Here, the inverse 1ℓ fRG antiferromagnetic susceptibility (blue line) is plotted as a function of temperature and compared to the one computed with 8ℓ mfRG calculation (green line): at any temperature considered the higher-loop corrections systematically suppress the value of the susceptibility, thus lowering the pseudocritical scale.

We note that the formal equivalence between the mfRG and the parquet approximation should guarantee the fulfillment of the Mermin-Wagner theorem [72] as this is fulfilled by the parquet approximation [64]. Hence, a frequency-momentum *and* loop converged mfRG calculation should yield a complete suppression of the pseudocritical temperature down to zero. It is, however, very hard to prove this result by means of direct calculations in the low-T regime, due to the quasi-long-range nature of the spatial fluctuations, responsible for the Mermin-Wagner theorem. In fact, the "avoided" onset of a true long-range antiferromagnetism at finite temperature T is associated with the appearance of antiferromagnetic fluctuations with an exponential growing correlation length (see, e.g, discussion in Ref. [73]). Their occurrence has been indeed explicitly verified in several many-body calculations [9, 10, 73, 77–80] compatible with the Mermin-Wagner theorem. While these low-temperature exponentially extended correlations make the overall physics of our system very similar to that of a true AF ordered phase [81], being associated with a rapid crossover towards a low-temperature insulating behavior, they also make it numerically impossible to access the $T \to 0$ limit, because of the finiteness of any momentum grid discretization. In fact, in the temperature range where we could achieve a satisfactory momentum-convergence of our 8ℓ results the antiferromagnetic susceptibility does not show yet any evidence of the exponential behavior expected in the low-temperature regime. On the contrary for almost all the data, one still observes a linear mean-field like behavior for the inverse susceptibility (though significantly renormalized w.r.t. the 1ℓ results). As a consequence, a reliable low-T extrapolation for estimating T_{pc} from our converged 8ℓ results is not possible: If trying to extrapolate the data of Fig. 11, one would rather obtain an estimation for the instability scale of an effectively renormalized mean-field description, valid in the high-T regime.

Our findings and considerations are consistent with the most recent estimates of the temperature range, below which the exponential behavior of χ_{AF} should become visible: According to the most recent DΓA and Dual Fermion studies [9, 10, 15, 80, 82] such a "crossover" temperature would be *lower* than the ordering temperature of DMFT. The latter, for $U = 2$ is $T_N^{DMFT} \sim 0.05$ ($\beta = 20$), i.e., already twice smaller than the lowest temperature considered in the present work. We also observe that this DMFT critical scale would be roughly in agreement with the linear extrapolation of our 8ℓ data for the inverse susceptibility discussed above.

Next, we analyze the effect of the fRG multiloop corrections on some d-wave physical susceptibilities which, although suppressed in the particle-hole symmetric case, play an important role in describing the phase diagram of the 2D Hubbard model, most notably away from half filling [28, 36, 58, 83, 84]. In particular we analyze the static ($\omega = 0$) d-wave susceptibility in the superconducting channel for $\mathbf{q} = (0, 0)$ (dSC), as well as the static d-wave susceptibility in the charge channel for a bosonic momentum transfer $\mathbf{q} = (0, 0)$ (dPom), which would become dominant in the case of the so-called "Pomeranchuk" instability. The staggered d-wave charge density wave (dCDW) susceptibility for $\mathbf{q} = (\pi, \pi)$ has not been shown because of its degeneracy with the correspondent d-wave superconducting one. In fact, one can formally demonstrate that in a SU(2) and particle-hole symmetric case, where the system becomes invariant under pseudospin rotation, the pairing susceptibility at $\mathbf{q} = (0, 0)$ associated to a specific symmetry of the order parameter is degenerate with the staggered ($\mathbf{q} = (\pi, \pi)$) CDW associated to that specific symmetry. In Fig. 12 we display the result of a fRG calculation where, in addition to the s-wave form factor, the form factors indicated as 1 and 2 in Table 1 have been used. As

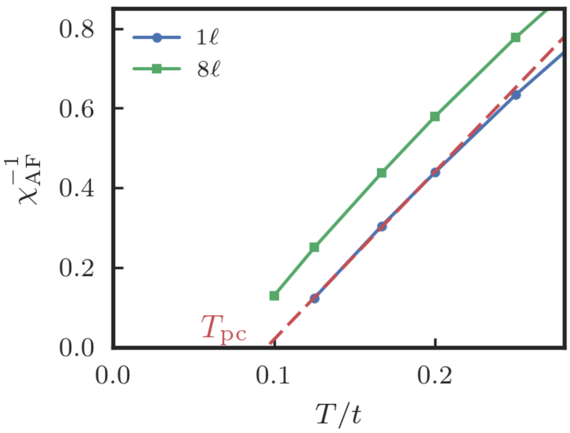

Figure 11: Inverse AF susceptibility as a function of temperature, for $U = 2t$.

in Fig. 8, the blue line indicates the fRG result obtained by the integration of Eq. (23a) up to a specific ℓ-loop order, alongside the corresponding (ℓ-loop) mfRG equations for Σ and γ_4. The green line represents the post-processed result for the d-wave susceptibilities calculated from a s+d-wave ℓ-loop order mfRG results for the self-energy (Σ) and the two-particle vertex (γ_4). The red line has been obtained, similarly to the green one, from s-wave ℓ-order mfRG results for Σ and γ_4. One notices that, differently to the antiferromagnetic case, the relative difference between blue and green lines with respect to the convergence value is, at the 1ℓ-level, of the order of few percents and lowers even down to less then $1‰$ at 8ℓ. Interestingly, the post-processed susceptibilities obtained from the s-wave fRG results (red curve) are almost on top of the correspondent ones where both s- and d-wave form factors have been considered during the fRG flow. This shows clearly that, as already known from previous studies on the single-band 2D Hubbard model, the d-wave tendencies in pairing and charge channels are triggered by the antiferromagnetic fluctuations of onsite (s-wave) spin bilinears. However, according to our data for the Fermi surface and the temperature considered, the flow of d-wave pairing and charge channels, which are not captured if only s-wave interactions flow, does not seem to be particularly relevant. This means that in the full system where all channels (s-wave, d-wave, etc.) are allowed to flow, the d-wave attractions triggered by the s-wave AF fluctuations would not fall on a too fertile ground at $T = 0.5t$, i.e., they would not flow strongly in their ‘native’ d-wave channels. Going to lower T and in particular out of half filling, this will likely change, as the particle-particle diagrams will enhance any attractive pairing component. Therefore, it is a priori not clear if the d-wave susceptibilities computed at lower T by projecting the vertex made up from s-wave bilinears could provide satisfactory physical results. Nevertheless, we argue that they serve as useful theoretical test objects for the convergence in the order of the multiloop corrections. This is because the effective d-wave interactions captured this way can be understood as two-particle irreducible (2PI) interactions in the d-wave pairing or charge channels, generated purely by s-wave one-loop processes. These 2PI d-wave quantities are non-singular but zero at lowest order in U in typical cases. Hence they can be expected to be dominated by diagrams of finite order in U that should exhibit stronger multiloop effects. In contrast with these terms, the missing boosts in the respective native channels, e.g., in the pairing channel, would just be a higher-order ladder summation of, for $T \to 0$, increasingly singular one-loop diagrams. Hence, if multiloop convergence is reached in the two-particle irreducible interactions, it is likely that the same degree of convergence would be found in the true susceptibilities. This idea leads us to consider the data shown in Fig. 13.

As already visible for $T = 0.5t$ in Fig. 12, the post-processing calculations exhibit a weak

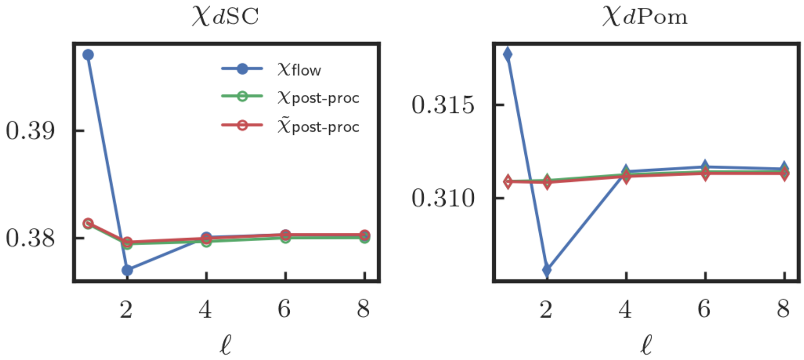

Figure 12: d-wave susceptibililties dSC, dPomeranchuk ($\mathbf{q} = (0,0)$) at $i\omega_m = 0$ as a function of the number of loops, for $U = 2t$ and $T = 0.5t$. The red line has been evaluated by means of Eq. (8), by inserting the two-particle vertex computed from a single (s-wave) form factor.

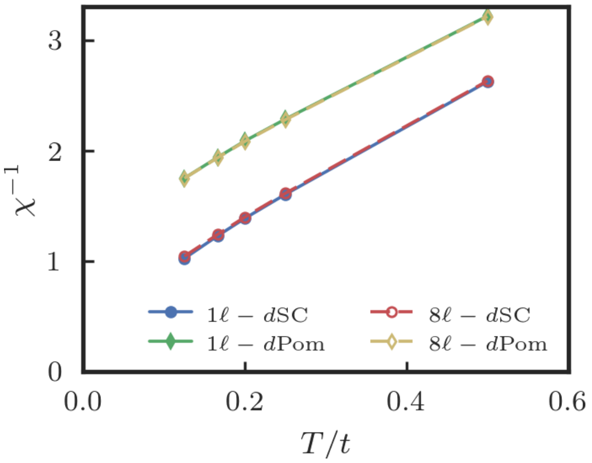

Figure 13: Inverse d-wave susceptibilities, computed by post-processing, as a function of temperature, for $U = 2t$ (fRG flow with only s-wave bilinear interactions).

dependence on the loop number (with a relative fluctuation less than 1‰). This is confirmed in Fig. 13 where the post-processed inverse d-wave susceptibilities in the aforementioned channels are calculated out of an s-wave 1ℓ (blue and green lines) and 8ℓ (red and yellow dashed lines) fRG flow. As it is apparent in the figure, the effects of the multiloop corrections are insignificant compared to the variation of the inverse susceptibilities in temperature.

To conclude this section, we comment on the multiloop effects on the self-energy shown in Fig. 7. The bandwidth renormalization is changed insignificantly and the scattering on the Fermi surface is reduced only slightly. Also the Fermi-surface shift remains zero in mfRG because the particle-hole symmetry is preserved in fRG, in PA and in the full solution and therefore also the multiloop corrections do not violate the particle-hole symmetry.

5 Conclusions

We have presented a comprehensive study of forefront algorithmic implementations of the fRG for interacting fermions on 2D lattices. While we focused on the 2D Hubbard model, the methodological improvements discussed here can provide a useful guidance for the generalization to other systems.

Our main goal is to illustrate the progress achieved when going beyond the approximations routinely made in most previous fRG computations. In particular, we have worked on the following aspects: (i) an accurate and converged treatment of both the momentum and frequency dependence of the vertex function together with its asymptotic structures; (ii) the inclusion of the self-energy and its feedback in the fRG flow; (iii) the implementation of the multiloop corrections beyond the standard 1ℓ.

Regarding the first aspect (i), we have kept the more general dependence of the two-particle vertex on all *three* Matsubara frequencies. We extend previous works [41, 44, 84–87] by exploiting an "economic" description [34] provided by an efficient parametrization of the high frequency asymptotics [32]. We could show that this parametrization can be brought to convergence in the number of frequencies employed, i.e., the results do not change if more frequencies are used. We combined this treatment of the frequency dependence with the truncated-unity technique for the momentum dependence, whose form-factor expansion was also shown to converge quickly for our test case [31].

With a frequency-dependent flowing interaction, we could also compute a momentum- and frequency-dependent self-energy, which has been fed back into the flow of the two-particle vertex. Through a systematic analysis of specific observables – in particular of the response functions – we could assess the effects of the improved algorithmic implementation with respect to previous results and demonstrate how, for the parameters studied, the fRG results can be converged in the number of considered frequencies. An analogous convergence could be also established for the 2D momentum dependence.

The major advancement achieved in this work is, however, the implementation of the multiloop corrections both for the flow of the two-particle vertex as well as for the flow of the coupling to external fields and the corresponding susceptibilities. The multiloop extension, so far only tested for a (prototypical) toy model [56], adds more virtual excitations to the flow of the two-particle vertex compared to the previously used 1ℓ truncation. As it was diagrammatically shown [55, 56], if truncated fRG results are converged with respect to the loop order, they exactly reproduce the parquet approximation (PA), not only concerning the topology of the summed diagrams, but also – quantitatively – their precise weight. This has been also recently confirmed by a formal analytical derivation of the multiloop fRG equations [57]. From this property, it follows that the results of a loop-converged fRG algorithm become completely independent from the employed cutoff scheme, at least if all modes are integrated out at sufficiently high temperature.

Previously, it was not clear how the contributions missing in the 1ℓ truncation would influence the results quantitatively. On the numerical level, the effort for including the multiloop corrections to order ℓ only rises linearly in ℓ, i.e. the situation is far better than if one really had to compute all higher-loop diagrams. Our studies show that the multiloop corrections can be included also in 2D up to rather high orders of $\ell = 8$. We find that the observables converge quite nicely when the multiloop order is increased. While it is not obvious that this quick convergence will hold for all model parameters and for all models of interest, our study shows that these checks can be performed with feasible numerical efforts. This adds a new important degree of quantitative control to the fRG, at least in the weak to intermediate coupling regime where the PA can be considered accurate. At stronger coupling, where low-frequency vertex corrections beyond the PA might appear [32, 50, 88–90], the mfRG could provide a much better [15] setup for the proposed combination with the DMFT [23,27,91]. The loop convergence of our fRG results is also reflected in the progressive reduction of the dependence of our fRG results on the chosen cutoff scheme, which appears completely suppressed at the 8ℓ level.

The incorporation of the multiloop contributions has also another rather appealing and quantitatively important aspect, giving rise to an additional very useful type of convergence. It has been known that response functions can be computed in two different ways in RG approaches and that the results differ due to the involved approximations. One way is to consider the flow of couplings of 'composite operator' bilinears in the primary degrees of freedom to external fields of appropriate type. Then the response function is obtained as renormalization of the propagator of the external field.

The other way, referred to as post-processing, is to compute the response functions by means of their diagrammatic expression, evaluated from the dressed bare fermion bubbles and the two-particle vertex at the end of the flow. In fact, in some cases arguments were made (see, e.g., Ref. [92] and references therein) that the external field methods should give more controlled results, i.e., that composite operators should be renormalized separately, because, at the level of the approximations made, the post-processed quantities, which involve the integration over all energies and momenta, are more affected by approximation errors. In our study, the multiloop extension of the response function flow allows us to show that *also* the flow of the response functions becomes an exact scale derivative of the post-processed response function. This establishes the formal equivalence of the two ways to compute response functions on the multiloop level. This formal equivalence is remarkably reflected by our numerical results, which exhibit a clear convergence of the two approaches: If the multiloop convergence is achieved, and frequency and momentum dependencies as well as the self-energy feedback are included appropriately, the fRG results for the response functions are unambiguous. The corresponding data can be used for quantitative studies and directly compared with other numerical techniques or with experiments, if the effective modelling of the problem is sufficiently realistic.

In summary, our study shows how the fRG algorithms for two-dimensional fermionic lattice models can be brought to a quantitatively reliable level at weak to moderate couplings, as long as the parquet approximation is appropriate. This goal has been reached by means of an economic, but accurate, treatment of the momentum and frequency dependencies which takes into account the asymptotic structure of the two-particle vertex and the self-energy during the fRG flow. This fRG framework has been supplemented with the implementation of the multiloop corrections to the 1ℓ truncation scheme.

The current work concentrates on testing the improved fRG method in a situation that is reasonably well understood. The fRG method itself is however not limited to this situation and can be applied to situation where the landscape of instabilities and emergent energy scales is less explored. For instance, within the framework of the 2D Hubbard model, we could apply our algorithmic implementation to broader parameter regimes in future works. If the Fermi surface displays a given curvature, due to the inclusion of, e.g., more hopping terms or changes of the band filling, the dominance of the AF channel will be weakened and the pseudo-critical scales will become smaller. For such cases the convergences of the different approximation might possibly vary. In particular, since the generation of d-wave pairing tendencies in third order of the bare coupling involves 2ℓ diagrams that are only partially captured in the 1ℓ truncation, we would expect the impact of the multiloop corrections to become more noticeable.

Acknowledgements

The authors thank A. Eberlein, J. Ehrlich, P. Hansmann, J. Lichtenstein, W. Metzner, T. Reckling, D. Sánchez de la Peña, G. Schober, C. Taranto, J. von Delft, D. Vilardi, and N. Wentzell for valuable discussions, D. Rohe (FZ Jülich) for major help on the parallelization of the code, and W. Metzner for a careful reading of the manuscript.

Author information A. Tagliavini and C. Hille contributed equally to this work.

Funding information We acknowledge financial support from the Deutsche Forschungsgemeinschaft (DFG) through ZUK 63, RTG 1995, HO 2422/11-1, and Projects No. AN 815/5-1 and No. AN 815/6-1, and the Austrian Science Fund (FWF) within the Project F41 (SFB ViCoM) and I2794-N35. Calculations were performed on the Vienna Scientific Cluster (VSC), at Jülich Supercomputing Centre (JSC) in the frame of project jjsc28, and at the MPI for Solid State Research in Stuttgart.

A Symmetries and symmetrized notation

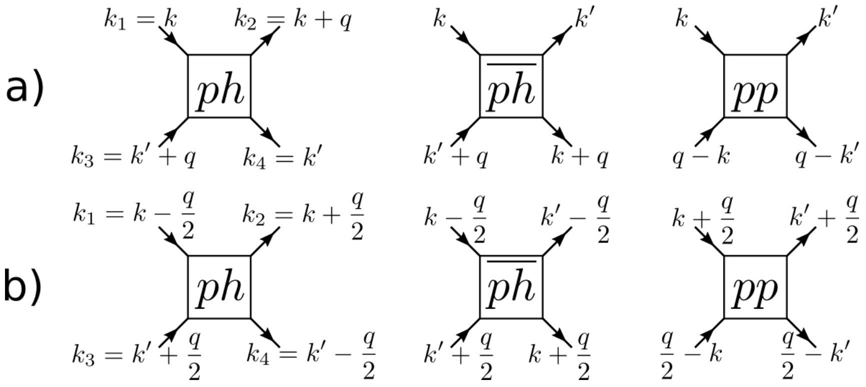

Figure 14: (a) Non-symmetrized and (b) symmetrized notation for the vertices, reducible vertices and irreducible vertices in the diagrammatic channel notation. The non-symmetrized notation is used primarily here, while the symmetrized notation is used only in App. A.

Here we illustrate how diagrammatic and lattice related symmetries can be expressed in an easy way and how they are implemented in our code. Directly related to the symmetries is the question if one uses the symmetrized or the non-symmetrized notation illustrated in Fig. 14 for the momentum and frequency dependence of the channels. In Section 3.1 we argued that the non-symmetrized notation leads to more readable flow equations, bubbles and projection matrices. Therefore we adopted primarily this notation. The symmetries, however, are much easier to express in the symmetrized notation. While in the non-symmetrized notation, simple relations like the crossing relation involve multiple form factor combinations, in the symmetrized notation we find a one-to-one correspondence. Therefore we here use for both momentum and frequency the symmetrized notation (s), which is related to the non-symmetrized (ns) by

$$\phi^{s}_{ph}(q,k,k') = \phi^{ns}_{ph}\left(q, k - \frac{q}{2}, k' - \frac{q}{2}\right) \tag{53a}$$

$$\phi^{s}_{\overline{ph}}(q,k,k') = \phi^{ns}_{\overline{ph}}\left(q, k - \frac{q}{2}, k' - \frac{q}{2}\right) \tag{53b}$$

$$\phi^{s}_{pp}(q,k,k') = \phi^{ns}_{pp}\left(q, k + \frac{q}{2}, k' + \frac{q}{2}\right) . \tag{53c}$$

A.1 Lattice related symmetries

First we specify how lattice related symmetries are reflected in the form factor expansion of the channels in the symmetrized notation. The lattice symmetries always depend on the system and we here focus on the 2D Hubbard model on a square lattice, where we have for example the rotation of $\pi/2$ around the z-axis and the mirroring at the y-axis as independent symmetry operations. Under any of these operations, or combinations of them, applied simultaneously to all momentum dependencies, the expressions of the channels are invariant. This can be translated into the form factor expansion by

$$\begin{aligned}\hat{P}[F]_{n,n'}(\mathbf{q}) &= \int d\mathbf{k}d\mathbf{k}' f_n^*(\mathbf{k}) f_{n'}(\mathbf{k}') F(\mathbf{q},\mathbf{k},\mathbf{k}') \\ &= \int d\mathbf{k}d\mathbf{k}' f_n^*(\mathbf{k}) f_{n'}(\mathbf{k}') F(\hat{R}(\mathbf{q}),\hat{R}(\mathbf{k}),\hat{R}(\mathbf{k}')) \\ &= \int d\mathbf{k}d\mathbf{k}' f_n^*(\hat{R}^{-1}(\mathbf{k})) f_{n'}(\hat{R}^{-1}(\mathbf{k}')) F(\hat{R}(\mathbf{q}),\mathbf{k},\mathbf{k}')\,, \end{aligned} \tag{54}$$

where F is any of the channels D, C or P. The frequency dependence is not affected and is therefore omitted. We here exploited the symmetry under consideration and introduced a variable change. If the form factors are chosen in such a way that under this symmetry operation any form factor is related to a linear combination of others, described by the matrix $\mathbf{M}_{\hat{R}^{-1}}(\mathbf{k})$, it holds in addition

$$\hat{P}[F]_{n,n'}(\mathbf{q}) = \int d\mathbf{k}d\mathbf{k}' \sum_m f_m^*(\mathbf{k}) M_{\hat{R}^{-1}}(\mathbf{k})_{mn} \sum_{m'} M_{\hat{R}^{-1}}(\mathbf{k}')_{n'm'} f_{m'}(\mathbf{k}') F(\hat{R}(\mathbf{q}),\mathbf{k},\mathbf{k}')\,. \tag{55}$$

If moreover, the symmetry operation on every form factor yields a single other form factor expressed by the vector $\mathbf{V}_{\hat{R}^{-1}}$, the above relation simplifies to

$$\hat{P}[F]_{n,n'}(\mathbf{q}) = \hat{P}[F]_{V_{\hat{R}^{-1}}(n) V_{\hat{R}^{-1}}(n')}(\mathbf{q}) S_{V_{\hat{R}}(n)} S_{V_{\hat{R}}(n')}\,, \tag{56}$$

where the only difference is a possible sign change taken into account by $S_{V_{\hat{R}}(n)}$. These assumptions hold for the form factors used in the present implementation (see Table 1), but are not necessarily valid for an arbitrary choice of form factors.

A.2 Diagrammatic symmetries

In addition to the lattice related symmetries, there are diagrammatic symmetries which are independent of the geometry of the system. Considering a two-particle fermionic vertex, we can apply the crossing symmetry simultaneously to the annihilation and the creation operators, recovering the following relations:

$$F_{\sigma_1,\sigma_2,\sigma_3}(i\nu_{o_1}, i\nu_{o_2}, i\nu_{o_3}, k_1, k_2, k_3) = F_{\sigma_3,\sigma_4,\sigma_1}(i\nu_{o_3}, i\nu_{o_4}, i\nu_{o_1}, k_3, k_4, k_1)\,, \tag{57}$$

time reversal

$$F_{\sigma_1,\sigma_2,\sigma_3}(i\nu_{o_1}, i\nu_{o_2}, i\nu_{o_3}, k_1, k_2, k_3) = F_{\sigma_2,\sigma_1,\sigma_4}(i\nu_{o_2}, i\nu_{o_1}, i\nu_{o_4}, k_2, k_1, k_4)\,, \tag{58}$$

and complex conjugation

$$F^*_{\sigma_1,\sigma_2,\sigma_3}(i\nu_{o_1}, i\nu_{o_2}, i\nu_{o_3}, k_1, k_2, k_3) = F_{\sigma_2,\sigma_1,\sigma_4}(-i\nu_{o_2}, -i\nu_{o_1}, -i\nu_{o_4}, k_2, k_1, k_4)\,, \tag{59}$$

for which we refer to Ref. [93]. In the SU(2) symmetric case, by projecting the vertex ϕ to the form factor basis and adopting the symmetrized notation, one has that Eq. (57) gives

$$P_{n,n'}(i\omega_m, i\nu_o, i\nu_{o'}, \mathbf{q}) = \Pi_n \Pi_{n'} P_{n,n'}(i\omega_m, -i\nu_o, -i\nu_{o'}, \mathbf{q}) \tag{60a}$$

$$D_{n,n'}(i\omega_m, i\nu_o, i\nu_{o'}, \mathbf{q}) = D_{n,n'}(-i\omega_m, i\nu_{o'}, i\nu_o, -\mathbf{q}) \tag{60b}$$

$$C_{n,n'}(i\omega_m, i\nu_o, i\nu_{o'}, \mathbf{q}) = C_{n,n'}(-i\omega_m, i\nu_{o'}, i\nu_o, -\mathbf{q})\,, \tag{60c}$$

where Π_m is the parity associated to the momentum inversion of the form factor m defined as

$$f_n(-\mathbf{k}) = \Pi_n f_n(\mathbf{k})\,. \tag{61}$$

The time reversal symmetry reads

$$P_{n,n'}(i\omega_m, i\nu_o, i\nu_{o'}, \mathbf{q}) = P_{n',n}(i\omega_m, i\nu_{o'}, i\nu_o, \mathbf{q}) \tag{62a}$$
$$D_{n,n'}(i\omega_m, i\nu_o, i\nu_{o'}, \mathbf{q}) = D_{n,n'}(-i\omega_m, i\nu_o, i\nu_{o'}, -\mathbf{q}) \tag{62b}$$
$$C_{n,n'}(i\omega_m, i\nu_o, i\nu_{o'}, \mathbf{q}) = C_{n',n}(i\omega_m, i\nu_{o'}, i\nu_o, \mathbf{q})\,, \tag{62c}$$

and the complex conjugation

$$P^*_{n,n'}(i\omega_m, i\nu_o, i\nu_{o'}, \mathbf{q}) = P_{n',n}(-i\omega_m, -i\nu_{o'}, -i\nu_o, \mathbf{q}) \tag{63a}$$
$$D^*_{n,n'}(i\omega_m, i\nu_o, i\nu_{o'}, \mathbf{q}) = D_{n,n'}(i\omega_m, -i\nu_o, -i\nu_{o'}, -\mathbf{q}) \tag{63b}$$
$$C^*_{n,n'}(i\omega_m, i\nu_o, i\nu_{o'}, \mathbf{q}) = C_{n',n}(-i\omega_m, -i\nu_{o'}, -i\nu_o, \mathbf{q})\,. \tag{63c}$$

A.3 Connection between $\mathcal{K}_2$ and $\bar{\mathcal{K}}_2$

In Section 3.1.2 we argued that $\bar{\mathcal{K}}_2$ can be obtained from $\mathcal{K}_2$ by symmetry. For the pp and $\overline{ph}$ channel the time reversal symmetry exchanges the two fermionic dependencies while keeping the transfer frequency and momentum fixed. The same holds for the ph-channel by using the combination of the crossing and the time reversal symmetry. Taking the limit of large frequencies for the first and second fermionic frequency respectively, we obtain trivially

$$\mathcal{K}_{2,P,n}(i\omega_m, i\nu_o, \mathbf{q}) = \bar{\mathcal{K}}_{2,P,n}(i\omega_n, i\nu_o, \mathbf{q}) \tag{64a}$$
$$\mathcal{K}_{2,D,n}(i\omega_m, i\nu_o, \mathbf{q}) = \bar{\mathcal{K}}_{2,D,n}(i\omega_n, i\nu_o, \mathbf{q}) \tag{64b}$$
$$\mathcal{K}_{2,C,n}(i\omega_m, i\nu_o, \mathbf{q}) = \bar{\mathcal{K}}_{2,C,n}(i\omega_n, i\nu_o, \mathbf{q})\,. \tag{64c}$$

B Formal derivation of the fRG flow equations for χ and γ_3

In this section we provide an explicit derivation of the flow equations for the response functions. As anticipated in Sec. 2.2, we start by coupling the fermionic bilinears to an external source field J, by adding the following scalar product

$$(J^n_\eta, \rho^n_\eta) = \int dk J^n_\eta(k)\rho^n_\eta(k)\,, \tag{65}$$

where n indicates the momentum structure of the fermionic bilinears coupled to the field J^n_η. Since the density is in general not charge conserving, it is convenient to use the Nambu formalism that allows for a more concise derivation of the flow equations of the physical response functions. We rewrite Eqs. (1) and (2) in the Nambu basis [94, 95]

$$\rho^n_\eta(q) = \sum_{s,s'=\pm} \alpha^\eta_{s,s'} \int dp\, \bar{\phi}_s(p-q) f_n(\mathbf{p}) \phi_{s'}(p)\,, \tag{66}$$

where $s = \pm$ represents the Nambu index and

$$\phi_+(k) = \psi_\uparrow(k) \qquad \bar{\phi}_+(k) = \bar{\psi}_\uparrow(k)$$
$$\phi_-(k) = \bar{\psi}_\downarrow(-k) \qquad \bar{\phi}_-(k) = \psi_\downarrow(-k)\,.$$

The matrices $\boldsymbol{\alpha}^\eta$ (with $\eta = \{\mathrm{d},\mathrm{m},\mathrm{sc}\}$), which define the Nambu index structure in the different physical channels, are given by

$$\boldsymbol{\alpha}^{\mathrm{d}} = \begin{pmatrix} 1 & 0 \\ 0 & -1 \end{pmatrix} \quad \boldsymbol{\alpha}^{\mathrm{m}} = \begin{pmatrix} 1 & 0 \\ 0 & 1 \end{pmatrix} \quad \boldsymbol{\alpha}^{\mathrm{sc}} = \begin{pmatrix} 0 & 1 \\ -1 & 0 \end{pmatrix} . \tag{67}$$

In order to derive the flow equations for the fermion-boson vertex of Eq. (15) and the susceptibility of Eq. (14) we start from the so-called Wetterich equation [96]

$$\partial_\Lambda \Gamma^\Lambda[J_\eta,\phi] = -(\bar{\phi},\dot{Q}_0^\Lambda\phi) - \frac{1}{2}\mathrm{tr}\{\dot{\mathbf{Q}}_0^\Lambda(\boldsymbol{\Gamma}^{(2)\Lambda}[J_\eta,\phi])^{-1}\} , \tag{68}$$

where Γ^Λ represents the scale-dependent effective action, which is a function of the functional variable J_η and the Nambu field ϕ, Q_0^Λ is the inverse non-interacting Green's function and the dot denotes the derivative with respect to the flow parameter Λ. Further, the matrix $\mathbf{Q}_0^\Lambda = \mathrm{diag}(Q_0^\Lambda, -Q_0^{\Lambda,t})$ and

$$\boldsymbol{\Gamma}^{(2)\Lambda}[J_\eta,\phi] = \begin{pmatrix} \bar{\partial}\partial\Gamma^\Lambda[J_\eta,\phi] & \bar{\partial}\bar{\partial}\Gamma^\Lambda[J_\eta,\phi] \\ \partial\partial\Gamma^\Lambda[J_\eta,\phi] & \partial\bar{\partial}\Gamma^\Lambda[J_\eta,\phi] \end{pmatrix} \tag{69}$$

were we used, where ∂ and $\bar{\partial}$ applied to the effective action Γ^Λ are a shorthand notation for the functional derivative with respect to ϕ and $\bar{\phi}$, respectively. Following the derivation of Ref. [2], we introduce the matrix

$$\mathbf{U}^\Lambda[J_\eta,\phi] = (\mathbf{G}^\Lambda)^{-1} - \boldsymbol{\Gamma}^{(2)\Lambda}[J_\eta,\phi] . \tag{70}$$

Thus, we can recast $(\boldsymbol{\Gamma}^{(2)\Lambda}[J_\eta,\phi])^{-1} = (\mathbf{1} - \mathbf{G}^\Lambda\mathbf{U}^\Lambda)^{-1}\,\mathbf{G}^\Lambda$ and expand the inverse matrix in a geometric series

$$(\boldsymbol{\Gamma}^{(2)\Lambda}[J_\eta,\phi])^{-1} = \sum_{n=0}^{\infty}(\mathbf{G}^\Lambda\mathbf{U}^\Lambda)^n\,\mathbf{G}^\Lambda . \tag{71}$$

We can now insert Eq. (71) in Eq. (68). Expanding up to second order yields

$$\partial_\Lambda \Gamma^\Lambda[J_\eta,\phi] = -(\bar{\phi},\dot{Q}_0^\Lambda\phi) - \frac{1}{2}\mathrm{tr}\{\dot{\mathbf{Q}}_0^\Lambda\mathbf{G}^\Lambda\} - \frac{1}{2}\mathrm{tr}\{\mathbf{S}^\Lambda\mathbf{U}^\Lambda\} - \frac{1}{2}\mathrm{tr}\{\mathbf{S}^\Lambda\mathbf{U}^\Lambda\mathbf{G}^\Lambda\mathbf{U}^\Lambda\} + \ldots , \tag{72}$$

where $\mathbf{S}^\Lambda = \mathbf{G}^\Lambda\mathbf{Q}_0^\Lambda\mathbf{G}^\Lambda = \mathrm{diag}(S^\Lambda, -S^{\Lambda,t})$ represents the matrix diagonal form of the single scale propagator, and we exploited the cyclic property of the trace. After applying the trace to the matrices in the curly brackets, we can expand the effective action in powers of the fermionic Nambu fields and the external bosonic source field

$$\Gamma^\Lambda[J_\eta,\phi] = \sum_{m_1,n_1=0}^{\infty}\frac{(-1)^{m_1}}{n_1!\,(m_1!)^2}\times \sum_{\substack{x_1\ldots x_{m_1}\\ x'_1\ldots x'_{m_1}\\ y_1\ldots y_{n_1}}} \frac{\partial^{(2m_1+n_1)}\Gamma^\Lambda[J_\eta,\phi]}{\partial J_\eta(y_1)\ldots\partial J_\eta(y_{n_1})\partial\bar{\phi}(x'_1)\ldots\partial\bar{\phi}(x'_{m_1})\partial\phi(x_{m_1})\ldots\phi(x_1)}\Big|_{\phi=J_\eta=0}\times J_\eta(y_1)\ldots J_\eta(y_{n_1})\bar{\phi}(x'_1)\ldots\bar{\phi}(x'_{m_1})\phi(x_{m_1})\ldots\phi(x_1) \tag{73a}$$

$$= \sum_{m_1,n_1=0}^{\infty}\frac{(-1)^{m_1}}{n_1!\,(m_1!)^2}\sum_{\substack{x_1\ldots x_{m_1}\\ x'_1\ldots x'_{m_1}\\ y_1\ldots y_{n_1}}}\gamma^\Lambda_{2m_1+n_1,y_1..y_{n_1},x'_1..x'_{m_1},x_1..x_{m_1}}\times J_\eta(y_1)\ldots J_\eta(y_{n_1})\bar{\phi}(x'_1)\ldots\bar{\phi}(x'_{m_1})\phi(x_{m_1})\ldots\phi(x_1) . \tag{73b}$$

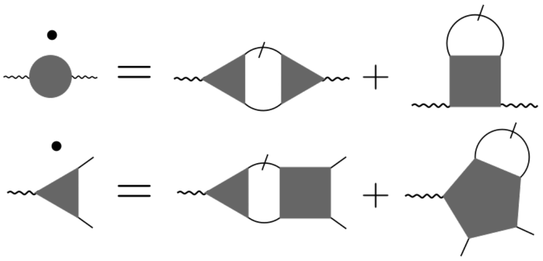

Figure 15: Simplified diagrammatic representation of the flow equations for the susceptibily (first line) and the fermion-boson vertex (second line) illustrating the topological structure of the diagrams. The circle, triangle and the square represent the susceptibility χ, the fermion-boson vertex γ_3, and the two-particle vertex γ_4, respectively.

Note that the index $x = \{s, k\}$ combines the Nambu index s and the fermionic quadrivector $k = (\nu, \mathbf{k})$ (here we disregard additional quantum numbers, as e.g., orbital), while $y = \{n, q\}$ combines the momentum structure of the coupling to the bilinears, n, with the bosonic quadrivector $q = (\omega, \mathbf{q})$. Inserting this expansion in Eq. (72), we compare the expansion coefficient related to the same order on the fields on both sides of the equation.

For $n_1 = 0$ we recover the standard fermionic hierarchy of flow equations [1,2]. For $n_1 > 0$ we can derive the flow equations for the fermion-boson vertex ($n_1 = 1$, $m_1 = 1$) as well as for the boson-boson vertices or susceptibilities ($n_1 = 2$, $m_1 = 0$). In Nambu notation, the flow equation for the susceptibility reads

$$\begin{aligned}\partial_\Lambda \chi^\Lambda(y, y') = &\sum_{\substack{x_1, x_1' \\ x_2, x_2'}} \gamma_3^\Lambda(y, x_1', x_1)[G^\Lambda(x_1, x_2')S^\Lambda(x_2, x_1') + (S \leftrightarrow G)]\gamma_3^{\Lambda\dagger}(y', x_2, x_2') + \\ &\sum_{x_1, x_1'} S^\Lambda(x_1, x_1')\tilde{\gamma}_4^\Lambda(y, y', x_1', x_1)\,, \end{aligned} \tag{74}$$

and the one for the fermion-boson vertex is

$$\begin{aligned}\partial_\Lambda \gamma_3^\Lambda(y, x', x) = &\sum_{x_1, x_1'} S^\Lambda(x_1, x_1')\gamma_5^\Lambda(y, x', x_1', x_1, x) + \\ &\sum_{\substack{x_1, x_1' \\ x_2, x_2'}} \gamma_3^\Lambda(y, x_1', x_1)[G^\Lambda(x_1, x_2')S^\Lambda(x_2, x_1') + (S \leftrightarrow G)]\gamma_4^\Lambda(x', x_2, x_2', x)\,. \end{aligned} \tag{75}$$

In the second term on the r.h.s. of Eq. (74), $\gamma^\Lambda_{2m_1+n_1} = \tilde{\gamma}^\Lambda_{2+2}$ represents the functional derivative of the effective action with respect to two bosonic and two fermionic Nambu fields. The two Eqs. (74) and (75) are schematically shown in Fig. 15. If one neglects the second term in both r.h.s., they correspond to the 1ℓ fRG equations for the response functions. Both γ_3 and χ do not feed back into the flow equations for γ_4 and Σ.

C Connection between the vertex asymptotics and the response functions

In this appendix we demonstrate that the integration of the fRG flow equations for the so-called kernel functions $\mathcal{K}_1$ and $\mathcal{K}_2$ mentioned in Section 3, coincide with the s-wave susceptibility and fermion-boson vertex resulting from the flow.

Let us write explicitly the flow equation for the asymptotics $\mathcal{K}^{\Lambda}_{1,\eta}$ and $\bar{\mathcal{K}}^{\Lambda}_{2,\eta}$, with $\eta = \{\text{sc,d,m}\}$, obtained from Eq. (43) in the limit of infinite fermionic Matsubara frequencies ν and ν'

$$\begin{aligned}\lim_{\substack{\nu\to\infty\\ \nu'\to\infty}} \dot{\boldsymbol{\phi}}^{\Lambda}_{\eta} = \dot{\mathcal{K}}^{\Lambda}_{1,\eta} = (\boldsymbol{\gamma}^{0}_{4,\eta} + \mathcal{K}^{\Lambda}_{1,\eta} + \bar{\mathcal{K}}^{\Lambda}_{2,\eta}) \circ \dot{\boldsymbol{\Pi}}^{\Lambda}_{\eta} \circ (\boldsymbol{\gamma}^{0}_{4,\eta} + \mathcal{K}^{\Lambda}_{1,\eta} + \mathcal{K}^{\Lambda}_{2,\eta}) + \\ (\boldsymbol{\gamma}^{0}_{4,\eta} + \mathcal{K}^{\Lambda}_{1,\eta} + \bar{\mathcal{K}}^{\Lambda}_{2,\eta}) \circ\ \boldsymbol{\Pi}^{\Lambda}_{\eta} \circ \dot{\mathbf{I}}^{\Lambda}_{\eta} \circ \boldsymbol{\Pi}^{\Lambda}_{\eta} \circ (\boldsymbol{\gamma}^{0}_{4,\eta} + \mathcal{K}^{\Lambda}_{1,\eta} + \mathcal{K}^{\Lambda}_{2,\eta})\end{aligned} \tag{76}$$

and

$$\begin{aligned}\lim_{\nu\to\infty} \dot{\boldsymbol{\phi}}^{\Lambda}_{\eta} = \dot{\mathcal{K}}^{\Lambda}_{1,\eta} + \dot{\bar{\mathcal{K}}}^{\Lambda}_{2,\eta} = (\boldsymbol{\gamma}^{0}_{4,\eta} + \mathcal{K}^{\Lambda}_{1,\eta} + \bar{\mathcal{K}}^{\Lambda}_{2,\eta}) \circ \dot{\boldsymbol{\Pi}}^{\Lambda}_{\eta} \boldsymbol{\gamma}^{\Lambda}_{4,\eta} + \\ (\boldsymbol{\gamma}^{0}_{4,\eta} + \mathcal{K}^{\Lambda}_{1,\eta} + \bar{\mathcal{K}}^{\Lambda}_{2,\eta}) \circ \boldsymbol{\Pi}^{\Lambda}_{\eta} \circ \dot{\mathbf{I}}^{\Lambda}_{\eta} + \\ (\boldsymbol{\gamma}^{0}_{4,\eta} + \mathcal{K}^{\Lambda}_{1,\eta} + \bar{\mathcal{K}}^{\Lambda}_{2,\eta}) \circ \boldsymbol{\Pi}^{\Lambda}_{\eta} \circ \dot{\mathbf{I}}^{\Lambda}_{\eta} \circ \boldsymbol{\Pi}^{\Lambda}_{\eta} \circ \boldsymbol{\gamma}^{\Lambda}_{4,\eta}\,,\end{aligned} \tag{77}$$

where $\dot{\boldsymbol{\phi}}^{\Lambda}_{\eta}$ is given by

$$\dot{\boldsymbol{\phi}}^{\Lambda}_{\text{sc}} = \dot{\boldsymbol{P}}^{\Lambda} \tag{78a}$$

$$\dot{\boldsymbol{\phi}}^{\Lambda}_{\text{d}} = 2\dot{\boldsymbol{D}}^{\Lambda} - \dot{\boldsymbol{C}}^{\Lambda} \tag{78b}$$

$$\dot{\boldsymbol{\phi}}^{\Lambda}_{\text{m}} = -\dot{\boldsymbol{C}}^{\Lambda}\,, \tag{78c}$$

the bare vertex $\boldsymbol{\gamma}^{0}_{4,\eta} = \mp U$ corresponds to the Hubbard interaction (with the minus sign for $\eta = \text{sc, d}$ and the plus sign for $\eta = \text{m}$), and the asymptotic vertex function $\bar{\mathcal{K}}^{\Lambda}_{2,\eta}$ is related to $\mathcal{K}^{\Lambda}_{2,\eta}$ by symmetry (see Appendix A). For local bare interactions, the only non-zero elements of the matrices $\dot{\mathcal{K}}^{\Lambda}_{1,\eta}$ and $\boldsymbol{\gamma}^{0}_{4,\eta}$ correspond to both form factors being equal to zero, and of $\mathcal{K}^{\Lambda}_{2,\eta}$ ($\bar{\mathcal{K}}^{\Lambda}_{2,\eta}$) to a vanishing second (first) form factor.

The connection between the vertex asymptotics and the response function is shown by induction using the assumption

$$\boldsymbol{\gamma}^{0}_{4,\eta} + \mathcal{K}^{\Lambda}_{1,\eta} + \bar{\mathcal{K}}^{\Lambda}_{2,\eta} = \alpha \boldsymbol{\gamma}^{\Lambda}_{3,\eta}(\omega, \nu, \mathbf{q})\,. \tag{79}$$

For the initial condition, it holds $\boldsymbol{\gamma}^{\Lambda_{\text{init}}}_{3,\eta} = \boldsymbol{\gamma}^{0}_{3,\eta} = \mathbb{1}$. Since $\mathcal{K}^{\Lambda_{\text{init}}}_{1}$ and $\mathcal{K}^{\Lambda_{\text{init}}}_{2}$ both vanish, one has $\alpha = \boldsymbol{\gamma}^{0}_{4,\eta} = \mp U \delta_{n,0}\delta_{n',0}$. Considering $(\boldsymbol{\gamma}^{0}_{4,\eta} + \mathcal{K}^{\Lambda}_{1,\eta} + \bar{\mathcal{K}}^{\Lambda}_{2,\eta})$ for an arbitrary value of Λ, we can identify the flow equation of the asymptotics with the one of γ_3, see Eq. (23a). Therefore Eq. (79) applies also for the following Λ step. As a consequence we can extract the fermion-boson vertex from the vertex asymptotics. Finally, inserting Eq. (79) into (76), we obtain the flow equation for the susceptibility (23a).

The s-wave fRG results for the susceptibility and the fermion-boson vertex can be extracted from the asymptotic vertex functions $\mathcal{K}^{\Lambda}_{1,\eta}$ and $\bar{\mathcal{K}}^{\Lambda}_{2,\eta}$ by dividing the s-wave form factor component by the bare interaction $\mp U$. Since $\boldsymbol{\gamma}^{0}_{4,\eta}$ vanishes for all other form factor combinations, other than s-wave response functions cannot be recovered by the asymptotics. This observation simplifies the fRG implementation, where the flow equations for χ and γ_3 can be omitted if only their s-wave components are needed.

D "Post-processed" flow equations for γ_3 and χ

In this section we explicitly provide the scale derivative of Eqs. (8) and (10) for the case in which the Σ and γ_4 entering the r.h.s. are obtained from the integration of the corresponding

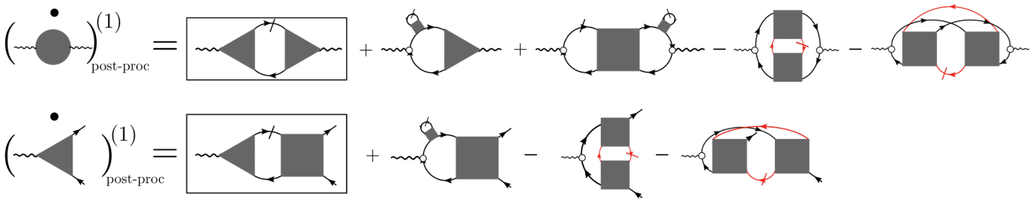

Figure 16: Diagrammatic representation of Eqs. (81) (first line) and (83) (second line), where the boxes indicate the conventional 1ℓ approximation. The internal loops in red provide the particle-hole and particle-particle contributions respectively. The empty dot represents the bare AF fermion-boson vertex $(\gamma^0_{3,\mathrm{m}})_{n,m} = \delta_{n,m}$.

1ℓ flow equations. We first consider Eq. (10) and, after introducing a Λ-dependence of the Green's functions and of γ_4 on the r.h.s., perform the full derivative with respect to Λ. For simplicity we here consider the magnetic vertex as example, which is directly related to the particle-hole crossed vertex by

$$\gamma_{4,\mathrm{m}}(q,k,k') = \gamma_{4,ph,\uparrow\uparrow}(q,k,k') - \gamma_{4,ph,\uparrow\downarrow}(q,k,k') = \gamma_{4,ph,\overline{\uparrow\downarrow}}(k'-k,k,k+q) = -\gamma_{4,\overline{ph},\uparrow\downarrow}(q,k,k')\,, \tag{80}$$

where we used the SU(2) and crossing symmetries [32]. The derivative of the fermion-boson vertex with respect to Λ, as obtained from Eq. (10), reads

$$\begin{aligned}
\partial_\Lambda\Big(\boldsymbol{\gamma}^\Lambda_{3,\mathrm{m}}\Big)^{(1)}_{\text{post-proc}} =&\partial_\Lambda\Big(\boldsymbol{\gamma}^0_{3,\mathrm{m}} + \boldsymbol{\gamma}^0_{3,\mathrm{m}} \circ \mathbf{\Pi}^\Lambda_{\mathrm{m}} \circ \boldsymbol{\gamma}^\Lambda_{4,\mathrm{m}}\Big)\\
=&\boldsymbol{\gamma}^0_{3,\mathrm{m}} \circ \Big(\dot{\mathbf{\Pi}}^{\Lambda,(1)}_{S,\mathrm{m}} + \dot{\tilde{\mathbf{\Pi}}}^{\Lambda,(1)}_{\mathrm{m}}\Big) \circ \boldsymbol{\gamma}^\Lambda_{4,\mathrm{m}} + \boldsymbol{\gamma}^0_{3,\mathrm{m}} \circ \mathbf{\Pi}^\Lambda_{\mathrm{m}} \circ \dot{\boldsymbol{\gamma}}^{\Lambda,(1)}_{4,\mathrm{m}}\\
=&\boldsymbol{\gamma}^0_{3,\mathrm{m}} \circ \Big(\dot{\mathbf{\Pi}}^{\Lambda,(1)}_{S,\mathrm{m}} + \dot{\tilde{\mathbf{\Pi}}}^{\Lambda,(1)}_{\mathrm{m}}\Big) \circ \boldsymbol{\gamma}^\Lambda_{4,\mathrm{m}} -\\
&\boldsymbol{\gamma}^0_{3,\mathrm{m}} \circ \mathbf{\Pi}^\Lambda_{\mathrm{m}} \circ \Big(\dot{\boldsymbol{C}}^{\Lambda,(1)} - \hat{\boldsymbol{C}}[\dot{\phi}^{\Lambda,(1)}_{ph}] - \hat{\boldsymbol{C}}[\dot{\phi}^{\Lambda,(1)}_{pp}]\Big)\\
=&\boldsymbol{\gamma}^\Lambda_{3,\mathrm{m}} \circ \dot{\mathbf{\Pi}}^{\Lambda,(1)}_{S,\mathrm{m}} \circ \boldsymbol{\gamma}^\Lambda_{4,\mathrm{m}} + \boldsymbol{\gamma}^0_{3,\mathrm{m}} \circ \dot{\tilde{\mathbf{\Pi}}}^{\Lambda,(1)}_{\mathrm{m}} \circ \boldsymbol{\gamma}^\Lambda_{4,\mathrm{m}} - \boldsymbol{\gamma}^0_{3,\mathrm{m}} \circ \mathbf{\Pi}^\Lambda_{\mathrm{m}} \circ \hat{\boldsymbol{C}}[\dot{\phi}^{\Lambda,(1)}_{ph}] -\\
&\boldsymbol{\gamma}^0_{3,\mathrm{m}} \circ \mathbf{\Pi}^\Lambda_{\mathrm{m}} \circ \hat{\boldsymbol{C}}[\dot{\phi}^{\Lambda,(1)}_{pp}]\,,
\end{aligned} \tag{81}$$

where for sake of conciseness we used a tensor-product form. In contrary to the definition in Sec. 3.2, the bubble $\mathbf{\Pi}^\Lambda_{S,\mathrm{m}}$ does not have the Katanin substitution [45] and we define $\dot{\tilde{\mathbf{\Pi}}}_{\mathrm{m}} = \dot{\mathbf{\Pi}}_{S\to G\dot{\Sigma}G,\mathrm{m}}$ in order to take care of the scale derivative in the self-energy. Further $\boldsymbol{\gamma}^0_{3,\mathrm{m}} = \mathbb{1}$, and $\hat{\boldsymbol{C}}[\dot{\phi}_\eta]$ stands for

$$\hat{C}[\dot{\phi}^\Lambda_{ph}]_{n,n'} = \int d\mathbf{k}d\mathbf{k}' f^*_n(\mathbf{k})\, f_{n'}(\mathbf{k}')\dot{\phi}^\Lambda_{ph}(k'-k,k,k+q) \tag{82a}$$

$$\hat{C}[\dot{\phi}^\Lambda_{pp}]_{n,n'} = \int d\mathbf{k}d\mathbf{k}' f^*_n(\mathbf{k})\, f_{n'}(\mathbf{k}')\dot{\phi}^\Lambda_{pp}(q+k+k',k,k+q)\,. \tag{82b}$$

The superscript (1) indicates that flowing objects (Σ and the ϕ's) are computed within 1ℓ from their corresponding differential equations. From the second to the third line of Eq. (81) we used Eq. (80) and the parquet decomposition in Eq. (32). The diagrammatic representation of the last line of Eq. (81) is shown in the first line of Fig. 16.

Let us now turn to Eq. (8) for the susceptibility, where we again restrict ourselves to the magnetic channel. Following the derivation of Eq. (81) one obtains

$$\begin{aligned}\partial_\Lambda\Big(\boldsymbol{\chi}^{\Lambda}_{\mathrm{m}}\Big)^{(1)}_{\text{post-proc}} &= \partial_\Lambda\Big(\boldsymbol{\gamma}^{0}_{3,\mathrm{m}}\circ\boldsymbol{\Pi}^{\Lambda}_{\mathrm{m}}\circ\boldsymbol{\gamma}^{\dagger,0}_{3,\mathrm{m}}+\boldsymbol{\gamma}^{0}_{3,\mathrm{m}}\circ\boldsymbol{\Pi}^{\Lambda}_{\mathrm{m}}\circ\boldsymbol{\gamma}^{\Lambda}_{4,\mathrm{m}}\circ\boldsymbol{\Pi}^{\Lambda}_{\mathrm{m}}\circ\boldsymbol{\gamma}^{\dagger,0}_{3,\mathrm{m}}\Big)\\ &= \boldsymbol{\gamma}^{\Lambda}_{3,\mathrm{m}}\circ\dot{\boldsymbol{\Pi}}^{\Lambda,(1)}_{S,\mathrm{m}}\circ\boldsymbol{\gamma}^{\Lambda,\dagger}_{3,\mathrm{m}}+\\ &\quad\boldsymbol{\gamma}^{0}_{3,\mathrm{m}}\circ\dot{\tilde{\boldsymbol{\Pi}}}^{\Lambda,(1)}_{\mathrm{m}}\circ\boldsymbol{\gamma}^{\Lambda,\dagger}_{3,\mathrm{m}}+\boldsymbol{\gamma}^{0}_{3,\mathrm{m}}\circ\boldsymbol{\Pi}^{\Lambda}_{\mathrm{m}}\circ\boldsymbol{\gamma}^{\Lambda}_{4,\mathrm{m}}\circ\dot{\tilde{\boldsymbol{\Pi}}}^{\Lambda,(1)}_{\mathrm{m}}\circ\boldsymbol{\gamma}^{\dagger,0}_{3,\mathrm{m}}-\\ &\quad\boldsymbol{\gamma}^{0}_{3,\mathrm{m}}\circ\boldsymbol{\Pi}^{\Lambda}_{\mathrm{m}}\circ\hat{\boldsymbol{C}}[\dot{\phi}^{\Lambda,(1)}_{ph}]\circ\boldsymbol{\Pi}^{\Lambda}_{\mathrm{m}}\circ\boldsymbol{\gamma}^{\dagger,0}_{3,\mathrm{m}}-\\ &\quad\boldsymbol{\gamma}^{0}_{3,\mathrm{m}}\circ\boldsymbol{\Pi}^{\Lambda}_{\mathrm{m}}\circ\hat{\boldsymbol{C}}[\dot{\phi}^{\Lambda,(1)}_{pp}]\circ\boldsymbol{\Pi}^{\Lambda}_{\mathrm{m}}\circ\boldsymbol{\gamma}^{\dagger,0}_{3,\mathrm{m}}\,,\end{aligned}\tag{83}$$

with the diagrammatic representation is provided in Fig. 16 (second line). One observes the appearance of additional terms on the r.h.s. of the post-processing flow equations for γ_3 and χ with respect to their standard 1ℓ equations, indicated by the boxes in Fig. 16. Besides the terms containing the Λ derivative of the self-energy (which are included in the Katanin corrections [45]), let us draw the attention to the last two diagrams appearing on the r.h.s. for both $\partial_\Lambda(\gamma_3^\Lambda)_{\text{post-proc}}$ and $\partial_\Lambda(\chi^\Lambda)_{\text{post-proc}}$. The diagrammatic structure in terms of loops is of second order for γ_3 and of third for χ. The integration of these post-processed flow equations, along with the 1ℓ flow equations for Σ and γ_4, would generate the last two diagrams already at the first integration step $\Lambda_{\text{init}}+d\Lambda$ (with $d\Lambda<0$ in the Ω-flow), providing the following contribution to $\dot{\boldsymbol{\chi}}^{\Lambda_{\text{init}}}_{\mathrm{m}}$

$$-\boldsymbol{\gamma}^{0}_{3,\mathrm{m}}\circ\Big(\boldsymbol{\Pi}^{\Lambda_{\text{init}}}_{\mathrm{m}}\circ\hat{\boldsymbol{C}}[\dot{\phi}^{\Lambda_{\text{init}}}_{ph}]\circ\boldsymbol{\Pi}^{\Lambda_{\text{init}}}_{\mathrm{m}}+\boldsymbol{\Pi}^{\Lambda_{\text{init}}}_{\mathrm{m}}\circ\hat{\boldsymbol{C}}[\dot{\phi}^{\Lambda_{\text{init}}}_{pp}]\circ\boldsymbol{\Pi}^{\Lambda_{\text{init}}}_{\mathrm{m}}\Big)\circ\boldsymbol{\gamma}^{\dagger,0}_{3,\mathrm{m}}\,.\tag{84}$$

The first term vanishes due to the Pauli principle ($\dot{\phi}^{\Lambda_{\text{init}}}_{ph}=0$, see Ref. [34]), and the last one provides a negative contribution which reduces the 1ℓ term. In fact, the unscreened particle-particle bubble entering $\hat{C}[\dot{\phi}^{\Lambda_{\text{init}}}_{pp}]_{n,m}$ has the same sign of the unscreened (magnetic) $S-G$ bubble. This overall suppression by the additional 3ℓ-like terms is a general feature of the post-processed fRG scheme. The unbalance between the 1ℓ γ_4 flow, which topologically cuts part of the parquet diagrams, and the additional 3ℓ-like diagrams of the susceptibility flow, leads to an artificial overscreening of the conventional 1ℓ calculation. Analogous conclusions can be drawn for the density and superconducting channels. Thus one expects a pronounced effect in the secondary channels because the dominant channel enters the internal loop of one of the two 3ℓ-like additional diagrams, resulting in a reduction with respect to the converged data. In contrast, the dominant channel will not be affected that strongly, presenting only a slight overestimation of the post-processed susceptibility at the 1ℓ level (see Fig. 8). Moreover, since this overscreening affects all frequencies, it may be responsible for the unphysical negative value of the density susceptibility observed at finite frequencies in Fig. 9. In particular, since the parquet diagrams disregarded in the 1ℓ approximation depend on the cutoff, the detected unphysical results in the secondary channels were observed to be more severe for the interaction flow. We finally note that this opposite effect of the density and the superconducting channels with respect to the dominant magnetic channel has been observed also in Ref. [97] by analyzing the effect of the parquet decomposition of the vertex on the self-energy.

E Two-loop approximation for γ_3's flow equation

We here provide the derivation of the 2ℓ corrections to the conventional 1ℓ truncated flow equations. The derivation follows the scheme adopted for the flow equation of the two-particle vertex as reported in Ref. [17]. Our goal is to include the feedback of γ_5^Λ onto the flow equation for γ_3^Λ, see Eq. (75), at the second order in the effective interaction. From the derivation

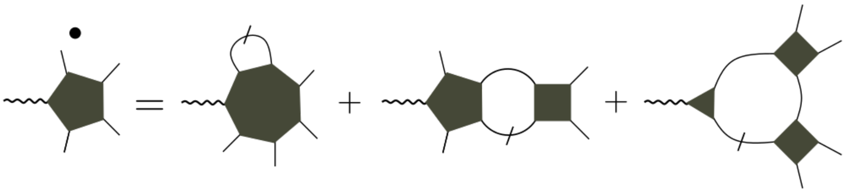

Figure 17: Simplified diagrammatic representation of the flow equation for γ_5^Λ illustrating the topological structure of the diagrams.

provided in Appendix B, one sees that the differential equation for γ_5^Λ is given by the sum of all diagrams which have the topological structure depicted in Fig. 17. The first and the second diagrams on the r.h.s. are at least of third order in the effective interaction since γ_7^Λ (depicted by a heptagon) and γ_5 (depicted by a pentagon) are at least $O((\gamma_4^\Lambda)^3)$ and $O((\gamma_4^\Lambda)^2)$, respectively. Therefore, we can restrict ourselves to diagrams with a topological structure of the third one. Its contribution can be obtained by taking the following functional derivative evaluated at zero fields

$$\partial_\Lambda \gamma_5^\Lambda(y, x_1', x_2, x_1, x_2) = \frac{\partial^5}{\partial J_\eta(y) \partial \bar{\phi}(x_1') \partial \bar{\phi}(x_2') \partial \phi(x_2) \partial \phi(x_1)} \times \\ \Big[\frac{1}{3} \partial_{\Lambda,S} \mathrm{tr}\big(G^\Lambda \bar{\partial}\partial\Gamma^\Lambda G^\Lambda \bar{\partial}\partial\Gamma^\Lambda G^\Lambda \bar{\partial}\partial\Gamma^\Lambda\big) - \partial_{\Lambda,S} \mathrm{tr}\big(G^\Lambda \bar{\partial}\partial\Gamma^\Lambda G^\Lambda \bar{\partial}\bar{\partial}\Gamma^\Lambda G^{\Lambda,t} \partial\partial\Gamma^\Lambda\big)\Big]\Big|_{J=\phi=0}, \tag{85}$$

where $x = \{s, k\}$, $y = \{\eta, q\}$ and $\partial_{\Lambda,S}$ acts only on G^Λ and returns the single-scale propagator S^Λ. At this point we integrate the r.h.s. which is an easy operation once we take into account that i) one can replace $S^\Lambda = \partial_{\Lambda,S} G^\Lambda$ by the full derivative $\partial_\Lambda G^\Lambda$ since their difference due the derivative of the self-energy is of higher order in the effective interaction γ_4^Λ, and ii) one can let the scale derivative act also on γ_4^Λ since its derivative is at least of order $O((\gamma_4^\Lambda)^2)$. According to these arguments, the r.h.s. of Eq. (85) can be approximated by the total derivative with respect to the Λ and integrated to

$$\gamma_5^\Lambda(y, x_1', x_2, x_1, x_2) = \frac{\partial^5}{\partial J_\eta(y) \partial \bar{\phi}(x_1') \partial \bar{\phi}(x_2') \partial \phi(x_2) \partial \phi(x_1)} \\ \Big[\frac{1}{3} \mathrm{tr}\big(G^\Lambda \bar{\partial}\partial\Gamma^\Lambda G^\Lambda \bar{\partial}\partial\Gamma^\Lambda G^\Lambda \bar{\partial}\partial\Gamma^\Lambda\big) - \mathrm{tr}\big(G^\Lambda \bar{\partial}\partial\Gamma^\Lambda G^\Lambda \bar{\partial}\bar{\partial}\Gamma^\Lambda G^{\Lambda,t} \partial\partial\Gamma^\Lambda\big)\Big]\Big|_{J=\phi=0}. \tag{86}$$

The only terms surviving the functional derivative are all connected diagrams composed by two two-particle vertices γ_4^Λ and one fermion-boson vertex γ_3^Λ. What distinguishes the first and the second contributions of Eq. (86) is the position of γ_3^Λ which can be inserted at all $\bar{\partial}\partial$ in the first line, while is restricted to a single $\bar{\partial}\partial$ in the second one because of the conservation of Nambu particles. Moreover, the first term accounts for two-particle vertices whose external lines are always a particle and a hole, whereas in the second term they are attached to two particles $\partial\partial\Gamma^\Lambda$ and two holes $\bar{\partial}\bar{\partial}$, respectively. The topological structure of these two contributions is schematically shown in Fig. 18.

The last step consists in closing these diagrams in all possible ways by means of the single-scale propagator and adding them to the flow equation of γ_3^Λ. Hence, one obtains 2ℓ approximated flow equations for γ_3^Λ which contain terms of the order $O((\gamma_4^\Lambda)^2)$ in the effective interaction. We can classify [17,40] the 2ℓ corrections according to their topological structure, with overlapping loops (Fig. 19 (b)) and non-overlapping loops (Fig. 19 (a)). We observe that the latter can be included in the 1ℓ equations by using the Katanin correction [45] where

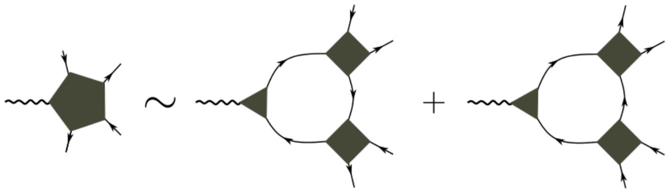

Figure 18: Diagrammatic contributions for γ_5^Λ up to the second oder in the effective interaction γ_4^Λ.

$S^\Lambda \to S^\Lambda + G^\Lambda \dot{\Sigma}^\Lambda G^\Lambda$. The remaining 2ℓ corrections have as building block the 1ℓ diagrams of the flow equation of γ_4^Λ. Translating our Nambu formalism to the physical fields, those corrections yield Eq. (24).

F Implementation details

Here we provide the explicit form of $\boldsymbol{\gamma}_{4,\{P,D,C\}}$ appearing on the r.h.s. of Eq. (36). By using the parquet decomposition in the diagrammatic channels (see Eq. (32)), the first contribution of the projections of the four-point vertex onto the different channels is the projection of the fully two-particle irreducible vertex, approximated by its first order in the on-site Hubbard interaction U, onto the form-factor basis. The projected bare interaction is

$$\begin{aligned}[][\hat{P}[U](i\omega_l, i\nu_o, i\nu_{o'}, \mathbf{q})]_{n,n'} &= [\hat{D}[U](i\omega_l, i\nu_o, i\nu_{o'}, \mathbf{q})]_{n,n'} \\ &= [\hat{C}[U](i\omega_l, i\nu_o, i\nu_{o'}, \mathbf{q})]_{n,n'} = -U\delta_{n,0}\delta_{n',0} \,. \end{aligned} \tag{87}$$

Secondly, every channel, written in its natural bosonic-fermionic notation on the l.h.s. of Eq. (36), needs to be projected onto the complementary channels. The projection of one channel ϕ_r to another leads to a linear combination of its frequency arguments (see Eq. (22) for the physical channels and Eq. (91a) to Eq. (91f) for the diagrammatic channels). In momentum space, the projection is more involved due to the form factor dependence. Following the procedure of Ref. [31], we identify the projection matrices which describe the momentum translation from one channel to another using a matrix multiplication

$$[\hat{B}[\phi_{B'}](i\omega_l, i\nu_o, i\nu_{o'}, \mathbf{q})]_{n,n'} = \sum_{m,m',\mathbf{l}} A^{B,B'}_{n,n',m,m'}(\mathbf{l},\mathbf{q}) B'_{m,m'}(\ldots,\mathbf{l}) \,, \tag{88}$$

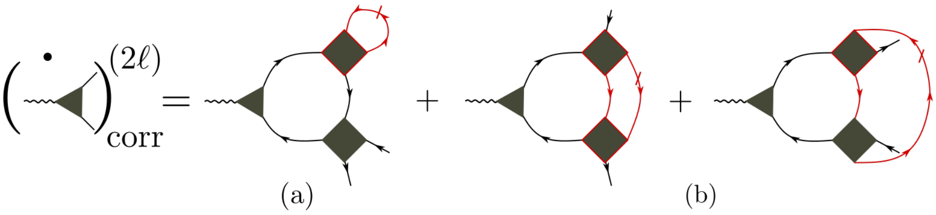

Figure 19: Simplified diagrammatic representation of the 2ℓ correcting diagrams for the flow equation of γ_3^Λ illustrating the topological structure of the diagrams. Diagram (a) can be reabsorbed in the single-scale propagator according to the “Katanin correction”, while the second and the third contributions (b) represent the so-called “overlapping-diagrams”.

where … stands for the channel specific translation of the frequency dependencies.

We exemplify the projection for the channel D to P. In momentum space, it reads

$$\begin{aligned}
[\hat{P}[\phi_{ph}](i\omega_l, i\nu_o, i\nu_{o'}, \mathbf{q})]_{n,n'} &= \int d\mathbf{k}d\mathbf{k}' f_n^*(\mathbf{k})\, f_{n'}(\mathbf{k}')\times \\
&\quad \phi_{ph}\Big(i\omega_l - i\nu_{o'}, i\nu_o, i\nu_{o'}, \mathbf{q}-\mathbf{k}'-\mathbf{k}, \mathbf{k}, \mathbf{k}'\Big) \\
&= \sum_{m,m'} \int d\mathbf{k}d\mathbf{k}' f_n^*(\mathbf{k})\, f_{n'}(\mathbf{k}')\, f_m(\mathbf{k})\, f_{m'}^*(\mathbf{k}')\times \\
&\quad D_{m,m'}(i\omega_l - i\nu_{o'}, i\nu_o, i\nu_{o'}, \mathbf{q}-\mathbf{k}'-\mathbf{k})\,. \qquad (89)
\end{aligned}$$

We now transform the form factors to real space and shift the momentum dependence in order to get the matrix form of (88)

$$\begin{aligned}
[\hat{P}[\phi_{ph}](i\omega_l, i\nu_o, i\nu_{o'}, \mathbf{q})]_{n,n'} &= \sum_{m,m'} \int_{-\pi}^{\pi} d\mathbf{K} \sum_{\mathbf{R}\mathbf{R}_1\mathbf{R}_2} e^{i\mathbf{l}\mathbf{R}-i\mathbf{q}\mathbf{R}} f_n^*(\mathbf{R}_1-\mathbf{R}) f_{n'}(\mathbf{R}_2+\mathbf{R})\times \\
&\quad f_m(\mathbf{R}_1) f_{m'}^*(\mathbf{R}_2) D_{m,m'}\Big(i\omega_l - i\nu_{o'} - i\nu_o, i\nu_o, i\nu_{o'}, \mathbf{l}\Big)\,. \qquad (90)
\end{aligned}$$

The same procedure for every channel projection leads to the matrix equations

$$[\hat{P}[\phi_{ph}](i\omega_l, i\nu_o, i\nu_{o'}, \mathbf{q})]_{n,n'} = \sum_{m,m',\mathbf{l}} A^{P,D}_{n,n',m,m'}(\mathbf{l},\mathbf{q}) D_{m,m'}\Big(i\omega_l - i\nu_{o'} - i\nu_o, i\nu_o, i\nu_{o'}, \mathbf{l}\Big) \qquad (91a)$$

$$[\hat{P}[\phi_{\overline{ph}}](i\omega_l, i\nu_o, i\nu_{o'}, \mathbf{q})]_{n,n'} = \sum_{m,m',\mathbf{l}} A^{P,C}_{n,n',m,m'}(\mathbf{l},\mathbf{q}) C_{m,m'}\Big(-i\nu_o + i\nu_{o'}, i\nu_o, i\omega_l - i\nu_{o'}, \mathbf{l}\Big) \qquad (91b)$$

$$[\hat{D}[\phi_{pp}](i\omega_l, i\nu_o, i\nu_{o'}, \mathbf{q})]_{n,n'} = \sum_{m,m',\mathbf{l}} A^{D,P}_{n,n',m,m'}(\mathbf{l},\mathbf{q}) P_{m,m'}\Big(i\omega_l + i\nu_o + i\nu_{o'}, i\nu_o, i\nu_{o'}, \mathbf{l}\Big) \qquad (91c)$$

$$[\hat{D}[\phi_{\overline{ph}}](i\omega_l, i\nu_o, i\nu_{o'}, \mathbf{q})]_{n,n'} = \sum_{m,m',\mathbf{l}} A^{D,C}_{n,n',m,m'}(\mathbf{l},\mathbf{q}) C_{m,m'}\Big(i\nu_{o'} - i\nu_o, i\nu_o, i\nu_o + i\omega_l, \mathbf{l}\Big) \qquad (91d)$$

$$[\hat{C}[\phi_{pp}](i\omega_l, i\nu_o, i\nu_{o'}, \mathbf{q})]_{n,n'} = \sum_{m,m',\mathbf{l}} A^{C,P}_{n,n',m,m'}(\mathbf{l},\mathbf{q}) P_{m,m'}\Big(i\omega_l + i\nu_o + i\nu_{o'}, i\nu_o, i\omega_l + i\nu_o, \mathbf{l}\Big) \qquad (91e)$$

$$[\hat{C}[\phi_{ph}](i\omega_l, i\nu_o, i\nu_{o'}, \mathbf{q})]_{n,n'} = \sum_{m,m',\mathbf{l}} A^{C,D}_{n,n',m,m'}(\mathbf{l},\mathbf{q}) D_{m,m'}\Big(i\nu_{o'} - i\nu_o, i\nu_o, i\nu_o + i\omega_l, \mathbf{l}\Big), \qquad (91f)$$

with the following projection matrices for the non-symmetrized notation

$$A^{P,D}_{n,n',m,m'}(\mathbf{l},\mathbf{q}) = \sum_{\mathbf{R}\mathbf{R}_1\mathbf{R}_2} e^{i\mathbf{l}\mathbf{R}-i\mathbf{q}\mathbf{R}} f_n^*(\mathbf{R}_1-\mathbf{R}) f_{n'}(\mathbf{R}_2+\mathbf{R}) f_m(\mathbf{R}_1) f_{m'}^*(\mathbf{R}_2) \qquad (92a)$$

$$A^{P,C}_{n,n',m,m'}(\mathbf{l},\mathbf{q}) = \sum_{\mathbf{R}\mathbf{R}_1\mathbf{R}_2} e^{i\mathbf{l}\mathbf{R}+i\mathbf{q}\mathbf{R}_2} f_n^*(\mathbf{R}_1-\mathbf{R}) f_{n'}(-\mathbf{R}_2-\mathbf{R}) f_m(\mathbf{R}_1) f_{m'}^*(\mathbf{R}_2) \qquad (92b)$$

$$A^{D,P}_{n,n',m,m'}(\mathbf{l},\mathbf{q}) = \sum_{\mathbf{R}\mathbf{R}_1\mathbf{R}_2} e^{i\mathbf{l}\mathbf{R}-i\mathbf{q}\mathbf{R}} f_n^*(\mathbf{R}_1+\mathbf{R}) f_{n'}(\mathbf{R}_2-\mathbf{R}) f_m(\mathbf{R}_1) f_{m'}^*(\mathbf{R}_2) \qquad (92c)$$

$$A^{D,C}_{n,n',m,m'}(\mathbf{l},\mathbf{q}) = \sum_{\mathbf{R}\mathbf{R}_1\mathbf{R}_2} e^{i\mathbf{l}\mathbf{R}+i\mathbf{q}\mathbf{R}_2} f_n^*(\mathbf{R}_1-\mathbf{R}_2-\mathbf{R}) f_{n'}(-\mathbf{R}) f_m(\mathbf{R}_1) f_{m'}^*(\mathbf{R}_2) \qquad (92d)$$

$$A^{C,P}_{n,n',m,m'}(\mathbf{l},\mathbf{q}) = \sum_{\mathbf{R}\mathbf{R}_1\mathbf{R}_2} e^{i\mathbf{l}(\mathbf{R}_2-\mathbf{R})+i\mathbf{q}\mathbf{R}} f_n^*(\mathbf{R}_1-\mathbf{R}) f_{n'}(\mathbf{R}-\mathbf{R}_2) f_m(\mathbf{R}_1) f_{m'}^*(\mathbf{R}_2) \qquad (92e)$$

$$A^{C,D}_{n,n',m,m'}(\mathbf{l},\mathbf{q}) = \sum_{\mathbf{R}\mathbf{R}_1\mathbf{R}_2} e^{i\mathbf{l}\mathbf{R}+i\mathbf{q}\mathbf{R}_2} f_n^*(\mathbf{R}_1-\mathbf{R}_2-\mathbf{R}) f_{n'}(-\mathbf{R}) f_m(\mathbf{R}_1) f_{m'}^*(\mathbf{R}_2)\,. \qquad (92f)$$

G Performance of the code

The results shown in this paper were obtained with an OpenMP parallelized code on a single node. In Fig. 3, the scaling in memory and calculation effort is illustrated. The use of symmetries can decrease the calculation effort considerably. The maximum computing time using 40 threads was obtained for the following set of parameters (see caption of Fig. 3)

$$N_\nu = 8 \quad N_{\mathbf{q}} = 256 \quad N_{FF} = 1 \quad T = 0.125 \quad \ell = 8,$$

giving $\tau_{\text{max}} = \text{total CPU time}/(40\text{CPUs}) \sim 10$ days. The memory usage of a process for this set of parameters is approximately 15 GiB.

References

[1] W. Metzner, M. Salmhofer, C. Honerkamp, V. Meden and K. Schönhammer, *Functional renormalization group approach to correlated fermion systems*, Rev. Mod. Phys. **84**, 299 (2012), doi:10.1103/RevModPhys.84.299.

[2] C. Platt, W. Hanke and R. Thomale, *Functional renormalization group for multi-orbital Fermi surface instabilities*, Adv. Phys. **62**, 453 (2013), doi:10.1080/00018732.2013.862020.

[3] J. Sólyom, *The Fermi gas model of one-dimensional conductors*, Adv. Phys. **28**, 201 (1979), doi:10.1080/00018737900101375.

[4] C. Bourbonnais, B. Guay and R. Wortis, *Renormalization group technique for quasi-one-dimensional interacting fermion systems at finite temperature*, (2002), arXiv:cond-mat/0204163.

[5] D. Sénéchal, A.-M. Tremblay and C. Bourbonnais, *Theoretical methods for strongly correlated electrons*, CRM Series in Mathematical Physics 75, Springer, New York, (2003).

[6] J. von Delft and H. Schoeller, *Bosonization for beginners - refermionization for experts*, Ann. Phys. **7**, 225 (1998), doi:10.1002/(SICI)1521-3889(199811)7:4<225::AID-ANDP225>3.0.CO;2-L.

[7] T. Giamarchi, *Quantum physics in one dimension*, Internat. Ser. Mono. Phys., Clarendon Press, Oxford (2004).

[8] E. Jeckelmann, *Ground-state phase diagram of a half-filled one-dimensional extended Hubbard model*, Phys. Rev. Lett. **89**, 236401 (2002), doi:10.1103/PhysRevLett.89.236401.

[9] T. Schäfer, F. Geles, D. Rost, G. Rohringer, E. Arrigoni, K. Held, N. Blümer, M. Aichhorn and A. Toschi, *Fate of the false Mott-Hubbard transition in two dimensions*, Phys. Rev. B **91**, 125109 (2015), doi:10.1103/PhysRevB.91.125109.

[10] G. Rohringer and A. Toschi, *Impact of nonlocal correlations over different energy scales: A dynamical vertex approximation study*, Phys. Rev. B **94**, 125144 (2016), doi:10.1103/PhysRevB.94.125144.

[11] A. Georges, G. Kotliar, W. Krauth and M. J. Rozenberg, *Dynamical mean-field theory of strongly correlated fermion systems and the limit of infinite dimensions*, Rev. Mod. Phys. **68**, 13 (1996), doi:10.1103/RevModPhys.68.13.

[12] G. Kotliar, S. Y. Savrasov, K. Haule, V. S. Oudovenko, O. Parcollet and C. A. Marianetti, *Electronic structure calculations with dynamical mean-field theory*, Rev. Mod. Phys. **78**, 865 (2006), doi:10.1103/RevModPhys.78.865.

[13] K. Held, *Electronic structure calculations using dynamical mean field theory*, Adv. Phys. **56**, 829 (2007), doi:10.1080/00018730701619647.

[14] T. Maier, M. Jarrell, T. Pruschke and M. H. Hettler, *Quantum cluster theories*, Rev. Mod. Phys. **77**, 1027 (2005), doi:10.1103/RevModPhys.77.1027.

[15] G. Rohringer, H. Hafermann, A. Toschi, A. A. Katanin, A. E. Antipov, M. I. Katsnelson, A. I. Lichtenstein, A. N. Rubtsov and K. Held, *Diagrammatic routes to nonlocal correlations beyond dynamical mean field theory*, Rev. Mod. Phys. **90**, 025003 (2018), doi:10.1103/RevModPhys.90.025003.

[16] S. Uebelacker and C. Honerkamp, *Multiband effects on superconducting instabilities driven by electron-electron interactions*, Phys. Rev. B **85**, 155122 (2012), doi:10.1103/PhysRevB.85.155122.

[17] A. Eberlein, *Fermionic two-loop functional renormalization group for correlated fermions: Method and application to the attractive Hubbard model*, Phys. Rev. B **90**, 115125 (2014), doi:10.1103/PhysRevB.90.115125.

[18] A. Eberlein and W. Metzner, *Superconductivity in the two-dimensional t-t'-Hubbard model*, Phys. Rev. B **89**, 035126 (2014), doi:10.1103/PhysRevB.89.035126.

[19] A. Eberlein, W. Metzner, S. Sachdev and H. Yamase, *Fermi surface reconstruction and drop in the Hall number due to spiral antiferromagnetism in high-T_c cuprates*, Phys. Rev. Lett. **117**, 187001 (2016), doi:10.1103/PhysRevLett.117.187001.

[20] J. Lichtenstein, S. A. Maier, C. Honerkamp, C. Platt, R. Thomale, O. K. Andersen and L. Boeri, *Functional renormalization group study of an eight-band model for the iron arsenides*, Phys. Rev. B **89**, 214514 (2014), doi:10.1103/PhysRevB.89.214514.

[21] M. M. Scherer, S. Uebelacker and C. Honerkamp, *Instabilities of interacting electrons on the honeycomb bilayer*, Phys. Rev. B **85**, 235408 (2012), doi:10.1103/PhysRevB.85.235408.

[22] M. M. Scherer, S. Uebelacker, D. D. Scherer and C. Honerkamp, *Interacting electrons on trilayer honeycomb lattices*, Phys. Rev. B **86**, 155415 (2012), doi:10.1103/PhysRevB.86.155415.

[23] C. Taranto, S. Andergassen, J. Bauer, K. Held, A. Katanin, W. Metzner, G. Rohringer and A. Toschi, *From infinite to two dimensions through the functional renormalization group*, Phys. Rev. Lett. **112**, 196402 (2014), doi:10.1103/PhysRevLett.112.196402.

[24] W. Metzner, *Functional renormalization group approach to interacting fermi systems: DMFT as a booster rocket. Chapter 11*, Vol. **4**, Verlag des Forschungszentrum Jülich (2015).

[25] A. Toschi, A. A. Katanin and K. Held, *Dynamical vertex approximation: A step beyond dynamical mean-field theory*, Phys. Rev. B **75**, 045118 (2007), doi:10.1103/PhysRevB.75.045118.

[26] A. N. Rubtsov, M. I. Katsnelson and A. I. Lichtenstein, *Dual fermion approach to nonlocal correlations in the Hubbard model*, Phys. Rev. B **77**, 033101 (2008), doi:10.1103/PhysRevB.77.033101.

[27] N. Wentzell, C. Taranto, A. Katanin, A. Toschi and S. Andergassen, *Correlated starting points for the functional renormalization group*, Phys. Rev. B **91**, 045120 (2015), doi:10.1103/PhysRevB.91.045120.

[28] C. Husemann and M. Salmhofer, *Efficient parametrization of the vertex function, Ω scheme, and the t, t' Hubbard model at van Hove filling*, Phys. Rev. B **79**, 195125 (2009), doi:10.1103/PhysRevB.79.195125.

[29] K.-U. Giering and M. Salmhofer, *Self-energy flows in the two-dimensional repulsive Hubbard model*, Phys. Rev. B **86**, 245122 (2012), doi:10.1103/PhysRevB.86.245122.

[30] W.-S. Wang, Z.-Z. Li, Y.-Y. Xiang and Q.-H. Wang, *Competing electronic orders on kagome lattices at van Hove filling*, Phys. Rev. B **87**, 115135 (2013), doi:10.1103/PhysRevB.87.115135.

[31] J. Lichtenstein, D. Sánchez de la Peña, D. Rohe, E. Di Napoli, C. Honerkamp and S. A. Maier, *High-performance functional renormalization group calculations for interacting fermions*, Comput. Phys. Commun. **213**, 100 (2017), doi:10.1016/j.cpc.2016.12.013.

[32] G. Rohringer, A. Valli and A. Toschi, *Local electronic correlation at the two-particle level*, Phys. Rev. B **86**, 125114 (2012), doi:10.1103/PhysRevB.86.125114.

[33] G. Li, N. Wentzell, P. Pudleiner, P. Thunström and K. Held, *Efficient implementation of the parquet equations: Role of the reducible vertex function and its kernel approximation*, Phys. Rev. B **93**, 165103 (2016), doi:10.1103/PhysRevB.93.165103.

[34] N. Wentzell, G. Li, A. Tagliavini, C. Taranto, G. Rohringer, K. Held, A. Toschi and S. Andergassen, *High-frequency asymptotics of the vertex function: diagrammatic parametrization and algorithmic implementation*, (2016), arXiv:1610.06520.

[35] C. Honerkamp, M. Salmhofer, N. Furukawa and T. M. Rice, *Breakdown of the Landau-Fermi liquid in two dimensions due to umklapp scattering*, Phys. Rev. B **63**, 035109 (2001), doi:10.1103/PhysRevB.63.035109.

[36] D. Zanchi, *Angle-resolved loss of Landau quasiparticles in 2D Hubbard model*, Europhys. Lett. **55**, 376 (2001), doi:10.1209/epl/i2001-00413-7.

[37] C. Honerkamp, *Electron-doping versus hole-doping in the 2D t-t' Hubbard model*, Eur. Phys. J. B **21**, 81 (2001), doi:10.1007/PL00011117.

[38] C. Honerkamp and M. Salmhofer, *Flow of the quasiparticle weight in the N-patch renormalization group scheme*, Phys. Rev. B **67**, 174504 (2003), doi:10.1103/PhysRevB.67.174504.

[39] D. Rohe and W. Metzner, *Pseudogap at hot spots in the two-dimensional Hubbard model at weak coupling*, Phys. Rev. B **71**, 115116 (2005), doi:10.1103/PhysRevB.71.115116.

[40] A. A. Katanin, A. P. Kampf and V. Yu. Irkhin, *Anomalous self-energy and Fermi surface quasisplitting in the vicinity of a ferromagnetic instability*, Phys. Rev. B **71**, 085105 (2005), doi:10.1103/PhysRevB.71.085105.

[41] C. Husemann, K.-U. Giering and M. Salmhofer, *Frequency-dependent vertex functions of the (t, t') Hubbard model at weak coupling*, Phys. Rev. B **85**, 075121 (2012), doi:10.1103/PhysRevB.85.075121.

[42] S. Uebelacker and C. Honerkamp, *Self-energy feedback and frequency-dependent interactions in the functional renormalization group flow for the two-dimensional Hubbard model*, Phys. Rev. B **86**, 235140 (2012), doi:10.1103/PhysRevB.86.235140.

[43] A. Eberlein, *Self-energy effects in functional renormalization group flows of the two-dimensional t-t' Hubbard model away from van Hove filling*, Phys. Rev. B **92**, 235146 (2015), doi:10.1103/PhysRevB.92.235146.

[44] D. Vilardi, C. Taranto and W. Metzner, *Nonseparable frequency dependence of the two-particle vertex in interacting fermion systems*, Phys. Rev. B **96**, 235110 (2017), doi:10.1103/PhysRevB.96.235110.

[45] A. A. Katanin, *Fulfillment of Ward identities in the functional renormalization group approach*, Phys. Rev. B **70**, 115109 (2004), doi:10.1103/PhysRevB.70.115109.

[46] N. E. Bickers, *Self-consistent many-body theory for condensed matter systems*, in Theoretical Methods for Strongly Correlated Electrons, Springer-Verlag, New York, ISBN 0387008950 (2004), doi:10.1007/0-387-21717-7_6.

[47] V. Janiš, *Stability of self-consistent solutions for the Hubbard model at intermediate and strong coupling*, Phys. Rev. B **60**, 11345 (1999), doi:10.1103/PhysRevB.60.11345.

[48] S. X. Yang, H. Fotso, J. Liu, T. A. Maier, K. Tomko, E. F. D'Azevedo, R. T. Scalettar, T. Pruschke and M. Jarrell, *Parquet approximation for the 4×4 Hubbard cluster*, Phys. Rev. E **80**, 046706 (2009), doi:10.1103/PhysRevE.80.046706.

[49] K.-M. Tam, H. Fotso, S.-X. Yang, T.-W. Lee, J. Moreno, J. Ramanujam and M. Jarrell, *Solving the parquet equations for the Hubbard model beyond weak coupling*, Phys. Rev. E **87**, 013311 (2013), doi:10.1103/PhysRevE.87.013311.

[50] A. Valli, T. Schäfer, P. Thunström, G. Rohringer, S. Andergassen, G. Sangiovanni, K. Held and A. Toschi, *Dynamical vertex approximation in its parquet implementation: Application to Hubbard nanorings*, Phys. Rev. B **91**, 115115 (2015), doi:10.1103/PhysRevB.91.115115.

[51] C. Taranto, *Diagrammatic methods beyond DMFT*, Ph.D. thesis, Vienna University of Technology (2014).

[52] N. E. Bickers and D. J. Scalapino, *Critical behavior of electronic parquet solutions*, Phys. Rev. B **46**, 8050 (1992), doi:10.1103/PhysRevB.46.8050.

[53] A. A. Katanin, *Two-loop functional renormalization group approach to the one- and two-dimensional Hubbard model*, Phys. Rev. B **79**, 235119 (2009), doi:10.1103/PhysRevB.79.235119.

[54] S. A. Maier and C. Honerkamp, *Effective three-particle interactions in low-energy models for multiband systems*, Phys. Rev. B **85**, 064520 (2012), doi:10.1103/PhysRevB.85.064520.

[55] F. B. Kugler and J. von Delft, *Multiloop functional renormalization group for general models*, Phys. Rev. B **97**, 035162 (2018), doi:10.1103/PhysRevB.97.035162.

[56] F. B. Kugler and J. von Delft, *Multiloop functional renormalization group that sums up all parquet diagrams*, Phys. Rev. Lett. **120**, 057403 (2018), doi:10.1103/PhysRevLett.120.057403.

[57] F. B. Kugler and J. von Delft, *Derivation of exact flow equations from the self-consistent parquet relations*, New J. Phys. **20**, 123029 (2018), doi:10.1088/1367-2630/aaf65f.

[58] C. J. Halboth and W. Metzner, *Renormalization-group analysis of the two-dimensional Hubbard model*, Phys. Rev. B **61**, 7364 (2000), doi:10.1103/PhysRevB.61.7364.

[59] T. Ayral and O. Parcollet, *Mott physics and spin fluctuations: A unified framework*, Phys. Rev. B **92**, 115109 (2015), doi:10.1103/PhysRevB.92.115109.

[60] M. Salmhofer and C. Honerkamp, *Fermionic renormalization group flows: technique and theory*, Prog. Theor. Phys. **105**, 1 (2001), doi:10.1143/PTP.105.1.

[61] P. Kopietz, L. Bartosch and F. Schütz, *Introduction to the functional renormalization group (Lecture Notes in Physics)*, Springer, Berlin, (2010), ISBN 364205093X.

[62] F. Schütz, L. Bartosch and P. Kopietz, *Collective fields in the functional renormalization group for fermions, Ward identities, and the exact solution of the Tomonaga-Luttinger model*, Phys. Rev. B **72**, 035107 (2005), doi:10.1103/PhysRevB.72.035107.

[63] F. B. Kugler and J. von Delft, *Fermi-edge singularity and the functional renormalization group*, J. Phys.: Condens. Matter **30**, 195501 (2018), doi:10.1088/1361-648X/aaba2e.

[64] N. E. Bickers, *Parquet equations for numerical self-consistent-field theory*, Int. J. Mod. Phys. B **05**, 253 (1991), doi:10.1142/s021797929100016x.

[65] W.-S. Wang, Y.-Y. Xiang, Q.-H. Wang, F. Wang, F. Yang and D.-H. Lee, *Functional renormalization group and variational Monte Carlo studies of the electronic instabilities in graphene near $\frac{1}{4}$ doping*, Phys. Rev. B **85**, 035414 (2012), doi:10.1103/PhysRevB.85.035414.

[66] S. A. Maier, J. Ortloff and C. Honerkamp, *Multiorbital effects in the functional renormalization group: A weak-coupling study of the Emery model*, Phys. Rev. B **88**, 235112 (2013), doi:10.1103/PhysRevB.88.235112.

[67] D. Sánchez de la Peña, J. Lichtenstein and C. Honerkamp, *Competing electronic instabilities of extended Hubbard models on the honeycomb lattice: A functional renormalization group calculation with high-wave-vector resolution*, Phys. Rev. B **95**, 085143 (2017), doi:10.1103/PhysRevB.95.085143.

[68] A. Auerbach, *Interacting electrons and quantum magnetism*, Springer-Verlag (1994).

[69] P. Fazekas, *Lecture notes on electron correlation and magnetism*, World Scientific (1999).

[70] S. R. White, D. J. Scalapino, R. L. Sugar, E. Y. Loh, J. E. Gubernatis and R. T. Scalettar, *Numerical study of the two-dimensional Hubbard model*, Phys. Rev. B **40**, 506 (1989), doi:10.1103/PhysRevB.40.506.

[71] J. P. F. LeBlanc, A. E. Antipov, F. Becca, I. W. Bulik, G. K. L. Chan, C.-M. Chung, Y. Deng, M. Ferrero, T. M. Henderson, C. A. Jiménez-Hoyos, E. Kozik, X.-W. Liu, A. J. Millis, N. V. Prokof'ev, M. Qin, G. E. Scuseria, H. Shi, B. V. Svistunov, L. F. Tocchio, I. S. Tupitsyn, S. R. White, S. Zhang, B.-X. Zheng, Z. Zhu, E. Gull, *Solutions of the two-dimensional Hubbard model: benchmarks and results from a wide range of numerical algorithms*, Phys. Rev. X **5**, 041041 (2015), doi:10.1103/PhysRevX.5.041041.

[72] N. D. Mermin and H. Wagner, *Absence of ferromagnetism or antiferromagnetism in one- or two-dimensional isotropic Heisenberg models*, Phys. Rev. Lett. **17**, 1133 (1966), doi:10.1103/PhysRevLett.17.1133.

[73] Y. M. Vilk and A.-M. Tremblay, *Non-perturbative many-body approach to the Hubbard model and single-particle pseudogap*, J. Phys. I France **7**, 1309 (1997), doi:10.1051/jp1:1997135.

[74] D. Zanchi and H. J. Schulz, *Weakly correlated electrons on a square lattice: renormalization-group theory*, Phys. Rev. B **61**, 13609 (2000), doi:10.1103/PhysRevB.61.13609.

[75] A. A. Katanin and A. P. Kampf, *Quasiparticle anisotropy and pseudogap formation from the weak-coupling renormalization group point of view*, Phys. Rev. Lett. **93**, 106406 (2004), doi:10.1103/PhysRevLett.93.106406.

[76] C. Honerkamp, D. Rohe, S. Andergassen and T. Enss, *Interaction flow method for many-fermion systems*, Phys. Rev. B **70**, 235115 (2004), doi:10.1103/PhysRevB.70.235115.

[77] Y. M. Vilk and A.-M. S. Tremblay, *Destruction of Fermi-liquid quasiparticles in two dimensions by critical fluctuations*, Europhys. Lett. **33**, 159 (1996), doi:10.1209/epl/i1996-00315-2.

[78] K. Borejsza and N. Dupuis, *Antiferromagnetism and single-particle properties in the two-dimensional half-filled Hubbard model: A nonlinear sigma model approach*, Phys. Rev. B **69**, 085119 (2004), doi:10.1103/PhysRevB.69.085119.

[79] J. Otsuki, H. Hafermann and A. I. Lichtenstein, *Superconductivity, antiferromagnetism, and phase separation in the two-dimensional Hubbard model: A dual-fermion approach*, Phys. Rev. B **90**, 235132 (2014), doi:10.1103/PhysRevB.90.235132.

[80] T. Schäfer, A. A. Katanin, K. Held and A. Toschi, *Interplay of correlations and Kohn anomalies in three dimensions: quantum criticality with a twist*, Phys. Rev. Lett. **119**, 046402 (2017), doi:10.1103/PhysRevLett.119.046402.

[81] T. Baier, E. Bick and C. Wetterich, *Temperature dependence of antiferromagnetic order in the Hubbard model*, Phys. Rev. B **70**, 125111 (2004), doi:10.1103/PhysRevB.70.125111.

[82] E. G. C. P. van Loon, H. Hafermann and M. I. Katsnelson, *Precursors of the insulating state in the square-lattice Hubbard model*, Phys. Rev. B **97**, 085125 (2018), doi:10.1103/PhysRevB.97.085125.

[83] C. J. Halboth and W. Metzner, *d-Wave superconductivity and Pomeranchuk instability in the two-dimensional Hubbard model*, Phys. Rev. Lett. **85**, 5162 (2000), doi:10.1103/PhysRevLett.85.5162.

[84] C. Honerkamp, H. C. Fu and D.-H. Lee, *Phonons and d-wave pairing in the two-dimensional Hubbard model*, Phys. Rev. B **75**, 014503 (2007), doi:10.1103/PhysRevB.75.014503.

[85] C. Karrasch, R. Hedden, R. Peters, T. Pruschke, K. Schönhammer and V. Meden, *A finite-frequency functional renormalization group approach to the single impurity Anderson model*, J. Phys.: Condens. Matter **20**, 345205 (2008), doi:10.1088/0953-8984/20/34/345205.

[86] K.-M. Tam, S.-W. Tsai, D. K. Campbell and A. H. Castro Neto, *Retardation effects in the Holstein-Hubbard chain at half filling*, Phys. Rev. B **75**, 161103 (2007), doi:10.1103/PhysRevB.75.161103.

[87] K.-M. Tam, S.-W. Tsai, D. K. Campbell and A. H. Castro Neto, *Phase diagram of the Holstein-Hubbard two-leg ladder using a functional renormalization-group method*, Phys. Rev. B **75**, 195119 (2007), doi:10.1103/PhysRevB.75.195119.

[88] T. Schäfer, G. Rohringer, O. Gunnarsson, S. Ciuchi, G. Sangiovanni and A. Toschi, *Divergent precursors of the Mott-Hubbard transition at the two-particle level*, Phys. Rev. Lett. **110**, 246405 (2013), doi:10.1103/PhysRevLett.110.246405.

[89] T. Schäfer, S. Ciuchi, M. Wallerberger, P. Thunström, O. Gunnarsson, G. Sangiovanni, G. Rohringer and A. Toschi, *Nonperturbative landscape of the Mott-Hubbard transition: Multiple divergence lines around the critical endpoint*, Phys. Rev. B **94**, 235108 (2016), doi:10.1103/PhysRevB.94.235108.

[90] P. Chalupa, P. Gunacker, T. Schäfer, K. Held and A. Toschi, *Divergences of the irreducible vertex functions in correlated metallic systems: Insights from the Anderson impurity model*, Phys. Rev. B **97**, 245136 (2018), doi:10.1103/PhysRevB.97.245136.

[91] D. Vilardi, C. Taranto and W. Metzner, *Antiferromagnetic and d-wave pairing correlations in the strongly interacting two-dimensional hubbard model from the functional renormalization group*, (2018), arXiv:1810.02290.

[92] S. Andergassen, T. Enss, V. Meden, W. Metzner, U. Schollwöck and K. Schönhammer, *Functional renormalization group for Luttinger liquids with impurities*, Phys. Rev. B **70**, 075102 (2004), doi:10.1103/PhysRevB.70.075102.

[93] G. Rohringer, *New routes towards a theoretical treatment of nonlocal electronic correlations*, Ph.D. thesis, Vienna University of Technology (2013).

[94] M. Salmhofer, C. Honerkamp, W. Metzner and O. Lauscher, *Renormalization group flows into phases with broken symmetry*, Prog. Theor. Phys. **112**, 943 (2004), doi:10.1143/PTP.112.943.

[95] R. Gersch, C. Honerkamp and W. Metzner, *Superconductivity in the attractive Hubbard model: functional renormalization group analysis*, New J. Phys. **10**, 045003 (2008), doi:10.1088/1367-2630/10/4/045003.

[96] C. Wetterich, *Exact evolution equation for the effective potential*, Phys. Lett. B **301**, 90 (1993), doi:10.1016/0370-2693(93)90726-X.

[97] O. Gunnarsson, T. Schäfer, J. P. F. LeBlanc, J. Merino, G. Sangiovanni, G. Rohringer and A. Toschi, *Parquet decomposition calculations of the electronic self-energy*, Phys. Rev. B **93**, 245102 (2016), doi:10.1103/PhysRevB.93.245102.

IOP Publishing New J. Phys. 21 (2019) 099601 https://doi.org/10.1088/1367-2630/ab3d9b

New Journal of Physics
The open access journal at the forefront of physics

Deutsche Physikalische Gesellschaft DPG
IOP Institute of Physics

Published in partnership with: Deutsche Physikalische Gesellschaft and the Institute of Physics

CrossMark

OPEN ACCESS

PUBLISHED
12 September 2019

Original content from this work may be used under the terms of the Creative Commons Attribution 3.0 licence.

Any further distribution of this work must maintain attribution to the author(s) and the title of the work, journal citation and DOI.

ERRATUM

Erratum: Derivation of exact flow equations from the self-consistent parquet relations (2018 *New J. Phys.* **20** 123029)

Fabian B Kugler[1,2,3] and **Jan von Delft**[2]

[1] Max-Planck-Institut für Quantenoptik, Hans-Kopfermann-Str. 1, D-85748, Garching, Germany
[2] Physics Department, Arnold Sommerfeld Center for Theoretical Physics, and Center for NanoScience, Ludwig-Maximilians-Universität München, Theresienstr. 37, D-80333, Munich, Germany
[3] Author to whom any correspondence should be addressed.

E-mail: fabian.kugler@physik.lmu.de

Due to an error in the production processes, numerous indices in the following equations and symbols mistakenly appeared with a prime. The equations should read:

$$\langle c_{x_1} c_{x_2} \bar{c}_{x_2'} \bar{c}_{x_1'} \rangle = G_{x_1 x_1'} G_{x_2 x_2'} - G_{x_1 x_2'} G_{x_2 x_1'} + G_{x_1 y_1'} G_{x_2 y_2'} \Gamma_{y_1', y_2'; y_1, y_2} G_{y_1 x_1'} G_{y_2 x_2'} \tag{3}$$

$$\begin{aligned} B_a(\Gamma, \Gamma')_{x_1', x_2'; x_1, x_2} &= \sum_{y_1', y_1, y_2', y_2} \Gamma_{x_1', y_2'; y_1, x_2} G_{y_1, y_1'} G_{y_2, y_2'} \Gamma'_{y_1', x_2'; x_1, y_2} \\ &= \sum_{(y_2', y_1), (y_1', y_2)} \tilde{\Gamma}_{a;(x_1', x_2),(y_2', y_1)} \tilde{\Pi}_{a;(y_2', y_1),(y_1', y_2)} \tilde{\Gamma}'_{a;(y_1', y_2),(x_2', x_1)} \equiv (\Gamma \circ \Pi_a \circ \Gamma')_{x_1', x_2'; x_1, x_2} \end{aligned} \tag{A2a}$$

$$\begin{aligned} B_p(\Gamma, \Gamma')_{x_1', x_2'; x_1, x_2} &= \frac{1}{2} \sum_{y_1', y_1, y_2', y_2} \Gamma_{x_1', x_2'; y_1, y_2} G_{y_1, y_1'} G_{y_2, y_2'} \Gamma'_{y_1', y_2'; x_1, x_2} \\ &= \sum_{(y_1, y_2), (y_1', y_2')} \tilde{\Gamma}_{p;(x_1', x_2'),(y_1, y_2)} \tilde{\Pi}_{p;(y_1, y_2),(y_1', y_2')} \tilde{\Gamma}'_{p;(y_1', y_2'),(x_1, x_2)} \equiv (\Gamma \circ \Pi_p \circ \Gamma')_{x_1', x_2'; x_1, x_2} \end{aligned} \tag{A2b}$$

$$\begin{aligned} B_t(\Gamma, \Gamma')_{x_1', x_2'; x_1, x_2} &= - \sum_{y_1', y_1, y_2', y_2} \Gamma_{y_1', x_2'; y_1, x_2} G_{y_2, y_1'} G_{y_1, y_2'} \Gamma'_{x_1', y_2'; x_1, y_2} \\ &= \sum_{(y_1', y_1), (y_2', y_2)} \tilde{\Gamma}_{t;(x_2', x_2),(y_1', y_1)} \tilde{\Pi}_{t;(y_1', y_1),(y_2', y_2)} \tilde{\Gamma}'_{t;(y_2', y_2),(x_1', x_1)} \equiv (\Gamma \circ \Pi_t \circ \Gamma')_{x_1', x_2'; x_1, x_2} \end{aligned} \tag{A2c}$$

$$\hat{\Gamma}_{x_1', x_2'; x_1, x_2} = \Gamma_{x_1', x_2'; x_2, x_1} = \Gamma_{x_2', x_1'; x_1, x_2} \tag{A3}$$

$$\Gamma^{(3)}_{a; z, x_2', x_1} = \sum_{x_1', x_2} f_{z, x_1', x_2} \Gamma_{x_1', y_2'; y_1, x_2} \quad \Rightarrow \quad (\Gamma^{(3)}_a \circ \Pi_a \circ \Gamma')_{z, x_2', x_1} = \sum_{x_1', x_2} f_{z, x_1', x_2} (\Gamma \circ \Pi_a \circ \Gamma')_{x_1', x_2'; x_1, x_2} \tag{A4}$$

$$-L(\Gamma, G)_{x', x} = \sum_{y', y} \Gamma_{x', y'; x, y} G_{y, y'} = \sum_{(y', y)} \tilde{\Gamma}_{t;(x', x),(y', y)} \tilde{G}_{(y', y)} \equiv (\Gamma \cdot G)_{x', x}. \tag{A5}$$

The caption of figure A1 should include the sentence: The positions of the external (amputated) legs refer to the arguments of $\Gamma_{x_1', x_2'; x_1, x_2}$.

The sentence before equation (A2) should read: For this, we will use auxiliary objects that depend on channel-dependent tuples of quantum numbers (e.g. $\Gamma_{x_1', x_2'; x_1, x_2} = \tilde{\Gamma}_{a;(x_1', x_2),(x_2', x_1)}$) and define a contraction $\circ$ that always comes together with a two-particle propagator Π_r of a certain channel (consisting of two one-particle propagators G).

ORCID iDs

Fabian B Kugler https://orcid.org/0000-0002-3108-6607
Jan von Delft https://orcid.org/0000-0002-8655-0999

© 2019 The Author(s). Published by IOP Publishing Ltd on behalf of the Institute of Physics and Deutsche Physikalische Gesellschaft

IOP Publishing New J. Phys. 20 (2018) 123029 https://doi.org/10.1088/1367-2630/aaf65f

New Journal of Physics
The open access journal at the forefront of physics

Deutsche Physikalische Gesellschaft DPG
IOP Institute of Physics

Published in partnership with: Deutsche Physikalische Gesellschaft and the Institute of Physics

OPEN ACCESS

RECEIVED
24 August 2018

REVISED
14 November 2018

ACCEPTED FOR PUBLICATION
5 December 2018

PUBLISHED
21 December 2018

Original content from this work may be used under the terms of the Creative Commons Attribution 3.0 licence.

Any further distribution of this work must maintain attribution to the author(s) and the title of the work, journal citation and DOI.

PAPER

Derivation of exact flow equations from the self-consistent parquet relations

Fabian B Kugler[1,2,3] **and Jan von Delft**[2]

[1] Max-Planck-Institut für Quantenoptik, Hans-Kopfermann-Str. 1, D-85748 Garching, Germany
[2] Physics Department, Arnold Sommerfeld Center for Theoretical Physics, and Center for NanoScience, Ludwig-Maximilians-Universität München, Theresienstr. 37, D-80333 Munich, Germany
[3] Author to whom any correspondence should be addressed.

E-mail: fabian.kugler@physik.lmu.de

Keywords: exact flow equations, parquet equations, functional renormalization group, conservation laws

Abstract

We exploit the parquet formalism to derive exact flow equations for the two-particle-reducible four-point vertices, the self-energy, and typical response functions, circumventing the reliance on higher-point vertices. This includes a concise, algebraic derivation of the multiloop flow equations, which have previously been obtained by diagrammatic considerations. Integrating the multiloop flow for a given input of the totally irreducible vertex is equivalent to solving the parquet equations with that input. Hence, one can tune systems from solvable limits to complicated situations by variation of one-particle parameters, staying at the fully self-consistent solution of the parquet equations throughout the flow. Furthermore, we use the resulting differential form of the Schwinger–Dyson equation for the self-energy to demonstrate one-particle conservation of the parquet approximation and to construct a conserving two-particle vertex via functional differentiation of the parquet self-energy. Our analysis gives a unified picture of the various many-body relations and exact renormalization group equations.

1. Introduction

The many-body problem of nonrelativistic quantum-field theory is equipped with a well-known set of exact equations for its correlation functions [1, 2]. If these self-consistent many-body relations are expressed in their energy-momentum representation, they interrelate the different correlation functions between all energy scales, often involving integrations over all energy-momenta. However, a typical feature of interacting quantum many-body systems is that their relevant energy scales span several orders of magnitude. Conventional perturbative approaches or approaches that directly work with the self-consistent many-body relations treat all energy scales at once—they are therefore prone to inaccuracies and often plagued by infrared divergences. A very successful approach to such systems is instead given by the renormalization group (RG) technique which treats energy scales successively, starting from high ones and progressing towards lower ones [3].

The simplest realization of such a RG scheme considers the renormalization of effective couplings in analogy to Anderson's poor man's scaling [4]. There, the successive treatment of high-energy degrees of freedom is encoded in the evolution of running coupling constants. Since then, quantum-field-theoretical RG techniques have seen great development. A widely used, modern formulation is given by the functional RG (fRG), which allows one to study the flow of all coupling 'constants' in their full functional dependence [5, 6]. The respective couplings are nothing but the (field-theoretical) vertex functions; hence, the fRG can be directly applied to microscopic models.

The fRG flow is based on an exact functional flow equation for the generating functional of the (one-particle-irreducible) vertex functions [7]. If this flow equation is expanded in terms of the vertices, one obtains an infinite hierarchy of flow equations, where, in order to compute the flow of an n-point vertex, knowledge about the other vertices up to the $n + 2$-point vertex is required. The obvious way of truncating the hierarchy by disregarding higher-point vertices has led to a variety of successful applications of the fRG. However, one often wants to extend the usage of fRG beyond the validity of this approximation, and, in cutting-edge algorithmic development, this form of truncation may indeed be an exceedingly severe approximation.

© 2018 The Author(s). Published by IOP Publishing Ltd on behalf of Deutsche Physikalische Gesellschaft

In fact, considering a system of, say, interacting electrons, possibly subject to external fields, one may ask why it is necessary to include six- and higher-point vertices, i.e. *effective* interactions between three and more particles, if one is ultimately interested in one- and two-particle properties of the system. Although the fRG hierarchy of flow equations and also the hierarchy of Schwinger–Dyson equations (SDEs, or equations of motion) [8] interrelate all n-point vertices, the fundamental interaction is only of the (one- and) two-particle type; thus, it should suffice to work on the one- and two-particle level. Fortunately, a many-body framework that provides a complete description on the one- and two-particle level is available; it is the parquet formalism [2, 9].

The main idea of the approach presented in this paper is to apply the RG point of view neither to the generating functional of vertices [7] nor to the hierarchy of SDEs [8] but to the self-consistent many-body relations of the parquet formalism. Exploiting the organizational structure of the parquet formalism allows us to circumvent the inclusion of higher-point vertices and to freely navigate between different two-particle channels. Inspired by the fRG framework, we induce an internal scale dependence by using a scale-dependent propagator G^{Λ} that suppresses low-energy degrees of freedom and recovers the original theory at a final value Λ_f. It should be noted that this differs in technical aspects from more traditional RG schemes [3, 10], which, instead of solely using a scale-dependent propagator, restrict all involved energy-momenta to decreasing energy-momentum shells (often referred to as 'mode elimination'). Here, we simply substitute $G \to G^{\Lambda}$ in the well known many-body relations and study the behavior of the solution to these equations upon varying Λ.

As a result, we derive exact flow equations for the two-particle-reducible four-point vertices, the self-energy, and response functions. This provides a concise, algebraic derivation of the multiloop fRG (mfRG) flow equations, which have previously been obtained using diagrammatic arguments [11–13]. Our analysis also reveals how one can perform such multiloop flows beyond the parquet approximation (PA), thus including higher-order expressions for the totally irreducible vertex. Moreover, we establish an intimate connection between the functional derivative of the self-energy and the fRG flow equation for the self-energy: the latter constitutes an integration of the former along a specific path in the space of theories.

On a slightly different note, we use our approach to address fundamental questions of (traditional) parquet theory (i.e. without an explicit RG treatment): on the one hand, we demonstrate that the parquet self-energy can be obtained from the SDE using either of two possible orderings of the bare and full vertex. According to Baym and Kadanoff [14], it then follows that the PA fulfills one-particle conservation laws. On the other hand, we give an explicit construction to obtain a new, conserving vertex from the parquet self-energy, equivalent to taking the functional derivative. This construction not only allows one to quantify the degree to which the PA violates two-particle conservation laws. It can also be used to modify the PA, which fulfills the SDE but violates two-particle conservation, to obtain a fully conserving solution, albeit violating the SDE. As we show in the appendix, a fulfillment of both the SDE and the functional-derivative relation necessarily amounts to the exact solution of the many-body problem, in agreement with a result by Smith [15].

The paper is structured as follows. In section 2, we first focus (as is typical for RG approaches) on the effective interactions: we derive flow equations for the two-particle-reducible four-point vertices based on the parquet formalism, assuming the one-particle propagator to be given. Then, in section 3, we complement the flow of the four-point vertex by the flow of the self-energy, considering the various relations at hand. In section 4, we use our approach to discuss conservation properties of the PA. Finally, in section 5, we derive (dependent) flow equations for response functions, i.e. three-point vertices and suceptibilities, used to study collective excitations. In section 6, we summarize our results.

2. Derivation of the vertex flow

2.1. Preliminaries

We consider a general theory of interacting fermions, defined by the action

$$S = -\sum_{x',x} \bar{c}_{x'}[(G_0)^{-1}]_{x',x}c_x - \tfrac{1}{4}\sum_{x',x,y',y}\Gamma_{0;x',y';x,y}\bar{c}_{x'}\bar{c}_{y'}c_y c_x, \tag{1}$$

with a bare propagator G_0 and a bare four-point vertex Γ_0, which is antisymmetric in its first and last two arguments. The index x denotes all quantum numbers of the Grassmann field c_x. Correlation functions of fields, corresponding to time-ordered expectation values of operators, are given by the functional integral

$$\langle c_{x_1}\cdots\bar{c}_{x_n}\rangle = \frac{1}{Z}\int \mathcal{D}[\bar{c}]\mathcal{D}[c]\, c_{x_1}\cdots\bar{c}_{x_n}\mathrm{e}^{-S}, \tag{2}$$

where Z ensures normalization, such that $\langle 1\rangle = 1$. Two-point correlation functions are represented by the full propagator $G_{x,x'} = -\langle c_x\bar{c}_{x'}\rangle$; four-point correlation functions can be expressed via the full (one-particle-irreducible) four-point vertex Γ:

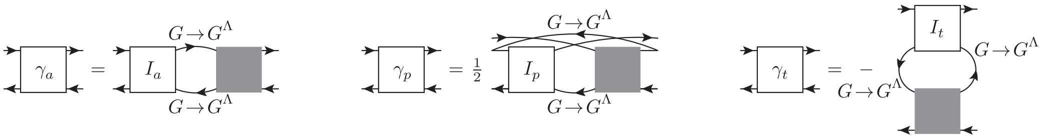

Figure 1. The Bethe–Salpeter equations for the channels $r = a, p, t$ are solved in an RG approach by introducing a scale (Λ) dependence to the propagators connecting the vertices. Consequently, γ_r, Γ, and I_r inherit a scale dependence while the totally irreducible vertex, R, remains as given input. (See appendix A for details on the diagrammatic notation.) As prime example for the scale dependence, one can multiply the frequency-dependent propagator by a step function, $G^\Lambda(\omega) = \Theta(|\omega| - \Lambda)G(\omega)$, such that the many-body relations are trivially solved at $\Lambda_i = \infty$ and reproduce the desired solution at $\Lambda_f = 0$.

$$\langle c_{x_1'} c_{x_2'} \bar{c}_{x_2'} \bar{c}_{x_1'} \rangle = G_{x_1' x_1'} G_{x_2' x_2'} - G_{x_1' x_2'} G_{x_2' x_1'} + G_{x_1' y_1'} G_{x_2' y_2'} \Gamma_{y_1', y_2'; y_1', y_2'} G_{y_1' x_1'} G_{y_2' x_2'}. \tag{3}$$

The notation given so far is identical to the one in [12]; all formulae further needed in this paper are defined in appendix A. In the following derivation of flow equations, we use a compact notation of contractions and need not write quantum numbers (such as x, x', etc) explicitly.

2.2. Parquet equations for the four-point vertex

The fRG flow equation for the four-point vertex, $\Gamma^{(4)} \equiv \Gamma$, contains the six-point vertex, $\Gamma^{(6)}$, which poses great difficulty for a numerical treatment. Similarly, the SDE (equation of motion) for Γ contains $\Gamma^{(6)}$ and therefore is likewise impractical. To circumvent the calculation of $\Gamma^{(6)}$, we revert to the parquet formalism [2, 9], which provides self-consistent equations for the two-particle-reducible contributions to the four-point vertex Γ but assumes as input a given, totally irreducible four-point vertex R. In a diagrammatic expansion, R is given by the bare vertex, Γ_0, with corrections starting at fourth order. The famous *parquet approximation* [16–18] (see section 4) consists of using $R = \Gamma_0$ and allows one to sum up all leading logarithmic contributions in logarithmically divergent perturbation theories [9, 19]. Importantly, however, the parquet equations can be used more generally as an exact classification of all diagrams of the four-point vertex.

In the parquet formalism, one decomposes the full four-point vertex, Γ, into the totally irreducible vertex, R, and the three two-particle-reducible vertices γ_r, $r \in \{a, p, t\}$[4]. Diagrams belonging to γ_r are reducible in channel r, i.e. they can be separated into two parts by cutting two *a*ntiparallel, *p*arallel, or *t*ransverse antiparallel lines, respectively. Diagrams that cannot be separated in this way belong to R. (For exemplary diagrams, see figure A1 in appendix A.) While the γ_r are subject to further equations, this set of coupled equations closes only for a fixed choice of R.

Let us assume a given expression for the totally irreducible vertex, R. Furthermore, we will for now assume the one-particle propagator, G, to be given; computation of G via the self-energy will be discussed later. The *parquet equations*, involving the two-particle-reducible vertices, γ_r, and two-particle-irreducible vertices, I_r, read

$$\Gamma = R + \sum_r \gamma_r, \qquad I_r = \Gamma - \gamma_r = R + \gamma_{\bar{r}}, \tag{4a}$$

$$\gamma_r = I_r \circ \Pi_r \circ \Gamma. \tag{4b}$$

For given R, these equations must be solved self-consistently to obtain the appropriate reducible vertices, γ_r, that complement the full vertex, Γ. In equation (4a), we use the notation $\bar{r}$ for the complementary channel of a given channel r, such that $\gamma_{\bar{r}} = \sum_{r' \neq r} \gamma_{r'}$. The *Bethe–Salpeter equation* (BSE) (4b) describes two vertices, I_r and Γ, connected by a bubble, Π_r, of two dressed propagators in channel r (see also figure 1). This bubble of vertices can be expressed as a matrix multiplication (given a suitable parametrization depending on the channel r, see appendix A), as indicated by the symbol $\circ$ attached to Π_r. Note that Π_p and Π_t implicitly contain a factor of $1/2$ and (-1), respectively.

In the following, we list relations that can be easily deduced from the parquet equations (4) and will be used repeatedly in the derivations of flow equations. The combination of equations (4a) and (4b) directly yields $\Gamma = I_r + I_r \circ \Pi_r \circ \Gamma$ (for all channels r). Exploiting the multiplicative structure, we can isolate Γ on the lhs to obtain the *inverted BSE*,

$$\Gamma = I_r + I_r \circ \Pi_r \circ \Gamma \quad \Leftrightarrow \quad \Gamma = (1 - I_r \circ \Pi_r)^{-1} \circ I_r. \tag{5}$$

A further straightforward manipulation yields an *extended BSE*,

---

[4] Our nomenclature follows the seminal application of the parquet equations to the x-ray-edge singularity by Roulet *et al* [9]. While we use Γ, R, γ_r, and I_r for the full, totally irreducible, two-particle-reducible, and -irreducible vertices, respectively, another common choice [20–22] is given by F, Λ, Φ_r, Γ_r, respectively. Similarly, a common notation [20–22] for the channels a, p, t is ph, pp, $\overline{ph}$, referring to the (longitudinal) particle-hole, the particle-particle, and the transverse (or vertical) particle-hole channel, respectively. One also finds the labels x, p, d in the literature [23], referring to the so-called exchange, pairing, and direct channel, respectively.

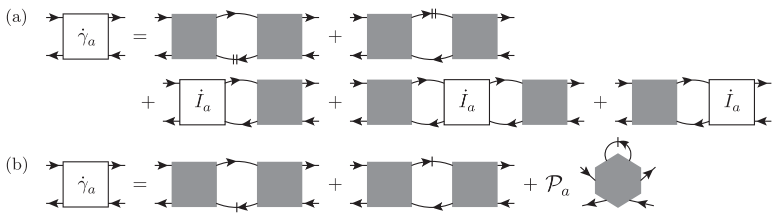

Figure 2. (a) Exact mfRG flow equation for the reducible vertex γ_a, involving the differentiated propagator, $\dot{G}$, (line with two vertical dashes) and the differentiated irreducible vertex given by $\dot{I}_r = \sum_{r'\neq r}\dot{\gamma}_{r'} \equiv \dot{\gamma}_{\bar{r}}$ (as $\dot{R} = 0$ in our construction). (b) Exact fRG flow equation for γ_a involving the single-scale propagator, $S = \partial_\Lambda G_{|\Sigma=\mathrm{const}}$, (line with one vertical dash) and the six-point vertex, whose contribution is (for conceptual purposes) reduced to the part reducible in the *a* channel via the projector $\mathcal{P}_a$.

$$1 + \Gamma \circ \Pi_r = 1 + (1 - I_r \circ \Pi_r)^{-1} \circ (I_r \circ \Pi_r - 1 + 1) = (1 - I_r \circ \Pi_r)^{-1}. \tag{6}$$

Using the inverted BSE (5), one directly sees (by isolating γ_r) that the order of the vertices in the BSE (4*b*) is irrelevant:

$$\gamma_r = I_r \circ \Pi_r \circ \Gamma = I_r \circ \Pi_r \circ (I_r + \gamma_r) \quad \Leftrightarrow \quad \gamma_r = (1 - I_r \circ \Pi_r)^{-1} \circ I_r \circ \Pi_r \circ I_r = \Gamma \circ \Pi_r \circ I_r. \tag{7}$$

2.3. Flow of the four-point vertex

The central aspect of our RG treatment is incorporated by attaching a scale (Λ) dependence to the propagator, $G \rightarrow G^\Lambda$, appearing in the self-consistent many-body relations. The physical picture is that Λ separates high- and low-energy degrees of freedom, and by using G^Λ we allow for successive renormalization of the low-energy ($<\Lambda$) theory by high-energy ($>\Lambda$) degrees of freedom as Λ is decreased. However, one can also simply consider Λ as some additional dependence in the propagators connecting the vertices in the BSEs: $G \rightarrow G^\Lambda$, $\Pi_r \rightarrow \Pi_r^\Lambda$ (cf figure 1). Hence, the reducible vertices γ_r^Λ—and consequently Γ^Λ and I_r^Λ—will inherit a scale (Λ) dependence, obtained from the requirement that the parquet relations be fulfilled for each value of Λ, while *R* remains as given input.

The scale dependence is auxiliary in the sense that we are ultimately interested in the fully renormalized theory: we are interested in $\gamma_r^{\Lambda_f} = \gamma_r$ where (at the final scale) $G^{\Lambda_f} = G$. Suppose we know the vertices at the initial scale, i.e. we can solve the BSEs using G^{Λ_i}. Then, we can obtain $\gamma_r^{\Lambda_f}$ by solving a differential equation specified by the initial condition together with the flow $\partial_\Lambda \gamma_r^\Lambda \equiv \dot{\gamma}_r^\Lambda$, which is induced by the scale dependence of G^Λ in the BSEs. We remark that it is natural to exclude the totally irreducible vertex *R* from the renormalization flow, as it constitutes precisely the part of the vertex that cannot be constructed iteratively and therefore does not have a flow equation that allows for an efficient (i.e. iterative one-loop) calculation.

2.3.1. Flow equation

To find the scale dependence of the two-particle-reducible vertices, γ_r, we start by differentiating the BSEs wrt Λ (suppressing the Λ dependence to lighten the notation) according to the product rule and decomposing the full vertex via the parquet equation (4*a*):

$$\begin{aligned}\dot{\gamma}_r &= I_r \circ \dot{\Pi}_r \circ \Gamma + \dot{I}_r \circ \Pi_r \circ \Gamma + I_r \circ \Pi_r \circ \dot{\Gamma} \\ &= I_r \circ \dot{\Pi}_r \circ \Gamma + \dot{I}_r \circ \Pi_r \circ \Gamma + I_r \circ \Pi_r \circ (\dot{I}_r + \dot{\gamma}_r).\end{aligned} \tag{8}$$

Similar to the manipulations in equation (7), we bring $\dot{\gamma}_r$ to the lhs and subsequently multiply by $(1 - I_r \circ \Pi_r)^{-1}$ from the left. According to the inverted BSE (5), we get

$$\dot{\gamma}_r = \Gamma \circ \dot{\Pi}_r \circ \Gamma + (1 - I_r \circ \Pi_r)^{-1} \circ \dot{I}_r \circ \Pi_r \circ \Gamma + \Gamma \circ \Pi_r \circ \dot{I}_r, \tag{9}$$

and, resolving the remaining inverse by the extended BSE (6), we find

$$\dot{\gamma}_r = \underbrace{\Gamma \circ \dot{\Pi}_r \circ \Gamma}_{\dot{\gamma}_r^{(1)}} + \underbrace{\dot{I}_r \circ \Pi_r \circ \Gamma}_{\dot{\gamma}_r^{(\mathrm{L})}} + \underbrace{\Gamma \circ \Pi_r \circ \dot{I}_r \circ \Pi_r \circ \Gamma}_{\dot{\gamma}_r^{(\mathrm{C})}} + \underbrace{\Gamma \circ \Pi_r \circ \dot{I}_r}_{\dot{\gamma}_r^{(\mathrm{R})}}. \tag{10}$$

The algebraic derivation of this exact flow equation, as the differential form of the BSE (4*b*), is our first main result. It is depicted diagrammatically in figure 2(a) (exemplified by the *a* channel) and contrasted with the corresponding standard fRG flow equation (figure 2(b)). It describes the flow of the reducible vertices, γ_r; the totally irreducible vertex, *R*, does not have an efficient flow equation and remains as input. Since $\dot{R} = 0$, we have $\dot{I}_r = \sum_{r'\neq r}\dot{\gamma}_{r'} \equiv \dot{\gamma}_{\bar{r}}$, and equation (10) constitutes a closed, coupled set of differential equations for all reducible vertices γ_r. The natural way to solve these equations is to start by computing the independent, *one-loop* part, $\dot{\gamma}_r^{(1)}$, for each channel, and then iteratively insert the results into the *left*, *right*, and *center* parts ($\dot{\gamma}_r^{(\mathrm{L})}$, $\dot{\gamma}_r^{(\mathrm{R})}$, $\dot{\gamma}_r^{(\mathrm{C})}$, respectively) of the various channels. If this is organized by the number of loops (connecting full vertices), we precisely recover the mfRG vertex flow which has been derived diagrammatically in [11, 12] (see figure 5 of [12]). It is worth mentioning that the numerical effort of this iterative mfRG flow grows only linearly with the number of loops that are kept (on average) as compared to the standard (truncated) fRG flow [11–13]. First implementations [11, 13] of this iterative scheme for moderate interaction strengths have found convergence for a number of loops $\lesssim 8$. In general, we expect that with increasing interacting strength the convergence with loop order will become slower—and possibly not occur at all for sufficiently strong interactions—in a way that will depend on the model at hand.

From the above derivation, it is clear that, if the scale dependence of G is chosen such that we are initially able to solve the BSEs (using G^{Λ_i}) and finally revert to the original theory ($G^{\Lambda_f} = G$), then solving the mfRG vertex flow (10) is equivalent to solving the BSEs (4*b*). An initial solution is always available by using $G^{\Lambda_i} = 0$, but can also be chosen differently, if desired (see below). In the same way that any solution of the BSEs depends on a certain choice of R, so do results of mfRG. However, the multiloop flow equation requires only the initial condition of the *full* vertex $\Gamma^{\Lambda_i} = R + \sum_r \gamma_r^{\Lambda_i}$ and not of the individual two-particle-reducible or -irreducible vertices; the decomposition into $\dot{\gamma}_r$ is only performed on the differential level. Nevertheless, the degree of approximation in our approach is encoded in the underlying expression for R, which can range from the simplest approximation, $R = \Gamma_0$, to the exact object, R^{ex}.

2.3.2. Examples

Let us give some examples for possible flows which are specified by the input R and the choice of G^{Λ_i} initializing the progression towards $G^{\Lambda_f} = G$. Recall that, in this section, we focus on the two-particle level, i.e. we study the influence of varying the full propagator, G^{Λ}, on the vertex, Γ^{Λ}. In practice, the variation of G^{Λ} will be realized by tuning the bare propagator, G_0^{Λ}, and complementing the vertex flow with a self-energy flow to compute G^{Λ} (see section 3).

(i) The BSEs at the initial scale are trivially solved if $G^{\Lambda_i} = 0$: Due to $\Pi_r^{\Lambda_i} = 0$, the corresponding initial condition for the reducible vertices is $\gamma_r^{\Lambda_i} = 0$. As we introduce the scale dependence only for the propagators connecting the vertices in the BSEs but leave the totally irreducible vertex R—the input to the parquet equations—unchanged, the initial condition for the full vertex is given by $\Gamma^{\Lambda_i} = R$[5]. Hence, the mfRG flow generates all two-particle-reducible diagrams given the irreducible building block R; the special case of $R = \Gamma_0$ yields all diagrams of the PA [11, 12].

(ii) The mfRG flow (10) is an *exact* flow equation for the two-particle-reducible vertices and thus gives us full control over the vertices corresponding to given propagators G^{Λ}. Immediate consequences are that (a) for given boundary conditions G^{Λ_i}, G^{Λ_f}, we are completely free to choose any *specific* Λ dependence in G^{Λ}—the results of the flow do not depend on this choice; and (b) that we can perform loops in theory space, going from G^{Λ_i} to $G^{\Lambda_f} = G^{\Lambda_i}$ without any loss of information. Conceptually, this underlines the power of the mfRG flow; practically, it can also be used as a consistency check for a numerical implementation (which might employ approximate parametrizations of the vertex functions, etc). We emphasize that, while both properties directly follow from the given derivation based on the BSEs, they are violated in the widely used one-loop form ($\dot{\gamma}_r \approx \dot{\gamma}_r^{(1)}$) of the truncated fRG flow.
A loop in theory space could for instance be realized via $G^{\Lambda} = f(\Lambda) G^{\Lambda_i}$ with $f(\Lambda_i) = f(\Lambda_f) = 1$. If we already have the result of the PA ($R = \Gamma_0$) in the form of $G^{\Lambda_i} = G^{\mathrm{PA}}$ and $\Gamma^{\Lambda_i} = \Gamma^{\mathrm{PA}}$, the vertex flow naturally gives the corresponding parquet vertex for all values of Λ (as $R = \Gamma_0$ throughout) and finally returns to the original result. If we assume (from a conceptual point of view) we had the exact solution of the many-body problem in the form of $G^{\Lambda_i} = G^{\mathrm{ex}}$, $\Gamma^{\Lambda_i} = \Gamma^{\mathrm{ex}}$, then such a vertex flow would return to the exact result, too. However, as the totally irreducible vertex remains fixed, the results at intermediate Λ do not correspond to the exact solution for that G^{Λ}. Instead, at each value of Λ, the reducible vertices γ_r^{Λ} solve the BSEs with propagators G^{Λ} and $R^{\mathrm{ex}} \neq R^{\Lambda}$. At Λ_f, the BSEs with $G^{\Lambda_f} = G^{\mathrm{ex}}$ and R^{ex} reproduce γ_r^{ex} and thus $\Gamma^{\mathrm{ex}} = R^{\mathrm{ex}} + \sum_r \gamma_r^{\mathrm{ex}}$.

(iii) As a highly correlated and, yet, numerically tractable initial condition [24], one can choose the solution of dynamical mean-field theory (DMFT) [25] and use the mfRG flow to generate nonlocal correlations [20, 26], thus extending the DMF^{2}RG idea [26] to *multiloop* DMF^{2}RG [11, 12] (or D(MF)^{2}RG [27]). A related approach that gives diagrammatic, nonlocal corrections to DMFT is given by the dynamical vertex approximation (DΓA) [28–30]. This approach directly employs the parquet equations, using as input R^{DMFT}, the totally irreducible vertex from the local DMFT solution [21]. If we used the same initial propagator $G^{\Lambda_i} = 0$ as in example (i) above, we would start the vertex flow from $\Gamma^{\Lambda_i} = R^{\mathrm{DMFT}}$, in perfect analogy to the DΓA algorithm. However, at this point we can leverage the flexibility of the RG framework and perform a continuous deformation starting directly from the full DMFT vertex: indeed, if we use $G^{\Lambda_i} = G^{\mathrm{DMFT}}$ (as opposed to $G^{\Lambda_i} = 0$), the vertex flow is not initiated by R^{DMFT}, but from the actual, full vertex Γ^{DMFT} [26]. (Recall that the decomposition into two-particle channels in equation (10) occurs only for *differentiated* vertices $\dot{\gamma}_r$, which are ultimately combined to give $\dot{\Gamma} = \sum_r \dot{\gamma}_r$.) Although the results are (in principle) independent of the specific Λ dependence, the choice $G^{\Lambda_i} = G^{\mathrm{DMFT}}$ with $\Gamma^{\Lambda_i} = \Gamma^{\mathrm{DMFT}}$ has the decisive numerical advantage that it avoids any explicit appearance of R^{DMFT}. The corresponding multiloop flow is hence not affected by the (likely) unphysical divergences of the totally irreducible vertex, which have been observed in strongly correlated systems [31–35], and can thus be used to analyze such systems in wider regimes of the phase diagram. The combination of vertex and self-energy flow in multiloop DMF^{2}RG, as used in practice, is further discussed in section 3.1.2 (iv).

---

[5] Whereas the initial condition $\Gamma^{\Lambda_i} = R$ at G^{Λ_i} is natural in the parquet approximation $R = \Gamma_0$, it might seem counter-intuitive for other cases, when thinking of the totally irreducible vertex, R, being itself composed of diagrams containing propagators. In this way of thinking, we have to treat propagators in R differently from those propagators that connect the building block R in the two-particle-reducible diagrams of the γ_r. This special treatment is necessary as R does not have an efficient flow equation.

So far, we have assumed the dressed propagator, G, to be known. However, as this is in general not the case, we now combine equation (10) with a self-energy flow, $\dot{\Sigma}^{\Lambda}$, to generate G^{Λ} during the flow. Via the Dyson equation, we then have $(G^{\Lambda})^{-1} = (G_0^{\Lambda})^{-1} - \Sigma^{\Lambda}$ in a flow controlled by the scale-dependent bare propagator, G_0^{Λ}.

3. Derivation of the self-energy flow

First, let us mention that the straightforward derivation of the vertex flow was based on the parquet equations (for given input R). These merely represent a classification of diagrams, reducing the need for an explicit input expression to the most fundamental building block. We did not use equations which provide a construction of the four-point vertex from higher-point vertices, such as the SDE involving $\Gamma^{(6)}$, or a functional derivative connecting four- and six-point vertices.

By contrast, we next want to construct the self-energy, Σ, from the four-point vertex, Γ. For this purpose, three equations are available: (i) the SDE relating Σ to Γ, typically used in the parquet formalism [2], (ii) a functional derivative between self-energy and two-particle-irreducible vertex, known from Hedin's equations [1] and Φ-derivable approaches [36, 37], and (iii) the fRG flow equation for Σ [5]. While all these equations are exact, their outcomes might differ when inserting an approximate vertex. In section 3.2, we show that the fRG flow for Σ can be easily derived from the functional derivative (as a necessary condition). However, as we show in appendix B, the SDE and the functional derivative are complementary in the sense that any solution that fulfills both equations must be the exact solution. It is therefore not surprising that it is complicated to relate a self-energy flow to the SDE for Σ. Nevertheless, we will use the SDE to derive a self-energy flow (different from the standard fRG flow), which is well-suited for the PA and allows us to gain insight into its conservation properties (see section 4). While this multiloop flow deduced from the SDE indeed proves beneficial in the PA [12], the general advantages and disadvantages of the different starting points (i) and (ii) are not entirely clear (see also section 3.1.2).

3.1. Self-energy flow from the SDE

Deriving a flow equation from the SDE of the self-energy is a difficult task since (as already mentioned) SDEs and differential equations are of fundamentally different nature—for instance, SDEs always contain the bare interaction whereas differential equations are typically phrased with renormalized objects only. In [8], the SDE was used to derive the fRG self-energy flow up to terms $O[(\Gamma)^3]$; here, we demonstrate agreement up to $O[(\Gamma)^4]$. In fact, we derive the mfRG self-energy flow from [12], which includes important terms that would be neglected if one simply inserts the approximate parquet vertex into the standard fRG self-energy flow equation [12]. The calculation with the main results given in equations (26) and (30) (see also figure 3) is presented in detail in the following section 3.1.1 and interpreted in section 3.1.2.

3.1.1. Flow equation

The starting point of our calculation is the *Schwinger–Dyson equation* for the self-energy (see figure 3(a)):

$$\Sigma = \Sigma_{\mathrm{SD}}(\Gamma_0, \Gamma, G) = -(\Gamma_0 + \Gamma_0 \circ \Pi_p \circ \Gamma) \cdot G = -(\Gamma_0 + \tfrac{1}{2}\Gamma_0 \circ \Pi_a \circ \Gamma) \cdot G. \tag{11}$$

Here, we have used bubbles in either the a or the p channel, as well as the contraction of two vertex legs with a propagator (denoted by $\Gamma \cdot G$, see appendix A, equation (A5)). As we can freely choose the specific propagator

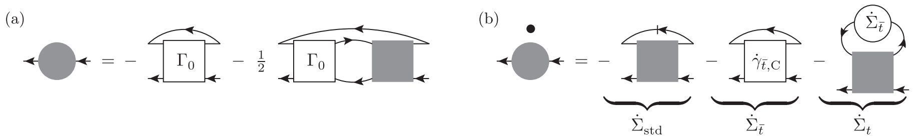

Figure 3. (a) Schwinger–Dyson equation (SDE) for the self-energy, where the second term contains two equivalent lines connected to antisymmetric vertices and hence requires a factor of 1/2. One notes that the three propagators in the second summand can be both viewed as contracting a parallel and antiparallel bubble of the vertices Γ_0 and Γ. (b) Multiloop fRG self-energy flow [12], derived from the SDE in the parquet approximation. The first term, $\dot\Sigma_{\mathrm{std}}$, constitutes the standard fRG self-energy flow.

for the final contraction, we can write the SDE with a bubble in either the p or the a channel—the factor of 1/2 is implicitly contained in Π_p and must be explicitly written when using Π_a.

The presence of two *equivalent* lines (i.e. parallel lines connected to (anti)symmetric vertices) in the second summand of the SDE opens the possibility for further manipulations. For this, let us explicitly denote the propagators contained in a bubble by $\Pi_{r;G_1,G_2}$; the standard bubble is then simply given by $\Pi_r \equiv \Pi_{r;G,G}$. In the SDE, we cannot only freely choose the propagator used in the final contraction (equation (12*a*)), we can also switch the equivalent lines by crossing two external legs of both vertices, $\Gamma_1 \to \hat\Gamma_1$, $\Gamma_2 \to \hat\Gamma_2$ (see equation (A3)). The relations deduced from this *contracted crossing* operation (see figure 4(a)) are

$$\left(\tfrac{1}{2}\Gamma_1 \circ \Pi_{a;G_1,G_2} \circ \Gamma_2\right) \cdot G_3 = (\Gamma_1 \circ \Pi_{p;G_1,G_3} \circ \Gamma_2) \cdot G_2 \tag{12a}$$

$$= \left(\tfrac{1}{2}\hat\Gamma_1 \circ \Pi_{a;G_3,G_2} \circ \hat\Gamma_2\right) \cdot G_1 = (\hat\Gamma_1 \circ \Pi_{p;G_3,G_1} \circ \hat\Gamma_2) \cdot G_2. \tag{12b}$$

We will use the contracted crossing relations extensively on the relevant vertices, which obey the crossing symmetries

$$\hat\Gamma = -\Gamma, \quad \hat\Gamma_0 = -\Gamma_0, \quad \hat R = -R, \quad \hat\gamma_p = -\gamma_p, \quad \hat\gamma_a = -\gamma_t, \quad \hat\gamma_t = -\gamma_a. \tag{13}$$

Note that the vertices in the particle-hole channels a, t are mapped onto each other upon crossing two external legs. For this reason, we will often combine contributions from the a and t channel in the following calculations.

The SDE yields a scale-dependent self-energy if we attach a Λ dependence to every propagator connecting the vertices in equation (11) and account for the Λ dependence of the four-point vertex, Γ, as discussed in section 2. In light of the functional derivative $\delta\Sigma/\delta G = -I_t$ (see section 3.2 below), we aim at generating the irreducible vertex I_t, for which we need the totally irreducible vertex, R, instead of the bare vertex, Γ_0. Hence, we define $R' = R - \Gamma_0$, and, since equation (11) is linear in Γ_0, we obtain

$$\Sigma = \Sigma_{\mathrm{SD}}(R,\ \Gamma,\ G) - \Sigma_{\mathrm{SD}}(R',\ \Gamma,\ G). \tag{14}$$

We now consider the flow of $\Sigma_{\mathrm{SD}}(R,\ \Gamma,\ G)$ and organize our computation according to (see figures 4(b) and (c))

$$\dot\Sigma = \underbrace{\partial_\Lambda\Sigma_{\mathrm{SD}}(R,\ \Gamma,\ G) - [-(R \circ \Pi_p \circ \dot\Gamma) \cdot G]}_{\dot\Sigma_1} + \underbrace{[-(R \circ \Pi_p \circ \dot\Gamma) \cdot G]}_{\dot\Sigma_2} - \underbrace{\partial_\Lambda\Sigma_{\mathrm{SD}}(R',\ \Gamma,\ G)}_{\dot\Sigma_3}. \tag{15}$$

Here, we have subtracted and added a term such that the first bracket, $\dot\Sigma_1$, contains only those terms of the differentiated SDE in which the derivative is explicitly applied to propagators. The second part, $\dot\Sigma_2$, accounts for the differentiated vertex for which we will insert the vertex flow (10). Finally, $\dot\Sigma_3$ contains all remaining contributions proportional to R'. In the PA, one has $R = \Gamma_0 \Leftrightarrow R' = 0$; thus, $\dot\Sigma_3$ will only be relevant in calculations that go beyond the PA. In fact, from equation (14), we see that the role of $\dot\Sigma_3$ is to cancel the extra terms that have been added to $\dot\Sigma_1 + \dot\Sigma_2$ by using $\Sigma_{\mathrm{SD}}(R,\ \Gamma,\ G)$ instead of $\Sigma_{\mathrm{SD}}(\Gamma_0,\ \Gamma,\ G)$. We begin our calculations with $\dot\Sigma_1$.

Generate $I_t \cdot \dot G$—As already mentioned, we want to single out the two-particle-irreducible vertex I_t (since it constitutes the functional derivative of the self-energy). The first summand in equation (11) (using R instead of Γ_0 with $\dot R = 0$) is easily differentiated as $-R \cdot \dot G$. In the remaining part of $\dot\Sigma_1$, we have three propagators to differentiate. Two of the resulting terms can be combined to factor out $\dot G$ if we use the contracted crossing symmetry (12) on R and Γ:

$$-\dot\Sigma_1 - R \cdot \dot G = (R \circ (\Pi_{p;\dot G,G} + \Pi_{p;G,\dot G}) \circ \Gamma) \cdot G + (R \circ \Pi_{p;G,G} \circ \Gamma) \cdot \dot G = (R \circ \Pi_a \circ \Gamma) \cdot \dot G + (R \circ \Pi_p \circ \Gamma) \cdot \dot G. \tag{16}$$

Next, we collect the terms for $I_t = R + \gamma_{\bar t} = R + I_a \circ \Pi_a \circ \Gamma + I_p \circ \Pi_p \circ \Gamma$ (see equation (4)) and find

$$-\dot\Sigma_1 = [R + (R \circ \Pi_a \circ \Gamma) + (R \circ \Pi_p \circ \Gamma)] \cdot \dot G = I_t \cdot \dot G - [(\gamma_p + \gamma_t) \circ \Pi_a \circ \Gamma + (\gamma_a + \gamma_t) \circ \Pi_p \circ \Gamma)] \cdot \dot G. \tag{17}$$

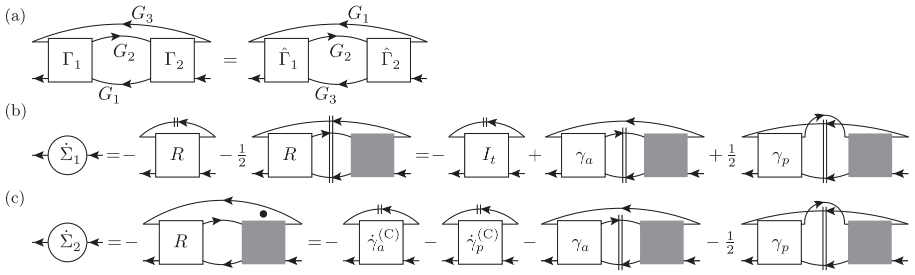

Figure 4. Illustrations for the derivation of the self-energy flow. (a) As stated in equation (12), a bubble of vertices closed with an additional loop can be viewed as a contracted *a* or *p* bubble and can be rewritten by exchanging two of the external legs ($\Gamma \to \hat\Gamma$) of the vertices (contracted crossing symmetry). Note that equation (12*a*) is fully encoded in the diagram on the lhs and equation (12*b*) in the one on the rhs. Thus, the individual equations (12*a*) and (12*b*) merely represent a redundancy in the algebraic description. (b) Rewriting of $\dot\Sigma_1$, the part of $\partial_\Lambda \Sigma_{\mathrm{SD}}$ where the derivative is applied to the propagators appearing explicitly in the SDE. The double dash crossing multiple lines denotes the derivative of the product of propagators, i.e. a sum of terms where each line is differentiated once. (c) Rewriting of $\dot\Sigma_2$, the part of $\partial_\Lambda \Sigma_{\mathrm{SD}}$ containing $\dot\Gamma$.

Use differentiated bubbles— The extra terms accompanying $I_t \cdot \dot G$ in equation (17) will later be combined with contributions from $\dot\Sigma_2$. Since $\dot\Sigma_2$ contains the differentiated vertex, which itself is built from differentiated bubbles $\dot\Pi_r$, we rewrite these contributions in terms of $\dot\Pi_r$. Using the contracted crossing symmetry (12), we find

$$(\gamma_p \circ \Pi_{a;G,G} \circ \Gamma) \cdot \dot G = (\gamma_p \circ \Pi_{p;G,\dot G} \circ \Gamma) \cdot G + (\gamma_p \circ \Pi_{p;\dot G,G} \circ \Gamma) \cdot G = (\gamma_p \circ \dot\Pi_p \circ \Gamma) \cdot G, \tag{18a}$$

$$(\gamma_t \circ \Pi_{a;G,G} \circ \Gamma) \cdot \dot G = (\gamma_a \circ \Pi_{a;\dot G,G} \circ \Gamma) \cdot G, \tag{18b}$$

$$[(\gamma_a + \gamma_t) \circ \Pi_{p;G,G} \circ \Gamma] \cdot \dot G = (2\gamma_a \circ \Pi_{p;G,G} \circ \Gamma) \cdot \dot G = (\gamma_a \circ \Pi_{a;G,\dot G} \circ \Gamma) \cdot G. \tag{18c}$$

This leads to the final expression for $\dot\Sigma_1$ (illustrated in figure 4(b)):

$$\dot\Sigma_1 = -I_t \cdot \dot G + (\gamma_a \circ \dot\Pi_a \circ \Gamma + \gamma_p \circ \dot\Pi_p \circ \Gamma) \cdot G. \tag{19}$$

Organize vertex derivative— The second contribution to equation (15), $\dot\Sigma_2$, contains the differentiated vertex. Inserting the decomposition $\dot\Gamma = \sum_r \dot\gamma_r$, we can combine the contributions from both particle-hole channels, *a* and *t*, by applying the contracted crossing symmetry (12) on *R* and $\dot\gamma_t$:

$$-\dot\Sigma_2 = (R \circ \Pi_p \circ \dot\Gamma) \cdot G = (R \circ \Pi_a \circ \dot\gamma_a) \cdot G + (R \circ \Pi_p \circ \dot\gamma_p) \cdot G. \tag{20}$$

Once we insert the flow equation (10) for $\dot\gamma_a$ and $\dot\gamma_p$ in equation (20), *R* will be connected to further bubbles of vertices. These connections can be simplified if we have I_r instead of *R*. Hence, we rewrite equation (20), using $I_r = R + \gamma_{\bar r}$, as

$$-\dot\Sigma_2 = (I_a \circ \Pi_a \circ \dot\gamma_a) \cdot G - [(\gamma_p + \gamma_t) \circ \Pi_a \circ \dot\gamma_a] \cdot G + (I_p \circ \Pi_p \circ \dot\gamma_p) \cdot G - [(\gamma_a + \gamma_t) \circ \Pi_p \circ \dot\gamma_p] \cdot G. \tag{21}$$

The next step consists of repeated use of the contracted crossing symmetry (12):

$$(\gamma_p \circ \Pi_a \circ \dot\gamma_a) \cdot G = (\gamma_p \circ \Pi_p \circ \dot\gamma_a) \cdot G + (\gamma_p \circ \Pi_p \circ \dot\gamma_t) \cdot G, \tag{22a}$$

$$(\gamma_t \circ \Pi_a \circ \dot\gamma_a) \cdot G = (\gamma_a \circ \Pi_a \circ \dot\gamma_t) \cdot G, \tag{22b}$$

$$[(\gamma_a + \gamma_t) \circ \Pi_p \circ \dot\gamma_p] \cdot G = (\gamma_a \circ \Pi_a \circ \dot\gamma_p) \cdot G. \tag{22c}$$

After using $\dot I_r = \dot\gamma_{\bar r}$, we then obtain

$$\dot\Sigma_2 = -\sum_{r=a,p} (I_r \circ \Pi_r \circ \dot\gamma_r - \gamma_r \circ \Pi_r \circ \dot I_r) \cdot G. \tag{23}$$

Insert vertex flow— Whereas the previous manipulations were possible due to the contracted crossing symmetry, the following insertion of the vertex flow for $\dot\gamma_r$, given by equation (10), can be simplified already on the vertex level. In fact, using the parquet equations (4) with $\gamma_r = I_r \circ \Pi_r \circ \Gamma$ and $\Gamma = I_r + \gamma_r$, we get

$$\begin{aligned} I_r \circ \Pi_r \circ \dot\gamma_r &= I_r \circ \Pi_r \circ (\Gamma \circ \dot\Pi_r \circ \Gamma + \dot I_r \circ \Pi_r \circ \Gamma + \Gamma \circ \Pi_r \circ \dot I_r \circ \Pi_r \circ \Gamma + \Gamma \circ \Pi_r \circ \dot I_r) \\ &= \gamma_r \circ \dot\Pi_r \circ \Gamma + \Gamma \circ \Pi_r \circ \dot I_r \circ \Pi_r \circ \Gamma + \gamma_r \circ \Pi_r \circ \dot I_r. \end{aligned} \tag{24}$$

The first term also occurs (with opposite sign) in equation (19), the second term reproduces $\dot\gamma_r^{(C)}$, and the third term gets canceled in equation (23). Hence, $\dot\Sigma_2$ can be simplified (as summarized in figure 4(c)) to

$$\dot{\Sigma}_2 = -\sum_{r=a,p} (\dot{\gamma}_r^{(\mathrm{C})} + \gamma_r \circ \dot{\Pi}_r \circ \Gamma) \cdot G. \tag{25}$$

With the definition $\dot{\gamma}_{\bar{t}}^{(\mathrm{C})} = \dot{\gamma}_a^{(\mathrm{C})} + \dot{\gamma}_p^{(\mathrm{C})}$, the full derivative of the self-energy is given by

$$\dot{\Sigma} = \dot{\Sigma}_1 + \dot{\Sigma}_2 - \dot{\Sigma}_3 = -I_t \cdot \dot{G} - \dot{\gamma}_{\bar{t}}^{(\mathrm{C})} \cdot G - \dot{\Sigma}_3. \tag{26}$$

This result for $\dot{\Sigma} \equiv \partial_\Lambda \Sigma_{\mathrm{SD}}$ in *skeleton* form (i.e. phrased with dressed propagators G, $\dot{G}$ only) will be considered more closely in section 4. Here, we move on by noting that equation (26) still contains $\dot{\Sigma}$ on both the lhs and the rhs (via $\dot{G}$).

Isolate $\dot{\Sigma}$—At this point in our derivation, we specify how the Λ dependence is supposed to enter G: it shall be incorporated in the bare propagator G_0 such that the Dyson equation, $G = G_0 + G_0 \cdot \Sigma \cdot G$, entails $\dot{G} = S + G \cdot \dot{\Sigma} \cdot G$ with the single-scale propagator $S = \partial_\Lambda G_{|\Sigma=\mathrm{const}} = -G \cdot (\partial_\Lambda G_0^{-1}) \cdot G$. Once we insert this expression for $\dot{G}$ into equation (26), we will face the contraction of a vertex with a composite line $G \cdot \dot{\Sigma} \cdot G$. In such a case, one can equivalently attribute the two propagators to either the self-energy or the vertex, such that we have the following equality for a *composite contraction* (recall the minus sign in Π_t; see equation (A6) for details):

$$I_t \cdot (G \cdot \dot{\Sigma} \cdot G) = -I_t \circ \Pi_t \cdot \dot{\Sigma}. \tag{27}$$

We insert equation (27) into equation (26) to isolate $\dot{\Sigma}$:

$$\begin{aligned} &\dot{\Sigma} = -I_t \cdot (S + G \cdot \dot{\Sigma} \cdot G) - \dot{\gamma}_{\bar{t}}^{(\mathrm{C})} \cdot G - \dot{\Sigma}_3 = -I_t \cdot S + I_t \circ \Pi_t \circ \dot{\Sigma} - \dot{\gamma}_{\bar{t}}^{(\mathrm{C})} \cdot G - \dot{\Sigma}_3 \\ \Leftrightarrow \quad &\dot{\Sigma} = -(1 - I_t \circ \Pi_t)^{-1} \circ I_t \cdot S - (1 - I_t \circ \Pi_t)^{-1} \cdot (\dot{\gamma}_{\bar{t}}^{(\mathrm{C})} \cdot G + \dot{\Sigma}_3). \end{aligned} \tag{28}$$

Next, we use the inverted BSE (5) as well as the extended BSE (6) to express this through Γ and $1 + \Gamma \circ \Pi_t$, respectively:

$$\dot{\Sigma} = -\Gamma \cdot S - (1 + \Gamma \circ \Pi_t) \cdot (\dot{\gamma}_{\bar{t}}^{(\mathrm{C})} \cdot G + \dot{\Sigma}_3). \tag{29}$$

For convenience, we finally write the contraction of $(\Gamma \circ \Pi_t)$ with both summands as composite contractions (using equation (27) for a general vertex and self-energy) and obtain

$$\dot{\Sigma} = \underbrace{[-\Gamma \cdot S]}_{\dot{\Sigma}_{\mathrm{std}}} + \underbrace{[-\dot{\gamma}_{\bar{t}}^{(\mathrm{C})} \cdot G]}_{\dot{\Sigma}_{\bar{t}}} + \underbrace{[-\Gamma \cdot (G \cdot \dot{\Sigma}_{\bar{t}} \cdot G)]}_{\dot{\Sigma}_t} - \dot{\Sigma}_3 - [-\Gamma \cdot (G \cdot \dot{\Sigma}_3 \cdot G)]. \tag{30}$$

This is our final result for the mfRG self-energy flow deduced from the SDE. It constitutes the bare ('nonskeleton') form of equation (26) as it involves G and S instead of G and $\dot{G}$. The first term in equation (30), $\dot{\Sigma}_{\mathrm{std}}$, is the standard fRG self-energy flow. The next two terms, $\dot{\Sigma}_{\bar{t}}$ and $\dot{\Sigma}_t$, constitute the multiloop corrections to the self-energy flow (see figure 3(b)), which have been derived diagrammatically in [12]. These contributions are needed to ensure that the self-energy flow generates all contributions to the self-energy arising within the PA. Finally, the two terms involving $\dot{\Sigma}_3$ remain in our final result and—in calculations beyond the PA—are required to cancel doubly counted terms coming from the replacement $\Sigma_{\mathrm{SD}}(\Gamma_0, \Gamma, G) \to \Sigma_{\mathrm{SD}}(R, \Gamma, G)$ in equation (14). We remark that $\dot{\Sigma}_3$ constitutes precisely the part that cannot be simplified further with our parquet tools, as it originates from the appearance of a *bare* instead of renormalized vertex in the SDE.

3.1.2. Interpretation

Let us interpret the flow equation (30) step by step:

(i) Since $\dot{\gamma}_{\bar{t}}^{(\mathrm{C})}$ and R' [and hence $\dot{\Sigma}_3 = \partial_\Lambda \Sigma_{\mathrm{SD}}(R', \Gamma, G)$] are of order $O[(\Gamma)^4]$, we have explicitly shown how to derive the standard fRG self-energy flow, $\dot{\Sigma}_{\mathrm{std}}$, from the SDE up to and including terms of fourth order in the (effective) interaction. If we were in the standard fRG setting where *every* line is Λ-dependent, further terms coming from $\dot{R} \neq 0$ would arise in our derivation. However, as these terms are similarly of order $O[(\Gamma)^4]$, the result $\partial_\Lambda \Sigma_{\mathrm{SD}} = \dot{\Sigma}_{\mathrm{std}} + O[(\Gamma)^4]$ would remain unchanged.

(ii) In the PA, the totally irreducible vertex is reduced to its simplest approximation, such that $R = \Gamma_0 \Leftrightarrow R' = 0$ and thus $\dot{\Sigma}_3 = 0$. In this case, equation (30) reproduces the mfRG self-energy flow from [12] including the corrections $\dot{\Sigma}_{\bar{t}}$ and $\dot{\Sigma}_t$ (see figure 3(b)), necessary to provide a total derivative of the SDE using the approximate parquet vertex.

(iii) Let us come back to the idea of a loop in theory space, which—including the self-energy flow—is now driven by the bare propagator G_0^Λ. A possible realization is given by $G_0^\Lambda = f(\Lambda) G_0$ with $f(\Lambda_i) = f(\Lambda_f) = 1$. If we start the flow from the solution in the PA ($R = \Gamma_0$) with $\Sigma^{\Lambda_i} = \Sigma^{\mathrm{PA}}$ and $\Gamma^{\Lambda_i} = \Gamma^{\mathrm{PA}}$, the combination of the mfRG vertex flow (10) and self-energy flow (30) (using $\dot{\Sigma}_3 = 0$) gives the corresponding result in the PA for all Λ (as $R = \Gamma_0$ throughout) and returns to the original solution at Λ_f. However, starting the flow from a solution with $R' \neq 0$, we would have to include $\dot{\Sigma}_3$ in the self-energy flow (30) in order to precisely return to the original self-energy, Σ, and vertex, Γ (dressed by Σ), at Λ_f; with $R' \neq 0$, setting $\dot{\Sigma}_3 = 0$ introduces an approximation in the full derivative of the SDE. Conversely, one can compare results of the flow at Λ_i and Λ_f to (numerically) gauge the importance of the individual terms in equation (30).

To better understand the effect of $\dot{\Sigma}_3$, we recall that $\dot{\Sigma}_{\bar{t}}$ and $\dot{\Sigma}_t$ were originally derived diagrammatically to compensate for missing diagrams of $\dot{\Sigma}^{\mathrm{PA}}$ when using the parquet vertex in $\dot{\Sigma}_{\mathrm{std}}$ [12]. With this perspective on $\dot{\Sigma}_{\bar{t}} + \dot{\Sigma}_t$ in mind, it is intuitively clear that higher-order contributions to R (i.e. $R' \neq 0$) generate doubly counted terms between $\dot{\Sigma}_{\mathrm{std}}$ and $\dot{\Sigma}_{\bar{t}} + \dot{\Sigma}_t$. Yet, as equation (30) is exact, these overcounted terms are precisely canceled by the parts involving $\dot{\Sigma}_3$.

For illustration, consider the (parquet) self-energy at fourth order in the interaction, which contains no approximation and whose flow is fully described by $\dot{\Sigma}_{\mathrm{std}} + \dot{\Sigma}_{\bar{t}} + \dot{\Sigma}_t$ using vertices in the PA. Now, fourth-order diagrams of $R' \neq 0$ generate fourth-order terms in $\dot{\Sigma}_{\mathrm{std}}$ but not in $\dot{\Sigma}_{\bar{t}}$ and $\dot{\Sigma}_t$ (due to their structure involving further vertices that raise the interaction order). The additional fourth-order contributions of $\dot{\Sigma}_{\mathrm{std}}$ are precisely canceled by $R' \cdot \dot{G}$ (containing only *one* Λ-dependent line) as part of $\dot{\Sigma}_3$. Generally, we believe that, for situations where $R' \neq 0$, the overcounting of differentiated diagrams in $\dot{\Sigma}_{\mathrm{std}} + \dot{\Sigma}_{\bar{t}} + \dot{\Sigma}_t$ has rather small weight and that, even if using $\dot{\Sigma}_3 \approx 0$, the multiloop additions $\dot{\Sigma}_{\bar{t}} + \dot{\Sigma}_t$ provide an improvement of the standard self-energy flow, $\dot{\Sigma}_{\mathrm{std}}$.

(iv) An interesting application with $R' \neq 0$ is the previously mentioned multiloop DMF^{2}RG approach. In its full form, combining the flow equations of the vertex (10) and self-energy (30), the mfRG flow is controlled by the bare propagator G_0^{Λ}, which interpolates between the local theory of DMFT and the actual lattice problem. The simplest realization [26] of a flow from $\Lambda_i = 1$ to $\Lambda_f = 0$, formulated in terms of Matsubara frequencies $\mathrm{i}\omega$ and momentum $\boldsymbol{k}$, is given by $(G_0^{\Lambda})^{-1} = \mathrm{i}\omega + \mu - \Lambda\Delta(\mathrm{i}\omega) - (1 - \Lambda)\epsilon_{\boldsymbol{k}}$. Here, $\Delta(\mathrm{i}\omega)$ is the self-consistently determined hybridization function of the auxiliary Anderson impurity model [25] and $\epsilon_{\boldsymbol{k}}$ the lattice dispersion. With $G_0^{\Lambda_i} = G_0^{\mathrm{DMFT}} = 1/[\mathrm{i}\omega + \mu - \Delta(\mathrm{i}\omega)]$, the flow is conveniently started from $\Sigma^{\Lambda_i} = \Sigma^{\mathrm{DMFT}}$ and $\Gamma^{\Lambda_i} = \Gamma^{\mathrm{DMFT}}$. While the vertex flow (10) exactly solves the BSEs (for given G^{Λ}), the differential form of the SDE contains $\dot{\Sigma}_3$ and therefore prevents complete equivalence to the DΓA approach. In this regard, it remains to be seen whether the standard fRG self-energy flow, $\dot{\Sigma}_{\mathrm{std}}$, with or without the multiloop corrections $\dot{\Sigma}_{\bar{t}} + \dot{\Sigma}_t$, or other realizations, incorporating parts of $\dot{\Sigma}_3$ in equation (30), lead to optimal results.

3.2. Self-energy flow from the functional derivative

We now show how the standard fRG self-energy flow, $\dot{\Sigma}_{\mathrm{std}}$, can be directly derived from the equality between the functional derivative of the self-energy and the (particle-hole) two-particle-irreducible vertex. To be in perfect accordance with the standard fRG setup, we have to require that *every* G line be Λ-dependent—even those in the totally irreducible vertex, $R = R^{\Lambda}$. Incorporating the Λ dependence in the bare propagator G_0, we again relate the differentiated propagator, $\dot{G}$, to the single-scale propagator, S, via $\dot{G} = S + G \cdot \dot{\Sigma} \cdot G$.

The functional derivative between self-energy and vertex, $\delta\Sigma/\delta G = -I_t$ (see equation (A8)), holds for any variation of G. If this variation is realized by having a scale-dependent propagator G^{Λ} and varying the scale parameter Λ, this equation *implies* $\dot{\Sigma} = -I_t \cdot \dot{G}$. Starting from this, we can perform the same steps as above: to obtain the standard fRG flow equation for the self-energy, it remains to insert $\dot{G} = S + G \cdot \dot{\Sigma} \cdot G$, express the composite contraction $I_t \cdot (G \cdot \dot{\Sigma} \cdot G)$ as $-I_t \circ \Pi_t \cdot \dot{\Sigma}$ (see equation (27)), and use the inverted BSE (5):

$$
\begin{aligned}
& \dot{\Sigma} = -I_t \cdot \dot{G} = -I_t \cdot (S + G \cdot \dot{\Sigma} \cdot G) = -I_t \cdot S + I_t \circ \Pi_t \cdot \dot{\Sigma} \\
\Leftrightarrow \quad & \dot{\Sigma} = -(1 - I_t \circ \Pi_t)^{-1} \circ I_t \cdot S = -\Gamma \cdot S.
\end{aligned}
\tag{31}
$$

Solving for Σ in a specific fRG flow via equation (31) amounts to integrating $\delta\Sigma = -I_t \cdot \delta G$ along a specific path in the space of theories defined by the bare propagator $G_0 = G_0^{\Lambda}$ (and the bare interaction Γ_0, see equation (1)). Only if this integration is independent of the path, i.e. if $\dot{\Sigma}$ contains a total derivative of diagrams, the standard self-energy flow (31) yields results consistent with the functional derivative. In the scenarios considered so far, this is not the case: the truncated fRG flow (without $\Gamma^{(6)}$ and more than one channel) employs equation (31) but does not generate a total derivative of diagrams [11, 12]; the mfRG flow of figure 3 with $R = \Gamma_0$ does provide a total derivative of diagrams but deviates from equation (31) by the additions $\dot{\Sigma}_{\bar{t}}$ and $\dot{\Sigma}_t$. (In fact, the latter reproduces precisely the self-energy diagrams generated by the SDE using the vertex in the PA. However, as shown in appendix B, the requirement of fulfilling both the functional derivative and the SDE necessitates the exact solution.)

As a direct application of the above calculations, we can derive a fRG flow which is equivalent to self-consistent Hartree–Fock (HF), in agreement with a result by Katanin [38]. This conserving fRG flow provides a simple example for which the integration of $\delta\Sigma = -I_t \cdot \delta G$ is indeed independent of the path. In HF theory, the

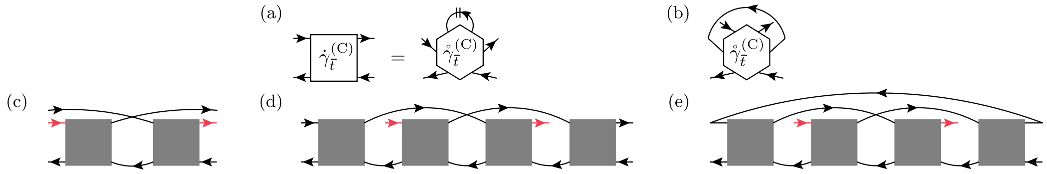
(a)
$\dot{\gamma}_{\bar{t}}^{(C)}$
=
$\mathring{\gamma}_{\bar{t}}^{(C)}$
(b)
$\mathring{\gamma}_{\bar{t}}^{(C)}$
(c)
(d)
(e)

Figure 5. Illustrations for $\mathring{\gamma}_r^{(C)}$. (a) The six-point vertex $\mathring{\gamma}_r^{(C)}$ is obtained from $\dot{\gamma}_r^{(C)}$ by removing its differentiated line; hence, $\dot{\gamma}_r^{(C)}$ is recovered by contracting $\mathring{\gamma}_r^{(C)}$ with $\dot{G}$. (b) A contraction of $\mathring{\gamma}_r^{(C)}$ denoted as $\mathring{\gamma}_r^{(C)} \cdot G$, such that $\dot{\gamma}_r^{(C)} \cdot G$ is reproduced by $(\mathring{\gamma}_r^{(C)} \cdot G) \cdot \dot{G}$. (c) As an example for the construction of $\mathring{\gamma}_r^{(C)}$, we consider the six-point vertex $\mathring{\gamma}_p^{(1)}$ obtained by removing the differentiated line in the *one-loop* part of the vertex flow in p channel, leaving two further amputated legs (marked in light red). (d) Inserting the vertex from (c) into the *center* part of the flow in the a channel, we generate a contribution to the six-point vertex $\mathring{\gamma}_a^{(C)}$ (being part of $\mathring{\gamma}_{\bar{t}}^{(C)}$). (e) By contracting two upper legs of the vertex from (d) according to $\mathring{\gamma}_{\bar{t}}^{(C)} \cdot G$, we get a contribution to the new, two-particle-irreducible vertex I_t'. The lowest-order realization of this, obtained by inserting a bare vertex for Γ, constitutes an envelope diagram, which is not contained in the initial I_t in the PA.

functional derivative of the self-energy is given by the bare vertex, $\delta\Sigma^{\mathrm{HF}}/\delta G = -\Gamma_0$. By replacing $I_t \to \Gamma_0$ in equation (31), we immediately find

$$\dot{\Sigma}^{\mathrm{HF}} = -\Gamma_0 \cdot \dot{G} = -(1 - \Gamma_0 \circ \Pi_t)^{-1} \circ \Gamma_0 \cdot S = -\Gamma_t^{\mathrm{lad}} \cdot S, \tag{32a}$$

$$\Gamma_t^{\mathrm{lad}} = \Gamma_0 + \Gamma_0 \circ \Pi_t \circ \Gamma_t^{\mathrm{lad}} \quad \Leftrightarrow \quad \Gamma_t^{\mathrm{lad}} = (1 - \Gamma_0 \circ \Pi_t)^{-1} \circ \Gamma_0, \tag{32b}$$

$$\dot{\Gamma}_t^{\mathrm{lad}} = \Gamma_0 \circ \dot{\Pi}_t \circ \Gamma_t^{\mathrm{lad}} + \Gamma_0 \circ \Pi_t \circ \dot{\Gamma}_t^{\mathrm{lad}} \;\Leftrightarrow\; \dot{\Gamma}_t^{\mathrm{lad}} = (1 - \Gamma_0 \circ \Pi_t)^{-1} \circ \Gamma_0 \circ \dot{\Pi}_t \circ \Gamma_t^{\mathrm{lad}} = \Gamma_t^{\mathrm{lad}} \circ \dot{\Pi}_t \circ \Gamma_t^{\mathrm{lad}}. \tag{32c}$$

Equation (32*c*) describes the vertex flow in the truncated Katanin form[6], restricted to the t channel. If the same vertex is used for the standard self-energy flow (equation (32*a*)), the fRG flow yields the HF self-energy together with a particle-hole ladder vertex (note $\hat{\Gamma}_t^{\mathrm{lad}} = -\Gamma_a^{\mathrm{lad}}$). As this vertex consists of ladder diagrams in only one channel, it clearly violates crossing symmetry.

4. Conservation laws in the PA

In this section, we take a slightly different perspective and are not concerned with RG flows. Instead, we use our insight into the structure of the many-body relations gained from the above derivations to address conceptual questions of many-body (parquet) theory. First, we derive two technical results: (i) we show how one can *construct* a two-particle-irreducible vertex which equals the functional derivative of the parquet self-energy. Evidently, the operation $\delta\Sigma/\delta G$ can be performed in an analytical study of Feynman diagrams [39]. However, in a numerical treatment, one never has access to the self-energy as a *functional* of the full propagator. Instead, one only has its value for the specific, given propagator, and the general construction for such a vertex remains unknown [15]. Here, we provide its construction for the case of the parquet self-energy. (ii) We demonstrate that the parquet self-energy can be obtained from the SDE using either of two possible orderings of the bare and full vertex. While it is believed that most approximations for Σ obtained from the SDE obey this property [14], it has (to our knowledge) not been shown for the PA. These results can then be interpreted in the context of conservation laws in the PA using arguments from Baym and Kadanoff [14].

4.1. Functional derivative of the parquet self-energy

We start from the flow equation for the self-energy in skeleton form: in the PA, we have $R = \Gamma_0$, and thus $R' = 0$ and $\dot{\Sigma}_3 = 0$, such that equation (26) reads

$$\dot{\Sigma}^{\mathrm{PA}} = -I_t \cdot \dot{G} - \dot{\gamma}_{\bar{t}}^{(C)} \cdot G. \tag{33}$$

As R is here given by the bare vertex, our construction of a scale-dependent Γ (section 2) and Σ (section 3) actually makes *every* propagator scale-dependent. Furthermore, this scale dependence is completely arbitrary, and we can view the scale derivative of the self-energy as coming from the chain rule, $\dot{\Sigma} = (\delta\Sigma/\delta G) \cdot \dot{G}$. Regarding equation (33), we want to similarly factorize $\dot{G}$ from the term $\dot{\gamma}_{\bar{t}}^{(C)} \cdot G$. For this, let $\mathring{\gamma}_{\bar{t}}^{(C)}$ be the six-point vertex obtained from $\dot{\gamma}_{\bar{t}}^{(C)}$ be removing the differentiated line, such that $\dot{\gamma}_{\bar{t}}^{(C)}$ is recovered by a contraction with $\dot{G}$, and $\dot{\gamma}_{\bar{t}}^{(C)} \cdot G = (\mathring{\gamma}_{\bar{t}}^{(C)} \cdot G) \cdot \dot{G}$ (see figures 5 (a) and (b)). It then follows from equation (33) that

---

[6] The substitution $S \to \dot{G}$ in the truncated fRG vertex flow is often called Katanin substitution [38].

$$\frac{\delta \Sigma^{\mathrm{PA}}}{\delta G} = -I_t - \mathring{\gamma}_{\bar{t}}^{(\mathrm{C})} \cdot G \equiv -I_t'. \tag{34}$$

Here, Σ^{PA} is the self-energy obtained from the SDE in the PA (using the vertex $\Gamma = I_t + I_t \circ \Pi_t \circ \Gamma$), and I_t' is the (new) two-particle-irreducible vertex that results from a functional derivative of the parquet self-energy. (The corresponding full vertex Γ' can be obtained by solving $\Gamma' = I_t' + I_t' \circ \Pi_t \circ \Gamma'$.) The crucial point is that —instead of taking the functional derivative—we can *construct* this vertex I_t' by taking the (initial) vertex I_t in the PA and adding the term $\mathring{\gamma}_{\bar{t}}^{(\mathrm{C})} \cdot G$; the six-point vertex $\mathring{\gamma}_{\bar{t}}^{(\mathrm{C})}$ needed for this can be constructed *iteratively*.

To elaborate this point, recall that the four-point vertex $\dot{\gamma}_{\bar{t}}^{(\mathrm{C})}$ constitutes a certain part of the vertex flow (10), which can be computed in a iterative one-loop fashion. To generate the six-point vertex $\mathring{\gamma}_{\bar{t}}^{(\mathrm{C})}$, one simply has to remove the differentiated line, $\dot{G}$, in this construction: one starts from a six-point vertex obtained by removing the differentiated line in the *one-loop part* of equation (10). Let us call the resulting object from the p channel $\mathring{\gamma}_p^{(1)}$. Then, $\mathring{\gamma}_p^{(1)}$ can be inserted into the *center part* of equation (10) to generate a first contribution for $\mathring{\gamma}_a^{(\mathrm{C})}$. These steps are illustrated in figures 5(c)–(e). Further contributions of $\mathring{\gamma}_r^{(\mathrm{C})}$ (for a certain channel r) are obtained as, e.g. $\mathring{\gamma}_r^{(1)}$ is inserted into the *left*, *right*, or *center* parts (see equation (10)) of channels $r' \neq r$ before inserting the resulting objects into $\mathring{\gamma}_r^{(\mathrm{C})}$. We remark that this scheme is directly accessible numerically by computing one-loop integral equations with six-point vertices. Though this will be computationally costly, it is conceptually not more complicated than computing the four-point mfRG flow. In fact, it is not surprising that one has to deal with six-point objects to go beyond the initial parquet vertex, since the PA exhausts (by construction) all diagrams that can be obtained in an iterative one-loop computation involving only four-point objects.

4.2. SDE with reversed order

Next, we show that the self-energy in the PA can equivalently be obtained from the SDE with either ordering of the involved vertices, i.e.

$$\Sigma^{\mathrm{PA}} = \Sigma_{\mathrm{SD}}(\Gamma_0, \Gamma, G) = \Sigma_{\mathrm{SD}}(\Gamma, \Gamma_0, G). \tag{35}$$

In section 3.1, we have used the expression $\Sigma_{\mathrm{SD}}(\Gamma_0, \Gamma, G)$ to derive the self-energy flow (26), which finally yielded equation (34) for the functional derivative in the PA. If we use the SDE in the 'reversed' order, we can actually follow these steps in close analogy to find the same relation for the functional derivative. First, starting from $\Sigma = \Sigma_{\mathrm{SD}}(\Gamma, \Gamma_0, G)$, we find a replication of equation (19) with reversed order:

$$\dot{\Sigma}_1 = -I_t \cdot \dot{G} + (\Gamma \circ \dot{\Pi} \circ \gamma_a + \Gamma \circ \dot{\Pi}_p \circ \gamma_p) \cdot G. \tag{36}$$

Concerning the simplifications of $\dot{\Sigma}_2$, we start from $(\dot{\Gamma} \circ \Pi_p \circ R) \cdot G$ to get (instead of equation (23))

$$\dot{\Sigma}_2 = -\sum_{r=a,p} (\dot{\gamma}_r \circ \Pi_r \circ I_r - \dot{I}_r \circ \Pi_r \circ \gamma_r) \cdot G. \tag{37}$$

Then, we use the BSE with 'reversed' order, $\gamma_r = \Gamma \circ \Pi_r \circ I_r$ (see equation (7)), to find the appropriate version of equation (25)

$$\dot{\Sigma}_2 = -\sum_{r=a,p} (\dot{\gamma}_r^{(\mathrm{C})} + \Gamma \circ \dot{\Pi}_r \circ \gamma_r) \cdot G. \tag{38}$$

The final manipulations can be made in complete analogy to obtain

$$\dot{\Sigma}^{\mathrm{PA}} = \dot{\Sigma}_1 + \dot{\Sigma}_2 = -I_t \cdot \dot{G} - \dot{\gamma}_{\bar{t}}^{(\mathrm{C})} \cdot G \quad \Rightarrow \quad \frac{\delta \Sigma^{\mathrm{PA}}}{\delta G} = -I_t - \mathring{\gamma}_{\bar{t}}^{(\mathrm{C})} \cdot G, \tag{39}$$

i.e. the identical differential equation (34). Since, for the specific propagator $G = 0$, one has $\Sigma_{\mathrm{SD}}(\Gamma_0, \Gamma, 0) = 0 = \Sigma_{\mathrm{SD}}(\Gamma, \Gamma_0, 0)$, it follows that the self-energy in the PA can indeed be obtained from any of the two versions of the SDE.

The strategy of generating, first, a self-energy via the SDE and, then, obtaining a vertex by functional differentiation has been famously put forward by Baym and Kadanoff [14]. They showed that, if the self-energy can equivalently be constructed via the SDE with either order of the vertices, then, the one-particle propagator is conserving. Thus, using this argument together with equation (35), one finds that the PA fulfills one-particle conservation laws. Baym and Kadanoff further showed that, if the vertices are subsequently constructed from $I_t' = -\delta\Sigma/\delta G$ and $\Gamma' = I_t' + I_t' \circ \Pi_t \circ \Gamma'$, two-particle conservation laws are fulfilled as well. As is well known, the PA does not fulfill two-particle conservation laws. In fact, equation (34) shows how the parquet vertex I_t needs to be modified to be conserving; in other words, the correction term $\mathring{\gamma}_{\bar{t}}^{(\mathrm{C})} \cdot G$ allows one to quantify to what degree the vertex I_t in the PA violates conservation laws.

Furthermore, equation (34) provides a construction how to generate a fully conserving solution originating from the parquet self-energy. After both the vertex I_t and the self-energy Σ^{PA} in the PA have been obtained, one computes $\mathring{\gamma}_{\bar{t}}^{(\mathrm{C})} \cdot G$ and adds this to I_t to get a conserving vertex I_t'. Note that the original parquet self-energy need not be modified. Similarly as one computes $\Gamma' = I_t' + I_t' \circ \Pi_t \circ \Gamma'$ with the original Π_t (containing Σ^{PA}),

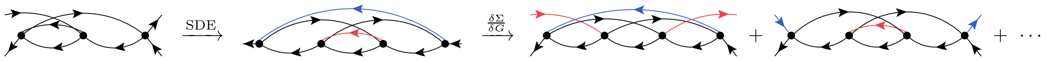

Figure 6. Illustration for the relation between (skeleton) diagrams of the vertex and the self-energy at fourth order in the interaction: inserting the first (parquet) vertex diagram into the SDE, we generate the second diagram as part of Σ^{PA}. Upon taking the functional derivative wrt to the full propagator, this self-energy diagram relates to multiple diagrams of the two-particle-irreducible vertex I_t. Among those, the third diagram, obtained by cutting the (light) red line, is an envelope diagram and not part of I_t in the PA. However, the fourth diagram, obtained by cutting the blue line, belongs to it. Note that we ignore signs and prefactors in these diagrams.

physical quantities (such as susceptibilities, conductivities, etc) are computed using I_t' (or Γ') together with Σ^{PA}. The resulting solution fulfills one- and two-particle conservation laws, but, clearly, it does not fulfill the SDE anymore. This is not surprising since, as shown in appendix B, a solution that fulfills both the SDE and the functional derivative must be the exact solution. The preferential choice between Γ and Γ' will surely depend on the physical application.

We remark that there have also been suggestions of how to keep the vertex I_t in the PA but modify the self-energy, Σ^{PA}, to obtain a thermodynamically consistent description [40]. While these ideas might be useful in practical situations, it is, however, not possible to construct a combination of the skeleton two-particle-irreducible vertex $I_t[G]$ in the PA together with *any* skeleton self-energy $\tilde{\Sigma}[G]$, such that the functional derivative $I_t = -\delta\tilde{\Sigma}/\delta G$ is fulfilled. The reason is that the functional derivative generates from any diagram of $\tilde{\Sigma}$ a multitude of diagrams for I_t—the same self-energy diagram related to missing diagrams of I_t in the PA also relates to diagrams that are contained in I_t (see figure 6). Therefore, the functional derivative cannot be fulfilled by starting from the PA and simply removing diagrams from the self-energy.

5. Response functions

Finally, we use our results from section 2 to derive dependent, mfRG flow equations for response functions. In fact, the (fermionic) four-point vertex, Γ, and the self-energy, Σ, give us full control over correlation functions up to the four-point level, and thus they suffice to compute response functions such as three-point vertices, $\Gamma^{(3)}$, and susceptibilities, χ. If Γ and Σ are obtained by an RG flow, the response functions can be deduced from the scale-dependent Γ^{Λ}, Σ^{Λ} at any stage during the flow. Alternatively, the response functions $\Gamma^{(3),\Lambda}$ and χ^{Λ} are often deduced from their own RG flows [5]. In this case, the flow equations provided by the standard fRG hierarchy again require knowledge about unknown, higher-point vertices (namely a five-point vertex for the flow of $\Gamma^{(3)}$ and a boson-fermion four-point vertex for χ) [6]. In particular, the inevitable truncation in the fRG hierarchy leads to ambiguities in the computation of the response function [13, 41]. These ambiguities have been recently resolved by a diagrammatic derivation of the mfRG flow equations for the response functions [13]. Here, we provide algebraic derivations of these flow equations. We find that one can circumvent the influence of unknown, higher-point vertices by using exact flow equations for the response functions, which follow from the standard relations between the response functions and the (known) fermionic four-point vertex and self-energy.

5.1. Three-point vertex

The SDE relating the (full) three-point vertex to the bare three-point vertex (often taken to be unity) and the four-point vertex [6] is given by (see figure 7)

$$\Gamma^{(3)}_r = \Gamma^{(3)}_{r,0} + \Gamma^{(3)}_{r,0} \circ \Pi_r \circ \Gamma. \tag{40}$$

Employing the scale dependence described in the previous sections, we can differentiate equation (40) to get

$$\dot{\Gamma}^{(3)}_r = \Gamma^{(3)}_{r,0} \circ \dot{\Pi}_r \circ \Gamma + \Gamma^{(3)}_{r,0} \circ \Pi_r \circ \dot{\Gamma} = \Gamma^{(3)}_{r,0} \circ \dot{\Pi}_r \circ \Gamma + \Gamma^{(3)}_{r,0} \circ \Pi_r \circ (\dot{I}_r + \dot{\gamma}_r). \tag{41}$$

We insert the mfRG vertex flow (10), combine several terms according to equation (40), and obtain

$$\begin{aligned}\dot{\Gamma}^{(3)}_r &= \Gamma^{(3)}_{r,0} \circ \dot{\Pi}_r \circ \Gamma + \Gamma^{(3)}_{r,0} \circ \Pi_r \circ \dot{I}_r + \Gamma^{(3)}_{r,0} \circ \Pi_r \circ (\Gamma \circ \dot{\Pi}_r \circ \Gamma + \Gamma \circ \Pi_r \circ \dot{I}_r + \dot{I}_r \circ \Pi_r \circ \Gamma + \Gamma \circ \Pi_r \circ \dot{I}_r \circ \Pi_r \circ \Gamma)\\ &= \Gamma^{(3)}_r \circ \dot{\Pi}_r \circ \Gamma + \Gamma^{(3)}_r \circ \Pi_r \circ (\dot{I}_r + \dot{I}_r \circ \Pi_r \circ \Gamma).\end{aligned} \tag{42}$$

The first term occurs similarly in the fRG flow equation (with the typical replacement $\dot{G} \leftrightarrow S$). However, the remaining part of our flow equation successfully replaces the contributions from the unknown five-point vertex in the fRG flow.

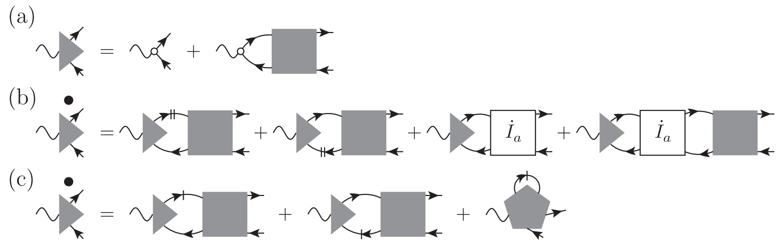

Figure 7. Illustration of three exact equations for the three-point vertex in the *a* channel: (a) Schwinger–Dyson equation between three- and four-point vertex; the white dot denotes the bare three-point vertex; (b) mfRG flow equation containing differentiated vertices from the complementary channel, $\dot{I}_a = \dot{\gamma}_{\bar{a}}$; and (c) standard fRG flow equation containing an unknown five-point vertex.

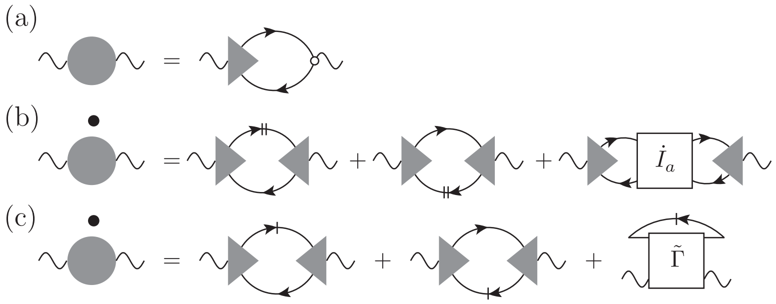

Figure 8. Illustration of three exact equations for the susceptibility in the *a* channel: (a) Schwinger–Dyson equation relating the susceptibility to the full and bare three-point vertex; (b) mfRG flow equation containing differentiated vertices from the complementary channel, $\dot{I}_a = \dot{\gamma}_{\bar{a}}$; and (c) standard fRG flow equation containing an unknown fermion-boson four-point vertex $\tilde{\Gamma}$.

5.2. Susceptibility

The susceptibility is fully determined by the three-point vertex or (via equation (40)) the four-point vertex [6], according to (see figure 8)

$$\chi_r = \Gamma_r^{(3)} \circ \Pi_r \circ \Gamma_{r,0}^{(3)\dagger} = \Gamma_{r,0}^{(3)} \circ \Pi_r \circ \Gamma_{r,0}^{(3)\dagger} + \Gamma_{r,0}^{(3)} \circ \Pi_r \circ \Gamma \circ \Pi_r \circ \Gamma_{r,0}^{(3)\dagger}. \tag{43}$$

We can differentiate either relation; choosing the first one, we insert the mfRG flow (42) of $\Gamma^{(3)}$ to find the mfRG flow of the susceptibility:

$$\begin{aligned} \dot{\chi}_r &= \Gamma_r^{(3)} \circ \dot{\Pi}_r \circ \Gamma_{r,0}^{(3)\dagger} + \dot{\Gamma}_r^{(3)} \circ \Pi_r \circ \Gamma_{r,0}^{(3)\dagger} \\ &= \Gamma_r^{(3)} \circ \dot{\Pi}_r \circ \Gamma_{r,0}^{(3)\dagger} + (\Gamma_r^{(3)} \circ \dot{\Pi}_r \circ \Gamma \circ \ + \Gamma_r^{(3)} \circ \Pi_r \circ \dot{I}_r + \Gamma_r^{(3)} \circ \Pi_r \circ \dot{I}_r \circ \Pi_r \circ \Gamma) \circ \Pi_r \circ \Gamma_{r,0}^{(3)\dagger} \\ &= \Gamma_r^{(3)} \circ \dot{\Pi}_r \circ \Gamma_r^{(3)\dagger} + \Gamma_r^{(3)} \circ \Pi_r \circ \dot{I}_r \circ \Pi_r \circ \Gamma_r^{(3)\dagger}. \end{aligned} \tag{44}$$

Again, the first term occurs similarly in the fRG flow equation (with $\dot{G} \leftrightarrow S$), and the remaining terms in our flow equation replace the contributions from the unknown boson-fermion four-point vertex in the fRG flow.

Let us briefly summarize: the response functions $\Gamma^{(3)}$, χ can be deduced from the four-point vertex, Γ, and the self-energy, Σ, at any point of the RG fow. As Γ and Σ evolve with Λ, so do $\Gamma^{(3)}$ and χ. With the above derivation, we have cast this evolution into exact, mfRG flow equations for the response function, each containing the vertex flow from the complementary channel ($\dot{I}_r = \dot{\gamma}_{\bar{r}}$). The two-particle-reducible vertices still obey the mfRG flow (10); approximations come from the chosen expression for the totally irreducible vertex, *R*, which affects the initial conditions but is itself not part of the flow.

6. Conclusion

We have used the well-known self-consistent relations of the parquet formalism to derive exact flow equations for various vertex and correlation functions. Compared to the standard fRG framework, these mfRG flow equations can be advantageous as they circumvent the reliance on higher-point vertices. In fact, our calculations include concise, algebraic derivations of the mfRG flow equations that have previously been derived diagrammatically [11–13] and have already been used [11, 13] to improve the approximations of the truncated fRG flow (for results of two-loop fRG, see [22, 42, 43]).

The analysis presented in this paper puts the mfRG approach on a general basis. The algebraic derivations open the route to RG flows beyond the diagrams of the PA. Since the totally irreducible vertex, R, is precisely the part of the vertex that cannot be efficiently included in the flow, the focus can now shift to systematic ways of computing R. If one chooses a scale dependence in the propagators that starts from $G_0^{\Lambda_i} = 0$, all reducible contributions built on R will be fully included by the mfRG flow. Other starting points for the flow are a possible as well. In particular, if one uses as initial, bare propagator the (self-consistently determined) one from DMFT, $G_0^{\Lambda_i} = G_0^{\mathrm{DMFT}}$, the nonlocal correlations not contained in DMFT will be added by a flow that starts from the self-energy Σ^{DMFT} and the full vertex Γ^{DMFT} [26], thus circumventing potential divergences of R^{DMFT}. Similarly, if the system in question is related to another, solvable reference system [22] by variation of one-particle parameters, mfRG can be used to tune between these systems via G_0^{Λ}, with the guarantee that the self-consistent parquet equations are fulfilled throughout the flow. As examples, let us mention Fermi polarons [44, 45], where one can tune the chemical potential of the majority species, and nonequilibrium transport (see below), where one can gradually increase the bias voltage. Our computations also provide a basis for setting up mfRG flows for more complicated theories, including, for instance, further bosonic degrees of freedom. Generally, we believe that the insights presented in this paper will be useful for further development of quantum-field-theoretical RG techniques.

Additionally, we have demonstrated an intimate relation between the functional derivative of the self-energy (inducing a conserving solution) and the (standard) fRG self-energy flow: the flow equation directly follows from the functional derivative for the case that the propagator is varied through a scale parameter. However, a solution of the fRG flow is consistent with the functional derivative only if the flow is independent of the specific scale dependence, i.e. only if $\Gamma \cdot S$ constitutes a total derivative of diagrams. A simple example for which this is indeed the case is given by a truncated fRG flow with a (particle-hole) ladder vertex that reproduces self-consistent HF. Building on this, it would be worthwhile to devise other approximate flows that comply with the functional derivative but go beyond HF, thereby including an interplay between different two-particle channels.

Lastly, we have used our approach to address important general questions of (traditional) parquet theory. Using an argument of Baym and Kadanoff [14], we have demonstrated that the PA fulfills one-particle conservation laws. Furthermore, we have shown how to *construct* a two-particle-irreducible vertex equivalent to taking the functional derivative of the parquet self-energy. With this, one can quantify to what extent the PA violates two-particle conservation laws, and one can modify the PA to obtain a fully conserving approximation. It would be interesting to apply this modified parquet approach in situations where conservation properties are crucial, such as studies of transport phenomena.

The generality of our formalism opens up a vast field of applications. mfRG flows have already yielded impressive results for the prototypical 2D Hubbard model [13] (see [42] for results using two-loop fRG) and promise a better understanding of strongly correlated electron systems [5, 12, 20]. In the study of quantum magnetism, the pseudo-fermion fRG approach [46] has become a competing method, and first calculations with two-loop corrections [43] suggest that a full multiloop treatment would yield further improvements. Moreover, mfRG can be directly applied to a variety of interesting physical problems where the most relevant properties are expected to emerge within the PA, such as various forms of mobile impurity problems [45, 47] or one-dimensional fermion systems [48] beyond the Luttinger liquid paradigm [49]. In the field of transport phenomena in disordered systems, our mfRG approach could provide unprecedented insight into many-body localization in large systems [50, 51] or interaction effects on the Anderson localization transition [52]. Finally, we remark that mfRG flows can also be naturally set up within the Keldysh formalism [23, 53] to provide real-frequency information, both in and out of equilibrium.

Acknowledgments

We thank S Andergassen, P Chalupa, A Tagliavini, and A Toschi for useful discussions at TU Wien. We thank O Yevtushenko as well as A Toschi for a careful reading of the manuscript and A A Katanin for helpful correspondence. We acknowledge support by the Cluster of Excellence Nanosystems Initiative Munich; FBK acknowledges funding from the research school IMPRS-QST.

Appendix A. Matrix notation of bubbles and loops

In this section, we define our notation for the contraction of various vertex functions. It is common to view the contraction of one-particle quantities as matrix multiplications, such that e.g. the Dyson equation between

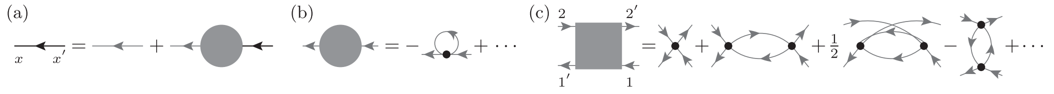

Figure A1. (a) Dyson's equation relating the full propagator $G_{x,x'}$ (black, thick line) to the bare propagator G_0 (gray, thin line) and the self-energy Σ (circle). (b) First-order diagram for the self-energy using the (antisymmetrized) bare vertex Γ_0 (solid dot). (c) Diagrammatic expansion of the four-point vertex Γ (square) up to second order in the interaction. The positions of the external (amputated) legs refer to the arguments of $\Gamma_{x_1',x_2';x_1',x_2'}$. Diagrams from left to right belong to R, γ_a, γ_p, and γ_t, respectively; diagrams for I_r follow from the relation $I_r = \Gamma - \gamma_r$.

propagator, $G_{x,x'} = -\langle c_x \bar{c}_{x'} \rangle$, and the self-energy, $\Sigma_{x',x}$, (see figures A1(a) and (b)) reads

$$G = G_0 + G_0 \cdot \Sigma \cdot G, \qquad (A \cdot B)_{x,x'} = \sum_y A_{x,y} B_{y,x'}. \tag{A1}$$

For the contraction of two four-point vertices, we have three inequivalent possibilities corresponding to the three two-particle channels $r = a, p, t$ (standing for antiparallel, parallel, transverse, respectively; see also figure A1(c)). In [12], the different combinations have been labeled as 'bubble functions' $B_r(\Gamma,\ \Gamma')$. Here, we repeat the corresponding equations and show that they can be conveniently written as matrix multiplications. For this, we will use auxiliary objects that depend on channel-dependent tuples of quantum numbers (e.g. $\Gamma_{x_1',x_2';x_1',x_2'} = \tilde{\Gamma}_{a;(x_1',x_2'),(x_2',x_1')}$) and define a contraction $\circ$ that always comes together with a two-particle propagator Π_r of a certain channel (consisting of two one-particle propagators G):

$$\begin{aligned} B_a(\Gamma,\ \Gamma')_{x_1',x_2';x_1',x_2'} &= \sum_{y_1',y_1',y_2',y_2'} \Gamma_{x_1',y_2';y_1',x_2'} G_{y_1',y_1'} G_{y_2',y_2'} \Gamma'_{y_1',x_2';x_1',y_2'} \\ &= \sum_{y_1',y_1',y_2',y_2'} \tilde{\Gamma}_{a;(x_1',x_2'),(y_2',y_1')} \tilde{\Pi}_{a;(y_2',y_1'),(y_1',y_2')} \tilde{\Gamma}'_{a;(y_1',y_2'),(x_2',x_1')} \equiv (\Gamma \circ \Pi_a \circ \Gamma')_{x_1',x_2';x_1',x_2'}, \end{aligned} \tag{A2a}$$

$$\begin{aligned} B_p(\Gamma,\ \Gamma')_{x_1',x_2';x_1',x_2'} &= \frac{1}{2} \sum_{y_1',y_1',y_2',y_2'} \Gamma_{x_1',x_2';y_1,y_2'} G_{y_1',y_1'} G_{y_2',y_2'} \Gamma'_{y_1',y_2';x_1',x_2'} \\ &= \sum_{y_1',y_1',y_2',y_2'} \tilde{\Gamma}_{p;(x_1',x_2'),(y_1',y_2')} \tilde{\Pi}_{p;(y_1',y_2'),(y_1',y_2')} \tilde{\Gamma}'_{p;(y_1',y_2'),(x_1',x_2')} \equiv (\Gamma \circ \Pi_p \circ \Gamma')_{x_1',x_2';x_1',x_2'}, \end{aligned} \tag{A2b}$$

$$\begin{aligned} B_t(\Gamma,\ \Gamma')_{x_1',x_2';x_1',x_2'} &= -\sum_{y_1',y_1',y_2',y_2'} \Gamma_{y_1',x_2';y_1',x_2'} G_{y_2',y_1'} G_{y_1',y_2'} \Gamma'_{x_1',y_2';x_1',y_2'} \\ &= \sum_{(y_1',y_1'),(y_2',y_2')} \tilde{\Gamma}_{t;(x_2',x_2'),(y_1',y_1')} \tilde{\Pi}_{t;(y_1',y_1'),(y_2',y_2')} \tilde{\Gamma}'_{t;(y_2',y_2'),(x_1',x_1')} \equiv (\Gamma \circ \Pi_t \circ \Gamma')_{x_1',x_2';x_1',x_2'}. \end{aligned} \tag{A2c}$$

Note that a factor of $1/2$ has been absorbed into Π_p and a minus sign into Π_t. From equations (1) and (3), it is clear that Γ_0 and Γ are antisymmetric in their indices. Using the bubble functions (A2) together with the parquet equations (4), one finds the further crossing symmetries stated in equation (13), which use the symbol

$$\hat{\Gamma}_{x_1',x_2';x_1',x_2'} = \Gamma_{x_1',x_2';x_2',x_1'} = \Gamma_{x_2',x_1';x_1',x_2'}. \tag{A3}$$

If we combine two fermionic indices into one bosonic index, the above equations directly translate to three-point vertices. For instance, one could combine the two external legs of the first vertex in the a bubble according to some function f and interpret

$$\Gamma^{(3)}_{a;z,x_2',x_1'} = \sum_{x_1',x_2'} f_{z,x_1',x_2'} \Gamma_{x_1',y_2';y_1',x_2'} \quad \Rightarrow \quad (\Gamma^{(3)}_a \circ \Pi_a \circ \Gamma')_{z,x_2',x_1'} = \sum_{x_1',x_2'} f_{z,x_1',x_2'} (\Gamma \circ \Pi_a \circ \Gamma')_{x_1',x_2';x_1',x_2'}. \tag{A4}$$

Furthermore, one can contract a four-point vertex with a one-particle propagator to obtain another one-particle object. We define the symbol $\cdot$ between vertex and propagator to be such a contraction applied to the 'upper' external legs of the vertex (i.e. legs 2 and 2′ in figure A1(c)). In [12], this has been dubbed a 'self-energy loop', L, defined as

$$-L(\Gamma,\ G)_{x',x'} = \sum_{y',y} \Gamma_{x',y';x,y} G_{y,y'} = \sum_{(y',y)} \tilde{\Gamma}_{t;(x',x),(y',y)} \tilde{G}_{(y',y)} \equiv (\Gamma \cdot G)_{x',x'}. \tag{A5}$$

If the contracting line is a composite object of the type $G \cdot \Sigma \cdot G$, we can view the G lines as a t bubble attached to the vertex, according to

$$
\begin{aligned}
(\Gamma \cdot (G \cdot \Sigma \cdot G))_{x',x} &= \sum_{y',y,z',z} \Gamma_{x',y';x,y} G_{y,z'} \Sigma_{z',z} G_{z,y'} \\
&= -\sum_{(y',y),(z',z)} \tilde{\Gamma}_{t;(x',x),(y',y)} \tilde{\Pi}_{t;(y',y),(z',z)} \tilde{\Sigma}_{(z',z)} \equiv -(\Gamma \circ \Pi_t \cdot \Sigma)_{x',x}. \qquad \text{(A6)}
\end{aligned}
$$

The SDE for the self-energy contains a contraction of three propagators. Using the bubble functions defined above, this can equivalently be written with Π_p and Π_a:

$$
\begin{aligned}
-\Sigma_{x',x} &= \sum_{y',y} \Gamma_{0;x',y';x,y} G_{y,y'} + \tfrac{1}{2} \sum_{y',y,z',z,w',w} \Gamma^{0}_{x',z';y,w} G_{y,y'} G_{z,z'} G_{w,w'} \Gamma_{y',w';x,z} \\
&= \Big((\Gamma_0 + \Gamma_0 \circ \Pi_p \circ \Gamma) \cdot G \Big)_{x',x} = \Big((\Gamma_0 + \tfrac{1}{2} \Gamma_0 \circ \Pi_a \circ \Gamma) \cdot G \Big)_{x',x}. \qquad \text{(A7)}
\end{aligned}
$$

The functional derivative between self-energy and two-particle-irreducible vertex (in the *t* or *a* channel) is given by

$$
\frac{\delta \Sigma_{x',x}}{\delta G_{y,y'}} = -I_{t;x',y';x,y} = I_{a;x',y';y,x}. \qquad \text{(A8)}
$$

Note that in order to obtain the two-particle-irreducible vertex in the *p* channel from functional differentiation, $I_{p;x',y';x,y} = \delta \Sigma_{x',y'} / \delta G_{x,y}$, one has to allow for variations around the physical solution which break charge conservation.

Appendix B. SDE and functional derivative

We consider the SDE for the self-energy as well as the functional derivative between self-energy and vertex (see equation (A8)),

$$
\Sigma = -\Gamma_0 \cdot G - (\Gamma_0 \circ \Pi_p \circ \Gamma) \cdot G, \qquad \text{(B1}a\text{)}
$$

$$
I_t = -\frac{\delta \Sigma}{\delta G}, \qquad \Gamma = I_t + I_t \circ \Pi_t \circ \Gamma, \qquad \text{(B1}b\text{)}
$$

and show that a solution for Σ and Γ that fulfills both equations (B1*a*) and (B1*b*) must necessarily be the exact solution. In essence, this proof has already been given by Smith [15]. However, we find it useful to present it here in our notation, which exclusively consists of properly symmetrized objects. In fact, this proof puts on solid ground what has long been known to the community [2]: in any approximate solution to the many-body problem, one has to decide whether to comply with *either* conservation laws *or* crossing symmetry; achieving both amounts to finding the exact solution.

To be able to apply the functional derivative, we consider the self-energy as a functional of the full propagator, $\Sigma[G]$. This is perfectly compatible with the SDE (B1*a*), which is formulated using full propagators only. Furthermore, all vertex functions depend on the given theory's bare vertex Γ_0 (which we here label $\Gamma_0 = U$ for ease of notation); in particular, this holds for $\Sigma[G, U]$ and $\Gamma[G, U]$. Since U is the bare vertex, we have $\Gamma[G, U] = U + O(G^2, U^2)$; by use of either the SDE (B1*a*) or the functional derivative (B1*b*), it is clear that $\Sigma[G, U] = U \cdot G + O(G^3, U^2)$.

Assume that we know the exact vertex up to terms of order $n \geqslant 2$ in both G and U, i.e., $\Gamma = \Gamma^{\text{ex}} + O(G^n, U^n)$. If we apply the SDE (B1*a*), we obtain (inserting into the second term) $\Sigma = \Sigma^{\text{ex}} + O(G^{n+3}, U^{n+1})$. Now, we apply the functional derivative (B1*b*) and get $I_t = I_t^{\text{ex}} + O(G^{n+2}, U^{n+1})$. Finally, using the BSE (B1*b*) yields $\Gamma = \Gamma^{\text{ex}} + O(G^{n+2}, U^{n+1})$, i.e. the exact vertex one order higher in G^2 and U than we started with. Since we do know the exact vertex up to terms of second order, $\Gamma[G, U] = U + O(G^2, U^2)$, it follows by induction that a solution which fulfills both equation (B1*a*) and (B1*b*) consists of the exact functionals $\Sigma^{\text{ex}}[G, U]$, $\Gamma^{\text{ex}}[G, U]$.

We remark that this proof applies equivalently to finite-order approximations of Σ and Γ as well as to approximations of infinite order in U. As soon as an expression for Γ contains the bare vertex U [15], the combination of equation (B1*a*) and (B1*b*) requires *all* expansion coefficients of Σ and Γ to be the ones of the exact solution.

ORCID iDs

Fabian B Kugler https://orcid.org/0000-0002-3108-6607
Jan von Delft https://orcid.org/0000-0002-8655-0999

References

[1] Hedin L 1965 *Phys. Rev.* **139** A796
[2] Bickers N 2004 *Theoretical Methods for Strongly Correlated Electrons* (*CRM Series in Mathematical*) ed D Sénéchal, A-M Tremblay and C Bourbonnais (New York: Springer) pp 237–96

[3] Wilson K G 1975 *Rev. Mod. Phys.* **47** 773–840

[4] Anderson P W 1970 *J. Phys.* C **3** 2436

[5] Metzner W, Salmhofer M, Honerkamp C, Meden V and Schönhammer K 2012 *Rev. Mod. Phys.* **84** 299

[6] Kopietz P, Bartosch L and Schütz F 2010 *Introduction to the Functional Renormalization Group* (*Lecture Notes in Physics*) (Berlin: Springer)

[7] Wetterich C 1993 *Phys. Lett.* B **301** 90

[8] Veschgini K and Salmhofer M 2013 *Phys. Rev.* B **88** 155131

[9] Roulet B, Gavoret J and Nozières P 1969 *Phys. Rev.* **178** 1072

[10] Shankar R 1994 *Rev. Mod. Phys.* **66** 129

[11] Kugler F B and von Delft J 2018 *Phys. Rev. Lett.* **120** 057403

[12] Kugler F B and von Delft J 2018 *Phys. Rev.* B **97** 035162

[13] Tagliavini A, Hille C, Kugler F B, Andergassen S, Toschi A and Honerkamp C 2018 arXiv:1807.02697

[14] Baym G and Kadanoff L P 1961 *Phys. Rev.* **124** 287

[15] Smith R A 1992 *Phys. Rev.* A **46** 4586

[16] Yang S X, Fotso H, Liu J, Maier T A, Tomko K, D'Azevedo E F, Scalettar R T, Pruschke T and Jarrell M 2009 *Phys. Rev.* E **80** 046706

[17] Tam K-M, Fotso H, Yang S-X, Lee T-W, Moreno J, Ramanujam J and Jarrell M 2013 *Phys. Rev.* E **87** 013311

[18] Li G, Wentzell N, Pudleiner P, Thunström P and Held K 2016 *Phys. Rev.* B **93** 165103

[19] Abrikosov A A 1965 *Physics* **2** 5

[20] Rohringer G, Hafermann H, Toschi A, Katanin A A, Antipov A E, Katsnelson M I, Lichtenstein A I, Rubtsov A N and Held K 2018 *Rev. Mod. Phys.* **90** 025003

[21] Rohringer G, Valli A and Toschi A 2012 *Phys. Rev.* B **86** 125114

[22] Wentzell N, Li G, Tagliavini A, Taranto C, Rohringer G, Held K, Toschi A and Andergassen S 2016 arXiv:1610.06520

[23] Jakobs S G, Pletyukhov M and Schoeller H 2010 *Phys. Rev.* B **81** 195109

[24] Wentzell N, Taranto C, Katanin A, Toschi A and Andergassen S 2015 *Phys. Rev.* B **91** 045120

[25] Georges A, Kotliar G, Krauth W and Rozenberg M J 1996 *Rev. Mod. Phys.* **68** 13

[26] Taranto C, Andergassen S, Bauer J, Held K, Katanin A, Metzner W, Rohringer G and Toschi A 2014 *Phys. Rev. Lett.* **112** 196402

[27] Tagliavini A 2018 *PhD Thesis* Universität Tübingen

[28] Toschi A, Katanin A A and Held K 2007 *Phys. Rev.* B **75** 045118

[29] Held K, Katanin A A and Toschi A 2008 *Prog. Theor. Phys. Supp.* **176** 117

[30] Valli A, Schäfer T, Thunström P, Rohringer G, Andergassen S, Sangiovanni G, Held K and Toschi A 2015 *Phys. Rev.* B **91** 115115

[31] Schäfer T, Rohringer G, Gunnarsson O, Ciuchi S, Sangiovanni G and Toschi A 2013 *Phys. Rev. Lett.* **110** 246405

[32] Schäfer T, Ciuchi S, Wallerberger M, Thunström P, Gunnarsson O, Sangiovanni G, Rohringer G and Toschi A 2016 *Phys. Rev.* B **94** 235108

[33] Gunnarsson O, Rohringer G, Schäfer T, Sangiovanni G and Toschi A 2017 *Phys. Rev. Lett.* **119** 056402

[34] Chalupa P, Gunacker P, Schäfer T, Held K and Toschi A 2018 *Phys. Rev.* B **97** 245136

[35] Thunström P, Gunnarsson O, Ciuchi S and Rohringer G 2018 *Phys. Rev.* B **98** 235107

[36] Luttinger J M and Ward J C 1960 *Phys. Rev.* **118** 1417

[37] Baym G 1962 *Phys. Rev.* **127** 1391

[38] Katanin A A 2004 *Phys. Rev.* B **70** 115109

[39] Kugler F B 2018 *Phys. Rev.* E **98** 023303

[40] Janiš V, Kauch A and Pokorný V 2017 *Phys. Rev.* B **95** 045108

[41] Kugler F B and von Delft J 2018 *J. Phys.: Condens. Matter* **30** 195501

[42] Eberlein A 2014 *Phys. Rev.* B **90** 115125

[43] Rück M and Reuther J 2018 *Phys. Rev.* B **97** 144404

[44] Mitra T, Chatterjee A and Mukhopadhyay S 1987 *Phys. Rep.* **153** 91

[45] Schmidt R, Knap M, Ivanov D A, You J-S, Cetina M and Demler E 2018 *Rep. Prog. Phys.* **81** 024401

[46] Reuther J and Wölfle P 2010 *Phys. Rev.* B **81** 144410

[47] Schmidt R and Enss T 2011 *Phys. Rev.* A **83** 063620

[48] Meden V, Andergassen S, Enss T, Schoeller H and Schönhammer K 2008 *New J. Phys.* **10** 045012

[49] Imambekov A, Schmidt T L and Glazman L I 2012 *Rev. Mod. Phys.* **84** 1253

[50] Abanin D A and Papić Z 2017 *Ann. Phys.* **529** 1700169

[51] Pietracaprina F, Macé N, Luitz D J and Alet F 2018 *SciPost Phys.* **5** 045

[52] Amini M, Kravtsov V E and Müller M 2014 *New J. Phys.* **16** 015022

[53] Jakobs S G, Pletyukhov M and Schoeller H 2010 *J. Phys.* A **43** 103001

4 Counting of Feynman diagrams

4.1 Overview

Feynman diagrams, graphical representations for the myriad of mathematical expressions in quantum field theory, “have revolutionized nearly every aspect of theoretical physics” [Kai05]. They are an indispensable tool of many-body theory and have already appeared in various forms within this thesis: They allow one to (i) perform and organize the many-body perturbation theory (Sec. 2.1); (ii) construct resummations of the perturbation series as well as renormalization group flows (Sec. 2.3 and Chapter 3); and (iii) characterize fully nonperturbative approaches such as DMFT (Sec. 2.4.1) and especially diagrammatic extensions thereof (Sec. 2.5). In order to estimate the power of a given diagrammatic resummation or to compare different approximate approaches, it is often useful to count the number of Feynman diagrams involved. Furthermore, the asymptotic number of Feynman diagrams with the interaction order is of particular interest as it can be linked to convergence properties of the corresponding perturbation series [NO98].

The following article [P6] presents an algorithm to count the number of Feynman diagrams of various quantities from the set of many-body relations that generates their solution. The algorithm, inspired by the comparison of diagrams in the PA and truncated fRG flows in [P2, P3], can be applied to diverse approximations and even the exact solution. Its iterative form ensures numerical access to arbitrarily large interaction orders, and its general structure enables analytic statements about the asymptotic number of Feynman diagrams.

P6 *Counting Feynman diagrams via many-body relations*
F. B. Kugler
Phys. Rev. E **98**, 023303 (2018)
DOI: 10.1103/PhysRevE.98.023303
© 2018 American Physical Society
reprinted on pages 141–149.

Counting Feynman diagrams via many-body relations

Fabian B. Kugler
Physics Department, Arnold Sommerfeld Center for Theoretical Physics, and Center for NanoScience, Ludwig-Maximilians-Universität München, Theresienstr. 37, 80333 Munich, Germany

(Received 13 May 2018; published 7 August 2018)

We present an iterative algorithm to count Feynman diagrams via many-body relations. The algorithm allows us to count the number of diagrams of the exact solution for the general fermionic many-body problem at each order in the interaction. Further, we apply it to different parquet-type approximations and consider spin-resolved diagrams in the Hubbard model. Low-order results and asymptotics are explicitly discussed for various vertex functions and different two-particle channels. The algorithm can easily be implemented and generalized to many-body relations of different forms and levels of approximation.

DOI: 10.1103/PhysRevE.98.023303

I. INTRODUCTION

In the study of many-particle systems, Feynman diagrams are a ubiquitous, powerful tool to perform and organize perturbation series as well as partial resummations thereof. To gain intuition about the strength of a diagrammatic resummation or to compare different variants of resummation, it can be useful to count the number of diagrams involved, ideally for several kinds of vertex functions. Moreover, the factorial growth in the number of diagrams with the interaction order is often linked with the nonconvergent, asymptotic nature of (bare) perturbation series [1]. The asymptotic number of diagrams generated by approximate solutions is therefore of particular interest.

In this paper, we present an algorithm to count the number of Feynman diagrams inherent in many-body integral equations. Its iterative structure allows us to numerically access arbitrarily large interaction orders and to gain analytical insights about the asymptotic behavior. In Sec. II we recapitulate typical many-body relations as a basis for the algorithm. The algorithm is explained in Sec. III, where some general parts of the discussion follow Ref. [2] quite closely; some of the ideas have also been formulated by Smith [3]. In Sec. IV we use the algorithm to count the exact number of bare and skeleton diagrams of the general many-body problem for various vertex functions and to discuss their asymptotics. Subsequently, we consider parquet-type approximations as examples for approximate solutions, and we focus on the Hubbard model to discuss spin-resolved diagrams. Finally, we present our conclusions in Sec. V.

II. MANY-BODY RELATIONS

A general theory of interacting fermions is defined by the action

$$S = -\sum_{x',x} \bar{c}_{x'} \left(G_0^{-1}\right)_{x',x} c_x - \frac{1}{4} \sum_{x',x,y',y} \Gamma^{(4)}_{0;x',y';x,y} \bar{c}_{x'} \bar{c}_{y'} c_y c_x, \tag{1}$$

where G_0 is the bare propagator, $\Gamma^{(4)}_0$ the bare four-point vertex, which is antisymmetric in its first and last two arguments, and x denotes all quantum numbers of the Grassmann field c_x. If we choose, e.g., Matsubara frequency, momentum, and spin, with $x = (i\omega, \boldsymbol{k}, \sigma) = (k, \sigma)$, and consider a translationally invariant system with interaction $U_{|\boldsymbol{k}|}$, the bare quantities read

$$G_{0;x',x} \overset{\text{e.g.}}{=} G_{0;k,\sigma} \delta_{k',k}\, \delta_{\sigma',\sigma}\,, \tag{2a}$$

$$-\Gamma^{(4)}_{0;x_1',x_2';x_1,x_2} \overset{\text{e.g.}}{=} \big(U_{|\boldsymbol{k}_1'-\boldsymbol{k}_1|} \delta_{\sigma_1',\sigma_1} \delta_{\sigma_2',\sigma_2} - U_{|\boldsymbol{k}_1'-\boldsymbol{k}_2|} \delta_{\sigma_1',\sigma_2} \delta_{\sigma_2',\sigma_1}\big)\, \delta_{k_1'+k_2',k_1+k_2}. \tag{2b}$$

Interested in one- and two-particle correlations, the many-body theory is usually focused on the full propagator G with self-energy Σ and the full one-particle-irreducible (1PI) four-point vertex $\Gamma^{(4)}$, which can be decomposed into two-particle-irreducible vertices I_r in different two-particle channels $r \in \{a, p, t\}$ (see below). The quantities G, Σ, $\Gamma^{(4)}$ are related by the exact and closed set of equations [4–7]

$$G = G_0 + G_0 \cdot \Sigma \cdot G, \tag{3a}$$

$$\Sigma = -\Gamma^{(4)}_0 \circ G - \frac{1}{2} \Gamma^{(4)}_0 \circ G \circ G \circ G \circ \Gamma^{(4)}, \tag{3b}$$

$$\Gamma^{(4)} = I_t - I_t \circ G \circ G \circ \Gamma^{(4)}, \quad I_t = -\frac{\delta \Sigma}{\delta G}, \tag{3c}$$

where $\cdot$ represents a matrix product and $\circ$ a suitable contraction of indices [8]. The first equation is the well-known Dyson equation, the second one the Schwinger-Dyson equation (SDE, or equation of motion) for the self-energy, and the last one a Bethe-Salpeter equation (BSE), where the irreducible vertex I_t is obtained by a functional derivative of Σ w.r.t. G. These equations together with further equations discussed below are illustrated in Fig. 1.

The relation between I_t and Σ is closely related [7] to an exact flow equation of the functional renormalization group (fRG) framework [9,10]. There, the theory evolves under the RG flow by variation of a scale parameter Λ, introduced in the bare propagator. Consequently, all vertex functions develop a scale dependence (which is suppressed in the notation),

©2018 American Physical Society

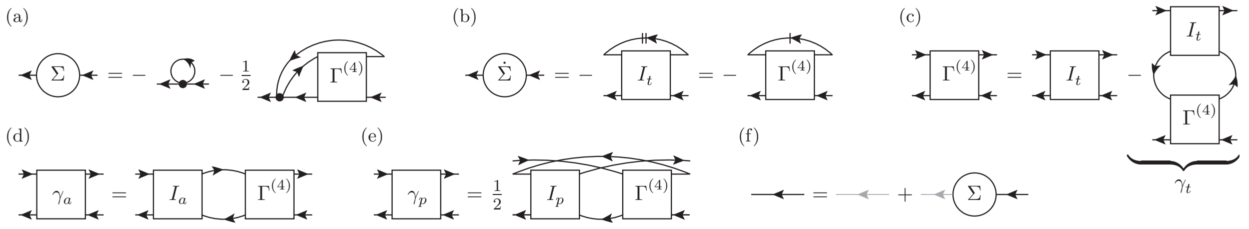

FIG. 1. Graphical representation of many-body relations, where solid lines represent dressed propagators G and dots represent bare four-point vertices $\Gamma_0^{(4)}$. (a) Schwinger-Dyson equation (3b) for the self-energy. (b) To perform the functional derivative $\delta\Sigma/\delta G$ in Eq. (3c), one sums all copies of diagrams where one G line is removed. Conversely, the self-energy differentiated w.r.t. a scalar parameter (see main text), $\dot{\Sigma}$, is obtained by contracting [cf. Eq. (5a)] the vertex I_t with $\dot{G}$ (line with double dash) or [cf. Eq. (5b)] the full vertex $\Gamma^{(4)}$ with the singled-scale propagator S [cf. Eq. (4), line with one dash]. (c) $\Gamma^{(4)}$ deduced from the Bethe-Salpeter equation (BSE) in the transverse channel (3c). (d)–(e) BSEs (7) for the reducible vertices in (d) the antiparallel channel and (e) the parallel channel. (f) Dyson equation (3a) involving the bare propagator G_0 (gray line). Note that the relations (a)–(c) suffice to generate all skeleton diagrams for the self-energy and the vertex (with all signs and prefactors written explicitly). Relations (c)–(e) together with Eq. (6) enable the parquet decomposition of the four-point vertex. Finally, the Dyson equation (f) makes the connection between bare and skeleton diagrams.

and an important role is attached to the so-called single-scale propagator

$$S = \dot{G} - G \cdot \dot{\Sigma} \cdot G = (\mathbb{1} + G \cdot \Sigma) \cdot \dot{G}_0 \cdot (\Sigma \cdot G + \mathbb{1}), \quad (4)$$

where $\dot{G} = \partial_\Lambda G$, etc. If the variation of G in Eq. (3c) is realized by varying Λ, one obtains by inserting Eq. (4)

$$\dot{\Sigma} = -I_t \circ \dot{G} = -I_t \circ (S + G \cdot \dot{\Sigma} \cdot G) \quad (5a)$$

$$= -(I_t - I_t \circ G \circ G \circ I_t + \cdots)S = -\Gamma^{(4)} \circ S. \quad (5b)$$

The iterative insertion of $\dot{\Sigma}$ on the r.h.s. yields a ladder construction in the t channel that produces the full vertex $\Gamma^{(4)}$ from I_t [cf. Eq. (3c)] and results in the well-known flow equation of the self-energy [9,10].

Finally, the relation between the full and the two-particle-irreducible vertices is made precise by the parquet equation [5,11]

$$\Gamma^{(4)} = R + \sum_r \gamma_r, \quad I_r = R + \sum_{r' \neq r} \gamma_{r'}. \quad (6)$$

Here R is the totally irreducible vertex, whereas the vertices γ_r with $r \in \{a, p, t\}$ are reducible by cutting two *antiparallel* lines, two *parallel* lines, or two *transverse* (antiparallel) lines, respectively [12]. They are obtained from the irreducible ones via the BSEs [cf. Eq. (3c) and Figs. 1(c)–1(e)]

$$\gamma_r = \sigma_r \, I_r \circ G \circ G \circ \Gamma^{(4)}, \quad \sigma_a = 1 = -\sigma_t, \ \sigma_p = \tfrac{1}{2}. \quad (7)$$

The relative minus sign in the a and t channel stems from the fact that γ_a and γ_t are related by exchange of fermionic legs. Following the conventions of Bickers [5], the factor of 1/2 used in the p channel and in Eq. (3b) ensures that, when summing over all internal indices, one does not overcount the effect of the two indistinguishable (parallel) lines connected to the antisymmetric vertices.

III. COUNTING OF DIAGRAMS

A key aspect in the technique of many-body perturbation theory is that all quantities have (under certain conventions) a unique representation as a sum of diagrams, which can be obtained by following the so-called Feynman rules. In order to *count* the number of diagrams via many-body integral equations, we express all quantities as sums of diagrams (i.e., we expand in the interaction) and collect all combinations that lead to the same order in the interaction. These combinations of different numbers of diagrams yield the number of diagrams for the resulting object. In fact, the multiplicative structure in the interaction translates into discrete convolutions of the individual numbers of diagrams. Since the interaction vertices start at least at first order in the interaction, the resulting equations can be solved iteratively.

As a first example, we count the number of diagrams in the full propagator G at order n in the interaction, $\mathcal{N}_G(n)$, given the number of diagrams in the self-energy, $\mathcal{N}_\Sigma(n)$. We know that the bare propagator has only one contribution, $\mathcal{N}_{G_0}(n) = \delta_{n,0}$, and that the self-energy starts at first order, i.e., $\mathcal{N}_\Sigma(0) = 0$. From Dyson's equation (3a), we then see that the number of diagrams in the full propagator can be generated iteratively via

$$\mathcal{N}_G(n) = \delta_{n,0} + \sum_{m=1}^{n} \mathcal{N}_\Sigma(m) \mathcal{N}_G(n-m). \quad (8)$$

As already indicated, it is useful to define a convolution of sequences according to

$$\mathcal{N}_1 = \mathcal{N}_2 * \mathcal{N}_3 \ \Leftrightarrow \ \mathcal{N}_1(n) = \sum_{m=0}^{n} \mathcal{N}_2(m) \mathcal{N}_3(n-m) \ \forall n. \quad (9)$$

With this, we can write Eq. (8) in direct analogy to the original equation (3a) as

$$\mathcal{N}_G = \mathcal{N}_{G_0} + \mathcal{N}_{G_0} * \mathcal{N}_\Sigma * \mathcal{N}_G. \quad (10)$$

Similarly, we use the SDE (3b) and the number of diagrams in the bare vertex $\mathcal{N}_{\Gamma_0^{(4)}}(n) = \delta_{n,1}$ to get

$$\mathcal{N}_\Sigma = \mathcal{N}_{\Gamma_0^{(4)}} * \mathcal{N}_G + \tfrac{1}{2} \mathcal{N}_{\Gamma_0^{(4)}} * \mathcal{N}_G * \mathcal{N}_G * \mathcal{N}_G * \mathcal{N}_{\Gamma^{(4)}}. \quad (11)$$

We can ignore the extra minus signs when collecting topologically distinct diagrams (for an example of many-body relations where the relative minus signs do matter, see the Appendix). However, we have to keep track of prefactors of magnitude not equal to unity to avoid double counting of diagrams [5]. This is necessary as we use the antisymmetric bare four-point vertex as building block for diagrams. If one counts direct and exchange interactions separately, corresponding to an expansion in terms

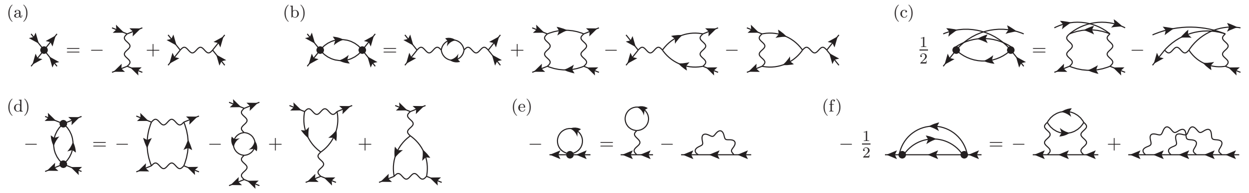

FIG. 2. Examples and translation from Hugenholtz to Feynman diagrams. (a) Bare (antisymmetric) four-point vertex (dot) as used for Hugenholtz diagrams expressed by direct and exchange interactions [cf. Eq. (2b), wavy lines] as used for Feynman diagrams. (b)–(d) Diagrams for the reducible vertices γ_r in the two-particle channels a, p, t, respectively. Whereas γ_a and γ_t have four Feynman diagrams, γ_p has only two. In fact, inserting the direct and exchange interactions from (a) into the Hugenholtz diagram containing two equivalent propagators (parallel lines connected to antisymmetric vertices) yields only two topologically distinct diagrams, properly canceling the factor of 1/2. (e) First- and (f) second-order diagrams for the self-energy. The prefactor of 1/2 is again canceled upon decomposing Γ_0. Note that, if the electron propagators (lines) are considered as dressed ones, the above diagrams comprise all skeleton diagrams of the four-point vertex and the self-energy up to second order.

of the amplitude U instead of the antisymmetric matrix Γ_0 in Eq. (2b), one attributes two diagrams to the bare vertex [$\mathcal{N}_{\Gamma_0^{(4)}}(n) = 2\delta_{n,1}$], and the number of diagrams at each order is magnified by $\mathcal{N}_X(n) \to \mathcal{N}_X(n)2^n$. This corresponds to the translation from Hugenholtz to Feynman diagrams [1] and cancels the fractional prefactors (cf. Fig. 2).

The further relations for the number of diagrams that follow from Eq. (3c) close the set of equations and will allow us to generate the exact numbers of diagrams in all involved quantities. The crucial point for this to work is that, on the one hand, as $\mathcal{N}_{\Gamma_0^{(4)}}(n) \propto \delta_{n,1}$, the self-energy at order n is generated by G (containing Σ) and $\Gamma^{(4)}$ up to order $n-1$ via Eq. (3b). On the other hand, Eq. (5) [deduced from Eq. (3c)] relates $\dot\Sigma$ at order n to Σ at orders $1, \dots, n-1$ and $\Gamma^{(4)}$ at orders $1, \dots, n$. Knowing $\mathcal{N}_\Sigma(n)$ from the SDE, we can thus infer $\mathcal{N}_{\Gamma^{(4)}}(n)$. Then the algorithm proceeds iteratively.

To use the differential equations, note that a diagram of the propagator G at order n contains $2n+1$ lines, and a diagram of an m-point vertex $\Gamma^{(m)}$ (we use $\Sigma = \Gamma^{(2)}$ as in Ref. [10]) has $(4n-m)/2$ lines. According to the product rule, the number of differentiated diagrams is thus given by

$$\mathcal{N}_{\dot G}(n) = \mathcal{N}_G(n)(2n+1), \tag{12a}$$

$$\mathcal{N}_{\dot\Gamma^{(m)}}(n) = \mathcal{N}_{\Gamma^{(m)}}(n)\left(2n - \frac{m}{2}\right). \tag{12b}$$

Further, Eq. (5) is easily translated into

$$\mathcal{N}_{\dot\Sigma} = \mathcal{N}_{\Gamma^{(4)}} * \mathcal{N}_S \tag{13a}$$

$$= \mathcal{N}_{I_t} * \mathcal{N}_{\dot G} \tag{13b}$$

and can be transformed to give an equation for the number of diagrams in the vertices $\Gamma^{(4)}$ and I_t. From Eq. (13a), we get

$$\mathcal{N}_{\Gamma^{(4)}}(n) = \left[\mathcal{N}_{\dot\Sigma}(n) - \sum_{m=1}^{n-1} \mathcal{N}_{\Gamma^{(4)}}(m)\mathcal{N}_S(n-m)\right]\Big/\mathcal{N}_S(0), \tag{14}$$

where the number of diagrams in the single-scale propagator S can be obtained from the equivalent relations

$$\mathcal{N}_S = \mathcal{N}_{\dot G} - \mathcal{N}_G * \mathcal{N}_{\dot\Sigma} * \mathcal{N}_G \tag{15a}$$

$$= (\mathcal{N}_{\mathbb{1}} + \mathcal{N}_G * \mathcal{N}_\Sigma) * \mathcal{N}_{\dot G_0} * (\mathcal{N}_{\mathbb{1}} + \mathcal{N}_\Sigma * \mathcal{N}_G), \tag{15b}$$

with $\mathcal{N}_{\dot G_0}(n) = \delta_{n,0} = \mathcal{N}_{\mathbb{1}}(n)$. If we alternatively use Eq. (13b) [combined with Eq. (3c)], we have

$$\mathcal{N}_{I_t}(n) = \left[\mathcal{N}_{\dot\Sigma}(n) - \sum_{m=1}^{n-1} \mathcal{N}_{I_t}(m)\mathcal{N}_{\dot G}(n-m)\right]\Big/\mathcal{N}_{\dot G}(0), \tag{16a}$$

$$\mathcal{N}_{\Gamma^{(4)}}(n) = \mathcal{N}_{I_t}(n) + \sum_{m=1}^{n-1} \mathcal{N}_{\Gamma^{(4)}}(m)\big(\mathcal{N}_G * \mathcal{N}_G * \mathcal{N}_{I_t}\big)(n-m). \tag{16b}$$

In an analogous fashion, one can also derive the number of diagrams in the 1PI six-point vertex $\Gamma^{(6)}$ from the exact fRG flow equation [9,10] of the four-point vertex $\Gamma^{(4)}$,

$$\mathcal{N}_{\dot\Gamma^{(4)}} = 5\,\mathcal{N}_{\Gamma^{(4)}} * \mathcal{N}_G * \mathcal{N}_S * \mathcal{N}_{\Gamma^{(4)}} + \mathcal{N}_{\Gamma^{(6)}} * \mathcal{N}_S, \tag{17}$$

together with Eq. (12b). A further relation is given by the SDE for $\Gamma^{(4)}$ [17] ($\mathcal{N}_\Pi = \mathcal{N}_G * \mathcal{N}_G$)

$$\begin{aligned}\mathcal{N}_{\Gamma^{(4)}} ={}& \mathcal{N}_{\Gamma_0^{(4)}} + \tfrac{5}{2}\,\mathcal{N}_{\Gamma_0^{(4)}} * \mathcal{N}_\Pi * \mathcal{N}_{\Gamma^{(4)}} \\ &+ 4\,\mathcal{N}_{\Gamma_0^{(4)}} * \mathcal{N}_\Pi * \mathcal{N}_\Pi * \mathcal{N}_{\Gamma^{(4)}} * \mathcal{N}_{\Gamma^{(4)}} \\ &+ \tfrac{1}{2}\,\mathcal{N}_{\Gamma_0^{(4)}} * \mathcal{N}_G * \mathcal{N}_\Pi * \mathcal{N}_{\Gamma^{(6)}}.\end{aligned} \tag{18}$$

Finally, the number of diagrams in the vertex $\Gamma^{(4)}$ can be decomposed into two-particle channels according to the parquet equations (6), (7). By symmetry, we have $\mathcal{N}_{\gamma_a} = \mathcal{N}_{\gamma_t}$ and obtain

$$\mathcal{N}_{\Gamma^{(4)}} = \mathcal{N}_R + 2\mathcal{N}_{\gamma_a} + \mathcal{N}_{\gamma_p}, \tag{19a}$$

$$\mathcal{N}_{\gamma_r} = |\sigma_r|\big(\mathcal{N}_{\Gamma^{(4)}} - \mathcal{N}_{\gamma_r}\big) * \mathcal{N}_G * \mathcal{N}_G * \mathcal{N}_{\Gamma^{(4)}}. \tag{19b}$$

Given $\mathcal{N}_{\Gamma^{(4)}}$, one can first deduce $\mathcal{N}_{\gamma_r}$ and then $\mathcal{N}_R$. If, conversely, the number of diagrams in the totally irreducible vertex R [with $\mathcal{N}_R(0) = 0$] is fixed, as is the case in parquet approximations, one can combine these equations with Eqs. (10) and (11) to generate all numbers of diagrams without the need to use the differential equations (13).

TABLE I. Exact number of Hugenholtz diagrams for various vertex functions and the propagator up to interaction order 6. The number of Feynman diagrams is obtained by $\mathcal{N}_X(n) \to \mathcal{N}_X(n)2^n$, which cancels all fractional parts (cf. Fig. 2).

n	1	2	3	4	5	6
$\mathcal{N}_{\Gamma^{(6)}}$	0	0	21	$319\frac{1}{2}$	$4180\frac{1}{2}$	$53612\frac{1}{4}$
$\mathcal{N}_{\Gamma^{(4)}}$	1	$2\frac{1}{2}$	$15\frac{1}{4}$	$112\frac{1}{8}$	$935\frac{1}{16}$	$8630\frac{5}{32}$
$\mathcal{N}_{\gamma_a}$	0	1	6	$42\frac{1}{4}$	332	$2854\frac{9}{16}$
$\mathcal{N}_{\gamma_p}$	0	$\frac{1}{2}$	$3\frac{1}{4}$	$23\frac{5}{8}$	$188\frac{1}{16}$	$1622\frac{17}{32}$
$\mathcal{N}_R$	1	0	0	4	83	$1298\frac{1}{2}$
$\mathcal{N}_\Sigma$	1	$1\frac{1}{2}$	$5\frac{1}{4}$	$25\frac{7}{8}$	$158\frac{1}{16}$	$1132\frac{19}{32}$
$\mathcal{N}_G$	1	$2\frac{1}{2}$	$9\frac{1}{4}$	$44\frac{1}{8}$	$255\frac{1}{16}$	$1725\frac{5}{32}$

IV. RESULTS

A. Bare diagrams

With the equations stated above, we can construct the exact number of diagrams of the general many-body problem for all involved quantities. Table I shows the number of diagrams in the different vertices, the self-energy, and the propagator up to order 6. After translation from the number of Hugenholtz to Feynman diagrams by $\mathcal{N}_X(n) \to \mathcal{N}_X(n)2^n$, $\mathcal{N}_G$ reproduces the numbers already given in Ref. [18] (their Table I, first column) and Ref. [19] [their Eq. (9.10)].

B. Skeleton diagrams

For many purposes, it is convenient to work with skeleton diagrams, i.e., diagrams in which all electron propagators are fully dressed ones. Then the bare propagator [with $\mathcal{N}_{G_0}(n) = \delta_{n,0} = \mathcal{N}_{\dot{G}_0}(n)$] is replaced as building block for diagrams by the full propagator, for which we now use $\mathcal{N}_G(n) = \delta_{n,0} = \mathcal{N}_{\dot{G}}(n)$. We can directly apply the previous methods by using those equations that are phrased with dressed propagators, such as Eqs. (11), (16), and (19).

Moreover, the numbers of bare and skeleton diagrams are directly related. According to the number of lines in an nth-order diagram of an m-point vertex [cf. Eq. (12b)], one has

$$\mathcal{N}_{\Gamma^{(m)}}(n) = \sum_{k=1}^{n} \mathcal{N}^{\mathrm{sk}}_{\Gamma^{(m)}}(k)\big(\underbrace{\mathcal{N}_G * \cdots * \mathcal{N}_G}_{2k-m/2}\big)(n-k) \tag{20}$$

and can transform the number of skeleton diagrams $\mathcal{N}^{\mathrm{sk}}_{\Gamma^{(m)}}$ to bare diagrams $\mathcal{N}_{\Gamma^{(m)}}$. For this, the numbers of bare diagrams in Σ and G are built up side by side, using Eq. (8). If we consider, e.g., the simplest approximation of a finite-order *skeleton* self-energy, namely, the Hartree-Fock approximation with $\mathcal{N}^{\mathrm{sk}}_\Sigma(n) = \delta_{n,1}$, Eq. (20) can be used to give $\mathcal{N}_\Sigma(n) = 0, 1, 2, 5, 14, 42, 132, \ldots$ for the number of *bare* self-energy diagrams.

If, conversely, the number of bare diagrams $\mathcal{N}_{\Gamma^{(m)}}$ is known, we can easily construct a recursion relation for $\mathcal{N}^{\mathrm{sk}}_{\Gamma^{(m)}}$ by inverting Eq. (20),

TABLE II. Exact number of skeleton Hugenholtz diagrams for various vertex functions up to interaction order 6. The number of Feynman diagrams is again obtained by $\mathcal{N}_X(n) \to \mathcal{N}_X(n)2^n$.

n	1	2	3	4	5	6
$\mathcal{N}^{\mathrm{sk}}_{\Gamma^{(6)}}$	0	0	21	$256\frac{1}{2}$	$2677\frac{1}{2}$	$28179\frac{3}{4}$
$\mathcal{N}^{\mathrm{sk}}_{\Gamma^{(4)}}$	1	$2\frac{1}{2}$	$10\frac{1}{4}$	$56\frac{1}{8}$	$375\frac{9}{16}$	$2931\frac{21}{32}$
$\mathcal{N}^{\mathrm{sk}}_{\gamma_a}$	0	1	4	$20\frac{1}{4}$	123	$866\frac{1}{16}$
$\mathcal{N}^{\mathrm{sk}}_{\gamma_p}$	0	$\frac{1}{2}$	$2\frac{1}{4}$	$11\frac{5}{8}$	$70\frac{9}{16}$	$493\frac{1}{32}$
$\mathcal{N}^{\mathrm{sk}}_R$	1	0	0	4	59	$706\frac{1}{2}$
$\mathcal{N}^{\mathrm{sk}}_\Sigma$	1	$\frac{1}{2}$	$1\frac{1}{4}$	$5\frac{1}{8}$	$28\frac{1}{16}$	$187\frac{25}{32}$

$$\mathcal{N}^{\mathrm{sk}}_{\Gamma^{(m)}}(n) = \Bigg[\mathcal{N}_{\Gamma^{(m)}}(n) - \sum_{k=1}^{n-1} \mathcal{N}^{\mathrm{sk}}_{\Gamma^{(4)}}(k) \times (\underbrace{\mathcal{N}_G * \cdots * \mathcal{N}_G}_{2k-m/2})(n-k)\Bigg] \Big/ (\underbrace{\mathcal{N}_G * \cdots * \mathcal{N}_G}_{2n-m/2})(0). \tag{21}$$

Table II shows the number of skeleton diagrams in the various quantities. The number of skeleton *Feynman* diagrams for the self-energy, $\mathcal{N}^{\mathrm{sk}}_\Sigma(n)2^n$, agrees with the numbers given in Ref. [20] [coefficients in their Eq. (17) using $\ell = 1$] and Ref. [21] (their Table 4.1, column 2 [22]).

C. Asymptotic behavior

From combinatorial arguments, it is clear that the number of diagrams exhibits a factorial growth with the interaction order n. Indeed, Fig. 3 (full lines) shows the number of diagrams in different vertex functions $\mathcal{N}_{\Gamma^{(m)}}$ divided by their (numerically determined) asymptote

$$\mathcal{N}_{\Gamma^{(m)}} \sim n!\, n^{(m-1)/2} 2^{(m-2)/2}, \quad n \gg 1 \tag{22}$$

as a function of $1/n$. The fact that the curves linearly approach a finite value demonstrates that, indeed, the correct asymptotic behavior has been identified. We find the same proportionality factor for all vertex functions.

The m dependence in Eq. (22) can be readily understood from the universal part of the exact fRG flow equations, $\dot{\Gamma}^{(m)} = -\Gamma^{(m+2)} \circ S + \ldots$ [9,10]. Due to the factorial growth, we have $\mathcal{N}_X(n) \gg \mathcal{N}_X(n-1)$ for $n \gg 1$, and the leading behavior is determined by [using $\mathcal{N}_S(0) = 1$ and Eq. (12b)]

$$\mathcal{N}_{\Gamma^{(m+2)}}(n)\mathcal{N}_S(0) \sim \mathcal{N}_{\dot{\Gamma}^{(m)}}(n) \sim 2n\, \mathcal{N}_{\Gamma^{(m)}}(n), \; n \gg 1. \tag{23}$$

The asymptotes of G and $\Sigma = \Gamma^{(2)}$ agree due to the simple relation deduced from Eq. (10) for $n \gg 1$,

$$\mathcal{N}_G(n) \sim \mathcal{N}_{G_0}(0)\mathcal{N}_\Sigma(n)\mathcal{N}_G(0) \sim \mathcal{N}_\Sigma(n) \sim n!\, n^{1/2}. \tag{24}$$

The number of diagrams in the reducible vertices γ_r divided by the same function as $\Gamma^{(4)}$ (dotted lines in Fig. 3) go to zero. In fact, the correct asymptote of the reducible vertices (as used for the dashed lines in Fig. 3) is found from the BSEs (19b)

$$\begin{aligned}\mathcal{N}_{\gamma_r}(n) &\sim 2|\sigma_r|\mathcal{N}_{\Gamma^{(4)}}(1)\mathcal{N}_G(0)\mathcal{N}_G(0)\mathcal{N}_{\Gamma^{(4)}}(n-1) \\ &\sim 4|\sigma_r|(n-1)!\, n^{3/2} = 4|\sigma_r|\, n!\, n^{1/2}, \quad n \gg 1.\end{aligned} \tag{25}$$

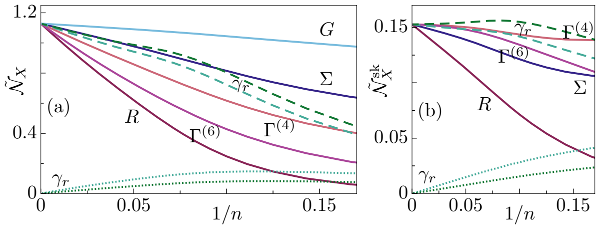

FIG. 3. Plots for the rescaled number of (a) bare and (b) skeleton diagrams with n ranging up to 1500. Numbers are rescaled as $\tilde{\mathcal{N}}_{\Gamma^{(m)}}(n) = \mathcal{N}_{\Gamma^{(m)}}(n)/(n!n^{(m-1)/2}2^{(m-2)/2})$ [Eq. (22)]; G is rescaled in the same way as $\Sigma = \Gamma^{(2)}$ [Eq. (24)]; R and γ_r ($r = a, p$, dotted) in the same way as $\Gamma^{(4)}$. Dashed lines for γ_r account for the correct asymptote, showing $\mathcal{N}_{\gamma_r}/(4|\sigma_r|n!n^{1/2})$ [Eq. (25)].

According to Eq. (19a), the number of diagrams in the totally irreducible vertex R must then grow as fast as $\mathcal{N}_{\Gamma^{(4)}}$,

$$\mathcal{N}_R(n) \sim \mathcal{N}_{\Gamma^{(4)}}(n) \sim 2n!n^{3/2}, \tag{26a}$$

$$\frac{\mathcal{N}_{\gamma_r}(n)}{\mathcal{N}_R(n)} \sim \frac{2|\sigma_r|}{n}, \quad n \gg 1. \tag{26b}$$

From Fig. 3, we indeed see that $\mathcal{N}_R > \mathcal{N}_{\gamma_a}, \mathcal{N}_{\gamma_p}$ for $n > 8$.

The proportionality factor of roughly 1.128 in the asymptotics of the bare number of diagrams can be derived from a combinatorial approach to count diagrams in m-point connected Green's function $G^{(m)}$ (with $G = G^{(2)}$). If the recursion relation for G given in Ref. [19] [their Eq. (9.10)] is translated to Hugenholtz diagrams and generalized to m-point functions, it reads

$$\mathcal{N}_{G^{(m)}}(n) = \frac{(2n+m/2)!}{n!4^n} - \sum_{k=1}^{n} \frac{(2k)!}{k!4^k}\mathcal{N}_{G^{(m)}}(n-k), \tag{27}$$

where the first summand accounts for all topologically distinct contractions and the second summand removes disconnected ones. For the asymptotic behavior, it suffices to subtract the *fully* disconnected part [the $k = n$ summand dominates since $\mathcal{N}_X(n) \gg \mathcal{N}_X(n-1)$], and we obtain, using $\mathcal{N}_{G^{(m)}}(0) = O(1)$ and Stirling's formula,

$$\mathcal{N}_{G^{(m)}}(n) \sim \frac{(2n+m/2)!}{n!4^n} - \frac{(2n)!}{n!4^n} \sim \frac{(2n)^{m/2}(2n)!}{n!4^n}$$
$$\sim \frac{2}{\sqrt{\pi}} n!n^{(m-1)/2}2^{(m-2)/2}, \quad n \gg 1. \tag{28}$$

Comparing this to Eq. (22), we indeed find a proportionality factor of $2/\sqrt{\pi} \approx 1.128$ [23].

D. Asymptotics of parquet approximations

In any type of parquet approximation, one has $\mathcal{N}_R(n) = 0$ for $n > n_p$ (i.e., n_p denotes the highest-order contribution retained for R), whereas the reducible vertices and the self-energy still extend to arbitrarily high orders, as determined by the self-consistent BSEs (7) and SDE (3b). However, in this case, a factorial growth in the number of diagrams $[\mathcal{N}_X(n) \gg \mathcal{N}_X(n-1)]$ leading to Eq. (26) would contradict a vertex R of finite order. Hence, the number of diagrams in any approximation of the parquet type can at most grow exponentially $[\mathcal{N}_X(n)/\mathcal{N}_X(n-1) \sim O(1)]$. Figure 4 shows how the quotient of two subsequent elements in $\mathcal{N}_X$ subject to (two different) parquet-type approximations approaches a constant; it confirms the exponential growth and reveals that the exponential rate only depends on n_p for *all* vertex functions. Curiously, one finds dampened oscillations modulating the growth in the number of diagrams for $n > n_p \gtrsim 10$.

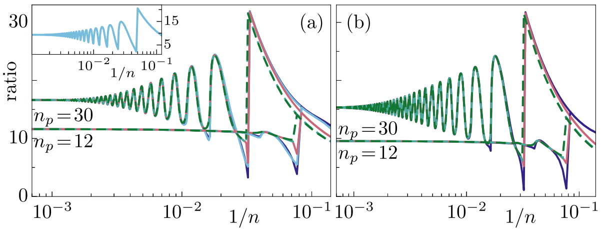

FIG. 4. Ratio of subsequent elements of (a) $\mathcal{N}_X$ and (b) $\mathcal{N}_X^{\mathrm{sk}}$ in the parquet-type approximations with $n_p = 30$ and $n_p = 12$ (see main text). We use the same color coding as in Fig. 3; dashed lines represent γ_r. The inset shows an analogous plot for $\mathcal{N}_G$, obtained from a finite-order self-energy ($n_s = 20$) [cf. Eq. (29)]. The cusp for $\Gamma^{(4)}$, Σ, G occurs at $1/n_p$ (inset: $1/n_s$), and for γ_r at $1/n_p + 1$, due to the structure of the BSEs [cf. (19b)].

An analogous phenomenon already occurs by using the Dyson equation with a self-energy of finite order (cf. Fig. 4, inset). Again, a factorial growth in the number of diagrams $[\mathcal{N}_X(n) \gg \mathcal{N}_X(n-1)]$ leading to Eq. (24) would contradict such an $\mathcal{N}_\Sigma$, and $\mathcal{N}_G$ can at most grow exponentially. If $\mathcal{N}_\Sigma(n) = 0$ for $n > n_s$, Eq. (8) is simplified to

$$\mathcal{N}_G(n) = \delta_{n,0} + \sum_{m=1}^{\min\{n,n_s\}} \mathcal{N}_\Sigma(m)\mathcal{N}_G(n-m). \tag{29}$$

For large n, the factor $\mathcal{N}_G(n-m)$ spans over the orders $n - n_s, \ldots, n$ and produces "fading echoes" of the abrupt fall in the quotient which stems from the first occurrence of $\mathcal{N}_\Sigma(n) = 0$ at $n = n_s + 1$.

Even if only the skeleton diagrams of, e.g., Σ or R are of finite order, the resulting numbers of bare diagrams can grow at most exponentially. The reasoning is similar: A factorial growth in the number of diagrams $[\mathcal{N}_X(n) \gg \mathcal{N}_X(n-1)]$ would imply $\mathcal{N}_{\Gamma^{(m)}}(n) \sim \mathcal{N}^{\mathrm{sk}}_{\Gamma^{(m)}}(n_{\min})\mathcal{N}_G(n-n_{\min})$, using Eq. (20) and $\mathcal{N}_G(0) = 1$. For Σ, one has $n_{\min} = 1$, and the result would directly contradict Eq. (24). For R, one has $n_{\min} = 4$ and would find a contradiction using Eqs. (23), (24), and (26). We conclude that for any of the typical diagrammatic resummation approaches, one generates numbers of (bare) diagrams that grow at most exponentially with interaction order n.

E. Hubbard model

The Hubbard model [24] is of special interest in condensed matter physics. In terms of diagrams, a simplification arises due to the SU(2) spin symmetry of the model with the restrictive bare vertex ($\sigma \in \{\uparrow, \downarrow\}$)

$$\Gamma^{(4)}_{0;x_1',x_2';x_1,x_2} \propto \left(\delta_{\sigma_1',\sigma_1}\delta_{\sigma_2',\sigma_2} - \delta_{\sigma_1',\sigma_2}\delta_{\sigma_2',\sigma_1}\right)\delta_{\sigma_1,\bar{\sigma}_2}, \tag{30}$$

TABLE III. Exact number of spin-resolved bare diagrams in the Hubbard model. By symmetry, we have $\mathcal{N}^{\uparrow\uparrow}_{\gamma_a} = \mathcal{N}^{\uparrow\uparrow}_{\gamma_t}$, and one further finds $\mathcal{N}^{\uparrow\downarrow}_{\gamma_a} = \mathcal{N}^{\uparrow\downarrow}_{\gamma_p}$ [cf. Fig. 5 and Eq. (A9)].

n	1	2	3	4	5	6	7
$\mathcal{N}_\Sigma$	1	2	8	44	296	2312	20 384
$\mathcal{N}^{\uparrow\downarrow}_{\Gamma^{(4)}}$	1	2	13	104	940	9352	101 080
$\mathcal{N}^{\uparrow\downarrow}_{\gamma_a}$	0	1	5	36	300	2760	27 544
$\mathcal{N}^{\uparrow\downarrow}_{\gamma_t}$	0	0	3	30	282	2758	28 526
$\mathcal{N}^{\uparrow\downarrow}_{R}$	1	0	0	2	58	1074	17 466
$\mathcal{N}^{\uparrow\uparrow}_{\Gamma^{(4)}}$	0	2	12	94	848	8468	92 016
$\mathcal{N}^{\uparrow\uparrow}_{\gamma_a}$	0	1	6	44	366	3354	33 334
$\mathcal{N}^{\uparrow\uparrow}_{\gamma_p}$	0	0	0	2	28	320	3532
$\mathcal{N}^{\uparrow\uparrow}_{R}$	0	0	0	4	88	1440	21 816
$\mathcal{N}^{\uparrow\downarrow\uparrow}_{\Gamma^{(6)}}$	0	0	8	144	2072	28 744	402 736
$\mathcal{N}^{\uparrow\uparrow\uparrow}_{\Gamma^{(6)}}$	0	0	12	144	1872	25 176	349 812

TABLE IV. Exact number of spin-resolved skeleton diagrams in the Hubbard model, where we again have $\mathcal{N}^{\text{sk}\uparrow\uparrow}_{\gamma_a} = \mathcal{N}^{\text{sk}\uparrow\uparrow}_{\gamma_t}$ and $\mathcal{N}^{\text{sk}\uparrow\downarrow}_{\gamma_a} = \mathcal{N}^{\text{sk}\uparrow\downarrow}_{\gamma_p}$.

n	1	2	3	4	5	6	7
$\mathcal{N}^{\text{sk}}_\Sigma$	1	1	2	9	54	390	3268
$\mathcal{N}^{\text{sk}\uparrow\downarrow}_{\Gamma^{(4)}}$	1	2	9	54	390	3268	30 905
$\mathcal{N}^{\text{sk}\uparrow\downarrow}_{\gamma_a}$	0	1	3	17	112	850	7289
$\mathcal{N}^{\text{sk}\uparrow\downarrow}_{\gamma_t}$	0	0	3	18	120	928	8029
$\mathcal{N}^{\text{sk}\uparrow\downarrow}_{R}$	1	0	0	2	46	640	8298
$\mathcal{N}^{\text{sk}\uparrow\uparrow}_{\Gamma^{(4)}}$	0	2	8	48	352	2978	28 376
$\mathcal{N}^{\text{sk}\uparrow\uparrow}_{\gamma_a}$	0	1	4	21	136	1028	8768
$\mathcal{N}^{\text{sk}\uparrow\uparrow}_{\gamma_p}$	0	0	0	2	16	126	1064
$\mathcal{N}^{\text{sk}\uparrow\uparrow}_{R}$	0	0	0	4	64	796	9776
$\mathcal{N}^{\text{sk}\uparrow\downarrow\uparrow}_{\Gamma^{(6)}}$	0	0	8	120	1376	15 648	185 296
$\mathcal{N}^{\text{sk}\uparrow\uparrow\uparrow}_{\Gamma^{(6)}}$	0	0	12	108	1188	13 464	160 236

where $\bar{\uparrow} = \downarrow$, $\bar{\downarrow} = \uparrow$. In this case, one can individually count diagrams with specific spin configuration. In other words, one can explicitly perform the spin sums in all diagrams and actually count only those diagrams that do not vanish under the spin restriction.

So far, we have considered diagrams that contain summations over *all* internal degrees of freedom—including spin. Generally, our algorithm cannot give the functional dependence of the diagrams and, in particular, does not give the spin dependence of the diagrams. If one writes the relations stated above with their explicit spin dependence (as done in the Appendix), one finds that the SDE relates the self-energy to the vertex with different spins at the external legs. However, the differential equations contain a summation over all spin configurations of the vertex. Thus, Eqs. (14) and (16a) cannot be used to deduce the number of spin-resolved vertex diagrams.

As already mentioned, for *approximate* many-body approaches that do allow for an iterative construction, such as parquet-type approximations, we need not make use of the differential equations. We could therefore easily construct the corresponding numbers of spin-resolved diagrams. However, here we prefer to give low-order results for the *exact* numbers of diagrams for all the different vertex functions by resorting to known results: We use exact numbers of diagrams for a specific quantity not considered in this work, which are obtained by Monte Carlo sampling up to order 7 in Ref. [25] (their Table I). From this, we can deduce the number of diagrams in the totally irreducible vertex R and, then, generate the numbers for all further vertex functions studied here.

Using spin symmetry, only a few spin configurations of the vertices are actually relevant: One-particle properties must be independent of spin; for two- and three-particle vertices, it suffices to consider those with identical spins and those with two different pairs of spins. In the Appendix we explain the labeling and give further relations that follow from the SU(2) spin symmetry and rely on cancelations of diagrams.

Table III gives the exact number of bare diagrams for the Hubbard model up to order 7; Table IV gives the corresponding numbers of skeleton diagrams. The numbers for $\mathcal{N}^{\text{sk}}_\Sigma$ up to order 6 agree with those of Ref. [21] (their Table 4.1, column 3). Note that, for spin-resolved diagrams of the Hubbard model, we can use the internal spin summations to express all Hugenholtz diagrams in terms of the bare vertex $\Gamma^{\uparrow\downarrow}_0$ with fixed spins, containing only one diagram. Hence, the number of spin-resolved Hugenholtz and Feynman diagrams for this model are equal (cf. Fig. 5).

It is interesting to compare the number of diagrams in the four-point vertex with identical and different spins. On top of the numbers given in Tables III and IV, our algorithm can also determine the asymptotic behavior of, e.g., the relation between $\mathcal{N}^{\uparrow\uparrow}_{\Gamma^{(4)}}$ and $\mathcal{N}^{\uparrow\downarrow}_{\Gamma^{(4)}}$. If we consider skeleton diagrams, the SDE (A7a) with $\mathcal{N}^{\text{sk}\uparrow\downarrow}_{\Gamma^{(4)}_0}(n) = \delta_{n,1}$ yields $\mathcal{N}^{\text{sk}}_\Sigma(n+1) = \mathcal{N}^{\text{sk}\uparrow\downarrow}_{\Gamma^{(4)}}(n)$. Combined with the (super) factorial growth of $\mathcal{N}^{\text{sk}}_\Sigma$, this gives

$$n\mathcal{N}^{\text{sk}}_\Sigma(n) \gtrsim \mathcal{N}^{\text{sk}}_\Sigma(n+1) = \mathcal{N}^{\text{sk}\uparrow\downarrow}_{\Gamma^{(4)}}(n), \quad n \gg 1. \tag{31}$$

On the other hand, Eq. (12b) and Eq. (A7c) together with the knowledge that $\mathcal{N}_R$ asymptotically dominates $\mathcal{N}_{\Gamma^{(4)}}$ can be used

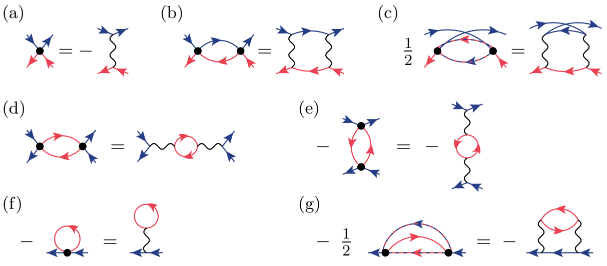

FIG. 5. Spin-resolved diagrams of the Hubbard model in the Hugenholtz and Feynman representation up to second order. Blue (dark) lines denote spin-up and red (light) lines spin-down propagators; dashed lines symbolize a sum over spin. Panels (a)–(c) give diagrams for $\Gamma^{\uparrow\downarrow}_0$, $\gamma^{\uparrow\downarrow}_a$, and $\gamma^{\uparrow\downarrow}_p$; (d)–(e) for $\gamma^{\uparrow\uparrow}_a$ and $\gamma^{\uparrow\uparrow}_t$; and (f)–(g) for Σ. Viewed with full propagators, these are all skeleton diagrams entering $\Gamma^{(4)}$ and Σ up to second order. We explicitly see that the numbers of Hugenholtz and Feynman diagrams are equal.

to obtain

$$\begin{aligned} 2n\mathcal{N}_{\Sigma}^{\mathrm{sk}}(n) &\lesssim \mathcal{N}_{I_t}^{\mathrm{sk}\uparrow\uparrow}(n)+\mathcal{N}_{I_t}^{\mathrm{sk}\uparrow\downarrow}(n) \\ &\lesssim \mathcal{N}_{\Gamma^{(4)}}^{\mathrm{sk}\uparrow\uparrow}(n)+\mathcal{N}_{\Gamma^{(4)}}^{\mathrm{sk}\uparrow\downarrow}(n), \quad n \gg 1. \end{aligned} \tag{32}$$

Dividing both equations, we find that, according to

$$\mathcal{N}_{\Gamma^{(4)}}^{\uparrow\uparrow}(n)/\mathcal{N}_{\Gamma^{(4)}}^{\uparrow\downarrow}(n) \sim \mathcal{N}_{\Gamma^{(4)}}^{\mathrm{sk}\uparrow\uparrow}(n)/\mathcal{N}_{\Gamma^{(4)}}^{\mathrm{sk}\uparrow\downarrow}(n) \gtrsim 1, \quad n \gg 1, \tag{33}$$

the number of diagrams for the effective interaction between same spins asymptotically approaches the one between different spins from above for large interaction orders.

V. CONCLUSION

We have presented an iterative algorithm to count the number of Feynman diagrams inherent in many-body integral equations. We have used it to count the exact number of bare and skeleton diagrams in various vertex function and different two-particle channels. Our algorithm can easily be applied to many-body relations of different forms and levels of approximation, such as the parquet formalism [5,11] and its simplified variant FLEX [5], other approaches based on Hedin's equations [4,20] including the famous GW approximation [26,27], Φ-derivable results deduced from a specific approximation of the Luttinger-Ward functional [5,28,29], and truncated flows of the functional renormalization group [2,9,10,30].

Due to its iterative structure, the algorithm allows us to numerically access arbitrarily large interaction orders and gain analytical insight into the asymptotic behavior. First, we have extracted a leading dependence of $n!n^{(m-1)/2}2^{(m-2)/2}$ in the number of diagrams of an m-point 1PI vertex. Second, we have shown that the number of diagrams in the totally irreducible four-point vertex exceeds those of the reducible ones for interaction orders $n > 8$ and asymptotically contains *all* diagrams of the four-point vertex [i.e., $\mathcal{N}_{\gamma_r}(n)/\mathcal{N}_R(n) \to 0$ as $n \to \infty$]. Third, we have argued that any of the typical diagrammatic resummation procedures, including any type of parquet approximation, can support an exponential growth only in the number of diagrams. This is in contrast to the factorial growth in the exact number of diagrams. It is therefore likely that the corresponding approximate series expansions do have a finite radius of convergence.

We believe that the techniques and results presented in this paper will be useful for various applications of Green's functions methods as well as approaches that directly sum diagrams, such as finite-order approximations or diagrammatic Monte Carlo [31].

ACKNOWLEDGMENTS

The author wishes to thank E. Kozik, D. Schimmel, J. von Delft, and F. Werner for useful discussions. Support by the Cluster of Excellence Nanosystems Initiative Munich and funding from the research school IMPRS-QST is acknowledged.

APPENDIX: RELATIONS FOR THE HUBBARD MODEL

The spin symmetry in the Hubbard model allows us to focus on a small set of vertex functions when counting diagrams. By spin conservation, an n-particle vertex depends on only n spins. Using the $\mathbb{Z}_2$ symmetry, it is clear that self-energy diagrams do not depend on spin, while, for the four-point vertex, it suffices to consider

$$\mathcal{N}_{\Gamma^{(4)}}^{\uparrow\uparrow} := \mathcal{N}_{\Gamma^{(4)}}^{\uparrow\uparrow;\uparrow\uparrow}, \quad \mathcal{N}_{\Gamma^{(4)}}^{\uparrow\downarrow} := \mathcal{N}_{\Gamma^{(4)}}^{\uparrow\downarrow;\uparrow\downarrow}. \tag{A1}$$

Here we write the spin indices of the vertex in the order of Eq. (1) as superscripts of $\mathcal{N}$. The classification of four-point diagrams into two-particle channels depends on the labels of the external legs. By crossing symmetry, we have $\mathcal{N}_{\gamma_a}^{\uparrow\uparrow} = \mathcal{N}_{\gamma_t}^{\uparrow\uparrow}$ and find for different spins

$$\mathcal{N}_{\gamma_p}^{\uparrow\downarrow} := \mathcal{N}_{\gamma_p}^{\uparrow\downarrow;\uparrow\downarrow} = \mathcal{N}_{\gamma_p}^{\uparrow\downarrow;\downarrow\uparrow}, \tag{A2a}$$

$$\mathcal{N}_{\gamma_a}^{\uparrow\downarrow} := \mathcal{N}_{\gamma_a}^{\uparrow\downarrow;\uparrow\downarrow} = \mathcal{N}_{\gamma_t}^{\uparrow\downarrow;\downarrow\uparrow}, \tag{A2b}$$

$$\mathcal{N}_{\gamma_t}^{\uparrow\downarrow} := \mathcal{N}_{\gamma_t}^{\uparrow\downarrow;\uparrow\downarrow} = \mathcal{N}_{\gamma_a}^{\uparrow\downarrow;\downarrow\uparrow}. \tag{A2c}$$

For the six-point vertex, we need to consider only (the semicolon again separates incoming and outgoing lines)

$$\mathcal{N}_{\Gamma^{(6)}}^{\uparrow\uparrow\uparrow} := \mathcal{N}_{\Gamma^{(6)}}^{\uparrow\uparrow\uparrow;\uparrow\uparrow\uparrow}, \quad \mathcal{N}_{\Gamma^{(6)}}^{\uparrow\downarrow\uparrow} := \mathcal{N}_{\Gamma^{(6)}}^{\uparrow\downarrow\uparrow;\uparrow\downarrow\uparrow}. \tag{A3}$$

The SU(2) spin symmetry further relates the remaining components of the four-point vertex by [13]

$$\Gamma^{(4)}_{p'\uparrow,q'\uparrow;p\uparrow,q\uparrow} = \Gamma^{(4)}_{p'\uparrow,q'\downarrow;p\downarrow,q\uparrow} - \Gamma^{(4)}_{p'\uparrow,q'\downarrow;q\downarrow,p\uparrow}, \tag{A4}$$

where we have decomposed the quantum number x into p and σ. However, this subtraction involves cancelations of diagrams as opposed to the summation of topologically distinct, independent diagrams we have encountered so far. This can already be seen at first order where $\mathcal{N}_{\Gamma_0^{(4)}}^{\uparrow\uparrow} = 0$. Such cancelations of diagrams can only change the number of diagrams by a multiple of 2. Consequently, we infer that

$$2\mathcal{N}_{\Gamma^{(4)}}^{\uparrow\downarrow} - \mathcal{N}_{\Gamma^{(4)}}^{\uparrow\uparrow} \in 2\mathbb{N}_0. \tag{A5}$$

If we further invoke the channel decomposition with crossing symmetries, we find that all of

$$2\mathcal{N}_{R}^{\uparrow\downarrow} - \mathcal{N}_{R}^{\uparrow\uparrow}, \quad 2\mathcal{N}_{\gamma_p}^{\uparrow\downarrow} - \mathcal{N}_{\gamma_p}^{\uparrow\uparrow}, \quad \mathcal{N}_{\gamma_a}^{\uparrow\downarrow} + \mathcal{N}_{\gamma_t}^{\uparrow\downarrow} - \mathcal{N}_{\gamma_a}^{\uparrow\uparrow} \tag{A6}$$

are nonnegative, even numbers (as can explicitly be checked in Tables III and IV).

Next, we perform the spin summation in the different many-body relations stated in Sec. III. Starting with Eqs. (11) and (13) for the self-energy, we get

$$\mathcal{N}_{\Sigma} = \mathcal{N}_{\Gamma_0^{(4)}}^{\uparrow\downarrow} * \mathcal{N}_G + \mathcal{N}_{\Gamma_0^{(4)}}^{\uparrow\downarrow} * \mathcal{N}_{\Pi} * \mathcal{N}_G * \mathcal{N}_{\Gamma^{(4)}}^{\uparrow\downarrow}, \tag{A7a}$$

$$\begin{aligned} \mathcal{N}_{\dot{\Sigma}} &= \left(\mathcal{N}_{\Gamma^{(4)}}^{\uparrow\downarrow} + \mathcal{N}_{\Gamma^{(4)}}^{\uparrow\uparrow}\right) * \mathcal{N}_S & \text{(A7b)} \\ &= \left(\mathcal{N}_{I_t}^{\uparrow\downarrow} + \mathcal{N}_{I_t}^{\uparrow\uparrow}\right) * \mathcal{N}_{\dot{G}}. & \text{(A7c)} \end{aligned}$$

From Eqs. (17) and (18), we similarly get for the four-point vertex ($\mathcal{N}_{\dot{\Pi}_S} = \mathcal{N}_G * \mathcal{N}_S$)

$$\begin{aligned}\mathcal{N}^{\uparrow\downarrow}_{\dot{\Gamma}^{(4)}} &= 2\,\mathcal{N}^{\uparrow\downarrow}_{\Gamma^{(4)}} * \mathcal{N}_{\dot{\Pi}_S} * \mathcal{N}^{\uparrow\downarrow}_{\Gamma^{(4)}} + 2\,\mathcal{N}^{\uparrow\downarrow}_{\Gamma^{(4)}} * \mathcal{N}_{\dot{\Pi}_S} * \mathcal{N}^{\uparrow\uparrow}_{\Gamma^{(4)}} \\ &\quad +2\,\mathcal{N}^{\uparrow\downarrow\uparrow}_{\Gamma^{(6)}} * N_S, \qquad \text{(A8a)}\\ \mathcal{N}^{\uparrow\uparrow}_{\dot{\Gamma}^{(4)}} &= \tfrac{5}{2}\,\mathcal{N}^{\uparrow\uparrow}_{\Gamma^{(4)}} * \mathcal{N}_{\dot{\Pi}_S} * \mathcal{N}^{\uparrow\uparrow}_{\Gamma^{(4)}} + 2\,\mathcal{N}^{\uparrow\downarrow}_{\Gamma^{(4)}} * \mathcal{N}_{\dot{\Pi}_S} * \mathcal{N}^{\uparrow\downarrow}_{\Gamma^{(4)}} \\ &\quad + \mathcal{N}^{\uparrow\downarrow\uparrow}_{\Gamma^{(6)}} * N_S + \mathcal{N}^{\uparrow\uparrow\uparrow}_{\Gamma^{(6)}} * N_S, \qquad \text{(A8b)}\\ \mathcal{N}^{\uparrow\downarrow}_{\Gamma^{(4)}} &= \mathcal{N}^{\uparrow\downarrow}_{\Gamma^{(4)}_0} + 2\,\mathcal{N}^{\uparrow\downarrow}_{\Gamma^{(4)}_0} * \mathcal{N}_{\Pi} * \mathcal{N}^{\uparrow\downarrow}_{\Gamma^{(4)}} \\ &\quad + \mathcal{N}^{\uparrow\downarrow}_{\Gamma^{(4)}_0} * \mathcal{N}_{\Pi} * \mathcal{N}^{\uparrow\uparrow}_{\Gamma^{(4)}} + \mathcal{N}^{\uparrow\downarrow}_{\Gamma^{(4)}_0} * \mathcal{N}_{\Pi} * \mathcal{N}^{\uparrow\downarrow\uparrow}_{\Gamma^{(6)}} \\ &\quad + 3\,\mathcal{N}^{\uparrow\downarrow}_{\Gamma^{(4)}_0} * \mathcal{N}_{\Pi} * \mathcal{N}_{\Pi} * \mathcal{N}^{\uparrow\downarrow}_{\Gamma^{(4)}} * \mathcal{N}^{\uparrow\downarrow}_{\Gamma^{(4)}} \\ &\quad + 4\,\mathcal{N}^{\uparrow\downarrow}_{\Gamma^{(4)}_0} * \mathcal{N}_{\Pi} * \mathcal{N}_{\Pi} * \mathcal{N}^{\uparrow\downarrow}_{\Gamma^{(4)}} * \mathcal{N}^{\uparrow\uparrow}_{\Gamma^{(4)}}, \qquad \text{(A8c)}\\ \mathcal{N}^{\uparrow\uparrow}_{\Gamma^{(4)}} &= 2\,\mathcal{N}^{\uparrow\downarrow}_{\Gamma^{(4)}_0} * \mathcal{N}_{\Pi} * \mathcal{N}^{\uparrow\downarrow}_{\Gamma^{(4)}} \\ &\quad + \mathcal{N}^{\uparrow\downarrow}_{\Gamma^{(4)}_0} * \mathcal{N}_{\Pi} * \mathcal{N}^{\uparrow\uparrow}_{\Gamma^{(4)}} + \mathcal{N}^{\uparrow\downarrow}_{\Gamma^{(4)}_0} * \mathcal{N}_{\Pi} * \mathcal{N}^{\uparrow\downarrow\uparrow}_{\Gamma^{(6)}} \\ &\quad + 4\,\mathcal{N}^{\uparrow\downarrow}_{\Gamma^{(4)}_0} * \mathcal{N}_{\Pi} * \mathcal{N}_{\Pi} * \mathcal{N}^{\uparrow\downarrow}_{\Gamma^{(4)}} * \mathcal{N}^{\uparrow\downarrow}_{\Gamma^{(4)}} \\ &\quad + 3\,\mathcal{N}^{\uparrow\downarrow}_{\Gamma^{(4)}_0} * \mathcal{N}_{\Pi} * \mathcal{N}_{\Pi} * \mathcal{N}^{\uparrow\downarrow}_{\Gamma^{(4)}} * \mathcal{N}^{\uparrow\uparrow}_{\Gamma^{(4)}}. \qquad \text{(A8d)}\end{aligned}$$

Finally, we resolve the parquet equations (19) in their spin configurations and obtain

$$\begin{aligned}\mathcal{N}^{\sigma\sigma'}_{\Gamma^{(4)}} &= \mathcal{N}^{\sigma\sigma'}_{R} + \sum_r \mathcal{N}^{\sigma\sigma'}_{\gamma_r}, \qquad \text{(A9a)}\\ \mathcal{N}^{\sigma\sigma'}_{I_r} &= \mathcal{N}^{\sigma\sigma'}_{\Gamma^{(4)}} - \mathcal{N}^{\sigma\sigma'}_{\gamma_r}, \qquad \text{(A9b)}\\ \mathcal{N}^{\uparrow\downarrow}_{\gamma_a} &= \mathcal{N}^{\uparrow\downarrow}_{I_a} * \mathcal{N}_{\Pi} * \mathcal{N}^{\uparrow\downarrow}_{\Gamma^{(4)}}, \qquad \text{(A9c)}\\ \mathcal{N}^{\uparrow\downarrow}_{\gamma_p} &= \mathcal{N}^{\uparrow\downarrow}_{I_p} * \mathcal{N}_{\Pi} * \mathcal{N}^{\uparrow\downarrow}_{\Gamma^{(4)}}, \qquad \text{(A9d)}\\ \mathcal{N}^{\uparrow\downarrow}_{\gamma_t} &= \mathcal{N}^{\uparrow\downarrow}_{I_t} * \mathcal{N}_{\Pi} * \mathcal{N}^{\uparrow\uparrow}_{\Gamma^{(4)}} + \mathcal{N}^{\uparrow\uparrow}_{I_t} * \mathcal{N}_{\Pi} * \mathcal{N}^{\uparrow\downarrow}_{\Gamma^{(4)}}, \qquad \text{(A9e)}\\ \mathcal{N}^{\uparrow\uparrow}_{\gamma_a} &= \mathcal{N}^{\uparrow\uparrow}_{I_a} * \mathcal{N}_{\Pi} * \mathcal{N}^{\uparrow\uparrow}_{\Gamma^{(4)}} + \mathcal{N}^{\uparrow\downarrow}_{I_t} * \mathcal{N}_{\Pi} * \mathcal{N}^{\uparrow\downarrow}_{\Gamma^{(4)}}, \qquad \text{(A9f)}\\ \mathcal{N}^{\uparrow\uparrow}_{\gamma_p} &= \tfrac{1}{2}\mathcal{N}^{\uparrow\uparrow}_{I_p} * \mathcal{N}_{\Pi} * \mathcal{N}^{\uparrow\uparrow}_{\Gamma^{(4)}}, \qquad \text{(A9g)}\\ \mathcal{N}^{\uparrow\uparrow}_{\gamma_t} &= \mathcal{N}^{\uparrow\uparrow}_{I_t} * \mathcal{N}_{\Pi} * \mathcal{N}^{\uparrow\uparrow}_{\Gamma^{(4)}} + \mathcal{N}^{\uparrow\downarrow}_{I_t} * \mathcal{N}_{\Pi} * \mathcal{N}^{\uparrow\downarrow}_{\Gamma^{(4)}}. \qquad \text{(A9h)}\end{aligned}$$

In Sec. III we combined the Schwinger-Dyson with differential (or flow) equations to iteratively construct the exact number of diagrams. Here we see that the Schwinger-Dyson equations of Σ [Eq. (A7a)] and $\Gamma^{(4)}$ [Eqs. (A8c) and (A8d)] contain the corresponding higher-point vertex $\Gamma^{(4)}$ and $\Gamma^{(6)}$, respectively, only in the configuration with different spins. However, the differential equations [Eqs. (A7b) and (A7c) and Eqs. (A8a) and (A8b)] involve the same higher-point vertex in all of its spin configurations. It is for this reason that one cannot iteratively construct the exact number of *spin-resolved* diagrams. However, the equations can easily be used to generate the number of diagrams in approximations that do allow for an iterative construction, such as parquet-type approximations or approximations that involve a finite number of known (bare or skeleton) diagrams.

---

[1] J. Negele and H. Orland, *Quantum Many-Particle Systems*, Advanced Books Classics (Perseus Books, New York, 1998).

[2] F. B. Kugler and J. von Delft, Phys. Rev. B **97**, 035162 (2018).

[3] R. A. Smith, Phys. Rev. A **46**, 4586 (1992).

[4] L. Hedin, Phys. Rev. **139**, A796 (1965).

[5] N. Bickers, in *Theoretical Methods for Strongly Correlated Electrons*, CRM Series in Mathematical Physics, edited by D. Sénéchal, A.-M. Tremblay, and C. Bourbonnais (Springer, New York, 2004), pp. 237–296.

[6] K. Held, C. Taranto, G. Rohringer, and A. Toschi, in *The LDA+DMFT Approach to Strongly Correlated Materials—Lecture Notes of the Autumn School 2011*, edited by E. Pavarini, E. Koch, D. Vollhardt, and A. Lichtenstein (Forschungszentrum Jülich, Jülich, 2011), Chap. 13.0.

[7] F. B. Kugler and J. von Delft, arXiv:1807.02898.

[8] The precise formulation can be found in Ref. [2]; the indices in the functional derivative are $\delta\Sigma_{x',x}/\delta G_{y,y'} = -I_{t;x',y';x,y} = I_{a;x',y';y,x}$.

[9] W. Metzner, M. Salmhofer, C. Honerkamp, V. Meden, and K. Schönhammer, Rev. Mod. Phys. **84**, 299 (2012).

[10] P. Kopietz, L. Bartosch, and F. Schütz, *Introduction to the Functional Renormalization Group*, Lecture Notes in Physics Vol. 798 (Springer, Berlin, 2010).

[11] B. Roulet, J. Gavoret, and P. Nozières, Phys. Rev. **178**, 1072 (1969).

[12] The term transverse refers to a horizontal space-time axis; in using the terms antiparallel and parallel, we adopt the nomenclature used by Roulet *et al.* [11]. Equivalently, a common notation [13–15] for the channels a, p, t is ph, pp, $\overline{ph}$, referring to the (longitudinal) particle-hole, the particle-particle, and the transverse (or vertical) particle-hole channel, respectively. One also finds the labels x, p, d in the literature [16], referring to the so-called exchange, pairing, and direct channel, respectively.

[13] G. Rohringer, A. Valli, and A. Toschi, Phys. Rev. B **86**, 125114 (2012).

[14] G. Rohringer, H. Hafermann, A. Toschi, A. A. Katanin, A. E. Antipov, M. I. Katsnelson, A. I. Lichtenstein, A. N. Rubtsov, and K. Held, Rev. Mod. Phys. **90**, 025003 (2018).

[15] N. Wentzell, G. Li, A. Tagliavini, C. Taranto, G. Rohringer, K. Held, A. Toschi, and S. Andergassen, arXiv:1610.06520.

[16] S. G. Jakobs, M. Pletyukhov, and H. Schoeller, Phys. Rev. B **81**, 195109 (2010).

[17] K. Veschgini and M. Salmhofer, Phys. Rev. B **88**, 155131 (2013).

[18] P. Cvitanović, B. Lautrup, and R. B. Pearson, Phys. Rev. D **18**, 1939 (1978).

[19] R. A. Jishi, *Feynman Diagram Techniques in Condensed Matter Physics* (Cambridge University Press, Cambridge, 2013).

[20] L. G. Molinari and N. Manini, Eur. Phys. J. B **51**, 331 (2006).

[21] W. Zhou, Ph.D. thesis, University of Georgia, Athens, 2008.

[22] Their number at order 6 should be 12 018 instead of 12 081.

[23] We conclude that in Ref. [18], Table I, first column, the factor C should read $\sqrt{2/\pi}$ instead of $\sqrt{2}/\pi$. We can numerically confirm their coefficients d_1 and d_2 for the subleading contributions.
[24] A. Montorsi, *The Hubbard Model: A Reprint Volume* (World Scientific, Singapore, 1992).
[25] K. Van Houcke, F. Werner, N. Prokof'ev, and B. Svistunov, arXiv:1305.3901.
[26] F. Aryasetiawan and O. Gunnarsson, Rep. Prog. Phys. **61**, 237 (1998).
[27] L. G. Molinari, Phys. Rev. B **71**, 113102 (2005).
[28] J. M. Luttinger and J. C. Ward, Phys. Rev. **118**, 1417 (1960).
[29] G. Baym, Phys. Rev. **127**, 1391 (1962).
[30] F. B. Kugler and J. von Delft, Phys. Rev. Lett. **120**, 057403 (2018).
[31] K. V. Houcke, E. Kozik, N. Prokof'ev, and B. Svistunov, Phys. Procedia **6**, 95 (2010), Computer Simulations Studies in Condensed Matter Physics XXI.

5 Transport through multilevel quantum dots

5.1 Overview

Quantum dots constitute fascinating and, at the same time, minimalist quantum systems, which play a central role in nanotechnology. Considering, e.g., their potential as single-electron transistors, transport through quantum dots is of particular interest. In the simplest version, a quantum dot can be occupied by at most two charge carriers, corresponding to electrons with two different spin states—a setup well studied in the literature [HKP⁺07]. The following articles[1] focus on transport through *generic* quantum dots, where a dot of N levels is enclosed between a right (R) and left (L) lead of N_R and N_L levels, respectively. The latter two can be chosen equal to N without loss of generality [P7], and the case $N = 3$ is given special attention.

The first article [P7] focuses on the Coulomb-blockade regime with a singly occupied dot at large Coulomb repulsion. It employs poor man's RG as well as NRG to show that the equilibrium three-level quantum dot hosts an SU(3)-symmetric fixed point. It further reveals that the situation is much richer in nonequilibrium, where, in particular, the finite bias voltage drives the system towards a fixed point of different symmetry compared to the equilibrium case. The second article [P8] considers the regime of strong charge fluctuations. By comparing results of NRG, fRG, and the real-time renormalization group (RTRG), it advertises RTRG as a versatile tool to describe charge fluctuations in general quantum dots both in and out of equilibrium.

P7 *Flavor fluctuations in three-level quantum dots: Generic SU(3) Kondo fixed point in equilibrium and non-Kondo fixed points in nonequilibrium*
C. J. Lindner, **F. B. Kugler**, H. Schoeller, J. von Delft
Phys. Rev. B **97**, 235450 (2018)
DOI: 10.1103/PhysRevB.97.235450
© 2018 American Physical Society
reprinted on pages 151–171.

P8 *Renormalization group transport theory for open quantum systems: Charge fluctuations in multilevel quantum dots in and out of equilibrium*
C. J. Lindner, **F. B. Kugler**, V. Meden, H. Schoeller
Phys. Rev. B **99**, 205142 (2019)
DOI: 10.1103/PhysRevB.99.205142
© 2019 American Physical Society
reprinted on pages 172–188.

---

[1] The author of this thesis implemented the NRG code, produced the NRG results for both publications, and contributed to writing the manuscripts, especially section III of [P7].

PHYSICAL REVIEW B **97**, 235450 (2018)

Flavor fluctuations in three-level quantum dots: Generic SU(3) Kondo fixed point in equilibrium and non-Kondo fixed points in nonequilibrium

Carsten J. Lindner,[1,2] Fabian B. Kugler,[3] Herbert Schoeller,[1,2,*] and Jan von Delft[3]
[1]*Institut für Theorie der Statistischen Physik, RWTH Aachen, 52056 Aachen, Germany*
[2]*JARA-Fundamentals of Future Information Technology, Aachen, Germany*
[3]*Physics Department, Arnold Sommerfeld Center for Theoretical Physics, and Center for NanoScience, Ludwigs-Maximilians-Universität München, Theresienstr. 37, 80333 Munich, Germany*

(Received 28 February 2018; published 29 June 2018)

We study a three-level quantum dot in the singly occupied cotunneling regime coupled via a generic tunneling matrix to several multichannel leads in equilibrium or nonequilibrium. Denoting the three possible states of the quantum dot by the quark flavors up (u), down (d), and strange (s), we derive an effective model where also each reservoir has three flavors labeled by u, d, and s with an effective density of states polarized with respect to an eight-dimensional F spin corresponding to the eight generators of SU(3). In *equilibrium* we perform a standard poor man's scaling analysis and show that tunneling via virtual intermediate states induces flavor fluctuations on the dot which become SU(3) symmetric at a characteristic and exponentially small low-energy scale T_K. Close to T_K the system is described by a single isotropic Kondo coupling $J > 0$ diverging at T_K. Using the numerical renormalization group, we study in detail the linear conductance and confirm the SU(3)-symmetric Kondo fixed point with universal conductance $G = 3\sin^2(\pi/3)\frac{e^2}{h} = 2.25\frac{e^2}{h}$ for various tunneling setups by tuning the level spacings on the dot. We also identify regions of the level positions where the SU(2) Kondo fixed point is obtained and find a rather complex dependence of the various Kondo temperatures as function of the gate voltage and the tunneling couplings. In contrast to the equilibrium case, we find in *nonequilibrium* that the fixed-point model is *not* SU(3) symmetric but characterized by rotated F spins for each reservoir with total vanishing sum. At large voltage we analyze the F-spin magnetization and the current in Fermi's golden rule as function of a longitudinal (h_z) and perpendicular ($h_\perp$) magnetic field for the isospin and the level spacing Δ to the strange quark. As a smoking gun to detect the nonequilibrium fixed point we find that the curve of zero F-spin magnetization in (h_z,$h_\perp$,Δ) space is a circle when projected onto the (h_z,$h_\perp$) plane. We propose that our findings can be generalized to the case of quantum dots with an arbitrary number N of levels.

DOI: 10.1103/PhysRevB.97.235450

I. INTRODUCTION

Over the last three decades, transport properties of correlated quantum dots have gained an enormous interest in many experimental and theoretical research activities in condensed matter physics. As artificial atoms they allow for a controlled study of interesting phenomena playing a central role in many different fields of applied and fundamental research in nanoelectronics, spintronics, quantum information processing, dissipative quantum mechanics, and many-body physics and nonequilibrium phenomena in correlated systems (see, e.g., Refs. [1,2] for reviews). Of particular interest is the cotunneling or Coulomb blockade regime of quantum dots with strong charging energy, where the charge is fixed and only the spin and orbital degrees of freedom can fluctuate by second-order tunneling processes via virtual intermediate states. In this regime, effective models can be derived which are equivalent to Kondo models well known from solid-state physics [3] (see, e.g., Ref. [4] for a review of the Kondo effect in quantum dots). The standard model is the SU(2) Kondo model, where a local spin-$\frac{1}{2}$ is coupled via an isotropic exchange coupling to the spins of two large reservoirs. Below a characteristic low-energy scale, called the Kondo temperature T_K, the local spin is completely screened and the remaining potential scattering leads to resonant transport through the system with universal conductance $2\frac{e^2}{h}$. This Kondo effect has been theoretically predicted for quantum dots [5] and has been experimentally observed [6]. After this discovery, the research for Kondo physics in quantum dots has gained an enormous interest and further realizations have been proposed and observed, such as, e.g., the realization of higher spin values [7], singlet-triplet fluctuations [8], non-Fermi-liquid behavior in two-channel realizations [9], and the SU(4) Kondo effect [10]. Recently, also the realization of SU(N) Kondo physics for arbitrary N has been proposed in coupled quantum dots [11–13].

The enormous variety of possible realizations of Kondo physics raises the question as to what happens in the generic case when a quantum dot in the regime of fixed charge with $N_{\rm dot} \geqslant 1$ electrons and $N \geqslant 2$ levels is coupled via a generic tunneling matrix to several multichannel reservoirs. Even for the simplest case $N_{\rm dot} = 1$ and $N = 2$, this issue is nontrivial since the quantum number $l = 1,2$ labeling the two dot levels is in general a nonconserved quantity in tunneling, such as, e.g., for ferromagnetic leads [14], orbital degrees of freedom

---

[*] schoeller@physik.rwth-aachen.de

©2018 American Physical Society

[15], Aharonov-Bohm geometries [16], and spin-orbit or Dzyaloshinski-Moriya interactions [17,18]. In Ref. [16] it was shown via a singular value decomposition of the total tunneling matrix (i.e., containing *all* reservoirs) that all these different cases can be mapped onto an effective model which is equivalent to the anisotropic spin-$\frac{1}{2}$ Kondo model which flows into the isotropic SU(2)-symmetric fixed point at low energies below the Kondo temperature. This explains why in all linear response transport calculations of quantum dot models with $N_{\text{dot}} = 1$ and $N = 2$, the Kondo effect with universal conductance is observed provided that local effective magnetic fields are explicitly canceled by external ones [19]. However, this result is only valid in the linear response regime and for proportional couplings to all the reservoirs where the linear conductance can be related to the equilibrium spectral density of the dot [20]. To calculate the latter, all reservoirs can be taken together to a single one and only the total tunneling matrix matters. However, when all reservoirs are coupled in a generic way to the dot or when they are characterized by different temperatures or chemical potentials, the analysis of Ref. [16] is no longer valid. This fact was emphasized in Ref. [21], where it was shown that in a generic *nonequilibrium* situation, the proper effective model for $N_{\text{dot}} = 1$ and $N = 2$ is a spin-valve model, where the spin polarizations of all reservoirs point in different directions, such that at the low-energy fixed point their sum is equal to zero. This has the consequence that the fixed-point model in nonequilibrium is essentially not SU(2) symmetric and new interesting nonequilibrium fixed-point models emerge with different non-Kondo-type properties in the weak- as well as in the strong-coupling regime. Only in the equilibrium situation when all reservoirs are characterized by the same temperature and chemical potential, all reservoirs can be taken together, resulting in an unpolarized reservoir with SU(2) symmetry at the fixed point. The nonequilibrium properties at and away from the fixed-point model have been studied for large voltages above the Kondo temperature [21], and a smoking gun was identified in the nontrivial magnetic field dependence of the magnetization and the transport current characterizing the fixed-point model.

The proposals of new nonequilibrium fixed-point models are of particular interest for the constant effort to generalize well-established analytical and numerical methods for the study of equilibrium properties of quantum impurity models [3,22] to the nonequilibrium case. Recent developments of perturbative renormalization group methods [23–26] have shown how the voltage dependence and the physics of cutoff scales by decay rates can be implemented [27] and how the time evolution into the stationary state can be calculated [28]. Even in the strong-coupling regime [29,30] results in agreement with experiments [31] were obtained, although the used methods are essentially perturbative and not capable of describing the strong-coupling regime in general. Therefore, numerically exact methods are required for the description of quantum dot systems in nonequilibrium, such as, e.g., the time-dependent numerical renormalization group (TD-NRG) [32], time-dependent density matrix renormalization group (TD-DMRG) [33], iterative stochastic path integrals [34], and quantum Monte Carlo methods [35]. Recently, a promising thermofield approach has been suggested by a combination of TD-NRG and TD-DMRG [36] showing a good agreement with the strong-coupling results for the nonequilibrium Kondo model of Refs. [29–31].

The aim of this paper is to analyze the generic case $N_{\text{dot}} = 1$ and arbitrary N to see how the results of Ref. [21] can be generalized to the case $N > 2$. In particular, we will study the case $N = 3$ and, starting from a generic tunneling matrix, will show that an effective tunneling model can be derived where also the reservoirs are characterized by three flavors which we will conveniently label by the up (u), down (d), and strange (s) quark flavors. The effective model in the cotunneling regime of a singly occupied quantum dot can be described by flavor fluctuations, and we will show by a poor man's scaling analysis that the low-energy fixed-point model is indeed the SU(3)-symmetric Kondo model. This result is shown to hold also for arbitrary N within the poor man's scaling analysis and will be explicitly confirmed for $N = 3$ by a numerically exact NRG analysis for the linear response conductance, similiar to Refs. [12,13]. In addition to these references, we will study the dependence of the SU(3) Kondo temperature on the tunneling matrix elements and will show how the SU(3)-symmetric point is obtained by a proper adjustment of the level spacings of the dot. Subsequently, we will analyze the nonequilibrium situation and generalize the spin-valve model of Ref. [21] for $N = 2$ to the case of three levels $N = 3$. In this case, a fixed-point model arises where the reservoirs are characterized by eight-dimensional F spins corresponding to the eight generators of the SU(3) group which cancel when all reservoirs are taken together. For large voltages and two reservoirs we find that the nonequilibrium fixed-point model has a characteristic dependence on the dot parameters for zero F-spin magnetization on the dot providing a *smoking gun* for the detection of the fixed point. Thus, we conclude that the results of Ref. [21] can indeed be generalized to the case of $N > 2$ levels with a great potential for a variety of new interesting nonequilibrium fixed-point models where the low-energy behavior in the strong-coupling regime is still unknown.

The paper is organized as follows. In Sec. II we will derive various effective models. We will set up effective tunneling models in Sec. II A and the effective model in the cotunneling regime in Sec. II B. The fixed-point model is obtained via a poor man's scaling analysis in Sec. II C for arbitrary N. In Sec. II D we consider the particular case $N = 3$ and will set up the relation to the representation of the SU(3) group and the physical picture in terms of F-spin interactions. In Sec. III we will use the NRG method to confirm the SU(3)-symmetric fixed-point model in the linear response regime. Finally, in Sec. IV we analyze the nonequilibrium properties of the fixed-point model in the perturbative regime of large voltage via a Fermi's golden rule approach. The general formulas are derived in Sec. IV A and the magnetization and the current are calculated as function of characteristic dot parameters for the case of two reservoirs in Sec. IV B where the smoking gun for the detection of the fixed-point model is derived. We close with a summary of our results in Sec. V. We use units $e = \hbar = 1$ throughout this paper.

II. DERIVATION OF EFFECTIVE MODELS

In this section we start from a quantum dot with N levels coupled via a generic tunneling matrix to N_{res} multichannel noninteracting reservoirs in grand-canonical equilibrium. We show in Sec. II A that this model is equivalent to an effective one where the number of channels in each reservoir is the same as the number N of the quantum dot levels. For the special case of $N = 3$ this sets the basis to use a notation in terms of three flavor states for the three channels and to characterize the reservoirs by rotated F spins with a certain isospin and hypercharge polarization. In addition, we will set up various effective tunneling models and characterize the properties of the central fixed-point model derived in Secs. II B–II D for the cotunneling regime, where the number N_{dot} of particles on the dot is fixed to $N_{\mathrm{dot}} = 1$, such that only flavor fluctuations via virtual intermediate states can occur. In this regime, we will derive an effective model describing flavor fluctuations and propose the fixed-point model from a poor man's scaling analysis.

A. Effective tunneling models

The starting point is a quantum dot consisting of N levels characterized by some quantum number $l = 1,2,\dots,N$, together with a Coulomb energy $E_{N_{\mathrm{dot}}}$ depending only on the total particle number operator $N_{\mathrm{dot}} = \sum_l c_l^\dagger c_l$ of the dot

$$H_{\mathrm{dot}} = \sum_{ll'} h_{ll'} c_l^\dagger c_{l'} + E_{N_{\mathrm{dot}}}, \tag{1}$$

$$E_{N_{\mathrm{dot}}} = E_C (N_{\mathrm{dot}} - n_x)^2, \tag{2}$$

where $c_l^\dagger / c_l$ are the creation/annihilation operators of the single-particle states of the dot. The charging energy E_c is assumed to be the largest energy scale in the problem such that, for small $h_{ll'}$, the parameter n_x determines the occupation of the dot. If $n_x = n$ is integer, the ground state will be dominated by $N_{\mathrm{dot}} = n$, whereas for half-integer $n_x = n + \frac{1}{2}$, states with $N_{\mathrm{dot}} = n, n+1$ are degenerate with respect to the Coulomb interaction. For convenience, we define the gate voltage by

$$V_g = E_c(2n_x - N), \tag{3}$$

such that $V_g = 0$ (or $n_x = N/2$) defines the particle-hole-symmetric point for $h_{ll'} = 0$. With this definition we can also write the dot Hamiltonian in second quantized form as

$$H_{\mathrm{dot}} = \sum_{ll'} \tilde{h}_{ll'} c_l^\dagger c_{l'} + \frac{U}{2} \sum_{ll'} c_l^\dagger c_{l'}^\dagger c_{l'} c_l, \tag{4}$$

with $U = 2E_c$ and $\tilde{h}_{ll'} = h_{ll'} - [V_g + (U/2)(N-1)]\delta_{ll'}$.

The quantum dot is coupled via a generic tunneling matrix to several infinitely large reservoirs $\alpha = 1,2,\dots,N_{\mathrm{res}}$ kept at grand-canonical equilibrium with temperature T and chemical potential μ_α, such that the total Hamiltonian reads as

$$H_{\mathrm{tot}} = H_{\mathrm{dot}} + H_{\mathrm{res}} + H_T, \tag{5}$$

with the reservoir Hamiltonian

$$H_{\mathrm{res}} = \sum_{\alpha\nu_\alpha k} \epsilon_{\alpha\nu_\alpha k}\, a_{\alpha\nu_\alpha k}^\dagger a_{\alpha\nu_\alpha k}, \tag{6}$$

and the tunneling Hamiltonian

$$H_T = \frac{1}{\sqrt{\rho^{(0)}}} \sum_{\alpha\nu_\alpha l k} \left\{ t_{\nu_\alpha l}^\alpha a_{\alpha\nu_\alpha k}^\dagger c_l + \left(t_{\nu_\alpha l}^\alpha\right)^* c_l^\dagger a_{\alpha\nu_\alpha k} \right\}. \tag{7}$$

Here, $\nu_\alpha = 1,2,\dots,N_\alpha$ is the channel index for reservoir α (with N_α channels in total), $\epsilon_{\alpha\nu_\alpha k}$ is the band dispersion of reservoir α for channel ν_α relative to the chemical potential μ_α and labeled by k (which becomes continuous in the thermodynamic limit), and $t_{\nu_\alpha l}^\alpha$ is the tunneling matrix between the dot and reservoir α. $\rho^{(0)}$ is some average density of states (DOS) in the reservoirs, which is set to $\rho^{(0)} = 1$ in the following defining the energy units. In vector-matrix notation, the tunneling Hamiltonian can be written in a more compact form as

$$H_T = \sum_{\alpha k} \{ \underline{a}_{\alpha k}^\dagger \underline{\underline{t}}_\alpha \underline{c} + \underline{c}^\dagger \underline{\underline{t}}_\alpha^\dagger \underline{a}_{\alpha k} \}, \tag{8}$$

where $\underline{c}^\dagger = (c_1^\dagger, \dots, c_N^\dagger)$, $\underline{a}_{\alpha k}^\dagger = (a_{\alpha 1 k}^\dagger, \dots, a_{\alpha N_\alpha k}^\dagger)$, and $\underline{\underline{t}}_\alpha$ is a $N_\alpha \times N$ matrix with matrix elements $t_{\nu_\alpha l}^\alpha$. For convenience, we have taken here a tunneling matrix independent of k which is usually a very good approximation for rather flat reservoir bands on the scale of the low-energy scales of interest.

Using Keldysh formalism. it is straightforward [20,37] to relate the stationary current $I_{\alpha\nu_\alpha}$ in reservoir α and channel ν_α to the stationary nonequilibrium greater/lesser Green's functions $G_{ll'}^{\gtrless}(\omega)$ of the dot via

$$I_{\alpha\nu_\alpha} = \frac{e}{h} \int d\omega\, \mathrm{Tr}\, \underline{\underline{\Gamma}}_{\alpha\nu_\alpha} \{ [1 - f_\alpha(\omega)]\, i \underline{\underline{G}}^<(\omega) + f_\alpha(\omega)\, i \underline{\underline{G}}^>(\omega) \}, \tag{9}$$

where Tr denotes the trace over the single-particle states of the dot, $f_\alpha(\omega) = (e^{\beta(\omega - \mu_\alpha)} + 1)^{-1}$ is the Fermi function of reservoir α, and the $(N \times N)$-hybridization matrix $\underline{\underline{\Gamma}}_{\alpha\nu_\alpha}$ is defined by

$$\left(\underline{\underline{\Gamma}}_{\alpha\nu_\alpha}\right)_{ll'} = 2\pi \rho_{\alpha\nu_\alpha} \left(t_{\nu_\alpha l}^\alpha\right)^* t_{\nu_\alpha l'}^\alpha. \tag{10}$$

Here, $\rho_{\alpha\nu_\alpha} = \sum_k \delta(\omega - \epsilon_{\alpha\nu_\alpha k})$ denotes the DOS in reservoir α for channel ν_α, which is assumed to be rather flat so that the energy dependence can be neglected. The influence of the reservoirs and the tunneling on the Green's functions is determined by the reservoir part of the lesser/greater self-energy given by

$$\underline{\underline{\Sigma}}_{\mathrm{res}}^<(\omega) = i \sum_\alpha f_\alpha(\omega) \underline{\underline{\Gamma}}_\alpha, \tag{11}$$

$$\underline{\underline{\Sigma}}_{\mathrm{res}}^>(\omega) = -i \sum_\alpha (1 - f_\alpha(\omega)) \underline{\underline{\Gamma}}_\alpha, \tag{12}$$

where

$$\underline{\underline{\Gamma}}_\alpha = \sum_{\nu_\alpha} \underline{\underline{\Gamma}}_{\alpha\nu_\alpha} = 2\pi\, \underline{\underline{t}}_\alpha^\dagger\, \underline{\underline{\rho}}_\alpha\, \underline{\underline{t}}_\alpha \tag{13}$$

is the hybridization matrix for reservoir α including all channels and $(\underline{\underline{\rho}}_\alpha)_{\nu_\alpha \nu_\alpha'} = \delta_{\nu_\alpha \nu_\alpha'} \rho_{\alpha\nu_\alpha}$ is the diagonal matrix for the DOS of reservoir α. As a consequence, we see that the Green's functions depend on the reservoirs and the tunneling matrix only via the hybridization matrices $\underline{\underline{\Gamma}}_\alpha$ of all the reservoirs. Thus, two models with the same hybridization matrices give exactly the same Green's functions. Once the Green's functions are known, the channel-resolved currents $I_{\alpha\nu_\alpha}$ can be calculated from (9), where the channel-resolved hybridization matrix $\underline{\underline{\Gamma}}_{\alpha\nu_\alpha}$ of the concrete model under consideration has to be inserted. The stationary expectation values of single-particle operators of the dot can be directly calculated from the lesser Green's functions via $\langle c^\dagger_{l'} c_l \rangle = \frac{1}{2\pi i}\int d\omega\, G^<_{ll'}(\omega)$ and thus are exactly the same for two models with the same hybridization matrices $\underline{\underline{\Gamma}}_\alpha$.

We note that for the equilibrium case, where all Fermi functions of the reservoirs are the same, the reservoir self-energies involve only the total hybridization matrix

$$\underline{\underline{\Gamma}} = \sum_\alpha \underline{\underline{\Gamma}}_\alpha, \tag{14}$$

with the result that the equilibrium Green's functions are the same for two models with the same $\underline{\underline{\Gamma}}$. However, the current in linear response can not be related to the single-particle Green's functions in equilibrium via (9) since also the Green's functions have to be expanded in the voltages. A special case is the one of proportional couplings where it is assumed that $\underline{\underline{\Gamma}}_\alpha = x_\alpha \underline{\underline{\Gamma}}$ with $\sum_\alpha x_\alpha = 1$. Using current conservation $\sum_\alpha I_\alpha = 0$, with $I_\alpha = \sum_{\nu_\alpha} I_{\alpha\nu_\alpha}$ denoting the total current in reservoir α, we get in this case from (9) the Landauer-Büttiker–type formula [20]

$$I_\alpha = \frac{e}{h}\sum_{\beta\neq\alpha}\int d\omega\, T_{\alpha\beta}(\omega)(f_\alpha - f_\beta)(\omega), \tag{15}$$

with the transmission probability

$$T_{\alpha\beta}(\omega) = 2\pi\, x_\alpha x_\beta \mathrm{Tr}\, \underline{\underline{\Gamma}}\, \underline{\underline{\rho}}(\omega), \tag{16}$$

where $\underline{\underline{\rho}}(\omega) = \frac{i}{2\pi}(\underline{\underline{G}}^R - \underline{\underline{G}}^A)(\omega)$ is the spectral density on the dot. From this formula one can see that in linear response, where $(f_\alpha - f_\beta)(\omega) \approx -f'(\omega)(\mu_\alpha - \mu_\beta)$, one needs only the spectral density in equilibrium and, with $\mu_\alpha = -eV_\alpha$, the current can be written as

$$I_\alpha = \sum_\beta G_{\alpha\beta}(V_\beta - V_\alpha), \tag{17}$$

with the conductance tensor

$$G_{\alpha\beta} = -\frac{e^2}{h}\int d\omega\, T_{\alpha\beta}(\omega)\, f'(\omega). \tag{18}$$

With the knowledge that the hybridization matrices $\underline{\underline{\Gamma}}_\alpha$ are the only input we need to characterize the reservoirs and the tunneling matrix, we can now proceed to define effective models with the same hybridization matrices. Since $\underline{\underline{\Gamma}}_\alpha$ is a positive-definite Hermitian matrix, we can diagonalize it with a unitary matrix $\underline{\underline{U}}_\alpha$,

$$\underline{\underline{\Gamma}}_\alpha = \underline{\underline{U}}_\alpha\, \underline{\underline{\Gamma}}^{\mathrm{d}}_\alpha\, \underline{\underline{U}}^\dagger_\alpha, \tag{19}$$

where $(\underline{\underline{\Gamma}}^{\mathrm{d}}_\alpha)_{ll'} = \delta_{ll'}\Gamma_{\alpha l}$ is a diagonal matrix with positive eigenvalues $\Gamma_{\alpha l} = 2\pi t^2_{\alpha l} > 0$. We exclude here the exotic case that one of the eigenvalues $\Gamma_{\alpha l}$ is zero since this would mean that one of the reservoir channels effectively decouples from the system. Following Ref. [21], we can write the hybridization matrix in two equivalent forms by shifting the whole information either to an effective tunneling matrix or to an effective DOS of the reservoirs. In the first case, we introduce an effective tunneling matrix $\underline{\underline{t}}^{\mathrm{eff}}_\alpha$ by

$$\left(\underline{\underline{t}}^{\mathrm{eff}}_\alpha\right)_{ll'} = t_{\alpha l}(\underline{\underline{U}}^\dagger_\alpha)_{ll'} \tag{20}$$

and get

$$\underline{\underline{\Gamma}}_\alpha = 2\pi \left(\underline{\underline{t}}^{\mathrm{eff}}_\alpha\right)^\dagger \underline{\underline{t}}^{\mathrm{eff}}_\alpha. \tag{21}$$

Since $\underline{\underline{t}}^{\mathrm{eff}}_\alpha$ is an $N \times N$ matrix, this effective model consists of reservoirs which have exactly the same number N of channels as we have levels on the dot, i.e., the quantum number on the dot is also the quantum number labeling the channels in the effective reservoirs but this quantum number is in general not conserved by tunneling. Comparing (21) to (13), we see that the effective DOS in the reservoirs is unity, i.e., we consider unpolarized reservoirs.

In the second case, we define an effective DOS $\underline{\underline{\rho}}^{\mathrm{eff}}_\alpha$ in reservoir α by

$$\underline{\underline{\rho}}^{\mathrm{eff}}_\alpha = N\, \underline{\underline{U}}_\alpha \left(\underline{\underline{\Gamma}}^d_\alpha / \Gamma_\alpha\right) \underline{\underline{U}}^\dagger_\alpha, \tag{22}$$

with $\Gamma_\alpha = \sum_l \Gamma_{\alpha l}$. Defining an average tunneling matrix element $t_\alpha > 0$ by $t^2_\alpha = \frac{1}{N}\sum_l t^2_{\alpha l}$, we can then write the hybridization matrix as

$$\underline{\underline{\Gamma}}_\alpha = 2\pi t^2_\alpha\, \underline{\underline{\rho}}^{\mathrm{eff}}_\alpha. \tag{23}$$

In this case, the effective tunneling matrix is proportional to unity, the tunneling conserves the flavor and is flavor independent. In contrast, the effective DOS contains the whole nontrivial information of the hybridization matrix and describes a unitary transformation of the diagonal matrix $N\underline{\underline{\Gamma}}^{\mathrm{d}}_\alpha/\Gamma_\alpha$. The latter matrix can be decomposed in a basis of all diagonal matrices and the coefficients can be interpreted as physical parameters characterizing the effective reservoirs. Using $\mathrm{Tr}\,\underline{\underline{\Gamma}}^{\mathrm{d}}_\alpha = \Gamma_\alpha$, we get for $N = 2$

$$2\, \underline{\underline{\Gamma}}^d_\alpha / \Gamma_\alpha = \underline{\underline{\mathbb{1}}}_2 + p_\alpha \underline{\underline{\sigma}}_z, \tag{24}$$

where σ_z is the Pauli matrix in the z direction and p_α describes the spin polarization in reservoir α. Since the matrix has only positive diagonal elements we get the condition $-1 < p_\alpha < 1$. If one orders the eigenvalues according to $\Gamma_{\alpha 1} \geqslant \Gamma_{\alpha 2}$, one gets $0 < p_\alpha < 1$.

For $N = 3$ we obtain

$$3\, \underline{\underline{\Gamma}}^{\mathrm{d}}_\alpha / \Gamma_\alpha = \underline{\underline{\mathbb{1}}}_3 + p_\alpha \underline{\underline{\lambda}}_3 + \frac{q_\alpha}{\sqrt{3}} \underline{\underline{\lambda}}_8, \tag{25}$$

where

$$\underline{\underline{\lambda}}_3 = \begin{pmatrix} 1 & 0 & 0 \\ 0 & -1 & 0 \\ 0 & 0 & 0 \end{pmatrix}, \tag{26}$$

$$\underline{\underline{\lambda}}_8 = \frac{1}{\sqrt{3}} \begin{pmatrix} 1 & 0 & 0 \\ 0 & 1 & 0 \\ 0 & 0 & -2 \end{pmatrix} \tag{27}$$

are the two diagonal generators of the SU(3) group, describing the isospin in z direction of the up/down quark and the hypercharge operator $\underline{\underline{Y}} = \frac{1}{\sqrt{3}}\underline{\underline{\lambda}}_8$, respectively. Therefore, we interpret p_α as the isospin polarization and q_α as the hypercharge polarization characterizing the reservoirs in the three-channel case. The fact that all matrix elements of (25) are positive leads to the two conditions

$$|p_\alpha| < 1 + \frac{q_\alpha}{3}, \quad 0 < 1 + \frac{q_\alpha}{3} < \frac{3}{2}. \tag{28}$$

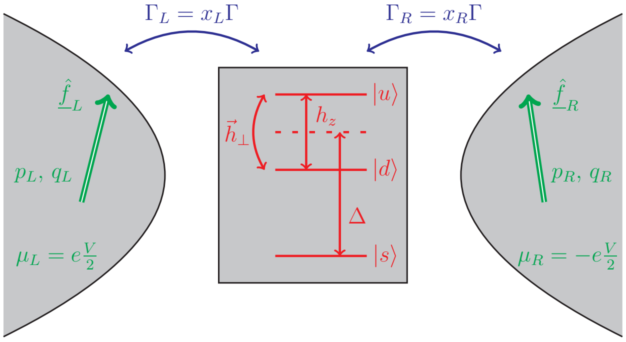

FIG. 1. Sketch of the effective model of two F-spin polarized leads $\alpha = L,R$ coupled to a three-level quantum dot via flavor-conserving tunneling rates $\Gamma_{L,R} = x_{L,R}\Gamma$. $\mu_{L,R} = \pm eV/2$ denote the chemical potentials of the leads with eight-dimensional F spins $\underline{f}_{L,R}$ characterized by an isospin polarization $p_{L,R}$ and hypercharge polarization $q_{L,R}$. $\vec{h} = (\vec{h}_\perp, h_z)$ with $\vec{h}_\perp = (h_x, h_y)$ denotes the magnetic field acting on the two isospin dot levels (up and down quarks), and Δ is the level spacing between the strange quark and the average of the two isospin levels.

If one orders the eigenvalues according to $\Gamma_{\alpha 1} \geqslant \Gamma_{\alpha 2} \geqslant \Gamma_{\alpha 3}$, one gets $0 < p_\alpha < q_\alpha < \frac{3}{2}$.

The unitary transformation $\underline{\underline{U}}_\alpha$ describes a rotation of the direction of the spin-$\frac{1}{2}$ in the $N = 2$ case, and a rotation of the eight-dimensional F spin with $\underline{\underline{F}}_i = \frac{1}{2}\underline{\underline{\lambda}}_i$ for $N = 3$ (see Fig. 1 for an illustration). Thus, the form (23) allows for a nice physical interpretation in terms of physical parameters characterizing the reservoirs. For $N = 3$, we can label the three flavors of the reservoirs and the dot by $l = u,d,s$ for the up, down, and strange quark and describe with the form (23) a system where the flavor is conserved in tunneling with equal tunneling amplitudes for all flavors. However, the polarization p_α of the isospin described by the up and down quarks and the hypercharge polarization q_α can be different for each reservoir, and the F spins in the reservoirs can all be rotated relative to the F spin of the dot. This naturally generalizes the effective spin-valve model set up in Ref. [21] for $N = 2$ to the $N = 3$ case, which is the main subject of this paper.

The form (21) in terms of an effective tunneling matrix allows for another representation of the hybridization matrix which will turn out to be crucial to interpret the fixed-point model derived in Sec. II C for the cotunneling regime. Taking all effective tunneling matrices together in a $N \cdot N_{\rm res} \times N$ matrix

$$\underline{\underline{t}}^{\rm eff} = \begin{pmatrix} \underline{\underline{t}}^{\rm eff}_1 \\ \cdot \\ \cdot \\ \cdot \\ \underline{\underline{t}}^{\rm eff}_{N_{\rm res}} \end{pmatrix}, \tag{29}$$

we can write this matrix via a singular value decomposition as

$$\underline{\underline{t}}^{\rm eff} = \underline{\underline{V}} \begin{pmatrix} \underline{\underline{\gamma}} \\ 0 \end{pmatrix} \underline{\underline{W}}^\dagger, \tag{30}$$

where $\underline{\underline{V}}$ is a unitary $N \cdot N_{\rm res} \times N \cdot N_{\rm res}$ matrix, $\underline{\underline{\gamma}}$ is an $N \times N$ diagonal matrix containing the positive singular values $\gamma_1 \geqslant \gamma_2 \geqslant \cdots \geqslant \gamma_N > 0$, and $\underline{\underline{W}}$ is a unitary $N \times N$ matrix. We assume here that N singular values exist, excluding exotic cases where some channels decouple effectively from the system. As a consequence, we can express all effective tunneling matrices in terms of the singular value matrix $\underline{\underline{\gamma}}$ as follows:

$$\underline{\underline{t}}^{\rm eff}_\alpha = \underline{\underline{V}}_\alpha \, \underline{\underline{\gamma}} \, \underline{\underline{W}}^\dagger, \tag{31}$$

where $\underline{\underline{V}}_\alpha$ are the $N \times N$ matrices occurring in the first N columns of $\underline{\underline{V}}$, which are in general *not* unitary. However, since $\underline{\underline{V}}$ is unitary, we note the important property

$$\sum_\alpha \underline{\underline{V}}^\dagger_\alpha \underline{\underline{V}}_\alpha = \underline{\underline{\mathbb{1}}}. \tag{32}$$

The unitary matrix $\underline{\underline{W}}$ can be eliminated by transforming the basis of the single-particle states of the dot using new field operators $\underline{c}' = \underline{\underline{W}}^\dagger \underline{c}$, such that the dot Hamiltonian (1) and the tunneling Hamiltonian (8) obtain the form

$$H_{\rm dot} = (\underline{c}')^\dagger \underline{\underline{h}}' \underline{c}' + E_{N_{\rm dot}}, \tag{33}$$

$$H_T = \sum_{\alpha k} \left\{ \underline{a}^\dagger_{\alpha k} \left(\underline{\underline{t}}^{\rm eff}_\alpha\right)' \underline{c}' + (\underline{c}')^\dagger \left(\left(\underline{\underline{t}}^{\rm eff}_\alpha\right)'\right)^\dagger \underline{a}_{\alpha k} \right\}, \tag{34}$$

with $\underline{\underline{h}}' = \underline{\underline{W}}^\dagger \, \underline{\underline{h}} \, \underline{\underline{W}}$ and

$$\left(\underline{\underline{t}}^{\rm eff}_\alpha\right)' = \underline{\underline{V}}_\alpha \, \underline{\underline{\gamma}}. \tag{35}$$

For simplicity, we will drop the prime in the following and replace $\underline{\underline{h}}' \to \underline{\underline{h}}$ and $(\underline{\underline{t}}^{\rm eff}_\alpha)' \to \underline{\underline{t}}^{\rm eff}_\alpha$ keeping in mind that these matrices result from the matrices of the original model by transforming the dot channels with the unitary matrix $\underline{\underline{W}}$.

In terms of the effective tunneling matrices (35), the hybridization matrices (21) obtain the form

$$\underline{\underline{\Gamma}}_\alpha = 2\pi \, \underline{\underline{\gamma}} \, \underline{\underline{V}}^\dagger_\alpha \, \underline{\underline{V}}_\alpha \, \underline{\underline{\gamma}}. \tag{36}$$

This form is of particular interest since it separates the hybridization matrix in a part $\underline{\underline{\gamma}}$ which is independent of the reservoirs and a reservoir-dependent part $\underline{\underline{V}}^\dagger_\alpha \underline{\underline{V}}_\alpha$. Comparing (36) with (13), we can interpret $\underline{\underline{\gamma}}$ as an effective tunneling matrix which conserves the flavor index and is the same for all reservoirs. This effective tunneling matrix contains the information of the eigenvalues $\Gamma_l = 2\pi\gamma_l^2$ of the total hybridization matrix since we get from (32)

$$\underline{\underline{\Gamma}} = \sum_\alpha \underline{\underline{\Gamma}}_\alpha = 2\pi \, \underline{\underline{\gamma}}^2. \tag{37}$$

The reservoir-dependent part $\underline{\underline{V}}^\dagger_\alpha \underline{\underline{V}}_\alpha$ can be interpreted as an effective DOS of the reservoirs. Taking $N = 3$ and decomposing this Hermitian matrix in the basis of the F-spin generators $\underline{\underline{F}}_i = \frac{1}{2}\underline{\underline{\lambda}}_i$ of SU(3) we get

$$\underline{\underline{V}}^\dagger_\alpha \underline{\underline{V}}_\alpha = x_\alpha \left(\underline{\underline{\mathbb{1}}} + \sum_{i=1}^{8} d^i_\alpha \, \underline{\underline{F}}_i \right), \tag{38}$$

with real coefficients x_α and d_α^i which, due to (32), fulfill the property

$$\sum_\alpha x_\alpha = 1, \quad \sum_\alpha x_\alpha d_\alpha^i = 0. \tag{39}$$

This means that the sum of the F spins of all reservoirs is zero. A similiar property holds for arbitrary N. In equilibrium, where all chemical potentials $\mu_\alpha = \mu$ are the same and all reservoirs can be taken together to one big reservoir, this means that an unpolarized reservoir with SU(3) symmetry couples to the dot. However, since the effective tunneling matrix elements γ_l still depend on the flavor index, SU(3) symmetry does not hold for the total system even in equilibrium.

Most importantly, we will see in Sec. II C by a poor man's scaling analysis in the cotunneling regime of a singly occupied dot $N_{\text{dot}} = 1$ that a generic fixed-point model with an isotropic matrix $\underline{\underline{\gamma}} = \gamma \underline{\underline{\mathbb{1}}}$ emerges, such that the effective tunneling matrix (35) reads as

$$\underline{\underline{t}}_\alpha^{\text{eff}} = \gamma \underline{\underline{V}}_\alpha. \tag{40}$$

$\gamma > 0$ can be related to an isotropic Kondo coupling J via

$$\gamma^2 = \frac{1}{4} J D, \quad \frac{1}{D} = \frac{1}{2}\left(\frac{1}{E_0} + \frac{1}{E_2}\right), \tag{41}$$

where $E_{N_{\text{dot}}}$ is given by (2) and J fulfils the poor man's scaling equation

$$\frac{dJ}{d\Lambda} = -\frac{N}{2}\frac{J^2}{\Lambda}, \tag{42}$$

with Λ denoting the effective bandwidth. In addition, a special potential scattering term emerges in the original tunneling model at the fixed point which is given by

$$V_{\text{sc}} = v_{\text{sc}} \sum_{kk'} \sum_{\alpha\alpha'} : \underline{a}_{\alpha k}^\dagger \underline{\underline{V}}_\alpha \underline{\underline{V}}_{\alpha'}^\dagger \underline{a}_{\alpha' k'} : , \tag{43}$$

where

$$v_{\text{sc}} = \frac{\gamma^2}{D}\left(\frac{N-2}{N} + \delta\right), \quad \delta = \frac{E_0 - E_2}{E_2 + E_0}, \tag{44}$$

with E_0 and E_2 from (2), and $: \cdots :$ denotes normal ordering. This potential scattering term vanishes for $N = 2$ and $\delta = 0$ (i.e., $n_x = 1$ where $E_0 = E_2$) and is such that it cancels the potential scattering term emerging in an effective model for the cotunneling regime (see Sec. II B). Due to V_{sc}, the reservoir part of the self-energy of the dot is more complicated than (11) and (12) and does not only depend on the hybridization matrix. However, as is shown in Appendix A, the effect of V_{sc} is just that γ is changed to an effective $\tilde{\gamma}$ given by

$$\tilde{\gamma} = \frac{\gamma}{\sqrt{1 + \pi^2 v_{\text{sc}}^2}}, \tag{45}$$

such that the self-energies (11) and (12) from the reservoirs can be written at the fixed point with effective hybridization matrices which can be either expressed via an effective tunneling matrix analog to (21):

$$\underline{\underline{\Gamma}}_\alpha = 2\pi \left(\underline{\underline{t}}_\alpha^{\text{eff}}\right)^\dagger \underline{\underline{t}}_\alpha^{\text{eff}}, \quad \underline{\underline{t}}_\alpha^{\text{eff}} = \tilde{\gamma} \underline{\underline{V}}_\alpha, \tag{46}$$

such that the DOS of the reservoirs is unity, or via an effective DOS analog to (23),

$$\underline{\underline{\Gamma}}_\alpha = 2\pi \tilde{\gamma}^2 \underline{\underline{\rho}}_\alpha^{\text{eff}}, \quad \underline{\underline{\rho}}_\alpha^{\text{eff}} = \underline{\underline{V}}_\alpha^\dagger \underline{\underline{V}}_\alpha, \tag{47}$$

with a trivial tunneling matrix given by $\tilde{\gamma}\underline{\underline{\mathbb{1}}}$ which is the same for all reservoirs and proportional to unity with respect to the flavor indices. The particular property of the effective DOS at the fixed point is the condition

$$\sum_\alpha \underline{\underline{\rho}}_\alpha^{\text{eff}} = \underline{\underline{\mathbb{1}}}, \tag{48}$$

following from (32). This means that in contrast to the general case depicted in Fig. 1 for $N = 3$, the particular property of the fixed-point model is that the sum over all reservoir F spins is equal to zero *and* the tunneling matrix $\underline{\underline{\gamma}} = \gamma \underline{\underline{\mathbb{1}}}$ is isotropic. As a consequence, we get overall SU(3) symmetry in equilibrium, whereas in nonequilibrium the fixed-point model is essentially *not* SU(3) symmetric since the F spins of the reservoirs are nonzero. A similar statement holds for any number N of dot levels, generalizing the picture found in Ref. [21] for $N = 2$ to a generic multilevel quantum dot.

We note that for the particular case of two reservoirs $N_{\text{res}} = 2$ with $\alpha = L,R$, we get from (32) that $\underline{\underline{V}}_L^\dagger \underline{\underline{V}}_L = \underline{\underline{\mathbb{1}}} - \underline{\underline{V}}_R^\dagger \underline{\underline{V}}_R$, such that we can find a common unitary matrix $\underline{\underline{U}}_V$ which diagonalizes both $\underline{\underline{V}}_\alpha^\dagger \underline{\underline{V}}_\alpha$ for $\alpha = L,R$

$$\underline{\underline{V}}_\alpha^\dagger \underline{\underline{V}}_\alpha = \underline{\underline{U}}_V \underline{\underline{A}}_\alpha^{\text{d}} \underline{\underline{U}}_V^\dagger, \tag{49}$$

where $\underline{\underline{A}}_\alpha^{\text{d}}$ are diagonal matrices with the property

$$\sum_{\alpha=L,R} \underline{\underline{A}}_\alpha^{\text{d}} = \underline{\underline{\mathbb{1}}}. \tag{50}$$

For $N = 3$, the matrix $\underline{\underline{A}}_\alpha^{\text{d}}$ can be decomposed analog to (25) as

$$\underline{\underline{A}}_\alpha^{\text{d}} = x_\alpha\left(\underline{\underline{\mathbb{1}}}_3 + p_\alpha \underline{\underline{\lambda}}_3 + \frac{q_\alpha}{\sqrt{3}} \underline{\underline{\lambda}}_8\right), \tag{51}$$

where, due to the property (50), we get

$$1 = x_L + x_R, \tag{52}$$

$$0 = x_L p_L + x_R p_R, \tag{53}$$

$$0 = x_L q_L + x_R q_R, \tag{54}$$

together with $0 < x_\alpha < 1$ and (28). Thus, the hybridization matrices at the fixed point obtain the following form for two reservoirs:

$$\underline{\underline{\Gamma}}_\alpha = 2\pi \tilde{\gamma}^2 \underline{\underline{U}}_V \underline{\underline{A}}_\alpha^{\text{d}} \underline{\underline{U}}_V^\dagger. \tag{55}$$

Omitting the unitary matrix $\underline{\underline{U}}_V$ by choosing a different single-particle basis for the dot states and redefining the parameters $h_{ll'}$ [analog to the transformation by the unitary matrix $\underline{\underline{W}}$, see (33) and (34)], we get finally the diagonal form

$$\underline{\underline{\Gamma}}_\alpha = 2\pi \tilde{\gamma}^2 \underline{\underline{A}}_\alpha^{\text{d}}, \tag{56}$$

which, for $N = 3$, by inserting the decomposition (51), can be written as

$$\underline{\underline{\Gamma}}_\alpha = \frac{1}{3}\Gamma_\alpha\left(\underline{\underline{\mathbb{1}}}_3 + p_\alpha\underline{\underline{\lambda}}_3 + \frac{q_\alpha}{\sqrt{3}}\underline{\underline{\lambda}}_8\right), \tag{57}$$

with $\Gamma_\alpha = 2\pi\bar{\gamma}^2 x_\alpha$. This form for the hybridization matrices constitutes the central generic fixed-point model for $N = 3$ and two reservoirs in the cotunneling regime of a singly occupied dot. This will be confirmed in Sec. III by NRG in equilibrium and analyzed in Sec. IV by a golden rule approach in nonequilibrium. It generalizes the spin-valve model for a two-level quantum dot with opposite spin polarizations in the two reservoirs analyzed in Ref. [21] to the case of a three-level quantum dot, where the isospin and hypercharge polarizations have to be opposite in the two reservoirs. An analog fixed-point model arises for an arbitrary number of dot levels, in this case one obtains in the two reservoirs opposite parameters corresponding to the $N - 1$ diagonal generators of SU(N). Whereas in equilibrium the fixed-point model is SU(N) symmetric (at least if the dot parmeters $h_{ll'}$ are adjusted properly, see Sec. III) and leads generically to the SU(N) Kondo effect, the nonequilibrium fixed-point model is *not* SU(N) symmetric and generically non-Kondo physics has to be expected. This will be analyzed in Sec. IV in the perturbative golden rule regime of large voltage, where we will see that zero F-spin magnetization on the dot occurs only for particular values of the dot parameters $h_{ll'}$ providing a *smoking gun* for the detection of the fixed-point model.

B. Effective model in the cotunneling regime

The effective model in the cotunneling regime where the particle number on the dot is fixed to $N_{\rm dot} = 1$ can easily be obtained by projecting the Hamiltonian matrix on this subspace analog to Brillouin-Wigner perturbation theory. Taking only one virtual process into the particle number sectors $N_{\rm dot} = 0{,}2$ into account we get

$$H_{\rm tot}^{\rm eff} = H_{\rm res} + P_1 H_{\rm dot} P_1 - \,:P_1 H_T Q_1 \frac{1}{H_{\rm dot}} Q_1 H_T P_1:\,, \tag{58}$$

where P_1 projects onto the one-particle subspace of the dot and $Q_1 = 1 - P_1$. We have introduced the normal-ordering $:\cdots:$ with respect to the reservoir field operators since we are not interested in terms renormalizing the dot Hamiltonian leading to effective parameters $h_{ll'}$. For $H_{\rm res}$ and H_T, we take a model with the effective tunneling matrix (35) and the unity matrix for the effective DOS in the reservoirs, as has been discussed in Sec. II. Inserting $H_{\rm dot}$ and H_T from (1) and (8) and using $E_{N_{\rm dot}}$ from (2) we get with $P_1 c_l^\dagger c_{l'} P_1 = |l\rangle\langle l'|$:

$$\begin{aligned} H_{\rm tot}^{\rm eff} &= H_{\rm res} + \sum_{ll'} h_{ll'}|l\rangle\langle l'| + E_1 \\ &\quad - \frac{1}{E_2}\sum_{\alpha\alpha'}\sum_{kk'} :P_1 \underline{a}_{\alpha k}^\dagger\, \underline{t}_\alpha^{\rm eff}\, \underline{c}\,\underline{c}^\dagger \left(\underline{t}_{\alpha'}^{\rm eff}\right)^\dagger \underline{a}_{\alpha' k'} P_1: \qquad (59) \\ &\quad - \frac{1}{E_0}\sum_{\alpha\alpha'}\sum_{kk'} :P_1 \underline{c}^\dagger \left(\underline{t}_{\alpha'}^{\rm eff}\right)^\dagger \underline{a}_{\alpha' k'}\, \underline{a}_{\alpha k}^\dagger\, \underline{t}_\alpha^{\rm eff}\, \underline{c} P_1:\,. \qquad (60) \end{aligned}$$

Using

$$\begin{aligned} P_1(\underline{c}\,\underline{c}^\dagger)_{ll'} P_1 &= -|l'\rangle\langle l| + \delta_{ll'} P_1, \\ :(\underline{a}_{\alpha' k'}\, \underline{a}_{\alpha k}^\dagger)_{l'l}: &= -:a_{\alpha lk}^\dagger a_{\alpha' l' k'}:\,, \end{aligned} \tag{61}$$

we get after inserting (35) for the tunneling matrix and leaving out the unimportant constant E_1

$$H_{\rm tot}^{\rm eff} = H_{\rm res} + \sum_{ll'} h_{ll'}|l\rangle\langle l'| + V_{\rm eff}, \tag{62}$$

with the effective interaction

$$V_{\rm eff} = \sum_{\alpha\alpha'}\sum_{kk'} :\underline{a}_{\alpha k}^\dagger\, \underline{\underline{V}}_\alpha\, \underline{\underline{\hat{J}}}\, \underline{\underline{V}}_{\alpha'}^\dagger\, \underline{a}_{\alpha' k'}: \tag{63}$$

and

$$\hat{J}_{ll'} = \gamma_l\gamma_{l'}\left(\frac{2}{D}|l'\rangle\langle l| - \frac{1}{E_2}\delta_{ll'}\hat{\mathbb{1}}\right), \tag{64}$$

with $2/D = 1/E_0 + 1/E_2$ [see (41)]. We note that the hat on $\hat{J}_{ll'}$ indicates that this object is a dot operator in the one-particle subspace for *each* fixed value of l and l', i.e., $\underline{\underline{\hat{J}}}$ represents a $N \times N$ matrix with dot operators in each matrix element. By using $\hat{\mathbb{1}} = \sum_l |l\rangle\langle l|$, a straightforward calculation leads to the decomposition

$$\begin{aligned} \hat{J}_{ll'} &= \xi_{ll'}|l'\rangle\langle l|(1 - \delta_{ll'}) \\ &\quad + \sum_{l_1 \neq l} \eta_{ll_1}\left(\frac{1}{N}\hat{\mathbb{1}} - |l_1\rangle\langle l_1|\right)\delta_{ll'} + v_l\delta_{ll'}\hat{\mathbb{1}}, \end{aligned} \tag{65}$$

with

$$\xi_{ll'} = \frac{2}{D}\gamma_l\gamma_{l'}, \quad \eta_{ll'} = \frac{2}{D}\gamma_l^2, \tag{66}$$

$$v_l = -\frac{1}{D}\gamma_l^2\left(\frac{N-2}{N} + \delta\right), \tag{67}$$

and $2\delta = D/E_2 - D/E_0$ [see (44)]. We note that the bare parameters $\eta_{ll'}$ are independent of l' but obtain a strong dependence on l' under the renormalization group flow described below. The decomposition (65) exhibits the nondiagonal matrix $|l'\rangle\langle l|$ for $l \neq l'$, all traceless diagonal matrices $\frac{1}{N}\hat{\mathbb{1}} - |l_1\rangle\langle l_1|$ for $l_1 \neq l$, and the unity matrix $\hat{\mathbb{1}}$ describing the effective potential scattering.

We note that the effective interaction (63) can also be written in terms of reservoir field operators for a single reservoir only:

$$V_{\rm eff} = \sum_{kk'} :\underline{\tilde{a}}_k^\dagger\, \underline{\underline{\hat{J}}}\, \underline{\tilde{a}}_{k'}:\,, \tag{68}$$

where

$$\underline{\tilde{a}}_k = \sum_\alpha \underline{\underline{V}}_\alpha^\dagger\, \underline{a}_{\alpha k} \tag{69}$$

fulfill commutation relations of field operators for a single effective reservoir with N flavors due to the property (32). However, this is only possible if all the reservoirs can be taken together, i.e., they must have the same temperature and chemical potential. In nonequilibrium this is not possible. Nevertheless, for the poor man's scaling analysis described in the next section, this form of the Hamiltonian can be applied since the poor man's scaling analysis integrates out only energy scales above the temperatures and chemical potentials of the reservoirs.

C. Poor man's scaling and fixed-point model for N levels

Taking the effective Hamiltonian in the cotunneling regime in the form (62) and (68), we now proceed to find an effective low-energy theory by integrating out all energy scales from the high-energy cutoff $\Lambda = D$ down to some low-energy scale Λ_c defined by the largest physical low-energy scale in the system set by the parameters $h_{ll'}$ of the dot Hamiltonian, the temperature T of the reservoirs, and the chemical potentials μ_α of the reservoirs

$$\Lambda_c = \max\{\{|h_{ll'}|\}_{ll'}, T, \{\mu_\alpha\}_\alpha\}. \tag{70}$$

This can be achieved by a standard poor man's scaling analysis leading to the RG equations

$$\frac{d\hat{J}_{ll'}}{ds} = -\sum_{l_1} [\hat{J}_{ll_1}, \hat{J}_{l_1 l'}], \tag{71}$$

where $[\cdot,\cdot]$ denotes the commutator and $s = \ln\frac{D}{\Lambda}$ is the flow parameter. This RG equation has obviously the two invariants $\mathrm{Tr}\hat{J}_{ll'}$ and $\sum_l \hat{J}_{ll}$. Defining

$$\eta_l = \sum_{l'\neq l} \eta_{ll'}, \quad \eta = \sum_l \eta_l, \quad v = \sum_l v_l, \tag{72}$$

we obtain from the decomposition (65)

$$\mathrm{Tr}\hat{J}_{ll'} = N v_l \delta_{ll'}, \tag{73}$$

$$\langle l|\sum_{l'} \hat{J}_{l'l'}|l\rangle = \frac{1}{N}\eta - \eta_l + v, \tag{74}$$

and get the invariants

$$0 = \frac{d}{ds} v_l, \tag{75}$$

$$0 = \frac{d}{ds}\Big(\eta_l - \frac{1}{N}\eta\Big). \tag{76}$$

The first equation means that there is no renormalization for the potential scattering. The second equation holds for all $l = 1,\dots,N$ and gives $N-1$ independent invariants.

Inserting the decomposition (65) in (71) we find after some straightforward algebra the RG equations for the parameters $\xi_{ll'}$ and $\eta_{ll'}$ characterizing the effective operator-valued matrix $\underline{\underline{\hat{J}}}$ at scale Λ in terms of (65) ($l \neq l'$ in all following equations):

$$\frac{d\xi_{ll'}}{ds} = 2\xi_{ll'}\bar{\eta}_{ll'} + \sum_{l_1\neq l,l'} \xi_{ll_1}\xi_{l_1 l'}, \tag{77}$$

$$\frac{d\eta_{ll'}}{ds} = 2\xi_{ll'}\xi_{l'l} + \sum_{l_1\neq l,l'} \xi_{ll_1}\xi_{l_1 l}, \tag{78}$$

where we defined the symmetric matrix

$$\bar{\eta}_{ll'} = \tfrac{1}{2}(\eta_{ll'} + \eta_{l'l}), \tag{79}$$

which fulfills the RG equation

$$\frac{d\bar{\eta}_{ll'}}{ds} = 2\xi_{ll'}^2 + \frac{1}{2}\sum_{l_1\neq l,l'} \big(\xi_{ll_1}^2 + \xi_{l_1 l'}^2\big) \tag{80}$$

since $\xi_{ll'}$ stays symmetric during the whole RG flow

$$\xi_{ll'} = \xi_{l'l}. \tag{81}$$

These differential equations have to be solved starting from the initial conditions at $s = 0$ given by (66).

The RG equation for $\eta_{ll'}$ can be solved by the ansatz

$$\eta_{ll'} = \bar{\eta}_{ll'} + r_l - r_{l'}, \tag{82}$$

where the r_l are determined from the RG equations

$$\frac{dr_l}{ds} = \frac{1}{2}\sum_{l'\neq l} \xi_{ll'}^2, \tag{83}$$

with initial condition $r_l = \gamma_l^2/D$. Using the form (82) we can express the $N-1$ independent invariants (76) as

$$0 = \frac{d}{ds}\Big(r - Nr_l + \bar{\eta}_l - \frac{1}{N}\bar{\eta}\Big), \tag{84}$$

where we have defined in analogy to (72)

$$\bar{\eta}_l = \sum_{l'\neq l} \bar{\eta}_{ll'}, \quad \bar{\eta} = \eta = \sum_l \bar{\eta}_l, \quad r = \sum_l r_l. \tag{85}$$

With these invariants all $N-1$ differences $r_l - r_{l'}$ can be expressed via the symmetric matrix $\bar{\eta}_{ll'}$ and it is only necessary to consider the RG equations (77) and (80) for the symmetric matrices $\xi_{ll'}$ and $\bar{\eta}_{ll'}$. As we will see in Sec. II D, these coupling constants can be interpreted as the transverse and longitudinal Kondo couplings $J_\perp$ and J_z corresponding to the SU(2) subgroup formed by the level pair (l,l').

As one can see from (78), the parameters $\eta_{ll'}$ obtain a significant dependence on l' not present in the initial condition. Furthermore, all parameters $\xi_{ll'}$ and $\eta_{ll'}$ stay positive and increase monotonously under the RG flow until they diverge at a certain low-energy scale T_K. The fixed point is the one where all parameters are the same and proportional to an isotropic Kondo-type coupling J:

$$\xi_{ll'} = \eta_{ll'} = \tfrac{1}{2}J, \tag{86}$$

where J fulfills the RG equation (42):

$$\frac{dJ}{ds} = \frac{N}{2}J^2 \quad \Rightarrow \quad T_K = \Lambda e^{-\frac{2}{NJ}} = \text{const.} \tag{87}$$

T_K is the energy scale where all coupling constants diverge and is called the Kondo temperature in the following. This scale is exponentially sensitive to the choice of the initial conditions. Therefore, one defines a typical initial coupling J_0 via

$$\frac{4\gamma_l^2}{D} = y_l\, J_0, \quad \sum_l y_l = 1, \tag{88}$$

such that $y_l \sim O(1)$ are fixed parameters, and defines formally the scaling limit by

$$J_0 \to 0, \quad D \to \infty, \quad T_K = \text{const.} \tag{89}$$

Close to the fixed point we can neglect the small potential scattering term and get from (65) the form

$$\hat{J}_{ll'} = \frac{1}{2}J|l'\rangle\langle l|(1-\delta_{ll'}) + \frac{1}{2}J\sum_{l_1\neq l}\Big(\frac{1}{N}\hat{\mathbb{1}} - |l_1\rangle\langle l_1|\Big)\delta_{ll'}, \tag{90}$$

which can also be written in the more compact form

$$\hat{J}_{ll'} = \frac{1}{2} J |l'\rangle\langle l| - \frac{1}{2N} J \hat{\mathbb{1}} \delta_{ll'}. \tag{91}$$

Using this form in the effective interaction (68) we get at the fixed point in the one-particle subspace of the dot

$$V_{\rm eff} = -\frac{1}{2N} J \sum_{kk'} : \underline{\tilde{a}}_k^\dagger \, \underline{\tilde{a}}_{k'} : + \frac{1}{2} J \sum_{kk'} \sum_{ll'} c_{l'}^\dagger c_l \; : \tilde{a}_{lk}^\dagger \, \tilde{a}_{l'k'} : . \tag{92}$$

At the fixed point the effective interaction is obviously SU(N) invariant under a common unitary transformation of the N flavors of the reservoir and dot field operators. We note that this holds only in the case of the single reservoir described by the field operators $\tilde{a}_{lk}$ but not for the original model in nonequilibrium where the reservoirs have different chemical potentials μ_α. In this case one has to insert (69) in (92) and finds that the effective interaction is *not* invariant under a common unitary transformation of all dot field operators c_l and reservoir field operators $a_{\alpha l k}$ due to the presence of the matrices $\underline{\underline{V}}_\alpha$.

We finally show that the fixed-point Hamiltonian corresponds to a projection of the effective tunneling model (40) together with the potential scattering term (43) on the $N = 1$ subspace of the dot. Comparing (86) with (66), we find that we get indeed a unity matrix for $\underline{\underline{\gamma}} = \gamma \underline{\underline{\mathbb{1}}}$ with γ given by (41). Furthermore, the potential scattering is absent in the fixed-point model (90) and, therefore, we have to introduce the potential scattering term (43) in the effective tunneling model with a coupling constant $v_{\rm sc}$ given by (44) of opposite sign compared to (67) (where γ_l is replaced by γ) such that (43) cancels the potential scattering generated by projecting the effective tunneling model on the $N = 1$ subspace.

D. Poor man's scaling in SU(3) representation

For the three-level case $N = 3$, which is the main subject of this paper, it is quite instructive to write the Hamiltonian and the poor man's scaling equations also in the representation of the generators of the SU(3) group. This provides a nice physical picture as to how the reservoir and dot F spins are coupled and how the interaction can be interpreted in terms of the dot and reservoir quark flavors.

Since each matrix element $\hat{J}_{ll'}$ is an operator in the three-dimensional dot space we can decompose it in the F-spin components $\hat{F}_i = \frac{1}{2}\hat{\lambda}_i$ of the dot as

$$\hat{J}_{ll'} = \sum_{i=1}^{8} J_{ll'}^i \hat{F}_i + v_l \delta_{ll'} \hat{\mathbb{1}}, \tag{93}$$

where the last term contains the potential scattering. Furthermore, each 3×3 matrix $\underline{\underline{J}}^i$ can again be decomposed in the generators $\underline{\underline{\lambda}}_j$ in reservoir space [note that we still consider here only one effective reservoir due to the form (68) of the effective interaction in the poor man's scaling regime]. Comparing (93) with (65) we find after some straightforward algebra

$$\underline{\underline{J}}^i = J_i \, \underline{\underline{\lambda}}_i \quad \text{for } i = 1,2,4,5,6,7, \tag{94}$$

$$\underline{\underline{J}}^3 = J_3 \, \underline{\underline{\lambda}}_3 + J_{38} \, \underline{\underline{\lambda}}_8 + \frac{2}{3} c_3 \, \underline{\underline{\mathbb{1}}}, \tag{95}$$

$$\underline{\underline{J}}^8 = J_8 \, \underline{\underline{\lambda}}_8 + J_{83} \, \underline{\underline{\lambda}}_3 + \frac{2}{3\sqrt{3}} c_8 \, \underline{\underline{\mathbb{1}}}, \tag{96}$$

where the various coupling constants are defined by

$$J_1 = J_2 = \xi_{12}, \quad K_1 = \bar{\eta}_{12}, \tag{97}$$

$$J_4 = J_5 = \xi_{13}, \quad K_4 = \bar{\eta}_{13}, \tag{98}$$

$$J_6 = J_7 = \xi_{23}, \quad K_6 = \bar{\eta}_{23}, \tag{99}$$

$$J_3 = K_1, \quad J_8 = \frac{1}{3}(2K_4 + 2K_6 - K_1), \tag{100}$$

$$J_{38} = J_{83} = \frac{1}{\sqrt{3}}(K_4 - K_6), \tag{101}$$

together with the two invariants

$$c_3 = \frac{\gamma_1^2 - \gamma_2^2}{D}, \quad c_8 = \frac{\gamma_1^2 + \gamma_2^2 - 2\gamma_3^2}{D}. \tag{102}$$

c_3 and c_8 must be invariants since

$$\sum_l \hat{J}_{ll} = \sum_{i=1}^{8} (\mathrm{Tr}\underline{\underline{J}}^i) \, \hat{F}_i + v \hat{\mathbb{1}} \tag{103}$$

is an invariant such that all coefficients $\mathrm{Tr}\underline{\underline{J}}^i$ must be invariants for $i = 1, \ldots 8$. Using (94)–(96), we see that the trace for $i = 1,2,4,5,6,7$ is trivially zero but for $i = 3,8$ we get that $\mathrm{Tr}\underline{\underline{J}}^3 = 2c_3$ and $\mathrm{Tr}\underline{\underline{J}}^8 = (2/\sqrt{3})c_8$ must be invariants.

We note that only the six coupling constants $(J_1, J_4, J_6) = (\xi_{12}, \xi_{13}, \xi_{23})$ and $(K_1, K_4, K_6) = (\bar{\eta}_{12}, \bar{\eta}_{13}, \bar{\eta}_{23})$ are independent. This is consistent with our general analysis in Sec. II C where we showed that only the parameters $\xi_{ll'}$ and $\bar{\eta}_{ll'}$ are needed.

Since all coupling constants grow under the RG flow and diverge at T_K, the small invariants c_3, c_8, and v_l can be omitted from the effective interaction $V_{\rm eff}$ defined in (68). Inserting $\underline{\underline{\hat{J}}} \approx \sum_{i=1}^{8} \underline{\underline{J}}^i \hat{F}_i$ from (93) and the decompositions (94)–(96) we can write $V_{\rm eff}$ in the compact form

$$V_{\rm eff} = 2 \sum_{i=1}^{8} J_i \, \hat{f}_i \, \hat{F}_i + 2J_{38} \, (\hat{f}_8 \hat{F}_3 + \hat{f}_3 \hat{F}_8), \tag{104}$$

where we defined the reservoir f-spin operator as

$$\hat{f}_i = \frac{1}{2} \sum_{kk'} \underline{\tilde{a}}_k^\dagger \, \underline{\underline{\lambda}}_i \, \underline{\tilde{a}}_{k'}. \tag{105}$$

The form (104) exhibits very clearly how the reservoir f spin couples to the dot F spin. There are three possible isospin pairs formed by the up/down quark ($i = 1,2$), the up/strange quark ($i = 4,5$), or the down/strange quark ($i = 6,7$), corresponding to the flavor pairs $l = 1,2$, $l = 1,3$, and $l = 2,3$, respectively. For each isospin pair we can define a transverse and longitudinal coupling, denoted by (J_1, K_1), (J_4, K_4), and (J_6, K_6), respectively, analog to the transverse and longitudinal Kondo couplings $(J_\perp, J_z)$ for a single spin $\frac{1}{2}$. The three transverse couplings belong to the six independent generators λ_i for $i = 1,2,4,5,6,7$. Therefore, the effective interaction does not contain any transverse couplings between different isospins of the reservoir and the dot but only the product $\hat{f}_i \, \hat{F}_i$ for $i = 1,2,4,5,6,7$. In contrast, the three longitudinal parts of the isospins are not independent. By convention, one chooses the longitudinal part of the up/down isospin (represented by λ_3) and the sum over the longitudinal parts of the up/strange and down/strange isospins (represented by the hypercharge generator $\sqrt{3}\lambda_8$) as basis for the two independent traceless matrices. Therefore, there is not only a longitudinal isospin coupling J_3 and a hypercharge coupling J_8 but also a mixed coupling J_{38} describing an interaction of the longitudinal reservoir isospin with the hypercharge polarization of the dot and vice versa. This picture naturally generalizes to arbitrary N providing a physical interpretation of the coupling constants ξ_{ij} and $\bar{\eta}_{ij}$ in terms of the transverse and longitudinal couplings for the isospin formed by the two flavors $l = i,j$.

Using (77) and (80) for $N = 3$, we obtain the RG equations

$$\frac{dJ_1}{ds} = 2J_1\,K_1 + J_4\,J_6, \tag{106}$$

$$\frac{dJ_4}{ds} = 2J_4\,K_4 + J_1\,J_6, \tag{107}$$

$$\frac{dJ_6}{ds} = 2J_6\,K_6 + J_1\,J_4, \tag{108}$$

$$\frac{dK_1}{ds} = 2J_1^2 + \frac{1}{2}\big(J_4^2 + J_6^2\big), \tag{109}$$

$$\frac{dK_4}{ds} = 2J_4^2 + \frac{1}{2}\big(J_1^2 + J_6^2\big), \tag{110}$$

$$\frac{dK_6}{ds} = 2J_6^2 + \frac{1}{2}\big(J_1^2 + J_4^2\big), \tag{111}$$

with the initial conditions at $s = 0$ given by (66):

$$J_1(0) = \frac{2\gamma_1\gamma_2}{D}, \quad J_4(0) = \frac{2\gamma_1\gamma_3}{D}, \tag{112}$$

$$J_6(0) = \frac{2\gamma_2\gamma_3}{D}, \quad K_1(0) = \frac{\gamma_1^2 + \gamma_2^2}{D}, \tag{113}$$

$$K_4(0) = \frac{\gamma_1^2 + \gamma_3^2}{D}, \quad K_6(0) = \frac{\gamma_2^2 + \gamma_3^2}{D}. \tag{114}$$

A numerical study of these RG equations shows that independent of the initial conditions, all couplings become equal during the RG flow and diverge at some low-energy scale T_K, in agreement with (86). Using (97)–(101), this means that all $J_i = J/2$ become the same for $i = 1,\dots,8$ and the mixed coupling J_{38} scales to zero. Thus, at the fixed point the effective interaction can be written in the isotropic and SU(3)-invariant form

$$V_{\rm eff} = J\sum_{i=1}^{8} \hat{f}_i\,\hat{F}_i, \tag{115}$$

which is identical with (92). Applying the analog scheme to an arbitrary number N of dot levels we obtain at the fixed point the same result, one just has to sum in (115) over all generators of SU(N). Figure 2 shows an example for the RG flow where the longitudinal and transverse couplings $K_i \approx J_i$ are initially nearly the same but different for each $i = 1,4,6$.

To obtain a feeling for the nature of the strong-coupling ground state, we assume a two-site model with Hamiltonian (115). In particular, we consider a tight-binding model for the reservoir and the two sites are the dot and the first site of the reservoir (i.e., the one that couples to the dot), respectively, while the other reservoir sites are not taken into account. The crucial point about determining the ground state lies in choosing the appropriate representation for the eigenstates of the SU(3)-symmetric interaction in (115). The SU(3) group has two fundamental representations [38], which we denote by the multiplet notation [3] and $[\bar{3}]$. We represent the eigenstates of the dot in the representation [3] where the F-spin components are $\hat{F}_i = \frac{1}{2}\hat{\lambda}_i$. Denoting the states by the quark flavors $l = 1,2,3 = u,d,s$, we have

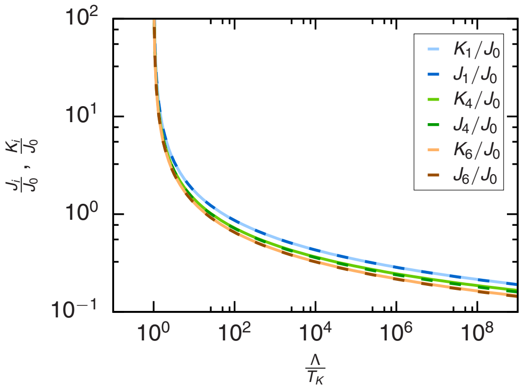

FIG. 2. Flow of the poor man's scaling RG for the couplings with similar initial values $(J_1,J_4,J_6)(0) = (0.018235, 0.015321, 0.013784)J_0$, $(K_1,K_4,K_6)(0) = (0.018337, 0.015924, 0.013994)J_0$, $J_0 = 0.096510$, and $D = 1000.0$. The couplings become degenerate at the Kondo scale T_K and diverge.

$$|u\rangle = \big|\tfrac{1}{2},\tfrac{1}{3}\big\rangle, \tag{116}$$

$$|d\rangle = \big|-\tfrac{1}{2},\tfrac{1}{3}\big\rangle, \tag{117}$$

$$|s\rangle = \big|0,-\tfrac{2}{3}\big\rangle, \tag{118}$$

where the states on the right-hand side are the eigenstates of $\hat{F}_3$ and $\hat{F}_8$ and the first (second) quantum number in the label is the corresponding eigenvalue of $\hat{F}_3$ ($\frac{2}{\sqrt{3}}\hat{F}_8$). Therefore, we refer to these eigenvalues as isospin (hypercharge) quantum numbers. Choosing the same representation for the first site in the reservoir is not useful since the states of the composite system are part of either the sextet [6] or the triplet $[\bar{3}]$ due to $[3]\otimes[3] = [6]\oplus[\bar{3}]$ [38]. Such a representation is not suitable since the system has a distinct nondegenerate ground state. Instead, we represent the first site of the reservoir with $[\bar{3}]$ and obtain $[3]\otimes[\bar{3}] = [8]\oplus[1]$ where all but one state of the two-site system form an octet together with the remaining state being a unique singlet state. $[\bar{3}]$ is the complex-conjugate representation of [3] and has therefore the generators $\hat{f}_i = -\frac{1}{2}\hat{\lambda}_i^*$. Consequently, we label the states of the second site with the antiquark flavor $\bar{l} = 1,2,3 = \bar{u},\bar{d},\bar{s}$ and get

$$|\bar{u}\rangle = \big|-\tfrac{1}{2},-\tfrac{1}{3}\big\rangle, \tag{119}$$

$$|\bar{d}\rangle = \big|\tfrac{1}{2},-\tfrac{1}{3}\big\rangle, \tag{120}$$

$$|\bar{s}\rangle = \big|0,\tfrac{2}{3}\big\rangle. \tag{121}$$

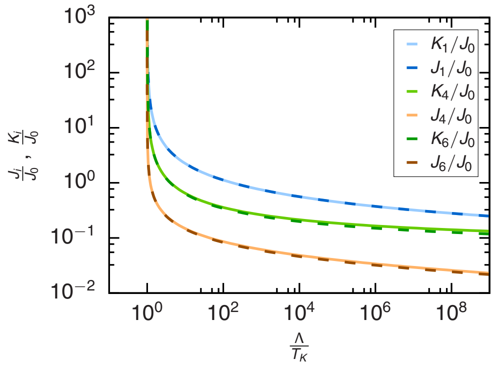

FIG. 3. Flow of the poor man's scaling RG for the couplings for $J_1(0) \gg J_4(0), J_6(0)$ with $(J_1,J_4,J_6)(0) = (0.0239873, 0.0022176, 0.0020878)J_0$, $(K_1,K_4,K_6)(0)=(0.0240310, 0.0128358, 0.0113882)J_0$, $J_0 = 0.0965099$, $D = 1000.0$. Each of the coupling pairs (J_1,K_1), (J_4,J_6), and (K_4,K_6) are quasidegenerate for the main part of the RG flow before all couplings obtain the same value at T_K.

In this basis, the operators $\hat{\lambda}_i^*$ have the same matrix representation as the Gell-Mann matrices $\hat{\lambda}_i$.

Indeed, we will show in Appendix B that the singlet state

$$|\text{gs}\rangle = \frac{1}{\sqrt{3}}(|u\bar{u}\rangle + |d\bar{d}\rangle + |s\bar{s}\rangle) \tag{122}$$

is the ground state with energy $E_{\text{gs}} = -\frac{4}{3}J$ while the octet states are degenerate with energy $E_8 = \frac{1}{6}J$. Since $|l\bar{l}\rangle = |l\rangle \otimes |\bar{l}\rangle$, it is straightforward to define the reduced dot density matrix

$$\hat{\rho} = \sum_{\bar{l}=\bar{u},\bar{d},\bar{s}} \langle \bar{l}|(|\text{gs}\rangle\langle\text{gs}|)|\bar{l}\rangle = \frac{1}{3}\hat{\mathbb{1}}, \tag{123}$$

which yields $n_l = \frac{1}{3}$ in perfect agreement with the NRG analysis in Sec. III.

Together with the SU(3)-symmetric interaction term, the outcome (122) motivates the term "quantum fluctuations" for the significant physical processes in the fixed-point model. The ground state is a symmetric linear combination of bound states with quark-antiquark flavor. This is in accordance with the observation that no free quarks exist, i.e., they always gather to form a particle with integer electric charge. The interaction term (115) preserves this since the fluctuation terms ($i = 1,2,4,5,6,7$) always annihilate a quark-antiquark pair while creating a different quark-antiquark bound state simultaneously. Furthermore, we will discuss in Appendix B that the eigenstates of (115) are identical to those of the quark model for light pseudoscalar mesons [39].

In this context, choosing $J_1 \approx K_1 \gg J_4 \approx J_6$ and $K_4 \approx K_6$ for the initial values reveals a nice physical picture in terms of the isospin of the up and down quarks. Figure 3 shows that in the whole regime from weak to intermediate coupling the couplings stay approximately degenerate with $J_1 \approx K_1$, $J_4 \approx J_6$, and $K_4 \approx K_6$. Here, the model exhibits an approximated SU(2) symmetry for the isospin with an isotropic isospin coupling $J_I = \frac{1}{2}(J_1 + K_1) \gg |J_1 - K_1|$. Furthermore, the interaction of isospin and hypercharge degrees of freedom disentangle in leading order since $J_{38} \ll J_3, J_8$. In the same way, $J_4 \approx J_6$ characterizes transitions between states differing in the hypercharge quantum number [compare with (116)–(118)]. In total, we find an isotropic isospin model where the presence of the third level (strange quark) mainly results in a potential scattering ($J_8 \sim J_I$) for the isospin with suppressed transitions to states with different hypercharge ($J_4, J_6 \ll J_I$). However, finally the RG flow approaches the generic SU(3)-symmetric fixed point on the Kondo scale T_K also in this case.

III. NRG ANALYSIS IN EQUILIBRIUM

In Sec. II D we have shown for a three-level quantum dot in the cotunneling regime that the generic fixed point model is an SU(3)-invariant isotropic effective interaction (115) between the F spins of the reservoir and the dot. This holds for the equilibrium case where all reservoirs can be taken together to a single reservoir and it requires also SU(3) symmetry of the dot. This means that the dot parameters $h_{ll'}$ have to be adjusted appropriately (including renormalizations arising from the coupling to the reservoir) such that the populations of all dot states are the same $n_l = \langle c_l^\dagger c_l \rangle = \frac{1}{3}$. The aim of this section is to confirm that in equilibrium the SU(3)-symmetric fixed point can be established independent of the tunneling matrix by an adjustment of the dot parameters. To this end, we use the numerically exact NRG method [40] and analyze the linear conductance G for $N = 3$ and two reservoirs ($\alpha = L,R$) for the case of proportional couplings $\underline{\underline{\Gamma}}_\alpha = x_\alpha \underline{\underline{\Gamma}}$ where G can be calculated from (18) and (16):

$$g = G/G_0 = -\frac{\pi}{2}\int d\omega \,\text{Tr}\, \underline{\underline{\Gamma}}\, \underline{\underline{\rho}}(\omega)\, f'(\omega), \tag{124}$$

with the dimensionless conductance g in units of $G_0 = (e^2/h)/(4x_L x_R)$. As explained in Sec. II A the equilibrium spectral density $\underline{\underline{\rho}}(\omega)$ depends only on the total hybridization matrix $\underline{\underline{\Gamma}}$, i.e., we can use a unitary transformation of the dot states such that this matrix is diagonal [see (37)] and the spectral density in this basis depends only on the eigenvalues $\Gamma_l = 2\pi\gamma_l^2$. In this case, the linear conductance (124) can be written as

$$g = -\frac{\pi}{2}\int d\omega \sum_l \Gamma_l\, \rho_{ll}(\omega)\, f'(\omega). \tag{125}$$

In the new dot basis we assume for simplicity that the dot Hamiltonian contains only diagonal elements

$$H = \sum_l h_l c_l^\dagger c_l. \tag{126}$$

Other cases with nondiagonal elements $h_{ll'}$ can also be studied but are of no interest because they just destroy SU(3) symmetry of the dot and drive the system away from the fixed-point model. Here, we are interested in a systematic study how, for *arbitrary* tunneling parameters Γ_l, SU(3) symmetry can be restored by tuning the level positions h_l appropriately. In addition, we will also study the dependence of the SU(3) Kondo temperature $T_K^{(3)}$ as function of Γ_l and compare it to the corresponding SU(2) Kondo temperature $T_K^{(2)}$, where only two levels contribute to transport. This analysis goes beyond the one of Ref. [13] which has concentrated on the linear conductance

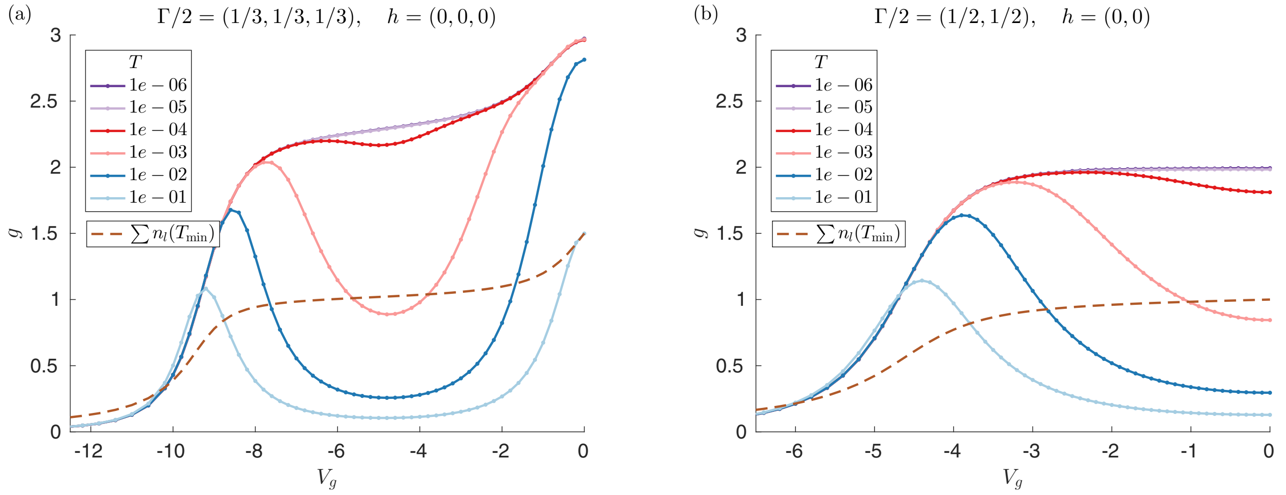

FIG. 4. Gate voltage dependence of the conductance at various temperatures for (a) $N = 3$ and (b) $N = 2$ at the SU(N)-symmetric point where all Γ_l are the same and all $h_l = 0$. By p-h symmetry the curves can be mirrored along $V_g = 0$. Also shown is the occupation n_l at the lowest temperature where the Friedel sum rule (127) is fulfilled.

for the SU(3)-symmetric case (i.e., all Γ_l are the same and $h_l = 0$) and the destruction of SU(3) symmetry by different Γ_l or finite values for $h_{ll'}$. As a signature of SU(3) symmetry we take the Friedel sum rule (used also in Refs. [12,13])

$$g = \sum_l \sin^2(\pi n_l), \tag{127}$$

which holds exactly at zero temperature and gives the value $g = 2.25$ for equal populations $n_l = \frac{1}{3}$ corresponding to the SU(3)-symmetric fixed point. The occupations n_l can be calculated from the spectral density via $n_l = \int d\omega\, \rho_{ll}(\omega) f(\omega)$. For the parameters in all figures we use

$$\frac{1}{2}\sum_l \Gamma_l = 1, \quad U = 10, \quad W = 10^4, \tag{128}$$

where $2W$ denotes the width of a flat DOS of the reservoirs [i.e., $|\omega| < W$ for the integral in (125)].

The calculations are performed using the full-density-matrix NRG [41], where we exploit either the individual charge conservation or the full SU(N) symmetry by means of the QSpace tensor library developed by Weichselbaum [42]. For the final results we employ a discretization parameter of $\Lambda = 3$, and we keep states up to a rescaled energy of $E_{\text{trunc}} = 9$ and maximal number N_{keep} during the NRG iteration. In the calculations without SU(N) symmetry we set $N_{\text{keep}} = 8000$. In the SU(N)-symmetric cases we can further increase the precision to very high level and explicitly confirm that results for g are converged up to 1% and results for n_l are converged up to 10^{-6} with respect to the numerical parameters. Note that in many calculations we optimize the level positions to achieve equal occupation of certain levels. Since the values of such optimized level positions h_l^* depend on the discretization of the bath, we refrain from using z averaging [40]. Finally, we need not broaden the NRG data as the computation of both g and n_l requires only discrete spectral weights.

To set the scene, we show in Fig. 4 known curves for the conductance depending on gate voltage and temperature in the SU(N)-symmetric cases for $N = 2,3$, where all Γ_l are the same and all $h_l = 0$. We find converged, plateaulike features when decreasing T below the Kondo temperature T_K in the cotunneling regime of a singly occupied dot. Note that n_l shows a very weak dependence on temperature in this regime and, at $T < T_K$, the Friedel sum rule (127) is fulfilled. Furthermore, we find that the Kondo temperatures $T_K^{(N)}$ are similar for $N = 2$ and 3 (recall that $\sum_l \Gamma_l$ is fixed). In contrast, the p-h symmetric point $V_g = 0$ corresponds to very different physics for the two cases since for $N = 3$ there are strong charge fluctuations due to $E_1 = E_2$, whereas for $N = 2$ spin fluctuations dominate. Therefore, at $V_g = 0$, the relevant low-energy scale is the hybridization Γ_l for $N = 3$ [13] and the Kondo temperature for $N = 2$.

Next, we study the case $\Gamma_1 = \Gamma_2 \neq \Gamma_3$ and $h_1 = h_2 = 0$. In this case, the different tunneling couplings lead to a different renormalization of h_3 of $O(\Gamma_1\Gamma_3/U)$ relative to $h_{1/2}$. Therefore, $h_1 = h_2 = h_3 = 0$ is *not* the SU(3)-symmetric point and the level position h_3 has to be adjusted appropriately to recover equal populations of the states and conductance $g = 2.25$ at zero temperature. Calling this optimized value h_3^* we show in Fig. 5 the conductance as function of $|h_3 - h_3^*|$. For temperatures $T < T_K^{(3)}$ we see that the conductance reaches the SU(3)-symmetric value $g = 2.25$ for $|h_3 - h_3^*| \sim T_K^{(3)}$ as expected. The Kondo temperature $T_K^{(3)}$ does not depend strongly on the value of Γ_3 and is nearly the same for $\Gamma_3 < \Gamma_{1/2}$ [Fig. 5(a)] and $\Gamma_3 > \Gamma_{1/2}$ [Fig. 5(b)]. For $|h_3 - h_3^*| > T_K^{(3)}$ and $h_3 > h_3^*$ (solid lines in Fig. 5), we see that the SU(2) Kondo effect with $g = 2$ appears at low enough temperatures $T < T_K^{(2)}$. Whereas $T_K^{(2)} \approx T_K^{(3)}$ for relatively small $\Gamma_3 < \Gamma_{1/2}$, we find that $T_K^{(2)} < T_K^{(3)}$ for $\Gamma_3 > \Gamma_{1/2}$. The latter can be explained by the fact that the two levels $l = 1,2$ form the SU(2) Kondo effect and therefore $T_K^{(2)}$ decreases if the coupling to these two levels Γ_1, Γ_2 is lowered. In contrast, when all three levels contribute to the SU(3) Kondo effect, we have a total coupling of $\sum_l \Gamma_l/2 = 1$ and find that the relative distribution of the Γ_l influences $T_K^{(3)}$ only weakly. Furthermore, in the regime where the SU(2) Kondo effect occurs, we see a strong

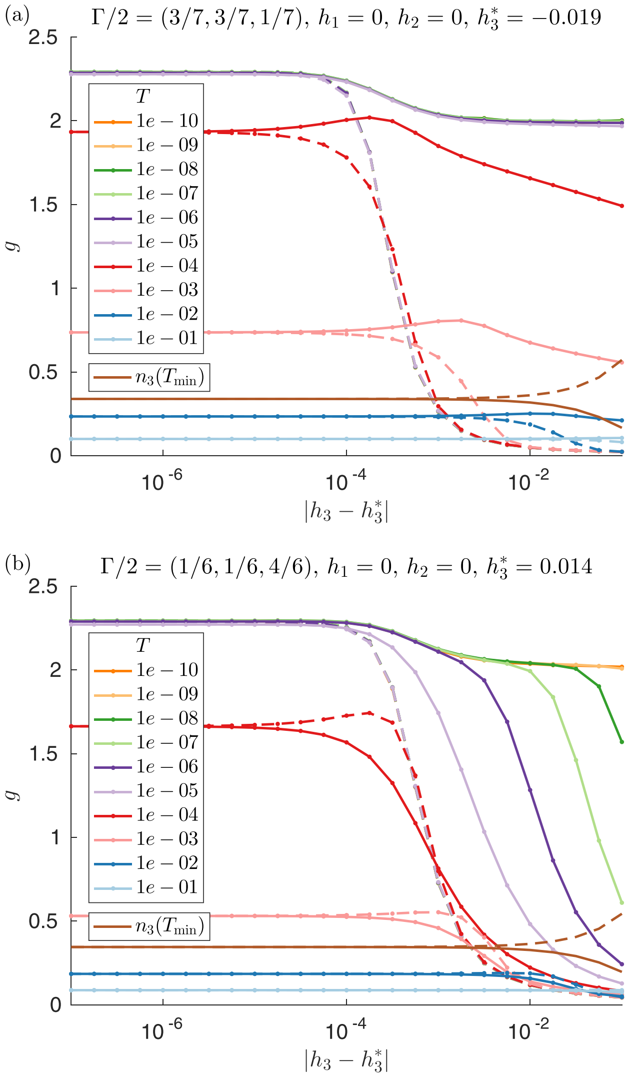

FIG. 5. Conductance at fixed $V_g = -U/2$ and $h_1 = h_2 = 0$ for (a) $\Gamma_1 = \Gamma_2 > \Gamma_3$ and (b) $\Gamma_1 = \Gamma_2 < \Gamma_3$ as function of $|h_3 - h_3^*|$ for various temperatures. We distinguish the case $h_3 > h_3^*$ (solid lines) from the case $h_3 < h_3^*$ (dashed lines), where h_3^* is the optimized value at which SU(3) symmetry is restored.

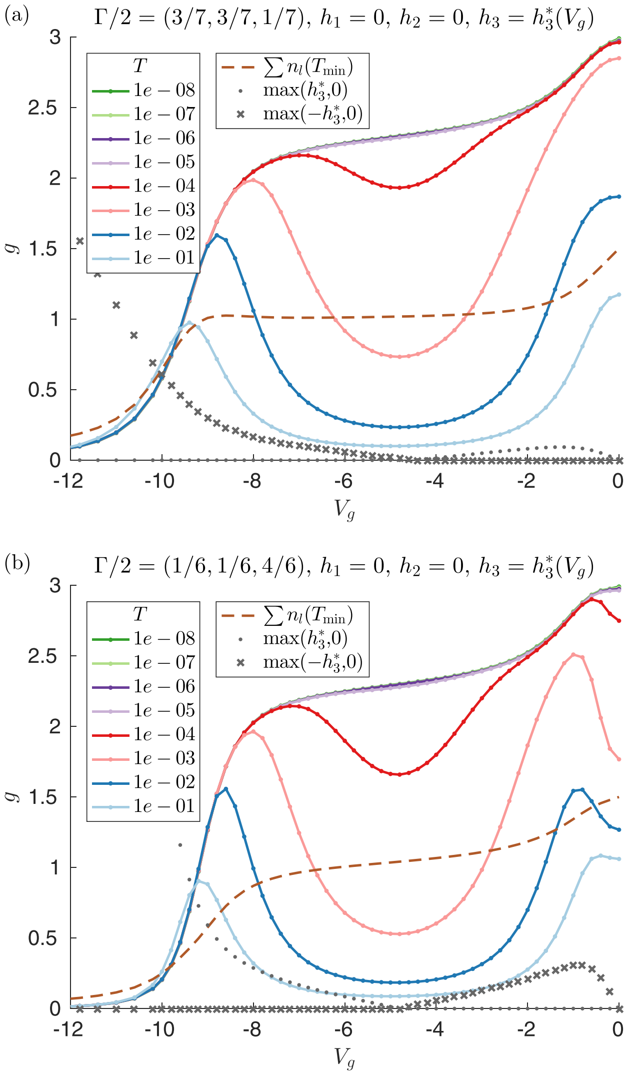

FIG. 6. Conductance for $h_1 = h_2 = 0$ and (a) $\Gamma_1 = \Gamma_2 > \Gamma_3$ and (b) $\Gamma_1 = \Gamma_2 < \Gamma_3$ as function of gate voltage for various temperatures. For each value of the gate voltage $h_3 = h_3^*(V_g)$ is optimized such that the populations of the three states are the same at zero temperature.

difference when moving over from $h_3 > h_3^*$ to $h_3 < h_3^*$ (dashed lines in Fig. 5) since then level 3 forms the ground state and thus the Kondo effect is much weaker compared to the case when the two levels $l = 1,2$ are lower in energy. In the regime of the SU(3) Kondo effect, it is hardly relevant whether level 3 approaches the other two levels from above or below.

In Fig. 6 we show the conductance as function of the gate voltage again for $h_1 = h_2 = 0$ and the two cases $\Gamma_1 = \Gamma_2 \gtrless \Gamma_3$ as in Fig. 5, but at each value of the gate voltage we choose the optimized value $h_3 = h_3^*(V_g)$ for which the populations of the three states are the same at zero temperature. As in Fig. 5 we confirm that $T_K^{(3)}$ depends only weakly on Γ_3 but the overall tendency is that $T_k^{(3)}$ decreases when increasing $|\Gamma_{1/2} - \Gamma_3|$. At the p-h symmetric point $V_g = 0$, the situation is completely different since charge fluctuations dominate for $N = 3$. Therefore, the conductance around $V_g = 0$ depends strongly on the relative distribution of the Γ_l. In fact, comparing various cases we find that the conductance at $V_g = 0$ (where also $h_3^* = 0$) decreases monotonously when increasing the variance of the couplings Γ_l. At large variance as in Fig. 6(b), g around $V_g = 0$ is strongly suppressed. In contrast, in the cotunneling regime $V_g \approx -U/2$ the conductance is rather insensitive to the distribution of the Γ_l. The combination of these phenomena leads to a surprising shape of the curve $g(V_g)$ which exhibits a local minimum at the p-h symmetric point for intermediate temperatures.

Finally, we consider in Fig. 7 three different hybridizations $\Gamma_1 < \Gamma_2 < \Gamma_3$ and tune h_2 and h_3 at fixed $h_1 = 0$, $V_g = -U/2$, and $T = 10^{-10}$. From the plots of the occupations n_l we can easily distinguish three regions where only one level is involved. At the intersections of two such regions we observe a two-level Kondo effect with conductance $g = 2$. The widths

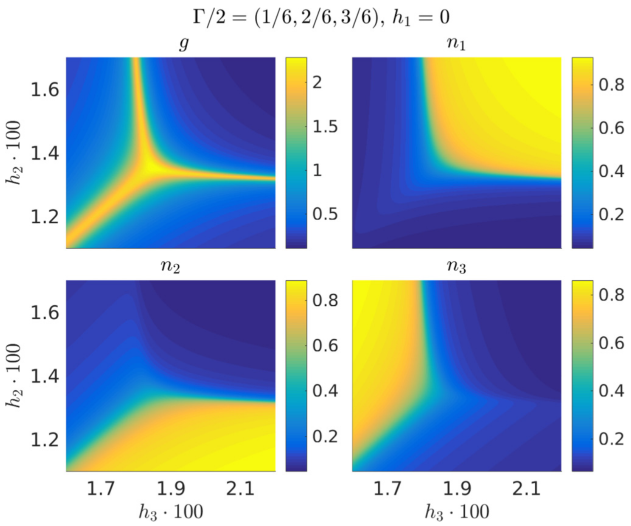

FIG. 7. Conductance and level occupations as functions of h_2 and h_3 for $\Gamma_1 < \Gamma_2 < \Gamma_3$, $h_1 = 0$, $V_g = -U/2$, and $T = 10^{-10}$.

of these intersections in the h_2-h_3 plane define three different Kondo temperatures $T_K^{(2)}$ which are ordered according to the size of the corresponding hybridizations $\Gamma_1 + \Gamma_2 < \Gamma_1 + \Gamma_3 < \Gamma_2 + \Gamma_3$. In the center, where all "one-level sections" intersect, we observe a wide region of a three-level Kondo effect with conductance $g = 2.25$. The corresponding Kondo temperature $T_K^{(3)}$ is of the same order as the maximum of the three two-level Kondo temperatures.

In summary, we find that for any kind of (diagonal) hybridization, whether with no, two, or three identical elements, we can find carefully optimized level positions (and low enough temperatures) to observe the behavior known from the SU(3)-symmetric quantum dot. For other hybridizations with two identical hybridization elements or, again, optimized level positions we can also reproduce the behavior of a two-level Kondo effect such that one level is (effectively) excluded. For arbitrary Γ_l and h_l (corresponding to most parts of a version of Fig. 7 zoomed out), the typical behavior is that of the single, (effectively) lowest-lying level.

IV. NONEQUILIBRIUM FIXED-POINT MODEL

The aim of this section is to analyze the *nonequilibrium* properties of the system for $N = 3$ in the perturbative regime where the cutoff scale Λ_c defined by (70) is much larger than the Kondo temperature $\Lambda_c \gg T_K$. Most importantly, as already emphasized several times in the previous sections, even if the fixed-point model (115) is reached at scale Λ_c [which will be the case if we take the formal scaling limit defined by (89)], it is essentially *not* SU(3) invariant if the chemical potentials of all reservoirs are different. This leads to new interesting nonequilibrium fixed-point models similar to the ones discussed in Ref. [21] for the $N = 2$ case which shows a completely different behavior of physical observables like the magnetization or the current compared to the SU(N)-symmetric Kondo model. Moreover, in practical situations the initial cutoff $D \sim E_c$ is fixed leading to deviations from the fixed-point model. Therefore, the aim of this section is to analyze the perturbative effects of the full effective interaction on physical observables and to identify a *smoking gun* for the fixed-point model together with a parameter measuring the distance from this fixed point.

A. Golden rule approach

We start from the effective interaction in the form (63) in terms of the original reservoir field operators $a_{\alpha l k}$. Inserting (93)–(96) and leaving out all small terms $\sim v_l, c_3, c_8$, we obtain

$$V_{\text{eff}} = \sum_{\alpha\alpha'} \sum_{kk'} :\underline{a}^\dagger_{\alpha k}\, \underline{\underline{V}}_\alpha\, \underline{\underline{\hat{J}}}\, \underline{\underline{V}}^\dagger_{\alpha'}\, \underline{a}_{\alpha' k'}, \tag{129}$$

with

$$\underline{\underline{\hat{J}}} \approx \sum_i \underline{\underline{J}}^i\, \hat{F}_i, \tag{130}$$

$$\underline{\underline{J}}^i = J_i\, \underline{\underline{\lambda}}_i + J_{38}(\delta_{i3}\, \underline{\underline{\lambda}}_8 + \delta_{i8}\, \underline{\underline{\lambda}}_3). \tag{131}$$

The total Hamiltonian is given by $H_{\text{tot}} = H_{\text{res}} + H_{\text{dot}} + V_{\text{eff}}$, with a unity DOS in the reservoirs and the dot Hamiltonian $H_{\text{dot}} = \sum_{ll'} h_{ll'} |l\rangle\langle l'|$ in the one-particle subspace. To apply the golden rule, we first diagonalize the dot Hamiltonian by a unitary transformation $\hat{U}$ such that

$$\tilde{H}_{\text{dot}} = \hat{U}^\dagger H_{\text{dot}} \hat{U} = \sum_l \epsilon_l |l\rangle\langle l|. \tag{132}$$

The golden rule rate for a transition from $l' \to l$ in the diagonalized basis is then given by

$$\Gamma_{l' \to l} = 2\pi \sum_{rr'} |\langle lr|\hat{U}^\dagger V_{\text{eff}} \hat{U}|l'r'\rangle|^2 \langle r'|\rho_{\text{res}}|r'\rangle \times \delta(\epsilon_l + E_r - \epsilon_{l'} - E_{r'}), \tag{133}$$

where $|r\rangle$ denote the many-particle states of the reservoirs with energy E_r and $\rho_{\text{res}} = \prod_\alpha \rho^\alpha_{\text{res}}$ is the product of the grand-canonical distributions of the reservoirs. Inserting the effective interaction (129) we find

$$\Gamma_{l' \to l} = 2\pi \sum_{\alpha\alpha'} \int d\omega \int d\omega' [1 - f_\alpha(\omega)] f_{\alpha'}(\omega') \times \delta(\epsilon_l - \epsilon_{l'} + \omega + \mu_\alpha - \omega' - \mu_{\alpha'}) \times \sum_{l_1 l'_1} |\langle l|\hat{U}^\dagger (\underline{\underline{V}}_\alpha\, \underline{\underline{\hat{J}}}\, \underline{\underline{V}}^\dagger_{\alpha'})_{l_1 l'_1} \hat{U}|l'\rangle|^2. \tag{134}$$

At zero temperature we get

$$\Gamma_{l' \to l} = 2\pi \sum_{\alpha\alpha'} w(\epsilon_l - \epsilon_{l'} + \mu_\alpha - \mu_{\alpha'}) \times \sum_{l_1 l'_1} |\langle l|\hat{U}^\dagger (\underline{\underline{V}}_\alpha\, \underline{\underline{\hat{J}}}\, \underline{\underline{V}}^\dagger_{\alpha'})_{l_1 l'_1} \hat{U}|l'\rangle|^2, \tag{135}$$

with $w(x) = |x|\theta(x)$. Here, $|\epsilon_l - \epsilon_{l'} + \mu_\alpha - \mu_{\alpha'}|$ is just the available energy phase space in the reservoirs for the energy gain $\epsilon_{l'} - \epsilon_l + \mu_{\alpha'} - \mu_\alpha > 0$. Inserting (130) we can write the golden rate in the compact form

$$\Gamma_{l'\to l} = 2\pi \sum_{\alpha\alpha'} w(\epsilon_l - \epsilon_{l'} + \mu_\alpha - \mu_{\alpha'}) \times \sum_{ij} \langle l|\hat{U}^\dagger \hat{F}_i \hat{U}|l'\rangle\, \langle l'|\hat{U}^\dagger \hat{F}_j \hat{U}|l\rangle\, \tau_{ij}^{\alpha\alpha'}, \tag{136}$$

where

$$\tau_{ij}^{\alpha\alpha'} = \mathrm{Tr}\, \underline{\underline{V}}_\alpha^\dagger\, \underline{\underline{V}}_\alpha\, \underline{\underline{J}}^i\, \underline{\underline{V}}_{\alpha'}^\dagger\, \underline{\underline{V}}_{\alpha'}\, \underline{\underline{J}}^j. \tag{137}$$

As expected, only the combination $\underline{\underline{V}}_\alpha^\dagger\, \underline{\underline{V}}_\alpha$ enters into this expression which is consistent with our discussion in Sec. II A where it was shown that the hybridization matrices $\underline{\underline{\Gamma}}_\alpha$ depend only on this combination [see (36)].

The stationary probability distribution p_l in the diagonalized basis follows from

$$\sum_{l'} p_{l'}\, \Gamma_{l'\to l} = 0, \quad \sum_l p_l = 1. \tag{138}$$

In an analog way one can calculate the stationary current I_β flowing in reservoir β from the current rates $W_{ll'}^\beta$ in golden rule:

$$I_\beta = \sum_{ll'} p_{l'}\, \Gamma_{l'\to l}^\beta, \tag{139}$$

with

$$\sum_l \Gamma_{l'\to l}^\beta = 2\pi \sum_{\alpha\alpha'} (\delta_{\alpha\beta} - \delta_{\alpha'\beta}) w(\epsilon_l - \epsilon_{l'} + \mu_\alpha - \mu_{\alpha'}) \times \sum_{ij} \langle l|\hat{U}^\dagger \hat{F}_i \hat{U}|l'\rangle\, \langle l'|\hat{U}^\dagger \hat{F}_j \hat{U}|l\rangle\, \tau_{ij}^{\alpha\alpha'}. \tag{140}$$

Once the input of the matrices $\underline{\underline{V}}_\alpha$, the coupling constants (J_1, J_4, J_6) and (K_1, K_4, K_6) (determining the matrices $\underline{\underline{J}}^i$ for $i = 1, \ldots, 8$), the unitary transformation $\hat{U}$, and the eigenvalues ϵ_l of the dot Hamiltonian are known, the stationary probabilities and the current can be calculated in a straightforward way from the above golden rule expressions. Thereby, we have neglected small renormalizations of the dot parameters induced by the coupling to the reservoirs which are assumed to be much smaller than the level spacings in the dot.

B. *F*-spin magnetization for two reservoirs

We now calculate the F-spin magnetization of the dot

$$m_F = \sqrt{\sum_{i=1}^{8} (\langle \hat{F}_i \rangle)^2} \tag{141}$$

for the special case of two reservoirs. We will show that the condition of zero F-spin magnetization requires special dot parameters characterizing the deviation from the fixed-point model. In the basis of the diagonalized dot Hamiltonian, the density matrix of the dot is diagonal in the golden rule approximation so that only the two diagonal generators $\hat{F}_3$ and $\hat{F}_8$ contribute to m_F:

$$m_F = \sqrt{(\langle \hat{F}_3 \rangle)^2 + \langle \hat{F}_8 \rangle)^2} = \tfrac{1}{2}\sqrt{(p_1 - p_2)^2 + \tfrac{1}{3}(p_1 + p_2 - 2p_3)^2}. \tag{142}$$

Zero F-spin magnetization is then equivalent to an equal population of the three states

$$m_F = 0 \quad \Leftrightarrow \quad p_1 = p_2 = p_3. \tag{143}$$

As explained in Sec. II A via (49), the case of two reservoirs has the advantage that both matrices $\underline{\underline{V}}_\alpha^\dagger\, \underline{\underline{V}}_\alpha = \underline{\underline{U}}_V\, \underline{\underline{A}}_\alpha^{\mathrm{d}}\, \underline{\underline{U}}_V^\dagger$ can be diagonalized by a common unitary matrix $\underline{\underline{U}}_V$ and the diagonal matrices $\underline{\underline{A}}_\alpha^{\mathrm{d}}$ are parametrized via (51) by the parameters x_α, p_α, and q_α, which fulfill the conditions (52)–(54) and (28). Furthermore, it was shown that the special property of the fixed-point model is that the unitary transformation $\underline{\underline{U}}_V$ can be shifted to the dot such that in the new basis an effective diagonal tunneling model (56) emerges. Thus, the particular property of the fixed-point model is that the expectation value of the F-spin magnetization and the current I_α are independent of the unitary matrix $\underline{\underline{U}}_V$. In contrast, for the model away from the fixed point this is no longer the case.

The unitary matrix $\underline{\underline{U}}_V$ provides a mean to parametrize the dot Hamiltonian by convenient parameters. After transforming the dot Hamiltonian with $\hat{U}_V = \sum_{ll'} (\underline{\underline{U}}_V)_{ll'} |l\rangle\langle l'|$, we take the form

$$\hat{U}_V^\dagger H_{\mathrm{dot}} \hat{U}_V = h_x \hat{F}_1 + h_y \hat{F}_2 + h_z \hat{F}_3 + \frac{2}{\sqrt{3}} \Delta \hat{F}_8, \tag{144}$$

such that $\vec{h}$ can be interpreted as an effective magnetic field acting on the isospin of the up/down quark, and Δ is the level distance between the strange quark and the average level position of the up and down quarks:

$$\Delta = \tfrac{1}{2}(\epsilon_1 + \epsilon_2) - \epsilon_3 \tag{145}$$

(see also Fig. 1 for an illustration). The eigenvalues ϵ_l of H_{dot} and the unitary operator $\hat{U}$ can then be expressed by the dot parameters $\vec{h}$ and Δ by

$$\epsilon_{1/2} = \pm\frac{1}{2} h + \frac{1}{3}\Delta, \quad \epsilon_3 = -\frac{2}{3}\Delta, \tag{146}$$

$$\hat{U} = \hat{U}_V\, \hat{U}_h, \quad \underline{\underline{U}}_h = \left(\begin{array}{c|c} \underline{x}_1\, \underline{x}_2 & 0 \\ \hline 0 & 1 \end{array}\right), \tag{147}$$

where $h = \sqrt{h_\perp^2 + h_z^2}$, $h_\perp^2 = h_x^2 + h_y^2$, and

$$\underline{x}_{1/2} = \frac{1}{\sqrt{2h(h \mp h_z)}} \begin{pmatrix} \pm(h_x - i h_y) \\ h \mp h_z \end{pmatrix}. \tag{148}$$

Inserting $\hat{U} = \hat{U}_V \hat{U}_h$ and $\underline{\underline{V}}_\alpha^\dagger\, \underline{\underline{V}}_\alpha = \underline{\underline{U}}_V\, \underline{\underline{A}}_\alpha^{\mathrm{d}}\, \underline{\underline{U}}_V^\dagger$ in the golden rate (136) we get

$$\Gamma_{l'\to l} = 2\pi \sum_{\alpha\alpha'} w(\epsilon_l - \epsilon_{l'} + \mu_\alpha - \mu_{\alpha'}) \times \sum_{ij} \langle l|\hat{U}^\dagger \hat{U}_V^\dagger \hat{F}_i \hat{U}_V \hat{U}_h|l'\rangle \times \langle l'|\hat{U}_h^\dagger \hat{U}_V^\dagger \hat{F}_j \hat{U}_V \hat{U}_h|l\rangle\, \tau_{ij}^{\alpha\alpha'}, \tag{149}$$

with

$$\tau_{ij}^{\alpha\alpha'} = \mathrm{Tr}\, \underline{\underline{A}}_{\alpha}^{d}(\underline{\underline{U}}_{V}^{\dagger}\, \underline{\underline{J}}^{i}\, \underline{\underline{U}}_{V})\, \underline{\underline{A}}_{\alpha'}^{d}(\underline{\underline{U}}_{V}^{\dagger}\, \underline{\underline{J}}^{j}\, \underline{\underline{U}}_{V}). \tag{150}$$

For the special case of the fixed-point model where $\underline{\underline{J}}^{i} = \frac{1}{2} J \underline{\underline{\lambda}}_{i}$, we can see that the unitary matrix $\underline{\underline{U}}_{V}$ indeed drops out as expected due to the invariant

$$\sum_{i=1}^{8} (\underline{\underline{U}}_{V}^{\dagger}\, \underline{\underline{\lambda}}_{i}\, \underline{\underline{U}}_{V})(\hat{U}_{V}^{\dagger} \hat{F}_{i} \hat{U}_{V}) = \sum_{i=1}^{8} \underline{\underline{\lambda}}_{i}\, \hat{F}_{i}. \tag{151}$$

An analog property holds for the current rate (139).

In the following, we consider the strong nonequilibrium regime where the bias voltage $V = \mu_L - \mu_R > 0$ is assumed to be larger than all level spacings, i.e.,

$$V > |h|, |\Delta \pm h/2|. \tag{152}$$

From (142) we see directly that the condition $m_F = 0$ is equivalent to $\langle \hat{F}_3 \rangle = \langle \hat{F}_8 \rangle = 0$. Consequently, these are two conditions revealing that $m_F = m_F(h_z, h_\perp, \Delta) = 0$ generically defines a closed curve in $(h_z, h_\perp, \Delta)$ space. Inserting (51) for $\underline{\underline{A}}_{\alpha}^{d}$, (131) for $\underline{\underline{J}}^{i}$, (146) for ϵ_l, and (147) for $\hat{U}_h$, we evaluate the golden rule rates (149) and (139) in Appendix C for the special case $\underline{\underline{U}}_{V} = \mathbb{1}$ from which we can determine the shape of this curve. This gives a generic result for the fixed-point model (where the matrix $\underline{\underline{U}}_{V}$ drops out), whereas for the model away from the fixed point we consider only the special case of a diagonal tunneling model.

From the condition $m_F(h_z, h_\perp, \Delta) = 0$ or $p_1 = p_2 = p_3 = 1/3$ we obtain in Appendix C the two equations

$$\Delta = x_L q_L V + \frac{J_4^2 - J_6^2}{J_4^2 + J_6^2}\left(x_L p_L V - \frac{1}{2} h_z\right), \tag{153}$$

$$\theta_2^2 x_L^2 p_L^2 V^2 = \theta_1^2 h_\perp^2 + \theta_2^2 (h_z - x_L p_L V)^2, \tag{154}$$

where

$$\theta_1^2 = J_1^2 + J_3^2 + J_{38}^2 + \tfrac{1}{2}(J_4^2 + J_6^2), \tag{155}$$

$$\theta_2^2 = 2J_1^2 + \tfrac{3}{2} J_4^2 - \tfrac{1}{2} J_6^2. \tag{156}$$

This means that the projection of the curve $m_F(h_z, h_\perp, \Delta) = 0$ on the $(h_z, h_\perp)$ plane is an ellipse with the ratio

$$s_1 = \theta_1/\theta_2 \tag{157}$$

of the two shape parameters. θ_1 is the major axis (minor axis) if $s_1 > 1$ $(s_1 < 1)$. We point out that this is different to the SU(2) model (i.e., $J_{38} = J_4 = J_6 = 0$) where θ_1 is always the major axis. Furthermore, the derivative of Δ with respect to h_z is given by

$$s_2 = \frac{d\Delta}{dh_z} = -\frac{1}{2} \frac{J_4^2 - J_6^2}{J_4^2 + J_6^2}. \tag{158}$$

The two parameters $s_{1/2}$ provide *smoking guns* for the detection of the fixed-point model since for $J_i = J/2$ and $J_{38} = 0$ we obtain

$$s_1 = 1, \quad s_2 = 0, \tag{159}$$

i.e., a circle in the $(h_z, h_\perp)$ plane as shown in Fig. 8 and no dependence of $\Delta = q_L V$ on h_z at the fixed point. In this sense $1 - s_1$ and s_2 can both be viewed as parameters measuring the distance from the fixed-point model. Furthermore, we see that the parameters $x_L p_L = -x_R p_R$ and $x_L q_L = -x_R q_R$ of the fixed-point model can be determined from the two equations

$$\Delta = x_L q_L V, \quad h_\perp^2 + (h_z - x_L p_L V)^2 = x_L p_L^2 V^2. \tag{160}$$

To fix the remaining parameter $x_L x_R$ and the coupling J from a physical quantity we have also evaluated the current in Appendix C and obtained at the fixed point and for $m_F = 0$

$$\begin{aligned} I_L &= -I_R \\ &= \pi x_L x_R J^2 \left\{ -\frac{q_L - q_R}{6} \Delta - \frac{p_L - p_R}{4} h_z \right. \\ &\quad \left. + \frac{1}{3}\left(4 - \frac{q_L q_R}{9} - \frac{p_L p_R}{3}\right) V \right\} \\ &= \pi J^2 \left\{ \frac{1}{6} x_R q_R \Delta + \frac{1}{4} x_R p_R h_z \right. \\ &\quad \left. + \frac{1}{3}\left(4 x_L x_R + \frac{1}{9} x_R^2 q_R^2 + \frac{1}{3} x_R^2 p_L^2\right) V \right\}, \end{aligned} \tag{161}$$

where we used $x_L x_R (q_L - q_R) = -x_R q_R$ and $x_L x_R (p_L - p_R) = -x_R p_R$ in the last equation. J^2 is just the overall scale of the current and the parameter $x_L x_R$ appears explicitly. Together with $x_L + x_R = 1$, the two parameters $x_{L/R}$ can thus be fixed.

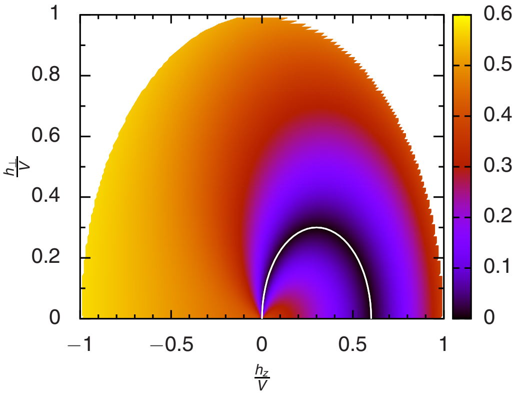

FIG. 8. The F-spin magnetization m_F in the strong nonequilibrium regime projected onto the $(h_z, h_\perp)$ plane at the fixed point with $x_L = x_R = 0.5$, $p_L = -p_R = 0.6$, $q_L = -q_R = 1.0$, $J = 0.0965103$, $V = 10^3\, T_K$, and $\Delta = 0.5V$. The white line $h_\perp^*(h_z)$ indicates where m_F is zero.

In summary, we have shown in the strong nonequilibrium regime that the condition of vanishing F-spin magnetization $m_F = 0$ defines a closed curve in $(h_z, h_\perp, \Delta)$ space that is an ellipse in the special case of a diagonal tunneling model. A golden rule calculation has revealed that the geometric properties of this ellipse are a measure for the distance to the fixed-point model where the ellipse turns into a circle being embedded in a plane defined by a constant value for Δ. At the fixed point, the parameters of the effective model can experimentally be obtained from identifying the position of this circle together with measuring the current at the corresponding dot parameters $\vec{h}$ and Δ.

V. SUMMARY

The results obtained in this paper show that the area of nonequilibrium low-temperature transport through generic quantum dot models contains a huge variety of interesting fixed-point models not accessible in the equilibrium case. Previous studies have analyzed many generic Kondo scenarios for equilibrium systems and used the finite voltage V just as a probe for the equilibrium dot spectral density for quantum dots coupled very asymmetrically to two reservoirs [4]. In addition, the finite voltage together with corresponding decay rates was just expected to act as a cutoff scale for RG flows in the weak-coupling regime [23,24,27] analog to the temperature, leading to quantitatively but *not* qualitatively different physical properties. In contrast, the analysis performed in this paper shows that, for generic tunneling matrices, the cutoff set by the voltage is essentially different from the temperature since it drives the system towards a fixed point characterized by a *different symmetry* compared to the equilibrium case. Our main result is that if an electron on a singly occupied dot in the cotunneling regime can occupy N levels, flavor fluctuations lead to a model in the nonequilibrium situation which is essentially *not* SU(N) invariant. In the scaling limit for fixed values of V and T_K, a fixed-point model appears at scale V where each reservoir is characterized by N effective flavors with (N^2-1)-dimensional polarizations [corresponding to the N^2-1 generators of the SU(N) group] pointing in different directions such that the total sum is equal to zero. This leads to a SU(N)-symmetric equilibrium fixed point where all reservoirs can be taken together, but to a SU(N)-*nonsymmetric* nonequilibrium fixed point with *qualitatively* different physical properties. We have demonstrated this for the special case $N=3$ and two reservoirs in the weak-coupling regime $V \gg T_K$ and have seen that the condition of equal population of all dot states is realized for special dot parameters providing a *smoking gun* to identify the special symmetry of the nonequilibrium fixed-point model.

Strictly speaking, the numerical solution of the RG flow shows that even for rather large ratios D/T_K, the coupling constants become all equal only very close to T_K, where the poor man's scaling approach is no longer valid. This means that the fixed-point model can not be reached for voltages $V \gg T_K$, except for cases where the initial parameters have already been set close to the fixed point. It is therefore of high interest for the future to develop numerically exact approaches to describe the strong-coupling regime in nonequilibrium. In particular, for voltages $V \sim T_K$ we expect that the fixed-point model has been reached and the scaling of the conductance and the F-spin magnetization as function of the dot parameters will be essentially different from the SU(N)-symmetric case. In agreement with Refs. [12,13] we have demonstrated in this paper that in equilibrium the fixed-point model is indeed reached for temperatures below the Kondo temperature T_K, providing evidence that a similar result will also hold in the nonequilibrium case when the voltage reaches T_K. It will be interesting for the future to test this conjecture and to provide signatures of the nonequilibrium fixed-point model in the strong-coupling regime.

Finally, it will also be very interesting for the future to study the nonequilibrium fixed points in regimes where the particle number of the dot is larger than one $N_{\rm dot} > 1$. Already in the equilibrium case it has been demonstrated that not only the Coulomb interaction, but also other kinds of interactions (e.g., spin-dependent terms) are very important to find the correct ground state (see, e.g., Ref. [4] for a review). Based on this and our results for $N_{\rm dot} = 1$ we expect that even a richer variety of new nonequilibrium fixed-point models has to be expected for $N_{\rm dot} > 1$.

ACKNOWLEDGMENTS

This work was supported by the Deutsche Forschungsgemeinschaft via RTG 1995 (C.J.L. and H.S.). We thank A. Weichselbaum and S.-S. B. Lee for helpful discussions on the NRG setup. F.B.K. and J.v.D. acknowledge support by the Cluster of Excellence Nanosystems Initiative Munich; F.B.K. acknowledges funding from the research school IMPRS-QST.

APPENDIX A: RESERVOIR SELF-ENERGY

In this Appendix we calculate the greater/lesser self-energies $\underline{\underline{\Sigma}}^{\gtrless}_{\rm res}(\omega)$ of the dot arising from the tunneling Hamiltonian (7) with an effective tunneling matrix given by (40) together with the potential scattering term $V_{\rm sc}$ [see (43)]. The effective DOS of the reservoirs is given by unity since the whole nontrivial information of the reservoirs is included in the effective tunneling matrix. Using standard Keldysh formalism we get

$$\underline{\underline{\Sigma}}^{\gtrless}_{\rm res}(\omega) = \gamma^2 \sum_{\alpha\alpha'} \sum_{kk'} \underline{\underline{V}}^{\dagger}_{\alpha}\, \underline{\underline{G}}^{\gtrless}_{\alpha k,\alpha' k'}(\omega)\, \underline{\underline{V}}_{\alpha'}, \tag{A1}$$

where $\underline{\underline{G}}^{\gtrless}_{\alpha k,\alpha' k'}(\omega)$ are the greater/lesser reservoir Green's functions arising from the reservoir part of the Hamiltonian including the potential scattering term. These Green's functions can be calculated from the Dyson equation with $V_{\rm sc}$ defining the self-energy

$$\begin{aligned}\underline{\underline{G}}^{\gtrless}_{\alpha k,\alpha' k'}(\omega) =& \underline{\underline{g}}^{\gtrless}_{\alpha k}(\omega)\delta_{\alpha\alpha'}\delta_{kk'} \\ &+ v_{\rm sc} \sum_{\alpha_1 k_1} \underline{\underline{g}}^{\gtrless}_{\alpha k}(\omega)\, \underline{\underline{V}}_{\alpha}\, \underline{\underline{V}}^{\dagger}_{\alpha_1}\, \underline{\underline{G}}^{A}_{\alpha_1 k_1,\alpha' k'}(\omega) \\ &+ v_{\rm sc} \sum_{\alpha_1 k_1} \underline{\underline{g}}^{R}_{\alpha k}(\omega)\, \underline{\underline{V}}_{\alpha}\, \underline{\underline{V}}^{\dagger}_{\alpha_1}\, \underline{\underline{G}}^{\gtrless}_{\alpha_1 k_1,\alpha' k'}(\omega),\end{aligned} \tag{A2}$$

where $\underline{\underline{G}}^{A}_{\alpha_1 k_1,\alpha' k'}(\omega)$ denotes the advanced Green's function which follows from the Dyson equation

$$\begin{aligned}\underline{\underline{G}}^{A}_{\alpha k,\alpha' k'}(\omega) =& \underline{\underline{g}}^{A}_{\alpha k}(\omega)\delta_{\alpha\alpha'}\delta_{kk'} \\ &+ v_{\rm sc} \sum_{\alpha_1 k_1} \underline{\underline{g}}^{A}_{\alpha k}(\omega)\, \underline{\underline{V}}_{\alpha}\, \underline{\underline{V}}^{\dagger}_{\alpha_1}\, \underline{\underline{G}}^{A}_{\alpha_1 k_1,\alpha' k'}(\omega).\end{aligned} \tag{A3}$$

$\underline{\underline{g}}^{x}_{\alpha k}$ (with $x = R, A, \gtrless$) denote the free Green's functions of reservoir α without $V_{\rm sc}$ given by

$$\underline{\underline{g}}^{R/A}_{\alpha k}(\omega) = \frac{1}{\omega - \epsilon_{\alpha k}\underline{\underline{\mathbb{1}}} \pm i\eta}, \tag{A4}$$

$$\underline{\underline{g}}^{<}_{\alpha k}(\omega) = -f_\alpha(\omega)(\underline{\underline{g}}^{R} - \underline{\underline{g}}^{A})(\omega), \tag{A5}$$

$$\underline{\underline{g}}^{>}_{\alpha k}(\omega) = [1 - f_\alpha(\omega)](\underline{\underline{g}}^{R} - \underline{\underline{g}}^{A})(\omega). \tag{A6}$$

Since the DOS of the reservoirs is unity we get

$$\sum_k \underline{\underline{g}}^{R/A}_{\alpha k}(\omega) = \mp i\pi\underline{\underline{\mathbb{1}}}, \tag{A7}$$

$$\sum_k \underline{\underline{g}}^{<}_{\alpha k}(\omega) = 2\pi i f_\alpha(\omega)\underline{\underline{\mathbb{1}}}, \tag{A8}$$

$$\sum_k \underline{\underline{g}}^{>}_{\alpha k}(\omega) = -2\pi i(1 - f_\alpha(\omega))\underline{\underline{\mathbb{1}}}. \tag{A9}$$

Using these properties together with $\sum_\alpha \underline{\underline{V}}^\dagger_\alpha \underline{\underline{V}}_\alpha = \underline{\underline{\mathbb{1}}}$ and defining

$$\underline{\underline{\bar{G}}}^x(\omega) = \sum_{\alpha\alpha'}\sum_{kk'} \underline{\underline{V}}^\dagger_\alpha \underline{\underline{G}}^x_{\alpha k,\alpha' k'}(\omega)\, \underline{\underline{V}}_{\alpha'}, \tag{A10}$$

with $x = R, A, \gtrless$, we obtain from the Dyson equations (A2) and (A3) after a straightforward calculation

$$\underline{\underline{\bar{G}}}^A = i\pi\underline{\underline{\mathbb{1}}} + i\pi v_{\text{sc}}\, \underline{\underline{\bar{G}}}^A, \tag{A11}$$

$$\begin{aligned}\underline{\underline{\bar{G}}}^<(\omega) &= -i\pi v_{\text{sc}}\, \underline{\underline{\bar{G}}}^<(\omega)\\ &\quad + 2\pi i \sum_\alpha f_\alpha(\omega)\, \underline{\underline{V}}^\dagger_\alpha \underline{\underline{V}}_\alpha\, (\underline{\underline{\mathbb{1}}} + v_{\text{sc}}\, \underline{\underline{\bar{G}}}^A),\end{aligned} \tag{A12}$$

$$\begin{aligned}\underline{\underline{\bar{G}}}^>(\omega) &= -i\pi v_{\text{sc}}\, \underline{\underline{\bar{G}}}^>(\omega)\\ &\quad - 2\pi i \sum_\alpha [1 - f_\alpha(\omega)]\, \underline{\underline{V}}^\dagger_\alpha \underline{\underline{V}}_\alpha\, (\underline{\underline{\mathbb{1}}} + v_{\text{sc}}\, \underline{\underline{\bar{G}}}^A).\end{aligned} \tag{A13}$$

Solving this set of matrix equations for $\underline{\underline{\bar{G}}}^\gtrless(\omega)$ and inserting the solution in

$$\underline{\underline{\Sigma}}^\gtrless_{\text{res}}(\omega) = \gamma^2\, \underline{\underline{\bar{G}}}^\gtrless(\omega), \tag{A14}$$

we finally get the result (11) and (12) for the self-energies with an effective hybridization matrix given by (47).

APPENDIX B: EQUILIBRIUM GROUND STATE OF THE FIXED-POINT MODEL

In Sec. II D, we have argued why the dot representation has the [3] fundamental representation while the first state of the reservoir the complex conjugate of this fundamental representation $[\bar{3}]$. Representing both sites by [3] (or, equivalently, by the complex conjugate of this representation $[\bar{3}]$) leads to a decomposition of the Hilbert space of the composite system into a sextet and a triplet. Accordingly, a SU(3)-symmetric Hamiltonian in this representation has an either threefold- or sixfold-degenerate ground state which is in contrast to the outcome of our analysis. Choosing the complex-conjugate representation $[\bar{3}]$ for the reservoir site instead leads to a Hilbert space that decomposes into an octet and a singlet. A SU(3)-symmetric Hamiltonian in this representation yields two different eigenenergies of which one is nondegenerate and the other eightfold degenerate.

We want to emphasize that this is fundamentally different to the situation in the corresponding SU(2) model. Generally, the fundamental representation of the spin $\frac{1}{2}$ [2] is equivalent to its complex conjugate, i.e., $[2] = [\bar{2}]$. This is consistent with the observation that no antispin $\frac{1}{2}$ exists. However, this a special property of the SU(2) group that holds no longer for SU(N) with $N > 2$ and we anticipate for an analog SU(N) model a ground state inspired by flavor-antiflavor pairs.

We consider the following set of basis states for the composite system:

$$|u\bar{s}\rangle = |u\rangle \otimes |\bar{s}\rangle, \tag{B1}$$

$$|d\bar{s}\rangle = |d\rangle \otimes |\bar{s}\rangle, \tag{B2}$$

$$|d\bar{u}\rangle = |d\rangle \otimes |\bar{u}\rangle, \tag{B3}$$

$$|u\bar{d}\rangle = |u\rangle \otimes |\bar{d}\rangle, \tag{B4}$$

$$|s\bar{u}\rangle = |s\rangle \otimes |\bar{u}\rangle, \tag{B5}$$

$$|s\bar{d}\rangle = |s\rangle \otimes |\bar{d}\rangle, \tag{B6}$$

$$|u\bar{u}\rangle = |u\rangle \otimes |\bar{u}\rangle, \tag{B7}$$

$$|d\bar{d}\rangle = |d\rangle \otimes |\bar{d}\rangle, \tag{B8}$$

$$|s\bar{s}\rangle = |s\rangle \otimes |\bar{s}\rangle. \tag{B9}$$

In a quark picture, these states are meaningful since they are all eigenstates of the total charge operator

$$\hat{q}_{\text{tot}} = \hat{Q} + \hat{q}, \tag{B10}$$

where $\hat{Q} = \hat{F}_3 + \frac{1}{\sqrt{3}}\hat{F}_8$ and $\hat{q} = \hat{f}_3 + \frac{1}{\sqrt{3}}\hat{f}_8$ are defined as usual in the quark model [38], with an integer eigenvalue. This is analog to the observation that no elementary particle with noninteger electrical charge exists in nature.

Let the effective Hamiltonian V_{eff} [Eq. (115)] act on the states (B1)–(B6), we find that $|u\bar{s}\rangle$, $|d\bar{s}\rangle$, $|d\bar{u}\rangle$, $|u\bar{d}\rangle$, $|s\bar{u}\rangle$, and $|s\bar{d}\rangle$ are eigenstates with eigenvalue $E_8 = \frac{1}{6}J$. Instead, the remaining states (B7)–(B9) are not eigenstates since

$$V_{\text{eff}}|u\bar{u}\rangle = -\frac{J}{3}|u\bar{u}\rangle - \frac{J}{2}(|d\bar{d}\rangle + |s\bar{s}\rangle), \tag{B11}$$

$$V_{\text{eff}}|d\bar{d}\rangle = -\frac{J}{3}|d\bar{d}\rangle - \frac{J}{2}(|u\bar{u}\rangle + |s\bar{s}\rangle), \tag{B12}$$

$$V_{\text{eff}}|s\bar{s}\rangle = -\frac{J}{3}|s\bar{s}\rangle - \frac{J}{2}(|u\bar{u}\rangle + |d\bar{d}\rangle). \tag{B13}$$

Finding the remaining eigenstates is a trivial diagonalization problem in the 3 × 3 subspace of $|u\bar{u}\rangle$, $|d\bar{d}\rangle$, and $|s\bar{s}\rangle$. The first two linear combinations

$$|1\rangle = \frac{1}{\sqrt{2}}(|u\bar{u}\rangle - |d\bar{d}\rangle), \tag{B14}$$

$$|2\rangle = \frac{1}{\sqrt{6}}(|u\bar{u}\rangle + |d\bar{d}\rangle - 2|s\bar{s}\rangle) \tag{B15}$$

with eigenvalue E_8 complement the octet. Being orthogonal to $|1\rangle$ and $|2\rangle$, the singlet eigenstate is the ground state (122) with eigenvalue $E_{\text{gs}} = -\frac{4}{3}J$. We note that this set of eigenstates is the same as for pseudoscalar mesons in the light quark model [39].

APPENDIX C: EVALUATION OF GOLDEN RULE RATE

In this Appendix we evaluate the golden rule rates (149) and (139) for the special case $\underline{\underline{U}}_V = \mathbb{1}$. We denote the three states by the quark flavors, i.e., $l = 1,2,3 \equiv u,d,s$. First, we evaluate the matrix elements $\tau_{ij}^{\alpha\alpha'}$ from (150) by employing the algebra of the Gell-Mann matrices. Writing

$$\tau_{ij}^{\alpha\alpha'} = x_\alpha x_{\alpha'} \bar{\tau}_{ij}^{\alpha\alpha'}, \tag{C1}$$

we obtain for the nonvanishing matrix elements

$$\bar{\tau}_{11}^{\alpha\alpha'} = \bar{\tau}_{22}^{\alpha\alpha'} = 2J_1^2 M_{1,\alpha\alpha'}^{-}, \tag{C2}$$

$$\bar{\tau}_{12}^{\alpha\alpha'} = -\bar{\tau}_{21}^{\alpha\alpha'} = 2iJ_1^2 M_{2,\alpha\alpha'}^{-}, \tag{C3}$$

$$\bar{\tau}_{44}^{\alpha\alpha'} = \bar{\tau}_{55}^{\alpha\alpha'} = J_4^2 M_{3,\alpha\alpha'}^{++}, \tag{C4}$$

$$\bar{\tau}_{45}^{\alpha\alpha'} = -\bar{\tau}_{54}^{\alpha\alpha'} = iJ_4^2 M_{3,\alpha\alpha'}^{+-}, \tag{C5}$$

$$\bar{\tau}_{66}^{\alpha\alpha'} = \bar{\tau}_{77}^{\alpha\alpha'} = J_6^2 M_{3,\alpha\alpha'}^{-+}, \tag{C6}$$

$$\bar{\tau}_{67}^{\alpha\alpha'} = -\bar{\tau}_{76}^{\alpha\alpha'} = iJ_6^2 M_{3,\alpha\alpha'}^{--}, \tag{C7}$$

$$\begin{aligned}\bar{\tau}_{ij}^{\alpha\alpha'}|_{i,j\in(3,8)} =& 2J_{3i}J_{3j}M_{1,\alpha\alpha'}^{+} + 2J_{i8}J_{j8}M_{4,\alpha\alpha'} \\ &+ \frac{2}{\sqrt{3}}(J_{3i}J_{j8} + J_{i8}J_{3j})M_{2,\alpha\alpha'}^{+},\end{aligned} \tag{C8}$$

where $J_{33} = J_3$, $J_{88} = J_8$, and

$$M_{1,\alpha\alpha'}^{\sigma} = \overline{q}_\alpha \overline{q}_{\alpha'} + \sigma p_\alpha p_{\alpha'}, \tag{C9}$$

$$M_{2,\alpha\alpha'}^{\sigma} = p_\alpha \overline{q}_{\alpha'} + \sigma \overline{q}_\alpha p_{\alpha'}, \tag{C10}$$

$$M_{3,\alpha\alpha'}^{\sigma\sigma'} = (\overline{q}_\alpha + \sigma p_\alpha)\tilde{q}_{\alpha'} + \sigma' \tilde{q}_\alpha(\overline{q}_{\alpha'} + \sigma p_{\alpha'}), \tag{C11}$$

$$M_{4,\alpha\alpha'} = 1 + \frac{p_\alpha p_{\alpha'} + q_\alpha q_{\alpha'}}{3} - \frac{q_\alpha + q_{\alpha'}}{3}, \tag{C12}$$

with $\overline{q}_\alpha = 1 + \frac{q_\alpha}{3}$ and $\tilde{q}_\alpha = 1 - \frac{2q_\alpha}{3}$. Introducing the notation

$$\chi_{1/3}^{\alpha\alpha'} = \frac{\pi}{2}\big(\tau_{11}^{\alpha\alpha'} \pm \tau_{33}^{\alpha\alpha'}\big), \tag{C13}$$

$$\chi_2^{\alpha\alpha'} = i\pi\tau_{12}^{\alpha\alpha'}, \quad \chi_s^\alpha = x_\alpha \tilde{q}_\alpha, \tag{C14}$$

$$\chi_{u/d}^{\alpha} = 2\pi x_\alpha[J_+^2(\overline{q}_\alpha \pm p_\alpha\phi_z) + J_-^2(p_\alpha \pm \overline{q}_\alpha\phi_z)], \tag{C15}$$

with $J_\pm^2 = \frac{1}{2}(J_4^2 \pm J_6^2)$ and $\phi_z = \frac{h_z}{h}$, we obtain by inserting (147) and (C1) in (149) after a straightforward calculation

$$\begin{aligned}\Gamma_{d\to u} =& \sum_{\alpha\alpha'} w(\mu_\alpha - \mu_{\alpha'} - h) \\ &\times \big[\chi_1^{\alpha\alpha'} - \chi_2^{\alpha\alpha'}\phi_z + \chi_3^{\alpha\alpha'}\phi_z^2\big],\end{aligned} \tag{C16}$$

$$\Gamma_{u\to d} = \sum_{\alpha\alpha'} w(\mu_\alpha - \mu_{\alpha'} + h)\big[\chi_1^{\alpha\alpha'} + \chi_2^{\alpha\alpha'}\phi_z + \chi_3^{\alpha\alpha'}\phi_z^2\big], \tag{C17}$$

$$\Gamma_{s\to u} = \sum_{\alpha\alpha'} w\left(\mu_\alpha - \mu_{\alpha'} - \Delta - \frac{h}{2}\right)\chi_u^\alpha \chi_s^{\alpha'}, \tag{C18}$$

$$\Gamma_{u\to s} = \sum_{\alpha\alpha'} w\left(\mu_\alpha - \mu_{\alpha'} + \Delta + \frac{h}{2}\right)\chi_s^\alpha \chi_u^{\alpha'}, \tag{C19}$$

$$\Gamma_{s\to d} = \sum_{\alpha\alpha'} w\left(\mu_\alpha - \mu_{\alpha'} - \Delta + \frac{h}{2}\right)\chi_d^\alpha \chi_s^{\alpha'}, \tag{C20}$$

$$\Gamma_{d\to s} = \sum_{\alpha\alpha'} w\left(\mu_\alpha - \mu_{\alpha'} + \Delta - \frac{h}{2}\right)\chi_s^\alpha \chi_d^{\alpha'}. \tag{C21}$$

In the following, we consider the case of two reservoirs in the strong nonequilibrium regime as defined in (152). From the properties (52)–(54) and the results (C1)–(C8) for $\tau_{ij}^{\alpha\alpha'}$, we obtain

$$\begin{aligned}\Gamma_{d\to u} =& \big[\chi_1^{LR} - \chi_2^{LR}\phi_z + \chi_3^{LR}\phi_z^2\big](V-h) \\ &+ w(-h)\sum_\alpha \big[\chi_1^{\alpha\alpha} + \chi_3^{\alpha\alpha}\phi_z^2\big],\end{aligned} \tag{C22}$$

$$\Gamma_{u\to d} = \Gamma_{d\to u} + 2\chi_2^{LR}\phi_z V + h\big(\chi_1 + \chi_3\phi_z^2\big), \tag{C23}$$

$$\Gamma_{s\to u} = \chi_u^L\chi_s^R\left(V - \Delta - \frac{h}{2}\right) + w\left(-\Delta - \frac{h}{2}\right)\sum_\alpha \chi_u^\alpha\chi_s^\alpha, \tag{C24}$$

$$\Gamma_{u\to s} = \Gamma_{s\to u} + \big(\chi_s^L\chi_u^R - \chi_u^L\chi_s^R\big)V + \left(\Delta + \frac{h}{2}\right)\chi_u\chi_s, \tag{C25}$$

$$\Gamma_{s\to d} = \chi_d^L\chi_s^R\left(V - \Delta + \frac{h}{2}\right) + w\left(-\Delta + \frac{h}{2}\right)\sum_\alpha \chi_d^\alpha\chi_s^\alpha, \tag{C26}$$

$$\Gamma_{d\to s} = \Gamma_{s\to d} + \big(\chi_s^L\chi_d^R - \chi_d^L\chi_s^R\big)V + \left(\Delta - \frac{h}{2}\right)\chi_d\chi_s, \tag{C27}$$

where we have defined

$$\chi_{1/3} = \sum_{\alpha\alpha'}\chi_{1/3}^{\alpha\alpha'} = \pi\big[J_1^2 \pm J_3^2 \pm J_{38}^2\big], \tag{C28}$$

$$\chi_{u/d} = \sum_\alpha \chi_{u/d}^\alpha = 2\pi(J_+^2 \pm J_-^2\phi_z), \tag{C29}$$

$$\chi_s = \sum_\alpha \chi_s^\alpha = 1, \tag{C30}$$

and note that

$$\chi_2^{LR} = -2\pi J_1^2 x_L p_L, \tag{C31}$$

$$\begin{aligned}&\chi_s^L\chi_{u/d}^R - \chi_{u/d}^L\chi_s^R \\ &\quad = -2\pi[x_L q_L(J_+^2 \pm J_-^2\phi_z) + x_L p_L(J_-^2 \pm J_+^2\phi_z)].\end{aligned} \tag{C32}$$

The stationary probability distribution p_l follows from inserting (C22)–(C27) in (138). Finally, we can compute m_F from (142).

We note that $m_F = 0$ is equivalent to $\langle\hat{F}_3\rangle = \langle\hat{F}_8\rangle = 0$. Therefore, we consider $\langle\hat{F}_3\rangle = \frac{1}{2}(p_u - p_d)$ and $\langle\hat{F}_8\rangle = \frac{1}{3}(p_u + p_d - 2p_s)$ in the following and analyze under which conditions both expectation values become zero in the strong nonequilibrium regime. A cumbersome but straightforward analysis yields

$$\langle\hat{F}_3\rangle = \frac{1}{2N}[\mathcal{F}_1(\Gamma_{s\to u}+\Gamma_{s\to d})+\mathcal{F}_2(\Gamma_{s\to u}-\Gamma_{s\to d})], \tag{C33}$$

$$\begin{aligned}\frac{2}{\sqrt{3}}\langle\hat{F}_8\rangle =& -\frac{1}{3N}\{\mathcal{F}_1[2\pi J_+^2(h-2x_Lp_L\phi_zV)\\ &+4\pi J_-^2(\Delta-x_Lq_LV)\phi_z+\Gamma_{s\to u}-\Gamma_{s\to d}]\\ &+\mathcal{F}_2[2\mathcal{F}_2+2(\Gamma_{d\to u}+\Gamma_{u\to d})+\Gamma_{s\to u}+\Gamma_{s\to d}]\}.\end{aligned} \tag{C34}$$

Here, the factor N follows from the normalization condition (138). Furthermore, we have defined the following functions in $(h_z,h_\perp,\Delta)$ space:

$$\begin{aligned}\mathcal{F}_1 =& -2\chi_2^{LR}\phi_zV-h(\chi_1+\chi_3\phi_z^2)-\pi[J_+^2(h-2x_Lp_L\phi_zV)\\ &+2J_-^2(\Delta-x_Lq_LV)\phi_z],\end{aligned} \tag{C35}$$

$$\mathcal{F}_2 = \pi[2J_+^2(\Delta-x_Lq_LV)+J_-^2(h_z-2p_lV)]. \tag{C36}$$

$\mathcal{F}_1=\mathcal{F}_2=0$ fulfills the condition $\langle\hat{F}_3\rangle=\langle\hat{F}_8\rangle=0$. Moreover, it defines a curve in $(h_z,h_\perp,\Delta)$ space that provides us with a tool to measure the distance to the fixed-point model. $\mathcal{F}_2=0$ directly yields (153) and defines the plane in $(h_z,h_\perp,\Delta)$ space where the curve lies in. The shape of the curve follows from $\mathcal{F}_1=0$. To that end, we insert (153) into (C35) and obtain (154). That is, we project the curve onto the $(h_z,h_\perp)$ plane.

Finally, we prove (161). To this end, we decompose (139) as

$$\begin{aligned}\langle I_\beta\rangle &= \sum_{ll'}\Gamma^\beta_{l'\to l}p_{l'}\\ &= I_0^\beta+I_3^\beta\langle\hat{F}_3\rangle+I_8^\beta\frac{2}{\sqrt{3}}\langle\hat{F}_8\rangle,\end{aligned} \tag{C37}$$

with

$$I_0^\beta = \frac{1}{3}\sum_{ll'}\Gamma^\beta_{l'\to l}, \tag{C38}$$

$$I_3^\beta = \sum_l(\Gamma^\beta_{u\to l}-\Gamma^\beta_{d\to l}), \tag{C39}$$

$$I_8^\beta = \frac{1}{2}\sum_l(\Gamma^\beta_{u\to l}+\Gamma^\beta_{d\to l}-2\Gamma^\beta_{s\to l}). \tag{C40}$$

Evaluating (140) for two reservoirs in the strong nonequilibrium regime (152), we can express (C38)–(C40) in terms of $\bar{\tau}_{ij}^{\alpha\alpha'}$:

$$I_0^L = \frac{\pi}{3}x_Lx_R\{[2\bar{\tau}_{11}^{LR}+\bar{\tau}_{33}^{LR}+2(\bar{\tau}_{44}^{LR}+\bar{\tau}_{66}^{LR})+\bar{\tau}_{88}^{LR}]V+2i(\bar{\tau}_{45}^{LR}+\bar{\tau}_{67}^{LR})\Delta+i(2\bar{\tau}_{12}^{LR}+\bar{\tau}_{45}^{LR}-\bar{\tau}_{67}^{LR})h_z\}, \tag{C41}$$

$$\begin{aligned}I_3^L =& \pi x_Lx_R\left\{\left[2i\bar{\tau}_{12}^{LR}+\frac{2}{\sqrt{3}}\bar{\tau}_{38}^{LR}+\bar{\tau}_{44}^{LR}-\bar{\tau}_{66}^{LR}+i(\bar{\tau}_{45}^{LR}-\bar{\tau}_{67}^{LR})\right]\phi_zV+[\bar{\tau}_{44}^{LR}-\bar{\tau}_{66}^{LR}+i(\bar{\tau}_{45}^{LR}-\bar{\tau}_{67}^{LR})]\phi_z\Delta\right.\\ &\left.+\left[\bar{\tau}_{11}^{LR}+\bar{\tau}_{33}^{LR}+(\bar{\tau}_{11}^{LR}-\bar{\tau}_{33}^{LR})\phi_z^2+\frac{1}{2}(\bar{\tau}_{44}^{LR}+\bar{\tau}_{66}^{LR})+\frac{i}{2}(\bar{\tau}_{45}^{LR}+\bar{\tau}_{67}^{LR})\right]h\right\},\end{aligned} \tag{C42}$$

$$\begin{aligned}I_8^L =& \frac{\pi}{2}x_Lx_R\left\{[2\bar{\tau}_{11}^{LR}+\bar{\tau}_{33}^{LR}-(\bar{\tau}_{44}^{LR}+\bar{\tau}_{66}^{LR}+\bar{\tau}_{88}^{LR})+3i(\bar{\tau}_{45}^{LR}+\bar{\tau}_{67}^{LR})]V+[3(\bar{\tau}_{44}^{LR}+\bar{\tau}_{66}^{LR})-i(\bar{\tau}_{45}^{LR}+\bar{\tau}_{67}^{LR})]\Delta\right.\\ &\left.+\left[2i\bar{\tau}_{12}^{LR}+\frac{3}{2}(\bar{\tau}_{44}^{LR}-\bar{\tau}_{66}^{LR})-\frac{i}{2}(\bar{\tau}_{45}^{LR}-\bar{\tau}_{67}^{LR})\right]h_z\right\}.\end{aligned} \tag{C43}$$

If we consider $m_F=0$, the current I^β is completely equal to I_0^β. Therefore, we can evaluate (C42) using (C2)–(C8) at the fixed point and obtain (161).

[1] R. Hanson, L. P. Kouwenhoven, J. R. Petta, S. Tarucha, and L. M. K. Vandersypen, Rev. Mod. Phys. **79**, 1217 (2007).

[2] S. Andergassen, V. Meden, H. Schoeller, J. Splettstoesser, and M. R. Wegewijs, Nanotechnology **21**, 272001 (2010).

[3] A. C. Hewson, *The Kondo Problem to Heavy Fermions* (Cambridge University Press, Cambridge, 1997).

[4] L. I. Glazman and M. Pustilnik, in *Nanophysics: Coherence and Transport*, edited by H. Bouchiat *et al.* (Elsevier, Amsterdam, 2005), p. 427.

[5] L. I. Glazman and M. E. Raikh, Pis'ma Zh. Eksp. Teor. Fiz. **47**, 378 (1988) [Sov. Phys.–JETP Lett. **47**, 452 (1988)]; T. K. Ng and P. A. Lee, Phys. Rev. Lett. **61**, 1768 (1988).

[6] D. Goldhaber-Gordon, H. Shtrikman, D. Mahalu, D. Abusch-Magder, U. Meirav, and M. A. Kastner, Nature (London) **391**, 156 (1998); S. M. Cronenwett, T. H. Oosterkamp, and L. P. Kouwenhoven, Science **281**, 540 (1998); F. Simmel, R. H. Blick, J. P. Kotthaus, W. Wegscheider, and M. Bichler, Phys. Rev. Lett. **83**, 804 (1999).

[7] S. Sasaki, S. De Franceschi, J. M. Elzerman, W. G. van der Wiel, M. Eto, S. Tarucha, and L. P. Kouwenhoven, Nature (London) **405**, 764 (2000); J. Nygård, D. H. Cobden, and P. E. Lindelof, *ibid.* **408**, 342 (2000); J. Schmid, J. Weis, K. Eberl, and K. v. Klitzing, Phys. Rev. Lett. **84**, 5824 (2000); M. Eto and Yu. V. Nazarov, *ibid.* **85**, 1306 (2000); M. Pustilnik and L. I. Glazman, *ibid.* **85**, 2993 (2000).

[8] W. G. van der Wiel, S. De Franceschi, J. M. Elzerman, S. Tarucha, L. P. Kouwenhoven, J. Motohisa, F. Nakajima, and T. Fukui, Phys. Rev. Lett. **88**, 126803 (2002); M. Pustilnik and L. I. Glazman, *ibid.* **87**, 216601 (2001); W. Hofstetter and H. Schoeller, *ibid.* **88**, 016803 (2001); A. Kogan, G. Granger, M. A.

Kastner, D. Goldhaber-Gordon, and H. Shtrikman, Phys. Rev. B **67**, 113309 (2003); W. Hofstetter and G. Zaránd, *ibid.* **69**, 235301 (2004).

[9] Y. Oreg and D. Goldhaber-Gordon, Phys. Rev. Lett. **90**, 136602 (2003); R. M. Potok, I. G. Rau, H. Shtrikman, Y. Oreg, and D. Goldhaber-Gordon, Nature (London) **446**, 167 (2007); A. J. Keller, L. Peeters, C. P. Moca, I. Weymann, D. Mahalu, V. Umansky, G. Zaránd, and D. Goldhaber-Gordon, *ibid.* **526**, 237 (2015).

[10] L. Borda, G. Zaránd, W. Hofstetter, B. I. Halperin, and J. von Delft, Phys. Rev. Lett. **90**, 026602 (2003); S. Sasaki, S. Amaha, N. Asakawa, M. Eto, and S. Tarucha, *ibid.* **93**, 017205 (2004); P. Jarillo-Herrero, J. Kong, H. S. J. van der Zant, C. Dekker, and L. Kouwenhoven, Nature (London) **434**, 484 (2005); R. López, D. Sanchez, M. Lee, M. S. Choi, P. Simon, and K. Le Hur, Phys. Rev. B **71**, 115312 (2005); M. S. Choi, R. López, and R. Aguado, Phys. Rev. Lett. **95**, 067204 (2005); S. Amasha, A. J. Keller, I. G. Rau, A. Carmi, J. A. Katine, H. Shtrikman, Y. Oreg, D. and Goldhaber-Gordon, *ibid.* **110**, 046604 (2013).

[11] A. Carmi, Y. Oreg, and M. Berkooz, Phys. Rev. Lett. **106**, 106401 (2011); C. Moca, A. Roman, M. Toderaş, and R. Chirla, AIP Conf. Proc. **1916**, 030003 (2017).

[12] C. P. Moca, A. Alex, J. von Delft, and G. Zaránd, Phys. Rev. B **86**, 195128 (2012).

[13] R. López, T. Rejec, J. Martinek, and R. Žitko, Phys. Rev. B **87**, 035135 (2013).

[14] J. König and J. Martinek, Phys. Rev. Lett. **90**, 166602 (2003); M. Braun, J. König, and J. Martinek, Phys. Rev. B **70**, 195345 (2004); I. Weymann and J. Barnas, *ibid.* **75**, 155308 (2007).

[15] D. Boese, W. Hofstetter, and H. Schoeller, Phys. Rev. B **64**, 125309 (2001); **66**, 125315 (2002).

[16] V. Kashcheyevs, A. Schiller, A. Aharony, and O. Entin-Wohlman, Phys. Rev. B **75**, 115313 (2007).

[17] J. Paaske, A. Andersen, and K. Flensberg, Phys. Rev. B **82**, 081309(R) (2010).

[18] M. Pletyukhov and D. Schuricht, Phys. Rev. B **84**, 041309 (2011).

[19] J. Martinek, Y. Utsumi, H. Imamura, J. Barnas, S. Maekawa, J. König, and G. Schön, Phys. Rev. Lett. **91**, 127203 (2003); J. Martinek, M. Sindel, L. Borda, J. Barnas, J. König, G. Schön, and J. von Delft, *ibid.* **91**, 247202 (2003); M. Sindel, L. Borda, J. Martinek, R. Bulla, J. König, G. Schön, S. Maekawa, and J. von Delft, Phys. Rev. B **76**, 045321 (2007).

[20] Y. Meir and N. S. Wingreen, Phys. Rev. Lett. **68**, 2512 (1992).

[21] S. Göttel, F. Reininghaus, and H. Schoeller, Phys. Rev. B **92**, 041103(R) (2015).

[22] T. A. Costi, A. C. Hewson, and V. Zlatic, J. Phys.: Condens. Matter **6**, 2519 (1994).

[23] A. Rosch, J. Kroha, and P. Wölfle, Phys. Rev. Lett. **87**, 156802 (2001); A. Rosch, J. Paaske, J. Kroha, and P. Wölfle, *ibid.* **90**, 076804 (2003).

[24] S. Kehrein, Phys. Rev. Lett. **95**, 056602 (2005); P. Fritsch and S. Kehrein, Phys. Rev. B **81**, 035113 (2010).

[25] H. Schoeller, Eur. Phys. J. Special Topics **168**, 179 (2009); Dynamics of open quantum systems, in *Lecture Notes of the 45th IFF Spring School Computing Solids: Models, Ab initio Methods and Supercomputing* (Forschungszentrum Jülich, 2014).

[26] S. G. Jakobs, M. Pletyukhov, and H. Schoeller, Phys. Rev. B **81**, 195109 (2010); J. Eckel *et al.*, New J. Phys. **12**, 043042 (2010).

[27] H. Schoeller and F. Reininghaus, Phys. Rev. B **80**, 045117 (2009); **80**, 209901(E) (2009).

[28] M. Pletyukhov, D. Schuricht, and H. Schoeller, Phys. Rev. Lett. **104**, 106801 (2010).

[29] M. Pletyukhov and H. Schoeller, Phys. Rev. Lett. **108**, 260601 (2012); F. Reininghaus, M. Pletyukhov, and H. Schoeller, Phys. Rev. B **90**, 085121 (2014).

[30] S. Smirnov and M. Grifoni, Phys. Rev. B **87**, 121302(R) (2013); New J. Phys. **15**, 073047 (2013).

[31] A. V. Kretinin, H. Shtrikman, and D. Mahalu, Phys. Rev. B **85**, 201301(R) (2012); O. Klochan, A. P. Micolich, A. R. Hamilton, D. Reuter, A. D. Wieck, F. Reininghaus, M. Pletyukhov, and H. Schoeller, *ibid.* **87**, 201104(R) (2013).

[32] F. B. Anders and A. Schiller, Phys. Rev. Lett. **95**, 196801 (2005); F. B. Anders, R. Bulla, and M. Vojta, *ibid.* **98**, 210402 (2007); A. Hackl, D. Roosen, S. Kehrein, and W. Hofstetter, *ibid.* **102**, 219902(E) (2009).

[33] A. J. Daley, C. Kollath, U. Schollwoeck, and G. Vidal, J. Stat. Mech.: Theory Exp. (2004) P04005; S. R. White and A. E. Feiguin, Phys. Rev. Lett. **93**, 076401 (2004); P. Schmitteckert, Phys. Rev. B **70**, 121302 (2004); F. Heidrich-Meisner, A. E. Feiguin, and E. Dagotto, *ibid.* **79**, 235336 (2009).

[34] S. Weiss, J. Eckel, M. Thorwart, and R. Egger, Phys. Rev. B **77**, 195316 (2008).

[35] T. L. Schmidt, P. Werner, L. Mühlbacher, and A. Komnik, Phys. Rev. B **78**, 235110 (2008).

[36] F. Schwarz, I. Weymann, J. von Delft, and A. Weichselbaum, arXiv:1708.06315.

[37] C. Caroli, R. Combescot, P. Nozières, and D. Saint-James, J. Phys. C: Solid State Phys. **4**, 916 (1971); **5**, 21 (1972).

[38] S. Coleman, *Aspects of Symmetry*, 1st ed. (Cambridge University Press, Cambridge, 1985); H. Georgi, *Lie Algebras in Particle Physics: From Isospin to Unified Theories*, 2nd ed., Frontiers in Physics, Vol. 54 (Westview, Boulder, CO, 1999).

[39] D. Griffiths, *Introduction to Elementary Particles*, 2nd ed. (Wiley, Weinheim, 2008).

[40] R. Bulla, T. A. Costi, and T. Pruschke, Rev. Mod. Phys. **80**, 395 (2008).

[41] A. Weichselbaum and J. von Delft, Phys. Rev. Lett. **99**, 076402 (2007); A. Weichselbaum, Phys. Rev. B **86**, 245124 (2012).

[42] A. Weichselbaum, Ann. Phys. **327**, 2972 (2012).

PHYSICAL REVIEW B **99**, 205142 (2019)

Renormalization group transport theory for open quantum systems: Charge fluctuations in multilevel quantum dots in and out of equilibrium

Carsten J. Lindner,[1] Fabian B. Kugler,[2] Volker Meden,[1] and Herbert Schoeller[1,*]
[1]*Institut für Theorie der Statistischen Physik, RWTH Aachen, 52056 Aachen, Germany and JARA-Fundamentals of Future Information Technology*
[2]*Physics Department, Arnold Sommerfeld Center for Theoretical Physics, and Center for NanoScience, Ludwigs-Maximilians-Universität München, Theresienstr. 37, 80333 Munich, Germany*

(Received 30 October 2018; revised manuscript received 21 February 2019; published 24 May 2019)

We present the real-time renormalization group (RTRG) method as a method to describe the stationary state current through generic multilevel quantum dots in nonequilibrium. The employed approach consists of a very rudimentary approximation for the renormalization group (RG) equations which neglects all vertex corrections while it provides a means to compute the effective dot Liouvillian self-consistently. Being based on a weak-coupling expansion in the tunneling between dot and reservoirs, the RTRG approach turns out to reliably describe charge fluctuations in and out of equilibrium for arbitrary coupling strength, even at zero temperature. We confirm this in the linear response regime with a benchmark against highly accurate numerical renormalization group data in the exemplary case of three-level quantum dots. For small to intermediate bias voltages and weak Coulomb interactions, we find an excellent agreement between RTRG and functional renormalization group data, which can be expected to be accurate in this regime. As a consequence, we advertise the presented RTRG approach as an efficient and versatile tool to describe charge fluctuations in quantum dot systems.

DOI: 10.1103/PhysRevB.99.205142

I. INTRODUCTION

Describing electron transport through mesoscopic systems like semiconductor heterostructures [1] or molecules (e.g., carbon nanotubes [2]) at low temperatures in nonequilibrium is a fundamental problem in the field of quantum statistics. The physics of these systems is highly affected by the repulsive Coulomb interaction between the electrons, leading to interesting correlation phenomena such as the Kondo effect [3,4]. Further attraction arose from possible applications of quantum nanostructures in future information technology, in particular in quantum computers.

Two competing mechanisms drive the physical behavior of an open quantum dot. First, electrons can tunnel in and out of the quantum dot via tunnel barriers, separating the dot from surrounding reservoirs held at different temperatures and chemical potentials. Second, the occupancy of the dot by the electrons is highly affected by the Pauli principle in concert with the repulsive Coulomb interaction between the electrons. The interplay of these two mechanisms causes correlation effects resulting in emergent phenomena such as the Kondo effect at sufficiently low temperatures.

Transport spectroscopy provides a means to analyze the physical processes in open quantum dots [1,5]. The idea is to scrutinize the current through the quantum dot as function of the bias voltage, gate voltage, or external magnetic fields. For instance, a resonance peak in the linear conductance as function of the gate voltage signals the change of the average dot electron number [1,5], while the emergence of a plateau is a hallmark of the Kondo effect [6]. In contrast, an increase in the steplike current away from equilibrium indicates the opening up of another transport channel, i.e., the possibility of occupying an excited state of the quantum dot [1,5]. Finding adequate approaches and methods to theoretically describe resonances in the current through nanostructures is therefore of great interest.

In equilibrium, numerically exact methods such as the numerical renormalization group (NRG) [7,8] or the density matrix renormalization group (DMRG) [9] are well established to describe the current through quantum nanostructures. Some progress has also been made in order to generalize these approaches to nonequilibrium, leading to the scattering state NRG [10], time-dependent NRG (TD-NRG) [11], and the time-dependent DMRG (TD-DMRG) [12]. Recently, a novel thermofield approach [13] was developed that combines the latter two methods to describe impurity models in nonequilibrium. Although all these approaches are very promising, reliable numerical data for the current across generic quantum dots with more than two levels out of equilibrium is missing in the literature at the moment.

Numerically exact methods are typically computationally demanding and one therefore often assumes certain symmetries for the model to reduce the numerical effort. Essentially analytic methods such as the real-time RG (RTRG) [14,15], functional RG (fRG)[16–18], or the flow equation method [19] are usually less demanding, allowing for a more efficient study of complex setups. For instance, the computational effort for determining the self-energy using the fRG method in lowest-order truncation is comparable to that of a mean-field calculation.

---

[*] schoeller@physik.rwth-aachen.de

©2019 American Physical Society

The downside of analytic methods is that they are usually perturbative with the consequence that their range of applicability is restricted. However, perturbative RG methods such as the fRG or the RTRG are based on a resummation of certain classes of diagrams. If these diagrams capture the essential physical processes, then these methods yield reliable results even beyond the range of validity of a corresponding approximation within plain perturbation theory. A notable example in this regard is the agreement between results for the Kondo model in nonequilibrium in the strong-coupling limit obtained from a RTRG approach [20,21], which is perturbative in the coupling between dot and reservoirs, and exact numerical methods [13]. Some results are also in accordance with experimental data [22].

In this paper, we report a similar observation for the description of charge fluctuations in generic three-level quantum dots with nondegenerate single-particle energies. Hereby, the regime of charge fluctuations is defined by the condition that real processes are possible changing the particle number on the quantum dot by $\Delta N = \pm 1$. In this regime, Kondo-induced correlations (as discussed in Ref. [28] for the Coulomb blockade regime) are suppressed and the main physics consists in resonances for the differential conductance as function of the gate voltage when one of the renormalized single-particle excitations of the dot is close to one of the chemical potentials of the reservoirs. Such resonances occur also in the sequential tunneling regime of high temperatures $T \gg \Gamma$, where Γ denotes the broadening of the single-particle excitations induced by the coupling to the leads. In this regime, the resonance positions correspond to the bare single-particle excitations of the dot and their line shape is mostly dominated by thermal smearing. This can be described by standard kinetic equations in Born-Markov approximation. In contrast, the aim of this paper is to calculate the position and line shape of these resonances at zero temperature $T = 0$ by including all diagrams of the RTRG describing charge fluctuation processes. In this essentially nonperturbative regime in Γ one obtains renormalized resonance positions and the line shape is dominated by quantum fluctuations leading to Breit-Wigner–type line shapes with a broadening of the order of Γ. Since orbital fluctuations are not taken into account, the solution is expected to be reliable when the distance δ of the gate voltage to one of the resonance positions is of the order of Γ. Furthermore, since the RTRG is derived from a diagrammatic expansion in Γ, at first glance this method is controlled only for small dot reservoir couplings, which means that Γ should be smaller than $\max\{T, \delta\}$. However, our study reveals that the self-consistent resummation of all charge fluctuation diagrams via the RTRG approach yields reliable results close to the resonances for arbitrary Coulomb interactions and arbitrary coupling to the reservoirs, respectively, even at zero temperature. Even when all energy scales become of the same order of magnitude $\delta, U \sim \Gamma$, where one can no longer distinguish between the regime of charge fluctuations (close to the resonances) and orbital fluctuations (between the resonances), the considered RTRG approximation describes quite well the line shape of the main resonances but not the conductance between the resonances (where orbital fluctuations dominate). This means a drastic extension of the range of validity of this approximation. To confirm this, highly accurate NRG data for the linear conductance as function of the gate voltage serve as a benchmark against the RTRG solution. In nonequilibrium, we find an excellent agreement between the fRG method, which employs the Coulomb interaction as the expansion parameter, and the RTRG for small Coulomb interactions and strong coupling, respectively. Additionally, one can show that our approximate RTRG approach becomes exact for large bias voltages (see Appendix A). As a consequence, we advertise the RTRG method as an efficient tool to describe charge fluctuations in multilevel quantum dots in nonequilibrium even at very low temperatures.

The fRG in static approximation serves in the following mainly as a benchmark for small Coulomb interactions in nonequilibrium, where this approach is strictly controlled. However, previous studies of transport through multilevel quantum dots with a complex setup [23] revealed that the fRG is reliable up to intermediate Coulomb interactions in the linear response regime. In general, fRG in static approximation is applicable if the physical behavior can be described by an effective single-particle picture. While this is clearly not the case for large bias, we compare fRG and RTRG data for the differential conductance also in this regime in order to estimate the range of applicability for the effective single-particle picture.

In this paper, we stick to simple approximation schemes for the RTRG and the fRG in order to keep the numerical effort as low as possible. However, both methods are flexible in the sense that approximations can be systematically extended by taking higher-order diagrams into account, as it was demonstrated, e.g., for a theoretical description of two-level quantum dots by the RTRG [24] and the fRG [18,25].

The outline of this paper is as follows. In Sec. II A, we introduce the multilevel generalization of the Anderson model together with a generic model for the tunneling between dot and reservoirs. The considered methods, RTRG, fRG, and NRG, are then introduced successively in Secs. II B–II D. Section III comprises the benchmark of the considered RTRG and fRG approximations against NRG data for the linear conductance for a model with proportional coupling. Afterward, we discuss the reliability of the RTRG and fRG approaches to describe the quantum dot with generic tunneling matrix in nonequilibrium in Sec. IV. The paper closes with a summary of the main results. We consider $\hbar = k_B = e = 1$ throughout this paper.

II. MODEL AND METHODS

In this section, we briefly introduce the considered model for the quantum dot as well as the methods applied in this work. To this end, we first discuss the Anderson model for multilevel quantum dots. Then, we set up the RG equations for this model using the RTRG method with the reservoir-dot couplings being the expansion parameter. Similarly, we set up RG equations in the static approximation within the fRG approach with the Coulomb interaction being the expansion parameter and comment on the applied NRG method. Results from the fRG are later on used to test the reliability of the RTRG solution out of equilibrium in the regime of weak Coulomb interactions and strong coupling, while the highly accurate

NRG data provide a benchmark for the linear conductance at arbitrary Coulomb interactions.

A. Multilevel Anderson model

We consider the multilevel generalization [26] of the single-impurity Anderson model [27] where the electron spin index σ is replaced by the flavor index l. This is a quantum number labeling one of the Z dot levels which is either empty or is occupied by exactly one electron. In general, l can be viewed as a multi-index that also includes the spin index σ. The corresponding Hamiltonian reads as

$$H_\mathrm{s} = H_0 + V_\mathrm{ee}, \tag{1}$$

$$H_0 = \sum_l \varepsilon_l \, c_l^\dagger \, c_l, \tag{2}$$

$$V_\mathrm{ee} = \frac{U}{2} \sum_{ll'} c_l^\dagger \, c_{l'}^\dagger \, c_{l'} \, c_l. \tag{3}$$

Here, U quantifies the strength of the Coulomb interaction between the dot electrons and $\varepsilon_l = h_l - V_\mathrm{g} - (Z-1)\frac{U}{2}$ are the single-particle dot levels. To avoid a proliferation of parameters, we assume a flavor-independent Coulomb interaction. However, our approaches can also handle more general two-particle interaction terms by incorporating these terms into the initial conditions of the RG equations. External fields (e.g., magnetic fields) are incorporated into the level spacing h_l and V_g is the gate voltage, allowing to uniformly tune the dot levels. The choice $h_l = V_\mathrm{g} = 0$ defines the particle-hole symmetric model.

The full Hamiltonian of the Z-level Anderson model is given by

$$H_\mathrm{tot} = H_\mathrm{s} + H_\mathrm{res} + V_\mathrm{c}, \tag{4}$$

with

$$H_\mathrm{res} = \sum_{k\alpha l} \varepsilon_{k\alpha l} \, a_{k\alpha l}^\dagger \, a_{k\alpha l}, \tag{5}$$

$$V_\mathrm{c} = \frac{1}{\sqrt{\rho^{(0)}}} \sum_{k\alpha ll'} \left(t_{ll'}^\alpha a_{k\alpha l}^\dagger c_{l'} + \left(t_{ll'}^\alpha\right)^* c_{l'}^\dagger a_{k\alpha l} \right), \tag{6}$$

where H_res is the part accounting for the Z_res reservoirs and V_c the coupling between the quantum dot and the reservoirs. Accordingly, $\alpha = 1, \dots Z_\mathrm{res}$ is the reservoir index, $\varepsilon_{k\alpha l}$ the band dispersion relative to the chemical potential μ_α for the channel l with some quantum number k that becomes continuous in the thermodynamic limit. Furthermore, $t_{ll'}^\alpha$ denotes the matrix elements of the tunneling between the reservoir and the dot. We assume flat reservoir bands (at least on the low-energy scale of interest) and take $t_{ll'}^\alpha$ as independent of k. Here, $\rho^{(0)}$ is some average reservoir density of states which we set to $\rho^{(0)} = 1$ for convenience, defining the energy units.

The reservoirs contribute to the self-energy and the current formula only via the *hybridization matrix*

$$\Gamma_{ll'}^\alpha(\omega) = 2\pi \sum_{l_1 l_2} \left(t_{l_1 l}^\alpha\right)^* \rho_{l_1 l_2}^\alpha(\omega) \, t_{l_2 l'}^\alpha, \tag{7}$$

where $\rho_{l_1 l_2}^\alpha(\omega) = \delta_{l_1 l_2} \sum_k \delta(\omega - \varepsilon_{k\alpha l_1} + \mu_\alpha)$ is the constant density of states in reservoir α. This together with the assumption that the reservoirs are infinitely large means that we can neglect the frequency dependence of $\Gamma_{ll'}^\alpha(\omega)$. In particular, we consider the *normal lead model* with

$$\Gamma_{ll'}^\alpha = 2\pi \sum_{l_l} \left(t_{l_1 l}^\alpha\right)^* t_{l_1 l'}^\alpha \tag{8}$$

in the following. We define $\Gamma = \sum_{\alpha ll'} \Gamma_{ll'}^\alpha$ as the characteristic energy scale for tunneling processes between the dot and the reservoirs.

Importantly, the dot expectation values and the current depend on the form of the hybridization matrices and *not* on the form of the tunneling matrices. This means that different models with the same hybridization matrices have the same properties. Accordingly, all these models can be mapped onto each other with rotations in the channel indices with an invariant hybridization matrix [28]. This is the reason why we can describe the generic case using the normal lead model (8) where the dot and channel indices coincide.

Finally, the Fermi distribution

$$f_\alpha(\omega) = \frac{1}{e^{\beta_\alpha \omega} + 1} \tag{9}$$

characterizes the thermodynamic state of the reservoir with the inverse temperature $\beta_\alpha = T_\alpha^{-1}$. We later consider reservoir temperatures $T_\alpha = 0$ implying $f_\alpha(\omega) = \Theta(-\omega)$ for the Fermi distribution function with $\Theta(\omega)$ being the Heaviside distribution.

B. Real-time RG

The state of the quantum dot can be quantified by the reduced density matrix

$$\rho_\mathrm{s}(t) = \mathrm{Tr}_\mathrm{res} \, \rho_\mathrm{tot}(t), \tag{10}$$

where Tr_res is the trace over the reservoir degrees of freedom and the total density matrix $\rho_\mathrm{tot}(t)$ is the solution of the von Neumann equation $i\frac{d}{dt}\rho_\mathrm{tot}(t) = [H_\mathrm{tot}, \rho_\mathrm{tot}(t)]$. The reduced density matrix $\rho_\mathrm{s}(t)$ is in turn the solution of the kinetic equation

$$i\frac{d}{dt}\rho_\mathrm{s}(t) = \int_0^t dt' \, L(t-t')\rho_\mathrm{s}(t') \tag{11}$$

with the effective Liouvillian $L(t-t')$ being the response function due to the coupling to the reservoirs. This equation can be formally solved in Fourier space, yielding

$$\rho_\mathrm{s}(E) = \frac{i}{E - L(E)} \rho_\mathrm{s}(t=0) \tag{12}$$

with $\rho_\mathrm{s}(E) = \int_0^\infty dt \, e^{iEt} \, \rho_\mathrm{s}(t)$ and $L(E) = \int_0^\infty dt \, e^{iEt} \, L(t)$.

Here, we are only interested in the solution in the stationary limit $(t \to \infty)$ which is defined as $\rho_\mathrm{st} = \lim_{E\to i0^+}(-iE)\rho_\mathrm{s}(E)$. It can be conveniently obtained from solving

$$L(i0^+)\rho_\mathrm{st} = 0. \tag{13}$$

The average electron current leaving reservoir γ is defined as $I_\gamma(t) = \langle -\frac{d}{dt}\hat{N}_\gamma \rangle$, where $\hat{N}_\gamma = \sum_{kl} a_{k\gamma l}^\dagger a_{k\gamma l}$ is the particle number in reservoir γ. The current can conveniently be computed using

$$I_\gamma(t) = -i \int_0^t dt' \, \mathrm{Tr}_\mathrm{s} \, \Sigma_\gamma(t-t')\rho_\mathrm{s}(t'), \tag{14}$$

or in Fourier space

$$I_\gamma(E) = -i\,\mathrm{Tr}_s\,\Sigma_\gamma(E)\,\rho_s(E), \tag{15}$$

where $\Sigma_\gamma(t-t')$ and $\Sigma_\gamma(E) = \int_0^\infty dt\, e^{iEt}\Sigma_\gamma(t)$, respectively, is the current kernel. The stationary state limit is given by

$$\begin{aligned} I_\gamma^{\mathrm{st}} &= \lim_{E\to i0^+}(-iE)I_\gamma(E) \\ &= -i\,\mathrm{Tr}_s\,\Sigma_\gamma(i0^+)\,\rho_{\mathrm{st}}, \end{aligned} \tag{16}$$

which we aim to compute.

The model Hamiltonians (2)–(6) provide two different starting points for a perturbative expansion. First, for weak Coulomb interactions ($U \ll \Gamma$), V_{ee} can be viewed as a perturbation and one can expand in the electron-electron interaction. This is the starting point of the fRG that is discussed in Sec. II C. Second, for arbitrary U, a weak-coupling expansion in Γ is favorable for $\Gamma \ll \max\{T_\alpha, \delta\}$. In this case, one can compute the effective Liouvillian $L(E)$ and the current kernel $\Sigma_\gamma(E)$ using the RTRG approach, as we discuss now.

Applying the diagrammatic technique presented in Refs. [14,15] on Anderson-type models with charge fluctuations yields the RG equation

$$\frac{d}{dE}L(E) = -$$ 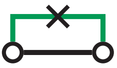 $$+\ \mathcal{O}(G^4)$$

$$\begin{aligned} &= -\int d\omega\, f'(\omega)\, G_1(E,\omega)\Pi(E_1+\omega) \\ &\quad \times G_{\bar{1}}(E_1+\omega,-\omega) + \mathcal{O}(G^4) \end{aligned} \tag{17}$$

for the effective Liouvillian, which was also already stated in the Supplemental Material of Ref. [29]. Here, $\Pi(E) = i[E - L(E)]^{-1}$ is the full propagator of the quantum dot and $G_1(E,\omega)$ is an effective vertex, accounting for the dot-reservoir interaction. Furthermore, $E_1 = E + \bar{\mu}_1$ is the Fourier variable plus the chemical potential $\bar{\mu}_1 = \eta\mu_\alpha$, $1 = \eta\alpha l$ is a multi-index, and η is a sign index that indicates whether a dot electron is created or annihilated during the interaction process. Accordingly, $\eta = +$ ($\eta = -$) corresponds to the dot annihilation (creation) operator, i.e., $c_{+l} = c_l$ ($c_{-l} = c_l^\dagger$).

The derivation of the RG equation (17) is not very difficult and can be sketched as follows (for details, see Refs. [15,20,29]). First, the perturbative series for $L(E)$ consists of a series of bare vertices G_1 connected by bare propagators $\Pi^{(0)}(E+X) = i[E + X - L_0]^{-1}$, where $L_0 = [H_0,\cdot]$ is the Liouvillian of the bare dot and X contains a certain sum of chemical potentials and frequencies of the reservoir contractions connecting the bare vertices. After resummation of self-energy insertions, all bare propagators are replaced by the full effective ones $\Pi(E+X)$. Differentiating this series with respect to E means that one of the propagators is replaced by its derivative $\frac{d}{dE}\Pi(E+X)$. Resumming vertex corrections left and right to $\frac{d}{dE}\Pi(E+X)$ and considering only the charge fluctuation process yields to lowest order

$$\begin{aligned} \frac{d}{dE}L(E) &= \int d\omega\, f(\omega)\, G_1(E,\omega) \\ &\quad \times \frac{d}{dE}\,\Pi(E_1+\omega)\, G_{\bar{1}}(E_1+\omega,-\omega) + O(G^4). \end{aligned} \tag{18}$$

Using $\frac{d}{dE}\Pi(E_1+\omega) = \frac{d}{d\omega}\Pi(E_1+\omega)$ and partial integration, one can shift the frequency derivative to the Fermi function and to the effective vertices. Since one can show that the frequency derivative of the vertices again leads to higher-order terms, they can be neglected and one obtains the RG equation (17).

The effective vertex $G_1(E,\omega)$ can be obtained as the solution of a similar RG equation. However, as it is explained in Appendix A, a resummation of logarithmic terms in the perturbative series expansion is not necessary since the self-consistently calculated Liouvillian does not suffer from any logarithmically divergent terms for $E = i0^+$. This has the consequence that vertex corrections can be neglected in leading order and we can replace the effective vertices $G_1(E,\omega)$ by the bare ones, i.e.,

$$G_1 = \sum_p G_1^p \tag{19}$$

with

$$G_1^p = G_{\eta\alpha l}^p = \sum_{l'} t_{ll'}^{\eta\alpha} C_{\eta l'}^p, \tag{20}$$

where $t_{ll'}^{\eta\alpha} = \delta_{\eta+}\, t_{ll'}^{\alpha} + \delta_{\eta-}\, t_{l'l}^{\alpha} = t_{l'l}^{-\eta\alpha}$ and

$$C_{\eta l}^p \bullet = p\sigma^p \begin{cases} c_{\eta l}\bullet & \text{if} \quad p = +, \\ \bullet\, c_{\eta l} & \text{if} \quad p = - \end{cases} \tag{21}$$

are the dot field superoperators fulfilling the anticommutation relation $\{C_{\eta l}^p, C_{\eta' l'}^{p'}\} = p\delta_{pp'}\delta_{\eta,-\eta'}\delta_{ll'}$. Here, the sign factor $(s_1 s_2|\sigma^p|s_1' s_2') = \delta_{s_1 s_1'}\delta_{s_2 s_2'}\, p^{N_{s_1}-N_{s_2}}$ measures the parity of the states [14,15] $|ss') = |s\rangle\langle s'|$, where $|ss') = |s\rangle\langle s'|$ are the basis states of the dot Liouville space, $(ss'|\ldots = \langle s|\ldots|s'\rangle$ are the basis states of the corresponding dual Liouville space, $|s\rangle$ are the many-body eigenstates of H_{s}, and N_s the dot electron number in state $|s\rangle$.

A similar RG equation for the current kernel follows from (17) by simply replacing the left vertex $G_1(E,\omega)$ by the current vertex $(I_\gamma)_1(E,\omega)$. This yields

$$\begin{aligned} \frac{d}{dE}\Sigma_\gamma(E) &= -\int d\omega\, f'(\omega)\,(I_\gamma)_1(E,\omega) \\ &\quad \times \Pi(E_1+\omega)\, G_{\bar{1}}(E_1+\omega,-\omega). \end{aligned} \tag{22}$$

For the same reasons as above, we neglect the vertex corrections to the current kernel which means that we insert [14,15]

$$(I_\gamma)_1, = \sum_{p=\pm}(I_\gamma)_1^p = c_1^\gamma\,\tilde{G}_1 \tag{23}$$

for the current vertex, where $c_1^\gamma = c_{\eta\alpha}^\gamma = -\frac{1}{2}\eta\delta_{\alpha\gamma}$ and $\tilde{G}_1 = \sum_{p=\pm} pG_1^p$.

The RG flow starts at $E = iD$, with D being the bandwidth of the reservoir density of states (see Appendix A), and stops at $E = i0^+$, where the effective Liouvillian and the current kernel needed to compute the stationary state properties are defined. Setting up the initial conditions for the RG equations as explained in Ref. [21], we obtain

$$L(E)\big|_{E=iD} = L^{(0)} + L^{(1s)}, \tag{24}$$

$$\Sigma_\gamma(E)\big|_{E=iD} = \Sigma_\gamma^{(1s)} \tag{25}$$

from lowest-order perturbation theory where $L^{(1s)}$ and $\Sigma_\gamma^{(1s)}$ are given by (A5) and (A7). The natural choice for the path of the RG flow is $E = i\Lambda$ with $D \geqslant \Lambda \geqslant 0^+$ and a *real* flow parameter. This is a special choice since, in general, the flow parameter E within the E-flow scheme [20,21] of the RTRG is complex with the consequence that two different paths for the RG flow connecting the same starting and end point yield the same solution at the end point, as long as they do not enclose any singularities of $L(E)$ and $\Sigma_\gamma(E)$, which lie in the lower half of the complex plane. This is fundamental for computing the transient dynamics [15,29].

At zero temperature $T_\alpha = 0$, the derivative of the Fermi distribution becomes the δ distribution $f'(\omega) = -\delta(\omega)$, and the frequency integrals in (17) and (22) become trivial. Thus, we obtain

$$\frac{d}{d\Lambda}\tilde{L}(\Lambda) = i\sum_{\eta\alpha l} G_{\eta\alpha l}\,\frac{1}{i\Lambda + \bar{\mu}_\alpha - \tilde{L}(\Lambda - i\bar{\mu}_\alpha)}\,G_{-\eta\alpha l}, \tag{26}$$

$$\frac{d}{d\Lambda}\tilde{\Sigma}_\alpha(\Lambda) = -\frac{i}{2}\sum_{l\eta}\eta\,\tilde{G}_{\eta\alpha l}\frac{1}{i\Lambda + \bar{\mu}_\alpha - \tilde{L}(\Lambda - i\bar{\mu}_\alpha)}G_{-\eta\alpha l}, \tag{27}$$

with $\tilde{L}(\Lambda) = L(i\Lambda)$ and $\tilde{\Sigma}(\Lambda) = \Sigma(i\Lambda)$.

We note that (26) defines an infinite hierarchy of differential equations since the Liouvillian evaluated at $\Lambda - i\bar{\mu}_\alpha$ is fed back and *not* the one evaluated at Λ. Thus, one also needs to solve an RG equation for $\tilde{L}(\Lambda - i\bar{\mu}_\alpha)$. The right-hand side of this equation in turn depends on $\tilde{L}(\Lambda - i\bar{\mu}_\alpha - i\bar{\mu}_{\alpha'})$. By proceeding this way, we arrive at an infinite hierarchy of RG equations for the effective Liouvillian where each RG equation is associated with a different shift in the energy argument of the effective Liouvillian. However, this hierarchy of RG equations can be straightforwardly truncated, as explained in Appendix B.

In total, the purpose of the RG treatment is a *self-consistent* computation of the effective Liouvillian $\tilde{L}(\Lambda)$. This is necessary since bare perturbation theory for the Liouvillian and the current kernel exhibits logarithmic singularities (see the discussion in Appendix A). These singularities are located at

$$\mu_\alpha = E_{s_1} - E_{s_2} \quad \text{with } N_{s_1} = N_{s_2} + 1, \tag{28}$$

where E_s are the eigenvalues of H_s. This equation represents the well-known condition for resonant tunneling through the quantum dot (see, e.g., Refs. [1,5] for a review). This means that the logarithmic singularities result in δ peaks in the differential conductance, i.e., the derivative of the current with respect to the reservoir bias voltage. As a consequence of the RG treatment, the eigenvalues $\lambda_k(E)$ of the effective Liouvillian, defined by $L(E)|x_k(E)) = \lambda_k(E)|x_k(E))$, replace $E_{s_1} - E_{s_2}$ in the argument of the logarithms of $L(E)$ and $\Sigma_\gamma(E)$. Importantly, the imaginary part $\mathrm{Im}\,\lambda_k(i0^+)$ provides a cutoff in the argument of the logarithm. This regularizes the logarithmic singularities and causes a finite height of the conductance peaks together with a finite broadening of width $\sim\Gamma$. In addition, the peak position is renormalized, i.e., the conductance peaks are now located at

$$\bar{\mu}_\alpha - \mathrm{Re}\,\lambda_k(\bar{\mu}_\alpha + i0^+) = 0. \tag{29}$$

This must be contrasted to the case of moderate temperatures $T_\alpha \gg \Gamma$, where, e.g., the width of the conductance peaks is given by the temperature $T = T_\alpha$ if all reservoir temperatures are equal. In this case, the sharp edge of the Fermi distribution, being fundamental for the emergence of logarithmic singularities at $T_\alpha = 0$, is broadened by the temperature and no logarithmic singularities occur. In this case, the full propagator on the right-hand sides of the RG equations (17) and (22) can be replaced by the bare one $\Pi^{(0)}(E) = i[E - L^{(0)}]^{-1}$, where $L^{(0)}$ is given by (A3). Thus, the RG equations can be formally solved, yielding the expressions for the first-order corrections in bare perturbation theory.

C. Functional RG

An alternative approach to compute the current across the quantum dot is the Keldysh Green's function formalism [30]. The current can be computed from

$$I_\gamma^{\mathrm{st}} = \frac{i}{4\pi}\int d\omega\,\mathrm{Tr}\,\underline{\underline{\Gamma}}^\gamma\{[1 - 2f_\gamma(\omega - \mu_\gamma)] \times [\underline{\underline{G}}^{\mathrm{R}}(\omega) - \underline{\underline{G}}^{\mathrm{A}}(\omega)] - \underline{\underline{G}}^{\mathrm{K}}(\omega)\}, \tag{30}$$

which is straightforwardly obtained from the current formula stated in Ref. [31] by replacing the lesser component of the Green's function by the Keldysh component. Accordingly, $\underline{\underline{G}}^{\mathrm{R,A,K}}(\omega)$ is the retarded, advanced, and Keldysh component of the dot Green's function, respectively,

$$\underline{\underline{G}}(\omega) = \begin{pmatrix} \underline{\underline{G}}^{\mathrm{R}}(\omega) & \underline{\underline{G}}^{\mathrm{K}}(\omega) \\ 0 & \underline{\underline{G}}^{\mathrm{A}}(\omega) \end{pmatrix}, \tag{31}$$

and $\underline{\underline{\Gamma}}^\gamma$ is the hybridization matrix in matrix notation, i.e., $(\underline{\underline{\Gamma}}^\gamma)_{ll'} = \Gamma^\gamma_{ll'}$. There are in total two independent components of the Green's function, that are

$$\underline{\underline{G}}^{\mathrm{R}}(\omega) = \frac{1}{\omega - \underline{\underline{\Sigma}}^{\mathrm{R}}(\omega)} = [\underline{\underline{G}}^{\mathrm{A}}(\omega)]^\dagger, \tag{32}$$

$$\underline{\underline{G}}^{\mathrm{K}}(\omega) = \underline{\underline{G}}^{\mathrm{R}}(\omega)\underline{\underline{\Sigma}}^{\mathrm{K}}(\omega)\underline{\underline{G}}^{\mathrm{A}}(\omega), \tag{33}$$

where

$$\underline{\underline{\Sigma}}(\omega) = \begin{pmatrix} \underline{\underline{\Sigma}}^{\mathrm{R}}(\omega) & \underline{\underline{\Sigma}}^{\mathrm{K}}(\omega) \\ 0 & \underline{\underline{\Sigma}}^{\mathrm{A}}(\omega) \end{pmatrix} \tag{34}$$

is the self-energy.

Here, we already consider the so-called *reservoir dressed* Green's function. This is an effective Green's function in dot space, hence doubly underlined in the matrix notation, which can be obtained from the Green's function of the total system by projecting out the reservoir degrees of freedom.

The projection results in an additional addend to the self-energy in terms of $\underline{\underline{\Gamma}}^{\alpha}$. In the noninteracting case, i.e., $U = 0$, we obtain $\underline{\underline{\Sigma}}^{\mathrm{R}} = \underline{\underline{\varepsilon}} + \underline{\underline{\Sigma}}^{\mathrm{R}}_{\mathrm{res}} = (\underline{\underline{\Sigma}}^{\mathrm{A}})^{\dagger}$ and $\underline{\underline{\Sigma}}^{\mathrm{K}}(\omega) = \underline{\underline{\Sigma}}^{\mathrm{K}}_{\mathrm{res}}(\omega)$ with $(\underline{\underline{\varepsilon}})_{ll'} = \varepsilon_{ll'}$ and

$$\underline{\underline{\Sigma}}^{\mathrm{R}}_{\mathrm{res}} = -\frac{i}{2}\underline{\underline{\Gamma}}, \tag{35}$$

$$\underline{\underline{\Sigma}}^{\mathrm{K}}_{\mathrm{res}}(\omega) = -i\sum_{\alpha}[1 - 2f_{\alpha}(\omega - \mu_{\alpha})]\underline{\underline{\Gamma}}^{\alpha}, \tag{36}$$

with $\underline{\underline{\Gamma}} = \sum_{\alpha}\underline{\underline{\Gamma}}^{\alpha}$. Accordingly, the reservoir dressed Green's function of the noninteracting system ($U = 0$) is given by

$$\underline{\underline{G}}^{\mathrm{R/A}}_{0}(\omega) = \frac{1}{\omega - \underline{\underline{\varepsilon}} - \underline{\underline{\Sigma}}^{\mathrm{R/A}}_{\mathrm{res}}}, \tag{37}$$

$$\underline{\underline{G}}^{\mathrm{K}}_{0}(\omega) = \underline{\underline{G}}^{\mathrm{R}}_{0}(\omega)\underline{\underline{\Sigma}}^{\mathrm{K}}_{\mathrm{res}}(\omega)\underline{\underline{G}}^{\mathrm{A}}_{0}(\omega). \tag{38}$$

The repulsive Coulomb interaction between the dot electrons leads to a renormalization of the self-energy. Here, we compute this renormalization using the fRG approach. This yields an RG equation for the self-energy, which can be expressed diagrammatically as [16]

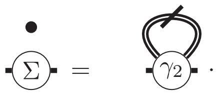

(39)

The diagram on the left-hand side represents the derivative of the self-energy with respect to the flow parameter Λ, while the diagram on the right-hand side is of Hartree-Fock form in Hugenholtz representation. Here, the single-scale propagator (crossed line) replaces the free contraction line and the interaction vertex represents the two-particle vertex function $\gamma_2(\Lambda)$.

In general, the two-particle vertex function $\gamma_2(\Lambda)$ can be obtained from a corresponding RG equation within the fRG approach. The right-hand side of the RG equations for the n-particle vertex $\gamma_n(\Lambda)$ with $n \geqslant 2$ depends on $\gamma_{n+1}(\Lambda)$. This leads to a hierarchy of infinitely many RG equations [16]. Here, we disregard all vertex corrections and insert the bare vertex

$$\bar{v}_{l_1l_2,l_1'l_2'} = \begin{cases} U & \text{if} \quad l_1 = l_1' \neq l_2 = l_2', \\ -U & \text{if} \quad l_1 = l_2' \neq l_2 = l_1', \\ 0 & \text{else} \end{cases} \tag{40}$$

for $\gamma_2(\Lambda)$. This means a truncation of the hierarchy of RG equations in lowest order. It corresponds to an RG-enhanced perturbation theory to leading order in U. Translating the diagram in (39) as explained in Ref. [17] yields

$$\frac{d}{d\Lambda}\Sigma^{\mathrm{R}}_{ll'}(\Lambda) = -\frac{i}{4\pi}\sum_{l_1l_1'}\bar{v}_{ll_1,l'l_1'}\int d\omega\, S^{\mathrm{K}}_{l_1'l_1}(\Lambda,\omega), \tag{41}$$

$$\frac{d}{d\Lambda}\Sigma^{\mathrm{K}}_{ll'}(\Lambda) = -\frac{i}{4\pi}\sum_{l_1l_1'}\bar{v}_{ll_1,l'l_1'}\int d\omega \times [\underline{\underline{S}}^{\mathrm{R}}(\Lambda,\omega) - \underline{\underline{S}}^{\mathrm{A}}(\Lambda,\omega)]_{l_1'l_1}, \tag{42}$$

where $\underline{\underline{S}}^{x}(\Lambda,\omega)$ denotes the three components ($x = \mathrm{R, A, K}$) of the single-scale propagator, which is defined as

$$\underline{\underline{S}}(\Lambda,\omega) = \begin{pmatrix} \underline{\underline{S}}^{\mathrm{R}}(\Lambda,\omega) & \underline{\underline{S}}^{\mathrm{K}}(\Lambda,\omega) \\ 0 & \underline{\underline{S}}^{\mathrm{A}}(\Lambda,\omega) \end{pmatrix} = -\underline{\underline{G}}(\Lambda,\omega)\left\{\frac{d}{d\Lambda}[\underline{\underline{G}}_{0}(\Lambda,\omega)]^{-1}\right\}\underline{\underline{G}}(\Lambda,\omega). \tag{43}$$

The Λ dependence of the Green's and vertex functions is established by supplementing an infrared cutoff Λ to the Green's function. It allows to treat the energy scales of the system successively from high to low energies. Starting from $\Lambda = \infty$, where the free propagation is completely suppressed, the fRG describes the scaling of the effective vertices and the self-energy during the process of successively turning on the free propagation of the model by reducing Λ. This means that the RG equations are solved along the RG path from $\Lambda = \infty$ to 0, where the original problem is recovered. Technically, this approach constitutes a means to resum systematically certain classes of diagrams in the perturbative series representation of the self-energy.

A crucial step is therefore to introduce an appropriate cutoff in the Green's function. The hybridization flow [32] has proved to be a convenient choice in nonequilibrium since it preserves fundamental symmetries as the Kubo-Martin-Schwinger conditions and causality. Physically, the idea is to couple the quantum dot uniformly to an auxiliary reservoir. This results in an additional addend to the self-energy of the form

$$\left(\underline{\underline{\Sigma}}^{\mathrm{R/A}}_{\mathrm{aux}}(\Lambda)\right)_{ll'} = \mp i\delta_{ll'}\Lambda, \tag{44}$$

$$\left(\underline{\underline{\Sigma}}^{\mathrm{K}}_{\mathrm{aux}}(\Lambda)\right)_{ll'} = -2i\delta_{ll'}[1 - 2f_{\mathrm{aux}}(\omega - \mu_{\mathrm{aux}})]\Lambda, \tag{45}$$

while the hybridization Λ serves as the cutoff. We assume $T_{\mathrm{aux}} = \infty$ which leads to $f_{\mathrm{aux}}(\omega - \mu_{\mathrm{aux}}) = \frac{1}{2}$, i.e., a flat distribution, with the consequence that the contribution to the Keldysh component vanishes, $\Sigma^{\mathrm{K}}_{\mathrm{aux}}(\Lambda) = 0$. This prevents the auxiliary reservoir from implying an additional structure like, e.g., Fermi edges, to the theoretical description of the nonequilibrium stationary state. Furthermore, the single-scale propagator becomes [18,32]

$$\underline{\underline{S}}^{\mathrm{R/A}}(\Lambda) = \mp i\underline{\underline{G}}^{\mathrm{R/A}}(\Lambda)\underline{\underline{G}}^{\mathrm{R/A}}(\Lambda), \tag{46}$$

$$\underline{\underline{S}}^{\mathrm{K}}(\Lambda) = -i\underline{\underline{G}}^{\mathrm{R}}(\Lambda)\underline{\underline{G}}^{\mathrm{K}}(\Lambda) + i\underline{\underline{G}}^{\mathrm{K}}(\Lambda)\underline{\underline{G}}^{\mathrm{A}}(\Lambda) \tag{47}$$

with

$$\underline{\underline{G}}^{\mathrm{R}}(\Lambda,\omega) = \frac{1}{i\Lambda + \omega - \underline{\underline{\Sigma}}^{\mathrm{R}}(\Lambda,\omega)} = [\underline{\underline{G}}^{\mathrm{A}}(\Lambda,\omega)]^{\dagger}, \tag{48}$$

and the Keldysh component follows from the relation (33) which holds also for the Λ-dependent Green's function. Here, we have separated the auxiliary reservoir contribution (44) from the self-energy $\underline{\underline{\Sigma}}^{\mathrm{R}}(\Lambda,\omega)$.

Solving the RG equations for the self-energy requires their initial conditions at the starting point $\Lambda = \infty$. Setting them up as explained in Ref. [18] gives

$$\Sigma^{\mathrm{R}}_{ll'}(\Lambda,\omega)\Big|_{\Lambda=\infty} = \varepsilon_{ll'} + \frac{1}{2}\sum_{l_1}\bar{v}_{ll_1,l'l_1} - \frac{i}{2}\Gamma_{ll'}$$

$$= (h_l - V_g)\delta_{ll'} - \frac{i}{2}\Gamma_{ll'}, \tag{49}$$

$$\Sigma^{\mathrm{K}}_{ll'}(\Lambda,\omega)\Big|_{\Lambda=\infty} = -i\sum_{\alpha}\Gamma^{\alpha}_{ll'}\,\mathrm{sgn}(\omega-\mu_\alpha), \tag{50}$$

where the second term on the right-hand side of the first line in (49) is the contribution from the Hartree diagram, which at $\Lambda = \infty$ is the only nonvanishing correction from the diagrammatic series representation of the self-energy.

The retarded (advanced) component of the Green's function as a function of the frequency ω is analytic in the upper (lower) half of the complex plane. This together with the frequency independence of the (bare) vertex has the important consequence that the integral on the right-hand side of (42) vanishes. This yields

$$\frac{d}{d\Lambda}\underline{\underline{\Sigma}}^{\mathrm{K}}(\Lambda) = 0, \tag{51}$$

i.e., the Keldysh component of the self-energy does not renormalize.

In contrast, the frequency integral on the right-hand side of (41) is nonvanishing and can be evaluated analytically using the spectral representation of the retarded component of the self-energy. This is possible since the (bare) two-particle interaction vertex is independent of the frequency. The resulting expressions can be found in Appendix C. As a result, the right-hand side of the RG equation (41) is a self-adjoint matrix since $(\underline{\underline{S}}^{\mathrm{K}}(\Lambda,\omega))^\dagger = -\underline{\underline{S}}^{\mathrm{K}}(\Lambda,\omega)$. Thus, we obtain a renormalized dot Hamiltonian

$$\tilde{H}_0 = \sum_{ll'}\tilde{\varepsilon}_{ll'}\,c_l^\dagger c_{l'}, \tag{52}$$

with $\underline{\underline{\tilde{\varepsilon}}} = \underline{\underline{\Sigma}}^{\mathrm{R}}(\Lambda = 0) - \underline{\underline{\Sigma}}^{\mathrm{R}}_{\mathrm{res}}$ for $\Lambda = 0$. The reservoir dressed Green's function is therefore the one of a noninteracting *open* system with

$$\underline{\underline{G}}^{\mathrm{R/A}}(\omega) = \frac{1}{\omega - \underline{\underline{\tilde{\varepsilon}}} - \underline{\underline{\Sigma}}^{\mathrm{R/A}}_{\mathrm{res}}}, \tag{53}$$

$$\underline{\underline{G}}^{\mathrm{K}}(\omega) = \underline{\underline{G}}^{\mathrm{R}}(\omega)\underline{\underline{\Sigma}}^{\mathrm{K}}_{\mathrm{res}}(\omega)\underline{\underline{G}}^{\mathrm{A}}(\omega). \tag{54}$$

This has the consequence that, as is shown in Ref. [31], the current formula (30) reduces to the Landauer-Büttiker formula

$$I^{\mathrm{st}}_\gamma = \frac{1}{2\pi}\sum_\alpha\int d\omega\,T_{\gamma\alpha}(\omega)[f_\gamma(\omega-\mu_\gamma) - f_\alpha(\omega-\mu_\alpha)], \tag{55}$$

where

$$T_{\gamma\alpha}(\omega) = \mathrm{Tr}\,\underline{\underline{\Gamma}}^\gamma\underline{\underline{G}}^{\mathrm{R}}(\omega)\underline{\underline{\Gamma}}^\alpha\underline{\underline{G}}^{\mathrm{A}}(\omega) \tag{56}$$

is the transmission probability.

To summarize, the fRG approach in lowest-order truncation is a means to compute the static self-energy with the effect of a renormalization of the single-particle dot Hamiltonian.

D. Numerical RG

We benchmark the solutions obtained from the RTRG and the fRG approaches, each constituting a *perturbative* RG method, against highly accurate NRG data in the linear response regime. To obtain the most accurate NRG data, we restrict the model to the case of proportional coupling, i.e., $\underline{\underline{\Gamma}}^\alpha = x_\alpha\underline{\underline{\Gamma}}$ with $\sum_\alpha x_\alpha = 1$. In this case, as shown in Ref. [31], one can again use the Landauer-Büttiker–type formula (55) but with the transmission probability (56) given by

$$T_{\gamma\alpha}(\omega) = 2\pi\,x_\gamma\,x_\alpha\,\mathrm{Tr}\,\underline{\underline{\Gamma}}\,\underline{\underline{\rho}}(\omega), \tag{57}$$

where $\underline{\underline{\rho}}(\omega) = \frac{i}{2\pi}(\underline{\underline{G}}^{\mathrm{R}} - \underline{\underline{G}}^{\mathrm{A}})(\omega)$ is the dot spectral function. This quantity characterizes completely the current across the dot in linear response. To see this, we first note that $f_\gamma(\omega - \mu_\gamma) - f_\alpha(\omega-\mu_\alpha) \approx -f'(\omega)(\mu_\gamma - \mu_\alpha)$. As a consequence, with $\mu_\alpha = -eV_\alpha$, the current is recast as

$$I_\gamma = \sum_\alpha G_{\gamma\alpha}\,(V_\gamma - V_\alpha), \tag{58}$$

with the conductance tensor

$$G_{\gamma\alpha} = -\frac{1}{2\pi}\int d\omega\,T_{\gamma\alpha}(\omega)\,f'(\omega) = \frac{1}{2\pi}T_{\gamma\alpha}(0), \tag{59}$$

where we used $f'(\omega) = -\delta(\omega)$ in the last step.

The calculations are performed using the full-density-matrix NRG [33] and make use of the QSpace tensor library developed by Weichselbaum [34]. We employ an efficient, interleaved NRG setup [35] with an overall discretization parameter of $\Lambda = 6$ (i.e., $\sqrt[3]{6}$ between each truncation), and we keep states up to a rescaled energy of $E_{\mathrm{trunc}} = 10$ and maximal number $N_{\mathrm{keep}} = 4000$ during the NRG iteration. Additionally, results are averaged between two realizations of the discretization (z averaging [8,36]). The wide-band and zero-temperature limits are practically realized by setting the half-bandwidth to 10^4 and temperature to 10^{-8}. We checked that our results are converged up to the percent level with respect to all involved numerical parameters. Finally, we note that one need not broaden the NRG data as the linear conductance can be inferred from discrete spectral weights.

III. CONDUCTANCE IN THE LINEAR RESPONSE REGIME

In order to demonstrate the strength of the RTRG method in describing charge fluctuations, we discuss results for a generic quantum dot with three ($Z = 3$) nondegenerate levels, i.e., $|h_l - h_{l'}| \sim \Gamma$, and two reservoirs held at different chemical potential and zero temperature. The difference between the chemical potentials of the reservoirs is quantified by the bias voltage, i.e., $\mu_L - \mu_R = V$ and $\mu_{L/R} = \pm\frac{V}{2}$. In particular, we consider the first derivative of the current I_γ, the differential conductance

$$G = G_{LR} = \frac{d}{dV}I_L = -\frac{d}{dV}I_R. \tag{60}$$

As a first step, we benchmark the RTRG (and the fRG) method in the chosen approximation against NRG data. We can do this for an arbitrary model with proportional coupling in the linear response regime.

TABLE I. Input parameters for the tunneling matrix $\underline{\underline{t}}^L$ of the left reservoir in the case of proportional coupling. These parameters define the matrix elements $t^L_{ll'}$ via (61). The tunneling matrix of the right reservoir follows from the relation $\underline{\underline{t}}^R = \sqrt{\kappa}\underline{\underline{t}}^L$.

$(\overline{\Gamma}_{\mathrm{L}11}, \overline{\varphi}_{\mathrm{L}11})$	(0.00680672,0.98)
$(\overline{\Gamma}_{\mathrm{L}12}, \overline{\varphi}_{\mathrm{L}12})$	(0.0605042,0.96)
$(\overline{\Gamma}_{\mathrm{L}13}, \overline{\varphi}_{\mathrm{L}13})$	(0.0332773,0.12)
$(\overline{\Gamma}_{\mathrm{L}21}, \overline{\varphi}_{\mathrm{L}21})$	(0.0627731, −0.99)
$(\overline{\Gamma}_{\mathrm{L}22}, \overline{\varphi}_{\mathrm{L}22})$	(0.0589916,0.79)
$(\overline{\Gamma}_{\mathrm{L}23}, \overline{\varphi}_{\mathrm{L}23})$	(0.024958, −0.16)
$(\overline{\Gamma}_{\mathrm{L}31}, \overline{\varphi}_{\mathrm{L}31})$	(0.00983193, −0.8)
$(\overline{\Gamma}_{\mathrm{L}32}, \overline{\varphi}_{\mathrm{L}32})$	(0.0468908,0.71)
$(\overline{\Gamma}_{\mathrm{L}33}, \overline{\varphi}_{\mathrm{L}33})$	(0.0559664,0.8)
κ	1.77778

We parametrize the tunneling matrix $t^\alpha_{ll'}$ of the model as

$$t^\alpha_{ll'} = \sqrt{\frac{\overline{\Gamma}_{\alpha ll'}}{2\pi}}\,\mathrm{e}^{i\overline{\varphi}_{\alpha ll'}\pi}, \tag{61}$$

leading to

$$\Gamma^\alpha_{ll'} = \sum_{l_1}\sqrt{\overline{\Gamma}_{\alpha l_1 l}\overline{\Gamma}_{\alpha l_1 l'}}\,e^{-i(\overline{\varphi}_{\alpha l_1 l}-\overline{\varphi}_{\alpha l_1 l'})\pi} \tag{62}$$

for the hybridization matrix. In the case of proportional coupling, we introduce the ratio $\kappa = \overline{\Gamma}_{Rll'}/\overline{\Gamma}_{Lll'}$.

We consider an arbitrary hybridization matrix. To this end, we present here the results for a model with hybridization matrix parametrized by random numbers. Table I contains the corresponding parameters $\overline{\Gamma}_{\alpha ll'}$ and $\overline{\varphi}_{\alpha ll'}$.

We found for arbitrary strengths of the Coulomb interaction three peaks for the conductance G as a function of the gate voltage V_{g}. Figures 1 and 2 show exemplary results. This outcome is commonly interpreted using the picture of the Coulomb blockade (see, e.g., Ref. [1] for a review). Accordingly, a peak occurs whenever the ground states of the N and $N+1$ particle sectors are degenerate and a resonant electron transport across the quantum dot is possible. This is the meaning of the condition (29) for resonant tunneling, which differs from (28) only due to the renormalization of the peak positions. In contrast, the conductance is drastically reduced between the peaks, resulting in so-called *Coulomb blockade valleys*. The dot electron number is fixed in this case and tunneling in and out of the dot involves the occupation of a dot state with a different particle number. These states are of higher energy and the occupation of these states becomes more and more suppressed for an increasing Coulomb interaction. Correspondingly, the Coulomb blockade valleys are more pronounced for increasing U/Γ.

The Green's function formalism provides an alternative interpretation. In this case, we deduce from (57) and (59) that the peaks in the conductance G are the maxima of the dot spectral function

$$\underline{\underline{\rho}}(0) = \frac{1}{\pi}\sum_k \mathrm{Im}\left\{\frac{1}{\tilde{h}_k - V_{\mathrm{g}} - i\frac{\tilde{\Gamma}_k}{2}}\underline{\underline{\tilde{P}}}_k\right\}. \tag{63}$$

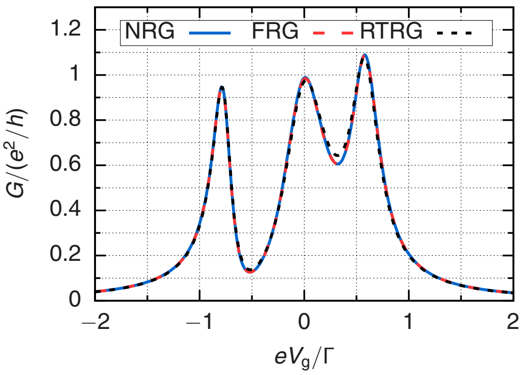

(a) $U/\Gamma = 0.1$

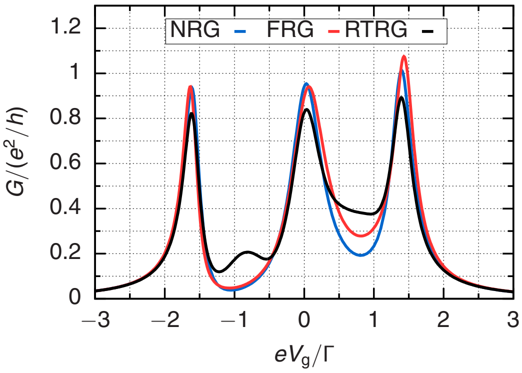

(b) $U/\Gamma = 1.0$

FIG. 1. Linear conductance G as function of the gate voltage for the model with $\underline{\underline{t}}^\alpha$ defined by Table I, and level spacings $h_l/\Gamma = (-0.7, 0.0, 0.5)$. We set $D = 1000.0\Gamma$ for all numerical RTRG calculations in this paper. All three applied methods (NRG, fRG, and RTRG) are in agreement regarding the position and shape of the conductance peaks.

Here, we inserted the spectral decomposition of $\underline{\underline{\Sigma}}^{\mathrm{R}}(\Lambda = 0) = \sum_k \tilde{\lambda}_k \underline{\underline{\tilde{P}}}_k$ where $\tilde{\lambda}_k = \tilde{h}_k - V_{\mathrm{g}} - i\frac{\tilde{\Gamma}_k}{2}$ are the eigenvalues and $\underline{\underline{\tilde{P}}}_k$ the corresponding projector. $\tilde{h}_k$ has the meaning of the position of a renormalized single-particle energy while $\tilde{\Gamma}_k$ is the corresponding level broadening. Due to (63), a conductance peak occurs for $\tilde{h}_k = V_{\mathrm{g}}$, i.e., resonant tunneling is obtained when the gate voltage equals a single-particle energy. Simultaneously, the very same level being unoccupied for $V_{\mathrm{g}} < \tilde{h}_k$ becomes populated with one electron at this point. In conclusion, the fRG solution in lowest-order truncation scheme complies with an effective single-particle picture for the three conductance peaks occurring in the linear response regime.

We find a very good agreement between all three considered methods in the regime of *small interaction strengths* $U \ll \Gamma$. For example, Fig. 1(a) shows the linear conductance as function of the gate voltage for $U = 0.1\Gamma$. While an agreement between fRG and NRG was expected in this regime, the RTRG data for the conductance is also reliable, as it was already noted for single-level [37] and for two-level quantum dots [24,38,39].

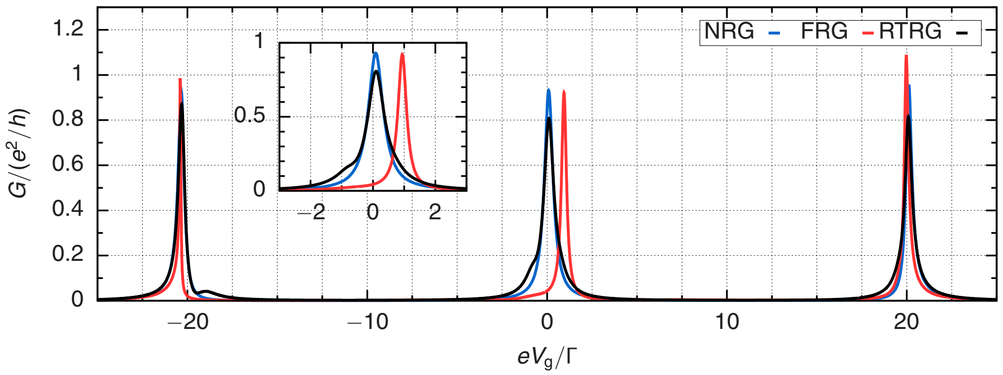

FIG. 2. Linear conductance G as function of the gate voltage V_g for the model with $\underline{\underline{t}}^\alpha$ defined by Table I, $U = 20.0\Gamma$ and level spacings $h_l/\Gamma = (-0.7, 0.0, 0.5)$. The inset shows a closeup of the central peak, clearly revealing the deviations in position and shape of the maximum within the fRG solution. In contrast, NRG and RTRG data are in good agreement regarding the position and the width of the conductance peak.

Figure 1(b) is exemplary for the solutions from the three methods in the regime of *intermediate interaction strengths* $U \sim \Gamma$. In this case, we still find a good agreement between fRG, NRG, and RTRG data regarding the position and width of the conductance peaks. However, the shape of the RTRG solution deviates from the NRG solution in the Coulomb blockade valleys. These deviations are perceptible imprints of the increasing significance of orbital fluctuations due to cotunneling processes in the quantum dot for increasing interaction strengths. Fourth-order terms in the tunneling are necessary for a reasonable description of the cotunneling processes. However, these terms are only taken partially into account within the considered truncation scheme for the RTRG approach, as is discussed in Appendix A. Thus, it is no surprise that the RTRG data are less reliable within the Coulomb blockade valleys. This means that the employed approximation for the RTRG equation describes charge fluctuations reliably, but is insufficient to study cotunneling processes. In contrast, these processes are fully taken into account by the fRG approach. The corresponding results thus show a good agreement with the NRG data also in the Coulomb blockade valleys.

Lastly, we considered the regime of large interaction strengths ($U \gg \Gamma$). Figure 2 shows the conductance as the function of the gate voltage for $U = 20.0\Gamma$. In this case, we find again a good accordance between RTRG and NRG data. In contrast, the fRG solution clearly shows deviations from the NRG solution for the position and shape of the conductance peaks. This is most pronounced for the peak arising from the transition from $N = 1$ to 2. In this case, the fRG method shifts the position of the peak further away from the particle-hole symmetric point than the other two methods (see the inset of Fig. 2).

The deviations between the fRG solution and the NRG solutions can be easily understood from the fact that the truncation of the RG equations from the fRG approach is motivated by means of an expansion in the Coulomb interaction. Obviously, this is justified formally only for small interaction strengths $U \ll \Gamma$. It is therefore no surprise that the fRG is not reliable for large interaction strengths $U \gg \Gamma$.

A closer look at Fig. 2 reveals that the RTRG produces a small peak close to the left conductance peak (referring to the transition $N = 0 \rightarrow N = 1$) and a small shoulder for the middle conductance peak (referring to the transition $N = 1 \rightarrow N = 2$). Again, these anomalies arise from the neglect of orbital fluctuations from higher-order diagrams, similar to the occurrence of the anomaly between the resonances for the case of intermediate Coulomb interaction strength [see Fig. 1(b)]. These features depend crucially on the choice of the tunneling matrix elements and the level spacings. However, they are very weak for strong Coulomb interaction and not relevant for the position and line shape of the main charge fluctuation resonances. It has to be studied in the future how these anomalies can be eliminated by a minimal extension of the RTRG, similar to the more refined but considerably more expensive versions of the RTRG used in Refs. [24,38], where vertex renormalizations were taken into account.

In total, the benchmark against the NRG data for a model with proportional coupling and nondegenerate dot levels in the linear response regime shows that the RTRG method yields reliable results for position and the width of the peaks of the linear conductance for arbitrary dot-reservoir couplings.

IV. STATIONARY STATE CURRENT IN NONEQUILIBRIUM

We now turn to a generic quantum dot coupled to two reservoirs with arbitrary values of the bias V. This means

TABLE II. Input parameters for the tunneling matrix $\underline{\underline{t}}^\alpha$ of the generic model. These parameters define the matrix elements $t^\alpha_{ll'}$ via (61).

α	L	R
$(\overline{\Gamma}_{\alpha 11}, \overline{\varphi}_{\alpha 11})$	(0.0434783, −0.8)	(0.101831, −0.88)
$(\overline{\Gamma}_{\alpha 12}, \overline{\varphi}_{\alpha 12})$	(0.0640732, −0.19)	(0.01373,0.32)
$(\overline{\Gamma}_{\alpha 13}, \overline{\varphi}_{\alpha 13})$	(0.0743707,0.71)	(0.0789474, −0.64)
$(\overline{\Gamma}_{\alpha 21}, \overline{\varphi}_{\alpha 21})$	(0.0446224,0.17)	(0.0480549, −0.72)
$(\overline{\Gamma}_{\alpha 22}, \overline{\varphi}_{\alpha 22})$	(0.0663616, −0.83)	(0.0915332, −0.08)
$(\overline{\Gamma}_{\alpha 23}, \overline{\varphi}_{\alpha 23})$	(0.00457666,0.45)	(0.0560641,0.41)
$(\overline{\Gamma}_{\alpha 31}, \overline{\varphi}_{\alpha 31})$	(0.01373, −0.1)	(0.100686, −0.22)
$(\overline{\Gamma}_{\alpha 32}, \overline{\varphi}_{\alpha 32})$	(0.0183066, −0.45)	(0.076659, −0.6)
$(\overline{\Gamma}_{\alpha 33}, \overline{\varphi}_{\alpha 33})$	(0.0469108,0.19)	(0.0560641, −0.15)

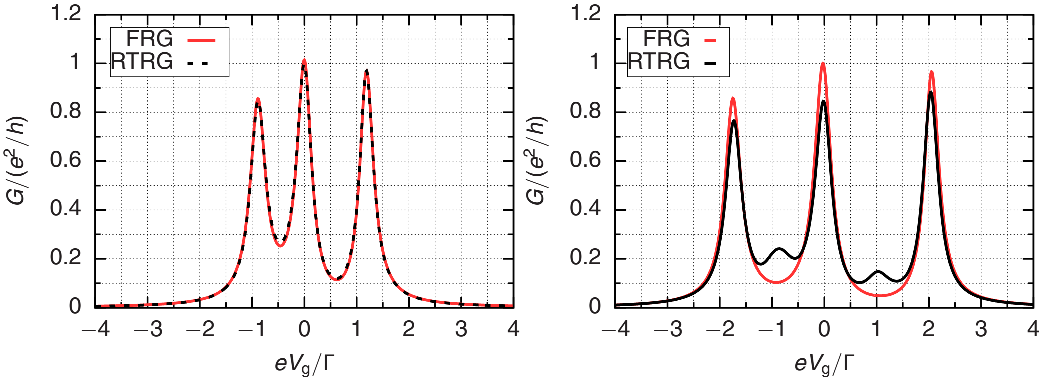

(a) $U/\Gamma = 0.1$, $V/\Gamma = 0.0$ (b) $U/\Gamma = 1.0$, $V/\Gamma = 0.0$

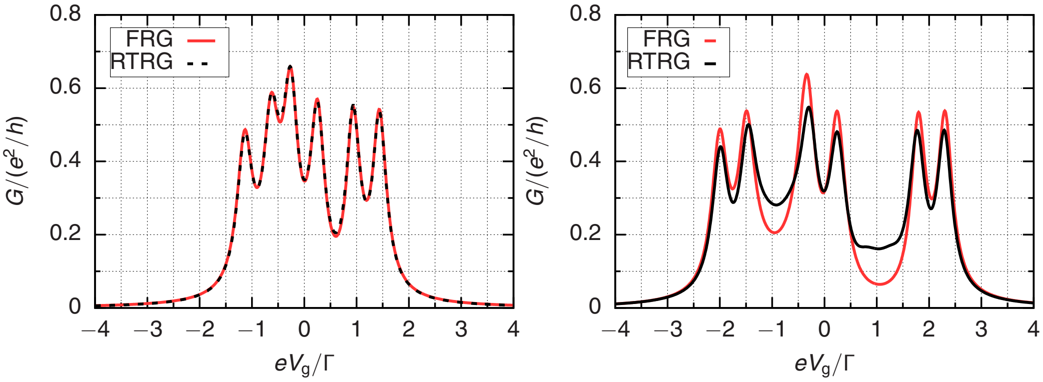

(c) $U/\Gamma = 0.1$, $V/\Gamma = 0.5$ (d) $U/\Gamma = 1.0$, $V/\Gamma = 0.5$

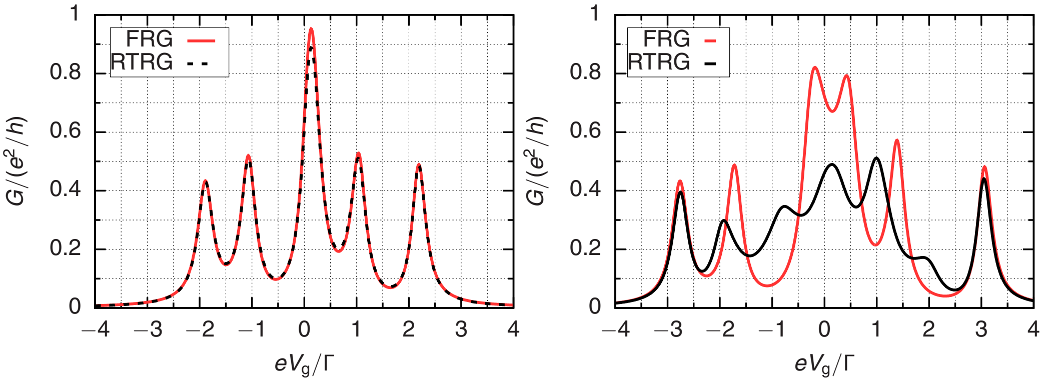

(e) $U/\Gamma = 0.1$, $V/\Gamma = 2.0$ (f) $U/\Gamma = 1.0$, $V/\Gamma = 2.0$

FIG. 3. Conductance G as function of the gate voltage V_g for a model with tunneling matrix $\underline{\underline{t}}^{\alpha}$ defined in Table II and $h_l/\Gamma = (-0.8, 0.0, 1.1)$ for small to intermediate Coulomb interactions, i.e., $U = 0.1\Gamma$ (left panel) and $U = 1.0\Gamma$ (right panel).

that the restriction of proportional coupling is lifted in the following. The parameters defining the tunneling matrix and the hybridization matrix, respectively, can be read off from Table II.

The fRG approach is controlled in the regime of small Coulomb interaction $U \ll \Gamma$ with the consequence that it can be used as a benchmark to test the reliability of the RTRG approximation in this limit. Our numerical study reveals an almost perfect agreement between RTRG and fRG data for arbitrary bias voltages in this regime. The left panel of Fig. 3 shows the exemplary conductance G as function of the gate voltage V_g for $U = 0.1\Gamma$ and selected values for V. This outcome generalizes our findings in the linear response regime, confirming that the RTRG approach yields accurate results for weak Coulomb interactions also in the limit of strong coupling already within the simplest approximation.

For small Coulomb interaction, the effective single-particle picture is valid. The mere effect of the fRG method in the lowest-order truncation scheme is a renormalization of the single-particle dot energy levels $\tilde{h}_k$. Resonant electron transport, causing the conductance peaks, occurs if one of these levels align with the chemical potential of one of the two reservoirs. As a consequence, the conductance peaks are now located at $V_g = \tilde{h}_k \pm \frac{V}{2}$. This means that each of the three peaks observed in equilibrium split into two peaks for increasing bias voltage. Eventually, the conductance shows six peaks constituting two groups of three peaks centered at $V_g = \tilde{h}_2 \pm \frac{V}{2}$ for large bias voltages $V \gg \Gamma$. There is a crossover between the cases of three and six resonances where the number of distinguishable peaks can be smaller than six. This is the case if the distance between two resonance lines is smaller than the peak widths.

In equilibrium, it is well established that the fRG yields reliable results from weak to intermediate Coulomb interactions [23]. However, for large bias voltages the effective single-particle picture is only applicable for small Coulomb interactions. Thus, we cannot use the static fRG data as a benchmark against the RTRG data beyond $U \ll \Gamma$. Nonetheless, we also compared the results for the differential conductance in order to estimate the parameter range where the solutions from both approaches are in qualitative agreement.

We find a more complex behavior for intermediate interaction strengths. The right panel of Fig. 3 shows exemplary the evolution of the differential conductance as function of the gate voltage with increasing bias for $U/\Gamma = 1.0$. Similar to Fig. 1(b), Fig. 3(b) reveals a good agreement between fRG and RTRG data for the position and width of the conductance peaks in the linear response regime. A qualitative agreement between results from both approaches is also obtained for $V/\Gamma = 0.5$ [cf. Fig. 3(d), where both approaches predict the same position of the six conductance peaks]. This is no longer the case already for moderate bias $V/\Gamma = 2.0$. Figure 3(f) shows that in this case the fRG and the RTRG approaches agree only for the outer conductance peaks, i.e., the leftmost and the rightmost peaks. In contrast, the RTRG solution shows an essentially different structure compared to the fRG solution in the region between these two peaks.

A corresponding picture emerges if we scrutinize the dependence of the differential conductance on the Coulomb interaction at large bias. Figure 4 shows the differential conductance as function of the gate voltage for $V/\Gamma = 5.0$ and different values for U. Starting from weak coupling [$U/\Gamma = 0.1$, Fig. 4(a)], where RTRG and fRG results are in very good agreement, we still find a qualitative agreement for $U/\Gamma = 0.5$ [see Fig. 4(b)]. In particular, both solutions are in accordance regarding the number and position of the conductance peaks but differ in the height of the inner conductance peaks. These are of reduced height in the RTRG solution for the differential conductance compared to the fRG data. In contrast, the solutions for the differential conductance from both approaches no longer comply in the region between the outer peaks for larger Coulomb interactions, as it is shown in Fig. 4(c) for $U/\Gamma = 2.0$.

For intermediate Coulomb interactions and moderate bias, e.g., Figs. 3(f) and 4(c), the number and positions of the inner conductance peaks are different for the solution from both approaches. In particular, the RTRG solution exhibits more than six local minima which we interpret as additional resonance lines. Their emergence is more pronounced for large Coulomb interaction, as can be seen in Fig. 5 for $U = 20.0\Gamma$ and $V = 5.0\Gamma$. This behavior of the RTRG solution for the differential conductance can be readily understood from the condition (29) for resonant tunneling within this approach

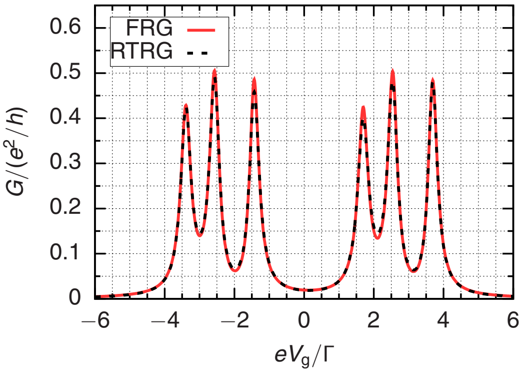

(a) $U/\Gamma = 0.1$

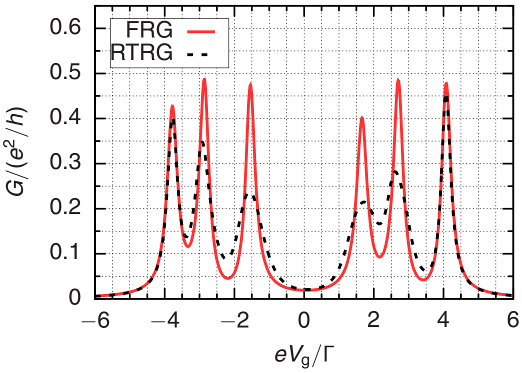

(b) $U/\Gamma = 0.5$

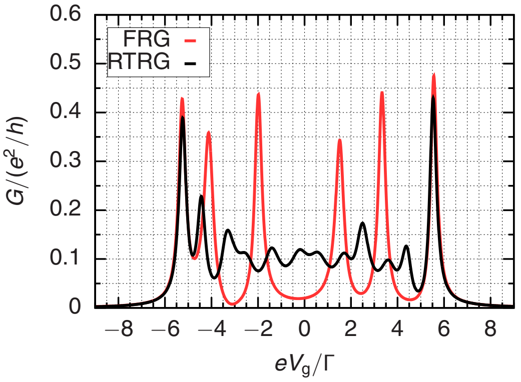

(c) $U/\Gamma = 2.0$

FIG. 4. Conductance G as function of the gate voltage V_g for a model with tunneling matrix $\underline{t}^{\alpha}$ defined in Table II, $h_l/\Gamma = (-0.8, 0.0, 1.1)$ and $V = 5.0\Gamma$. While there is a very good agreement between fRG and RTRG solution for small Coulomb interactions $U = 0.1\Gamma$, the results from both approaches coincide only for the outer, i.e., the very left and the very right, peaks for moderate interaction strengths $U = 2.0\Gamma$. In the latter case, the solutions differ significantly in the region between the outer peaks, as explained in the main text.

which is fulfilled if the real part of the eigenvalue $\lambda_k(E)$ of the effective Liouvillian aligns to the chemical potential of one of the two reservoirs. In order to interpret this condition, it is more instructive to consider (28), which determines the resonance lines using perturbation theory. The RG treatment

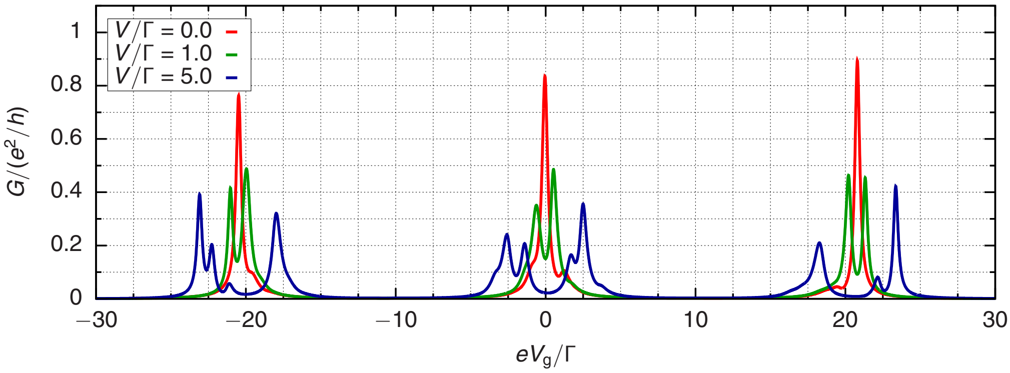

FIG. 5. RTRG solution for the conductance G as function of the gate voltage V_g for the model with $\underline{t}^\alpha$ defined by Table II, $U = 20.0\Gamma$, level spacings $h_l/\Gamma = (-0.8, 0.0, 1.1)$, and different values for the bias V. Each of the three peaks occurring in the linear response regime ($V = 0$) splits into two peaks of reduced height for increasing bias voltage $V = \Gamma$. In contrast, additional resonance lines emerge for large enough bias ($V = 5.0\Gamma$).

leads to a shift of the resonance lines in the conductance as a function of the gate voltage.

In the linear response regime, i.e., for $V \to 0$, condition (28) is only fulfilled if the ground-state energies of the N and $N+1$ electron sectors are degenerate. This means that for $V > 0$, one electron can tunnel from the left reservoir onto the dot, occupying the lowest-energy many-body state of the $N+1$ electron sector. Afterward, this electron can leave the dot by tunneling into the right reservoir, resulting in a total tunneling process involving the dot electron numbers $N \to N+1 \to N$. As a consequence, the three single-particle dot levels are successively populated with increasing gate voltage V_g. This complies with the single-particle picture and is also the reason why the linear conductance as function of the gate voltage has always three peaks.

If the bias is large enough, (28) can also be fulfilled for processes involving excited many-body dot states. For instance, transitions from the ground state of the N particle sector to an excited state of the $N+1$ particle sector can become possible if this condition is matched. Equivalently, these tunneling processes $s_2 \to s_1$ with $N_{s_1} = N_{s_2} + 1$ are possible if the corresponding energy difference $E_{s_1} - E_{s_2}$ lies within the transport window [1,5], i.e., $\mu_L > E_{s_1} - E_{s_2} > \mu_R$, provided that the initial state s_2 is occupied. As a consequence, additional resonance lines show up in the current, each corresponding to one of these tunneling processes. The emergence of such additional conductance peaks is clearly visible for $U = 20.0\Gamma$ and $V = 5.0\Gamma$ in Fig. 5. We note that each resonance can be split by the bias voltage in at most four resonances. For example, for the transition $N = 0 \to N = 1$ (corresponding to the left resonance in Fig. 5), three resonances occur when one of the three renormalized levels matches with the upper chemical potential $\mu_L = V/2$ but only one resonance can appear when the lowest level matches with the lower chemical potential $\mu_R = -V/2$. Once the lowest level is below μ_R, it is occupied and the resonances when the two higher levels match with μ_R are suppressed by Coulomb blockade. Therefore, for bias voltage significantly larger than Γ, four resonances are observed in Fig. 5 for the left resonance. Similar considerations hold for the middle and right resonances, but some of the peaks are hardly visible due to broadening effects. Similar findings were reported for an RTRG study of the Anderson model in the regime of strong Coulomb interactions in Ref. [24].

One must also distinguish between the deviations observed in the Coulomb blockade valleys in the linear response regime [see Figs. 1(b) and 3 (b)], and the behavior at intermediate bias $V \sim U \sim \Gamma$. While charge fluctuations are suppressed in the former case, the Coulomb blockade is lifted in the latter case. This means that charge fluctuations are dominant again for $V > U$. These processes are captured by the RTRG approximation considered in this work. Further evidence that the RTRG solution is reliable in this regime arises from the fact that it yields the exact Liouvillian in the limit $V \to \infty$. In this case, the right-hand side of the RG equation (26) is zero, which leads to

$$L(E) = L^{(0)} + L^{(1s)}. \tag{64}$$

This is an exact result in this limit since all higher-order terms vanish, as will be explained at the end of Appendix A.

To conclude, we expect a crossover from the effective single-particle behavior of the quantum dot for small Coulomb interactions $U \ll \Gamma$ to a more complex multiparticle situation, exhibiting further resonances, for large Coulomb interactions $U \gg \Gamma$. Figure 4 shows how this crossover sets in for intermediate Coulomb interactions $U \sim \Gamma$ and $V = 5.0\Gamma$ in the RTRG solution. In contrast, the effective single-particle picture applies for intermediate Coulomb interactions if the bias voltage is smaller than the Coulomb interaction. This is indicated by a qualitative agreement of the RTRG and fRG solutions [see Figs. 3(d) and 4(b)].

We refrain here from comparing fRG and RTRG results for the conductance in the regime of strong Coulomb interactions $U \gg \Gamma$ since no agreement can be expected, due to the aforementioned reasons. Figure 2 shows also clearly the deviations from fRG and RTRG data already in linear response in this regime.

In summary, we conclude that the RTRG method yields reliable results for the conductance in nonequilibrium at arbitrary Coulomb interaction or, equivalently, for arbitrary coupling to the reservoirs. From comparing the RTRG solution with fRG results, we estimate that the effective single-particle picture can be employed in nonequilibrium for bias voltages that are smaller than the Coulomb interaction.

V. SUMMARY

In this paper, we presented a comparative study of the electron transport through nondegenerate ($|h_l - h_{l'}| \sim \Gamma$) quantum dots coupled to two reservoirs via generic tunneling matrices in and out of equilibrium. To this end, we applied very basic approximations of the RTRG and fRG methods, where the effective Liouvillian and the self-energy were computed self-consistently while all vertex corrections were disregarded. Such basic approximations reduce the computational effort considerably but may also limit the range of applicability of the employed methods. We therefore analyzed to what degree such basic approaches take the dominant physical processes reliably into account.

An important test is the benchmark against numerical exact data. In equilibrium, we showed that the RTRG approximation yields reliable results for the position and width of the peaks of the linear conductance that are in very good agreement with highly accurate NRG data for arbitrary tunneling rates Γ, despite the fact that the RTRG is perturbative in the coupling between the dot and the reservoirs and is therefore *a priori* controlled only for small tunneling coupling $\Gamma \ll \max\{T, \delta\}$. This means that the charge fluctuations are captured largely by the contribution of the one-loop diagram to the RG equations whereas vertex renormalization seems to be less important to describe these processes. In contrast, cotunneling processes are only partly taken into account, causing deviations of the RTRG solution for the linear conductance from the NRG result in the Coulomb blockade regime, and leading to small anomalies close to the resonances in the case of strong Coulomb interactions. We conclude that the reliability of the RTRG solution depends essentially on the class of diagrams that are resummed and taken into account within the chosen approximation scheme. In this sense, the class of diagrams that is resummed into the renormalized one-loop diagram describes charge fluctuations, while (at least) two-loop diagrams and vertex renormalization are required for a reasonable description of cotunneling processes. The approximation of the RTRG equations can be systematically improved by taking such higher-order diagrams into account, as was already demonstrated in the past for the Kondo model [20,21] and the single-impurity Anderson model [24,38].

In nonequilibrium, we used reliable data for the conductance from the fRG approach in lowest-order truncation scheme as a benchmark for the RTRG data for small Coulomb interactions and strong coupling, respectively. Indeed, we find a nearly perfect agreement for the solutions from both approaches in this case, indicating again the drastic extension of the range of validity of the RTRG approximation to arbitrary Coulomb interactions in the regime of charge fluctuations.

We furthermore find from comparing RTRG and fRG solution that the single-particle picture of an *effectively* noninteracting open quantum dot with renormalized parameters is applicable (i) in the regime of small Coulomb interactions $U \ll \Gamma$ and arbitrary bias V, and (ii) for intermediate Coulomb interactions that are larger than the bias voltage. This means that the complex interplay between the Coulomb interaction and the tunneling processes away from equilibrium cannot be described by such an effective picture. In agreement with previous RTRG studies of the Anderson model [24], we showed that the RTRG method is capable of describing this interplay theoretically.

We note that in order to go beyond the effective single-particle picture with the fRG approach, one needs to extend the approximation for the RG equations to the next order. This was demonstrated in the two-level case [18,25], yielding accurate results also for intermediate Coulomb interactions at large bias [40].

In summary, we advertise the RTRG method as a versatile and flexible tool to describe transport phenomena in quantum dots with an arbitrary geometry in nonequilibrium. In particular, we demonstrated the reliability of this method in describing charge fluctuations in quantum dot systems with a very basic approximation that allows for an efficient numerical computation. We note that the formalism can easily be generalized to finite temperature by calculating the integral in Eq. (17) exactly in terms of the Matsubara poles of the Fermi distribution function. Furthermore, this equation can also be used to calculate the Liouvillian in the whole complex plane for arbitrary E such that the time evolution into the stationary state can be analyzed [15].

ACKNOWLEDGMENTS

This work was financially supported by the Deutsche Forschungsgemeinschaft via RTG 1995 (C.J.L., V.M., and H.S.). We thank J. von Delft, S. G. Jakobs, S.-S. B. Lee, M. R. Wegewijs, and A. Weichselbaum for fruitful discussions. F.B.K. acknowledges financial support by the Cluster of Excellence Nanosystems Initiative Munich and funding from the research school IMPRS-QST. Numerical calculations for the fRG and RTRG methods were performed with computing resources granted by RWTH Aachen University under Project No. rwth0287.

APPENDIX A: PERTURBATION THEORY FOR THE EFFECTIVE LIOUVILLIAN

In this Appendix, we discuss bare perturbation theory for the effective Liouvillian and the current kernel of the multilevel Anderson model. The perturbative series can be written as

$$L(E) = L^{(0)} + L^{(1)}(E) + L^{(2)}(E) + \cdots, \tag{A1}$$

$$\Sigma_\gamma(E) = \Sigma_\gamma^{(1)}(E) + \Sigma_\gamma^{(2)}(E) + \cdots, \tag{A2}$$

where $L^{(m)}(E)$ and $\Sigma_\gamma^{(m)}(E)$, respectively, comprise all diagrams with $m = 0, 1, 2, \ldots$ contraction lines. A contraction represents an excitation in the reservoirs and connects two vertices within a diagram within the diagrammatic language introduced in Refs. [14,15]. A diagram with m contraction lines is sometimes called an m-loop diagram.

The *zeroth-order* ($m = 0$) contribution to the effective Liouvillian is the Liouvillian of the isolated quantum dot, i.e., $L^{(0)}b = [H_{\mathrm{s}}, b]$, where b is an arbitrary operator acting on states of the dot Hilbert space. Denoting by E_s the eigenvalues of H_s and by $|s\rangle$ the corresponding many-body eigenstates, we can express the matrix elements of $L^{(0)}$ as

$$(s_1 s_2|L^{(0)}|s_1' s_2') = \delta_{s_1 s_1'} \delta_{s_2 s_2'} (E_{s_1} - E_{s_2}). \tag{A3}$$

Following Refs. [14,15], we obtain

$$L^{(1)}(E) =$$

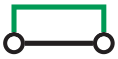

$$= L^{(1\mathrm{s})} + L^{(1\mathrm{a})}(E), \tag{A4}$$

with

$$\begin{aligned} L^{(1\mathrm{s})} &= \int d\omega\, \gamma^{\mathrm{s}}_{11'}(\omega) G_1 \frac{1}{E + \omega + \overline{\mu}_\alpha - L^{(0)}} \tilde{G}_{1'} \\ &= -i\frac{\pi}{2} G_1 \tilde{G}_{\overline{1}}, \end{aligned} \tag{A5}$$

$$\begin{aligned} L^{(1\mathrm{a})}(E) &= \int d\omega\, \gamma^{\mathrm{a}}_{11'}(\omega) G_1 \frac{1}{E + \omega + \overline{\mu}_\alpha - L^{(0)}} G_{1'} \\ &= G_1 \ln \frac{-i(E + \overline{\mu}_\alpha - L^{(0)})}{D} G_{\overline{1}} \end{aligned} \tag{A6}$$

for the *first-order* correction to the effective Liouvillian. The leading-order term for the current kernel can be obtained from these equations by simply replacing the left vertex G_1 by the current vertex (23) in all expressions, yielding

$$\Sigma^{(1\mathrm{s})}_\gamma = -i\frac{\pi}{2} c^\gamma_1 \tilde{G}_1 \tilde{G}_{\overline{1}}, \tag{A7}$$

$$\Sigma^{(1\mathrm{a})}_\gamma(E) = c^\gamma_1 \tilde{G}_1 \ln \frac{-i(E + \overline{\mu}_\alpha - L^{(0)})}{D} G_{\overline{1}}. \tag{A8}$$

In the first lines of Eqs. (A5) and (A6),

$$\gamma^{\mathrm{s,a}}_{11'}(\omega) = \delta_{\eta,-\eta'} \delta_{\alpha\alpha'} \rho_\mathrm{c}(\omega) f^{\mathrm{s,a}}_\alpha(\omega) \tag{A9}$$

are the symmetric and antisymmetric parts of the contraction $\gamma^{pp'}_{11'}(\omega) = p'\gamma^{\mathrm{s}}_{11'}(\omega) + \gamma^{\mathrm{a}}_{11'}(\omega)$. Accordingly, $f^{\mathrm{s,a}}_\alpha(\omega) = \frac{1}{2}[f(\omega) \pm f(-\omega)]$ are the symmetric and antisymmetric parts of the Fermi distribution. The former always gives $f^{\mathrm{s}}_\alpha(\omega) = \frac{1}{2}$ while the latter $f^{\mathrm{a}}_\alpha(\omega) = -\frac{1}{2}\,\mathrm{sgn}(\omega)$ for $T_\alpha = 0$. Furthermore, we have incorporated the factor p' in front of $\gamma^{\mathrm{s}}_{11'}(\omega)$ into the second vertex in (A5) and (A7), yielding $\tilde{G}_1 = \sum_{p=\pm} pG^p_1$.

We have introduced the Lorentzian high-frequency cut-off $\rho_\mathrm{c}(\omega) = D^2/(\omega^2 + D^2)$ with bandwidth $D \to \infty$ in order to regularize the frequency integral for high frequencies which results in the term $\sim \ln D$ in (A6). However, this term drops out since

$$\begin{aligned} G_1 G_{\overline{1}} &= \sum_{pp'} \sum_{\eta l_1 l_2} t^\eta_{\alpha l l_1} t^{-\eta}_{\alpha l l_2} C^p_{\eta l_1} C^{p'}_{-\eta l_2} \\ &= \frac{1}{2} \sum_{pp'} \sum_{\eta l_1 l_2} t^\eta_{\alpha l l_1} t^{-\eta}_{\alpha l l_2} \{ C^p_{\eta l_1} , C^{p'}_{-\eta l_2} \} \\ &= \frac{1}{2} \sum_{p} \sum_{l_1} t^\eta_{\alpha l l_1} t^{-\eta}_{\alpha l l_1} p \\ &= 0, \end{aligned} \tag{A10}$$

where we used the anticommutation relation $\{ C^p_{\eta l} , C^{p'}_{\eta' l'} \} = p\delta_{pp'}\delta_{\eta,-\eta'}\delta_{ll'}$ for the dot field superoperators after the second line. In order to show that the term $\sim \ln D$ in the last line in (A8) can be disregarded similarly, we note that we only need the combination $\mathrm{Tr}_\mathrm{s}\, \Sigma_\gamma(E)$ in order to compute the current I_γ from (14). From the general property [14,15] $\mathrm{Tr}_\mathrm{s}\, G^p_1 = 0$ one can deduce

$$\mathrm{Tr}_\mathrm{s}\, \tilde{G}_1 = 2\ \mathrm{Tr}_\mathrm{s}\, G^+_1 = -2\ \mathrm{Tr}_\mathrm{s}\, G^-_1 = -2p'\, \mathrm{Tr}_\mathrm{s}\, G^{-p'}_1, \tag{A11}$$

which leads to

$$\begin{aligned} \mathrm{Tr}_\mathrm{s}\, c^\gamma_1 \tilde{G}_1 G_{\overline{1}} &= -2\ \mathrm{Tr}_\mathrm{s} \sum_{p'} \sum_{\eta l_1 l_2} \eta p' t^\eta_{\alpha l l_1} t^{-\eta}_{\alpha l l_2} C^{-p'}_{\eta l_1} C^{p'}_{-\eta l_2} \\ &= -\,\mathrm{Tr}_\mathrm{s} \sum_{p'} \sum_{\eta l_1 l_2} \eta p' t^\eta_{\alpha l l_1} t^{-\eta}_{\alpha l l_2} \{ C^{-p'}_{\eta l_1} , C^{p'}_{-\eta l_2} \} \\ &= 0. \end{aligned} \tag{A12}$$

Thus, we can equivalently consider

$$L^{(1\mathrm{a})}(E) = G_1 \ln -i(E + \overline{\mu}_\alpha - L^{(0)}) G_{\overline{1}}, \tag{A13}$$

$$\Sigma^{(1\mathrm{a})}_\gamma(E) = c^\gamma_1 \tilde{G}_1 \ln -i(E + \overline{\mu}_\alpha - L^{(0)}) G_{\overline{1}}, \tag{A14}$$

instead of (A6) and (A8). Importantly, (A10) and (A12) have the consequence that perturbation theory yields no logarithmic divergences in the ultraviolet regime $|E| \to \infty$. A resummation of logarithmic terms is therefore not necessary in this case. This explains why we can neglect vertex corrections in lowest-order truncation for the RG treatment. Thus, we can simply insert the bare vertices G_1 and $(I_\gamma)_1$ into the RG equations.

In particular, the only logarithmic singularities of the effective Liouvillian and the current kernel for $E = i0^+$ are given by the condition (28). In order to treat these singularities, it is sufficient to calculate the effective Liouvillian self-consistently, which is achieved by the RTRG approach. The consequence is that the complex eigenvalues $\lambda_k(E)$ of the effective Liouvillian and *not* the real eigenvalues $E_{s_1} - E_{s_2}$ of the bare Liouvillian $L^{(0)}$ enter the argument of the complex logarithm in (A13) and (A14). The imaginary part of $\lambda_k(E)$ provides a cutoff that regularizes the logarithms. The sole exception is the nondegenerate eigenvalue $\lambda_\mathrm{st} = 0$ which, however, never appears in the argument of the logarithm, as discussed in more detail in Refs. [14,15].

Second-order diagrams ($m = 2$) are necessary to describe *cotunneling processes*. The two contraction lines in these diagrams account for the two excitations generated in the reservoir in a flavor fluctuation due to the coupling between dot and reservoir. One finds that the second-order contribution is given by the two diagrams

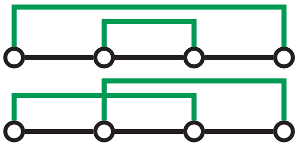

The upper diagram contains a connected first-order subdiagram as insertion on the propagator line. It belongs to the class of connected subdiagrams with no free contraction lines, i.e., all contraction lines connect two vertices of this subdiagram. These subdiagrams are sometimes called *self-energy insertion*, although they have nothing to do with the physical self-energy of a single-particle Green's function, apart from a formal equivalence. Resumming these insertions, one can replace all free propagators by full ones which leads to self-consistent perturbation theory [15]. Since the diagram on the right-hand side of the RG equation (17) contains only the full propagator, the upper diagram is also included in the RTRG approximation discussed in Sec. II B. In contrast, the diagram with the crossed contraction lines are not included within the considered truncation scheme. To include also this diagram, one needs to add the corresponding two-loop diagram on the right hand side of the RG equation (17) as well as to include the vertex correction by replacing the bare vertex by the effective one. The latter can then be obtained as solution of a corresponding RG equation.

Finally, we note that there are also no logarithmic divergent terms in the ultraviolet limit $|E| \to \infty$ in higher-order perturbation theory. An mth-order diagram consisting of m contraction lines and $2m$ vertices contains $2m-1$ resolvents $\sim(E_{1\dots n} + \underline{\omega}_{1\dots n} - L^{(0)})^{-1}$ with $E_{1\dots n} = E + \sum_{k=1}^{n} \overline{\mu}_k$ and $\overline{\omega}_{1\dots n} \sum_{k=1}^{n} \overline{\omega}_k$. Since each contraction gives rise to one frequency integral, one can estimate that the mth-order diagram with $m \geqslant 2$ falls off $\sim E^{1-m}$ for $|E| \to \infty$.

In the same way, all mth-order diagrams with $m \geqslant 2$ vanish in the limit $|\overline{\mu}_\alpha| \to \infty$. In the case $m = 1$, we find that the part of the diagram with the antisymmetric part of the contraction $\gamma^{\mathrm{a}}_{11'}(\omega)$ vanishes for $|\overline{\mu}_\alpha| \to \infty$ due to the property (A10). As a consequence, the effective Liouvillian is given by (64) in this case.

APPENDIX B: TRUNCATION OF THE RTRG EQUATION

After Eq. (27), we have explained that (26) defines effectively an infinite hierarchy of RG equations. In order to truncate this hierarchy of RG equations, we bring this system in a more transparent form for the special case of two reservoirs. Following Ref. [21], we define a chain of discrete points

$$\mu_k = \frac{k}{2} V, \tag{B1}$$

with an integer number k. Obviously, $k = 1$ and -1 correspond to the chemical potentials of the two reservoirs, i.e., $\mu_1 = \mu_L$ and $\mu_{-1} = \mu_R$, respectively. With the definition

$$\tilde{L}_k(\Lambda) = \tilde{L}(\Lambda - i\mu_k), \tag{B2}$$

the aforementioned hierarchy of RG equations is given by

$$\frac{d}{d\Lambda}\tilde{L}_k(\Lambda) = i \sum_{\eta\alpha l} G_{\eta\alpha l} \frac{1}{i\Lambda + \mu_{k+\nu_{\alpha\eta}} - \tilde{L}_{k+\nu_{\alpha\eta}}(\Lambda)} G_{-\eta\alpha l}, \tag{B3}$$

where we have introduced the sign factor

$$\nu_{\alpha\eta} = \begin{cases} +1 & \text{if} \quad \eta = +,\ \alpha = \mathrm{L} \quad \text{or} \quad \eta = -,\ \alpha = \mathrm{R}, \\ -1 & \text{if} \quad \eta = +,\ \alpha = \mathrm{R} \quad \text{or} \quad \eta = -,\ \alpha = \mathrm{L}. \end{cases} \tag{B4}$$

Within this notation scheme, the RG equation for the current kernel (27) recast as

$$\frac{d}{d\Lambda}\tilde{\Sigma}_\alpha(\Lambda) = -\frac{i}{2} \sum_{l\eta} \eta\, \tilde{G}_{\eta\alpha l} \frac{1}{i\Lambda + \mu_{\nu_{\alpha\eta}} - \tilde{L}_{\nu_{\alpha\eta}}(\Lambda)} G_{-\eta\alpha l}. \tag{B5}$$

The initial conditions are

$$\tilde{L}_k(\Lambda)\big|_{\Lambda=D} = L^{(0)} + L^{(1\mathrm{s})} \tag{B6}$$

since (24) holds for any k.

Truncation of the infinite hierarchy of RG equations is achieved by setting

$$\tilde{L}_{\pm(k_0+1)}(\Lambda) \approx \tilde{L}_{\pm k_0}(\Lambda) \tag{B7}$$

for some k_0. This is justified due to

$$\frac{\mu_{k+1} - \mu_k}{\mu_k} = \frac{1}{k}, \tag{B8}$$

which means that the relative change in the energy shift μ_k in the argument of the Liouvillian $\tilde{L}(\Lambda - i\mu_k)$ falls off $\sim k^{-1}$ for $k \to \infty$. In practice, we have checked convergence of the solution by comparing the results for different values of $|k_0|$. We consider a solution as reliable if the result for this choice does not deviate significantly from the one obtained for $|\tilde{k}_0| = |k_0| + 1$. For all numerical calculations, we observed a convergence already for quite small values of $|k_0|$. In particular, $|k_0| = 4$ proved to be a reliable choice for all cases considered in this paper.

APPENDIX C: CLOSED ANALYTIC EXPRESSIONS OF THE fRG EQUATION FOR THE SELF-ENERGY AND THE CURRENT

The integral on the right-hand side of (41) can be analytically evaluated, as we discuss now. Inserting (47) into (41) gives

$$\frac{d}{d\Lambda}\Sigma^{\mathrm{R}}_{ll'}(\Lambda) = -\frac{1}{4\pi} \sum_{l_1 l_1'} \overline{v}_{ll_1,l'l_1'} \int d\omega\, [\underline{\underline{G}}^{\mathrm{R}}(\Lambda,\omega)\underline{\underline{G}}^{\mathrm{K}}(\Lambda,\omega) - \underline{\underline{G}}^{\mathrm{K}}(\Lambda,\omega)\underline{\underline{G}}^{\mathrm{A}}(\Lambda,\omega)]_{l_1' l_1}. \tag{C1}$$

To evaluate the integral, we furthermore make use of the spectral representation of the retarded and advanced, respectively, components of the self-energy, i.e.,

$$\underline{\underline{\Sigma}}^{\mathrm{R}}(\Lambda) = \sum_k \lambda_k^\Lambda \underline{\underline{P}}_k^\Lambda, \tag{C2}$$

$$\underline{\underline{\Sigma}}^{\mathrm{A}}(\Lambda) = \sum_k \left(\lambda_k^\Lambda\right)^* \left(\underline{\underline{P}}_k^\Lambda\right)^\dagger. \tag{C3}$$

Inserting (32), (33), (C2), and (C3) into (C1) and using the integral

$$\int d\omega\ \mathrm{sgn}(\omega) \frac{1}{(\omega + z_1)^2} \frac{1}{\omega + z_2} = \frac{2}{z_1 - z_2} \left\{ \frac{1}{z_1 - z_2} [\ln(-i\sigma_1 z_1) - \ln(-i\sigma_2 z_2)] - \frac{1}{z_1} \right\} \tag{C4}$$

with $\sigma_i = \mathrm{sgn}(\mathrm{Im}\, z_i)$ yields

$$\begin{aligned}\frac{d}{d\Lambda}\Sigma^{\mathrm{R}}_{ll'}(\Lambda) = \frac{i}{2\pi}\sum_{l_1 l_1'}\overline{v}_{ll_1,l'l_1'}\sum_{\alpha k k'}\left[\underline{\underline{P}}^{\Lambda}_{k}\underline{\underline{\Gamma}}^{\alpha}\left(\underline{\underline{P}}^{\Lambda}_{k'}\right)^{\dagger}\right]_{l_1' l_1}&\frac{1}{\lambda^{\Lambda}_{k}-\left(\lambda^{\Lambda}_{k'}\right)^{*}-2i\Lambda}\\ \times\Bigg\{\frac{1}{\mu_\alpha-\lambda^{\Lambda}_{k}+i\Lambda}+\frac{1}{\mu_\alpha-\left(\lambda^{\Lambda}_{k'}\right)^{*}-i\Lambda}&+\frac{2}{\lambda^{\Lambda}_{k}-\left(\lambda^{\Lambda}_{k'}\right)^{*}-2i\Lambda}\\ \times\left[\ln -i(\mu_\alpha-\lambda^{\Lambda}_{k}+i\Lambda)-\ln i\left(\mu_\alpha-\left(\lambda^{\Lambda}_{k'}\right)^{*}-i\Lambda\right)\right]\Bigg\}&. \end{aligned} \tag{C5}$$

In the same way, we can evaluate the frequency integral in the current formula (30). Using the results

$$\int d\omega\ \mathrm{sgn}(\omega)\frac{1}{\omega+z_1}\frac{D^2}{D^2+\omega^2} = -2\frac{D^2}{D^2+z_1^2}\ln\frac{-i\sigma_1 z_1}{D} \xrightarrow{D\to\infty} -2\ \ln\frac{-i\sigma_1 z_1}{D}, \tag{C6}$$

$$\int d\omega\ \mathrm{sgn}(\omega)\,\frac{1}{\omega+z_1}\frac{1}{\omega+z_2} = \frac{2}{z_1-z_2}[\ln(-i\sigma_1 z_1)-\ln(-i\sigma_2 z_2)], \tag{C7}$$

we obtain

$$\begin{aligned} I^{\mathrm{st}}_{\alpha} &= \frac{i}{2\pi}\sum_{k}\mathrm{Tr}\{\underline{\underline{\Gamma}}^{\alpha}[\ln -i(\mu_\alpha-\tilde{\lambda}_k)\underline{\underline{\tilde{P}}}_{k}-\ln i(\mu_\alpha-\tilde{\lambda}^{*}_{k})\underline{\underline{\tilde{P}}}^{\dagger}_{k}]\}\\ &\quad-\frac{1}{2\pi}\sum_{\alpha' k k'}\frac{1}{\tilde{\lambda}_k-\tilde{\lambda}^{*}_{k'}}[\ln -i(\mu_{\alpha'}-\tilde{\lambda}_k)-\ln i(\mu_{\alpha'}-\tilde{\lambda}^{*}_{k'})]\,\mathrm{Tr}(\underline{\underline{\tilde{P}}}_{k}\underline{\underline{\Gamma}}^{\alpha'}\underline{\underline{\tilde{P}}}^{\dagger}_{k'}\underline{\underline{\Gamma}}^{\alpha})\\ &=\frac{1}{2\pi}\,\mathrm{Re}\,\mathrm{Tr}\left\{2i\sum_{k}\ln -i(\mu_\alpha-\tilde{\lambda}_k)\underline{\underline{\tilde{P}}}_{k}\underline{\underline{\Gamma}}^{\alpha}-\sum_{\alpha' k k'}\underline{\underline{\tilde{P}}}_{k}\underline{\underline{\Gamma}}^{\alpha'}\underline{\underline{\tilde{P}}}^{\dagger}_{k'}\underline{\underline{\Gamma}}^{\alpha}\frac{1}{\tilde{\lambda}_k-\tilde{\lambda}^{*}_{k'}}[\ln -i(\mu_{\alpha'}-\tilde{\lambda}_k)-\ln i(\mu_{\alpha'}-\tilde{\lambda}^{*}_{k'})]\right\}, \end{aligned} \tag{C8}$$

with $\tilde{\lambda}_k = \lambda^{\Lambda=0}_{k}$ and $\underline{\underline{\tilde{P}}}_{k} = \underline{\underline{P}}^{\Lambda=0}_{k}$.

[1] R. Hanson, L. P. Kouwenhoven, J. R. Petta, S. Tarucha, and L. M. K. Vandersypen, Rev. Mod. Phys. **79**, 1217 (2007).

[2] E. A. Laird, F. Kuemmeth, G. A. Steele, K. Grove-Rasmussen, J. Nygård, K. Flensberg, and L. P. Kouwenhoven, Rev. Mod. Phys. **87**, 703 (2015).

[3] L. I. Glazman and M. E. Raikh, Pis'ma Zh. Eksp. Teor. Fiz. **47**, 378 (1988) [Sov. Phys.–JETP Lett. **47**, 452 (1988)]; T. K. Ng and P. A. Lee, Phys. Rev. Lett. **61**, 1768 (1988).

[4] D. Goldhaber-Gordon, H. Shtrikman, D. Mahalu, D. Abusch-Magder, U. Meirav, and M. A. Kastner, Nature (London) **391**, 156 (1998); S. M. Cronenwett, T. H. Oosterkamp, and L. P. Kouwenhoven, Science **281**, 540 (1998); F. Simmel, R. H. Blick, J. P. Kotthaus, W. Wegscheider, and M. Bichler, Phys. Rev. Lett. **83**, 804 (1999).

[5] S. Andergassen, V. Meden, H. Schoeller, J. Splettstoesser, and M. R. Wegewijs, Nanotechnology **21**, 272001 (2010).

[6] L. I. Glazman and M. Pustilnik, in *Nanophysics: Coherence and Transport*, edited by H. Bouchiat *et al.* (Elsevier, Amsterdam, 2005), p. 427.

[7] K. G. Wilson, Rev. Mod. Phys. **47**, 773 (1975).

[8] R. Bulla, T. A. Costi, and T. Pruschke, Rev. Mod. Phys **80**, 395 (2008).

[9] S. R. White, Phys. Rev. Lett. **69**, 2863 (1992); Phys. Rev. B. **48**, 10345 (1993).

[10] F. B. Anders, Phys. Rev. Lett. **101**, 066804 (2008).

[11] F. B. Anders and A. Schiller, Phys. Rev. Lett. **95**, 196801 (2005); F. B. Anders, R. Bulla, and M. Vojta, *ibid.* **98**, 210402 (2007); A. Hackl, D. Roosen, S. Kehrein, and W. Hofstetter, *ibid.* **102**, 219902(E) (2009).

[12] A. J. Daley, C. Kollath, U. Schollwöck, and G. Vidal, J. Stat. Mech.: Theor. Exp. (2004) P04005; S. R. White and A. E. Feiguin, Phys. Rev. Lett. **93**, 076401 (2004); P. Schmitteckert, Phys. Rev. B **70**, 121302(R) (2004); F. Heidrich-Meisner, A. E. Feiguin, and E. Dagotto, *ibid.* **79**, 235336 (2009).

[13] F. Schwarz, I. Weymann, J. von Delft, and A. Weichselbaum, Phys. Rev. Lett. **121**, 137702 (2018).

[14] H. Schoeller, Eur. Phys. J. Special Topics **168**, 179 (2009).

[15] H. Schoeller, *Dynamics of Open Quantum Systems, in Lecture Notes of the 45th IFF Spring School Computing Solids: Models, ab initio Methods, and Supercomputing* (Forschungszentrum Jülich, Jülich, 2014).

[16] W. Metzner, M. Salmhofer, C. Honerkamp, V. Meden, and K. Schönhammer, Rev. Mod. Phys. **84**, 299 (2012).

[17] S. G. Jakobs, V. Meden, and H. Schoeller, Phys. Rev. Lett. **99**, 150603 (2007).

[18] S. G. Jakobs, M. Pletyukhov, and H. Schoeller, Phys. Rev. B **81**, 195109 (2010).

[19] F. Wegner, Ann. Phys. (Leipzig) **3**, 77 (1994); S. D. Głazek and K. G. Wilson, Phys. Rev. D. **48**, 5863 (1993); **49**, 4212 (1994); S. Kehrein, *The Flow Equation Approach to Many-Particle Systems*, Springer Tracts in Modern Physics, Vol. 217 (Springer, Berlin, 2006).

[20] M. Pletyukhov and H. Schoeller, Phys. Rev. Lett. **108**, 260601 (2012).

[21] F. Reininghaus, M. Pletyukhov, and H. Schoeller, Phys. Rev. B **90**, 085121 (2014).

[22] A. V. Kretinin, H. Shtrikman, and D. Mahalu, Phys. Rev. B **85**, 201301(R) (2012); O. Klochan, A. P. Micolich, A. R. Hamilton,

D. Reuter, A. D. Wieck, F. Reininghaus, M. Pletyukhov, and H. Schoeller, *ibid.* **87**, 201104(R) (2013).

[23] C. Karrasch, T. Hecht, A. Weichselbaum, Y. Oreg, J. von Delft, and V. Meden, Phys. Rev. Lett. **98**, 186802 (2007); C. Karrasch, T. Enss, and V. Meden, Phys. Rev. B **73**, 235337 (2006).

[24] R. B. Saptsov and M. R. Wegewijs, Phys. Rev. B **86**, 235432 (2012).

[25] C. Karrasch, R. Hedden, R. Peters, Th. Pruschke, K. Schönhammer, and V. Meden, J. Phys.: Condens. Matter **20**, 345205 (2008).

[26] N. E. Bickers, Rev. Mod. Phys. **59**, 845 (1987).

[27] P. W. Anderson, Phys. Rev. **124**, 41 (1961).

[28] S. Göttel, F. Reininghaus, and H. Schoeller, Phys. Rev. B **92**, 041103(R) (2015); C. J. Lindner, F. B. Kugler, H. Schoeller, and J. von Delft, **97**, 235450 (2018).

[29] O. Kashuba and H. Schoeller, Phys. Rev. B. **87**, 201402(R) (2013).

[30] L. V. Keldysh, Zh. Eksp. Thoer. Fiz. **47**, 1515 (1965) [Sov. Phys.–JETP **20**, 1018 (1965)].

[31] Y. Meir and N. S. Wingreen, Phys. Rev. Lett. **68**, 2512 (1992).

[32] S. G. Jakobs, M. Pletyukhov, and H. Schoeller, J. Phys. A: Math. Theor. **43**, 103001 (2010).

[33] A. Weichselbaum and J. von Delft, Phys. Rev. Lett **99**, 076402 (2007); Phys. Rev. B **86**, 245124 (2012).

[34] A. Weichselbaum, Ann. Phys. (NY) **327**, 2972 (2012).

[35] K. M. Stadler, A. K. Mitchell, J. von Delft, and A. Weichselbaum, Phys. Rev. B **93**, 235101 (2016).

[36] W. C. Oliveira and L. N. Oliveira, Phys. Rev. B **49**, 11986 (1994).

[37] H. Schoeller An introduction to real-time renormalization group, in *Low-Dimensional Systems*, edited by T. Brandes (Springer, Berlin, 1999).

[38] H. Schoeller and J. König, Phys. Rev. Lett. **84**, 3686 (2000).

[39] D. Boese, W. Hofstetter, and H. Schoeller, Phys. Rev. B **64**, 125309 (2001).

[40] J. Eckel, F. Heidrich-Meisner, S. G. Jakobs, M. Thorwart, M. Pletyukhov, and R. Egger, New J. Phys. **12**, 043042 (2010).

6 Hund metals with nondegenerate orbitals

6.1 Overview

Hund metals have opened a new chapter in the study of correlated electron systems. In these multiorbital systems, strong correlations are driven not by the Hubbard repulsion U but by the Hund's rule coupling J, even if the latter is much smaller than the electronic bandwidth [GdMM13, SKWvD19]. The most prominent appearance of Hund metals stems from the theoretical analysis of high-temperature iron-based superconductors (Fe-SCs), where the term "Hund metal" was coined [YHK11], but also ruthenates, including the famous unconventional, yet low-temperature superconductor Sr_2RuO_4 [MRS01, MSHM17], belong to this category. In Hund metals, orbital differentiation is a ubiquitous phenomenon [dM17]. For instance, in the normal state of Sr_2RuO_4, the xy orbital has heavier mass and shows stronger response in nuclear magnetic resonance measurements (see references in [P10]), and in many Fe-SCs, only the xy orbital disappears from photoemission spectra upon raising temperature (see references in [P9]).

The Hund-metal phase of multiorbital Hubbard models is hard to describe for many numerical methods because Hund J strongly suppresses the spin coherence scale. To analyze the Fermi-liquid regime, one must reach extremely low temperatures and energies. In a DMFT approach, unlike Quantum Monte Carlo, exact-diagonalization or DMRG-like impurity solvers, only NRG has access to arbitrarily small energy scales and is therefore the most suitable tool to study Hund metals. Building on recent progress in NRG methodology, we present in the following the first real-frequency studies of Hund metals with nondegenerate orbitals—both in the model and material context.

In [P9], we analyze a minimal model for orbital differentiation in Hund metals using a highly accurate method together with intuitive, conceptual arguments. We unravel several controversial aspects of the orbital-selective Mott transition and reveal interorbital doublon–holon excitations and suppressed coherence scales, leading to singular Fermi-liquid behavior, in Hund metals with strong orbital differentiation. In [P10], we demonstrate that NRG can also be used in the material context. This allows us to analyze the archetypal Hund-metal material Sr_2RuO_4 down to the lowest energy scales and follow the RG flow from fluctuating spin and orbital moments to the Fermi-liquid state below 25 K. We also show that the van Hove singularity in the xy orbital close to the Fermi level drives strong orbital differentiation in Sr_2RuO_4 and detect an attractive quasiparticle interaction in the spin-triplet sector.

P9 *Orbital differentiation in Hund metals*
F. B. Kugler, S.-S. B. Lee, A. Weichselbaum, G. Kotliar, J. von Delft
arXiv:1904.10774
© 2019 The Authors
reproduced on pages 190–200.

P10 *Strongly correlated materials from a numerical renormalization group perspective: How the Fermi-liquid state of* Sr_2RuO_4 *emerges*
F. B. Kugler, M. Zingl, H. U. R. Strand, S.-S. B. Lee, J. von Delft, A. Georges
arXiv:1909.02389
© 2019 The Authors
reproduced on pages 201–209.

arXiv:1904.10774v2 [cond-mat.str-el] 5 Sep 2019

Orbital differentiation in Hund metals

Fabian B. Kugler,[1] Seung-Sup B. Lee,[1] Andreas Weichselbaum,[2,1] Gabriel Kotliar,[2,3] and Jan von Delft[1]
[1] *Arnold Sommerfeld Center for Theoretical Physics, Center for NanoScience, and Munich Center for Quantum Science and Technology, Ludwig-Maximilians-Universität München, 80333 Munich, Germany*
[2] *Condensed Matter Physics and Materials Science Department, Brookhaven National Laboratory, Upton, NY 11973, USA*
[3] *Department of Physics and Astronomy, Rutgers University, Piscataway, NJ 08854, USA*

(Dated: September 6, 2019)

Orbital differentiation is a common theme in multi-orbital systems, yet a complete understanding of it is still missing. Here, we consider a minimal model for orbital differentiation in Hund metals with a highly accurate method: We use the numerical renormalization group as real-frequency impurity solver for a dynamical mean-field study of three-orbital Hubbard models, where a crystal field shifts one orbital in energy. The individual phases are characterized with dynamic correlation functions and their relation to diverse Kondo temperatures. Upon approaching the orbital-selective Mott transition, we find a strongly suppressed spin coherence scale and uncover the emergence of a singular Fermi liquid and interband doublon-holon excitations. Our theory describes the diverse polarization-driven phenomena in the t_{2g} bands of materials such as ruthenates and iron-based superconductors, and our methodological advances pave the way towards real-frequency analyses of strongly correlated materials.

I. INTRODUCTION

The discovery of superconductivity in the iron pnictides and chalcogenides [1, 2] (FeSCs) has led to renewed interest in multi-orbital systems. Both theoretical and experimental studies of these systems have uncovered the remarkable phenomenon of orbital differentiation: in an almost degenerate manifold of d states, some orbitals are markedly more correlated than others. For instance, in $\mathrm{FeSe}_x\mathrm{Te}_{1-x}$ [3], LiFeAs [4], and $\mathrm{K}_{0.76}\mathrm{Fe}_{1.72}\mathrm{Se}_2$ [5], among the t_{2g} states, only the xy orbital disappears from photoemission spectra as temperature is raised. Orbital differentiation is also seen in tunneling experiments [6] and is a key ingredient in theoretical frameworks to describe FeSCs [7–9]. It is not unique to the FeSCs; it has further been documented in the ruthenates [10] and likely takes place in all Hund metals [11, 12].

An extreme form of orbital differentiation is the orbital-selective Mott transition (OSMT) [13], where some orbitals become insulating, while others remain metallic. Despite its importance, the OSMT in three-band systems has not yet been systematically investigated with a controlled method enabling access to low temperatures, where Fermi liquids form. Controversial questions include: For a given sign of crystal-field splitting, which orbitals localize? Is the OSMT of first or second order? Do correlations enhance or reduce orbital polarization as one approaches the OSMT? Is it true that quenching of orbital fluctuations makes the orbitals behave independently? Do the itinerant electrons in the OSM phase (OSMP) form a Fermi liquid? Finally, how are the precursors of the OSMT related to the physics of Hund metals?

In this paper, we use a minimal model (see motivation below) for orbital differentiation in Hund metals to answer these questions in a unified picture. Our conceptual arguments are supported by a numerical method of unprecedented accuracy: we use the numerical renormalization group (NRG) [14] as real-frequency impurity solver for dynamical mean-field theory (DMFT) [15], extending the tools of Ref. 16 from full SU(3) to reduced orbital symmetry. Whereas different bandwidths directly lead to different effective interaction strengths among the orbitals (as extensively studied for two-orbital models; see [17] for a list of references), we focus here on the more intricate case where a crystal field shifts one orbital in energy w.r.t. two degenerate orbitals [18–22]. Thereby, we can isolate polarization effects and drive the system through band+Mott insulating, metallic, and OSM phases, reminiscent of $\mathrm{Ca}_2\mathrm{RuO}_4$ [13], $\mathrm{Sr}_2\mathrm{RuO}_4$ [23], and FeSCs, respectively.

Theoretically, the OSMP has been under debate both w.r.t. the precise form of the (conducting) self-energy [18, 21, 24–26] and w.r.t. subpeaks in the insulating spectral function [20, 26–28]. Whereas previous studies were limited by finite-size effects of exact diagonalization or finite temperature in Monte Carlo data (requiring analytic continuation), our NRG results yield conclusive numerical evidence down to the lowest energy scales. We give a detailed phase diagram including coexistence regimes (lacking hitherto) and characterize the individual phases with real-frequency properties and their relation to Kondo temperatures spanning several orders of magnitude. Upon approaching the OSMT, we find a strongly suppressed spin coherence scale and uncover the emergence of a singular Fermi liquid [24, 29–32] and interband doublon-holon excitations [33–36] (both of which were previously realized only separately and in two-orbital models).

II. MODEL AND METHOD

The Hamiltonian of our three-orbital Hubbard model is given by

$$\hat{H} = -t \sum_{\langle ij \rangle m\sigma} \hat{d}^\dagger_{im\sigma} \hat{d}_{jm\sigma} + \sum_i \hat{H}_{\mathrm{int}}[\hat{d}_{im\sigma}] + \sum_{im} \epsilon_m \hat{n}_{im},$$

where $\hat{d}^\dagger_{im\sigma}$ creates an electron on lattice site i in orbital $m \in \{1, 2, 3\}$ with spin $\sigma \in \{\uparrow, \downarrow\}$. The first term describes nearest-neighbor hopping within each orbital on the lattice of uniform amplitude $t = 1$, which thus sets the unit of energy. As local interaction, we use the following "minimal rotationally invariant" form [12, 16, 37, 38],

$$\hat{H}_{\rm int}[\hat{d}_{m\sigma}] = \tfrac{3}{4}J\hat{n} + \tfrac{1}{2}\big(U - \tfrac{3}{2}J\big)\hat{n}\big(\hat{n} - 1\big) - J\hat{\boldsymbol{S}}^2.$$

Here, $\hat{\boldsymbol{S}} = \sum_m \hat{\boldsymbol{S}}_m$ is the total spin operator; $\hat{n} = \sum_m \hat{n}_m$, $\hat{n}_m = \sum_\sigma \hat{n}_{m\sigma}$, and $\hat{n}_{m\sigma} = \hat{d}^\dagger_{m\sigma}\hat{d}_{m\sigma}$ are number operators with expectation values n, n_m, and $n_{m\sigma}$, respectively. This interaction yields an intraorbital Coulomb interaction of size U, interorbital Coulomb interactions of size $U - J$ and $U - 2J$ for opposite and equal spins, respectively, and a spin-flip term proportional to J [cf. Eq. (B1)]. With only two parameters, it exhibits the full SU(3) symmetry, as opposed to the SO(3) symmetry of the usual Hubbard-Kanamori Hamiltonian [12, 39]. We mostly fix these parameters to $U = 6$ and $J = 1$.

Our only source of orbital differentiation comes from the last term in $\hat{H}$ via the crystal-field splitting Δ, defined as relative shift among the onsite energies (cf. Fig. 1): $\epsilon_1 - \Delta = \epsilon_2 = \epsilon_3 \equiv \epsilon_{23}$. (The index "23" indicates shared properties of the degenerate doublet, e.g., $n_{23} \equiv n_2 = n_3$). The overall shift of ϵ_m is determined by the average filling $n = 2$, taken one away from half filling as characteristic for Hund metals. Note that, for J to act nontrivially, this setting requires at least three orbitals. While the effect of Δ in uncorrelated systems is rather straightforward, the interplay of Δ with U and especially J in Hund metals leads to intriguing phenomena.

Within the DMFT approximation, the lattice Hamiltonian is mapped to an impurity problem with self-consistently determined hybridization [15]. We use a semicircular lattice density of states (half-bandwidth 2), for convenience, and restrict ourselves to paramagnetic solutions at zero temperature ($T = 10^{-8}$, in practice). The impurity problem is solved on the real-frequency axis by means of the full-density matrix [40] NRG. The numerical challenge of three orbitals with reduced symmetry is overcome by interleaving the Wilson chains [41, 42] of the 1-orbital and 23-doublet, while fully exploiting the remaining $\mathrm{SU}(2)_{\rm spin} \otimes \mathrm{U}(1)_{\rm charge,1} \otimes \mathrm{U}(1)_{\rm charge,23} \otimes \mathrm{SU}(2)_{\rm orbital,23}$ symmetry, using the QSpace tensor library [43, 44]. We set the overall discretization parameter to $\Lambda = 6$ and keep up to 30000 multiplets ($\sim 2.5 \cdot 10^5$ states) during the iterative diagonalization. While NRG can famously resolve arbitrarily small energy scales very accurately, we also obtain a sufficiently accurate resolution at high energies via adaptive broadening [45, 46] of the discrete spectral data obtained for two different z shifts [47]. As dynamic correlation functions, we compute the impurity self-energy Σ [48], also used to extract the DMFT local spectral function $\mathcal{A}$, as well as spin and orbital susceptibilities $\chi = \chi' - i\pi\chi''$, defined in Appendix D.

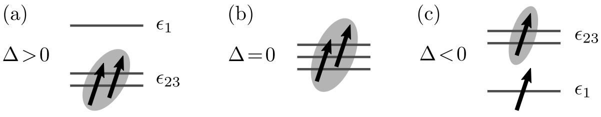

FIG. 1. Illustration of the onsite energies $\epsilon_1 - \Delta = \epsilon_2 = \epsilon_3$ and impurity occupations. Due to Hund's coupling, spins are aligned; shaded arrows symbolize a symmetric distribution among the degenerate orbitals. The different phases portrayed are (a) a band+Mott insulator for large, positive Δ, (b) an orbitally symmetric metal for vanishing Δ, and (c) the OSMP for large, negative Δ, yet $|\Delta| \lesssim 2J$. After a particle-hole transformation and the identification $1 \leftrightarrow xy$, $23 \leftrightarrow xz/yz$, (a) and (b) mimic properties of the t_{2g} orbitals of $\mathrm{Ca_2RuO_4}$ and $\mathrm{Sr_2RuO_4}$, respectively; with a half-filled xy-orbital and further metallic ones, (c) resembles the situation in FeSCs.

III. CRYSTAL-FIELD SPLITTING

As we tune Δ, the system undergoes (for suitable interaction strength) several phase transitions. The nature of the different phases can be easily understood by looking at the occupations in the atomic limit (Fig. 1) [19, 21]: For large $\Delta > 0$, the 1-orbital has highest energy; both electrons reside in the half-filled 23-doublet and are likely to form a Mott insulator [49]. For the symmetric model at $\Delta = 0$, the two electrons are equally distributed among the three degenerate orbitals with occupation $n_m = 2/3$ each, giving rise to metallic behavior (for not too strong interaction). Finally, for large $\Delta < 0$, the filling of the lowest orbital is eventually increased up to half filling, $n_1 = 1$, and the remaining electron occupies the quarter-filled 23-doublet. For intermediate interaction strengths [50], the half-filled 1-orbital is Mott-insulating while the quarter-filled 23-doublet remains metallic, thereby realizing an OSMP. By decreasing Δ even further, one reenters a metallic ($1 < n_1 < 2$) and ultimately a band-insulating phase ($n_1 = 2$).

These considerations anticipate the mechanism driving the phase transitions [18–22]: Δ primarily induces orbital polarization, i.e., it changes the relative *filling* of the orbitals. Starting from the orbitally symmetric, metallic phase, the different orbitals can become band-insulating or undergo a *filling-driven* Mott transition. If there are partially filled orbitals of different occupations and/or degeneracies, as in Fig. 1(c), this leads to different critical interaction strengths for the Mott transition, and an OSMP can be realized.

We now investigate the precise nature of these phase transitions as function of Δ for fixed U, J, n. Figure 2(a) shows the orbital polarization, $p = n_1 - n_{23}$. Starting from the symmetric case ($\Delta = 0$, $p = 0$) and increasing Δ, p decreases to its minimum $p = -1$ [cf. Fig. 1(a)]. For large $\Delta > 0$, we observe a coexistence region when approaching Δ from below or above, giving rise to the definitions $\Delta^{\rm pos}_{c1} \simeq 0.3$, $\Delta^{\rm pos}_{c2} \simeq 0.6$. If we decrease Δ starting from $\Delta = 0$, p increases until it saturates for $\Delta \le \Delta^{\rm neg}_{c} \simeq -0.85$ at $p = 0.5$. This regime constitutes the

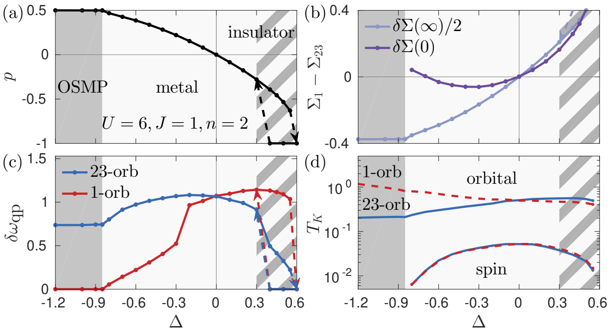

FIG. 2. Phase diagram for varying Δ. (a) The orbital polarization, $p = n_1 - n_{23}$, directly hints at the different phases portrayed in Fig. 1. We find coexisting solutions for $\Delta \in [0.3, 0.6]$ but no hysteresis between metal and OSMP. (b) The self-energy difference, $\delta\Sigma = \mathrm{Re}\Sigma_1 - \mathrm{Re}\Sigma_{23}$, adds to a renormalized Δ. Whereas $\delta\Sigma$ increases with increasing $\Delta > 0$ at both $\omega \in \{\infty, 0\}$, the $\delta\Sigma(0)$ curve (only shown for metallic solutions) bends upward for $\Delta < -0.3$, thereby counteracting the splitting. (c) The full width at half maximum of the quasiparticle peak, $\delta\omega_{\mathrm{qp}}$, confirms the metallic vs. insulating character. In the coexistence regime, either $\delta\omega_{\mathrm{qp}} = 0$ or $\delta\omega_{\mathrm{qp}} > 0$ for all orbitals alike. (d) The orbital and spin Kondo temperatures are clearly separated ($T_K^{\mathrm{orb}} \simeq 0.5$, $T_K^{\mathrm{sp}} \simeq 0.05$ at $\Delta = 0$). Strikingly, T_K^{sp} strongly decreases with increasing $|\Delta|$ and vanishes altogether in the OSMP (out of range on the log scale).

OSMP, for which we find *no* hysteresis w.r.t. Δ. Clearly, the Δ-driven OSMT is much more second-order-like than the ordinary Mott transition at $\Delta > 0$. We also note that, while p appears differentiable at the OSMT, $\mathrm{Var}(\hat{p})$ exhibits a kink [cf. Fig. 8(a)]. The OSMP is stable from Δ_c^{neg} down to $\Delta \simeq -1.5$, where one enters a strongly polarized ($p > 0.5$) metallic phase (not shown).

To address the effect of correlations on orbital differentiation, we examine the difference in the real part of the self-energies, $\delta\Sigma = \mathrm{Re}\Sigma_1 - \mathrm{Re}\Sigma_{23}$, which adds to a renormalized crystal field [20], $\Delta + \delta\Sigma$ [cf. also Fig. 8(b)]. The overall shift of the self-energies is given by the Hartree part, $\Sigma_{\mathrm{H}} = \Sigma(\omega = \infty)$, which can directly be calculated:

$$\Sigma_{\mathrm{H},m\sigma} = U n_{m\bar{\sigma}} + \sum_{m' \neq m} \Big[(U - J) n_{m'\bar{\sigma}} + (U - 2J) n_{m'\sigma} \Big].$$

The difference, $\delta\Sigma_{\mathrm{H}} = -(U - 3J)p/2$, increases monotonically with Δ (via p) for $U - 3J > 0$, such that interactions overall enhance orbital differentiation [12]. However, the renormalization of Δ at low energies must be determined numerically. Figure 2(b) displays $\delta\Sigma$ at $\omega \in \{0, \infty\}$: $\delta\Sigma(0)$ is smaller in magnitude than $\delta\Sigma_{\mathrm{H}}$ (plot shows $\delta\Sigma_{\mathrm{H}}/2$) and increases monotonically with Δ only for $\Delta > -0.3$. For $\Delta < -0.3$, $\delta\Sigma(0)$ bends upward and eventually increases with decreasing Δ, thereby counteracting the splitting.

Next, Fig. 2(c) shows the width of the quasiparticle peak, $\delta\omega_{\mathrm{qp}}$, of the spectral function (cf. Fig. 4) to confirm the conducting vs. insulating character of the different phases. For positive and negative Δ, we indeed find that the 23- and 1-orbital(s), respectively, undergo a Mott transition, with gradually decreasing $\delta\omega_{\mathrm{qp}}$. The sharp decline in $\delta\omega_{\mathrm{qp}}$ around $|\Delta| \sim 0.3$ corresponds to the formation of a subpeak (see below). For $\Delta > 0$, the 1-orbital shows a slight increase of $\delta\omega_{\mathrm{qp}}$ and eventually becomes band-insulating, while, for $\Delta < 0$, $\delta\omega_{\mathrm{qp}}$ of the 23-orbitals decreases until it saturates in the OSMP. Note that the quasiparticle weight, $Z_m = [1 - \partial_\omega \mathrm{Re}\Sigma_m(0)]^{-1}$, often used to describe the single-orbital Mott transition, is not ideal to characterize the full range of orbital differentiation: For $\Delta > 0$, when the 1-orbital gets emptied out, Z_1 increases although the whole quasiparticle peak gradually disappears; for large $\Delta < 0$, Z_1 of the insulating 1-orbital does not vanish throughout the OSMP, yet $Z_{23} = 0$ in the metallic 23-orbitals, as further explained below.

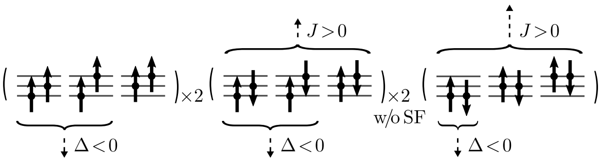

FIG. 3. Illustration of all 15 different impurity states for $n = 2$ in the $\hat{n}_m$, $\hat{S}_m^z$ basis. Finite J and Δ yield a relative shift in the eigenenergies (dashed arrows) and thus split the $J = 0 = \Delta$ groundstate manifold. The states in the middle are eigenstates of the impurity Hamiltonian only without spin-flip (SF) terms, where Hund's coupling merely shifts the density-density interactions by J and $2J$, cf. Eq. (B1); with SU(2) spin symmetry, they form singlet and triplet combinations. Subscripts $\times 2$ indicate that the number of states is counted twice due to spin degeneracy. Without SF terms, the groundstate degeneracy of 15 at $J = 0 = \Delta$ is reduced to 6 at $J > 0$, $\Delta = 0$ and to 4 at $J > 0$, $\Delta < 0$. Including SF terms, these are 15, 9, and 6.

We complete our phase diagram by showing in Fig. 2(d) the Δ-dependence of Kondo temperatures, defined as the energy scale at which the corresponding susceptibility, χ'', is maximal [cf. Fig. 4(c)]. As typical for Hund metals [12, 16], we observe spin–orbital separation in terms of Kondo scales: orbital fluctuations are screened at much higher energies than spin fluctuations ($T_K^{\mathrm{orb}} \gg T_K^{\mathrm{sp}}$). While $T_{K,23}^{\mathrm{orb}}$ characterizes orbital fluctuations within the 23-doublet, $T_{K,1}^{\mathrm{orb}}$ describes those between the (separated) 1-orbital and the 23-doublet [cf. Eq. (D2)] and reduces to the bare energy scale $\sim |\Delta|$ for large splitting. At sizable J, both orbitals have the same T_K^{sp} [53], and, strikingly, T_K^{sp} strongly decreases with increasing $|\Delta|$.

This can be understood as follows: It is well-known that finite J decreases T_K^{sp} [12, 54, 55], as it splits the impurity groundstate manifold. Intuitively, a smaller groundstate degeneracy implies a reduced effective hybridization and thus a reduced Kondo temperature. For $J > 0$ and finite Δ, the groundstate degeneracy is reduced even further, particularly for $\Delta < 0$, see Fig. 3. Moreover, the DMFT self-consistency suppresses the low-energy hybridization strength of the orbital approaching the Mott transition. In the OSMP, $\mathcal{A}_1(0)$ and T_K^{sp} eventually vanish altogether.

Let us now examine in detail how the spectral functions

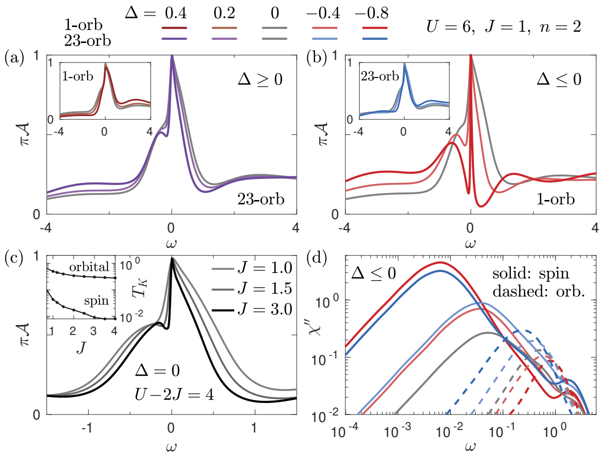

FIG. 4. (a,b) Spectral functions in the metallic phase for the orbitals approaching a Mott transition (main panels) and the remaining ones (insets). (b) Decreasing Δ sharpens the quasiparticle peak (reduced T_K^{sp}), destroys the orbital resonance if $|\Delta| \gtrsim T_K^{\mathrm{orb}}(\Delta = 0)/2$, and generates interband doublon-holon subpeaks. (c) Spectral functions and Kondo temperatures (inset) in the orbitally symmetric case for increasing J and fixed $U - 2J$. (d) Spin (solid lines) and orbital (dashed) susceptibilities corresponding to (b). (For $\Delta \neq 0$, we plot χ_1^{sp} and $4\chi_{23}^{\mathrm{sp}}$ to have the two curves for each Δ closer together.)

change with Δ in the metallic phase. Figures 4(a,b) show that, for both positive and negative Δ, the most important change with stronger correlations occurs in the orbital(s) approaching a Mott transition (main panels). The other orbitals (insets) mostly adjust the spectral weight. At $\Delta = 0$ [gray lines in Figs. 4(a–c)], the spectral functions exhibit the typical shoulder in the quasiparticle (qp) peak [16, 55] (below half filling at $\omega < 0$). In Ref. [55], this has been explained as the combination of a sharp SU(2) spin Kondo resonance ("needle" with width $\propto T_K^{\mathrm{sp}}$) and a wider SU(3) orbital Kondo resonance ("base" with width $\propto T_K^{\mathrm{orb}}$). If we first stay with the orbitally symmetric case [Fig. 4(c)] and use J and $E_{\mathrm{at}} = U - 2J$ as tuning parameters [55], we can reduce T_K^{sp} by increasing J while only mildly affecting T_K^{orb}. As a consequence, the needle sharpens while the wide base remains, revealing a subpeak.

Similarly, increasing $|\Delta|$ drastically decreases T_K^{sp} [Figs. 2(d), 4(d)] and causes a thin qp needle. Additionally, finite Δ, which acts in orbital space similar to a magnetic field in spin space, splits the qp base. For $|\Delta| \gtrsim T_K^{\mathrm{orb}}$, the orbital Kondo resonance is destroyed and subpeaks on both sides of $\omega = 0$ remain. In fact, the orbital-resonance shoulder is remarkably accurately centered at $-T_K^{\mathrm{orb}}(\Delta{=}0)/2$ [Fig. 4(c)], and crosses over to an interband doublon-holon excitation at $\Delta < 0$ (see below) for $|\Delta| \gtrsim T_K^{\mathrm{orb}}(\Delta{=}0)/2$. Note that the authors of Ref. [38] similarly marked strong influence of J by $J \gtrsim T_K^{\mathrm{orb}}(J{=}0)$.

Generally, finite Δ amplifies Hund-metal features in some orbitals while suppressing them in others. This is apparent in spectral functions (Fig. 4) as well as self-energies, see Fig. 5. For $\Delta = 0$, we find the typical [23, 56] inverted slope in $\mathrm{Re}\Sigma$ for small $\omega < 0$ and kink in $\mathrm{Re}\Sigma$ for small $\omega > 0$ (with $\mathrm{Im}\Sigma$ related by Kramers–Kronig transform). These features are enhanced as the orbital becomes more correlated, and suppressed as it becomes less correlated. The degree of correlation follows from proximity to half filling: n_1 approaches 1 as Δ decreases; n_{23} approaches 1 as Δ increases.

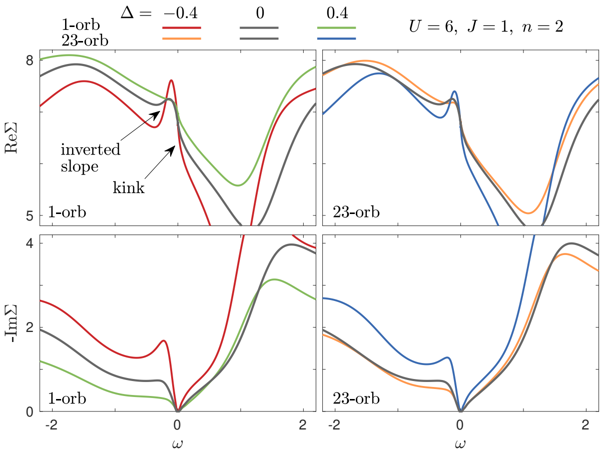

FIG. 5. Metallic self-energies for all orbitals, for different Δ. The characteristic features, such as an inverted slope and a kink, already present at $\Delta = 0$, are enhanced as the orbital becomes more correlated, induced by proximity to half filling: n_1 (n_{23}) approaches 1 with increasing (decreasing) Δ.

IV. OSMP

For $\Delta \leq -0.85$, T_K^{sp} and the qp needle vanish altogether; the 1-orbital becomes a Mott insulator while the 23-doublet retains spectral weight at $\omega = 0$ [Fig. 6(a)]. In the metallic orbitals, Luttinger pinning [57] via the semicircular lattice density of states ρ, with $\mathcal{A}_{23}(0) = \rho(x_n)$ and $\int_{-\infty}^{x_n} \rho(x)\mathrm{d}x = n_{23,\sigma}$, is fulfilled throughout [leading to $\pi\mathcal{A}_{23}(0) \approx 0.91$ at quarter filling $n_{23,\sigma} = 1/4$]. Yet, the spectral function of the half-filled 1-orbital strongly differs from a single-orbital Mott insulator. Next to the standard Hubbard bands, charge fluctuations in the 23-doublet enable interband doublon-holon excitations (previously identified in a two-band DMFT+DMRG study [35]; cf. [33, 34] for experimental signatures) in the insulating spectral function. Here, they occur at energies Δ and $\Delta + 2J$, as derived in Appendix B. These gap-filling states give $\mathcal{A}_1$ its soft form. They are shifted with Δ, leading to a "tilt" of $\mathcal{A}_1$ around $\omega = 0$. A hard gap is revealed when pushing the subpeaks apart (via J) and decreasing their weight (via $E_{\mathrm{at}} = U - 2J$) by suppressing 23-charge fluctuations [Fig. 6(b)]. The subpeaks' distinct nature [46, 58] is further underlined in plots of the momentum-

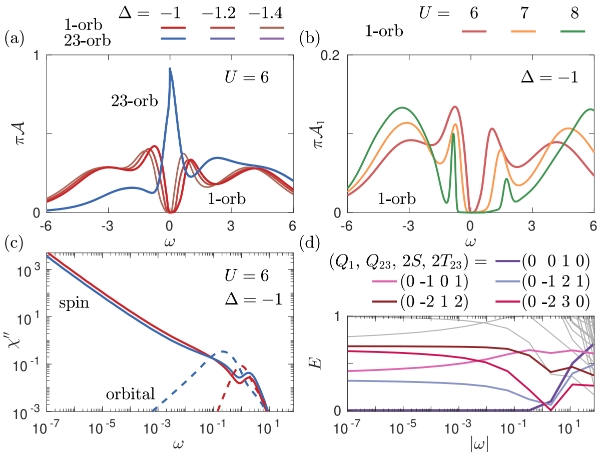

FIG. 6. Characterization of the OSMP. (a) Spectral functions showing the insulating and metallic character of the 1- and 23-orbital(s), respectively. Interband doublon-holon excitations are seen as subpeaks in $\mathcal{A}_1$, whose position shifts with Δ, leading to a tilt of $\mathcal{A}_1$ around $\omega = 0$; the $\mathcal{A}_{23}$ curves all lie on top of each other. (b) Close up of the insulating spectral function at variable U (only in this panel), with $J/U = 1/6$ fixed. Increasing J shifts the right subpeak towards larger energies, and increasing $E_{\text{at}} = U - 2J$ decreases the weight of the subpeaks by suppressing charge fluctuations in the 23-doublet. Both effects help to reveal a hard spectral gap. (c) Diverging spin (solid lines) and regular orbital (dashed) susceptibilities. (We again plot $4\chi^{\text{sp}}_{23}$.) (d) NRG flow diagram of the rescaled, lowest-lying energy levels at characteristic level spacing $\sim |\omega|$. The legend provides charge Q_m, total spin S, and SU(2) orbital T_{23} quantum numbers. The groundstate carries a residual spin 1/2 since the contribution to the impurity spin from the insulating 1-orbital cannot be screened. The SFL nature entails that the flow approaches the Fermi-liquid fixed point (where the first and second as well as third and fourth excitations become degenerate) only asymptotically.

resolved spectral function, shown in Appendix C, where one can also see how the widths of the 23-qp peak and 1-orbital subpeaks narrow together with increasing E_{at}.

As the insulating 1-orbital does not contribute to spin screening, the OSMP inherits properties of an underscreened (spin) Kondo effect [32], as manifested in a divergent spin susceptibility [Fig. 6(c)]. Within our DMFT description of the OSMP, the impurity electron in the 1-orbital and that in the 23-doublet form a combined spin 1, due to Hund's coupling. However, the 1-orbital hybridization ($\propto \mathcal{A}_1$) has zero weight at low enough energies. Hence, given the diagonal hybridization, only the 23-contribution to the impurity spin can be screened, while its 1-orbital contribution remains unscreened. The underscreened Kondo effect in turn leads to the singular Fermi-liquid (SFL) state of the OSMP, as strikingly evident in the NRG flow diagram [14, 16, 55]: Fig. 6(d) shows that the rescaled, lowest-lying energy levels of the iteratively diagonalized Wilson chain reach the Fermi-liquid (FL) fixed point only asymptotically [30].

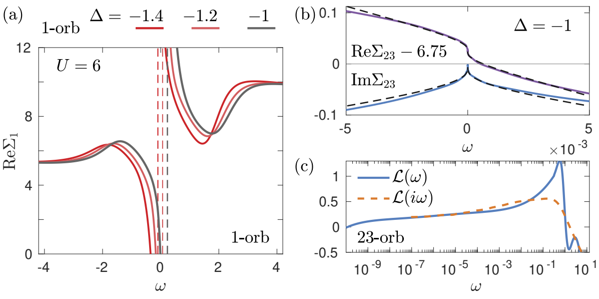

FIG. 7. Self-energies in the OSMP. (a) Real part of the insulating 1-orbital self-energy. Upon decreasing Δ in the OSMP, the position of the singularity in Σ_1 (marked by dashed lines) shifts through $\omega = 0$. (b) Low-energy zoom of the self-energy in the metallic 23-orbitals (solid lines) with fits (dashed) to the SFL logarithmic singularities. (c) The logarithmic derivative $\mathcal{L}(z)$ of $-\text{Im}\Sigma_{23}$ vanishes as $z \to 0$, providing additional confirmation of the logarithmic nature of the singularity.

The self-energy of the insulating 1-orbital diverges. In Fig. 7(a), we see that the singularity of Σ_1 is not bound to $\omega = 0$; instead, its position shifts with Δ. This implies that $Z_1 = 1/(1 - \partial_\omega \text{Re}\Sigma_1(0))$ does not vanish throughout the OSMP and is thus not suited to mark the insulating character of the 1-orbital in the OSMP. A low-energy zoom of the self-energy in the metallic 23-orbitals [Fig. 7(b)] reveals strong deviations from the standard zero-temperature FL form, $\text{Re}\Sigma_{\text{FL}} = a + b\omega$ and $\text{Im}\Sigma_{\text{FL}} = -|c|\omega^2$. Instead, it exhibits logarithmic singularities that can be well fitted [dashed lines in Fig. 7(b)] to the SFL relations [24, 32, 59]

$$\begin{aligned} \text{Re}\Sigma_{\text{SFL}} &= \tilde{a} + \tilde{b}\,\text{sgn}(\omega) \ln^{-3}|\omega/T^*|, \\ \text{Im}\Sigma_{\text{SFL}} &= -|\tilde{c}| \ln^{-2}|\omega/T^*|. \end{aligned}$$

The logarithmic singularity in Σ_{23} implies that $Z_{23} = 0$ despite the conducting character of the 23-orbitals with finite spectral weight at the Fermi level [Fig. 6(a)]. To further scrutinize the singularity, we consider the logarithmic derivative of the imaginary part of Σ_{23},

$$\mathcal{L}(z) = \frac{\mathrm{d}\ln[-\text{Im}\Sigma_{23}(z)]}{\mathrm{d}\ln z},$$

both for real frequencies, $z = \omega + i0^+$ with $\omega \in \mathbb{R}$, and for imaginary frequencies, $z = i\omega \in (2\mathbb{Z}+1)i\pi T$. This quantity is well suited to discriminate between singularities of logarithmic or fractional power-law type:

$$\begin{aligned} -\text{Im}\Sigma(z) &= |c'|z^\alpha &&\Rightarrow \quad \mathcal{L}(z) = \alpha, \\ -\text{Im}\Sigma(z) &= |\tilde{c}| \ln^{-2}(z/T^*) &&\Rightarrow \quad \mathcal{L}(z) = -2\ln^{-1}(z/T^*) \\ & && \qquad \xrightarrow[z\to 0]{} 0. \end{aligned}$$

In Fig. 7(c), we clearly see that $\mathcal{L}(0) = 0$, confirming the logarithmic nature of the singularity. Note that a smoothening postprocessing was used to suppress minor oscillations in very small values of ImΣ. The imaginary-frequency data $\mathcal{L}(i\omega)$, available for $|i\omega| \geq \pi T$, perfectly matches the low-frequency behavior but does not suffice to follow the decay up to $\mathcal{L}(0) = 0$. In fact, if the imaginary-frequency data were available only in a limited temperature range, as is the case in Monte Carlo studies, say, $T \gtrsim 10^{-3}$ and $|i\omega| \gtrsim \pi \cdot 10^{-3}$, one might easily be tempted to conclude that $\mathcal{L}(i\omega)$ saturates at $\alpha \approx 0.5$.

V. CONCLUSION

We have shown that DMFT+NRG can be used to study three-orbital Hubbard models with reduced orbital symmetry, used this method to accurately describe polarization-driven phase transitions induced by a crystal field Δ, and uncovered the rich real-frequency structure inherent in the interplay of Hund-metal physics and orbital differentiation. Our analysis leads to a conclusion of major conceptual significance: The popular notion that orbital screening, facilitated by J, makes the orbitals behave almost independently [8–10, 12, 18, 26, 49, 60] (as seen, e.g., in static correlations [18, 26, 60], cf. also Fig. 8(a)) misses the importance of spin fluctuations. It must be revised when looking at dynamic correlation functions, as (i) a suppressed hybridization in one orbital suppresses the spin Kondo temperature of *all* orbitals (at sizable J), (ii) charge fluctuations in some orbitals enable interband doublon-holon excitations [35] in the spectrum of other orbitals, and (iii) the presence of localized spins implies singular Fermi-liquid behavior of the remaining itinerant electrons [32].

With our methodological advances, NRG is ready to be used as real-frequency impurity solver in a DFT+DMFT description of three-orbital materials with reduced orbital symmetry. Future studies should further investigate the stability of the OSMP against interorbital hopping [61].

ACKNOWLEDGMENTS

We thank A. Georges and K. M. Stadler for fruitful discussions, and K. Hallberg for a helpful correspondence. FBK, S-SBL, and JvD were supported by the Deutsche Forschungsgemeinschaft under Germany's Excellence Strategy–EXC-2111–390814868; S-SBL further by Grant. No. LE3883/2-1. FBK acknowledges funding from the research school IMPRS-QST. AW was funded by DOE-DE-SC0012704. GK was supported by NSF-DMR-1733071.

Appendix A: Additions to the phase diagram

In the discussion oft the phase diagram in Fig. 2, we mentioned that the polarization $p = \langle \hat{p} \rangle$, with $\hat{p} = \hat{n}_1 - \hat{n}_{23}$ and $\hat{n}_{23} = (\hat{n}_2 + \hat{n}_3)/2$, varies with Δ in a differentiable way throughout the OSMT. Regarding the nature of the phase transition, it is then interesting to note that $\mathrm{Var}(\hat{p}) = \langle \hat{p}^2 \rangle - \langle \hat{p} \rangle^2$ exhibits a kink at the OSMT [Fig. 8(a)]. Further, we have elaborated on the intricate interorbital effects on dynamic correlation functions, such as a strongly suppressed spin coherence scale, singular Fermi-liquid behavior, and interband doublon-holon excitations. These effects are completely hidden when looking at static properties like the interorbital correlator $\mathrm{Cov}(\hat{n}_1, \hat{n}_{23}) = |\langle \hat{n}_1 \hat{n}_{23} \rangle - \langle \hat{n}_1 \rangle \langle \hat{n}_{23} \rangle|$, which, generally, is rather weak [Fig. 8(b)] and has a kink at Δ_c^{neg} analogous to $\mathrm{Var}(\hat{p})$ [18, 26].

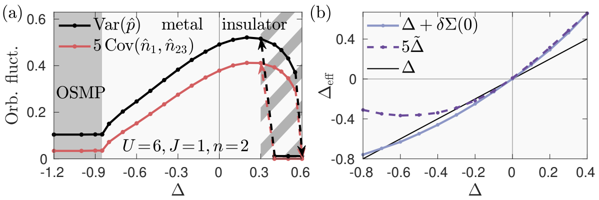

FIG. 8. Additions to the Δ phase diagram. (a) $\mathrm{Var}(\hat{p}) = \langle \hat{p}^2 \rangle - \langle \hat{p} \rangle^2$ and $\mathrm{Cov}(\hat{n}_1, \hat{n}_{23}) = |\langle \hat{n}_1 \hat{n}_{23} \rangle - \langle \hat{n}_1 \rangle \langle \hat{n}_{23} \rangle|$ exhibit a kink at the OSMT. The latter shows that static, interband correlations are rather weak (plot shows 5 Cov). (b) Two different versions of an effective crystal field (shown only for metallic solutions), $\Delta + \delta\Sigma(0)$ as relevant for electronic degrees of freedom and $\tilde{\Delta} = Z_1 \cdot (\epsilon_1 + \Sigma_1(0)) - Z_2 \cdot (\epsilon_{23} + \Sigma_{23}(0))$ for quasiparticle excitations. Both show similar behavior: They depend monotonically on Δ in a region around $\Delta = 0$ but bend upward for large, negative Δ, counteracting the splitting.

To gauge the influence of correlations on orbital differentiation, we investigated $\delta\Sigma(0) = \Sigma_1(0) - \Sigma_{23}(0)$, which contributes to a renormalized crystal field, $\Delta + \delta\Sigma(0)$, for electronic degrees of freedom. An alternative definition for an effective crystal field, Δ_{eff}, is given by $\tilde{\Delta} = Z_1 \cdot (\epsilon_1 + \Sigma_1(0)) - Z_2 \cdot (\epsilon_{23} + \Sigma_{23}(0))$, which constitutes a splitting for quasiparticle excitations [20]. Figure 8(b) shows that both variants of Δ_{eff} vary similarly with Δ: In a region around $\Delta = 0$, the self-energy difference $\delta\Sigma(0)$ increases the magnitude of Δ_{eff}, i.e., $\delta\Sigma(0) > 0$ for $\Delta > 0$ and $\delta\Sigma(0) < 0$ for moderate $\Delta < 0$. However, for large, negative Δ, we find that $\delta\Sigma(0) > 0$ for $\Delta < 0$, thus decreasing $|\Delta_{\mathrm{eff}}|$. The quasiparticle effective crystal field, $\tilde{\Delta}$, is much smaller in magnitude than the bare crystal field, but, nonetheless, shows a similar trend as $\Delta + \delta\Sigma(0)$: it depends monotonically on Δ in a region around $\Delta = 0$ but bends upward for large, negative Δ, thereby counteracting the splitting.

Appendix B: Doublon-holon excitations

The spectrum of the insulating 1-orbital in the OSMP can be qualitatively explained from the atomic level structure. In the atomic limit, the groundstate consists of eigenstates of the impurity Hamiltonian with one electron in the 1- and 23-orbital(s) each (the first contribution to $|G\rangle$ in Fig. 9(b), marked in red, is a representative).

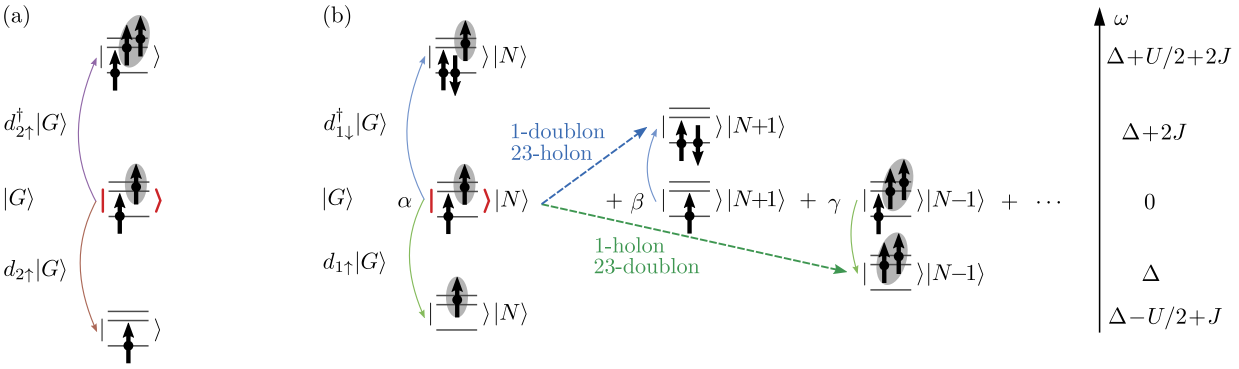

FIG. 9. (a) Groundstate $|G\rangle$ in the atomic limit at $\Delta < 0$, yet $|\Delta| \lesssim 2J$, and single-particle and -hole excitations in the 23-doublet. Shaded arrows symbolize a symmetric distribution over the degenerate orbitals. (b) Illustration of interband doublon-holon excitations in the OSMP. The occupation of the insulating 1-orbital is pinned to 1; however, the metallic 23-doublet still exhibits charge fluctuations. Then, $|G\rangle$ is a mixture of states, where the dominant impurity occupation is 2 (state marked red), and subleading contributions have impurity occupation 1 and 3 ($|\alpha|^2 \gg |\beta|^2, |\gamma|^2$). At fixed filling, the residual charge is carried by the bath (second "ket"). Single-particle and -hole excitations on top of the dominant contribution to the groundstate mark the 1-orbital Hubbard bands. Analogous excitations on the subleading terms lead to states which again have impurity occupation 2. If we relate these states to the dominant first part, we can identify them as interband doublon-holon excitations [35]: the charge on the impurity remains the same while an electron is removed in the 23-orbital and added in the 1-orbital (dashed blue line), or added in the 23-orbital and removed in the 1-orbital (dashed green). The location of the excitations in the 1-orbital spectral function (right, vertical axis) can be deduced from the atomic energy levels [see Eqs. (B7) and (B9)].

However, the metallic character of the 23-orbitals implies charge fluctuations, such that the actual groundstate also contains admixtures from states where the 23-levels of the impurity are empty or doubly occupied [second and third contribution to $|G\rangle$ in Fig. 9(b)]. At fixed filling, the residual charge is carried by the bath [second "ket" in the tensor-product notation of Fig. 9(b)].

At large interaction, the first term of $|G\rangle$ with impurity occupation 2 is dominant. Single-particle and -hole excitations in the 1-orbital on top of this state mark the Hubbard bands [first "column" in Fig. 9(b)]. Single-particle and -hole excitations to the other contributions make states accessible which are inaccessible in the atomic limit [second and third "column" in Fig. 9(b)]. If we relate these states to the *dominant* part of the groundstate, we can identify them as interband doublon-holon excitations [35]: the charge on the impurity remains 2 while an electron is removed in the 23-orbital and added in the 1-orbital [blue dashed line in Fig. 9(b)] or vice versa (green dashed line).

We can also estimate the positions of both the Hubbard bands and the doublon-holon peaks in $\mathcal{A}_1$ from the atomic level structure. To this end, we first recall the impurity Hamiltonian, $\hat H_\text{imp} = \sum_m \epsilon_m \hat n_m + \hat H_\text{int}$, with

$$H_\text{int} = U\sum_m \hat n_{m\uparrow}\hat n_{m\downarrow} + (U-J)\sum_{m\neq m'} \hat n_{m\uparrow}\hat n_{m'\downarrow} + (U-2J)\sum_{m<m',\sigma} \hat n_{m\sigma}\hat n_{m'\sigma} - J\sum_{m\neq m'} \hat d^\dagger_{m\uparrow}\hat d_{m\downarrow}\hat d^\dagger_{m'\downarrow}\hat d_{m'\uparrow}. \tag{B1}$$

The groundstate energy can be estimated from the impurity eigenstate with dominant weight, having one electron in the 1-orbital and another spin-aligned one in the 23-doublet, as $E_G = \epsilon_1 + \epsilon_{23} + (U-2J)$. The difference in onsite energies is determined by the crystal field, $\Delta = \epsilon_1 - \epsilon_{23}$, and the occupation of $n_1 = 1$ in the OSMP sets a range for their overall shift. Additionally, a specific value for ϵ_{23} can be found by looking at charge fluctuations in the 23-doublet, as shown next.

Charge fluctuations in the 23-orbitals

Charge fluctuations in the 23-doublet on top of the dominant groundstate contribution connect the states shown in Fig. 9(a) with atomic energies

$$E^+_\text{HB,23} = \epsilon_1 + 2\epsilon_{23} + 3(U-2J), \tag{B2a}$$
$$E^-_\text{HB,23} = \epsilon_1. \tag{B2b}$$

The energy cost for the respective transitions, giving the position of Hubbard bands in the 23-doublet, is

$$\delta E^+_\text{HB,23} = E^+_\text{HB,23} - E_G = \epsilon_{23} + 2(U-2J), \tag{B3a}$$
$$\delta E^-_\text{HB,23} = E^-_\text{HB,23} - E_G = -\epsilon_{23} - (U-2J). \tag{B3b}$$

Equilibrium at filling 2 is thus obtained when

$$\delta E^+_\text{HB,23} = \delta E^-_\text{HB,23} \quad \Rightarrow \quad \epsilon_{23} = -\tfrac{3}{2}(U-2J). \tag{B4}$$

Inserting the values $U = 6$ and $J = 1$ mostly used, this means $\epsilon_{23} = -6$ and $\delta E^\pm_\text{HB,23} = 2$, corresponding to the bumps in $\mathcal{A}_{23}$ at $\omega = \pm 2$ [Fig. 6(a)].

Hubbard bands in the 1-orbital

Single-particle and -hole excitations in the 1-orbital on top of the dominant groundstate contribution lead to the states shown in the first "column" of Fig. 9(b) with energies

$$E^+_{\mathrm{HB},1} = 2\epsilon_1 + \epsilon_{23} + U + (U-J) + (U-2J), \tag{B5a}$$

$$E^-_{\mathrm{HB},1} = \epsilon_{23}. \tag{B5b}$$

Excitations to these states mark the 1-orbital Hubbard bands, which are found in the spectral function at

$$\delta E^+_{\mathrm{HB},1} = E^+_{\mathrm{HB},1} - E_G = \epsilon_1 + 2U - J, \tag{B6a}$$

$$-\delta E^-_{\mathrm{HB},1} = E_G - E^-_{\mathrm{HB},1} = \epsilon_1 + U - 2J. \tag{B6b}$$

Inserting the value for $\epsilon_1 = \Delta + \epsilon_{23}$ from Eq. (B4) yields

$$\delta E^+_{\mathrm{HB},1} = \Delta + \tfrac{1}{2}U + 2J, \tag{B7a}$$

$$-\delta E^-_{\mathrm{HB},1} = \Delta - \tfrac{1}{2}U + J. \tag{B7b}$$

If we further insert the values $\Delta = -1$, $U = 6$, and $J = 1$ of Fig. 6(a), we get the peak positions -3 and 4. Increasing U up to 8, with $J = U/6$ as in Fig. 6(b), increases their magnitude up to $-3\frac{2}{3}$ and $5\frac{2}{3}$, respectively. These numbers match the curves in Fig. 6(a,b) very well.

Doublon-holon subpeaks

The doublon-holon excitation energies are found from single-particle or -hole excitations on top of the subleading contributions to the groundstate with an empty or doubly occupied 23-doublet [second and third "column" of Fig. 9(b)]. The atomic energies of the excited states are

$$E^+_{d_1h_{23}} = 2\epsilon_1 + U, \tag{B8a}$$

$$E^-_{h_1d_{23}} = 2\epsilon_{23} + (U-2J). \tag{B8b}$$

The energy difference to the dominant groundstate contribution [dashed lines in Fig.9(b)] gives the position of the subpeaks in the insulating spectral function. Using $\epsilon_1 - \epsilon_{23} = \Delta$, we have

$$\delta E^+_{d_1h_{23}} = E^+_{d_1h_{23}} - E_G = \Delta + 2J, \tag{B9a}$$

$$-\delta E^-_{h_1d_{23}} = E_G - E^-_{h_1d_{23}} = \Delta. \tag{B9b}$$

Interestingly, these peak positions only depend on the difference of the energy levels, Δ, and on Hund's coupling, J. Inserting the values for Fig. 6(a) gives -1 and $+1$, and those for Fig. 6(b) yield -1 and $1 + U/3$, in perfect agreement with the plots.

Both the charge fluctuations in the 23-doublet and the interband doublon-holon excitations are determined by the same subleading contributions to the groundstate (such as the terms with coefficients $|\beta|^2$ and $|\gamma|^2$ in Fig. 9). Hence, the widths of the quasiparticle peak in the 23-doublet and the subpeaks in the 1-orbital are closely tied together. By increasing $E_{\mathrm{at}} = U - 2J$, one can then decrease both the widths of the 23-quasiparticle peak and the 1-subpeaks. On the other hand, by tuning Δ and J at constant E_{at}, one can shift the positions of the 1-subpeaks, while the weights of the 23-quasiparticle peak and the 1-subpeaks remain roughly the same.

Appendix C: Momentum-resolved spectral function

In Fig. 10, we plot the local spectral function, $\mathcal{A}(\omega)$, together with the momentum-resolved one, $\mathcal{A}(\omega, \epsilon_{\mathbf{k}})$. As explained in the caption, strong particle-hole asymmetry, decreasing quasiparticle weight, and localization of the 1-electrons can be nicely seen. Moreover, it is interesting to observe that the crossover between the $\omega < 0$ shoulder and the interband doublon-holon subpeak at Δ is accompanied by a transfer of spectral weight from $\epsilon_{\mathbf{k}} < 0$ to $\epsilon_{\mathbf{k}} > 0$. In the OSMP, the doublon-holon subpeak at $\omega < 0$, $\epsilon_{\mathbf{k}} > 0$ can be very well distinguished from the Hubbard band at $\omega < 0$, $\epsilon_{\mathbf{k}} < 0$. Especially in the momentum-resolved plot, these *interband* doublon-holon subpeaks resemble the *intraband* doublon-holon subpeaks known from the single-orbital strongly correlated metallic phase [46, 58].

Appendix D: Susceptibilities

Here, we give the definitions for the various susceptibilities computed. The total spin operator is given by $\hat{\boldsymbol{S}} = \sum_m \hat{\boldsymbol{S}}_m$ with $\hat{\boldsymbol{S}}_m = \frac{1}{2}\sum_{\sigma\sigma'} \hat{d}^\dagger_{m\sigma} \boldsymbol{\tau}_{\sigma\sigma'} \hat{d}_{m\sigma'}$ and Pauli matrices $\boldsymbol{\tau}$. We further define $\hat{\boldsymbol{S}}_{23} = (\hat{\boldsymbol{S}}_2 + \hat{\boldsymbol{S}}_3)/2$, and mainly compute the spin susceptibilities

$$\chi^{\mathrm{sp}}_1 = \tfrac{1}{3}\sum_{\alpha=1}^{3} \langle \hat{S}^\alpha_1 || \hat{S}^\alpha_1 \rangle_\omega, \ \chi^{\mathrm{sp}}_{23} = \tfrac{1}{3}\sum_{\alpha=1}^{3} \langle \hat{S}^\alpha_{23} || \hat{S}^\alpha_{23} \rangle_\omega. \tag{D1}$$

Further, we use the angular-momentum operator $\hat{\boldsymbol{L}}$ with $\hat{L}_m = i\sum_\sigma \sum_{m'm''} \epsilon_{mm'm''} \hat{d}^\dagger_{m'\sigma} \hat{d}_{m''\sigma}$ and compute orbital susceptibilities according to $\hat{L}_{23} = (\hat{L}_2 + \hat{L}_3)/2$ and

$$\chi^{\mathrm{orb}}_1 = \langle \hat{L}_{23} || \hat{L}_{23} \rangle_\omega, \quad \chi^{\mathrm{orb}}_{23} = \langle \hat{L}_1 || \hat{L}_1 \rangle_\omega. \tag{D2}$$

In fact, as the system exhibits full SU(2) orbital symmetry in the 23-doublet, we can also use the fully symmetrized $\hat{\boldsymbol{T}}_{23} = \frac{1}{2}\sum_\sigma \sum_{m,m' \in \{2,3\}} \hat{d}^\dagger_{m\sigma} \boldsymbol{\tau}_{mm'} \hat{d}_{m'\sigma}$ and

$$\chi^{\mathrm{orb}}_{23} = \tfrac{1}{3}\sum_{\alpha=1}^{3} \langle \hat{T}^\alpha_{23} || \hat{T}^\alpha_{23} \rangle_\omega. \tag{D3}$$

In the literature, orbital susceptibilities are sometimes computed from charge fluctuations in the individual orbitals. In this language, with $\hat{n}_{23} = (\hat{n}_2 + \hat{n}_3)/2$, one has

$$\chi^{\mathrm{ch}}_1 = \langle \hat{n}_1 || \hat{n}_1 \rangle_\omega, \quad \chi^{\mathrm{ch}}_{23} = \langle \hat{n}_{23} || \hat{n}_{23} \rangle_\omega. \tag{D4}$$

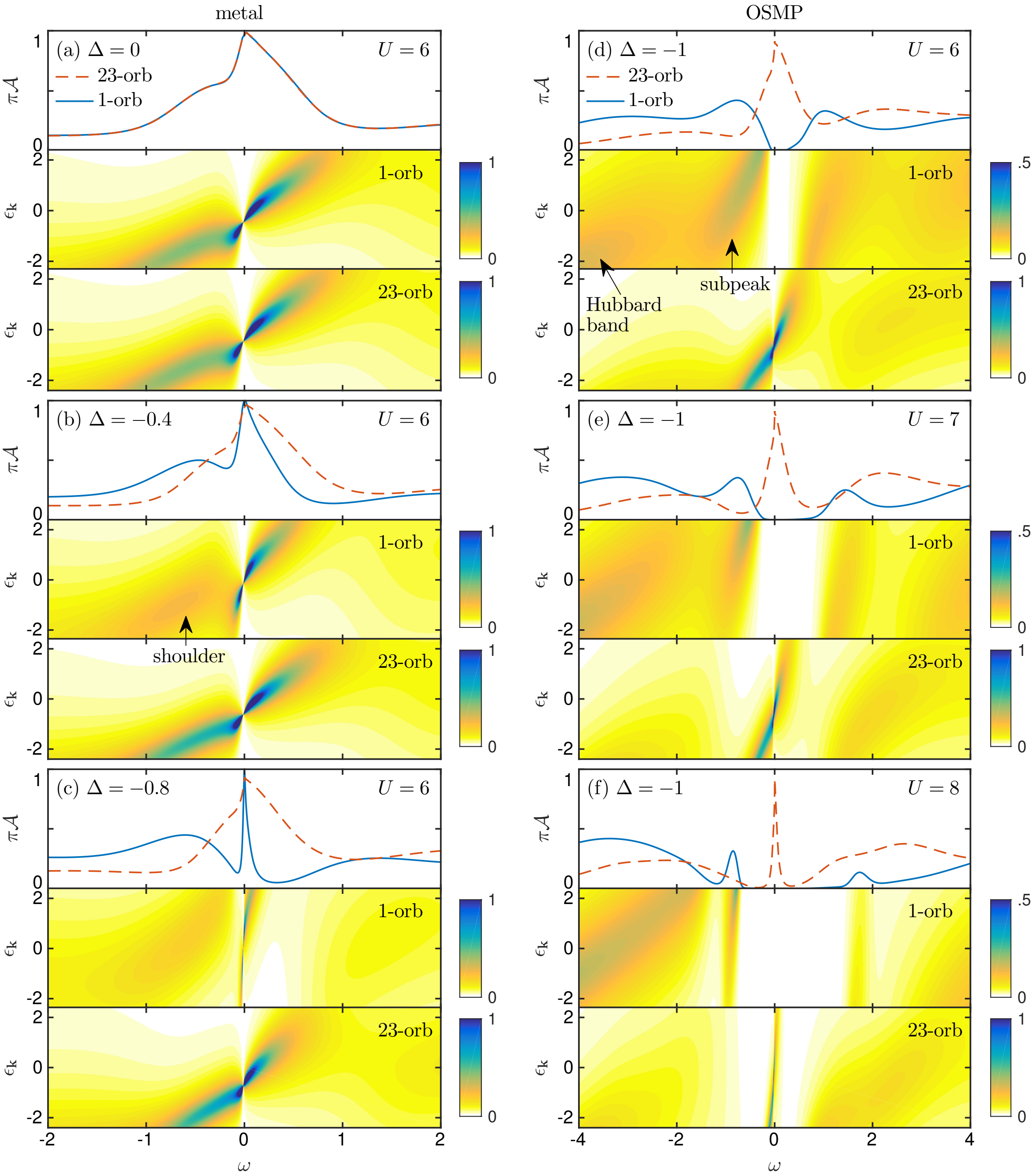

FIG. 10. Local $\mathcal{A}(\omega)$ and momentum-resolved $\mathcal{A}(\omega, \epsilon_{\mathbf{k}})$ spectral functions for varying Δ in the metallic phase (left panel) and for varying U ($J = U/6$ fixed) in the OSMP (right). Note that, within DMFT, the $\mathbf{k}$ dependence enters only via $\epsilon_{\mathbf{k}}$, and we set the half-bandwidth to 2. (a) Already at $\Delta = 0$, $\mathcal{A}(\omega)$ and $\mathcal{A}(\omega, \epsilon_{\mathbf{k}})$ reveal a strong particle-hole asymmetry. (b,c) As we decrease Δ, the 1-orbital is pushed towards half filling, the quasiparticle weight decreases, and $\mathcal{A}(\omega, \epsilon_{\mathbf{k}})$ reveals an almost flat dispersion. Interestingly, the spectral weight from the $\omega < 0$ shoulder is continuously transferred from negative to positive $\epsilon_{\mathbf{k}}$. (d) In the OSMP, the quasiparticle weight in the 1-orbital has vanished; the Hubbard band in $\mathcal{A}(\omega, \epsilon_{\mathbf{k}})$ at $\omega < 0$ is found at $\epsilon_{\mathbf{k}} < 0$ while the subpeak is distinctively centered at $\epsilon_{\mathbf{k}} > 0$ (note the altered color scale). The logarithmic singularities in the 23-orbitals are contained in the very sharp structure around $\omega = 0$. (e,f) With increasing $E_{\mathrm{at}} = U - 2J$, the widths of the 23-quasiparticle peak and, consequently, the widths of the 1-subpeaks decrease. With increasing J, the position of the right subpeak shifts to higher energies [cf. Eq. (B9)]. The distinct nature of the *interband* doublon-holon excitations and the Hubbard bands becomes clearly visible; they resemble the *intraband* doublon-holon subpeaks in the single-orbital strongly correlated metallic phase [46, 58].

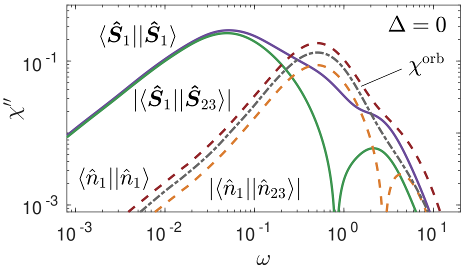

FIG. 11. Various intra- and inter-orbital susceptibilities. As the latter ones change sign within $0 < \omega < \infty$, they are shown in absolute value. The orbital Kondo scale can be read off from the position of the maximum of the orbital susceptibility, χ^{orb}, (dash-dotted line) as well as from orbital-resolved charge susceptibilities, $\langle n_1 || n_1 \rangle_\omega$ and $\langle n_1 || n_{23} \rangle_\omega$ (dashed lines).

Using orbital SU(2) symmetry with $\chi^{\mathrm{orb}}_{23} = \langle \hat{T}^3_{23} || \hat{T}^3_{23} \rangle_\omega$, one further obtains

$$\tfrac{1}{2} \sum_{m=2}^{3} \langle \hat{n}_m || \hat{n}_m \rangle_\omega = \langle \hat{n}_{23} || \hat{n}_{23} \rangle_\omega + \chi^{\mathrm{orb}}_{23}. \qquad \text{(D5)}$$

In the fully symmetric case at $\Delta = 0$, we can also extract the spin and orbital Kondo temperatures from

$$\chi^{\mathrm{sp}} = \tfrac{1}{3} \sum_{\alpha=1}^{3} \langle \hat{S}^\alpha || \hat{S}^\alpha \rangle_\omega, \quad \chi^{\mathrm{orb}} = \tfrac{1}{8} \sum_{a=1}^{8} \langle \hat{T}^a || \hat{T}^a \rangle_\omega, \quad \text{(D6)}$$

where $\hat{\boldsymbol{T}} = \frac{1}{2} \sum_\sigma \sum_{m,m' \in \{1,2,3\}} \hat{d}^\dagger_{m\sigma} \boldsymbol{g}_{mm'} \hat{d}_{m'\sigma}$ with SU(3) Gell-Mann matrices normalized as $\mathrm{Tr}[g^a, g^b] = 2\delta_{a,b}$.

For illustration, we finally show in Fig. 11 intra- and inter-orbital susceptibilities of spin and number operators. As the inter-orbital ones, $\langle \hat{\boldsymbol{S}}_1 || \hat{\boldsymbol{S}}_{23} \rangle_\omega = \frac{1}{3} \sum_{\alpha=1}^{3} \langle \hat{S}^\alpha_1 || \hat{S}^\alpha_{23} \rangle_\omega$ and $\langle \hat{n}_1 || \hat{n}_{23} \rangle_\omega$, change sign within $0 < \omega < \infty$, they are shown in absolute value. We see that the orbital Kondo scale, read off from the position of the maximum in χ^{orb} (dash-dotted line), can also be determined from orbital-resolved charge susceptibilities (dashed lines), corresponding to their explicit relation given in Eq. (D5). It is interesting to note that spins align, meaning $\langle \hat{\boldsymbol{S}}_1 || \hat{\boldsymbol{S}}_{23} \rangle_\omega > 0$, for $|\omega| \lesssim J = 1$ due to Hund's coupling, and the individual charges antagonize, meaning $\langle \hat{n}_1 || \hat{n}_{23} \rangle_\omega < 0$, for $|\omega| \lesssim U/2 = 3$ to minimize the Coulomb repulsion.

[1] Y. Kamihara, H. Hiramatsu, M. Hirano, R. Kawamura, H. Yanagi, T. Kamiya, and H. Hosono, J. Am. Chem. Soc. **128**, 10012 (2006).

[2] Y. Kamihara, T. Watanabe, M. Hirano, and H. Hosono, J. Am. Chem. Soc. **130**, 3296 (2008).

[3] Z. K. Liu, M. Yi, Y. Zhang, J. Hu, R. Yu, J.-X. Zhu, R.-H. He, Y. L. Chen, M. Hashimoto, R. G. Moore, S.-K. Mo, Z. Hussain, Q. Si, Z. Q. Mao, D. H. Lu, and Z.-X. Shen, Phys. Rev. B **92**, 235138 (2015).

[4] H. Miao, Z. P. Yin, S. F. Wu, J. M. Li, J. Ma, B.-Q. Lv, X. P. Wang, T. Qian, P. Richard, L.-Y. Xing, X.-C. Wang, C. Q. Jin, K. Haule, G. Kotliar, and H. Ding, Phys. Rev. B **94**, 201109 (2016).

[5] M. Yi, Z.-K. Liu, Y. Zhang, R. Yu, J.-X. Zhu, J. Lee, R. Moore, F. Schmitt, W. Li, S. Riggs, J.-H. Chu, B. Lv, J. Hu, M. Hashimoto, S.-K. Mo, Z. Hussain, Z. Mao, C. Chu, I. Fisher, Q. Si, Z.-X. Shen, and D. Lu, Nat. Commun. **6**, 7777 (2015).

[6] P. O. Sprau, A. Kostin, A. Kreisel, A. E. Böhmer, V. Taufour, P. C. Canfield, S. Mukherjee, P. J. Hirschfeld, B. M. Andersen, and J. C. S. Davis, Science **357**, 75 (2017).

[7] Z. P. Yin, K. Haule, and G. Kotliar, Nat. Mater. **10**, 932 (2011).

[8] L. de' Medici, G. Giovannetti, and M. Capone, Phys. Rev. Lett. **112**, 177001 (2014).

[9] L. de' Medici, in *Iron-Based Superconductivity* (Springer International Publishing, 2014) pp. 409–441.

[10] D. Sutter, M. Kim, C. E. Matt, M. Horio, R. Fittipaldi, A. Vecchione, V. Granata, K. Hauser, Y. Sassa, G. Gatti, M. Grioni, M. Hoesch, T. K. Kim, E. Rienks, N. C. Plumb, M. Shi, T. Neupert, A. Georges, and J. Chang, Phys. Rev. B **99**, 121115 (2019).

[11] K. Haule and G. Kotliar, New J. Phys. **11**, 025021 (2009).

[12] A. Georges, L. de' Medici, and J. Mravlje, Annu. Rev. Condens. Matter Phys. **4**, 137 (2013).

[13] V. Anisimov, I. Nekrasov, D. Kondakov, T. Rice, and M. Sigrist, Eur. Phys. J. B **25**, 191 (2002).

[14] R. Bulla, T. A. Costi, and T. Pruschke, Rev. Mod. Phys. **80**, 395 (2008).

[15] A. Georges, G. Kotliar, W. Krauth, and M. J. Rozenberg, Rev. Mod. Phys. **68**, 13 (1996).

[16] K. M. Stadler, Z. P. Yin, J. von Delft, G. Kotliar, and A. Weichselbaum, Phys. Rev. Lett. **115**, 136401 (2015).

[17] K. Inaba and A. Koga, J. Phys. Soc. Jpn. **76**, 094712 (2007).

[18] L. de' Medici, S. R. Hassan, M. Capone, and X. Dai, Phys. Rev. Lett. **102**, 126401 (2009).

[19] P. Werner, E. Gull, and A. J. Millis, Phys. Rev. B **79**, 115119 (2009).

[20] T. Kita, T. Ohashi, and N. Kawakami, Phys. Rev. B **84**, 195130 (2011).

[21] L. Huang, L. Du, and X. Dai, Phys. Rev. B **86**, 035150 (2012).

[22] Y. Wang, L. Huang, L. Du, and X. Dai, Chin. Phys. B **25**, 037103 (2016).

[23] J. Mravlje, M. Aichhorn, T. Miyake, K. Haule, G. Kotliar, and A. Georges, Phys. Rev. Lett. **106**, 096401 (2011).

[24] S. Biermann, L. de' Medici, and A. Georges, Phys. Rev. Lett. **95**, 206401 (2005).

[25] P. Werner and A. J. Millis, Phys. Rev. B **74**, 155107 (2006).

[26] L. de' Medici, Phys. Rev. B **83**, 205112 (2011).

[27] L. de' Medici, A. Georges, and S. Biermann, Phys. Rev. B **72**, 205124 (2005).

[28] M. Ferrero, F. Becca, M. Fabrizio, and M. Capone, Phys. Rev. B **72**, 205126 (2005).

[29] P. Coleman and C. Pépin, Phys. Rev. B **68**, 220405 (2003).

[30] P. Mehta, N. Andrei, P. Coleman, L. Borda, and

G. Zarand, Phys. Rev. B **72**, 014430 (2005).

[31] W. Koller, A. C. Hewson, and D. Meyer, Phys. Rev. B **72**, 045117 (2005).

[32] M. Greger, M. Sekania, and M. Kollar, arXiv:1312.0100.

[33] C.-H. Yee, G. Kotliar, and K. Haule, Phys. Rev. B **81**, 035105 (2010).

[34] K. Haule, C.-H. Yee, and K. Kim, Phys. Rev. B **81**, 195107 (2010).

[35] Y. Núñez Fernández, G. Kotliar, and K. Hallberg, Phys. Rev. B **97**, 121113 (2018).

[36] Y. Komijani, K. Hallberg, and G. Kotliar, Phys. Rev. B **99**, 125150 (2019).

[37] L. Dworin and A. Narath, Phys. Rev. Lett. **25**, 1287 (1970).

[38] A. Horvat, R. Žitko, and J. Mravlje, Phys. Rev. B **94**, 165140 (2016).

[39] J. Kanamori, Progr. Theor. Phys **30**, 275 (1963).

[40] A. Weichselbaum and J. von Delft, Phys. Rev. Lett. **99**, 076402 (2007).

[41] A. K. Mitchell, M. R. Galpin, S. Wilson-Fletcher, D. E. Logan, and R. Bulla, Phys. Rev. B **89**, 121105 (2014).

[42] K. M. Stadler, A. K. Mitchell, J. von Delft, and A. Weichselbaum, Phys. Rev. B **93**, 235101 (2016).

[43] A. Weichselbaum, Ann. Phys. **327**, 29723047 (2012).

[44] A. Weichselbaum, Phys. Rev. B **86**, 245124 (2012).

[45] S.-S. B. Lee and A. Weichselbaum, Phys. Rev. B **94**, 235127 (2016).

[46] S.-S. B. Lee, J. von Delft, and A. Weichselbaum, Phys. Rev. Lett. **119**, 236402 (2017).

[47] R. Žitko and T. Pruschke, Phys. Rev. B **79**, 085106 (2009).

[48] R. Bulla, A. C. Hewson, and T. Pruschke, J. Phys.: Condens. Matter **10**, 8365 (1998).

[49] L. de' Medici, J. Mravlje, and A. Georges, Phys. Rev. Lett. **107**, 256401 (2011).

[50] For $\Delta < 0$, the Mott transition of the half-filled 1-orbital depends mainly on U, with a critical $U_{c2} \approx 6$ similar to the single-orbital case [15]. The Mott transition in the quarter-filled, 23-doublet requires much stronger interaction [51, 52]. Hence, our choice $U = 6$ and $J = 1$ is close to the minimal interaction strength required for the OSMP.

[51] N. Blümer and E. V. Gorelik, Phys. Rev. B **87**, 085115 (2013).

[52] S.-S. B. Lee, J. von Delft, and A. Weichselbaum, Phys. Rev. B **97**, 165143 (2018).

[53] M. Greger, M. Kollar, and D. Vollhardt, Phys. Rev. Lett. **110**, 046403 (2013).

[54] I. Okada and K. Yosida, Progr. Theor. Phys. **49**, 1483 (1973).

[55] K. Stadler, G. Kotliar, A. Weichselbaum, and J. von Delft, Ann. Phys. (2018), 10.1016/j.aop.2018.10.017.

[56] H. Iwasawa, Y. Aiura, T. Saitoh, I. Hase, S. I. Ikeda, Y. Yoshida, H. Bando, M. Higashiguchi, Y. Miura, X. Y. Cui, K. Shimada, H. Namatame, and M. Taniguchi, Phys. Rev. B **72**, 104514 (2005).

[57] E. Müller-Hartmann, Z. Phys. B Condensed Matter **76**, 211 (1989).

[58] S.-S. B. Lee, J. von Delft, and A. Weichselbaum, Phys. Rev. B **96**, 245106 (2017).

[59] C. J. Wright, *Theoretical studies of underscreened Kondo physics in quantum dots*, Ph.D. thesis, Balliol College, Oxford (2011).

[60] L. Fanfarillo and E. Bascones, Phys. Rev. B **92**, 075136 (2015).

[61] R. Yu and Q. Si, Phys. Rev. B **96**, 125110 (2017).

arXiv:1909.02389v1 [cond-mat.str-el] 5 Sep 2019

Strongly Correlated Materials from a Numerical Renormalization Group Perspective: How the Fermi-liquid State of Sr_2RuO_4 Emerges

Fabian B. Kugler,[1] Manuel Zingl,[2] Hugo U. R. Strand,[2] Seung-Sup B. Lee,[1] Jan von Delft,[1] and Antoine Georges[3, 2, 4, 5]

[1] *Arnold Sommerfeld Center for Theoretical Physics, Center for NanoScience, and Munich Center for Quantum Science and Technology, Ludwig-Maximilians-Universität München, 80333 Munich, Germany*
[2] *Center for Computational Quantum Physics, Flatiron Institute, 162 5th Avenue, New York, NY 10010, USA*
[3] *Collège de France, 11 place Marcelin Berthelot, 75005 Paris, France*
[4] *Centre de Physique Théorique, CNRS, Ecole Polytechnique, IP Paris, 91128 Palaiseau, France*
[5] *Department of Quantum Matter Physics, University of Geneva, 1211 Geneva 4, Switzerland*

(Dated: September 6, 2019)

The crossover from fluctuating atomic constituents to a collective state as one lowers temperature/energy is at the heart of the dynamical mean-field theory description of the solid state. We demonstrate that the numerical renormalization group is a viable tool to monitor this crossover in a real-materials setting. The renormalization group flow from high to arbitrarily small energy scales clearly reveals the emergence of the Fermi-liquid state of Sr_2RuO_4. We find a two-stage screening process, where orbital fluctuations are screened at much higher energies than spin fluctuations, and Fermi-liquid behavior, concomitant with spin coherence, below a temperature of 25 K. By computing real-frequency correlation functions, we directly observe this spin–orbital scale separation and show that the van Hove singularity drives strong orbital differentiation. We extract quasiparticle interaction parameters from the low-energy spectrum and find an effective attraction in the spin-triplet sector.

Introduction.—Atoms with partially filled shells have a spectrum of many-body eigenstates with degeneracies associated with fluctuating spin and orbital moments. For instance, the isolated ruthenium atom in the Ru^{4+} configuration, subject to an octahedral crystal field, has a nine-fold degenerate groundstate corresponding to spin and orbital quantum numbers $S = L = 1$ [1, 2]. In materials with strong electronic correlations, these local fluctuations can be observed at high temperature and energy through, e.g., Curie–Weiss-like spin susceptibilities. In correlated metals, these fluctuations are suppressed as one reaches low temperature and energy. In the Fermi-liquid regime, a nondegenerate collective groundstate is formed, with long-lived coherent quasiparticle excitations and susceptibilities displaying Pauli behavior [3].

How the crossover from fluctuating atomic constituents to a collective state takes place is at the heart of the dynamical mean-field theory (DMFT) description of the solid state [4]. In this theory, each atom is viewed as exchanging electrons with an environment which self-consistently represents the whole solid. The gradual suppression of local fluctuations can be thought of as a self-consistent (multi-stage) Kondo screening process [5] of both spin and orbital moments [6, 7].

The renormalization group (RG) is the appropriate framework to describe and monitor these crossovers as a function of energy scale. Indeed, Wilson's numerical renormalization group (NRG) [8] has been a tool of choice for solving DMFT equations for lattice models with few orbital degrees of freedom [9], with the additional merit of providing real-frequency properties at any temperature. Following a number of two-particle applications [10–15], recently, even three-orbital studies have become possible [6, 7, 16–19]. Yet, all of these works operated in the model context. We demonstrate here that NRG can be successfully applied to an actual material, accounting for its electronic structure in a realistic manner using density functional theory (DFT) and DMFT [20].

The material we focus on, Sr_2RuO_4, is one of the more thoroughly studied quantum materials [21] and an ideal testbed for fundamental developments in quantum many-body theories. Besides the unconventional superconducting state below $\sim 1.5\,\mathrm{K}$ [22, 23], also the normal, Hund-metal state of Sr_2RuO_4 [2, 7, 24–27] attracts attention, due to text-book Fermi-liquid behavior below $T_{\mathrm{FL}} \approx 25\,\mathrm{K}$ [21, 28–33] (though signatures of quasiparticles are found up to elevated temperatures of $\sim 600\,\mathrm{K}$ [24]). However, temperatures below T_{FL} could not be reached with controlled computational methods hitherto.

In this Letter, we show that Sr_2RuO_4 undergoes a two-stage Kondo screening process [6, 7, 26], where orbital fluctuations are screened well before the spin degrees of freedom. We determine the associated Kondo temperatures to $T_{\mathrm{orb}} \approx 6000\,\mathrm{K}$ and $T_{\mathrm{sp}} \approx 500\,\mathrm{K}$, respectively, and show that Fermi-liquid behavior emerges when spin coherence is fully established below a scale of $T_{\mathrm{FL}} \approx 25\,\mathrm{K}$ [34]. With NRG as impurity solver, the entire DMFT calculation is performed on the real-frequency axis [35], and we can compute correlation functions at arbitrarily low energy scales and temperatures. Hence, we are able to go beyond previous Monte Carlo-based DFT+DMFT studies [24, 26, 27, 33, 38–41] and enter deep into the Fermi-liquid regime, even down to $T = 0$ [42]. This enables us to explore the counter-intuitive observation that the more itinerant (xy) orbital has the smaller quasiparticle weight [21, 24, 27, 38, 41, 44, 45]. We show that this effect is driven by a van Hove singularity close to the Fermi level, as elaborated in [24].

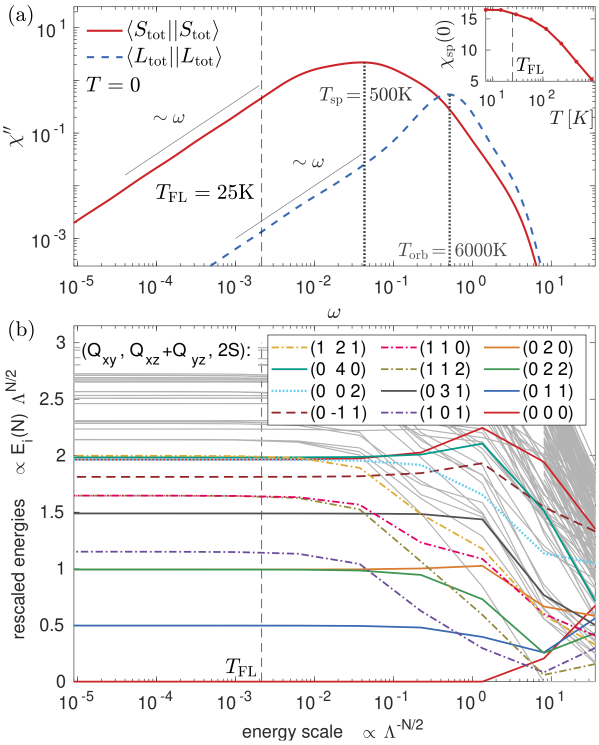

FIG. 1. (a) Dynamic spin and orbital susceptibilities, $\chi''_{\rm sp}(\omega)$ and $\chi''_{\rm orb}(\omega)$, showing spin–orbital scale separation. Inset: Static spin susceptibility as a function of temperature. (b) NRG flow diagram, showing the rescaled eigenenergies (with quantum numbers given in the legend) as a function of the energy scale [50], for the impurity model at self-consistency. The spin and orbital Kondo temperatures (maximum of χ'') and the Fermi-liquid scale, $T_{\rm FL}$, are marked by vertical lines.

Model.—The low-energy structure of $\mathrm{Sr_2RuO_4}$ can be well described by a local basis of three maximally localized Wannier functions [46, 47] with Ru-4d t_{2g} symmetry denoted by {xy, xz, yz}. The corresponding non-interacting Wannier Hamiltonian is characterized by the density of states (DOS) shown in Fig. 3(a) below, reflecting the quasi-2D tetragonal crystal structure of $\mathrm{Sr_2RuO_4}$, with quasi-2D xy orbitals and a strongly one-dimensional character of the degenerate xz/yz orbitals. We employ the same Wannier Hamiltonian as in [39, 40, 48] (without spin-orbit coupling) combined with a local Kanamori interaction [2, 49] parametrized by $U=2.3$ and $J=0.4$ [24]. Throughout this work, we use $\mathrm{eV}=1$ as unit of energy if not otherwise indicated. In the Hund-metal phase of $\mathrm{Sr_2RuO_4}$, the pair-hopping term of the Kanamori interaction is almost inactive and can be neglected to obtain a model with higher symmetry, more tractable for NRG [50].

Spin–orbital separation, Fermi liquid.—Since NRG can reach arbitrarily small energy scales, we are able to directly observe both spin–orbital scale separation and the onset of Fermi-liquid behavior. The zero-temperature real-frequency orbital and spin susceptibilities [50], $\chi''_{\rm orb}$ and $\chi''_{\rm sp}$, exhibit a separation of their maxima by more than one decade, see Fig. 1(a). This spin–orbital separation in Kondo scales, with $T_{\rm orb}\approx 6000\,\mathrm{K}$ and $T_{\rm sp}\approx 500\,\mathrm{K}$ as found from the maxima of χ'', is distinctive of correlated Hund metals [2, 6, 7, 19], where the Hund coupling J causes the screening of the respective fluctuations to occur at disparate energy scales. Further, completed screening of fluctuations is signaled by linear behavior, $\chi''\propto\omega$, found below roughly 1000 K and 25 K for $\chi''_{\rm orb}$ and $\chi''_{\rm sp}$, respectively. The fully coherent, Fermi-liquid state thus emerges below an energy scale of 25 K. The Fermi-liquid onset is also seen in the temperature dependence of the static spin susceptibility, $\chi_{\rm sp}(\omega=0)$, which crosses over from Curie–Weiss- to Pauli-like behavior, saturating below $T_{\rm FL}\approx 25\,\mathrm{K}$, see inset of Fig. 1(a). These results clearly establish spin–orbital scale separation in the low-temperature Fermi-liquid state of $\mathrm{Sr_2RuO_4}$, as proposed by previous studies above $T_{\rm FL}$ [7, 26].

A very direct observation of Fermi-liquid behavior is possible by studying the renormalization group flow diagram of the NRG algorithm [6, 9, 18, 19]. Figure 1(b) shows the NRG-Hamiltonian's (lowest) rescaled eigenenergies, $\Lambda^{N/2}E_i(N)$, depending on the energy scale $\Lambda^{-N/2}$ of the RG flow, where Λ is the NRG discretization parameter and N the length of the Wilson chain [50]. At high energy, the states are pure atomic eigenstates, which are screened by the bath when flowing down in energy. Below $T_{\rm FL}$, the Fermi liquid is formed. There, the flow reaches a fixed point, where the rescaled eigenenergies become independent of N, $\Lambda^{N/2}E_i(N)=E_i^*$. The Fermi-liquid nature of this fixed point is determined by "towers" [9] of equidistant excitation energies within the same symmetry sector, where each E_i^* is composed of n quasiparticle excitations, $E_i^*=n\cdot E_{\rm qp}$.

Each eigenstate has the quantum numbers $(Q_{\rm xy}, Q_{\rm xz}+Q_{\rm yz}, 2S)$, with orbital-resolved charge, Q_m, relative to the groundstate, and total spin, S. The most prominent tower of states stems from xz/yz quasiparticles, i.e., eigenstates with quantum numbers $(0,0,0)$, $(0,1,1)$, $(0,2,2)$, $(0,2,0)$, $(0,3,1)$, etc., see solid lines in Fig. 1(b). States with an additional xy quasiparticle are marked as dash-dotted

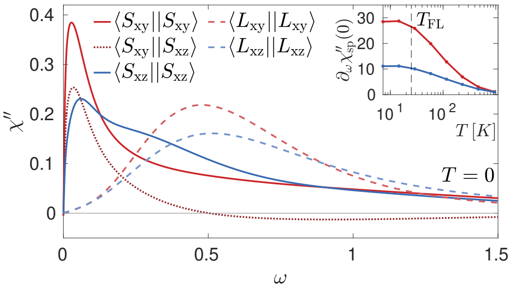

FIG. 2. Orbital-resolved, dynamic spin and angular-momentum susceptibilities, $\chi''(\omega)$. Inset: Temperature dependence of $\partial_\omega\chi''|_{\omega=0}$ in the spin sector, with $T_{\rm FL}$ marked as dashed line.

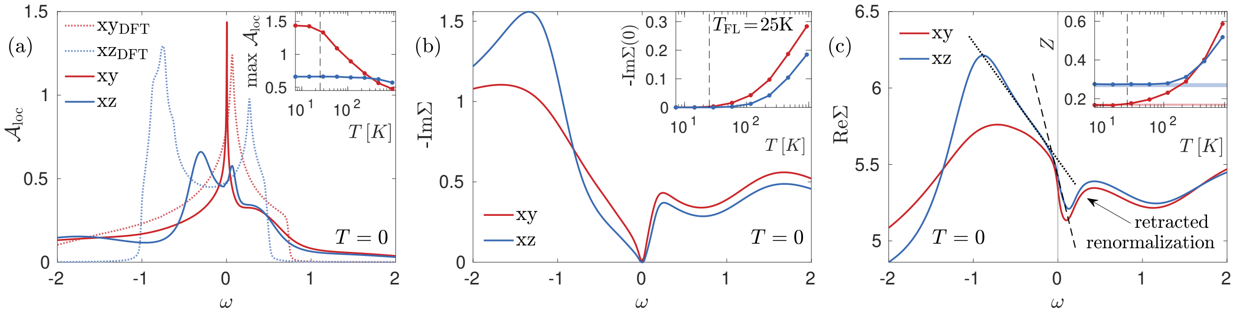

FIG. 3. Main panels: Real-frequency correlation functions at zero temperature. Insets: Characteristic values as function of temperature, converging below $T_{\rm FL}$ (dashed line). (a) Local spectral function, $\mathcal{A}_{\rm loc}(\omega)$, from DFT+DMFT (solid lines) and DFT (dotted lines). Inset: $\max_\omega \mathcal{A}_{\rm loc}(\omega)$. (b) Imaginary part of the self-energy, Im$\Sigma(\omega)$. Inset: Im$\Sigma(\omega\!=\!0)$. (c) Real part of the self-energy, Re$\Sigma(\omega)$, with the two linear regimes for $\omega\!<\!0$ and the low-energy, positive slope for $\omega\!>\!0$ highlighted. Inset: $Z\!=\!(1\!-\!\partial_\omega \mathrm{Re}\Sigma|_{\omega=0})^{-1}$; thick horizontal lines show the $T\!=\!0$ result for Z calculated via renormalized parameters.

lines. The Fermi-liquid scale, $T_{\rm FL}$, is seen in the RG flow as the point where eigenstates with equal charge but different spin become degenerate, see the pairs $(0,2,0)$, $(0,2,2)$ and $(1,1,0)$, $(1,1,2)$. Our direct evidence of the Fermi-liquid scale of Sr$_2$RuO$_4$, which conforms to the $T_{\rm FL}\!\approx\!25\,$K found in experiments [21, 28–31], is one of the main results of this work.

In order to understand how the different orbitals behave regarding spin–orbital scale separation, we investigate in Fig. 2 the orbitally resolved spin and angular-momentum susceptibilities [50]. We find strong orbital differentiation with larger amplitude in the xy than the xz spin response, and generally a shift of spectral weight to lower frequencies in the xy compared to the xz orbital. In nuclear magnetic resonance (NMR) spectroscopy, the inverse nuclear spin-lattice relaxation time, $1/(T_1T)$, is related to the zero-frequency slope of the electronic spin susceptibility, $1/(T_1T) \propto \partial_\omega \chi''|_{\omega=0}$ (neglecting matrix elements) [62, 63]. Computing the orbitally resolved $\partial_\omega \chi''|_{\omega=0}$ as a function of temperature, we find that the xy response is about 2.5 times stronger than the xz response, see inset of Fig. 2, in qualitative agreement with experimental [31, 64, 65] and theoretical works [66]. The temperature dependence changes from linear to constant at $T_{\rm FL}$, in a similar fashion for *both* orbitals, which we attribute to the strong orbital mixing on the two-particle level [39].

Single-particle spectrum.—Apart from the RG flow and the dynamic susceptibilities, our calculations also provide single-particle spectral information. Although the single-particle properties of Sr$_2$RuO$_4$ have been studied extensively [24, 26, 27, 33, 38, 45, 48] using continuous-time quantum Monte Carlo (CTQMC) solvers [67], these calculations have a challenging scaling with inverse temperature β, making it hard to reach the Fermi-liquid regime with $T < 25\,$K, i.e., $\beta > 464\,\mathrm{eV}^{-1}$. Additionally, the analytic continuation to real frequencies severely hampers spectral resolution [68]. Here, we go beyond previous works by analyzing Sr$_2$RuO$_4$ deep in the Fermi-liquid regime at low temperatures, and even $T\!=\!0$, directly on the real-frequency axis.

The local spectral function, $\mathcal{A}_{\rm loc}(\omega)$, of Sr$_2RuO_4$ is considerably renormalized compared to the DFT DOS [24, 45, 48], see Fig. 3(a). When accounting for correlations, the spectral features are retained but shifted towards the Fermi level—both for the double peak in the xz/yz orbitals and the narrow xy peak. The latter is generated by the van Hove singularity in the xy orbital, which is shifted towards the Fermi level by electronic correlations. The height of the van Hove peak grows with decreasing temperature and saturates below $T_{\rm FL}$, see inset of Fig. 3(a).

The imaginary part of the self-energy, Im$\Sigma(\omega)$, shown in Fig. 3(b), determines the lifetime of excitations. It has larger values at negative compared to positive frequencies, yielding shorter life times for hole excitations. Fermi-liquid behavior only emerges at frequencies below $T_{\rm FL}$. The real part of the self-energy, Re$\Sigma(\omega)$, displays linear (Fermi-liquid) behavior on the same small energy scale, see Fig. 3(c). However, at $\omega\approx -100\,$meV, it exhibits a “kink” leading to a second linear regime [lines in Fig. 3(c)], while, for ω in the range $+200-400\,$meV, the slope of Re$\Sigma(\omega)$ changes sign, “retracting” the renormalization of the quasiparticle dispersion. Hence, in this energy range, the quasiparticle velocity is larger than the bare one [33], as opposed to the usual low-energy reduction due to strong correlations. These single-particle properties are in qualitative agreement with previous Monte Carlo results [24, 26, 27, 33, 38, 45, 48].

The pronounced differentiation between the different orbitals, seen in Figs. 1(b) and 2, is also reflected in the self-energy. The xy orbital shows much stronger correlations than the xz/yz ones, with higher curvature in Im$\Sigma(\omega)$ and steeper slope in Re$\Sigma(\omega)$ at $\omega\!=\!0$, as visible in Figs. 3(b) and 3(c), respectively. The slope is related to the quasiparticle weight, $Z\!=\!(1\!-\!\partial_\omega \mathrm{Re}\Sigma|_{\omega=0})^{-1}$, shown in the inset of Fig. 3(c). The zero-temperature values of Z agree with renormalized parameters extracted directly from the spectrum (horizontal lines, see discussion below) and are also consistent with experiments [21, 48]. The low-temperature relation $Z_{\rm xy}\!<\!Z_{\rm xz}$ contrasts with $Z_{\rm xy}\!>\!Z_{\rm xz}$ at high temperature. Indeed, when lowering temperature,

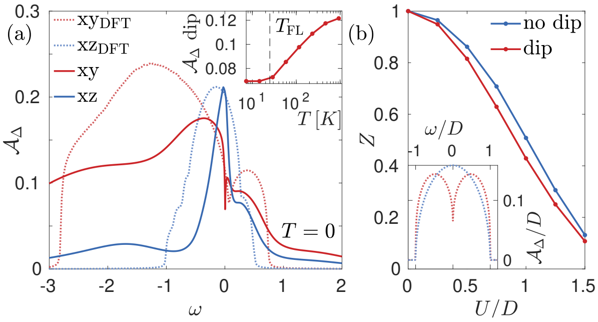

FIG. 4. (a) Spectral function of the hybridization, $\mathcal{A}_\Delta(\omega)$, in DFT+DMFT (solid lines) and DFT (dotted lines). Inset: temperature dependence of the van Hove dip in $\mathcal{A}_{\Delta,\rm xy}(\omega)$. (b) Quasiparticle weight, Z, as a function of Hubbard U, for a simple two-orbital model with identical half bandwidth, D. The hybridization functions at $U=0$ are shown in the inset.

the quasiparticle weights cross at $\sim 350\,$K, and, while $Z_{\rm xz}$ levels off at $T \sim 100\,$K, $Z_{\rm xy}$ only saturates below $T_{\rm FL}$. This shows that the coherence-to-incoherence crossover and the corresponding coherence scales in Sr$_2$RuO$_4$ are strongly orbital-dependent [24, 40]. It is only below $T_{\rm FL}$ that *all* orbitals are in the coherent Fermi-liquid regime.

At first sight, the stronger correlation in the xy orbital as compared to the xz/yz orbitals, indicated by $Z_{\rm xy} < Z_{\rm xz}$, is rather counterintuitive. Usually, the ratio between local Hubbard interaction U and the bandwidth W, U/W, is a good estimator for the strength of correlations. However, this clearly does not hold for Sr$_2$RuO$_4$, since the xy orbital has a significantly larger bandwidth, $W_{\rm xy} > W_{\rm xz}$, see Fig. 3(a). In [24], it has been argued that the strong xy correlations result from the proximity of its van Hove singularity to the Fermi level, see Fig. 3(a).

To understand this, we consider the spectral part of the hybridization function, $\mathcal{A}_\Delta(\omega)$, of the self-consistent impurity model. The van Hove singularity in $\mathcal{A}_{\rm loc,xy}(\omega)$ generates a dip in $\mathcal{A}_{\Delta,\rm xy}(\omega)$ [50] close to zero frequency, see Fig. 4(a), which implies a reduction of the effective coupling between impurity and bath at low energies for the xy orbital. The weaker coupling, in turn, increases the correlations and reduces the quasiparticle weight. The temperature dependence of the dip, inset of Fig. 4(a), matches the one of $\max_\omega \mathcal{A}_{\rm loc,xy}$ in the inset of Fig. 3(a).

To disentangle the effect of the van Hove singularity from other factors, we consider a simple, half-filled two-orbital model with both orbitals having the same bandwidth. We choose a semicircular lattice DOS for one orbital and set the second one such that its hybridization function has a dip at zero energy, see Fig. 4(b). Even in this simplified model, we find that Z is smaller in the orbital with a dip in the hybridization. This suggests that the relevant measure of the correlations strength is the Hubbard interaction divided by the effective low-energy hybridization strength, $U/\mathcal{A}_\Delta(\omega=0)$, rather than U/W.

Quasiparticle parameters.—Within the NRG framework, we can extract information about the Fermi liquid and its quasiparticles not only from correlation functions but directly from the RG flow. To this end, we compute (zero-temperature) renormalized parameters from the low-energy spectrum of the (self-consistent) impurity model [69–71]. The impurity Green's function has the low-energy expansion

$$G(\omega) \approx Z \cdot \big(\omega - \tilde{\epsilon} - Z\Delta(\omega)\big)^{-1}, \quad \tilde{\epsilon} = Z \cdot \big(\epsilon + \Sigma(0)\big).$$

For a (finite) Wilson chain of length N, $G(\omega)$ has first-order poles at the single-particle excitation energies. Taking the lowest particle- and hole-excitation energy $E_i(N)$ from Fig. 1(b), we have two equations that can be solved for Z and $\tilde{\epsilon}$ and converged in N [69]. The results for Z [and $\tilde{\epsilon}$ or $\Sigma(0)$] are reported in [50] and agree quantitatively with those taken from $\Sigma(\omega)$, see inset of Fig. 3(c).

To go beyond the single-particle picture, we exploit that, at any finite N, there are residual quasiparticle interactions in the form of exponentially small corrections to the equidistant tower of quasiparticle excitations. By comparing two-particle-excitation energies $E^S_{mm'}$, with orbital indices m and m' and spin index S, to two single-particle excitations E_m and $E_{m'}$, the quasiparticle interaction $\tilde{U}^S_{mm'}$ is given by [69]

$$E^S_{mm'} - E_m - E_{m'} = \tilde{U}^S_{mm'}\,|\psi_m(0)|^2\,|\psi_{m'}(0)|^2,$$

where $|\psi_m(0)|^2$ is the quasiparticle density at the impurity [50]. Hence, we are in the unique position to compute quasiparticle interactions $\tilde{U}^S_{mm'}$ as well as the zero-energy real-frequency vertex Γ, related via $\tilde{U}^S_{mm'} = Z_m Z_{m'} \Gamma^S_{mm'}$ [69, 71], for Sr$_2$RuO$_4$. The results, listed in [50], show that the orbital dependence of $\tilde{U}^S_{mm'}$ is governed by Z_m, while $\Gamma^S_{mm'}$ displays only weak orbital dependence. Strikingly, the effective interaction in the spin-triplet sector is *attractive*. We attribute this to the same mechanism as the Hund-metal s-wave spin-triplet superconducting instability found in model studies [72, 73].

Conclusion.—By following the NRG flow starting from high and proceeding to the lowest temperature and energy scales, we have analyzed spin–orbital scale separation and the emergence of the Fermi liquid in Sr$_2$RuO$_4$ within a real-materials DFT+DMFT setting. Through linear frequency behavior of zero-temperature dynamic susceptibilities and fixed-point analysis of the NRG flow, we provide theoretical evidence for a Fermi-liquid scale, in remarkable agreement with the experimentally observed $T_{\rm FL} \approx 25\,$K [21, 28–31]. Characteristic quantities, like $\chi_{\rm sp}$ and Z, are found to converge below $25\,$K. Further, our real-frequency and zero-temperature results substantiate a number of features, such as strongly shifted spectral peaks and the peculiar frequency dependence of the self-energy, previously found from analytically-continued Monte Carlo data [24, 26, 27, 33, 38–41]. We showed that the proximity of the van Hove singularity to the Fermi level drives strong orbital differentiation in Sr$_2$RuO$_4$. Notably, the effect of van Hove singularities on the correlated state is of importance even in non-transition metal systems like twisted bilayer graphene [74–76]. Finally, the extracted quasiparticle interactions $\tilde{U}^{S}_{mm'}$ reveal attractive coupling in the spin-triplet sector within our *ab initio* analysis. This paves the way towards a complete description of quasiparticles and their interactions in Sr_2RuO_4, which are of crucial importance for the understanding of the still puzzling superconducting state [23, 77].

Generally, our work demonstrates the potential of DFT+DMFT+NRG as a new computational paradigm for real-material systems to (i) directly access real-frequency properties at arbitrarily low temperatures and (ii) reveal and elucidate the intricate renormalization process that occurs during the dressing of atomic excitations by their solid-state environment.

We thank G. Kotliar, J. Mravlje, and A. Weichselbaum for fruitful discussions. The NRG results were obtained using the QSpace tensor library [78, 79], and TRIQS applications [80–82] were used; see [50] for details. FBK, S-SBL, and JvD are supported by the Deutsche Forschungsgemeinschaft under Germany's Excellence Strategy–EXC-2111–390814868; S-SBL further by Grant. No. LE3883/2-1. FBK acknowledges funding from the research school IMPRS-QST and is grateful for hospitality at the Flatiron Institute, where most of this work was carried out. The Flatiron Institute is a division of the Simons Foundation.

[1] S. Sugano, Y. Tanabe, and H. Kamimura, *Multiplets of Transition-Metal Ions in Crystals* (Academic Press Inc., 111 Fifth Avenue, New York, New York, 10003, 1970).
[2] A. Georges, L. de' Medici, and J. Mravlje, Annu. Rev. Condens. Matter Phys. **4**, 137 (2013).
[3] M. Imada, A. Fujimori, and Y. Tokura, Rev. Mod. Phys. **70**, 1039 (1998).
[4] A. Georges, G. Kotliar, W. Krauth, and M. J. Rozenberg, Rev. Mod. Phys. **68**, 13 (1996).
[5] J. Kondo, Prog. Theor. Phys. **32**, 37 (1964).
[6] K. M. Stadler, Z. P. Yin, J. von Delft, G. Kotliar, and A. Weichselbaum, Phys. Rev. Lett. **115**, 136401 (2015).
[7] X. Deng, K. M. Stadler, K. Haule, A. Weichselbaum, J. von Delft, and G. Kotliar, Nat. Comm. **10**, 2721 (2019).
[8] K. G. Wilson, Rev. Mod. Phys. **47**, 773 (1975).
[9] R. Bulla, T. A. Costi, and T. Pruschke, Rev. Mod. Phys. **80**, 395 (2008).
[10] T. Pruschke and R. Bulla, Eur. Phys. J. B **44**, 217 (2005).
[11] R. Peters and T. Pruschke, Phys. Rev. B **81**, 035112 (2010).
[12] R. Peters and T. Pruschke, J. Phys. Conf. Ser. **200**, 012158 (2010).
[13] R. Peters, N. Kawakami, and T. Pruschke, Phys. Rev. B **83**, 125110 (2011).
[14] M. Greger, M. Kollar, and D. Vollhardt, Phys. Rev. Lett. **110**, 046403 (2013).
[15] M. Greger, M. Sekania, and M. Kollar, arXiv:1312.0100.
[16] A. Horvat, R. Žitko, and J. Mravlje, Phys. Rev. B **94**, 165140 (2016).
[17] A. Horvat, R. Žitko, and J. Mravlje, Phys. Rev. B **96**, 085122 (2017).
[18] K. Stadler, G. Kotliar, A. Weichselbaum, and J. von Delft, Ann. Phys. **405**, 365 (2019).
[19] F. B. Kugler, S.-S. B. Lee, A. Weichselbaum, G. Kotliar, and J. von Delft, arXiv:1904.10774.
[20] G. Kotliar, S. Y. Savrasov, K. Haule, V. S. Oudovenko, O. Parcollet, and C. A. Marianetti, Rev. Mod. Phys. **78**, 865 (2006).
[21] A. P. Mackenzie and Y. Maeno, Rev. Mod. Phys. **75**, 657 (2003).
[22] Y. Maeno, H. Hashimoto, K. Yoshida, S. Nishizaki, T. Fujita, J. G. Bednorz, and F. Lichtenberg, Nature **372**, 532 (1994).
[23] A. P. Mackenzie, T. Scaffidi, C. W. Hicks, and Y. Maeno, npj Quantum Mater. **2**, 40 (2017).
[24] J. Mravlje, M. Aichhorn, T. Miyake, K. Haule, G. Kotliar, and A. Georges, Phys. Rev. Lett. **106**, 096401 (2011).
[25] L. de' Medici, J. Mravlje, and A. Georges, Phys. Rev. Lett. **107**, 256401 (2011).
[26] J. Mravlje and A. Georges, Phys. Rev. Lett. **117**, 036401 (2016).
[27] M. Kim, J. Mravlje, M. Ferrero, O. Parcollet, and A. Georges, Phys. Rev. Lett. **120**, 126401 (2018).
[28] N. E. Hussey, A. P. Mackenzie, J. R. Cooper, Y. Maeno, S. Nishizaki, and T. Fujita, Phys. Rev. B **57**, 5505 (1998).
[29] T. Katsufuji, M. Kasai, and Y. Tokura, Phys. Rev. Lett. **76**, 126 (1996).
[30] Y. Maeno, K. Yoshida, H. Hashimoto, S. Nishizaki, S.-I. Ikeda, M. Nohara, T. Fujita, A. P. Mackenzie, N. E. Hussey, J. G. Bednorz, and F. Lichtenberg, J. Phys. Soc. Japan **66**, 1405 (1997).
[31] T. Imai, A. W. Hunt, K. R. Thurber, and F. C. Chou, Phys. Rev. Lett. **81**, 3006 (1998).
[32] A. Mackenzie, S. Julian, A. Diver, G. Lonzarich, N. Hussey, Y. Maeno, S. Nishizaki, and T. Fujita, Phys. C: Superconductivity **263**, 510 (1996).
[33] D. Stricker, J. Mravlje, C. Berthod, R. Fittipaldi, A. Vecchione, A. Georges, and D. van der Marel, Phys. Rev. Lett. **113**, 087404 (2014).
[34] The orbital and spin Kondo temperatures, T_{orb} and T_{sp}, give the characteristic energy scale of the corresponding screening process and are here deduced from the maxima of the respective zero-temperature real-frequency susceptibilities [6, 18, 19]. Similarly, the Fermi-liquid crossover is associated with a scale as opposed to an exact number. Hence, we do not extract a specific value but rather compare the experimentally observed 25 K [21, 28–31] to our numerical data and demonstrate excellent agreement.
[35] We note that also tensor networks have been successfully used to carry out DFT+DMFT calculations directly on the real-frequency axis [36, 37].
[36] D. Bauernfeind, M. Zingl, R. Triebl, M. Aichhorn, and H. G. Evertz, Phys. Rev. X **7**, 031013 (2017).
[37] D. Bauernfeind, R. Triebl, M. Zingl, M. Aichhorn, and H. G. Evertz, Phys. Rev. B **97**, 115156 (2018).
[38] G. Zhang, E. Gorelov, E. Sarvestani, and E. Pavarini, Phys. Rev. Lett. **116**, 106402 (2016).
[39] H. U. R. Strand, M. Zingl, N. Wentzell, O. Parcollet, and A. Georges, arXiv:1904.07324.
[40] M. Zingl, J. Mravlje, M. Aichhorn, O. Parcollet, and A. Georges, npj Quantum Mater. **4**, 35 (2019).
[41] X. Deng, K. Haule, and G. Kotliar, Phys. Rev. Lett. **116**,

256401 (2016).
[42] Currently, also a matrix product states (MPS) based impurity solver is being used to study $\mathrm{Sr_2RuO_4}$ at $T = 0$, although on the Matsubara axis [43].
[43] N.-O. Linden, M. Zingl, C. Hubig, O. Parcollet, and U. Schollwöck, unpublished.
[44] C. Bergemann, A. P. Mackenzie, S. R. Julian, D. Forsythe, and E. Ohmichi, Adv. Phys. **52**, 639 (2003).
[45] E. Sarvestani, G. Zhang, E. Gorelov, and E. Pavarini, Phys. Rev. B **97**, 085141 (2018).
[46] N. Marzari and D. Vanderbilt, Phys. Rev. B **56**, 12847 (1997).
[47] I. Souza, N. Marzari, and D. Vanderbilt, Phys. Rev. B **65**, 035109 (2001).
[48] A. Tamai, M. Zingl, E. Rozbicki, E. Cappelli, S. Riccò, A. de la Torre, S. McKeown Walker, F. Y. Bruno, P. D. C. King, W. Meevasana, M. Shi, M. Radović, N. C. Plumb, A. S. Gibbs, A. P. Mackenzie, C. Berthod, H. U. R. Strand, M. Kim, A. Georges, and F. Baumberger, Phys. Rev. X **9**, 021048 (2019).
[49] J. Kanamori, Prog. Theor. Phys **30**, 275 (1963).
[50] See the Supplemental Material at [url], which additionally contains the Refs. [51–61] listed below.
[51] P. Werner, A. Comanac, L. de' Medici, M. Troyer, and A. J. Millis, Phys. Rev. Lett. **97**, 076405 (2006).
[52] P. Blaha, K. Schwarz, G. K. H. Madsen, D. Kvasnicka, J. Luitz, R. Laskowski, F. Tran, and L. D. Marks, *WIEN2k, An Augmented Plane Wave + Local Orbitals Program for Calculating Crystal Properties* (K. Schwarz, Techn. Univ. Wien, Austria, 2018).
[53] K. Kuneš, R. Arita, P. Wissgott, A. Toschi, H. Ikeda, and K. Held, Comput. Phys. Commun. **181**, 1888 (2010).
[54] A. A. Mostofi, J. R. Yates, G. Pizzi, Y.-S. Lee, I. Souza, D. Vanderbilt, and N. Marzari, Comput. Phys. Commun. **185**, 2309 (2014).
[55] A. Weichselbaum and J. von Delft, Phys. Rev. Lett. **99**, 076402 (2007).
[56] A. K. Mitchell, M. R. Galpin, S. Wilson-Fletcher, D. E. Logan, and R. Bulla, Phys. Rev. B **89**, 121105 (2014).
[57] K. M. Stadler, A. K. Mitchell, J. von Delft, and A. Weichselbaum, Phys. Rev. B **93**, 235101 (2016).
[58] R. Žitko and T. Pruschke, Phys. Rev. B **79**, 085106 (2009).
[59] S.-S. B. Lee and A. Weichselbaum, Phys. Rev. B **94**, 235127 (2016).
[60] S.-S. B. Lee, J. von Delft, and A. Weichselbaum, Phys. Rev. Lett. **119**, 236402 (2017).
[61] H. U. R. Strand, github.com/TRIQS/tprf (2019), doi:10.5281/zenodo.2638059.
[62] H. Alloul, Scholarpedia **9**, 32069 (2014), arXiv:1504.06992.
[63] H. Alloul, Scholarpedia **10**, 30632 (2015), arXiv:1505.04699.
[64] H. Mukuda, K. Ishida, Y. Kitaoka, K. Asayama, Z. Mao, Y. Mori, and Y. Maeno, J. Phys. Soc. Japan **67**, 3945 (1998).
[65] K. Ishida, H. Mukuda, Y. Minami, Y. Kitaoka, Z. Q. Mao, H. Fukazawa, and Y. Maeno, Phys. Rev. B **64**, 100501 (2001).
[66] J. Mravlje, M. Aichhorn, T. Miyake, K. Haule, G. Kotliar, and A. Georges, Phys. Rev. Lett. **106**, 096401 (2011).
[67] E. Gull, A. J. Millis, A. I. Lichtenstein, A. N. Rubtsov, M. Troyer, and P. Werner, Rev. Mod. Phys. **83**, 349 (2011).
[68] J. E. Gubernatis, M. Jarrell, R. N. Silver, and D. S. Sivia, Phys. Rev. B **44**, 6011 (1991).
[69] A. C. Hewson, A. Oguri, and D. Meyer, Eur. Phys. J. B **40**, 177 (2004).
[70] J. Bauer and A. C. Hewson, Phys. Rev. B **76**, 035118 (2007).
[71] Y. Nishikawa, D. J. G. Crow, and A. C. Hewson, Phys. Rev. B **82**, 115123 (2010).
[72] S. Hoshino and P. Werner, Phys. Rev. Lett. **115**, 247001 (2015).
[73] S. Hoshino and P. Werner, Phys. Rev. B **93**, 155161 (2016).
[74] G. Li, A. Luican, J. M. B. Lopes dos Santos, A. H. Castro Neto, A. Reina, J. Kong, and E. Y. Andrei, Nat. Phys. **6**, 109 (2009).
[75] A. Kerelsky, L. J. McGilly, D. M. Kennes, L. Xian, M. Yankowitz, S. Chen, K. Watanabe, T. Taniguchi, J. Hone, C. Dean, A. Rubio, and A. N. Pasupathy, Nature **572**, 95 (2019).
[76] Y. Choi, J. Kemmer, Y. Peng, A. Thomson, H. Arora, R. Polski, Y. Zhang, H. Ren, J. Alicea, G. Refael, F. von Oppen, K. Watanabe, T. Taniguchi, and S. Nadj-Perge, Nat. Phys. (2019).
[77] A. Pustogow, Y. Luo, A. Chronister, Y. S. Su, D. A. Sokolov, F. Jerzembeck, A. P. Mackenzie, C. W. Hicks, N. Kikugawa, S. Raghu, E. D. Bauer, and S. E. Brown, arXiv:1904.00047.
[78] A. Weichselbaum, Ann. Phys. **327**, 29723047 (2012).
[79] A. Weichselbaum, Phys. Rev. B **86**, 245124 (2012).
[80] O. Parcollet, M. Ferrero, T. Ayral, H. Hafermann, I. Krivenko, L. Messio, and P. Seth, Comput. Phys. Commun. **196**, 398 (2015).
[81] P. Seth, I. Krivenko, M. Ferrero, and O. Parcollet, Comput. Phys. Commun. **200**, 274 (2016).
[82] M. Aichhorn, L. Pourovskii, P. Seth, V. Vildosola, M. Zingl, O. E. Peil, X. Deng, J. Mravlje, G. J. Kraberger, C. Martins, M. Ferrero, and O. Parcollet, Comput. Phys. Commun. **204**, 200 (2016).

Supplemental Material for
“Strongly Correlated Materials from a Numerical Renormalization Group Perspective: How The Fermi-liquid State of $\mathrm{Sr_2RuO_4}$ Emerges”

Fabian B. Kugler,[1] Manuel Zingl,[2] Hugo U. R. Strand,[2] Seung-Sup B. Lee,[1] Jan von Delft,[1] and Antoine Georges[3,2,4,5]
[1] *Arnold Sommerfeld Center for Theoretical Physics, Center for NanoScience, and Munich Center for Quantum Science and Technology, Ludwig-Maximilians-Universität München, 80333 Munich, Germany*
[2] *Center for Computational Quantum Physics, Flatiron Institute, 162 5th Avenue, New York, NY 10010, USA*
[3] *Collège de France, 11 place Marcelin Berthelot, 75005 Paris, France*
[4] *Centre de Physique Théorique, CNRS, Ecole Polytechnique, IP Paris, 91128 Palaiseau, France*
[5] *Department of Quantum Matter Physics, University of Geneva, 1211 Geneva 4, Switzerland*
(Dated: September 6, 2019)

In this Supplemental Material, we first provide the definitions of the susceptibilities shown in the main text, discuss the Hamiltonians and the neglect of pair hopping, and give some algorithmic details. Next, we list the quasiparticle parameters deduced from the NRG flow. Finally, we benchmark our NRG results at various temperatures against continuous-time Quantum Monte Carlo (CTQMC) [67] data obtained in the hybridization expansion (CTHYB) [51, 67, 81]. Citations refer to the list of references given in the main text.

SUSCEPTIBILITIES

We compute susceptibilities as retarded two-point correlation functions of bosonic operators A, B on the impurity, $\chi(t) = \langle A||B\rangle(t) = -i\Theta(t)\langle[A(t), B]\rangle$. Focusing on their spectral density, we have $\chi = \chi' - i\pi\chi''$ and $\chi''(\omega) = \frac{1}{2\pi}\int \mathrm{d}t\, e^{i\omega t}\langle[A(t), B]\rangle$. Spin susceptibilities are computed via the spin operator in z direction,

$$S_m = \frac{1}{2}\sum_{\sigma\sigma'} d^\dagger_{m\sigma}\tau^z_{\sigma\sigma'}d_{m\sigma'},$$

using the Pauli matrix $\tau^z = \mathrm{diag}(1, -1)$ and the creation operator $d^\dagger_{m\sigma}$ of an electron in orbital m with spin σ on the impurity. Orbital (or angular-momentum) susceptibilities are computed via

$$L_m = \frac{i}{\sqrt{2}}\sum_{\sigma m'm''}\epsilon_{mm'm''}d^\dagger_{m'\sigma}d_{m''\sigma}$$

with the Levi-Civita symbol $\epsilon_{mm'm''}$. The factor of $1/\sqrt{2}$ is chosen for convenience, such that χ''_{sp} and χ''_{orb} have roughly the same integral weight $\int_0^\infty \chi''(\omega)\,\mathrm{d}\omega$. Total susceptibilities are obtained from $S_{\mathrm{tot}} = \sum_m S_m$ and $L_{\mathrm{tot}} = \sum_m L_m$. Finally, the orbital susceptibilities, $\langle L_m||L_m\rangle$, behave very similar to orbital-resolved charge susceptibilities [19], $\langle N_m||N_m\rangle$ with $N_m = \sum_\sigma d^\dagger_{m\sigma}d_{m\sigma}$.

HAMILTONIANS

To construct the non-interacting Hamiltonian, we use maximally localized Wannier functions [46, 47] for the three t_{2g}-like orbitals centered on the Ru atoms, employing the software packages WIEN2K [52] wien2wannier [53], wannier90 [54] and TRIQS/DFTTools [80, 82]; see [48] for further details. The resulting Wannier Hamiltonian, $h_{mm'}(\boldsymbol{k})$, is nondiagonal in orbital space. However, without spin-orbital coupling, which we neglect in this work, local single-particle quantities are orbital-diagonal due to the crystal symmetry of $\mathrm{Sr_2RuO_4}$. This applies to the impurity energy levels, $\boldsymbol{\epsilon}_d = \sum_{\boldsymbol{k}}\boldsymbol{h}(\boldsymbol{k})$ (momentum sum normalized), the local propagator

$$\boldsymbol{G}(\omega) = \sum_{\boldsymbol{k}}[\omega + i0^+ + \mu - \boldsymbol{h}(\boldsymbol{k}) - \boldsymbol{\Sigma}(\omega)]^{-1},$$

and the hybridization function $\boldsymbol{\Delta}(\omega)$.

The spectral density of the hybridization is evaluated as $\mathcal{A}_{\Delta,m}(\omega) = \frac{1}{\pi}\mathrm{Im}[G^{-1}_m(\omega) + \Sigma_m(\omega)]$. This already indicates the inverse relation between $\mathcal{A}_\Delta$ and the spectral function $\mathcal{A} = -\frac{1}{\pi}\mathrm{Im}G$, responsible for producing a dip in the hybridization from a van Hove peak in the spectrum. Indeed, if consider small frequencies ω, where $|\mathrm{Im}\Sigma(\omega)|, |\mathrm{Re}G(\omega)| \ll |\mathrm{Im}G(\omega)|$, we directly get $\mathcal{A}_\Delta(\omega) \propto \mathcal{A}^{-1}(\omega)$.

The widely used, local, SO(3)-symmetric Kanamori interaction Hamiltonian [2], consisting of a density-density, spin-flip, and pair-hopping part, is given by

$$\begin{aligned}
H_{\mathrm{int}} &= H_{\mathrm{dd}} + H_{\mathrm{sf}} + H_{\mathrm{ph}},\\
H_{\mathrm{dd}} &= U\sum_m n_{m\uparrow}n_{m\downarrow} + U'\sum_{m\neq m'} n_{m\uparrow}n_{m'\downarrow}\\
&\quad + (U' - J)\sum_{m<m',\sigma} n_{m\sigma}n_{m'\sigma},\\
H_{\mathrm{sf}} &= -J\sum_{m\neq m'} d^\dagger_{m\uparrow}d_{m\downarrow}d^\dagger_{m'\downarrow}d_{m'\uparrow},\\
H_{\mathrm{ph}} &= J\sum_{m\neq m'} d^\dagger_{m\uparrow}d^\dagger_{m\downarrow}d_{m'\downarrow}d_{m'\uparrow},
\end{aligned}$$

(a)	Z	$\tilde{\epsilon}$	ϵ	$\Sigma(0)$
xy	0.17	−0.076	−5.80	5.35
xz	0.26	−0.078	−5.72	5.42

(b)	$S=0$ (singlet)				$S=1$ (triplet)	
	xy-xy	xz-xz	xy-xz	xz-yz	xy-xz	xz-yz
$\tilde{U}$	0.17	0.40	0.27	0.40	−0.085	−0.12
Γ	6.1	5.9	6.1	5.9	−2.0	−1.7

TABLE I. Zero-temperature quasiparticle parameters deduced from the NRG low-energy spectrum. (a) Quasiparticle weight Z, quasiparticle energy level $\tilde{\epsilon}$, bare energy level ϵ, and the resulting self-energy at zero frequency, $\Sigma(0)$. (b) Quasiparticle interactions $\tilde{U}^{S}_{mm'}$ and the zero-energy vertex $\Gamma^{S}_{mm'}$, revealing an effective attraction in the spin-triplet sector. The two significant digits in all values give a rough estimate of the numerical accuracy.

with $U' = U - 2J$. The spin-flip term is crucial for the SU(2) spin symmetry and Hund-metal physics. By contrast, we argue in the following that the pair-hopping term is almost inactive in the Hund-metal phase of $\mathrm{Sr_2RuO_4}$ and can be neglected to obtain a model with higher symmetry that is more tractable for NRG (see below).

PAIR HOPPING

Considering the identical prefactor J of the spin-flip and pair-hopping term, it seems *a priori* hardly justified to neglect H_{ph}. However, it is readily understood that the effect of H_{ph} is a high-energy process, requiring states with one fully occupied and one completely empty orbital at the impurity site. At low energies, these contributions are suppressed; the dominant contributions instead have an impurity occupation of four electrons almost equally distributed among the three orbitals in the case of $\mathrm{Sr_2RuO_4}$.

Furthermore, we can *a posteriori* justify neglecting H_{ph} by evaluating the probability for an empty and doubly occupied orbital in the thermal state ρ. For this, we use the projectors

$$P_{m\uparrow\downarrow} = n_{m\uparrow} n_{m\downarrow}, \quad P_{m0} = (1 - n_{m\uparrow})(1 - n_{m\downarrow}),$$

to find that the probabilities

$$\mathrm{prob}_{\mathrm{ph},m\to m'} = \mathrm{Tr}[\,\rho\, P_{m\uparrow\downarrow} P_{m'0}]$$

are all on the level of a few percent. We also compared imaginary-time CTHYB results with and without pair hopping and found deviations of similar magnitude.

ALGORITHMIC DETAILS

Combining the quadratic part of the Hamiltonian, with $\Delta_{\mathrm{xy}}(\omega) \neq \Delta_{\mathrm{xz}}(\omega) = \Delta_{\mathrm{yz}}(\omega)$, with the SO(3)-symmetric interaction Hamiltonian, we have a **ch**arge, **orb**ital, and **sp**in symmetry of $\mathrm{U(1)_{ch}} \otimes \mathrm{SO(2)_{orb}} \otimes \mathrm{SU(2)_{sp}}$. Computationally, the one-dimensional SO(2) symmetry is rather weak. However, by neglecting the pair-hopping term, we obtain the larger symmetry $\mathrm{U(1)_{ch,xy}} \otimes \mathrm{U(1)_{ch,xz}} \otimes \mathrm{U(1)_{ch,yz}} \otimes \mathrm{SU(2)_{sp}}$.

We employ the full density-matrix (fdm) NRG [55] and exploit these symmetries using the QSpace tensor library [78, 79]. For further efficiency, we interleave [56, 57] the Wilson chains of all orbitals and thereby artificially break the symmetry between the xz and yz orbitals, but restore it by averaging results for these orbitals at each DMFT iteration. We use an NRG discretization parameter of $\Lambda = 6$ and keep up to 10^5 SU(2)-spin multiplets (roughly $4 \cdot 10^5$ individual states) during the iterative diagonalization. Sufficient resolution at finite energies is obtained by averaging results over four shifted discretization grids [58] and by using an adaptive broadening scheme [59, 60].

In the illustration of the NRG flow in Fig. 1(b), xz and yz contributions are averaged as well. To understand the rescaling of the axes in Fig. 1(b), we recall that the iterative diagonalization with a successively increasing Wilson chain length N sets a characteristic energy splitting of $a\Lambda^{-N/2}$, with a of order unity [9]. The y-axis is thus rescaled $\propto \Lambda^{-N/2}$ to have converged energy levels with convenient values. Further, in fdm-NRG, temperature-dependent quantities are computed unambiguously by including all Wilson shells N (of characteristic energy scale $E_N = a\Lambda^{-N/2}$) with their respective, temperature-dependent weight w_N^T [78]. Typically, w_N^T is maximal close to $E_N \approx T$ [78]. For the x-axis of Fig. 1(b), we fix the prefactor a by actually requiring $(\sum_N w_N^T E_N)/(\sum_N w_N^T) = T$ and thus have a unique assignment of shell index to energy scale and temperature.

Finally, to obtain a smooth hybridization in the DMFT self-consistency iteration, performed entirely on the real-frequency axis, we use a momentum summation with a large number of $4 \cdot 10^6$ $\boldsymbol{k}$ points in the irreducible Brillouin zone and manually set $-\mathrm{Im}\Sigma_{xy} \geq 0.005$ and $-\mathrm{Im}\Sigma_{xz/yz} \geq 0.01$.

QUASIPARTICLE PARAMETERS

In the main text, we explained that the quasiparticle weight Z and energy level $\tilde{\epsilon}$ can be extracted from the low-energy spectrum. The results are reported in Tab. I(a). The values for Z agree quantitatively with those obtained from the dynamic self-energy via $Z = [1 - \partial_\omega \mathrm{Re}\Sigma(0)]^{-1}$; the same is true when comparing $\tilde{\epsilon} = Z \cdot \big(\epsilon + \Sigma(0)\big)$ to the zero-frequency value of the dynamic self-energy.

The results for the quasiparticle interaction $\tilde{U}^{S}_{mm'}$ and the zero-energy vertex $\Gamma^{S}_{mm'}$ are listed in Tab. I(b). For their computation, we employed the quasiparticle density at the impurity, $|\psi_m(0)|^2$. It is conceptually related to

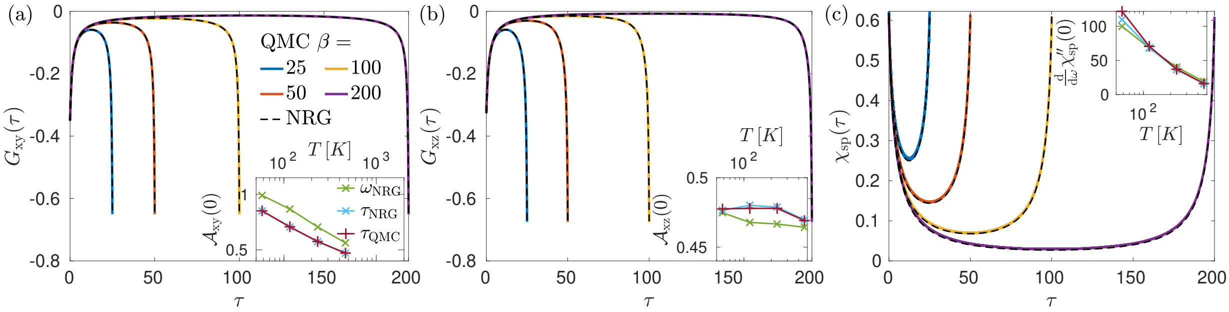

FIG. 5. Benchmark of NRG results against imaginary-time CTHYB data at various temperatures. (a) Single-particle Green's function in the xy orbital. Inset: Spectral weight at zero frequency, $\mathcal{A}(0)$, computed from the NRG real-frequency result (label $\omega_{\rm NRG}$) and the imaginary-time proxy, $-\frac{\beta}{\pi}G(\tau = \beta/2)$, both in NRG and CTHYB (labels $\tau_{\rm NRG}$ and $\tau_{\rm QMC}$). (b) Analogous plot for the xz orbital. (c) Total spin susceptibility. Inset: Zero-frequency slope of its spectral density, $\chi''_{\rm sp}$, computed from the NRG real-frequency result and the imaginary-time proxy, $-(\frac{\beta}{\pi})^2\chi(\tau = \beta/2)$.

the excited state $|E_m\rangle$ and groundstate $|\mathcal{G}\rangle$ of the renormalized impurity model according to $\psi_m(0) = \langle E_m|d^\dagger_\sigma|\mathcal{G}\rangle$, and practically evaluated as

$$|\psi_m(0)|^2 = \mathrm{Res}_{\omega=E_m} G_m(\omega) = \frac{1}{1 - \partial_\omega \Delta(\omega)|_{\omega=E_m}}.$$

BENCHMARKING NRG AGAINST QMC

We benchmark our NRG results against CTHYB imaginary-time data at various temperatures. All results are computed without pair hopping and are converged on their respective DMFT self-consistency cycle. We find very good agreement for the single-particle Green's function $G_{\rm xy}$ and $G_{\rm xz}$, see Fig. 5(a) and (b). The (total) spin susceptibilities show satisfactory agreement as well, with slightly higher deviations, see Fig. 5(c).

In the insets of Fig. 5, we show the real-frequency quantities $\mathcal{A}(0)$ and $\frac{\rm d}{{\rm d}\omega}\chi''|_{\omega=0}$ and their imaginary-time proxies, given by the l.h.s. of the relations

$$-\frac{\beta}{\pi}G(\tau\!=\!\beta/2) = \mathcal{A}(0) + \frac{\pi^2}{2\beta^2}\frac{{\rm d}^2}{{\rm d}^2\omega}\mathcal{A}(0) + O(\beta^{-4}),$$

$$\left(\frac{\beta}{\pi}\right)^2\chi(\tau\!=\!\beta/2) = \frac{\rm d}{{\rm d}\omega}\chi''(0) + \frac{\pi^2}{3\beta^2}\frac{{\rm d}^3}{{\rm d}^3\omega}\chi''(0) + O(\beta^{-4}).$$

By fitting the corresponding polynomials to the real-frequency curves, we find that the β^{-2} corrections on the r.h.s. amount to roughly 10%, 5%, and 30% for $G_{\rm xy}$, $G_{\rm xz}$, $\chi_{\rm sp}$, respectively. This is consistent with the notable deviations between the real-frequency values and their imaginary-time proxies in the insets of Fig. 5. The CTHYB results have been obtained using the TRIQS/CTHYB solver [81] and the TRIQS/TPRF package [61], which are based on the TRIQS library [80].

7 Summary and discussion

In this chapter, we summarize and discuss the main insights of all publications and explain further interpretations (Sec. 7.1.2), details (Sec. 7.2), and methodological challenges (Sec. 7.4.2). In the broader context of using RG approaches for strongly correlated systems, the works of *Chapter 3* present the novel approach of mfRG for the general fermionic many-body problem and apply it to the most prominent setting of correlated electrons, the 2D Hubbard model. Accurate results were obtained for weak to intermediate coupling strength and the prospects of reaching the strong-coupling regime by starting the flow from DMFT outlined. In Sec. 7.1.2, we expand on the idea of incorporating the RG notion into the parquet equations.

Before we established the direct connection between mfRG and the PA by a general, algebraic derivation of flow equations from self-consistent many-body relations, we had compared all the respective diagrammatic contributions. The devised algorithm to count Feynman diagrams from many-body equations led to the results of *Chapter 4*, where we count the number of diagrams in various quantities, relevant to cutting-edge many-body techniques, in approximate approaches as well as the exact solution. The implications for the radius of convergence of parquet resummations are also discussed in Sec. 7.2.

When targeting interacting electron systems of even higher complexity and closer to actual materials, multiple orbital degrees of freedom have to be taken into account. Then, an analysis of all the nonlocal fluctuations, as in mfRG, is extremely challenging, and, already on the level of the purely local correlations in DMFT, a variety of intriguing features can be explored. Particularly interesting are three-orbital models for the t_{2g} physics of Hund metals. Using NRG as DMFT impurity solver for these systems holds many advantages and has become feasible with recent methodological advances. However, DMFT+NRG studies of Hund metals in the general case of nondegenerate orbitals could not be realized before.

To get familiar with the iNRG approach (Sec. 2.4.2) to three-orbital systems, we first applied it to the technically much simpler setting of spinless impurity models and studied transport through three-level quantum dots in a collaboration led by H. Schoeller (*Chapter 5*). In this context, NRG is indeed the gold standard and can provide important (equilibrium) benchmark data for other RG methods reaching into the nonequilibrium regime. Finally, *Chapter 6* contains applications of DMFT+iNRG to three-orbital lattice systems, where we investigated orbital differentiation in Hund metals both in the model and material context. In Sec. 7.4.2, we discuss the main challenges for treating systems with an even higher number of orbitals.

7.1 Multiloop functional renormalization group

The mfRG framework achieves a unification and, at the same time, significant improvement of the fRG and parquet approaches. On the one hand, it provides an optimal truncation of the fRG hierarchy of flow equations: Instead of simply neglecting the influence of higher-point vertices, it incorporates all contributions from the six-point vertex to the flow of the four-point vertex and self-energy which can be kept efficiently, i.e., at numerical costs $O(N_k^4)$ (see Chapter 2). On the other hand, it enables a differential treatment of the parquet equations: It solves the notoriously difficult self-consistent parquet equations via a numerically more stable differential equation and guarantees the full parquet self-consistency throughout the entire flow.

The series of papers on mfRG, presented in Chapter 3, can be viewed along a continuous train of thought, which we retrace in the following. First, we recap the key points of the diagrammatic formulation of mfRG and discuss the improvements over the conventional, one-loop fRG. These are nicely brought to bear by the application to the 2D Hubbard model and encapsulated in two important figures. Then, we summarize the algebraic formulation of mfRG and the implications for diagrammatic extensions of DMFT. Finally, we elaborate on the interpretation of mfRG as differential form of the parquet equations.

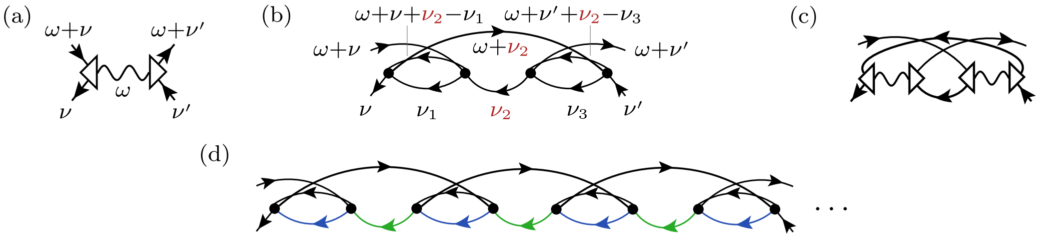

Figure 7.1 (a) The fermionic four-point interaction mediated by a Hubbard–Stratonovich boson is of the separable type $\Gamma_r^{(3)}(\omega_r,\nu)\Xi_r(\omega_r)\Gamma_r^{(3)}(\omega_r,\nu')$. (b) The separable form is violated already by the simplest parquet diagram with an explicit dependence on ν and ν'. (c) Second-order diagram of the four-point vertex in the transformed system. (d) Simple parquet diagram with alternating parallel and antiparallel lines. Whereas cutting any green lines generates 1PR diagrams, cutting n blue lines yields 1PI $(4+2n)$-point diagrams. Thus, *full* inclusion of such a parquet diagram with n blue lines via the fRG hierarchy of flow equations requires vertices up to the $(4+2n)$-point level.

7.1.1 Summary

Our interest in comparing fRG and the PA was triggered by the publication [LDSK15]. It claims that the parquet diagrams (short for the diagrams of the PA) of the X-ray–edge singularity can be resummed using a multichannel Hubbard–Stratonovich (HS) transformation followed by a simple truncation of the corresponding fRG flow. The idea is intriguing: The simplest self-energy of a HS boson already yields a ladder resummation for the effective fermionic interaction. Can a simple realization of coupled HS bosons represent the whole parquet resummation?

An important message of [P1] is that the way [LDSK15] obtained the parquet result for the particle-hole susceptibility is subject to a “fortuitous partial cancellation of diagrams specific to the X-ray–edge singularity” [P1]. Indeed, we clarified some of their approximations, rederived the result via a flowing susceptibility in a transparent and *regulator-independent* fashion, and thereby revealed the simple ladder structure of the underlying resummation. We also showed that a HS transformation does not save one from having to calculate the fermionic four-point vertex. This is easily understood: The parquet vertex (here composed of only two channels $r\in\{a,p\}$) develops a nontrivial three-dimensional frequency structure in the 2PR vertices $\gamma_r(\omega_r,\nu,\nu')$. However, the (effective) fermionic interaction mediated by a HS boson in channel r is of the type $\Gamma_r^{(3)}(\omega_r,\nu)\Xi_r(\omega_r)\Gamma_r^{(3)}(\omega_r,\nu')$, as illustrated in Fig. 7.1(a). This separable dependence on ν and ν' is far from general and breaks down already at the simplest parquet diagram with an explicit dependence on ν and ν', see Fig. 7.1(b). The HS transformation eliminates the first-order four-point diagrams, but the general four-point vertex persists and contains important contributions starting at second order; see, e.g., the diagram shown in Fig. 7.1(c) (irrespective of performing a flow or not). Even a subsequent rebosonization [BBW04], which uses counter terms that originate from a flowing rescaling of the field variables, can only eliminate contributions of a simple one-dimensional dependence.

Nevertheless, the multichannel HS transformation hints at the importance of a channel-dependent parametrization of the effective interaction, decomposed into physically relevant and diagrammatically justified contributions. Such a frequency parametrization was achieved by [WLT$^+$16] in a purely fermionic language (see Sec. 2.5).

We argued in [P1] that the parquet diagrams include 1PI n-point vertices of arbitrarily high n in the fRG hierarchy of flow equations, with or without HS transformation. Such vertices follow from (simple) parquet diagrams by cutting the corresponding number of lines, as long as there is no single, left-over (fermionic or bosonic) line inducing the one-particle reducibility, see Fig. 7.1(d). We also considered a 2PI formulation of fRG, finding that the simple Λ dependence of the generating LW functional, induced by only the full propagator as its argument, does not provide additional possibilities for summing the parquet diagrams compared to the 1PI framework.

The most important points of [P1] regarding mfRG are:

- One cannot deduce the content of a diagrammatic resummation from only the final result or, e.g., the power-law form of a specific quantity (here the particle-hole susceptibility).
- Solving the purely fermionic fRG flow truncated at $\Gamma^{(6)}=0$ does not reproduce the PA. Moreover, two- and three-point vertices of a multichannel HS transformation are unable to

replace the (parquet) contribution of the fermionic four-point vertex. With or without HS transformation, the parquet diagrams include 1PI n-point vertices for arbitrarily high n in the standard fRG hierarchy of flow equations.

In light of these findings, (i) we aimed at reproducing the PA from an fRG flow on an exact, diagrammatic level and did not satisfy ourselves with agreement for a specific quantity to a specific accuracy (e.g. leading log); (ii) we retained the purely fermionic formulation, but abandoned the rigid fRG hierarchy of flow equations, which assigns simple parquet contributions to arbitrarily high n-point vertices. After all, the parquet algorithm generates all diagrams of complexity $O(N_k^4)$—the same must be possible in fRG.

The main idea for the diagrammatic derivation of mfRG in [P2, P3] is the following: First, consider a diagrammatic resummation (here the PA) and make all diagrams Λ-dependent by replacing $G_0 \to G_0^\Lambda$. Then, find all *differentiated* diagrams of a specific object (e.g. the vertex Γ) by taking the Λ derivative according to the product rule (summing all copies of diagrams with one G_0 line replaced by $\dot{G}_0$). Now, check whether this resummation fulfills a certain flow equation (such as $\dot{\Gamma} = f_\Gamma$) by expanding both sides in the interaction and comparing each order, i.e., by comparing the differentiated diagrams. If certain contributions are missing in f_Γ, try to express them through the basic ingredients of the flow (Γ^Λ, G^Λ, etc.) and add them to the approximate flow equation, ideally using previously computed objects.

The mfRG flow, developed in [P2, P3], iteratively sums up all differentiated parquet diagrams. The procedure is very efficient as it consists of successive one-loop calculations and follows the typical RG structure of loops connecting full vertices (i.e. the effective interaction). The one-loop flow fully captures all ladder diagrams and contains at least a portion of each parquet diagram (namely the integral of those differentiated parquet diagrams where the differentiated line induces a two-particle reducibility). Diagrams where the differentiated line is increasingly nested are added by higher-loop contributions. Since the standard, one-loop fRG already contains some part of all parquet diagrams, the multiloop corrections are the minimal additions to make the fRG flow independent from the choice of regulator.

The diagrammatic construction in [P2] is facilitated by the minimal structure of the X-ray–edge singularity. For this toy model, we proved algebraically that the number of differentiated parquet diagrams precisely matches the number of differentiated diagrams generated by mfRG. In [P3], we extended the analysis to the general many-body problem. Next to the natural generalization to three two-particle channels and full propagators, we described corrections to the—in principle—exact self-energy flow, required when using the vertex in the PA. Equivalence to the parquet equations in conjunction with the SDE was established by a numerical procedure to count all involved diagrams. We clarified the numerically simple structure of the multiloop corrections by giving a pseudocode formulation of the mfRG flow in the appendix of [P3].

Key insights of [P2, P3] are

- One can diagrammatically derive multiloop corrections to the standard, one-loop fRG flow (obtained by setting $\Gamma^{(6)} = 0$ in the fRG hierarchy of flow equations), which consist of iterative one-loop calculations and successively complete the parquet resummation. These additions incorporate all contributions of $\Gamma^{(6)}$ to the flow of $\Gamma^{(4)}$ and Σ that can be kept efficiently, i.e., at the cost $O(N_k^4)$ of the PA.

- The mfRG flow improves the one-loop fRG flow in a number of ways: it restores the independence on the choice of regulator; it fulfills the diagrammatic identities of the PA (see Sec. 2.3.1.7) throughout the flow; it provides the full feedback between different two-particle channels and thereby increases the stability of the flow towards larger interaction strengths, suppressing ladder-type vertex divergences.

- The mfRG flow is advantageous over directly solving the parquet equations as it replaces *self-consistent* by numerically more stable *differential* equations. It naturally provides a regulator, which is needed to study infrared instabilities and can be adapted to one's needs (e.g. for a fast convergence in the number of loops). Finally, it retains the generality of fRG to flow between any two actions and is ideal for diagrammatic extensions of DMFT, as further discussed below.

Whereas [P2] contains mfRG results for a toy model and [P3] provides the general formulation, [P4] applies mfRG to the prominent 2D Hubbard model. It contains the diagrammatic derivation

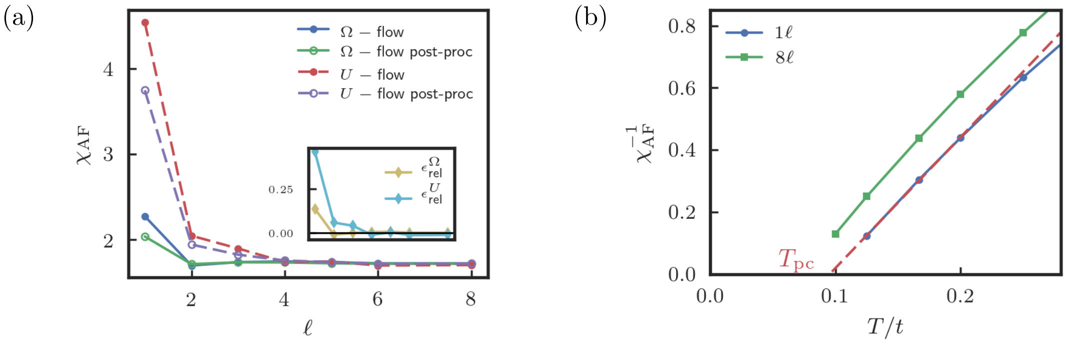

Figure 7.2 Plots for the antiferromagnetic susceptibility, χ_{AF}, in the half-filled 2D Hubbard model at interaction strength $U = 2t$ (where t is the hopping amplitude), taken from [P4]. (a) χ_{AF} (at $T = 0.2t$) obtained in an ℓ-loop flow in four different ways, choosing one of two regulators (dubbed Ω and U flow) and one of two schemes to compute response functions (directly from the flow or "post-processed"). Upon convergence in the number of loops, mfRG yields unique results for all schemes. (b) Computing χ_{AF}^{-1} at decreasing temperature, mfRG gives a finite value at $T = 0.1t$, where one-loop results already diverge.

of the mfRG flow of response functions, i.e., fermion-boson three-point vertices and susceptibilities. The latter are directly observable in experiment and hence of prime interest in any many-body framework. In fRG, there are two ways to obtain the response functions: They can either be computed from the four-point vertex and self-energy at the end of the flow ("post-processed"), or themselves included in the flow and analyzed at variable scale ("flowing"). Both procedures are equivalent in an exact solution but differ considerably in one-loop fRG. The multiloop flow, generating all parquet diagrams, restores the equivalence between the different ways of computing response functions.

Publication [P4] presents an fRG analysis of the 2D Hubbard model that goes beyond previous such studies in several ways: (i) It accounts for the full momentum and frequency dependence of the vertex. The parametrization, adapted to each two-particle channel, incorporates high-frequency asymptotics, a Brillouin-zone discretization for the (bosonic) transfer momentum, and a form-factor expansion for the weak dependence on fermionic momenta (cf. Chapter 2). (ii) Many fRG treatments of 2D lattice models neglect the self-energy because a frequency-independent vertex yields a similarly frequency-independent self-energy. Given our accurate parametrization of the vertex, the self-energy can easily be included. (iii) We employed an mfRG flow for all involved quantities: four-point vertex, self-energy, three-point vertices, and susceptibilities.

Two highlights of [P4] are illustrated by the plots reproduced in Fig. 7.2 (system parameters are given in the caption). Panel (a) shows results for the antiferromagnetic susceptibility, i.e., the static spin susceptibility at momentum (π, π). They are obtained from an ℓ-loop flow in four different ways, using either the flowing or post-processed scheme with one of two regulators (called Ω and U flow). At one-loop accuracy, one finds four different results ranging from 2 to 4.5. Clearly, there is hardly any quantitative meaning in this outcome. However, as the number of loops is increased, the results of all four procedures converge to a unique value[1] of roughly 1.7. Panel (b) shows that one-loop fRG predicts a divergent antiferromagnetic susceptibility and thus a finite critical Néel temperature T_N for the half-filled model, in conflict with the Mermin–Wagner theorem (see Chapter 2). In other words, one-loop fRG at $T = 0.1t$ already yields diverging vertices. By contrast, mfRG suppresses ladder-type vertex divergences and makes lower temperatures accessible. Indeed, we obtain a finite susceptibility at the lowest considered temperature[2] $T = 0.1t$.

---

[1] In an ongoing benchmark project, this value is found to agree within 0.5% with determinant Monte Carlo data [HH19]. This demonstrates that, at these system parameters, the PA is still very accurate while the multiloop corrections are already sizable. Note that our converged mfRG results constitute the first thermodynamic-limit results for the 2D Hubbard model that are equivalent to the PA.

[2] It is numerically hard to access lower temperatures: First, with decreasing T, the grid of Matsubara frequencies becomes finer and the size of vertices larger. Second, the nonseparable three-dimensional frequency-dependence of the vertices gets more pronounced such that a higher number of loops is needed for convergence. Third, it is hard to check the suppression of T_N by an explicit calculation at low temperatures when the system exhibits quasi-long-range spatial fluctuations and the exponentially growing correlation length renders any finite momentum discretization insufficient. As discussed in [P4], estimates for the temperature range where χ_{AF}^{-1} starts to show an exponential decrease are below $T = 0.05t$ and thus below the temperatures accessible to us so far. Hence, the

Two important points of [P4] are:

- The application to the 2D Hubbard model confirms the improvements of mfRG over one-loop fRG expected from general grounds. Most importantly, this includes the independence from the choice of the regulator and formula for the response functions and a stabilized flow, which suppresses vertex divergences and permits access to the more strongly correlated regime (higher U and/or lower T).
- Altogether, with an accurate parametrization of vertex functions and the multiloop formulation, fRG flows can be brought under quantitative control.

In publications [P2, P3, P4], the multiloop flow equations were derived from a diagrammatic point of view, following the strategy of amending the truncated fRG flow in a way that fully includes all parquet diagrams. In [P5], we instead started from the parquet equations and algebraically derived flow equations, without any reference to Feynman diagrams. The general idea is to derive exact flow equations not from generating functionals but directly from the self-consistent parquet equations. A scale (Λ) dependence is induced by substituting $G_0 \to G_0^\Lambda$ in these relations and by requiring that the parquet equations be fulfilled for all values of Λ, considering the totally irreducible vertex, $R \neq R^\Lambda$, fixed. It is indeed “natural to exclude … R from the renormalization flow, as it constitutes precisely the part of the vertex that cannot be constructed iteratively and therefore does not have a flow equation that allows for an efficient (i.e. iterative one-loop) calculation” [P5]. Under the approximation of $R \neq R^\Lambda$, we derived exact flow equations for the 2PR vertices γ_r^Λ. The mfRG vertex flow emerges directly as iterative solution to these coupled differential equations. Furthermore, we showed how the standard self-energy flow follows from the functional derivative $\delta\Sigma/\delta G = -I_t$, and we showed how the diagrammatically rather intricate mfRG self-energy flow follows from the well-known SDE within the PA. In this approach, the reliance on higher-point vertices is avoided from the outset. The resulting flow does not suffer from a questionable truncation but operates within a closed set of self-consistent equations.

The analysis of [P5] reveals clearly how to perform mfRG flows beyond the PA by taking a totally irreducible contribution different from the bare vertex. Importantly, the assumption of fixed R underlies the formalism, but the flow is still exclusively formulated in terms of the full vertex, Γ. Only if the bare propagator at the beginning of the flow vanishes, $G_0^{\Lambda_i} = 0$, the vertex starts from the totally irreducible building block, $\Gamma^{\Lambda_i} = R$, while reducible contributions are generated during the flow. However, the flow can be started from any $G_0^{\Lambda_i}$ as long as Γ^{Λ_i} and Σ^{Λ_i} are known, i.e., as long as the BSEs and the SDE can be solved initially. This is illustrated in Fig. 7.3(a).

An important example is the DMF^{2}RG flow starting from DMFT, where the initial $G_0^{\Lambda_i} = G_0^{\mathrm{DMFT}}$ implies $\Sigma^{\Lambda_i} = \Sigma^{\mathrm{DMFT}}$ and $\Gamma^{\Lambda_i} = \Gamma^{\mathrm{DMFT}}$, as taken from the self-consistently determined Anderson impurity model. Such DMF^{2}RG flows have so far only been implemented in the one-loop scheme [TAB$^+$14], where a notable improvement was achieved [VTM19] with a refined choice for the specific Λ dependence in the bare propagator between $G_0^{\Lambda_i}$ and $G_0^{\Lambda_f}$. Nevertheless, the neglect of the six-point vertex remains the crucial approximation that limits the accuracy of one-loop DMF^{2}RG. In the multiloop extension, this approximation is ameliorated by including all effective three-particle interactions of complexity $O(N_k^4)$. In particular, results in mfRG are independent from the specific Λ dependence in G_0^Λ (up to a subtlety in the self-energy flow due to $R \neq \Gamma_0$); a clever choice, like the one of [VTM19], stated in Eq. (2.55), will then accelerate the convergence in the number of loops.

The benefit of multiloop DMF^{2}RG can also be seen from the parquet perspective. The DΓA approach, the direct application of the parquet equations taking the totally irreducible vertex, R, from the self-consistent impurity model (Sec. 2.5), is a very accurate diagrammatic extension of DMFT. However, it requires the diagrammatic decomposition $\Gamma = R + \sum_r \gamma_r$ of the nonperturbative DMFT vertex, which yields diverging results in strongly correlated systems [SRG$^+$13, SCW$^+$16, GRS$^+$17, CGS$^+$18, TGCR18]. This fundamental problem is resolved by the mfRG flow, which provides a solution of the parquet equations but is entirely based on the *regular* full vertex. The DMFT solution is not broken apart (into R) and then glued back together (solving the parquet equations with nonlocal propagators), but the internal lines in all diagrams of Σ

---

extrapolation of our χ_{AF}^{-1} data with temperature to a finite pseudocritical temperature T_{pc} does not contradict the fulfillment of the Mermin–Wagner theorem in the PA (see Sec. 2.3.1.7) and thus converged mfRG flows.

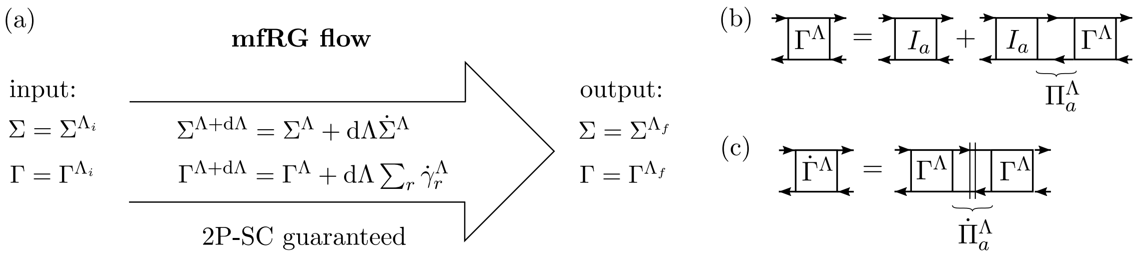
(a)
mfRG flow
input:
$\Sigma = \Sigma^{\Lambda_i}$
$\Gamma = \Gamma^{\Lambda_i}$
$\Sigma^{\Lambda+\mathrm{d}\Lambda} = \Sigma^{\Lambda} + \mathrm{d}\Lambda\dot{\Sigma}^{\Lambda}$
$\Gamma^{\Lambda+\mathrm{d}\Lambda} = \Gamma^{\Lambda} + \mathrm{d}\Lambda \sum_r \dot{\gamma}_r^{\Lambda}$
2P-SC guaranteed
output:
$\Sigma = \Sigma^{\Lambda_f}$
$\Gamma = \Gamma^{\Lambda_f}$
(b)
Γ^{Λ} = I_a + I_a Γ^{Λ}
Π_a^{Λ}
(c)
$\dot{\Gamma}^{\Lambda}$ = Γ^{Λ} Γ^{Λ}
$\dot{\Pi}_a^{\Lambda}$

Figure 7.3 (a) Illustration of the multiloop fRG (mfRG) flow [P2, P3]. It starts from an initial pair of self-energy, Σ, and vertex, Γ, that solve the parquet equations with bare propagator $G_0^{\Lambda_i}$ and fixed, underlying totally irreducible vertex, R [P5]. Both Σ and Γ evolve along the trajectory of two-particle self-consistent (2P-SC) solutions to the parquet equations, as defined by G_0^{Λ} and fixed, underlying R. At the end of the flow, where $G_0^{\Lambda_f} = G_0$, one obtains the desired Σ and Γ. (b) BSE in a single channel (as in ladder DΓA) made scale-dependent via $\Pi_a \to \Pi_a^{\Lambda}$ at fixed I_a (e.g. I_a^{DMFT}). (c) Equivalent formulation as flow equation, which involves only $\dot{\Pi}_a$ and the initial condition of the *full* vertex Γ^{Λ_i} (e.g. Γ^{DMFT}).

and Γ smoothly evolve from the local to their $\boldsymbol{k}$-dependent form, while retaining the parquet self-consistency throughout the flow.

Finally, from a somewhat different point of view, the differential diagrammatics of mfRG allowed us to settle a long-standing (and partly confusing[3]) question regarding conserving properties of the PA. We showed that the PA fulfills conservation laws on the one- but not the two-particle level. In particular, it does not fulfill the functional Ward identity $I_t = -\delta\Sigma/\delta G$, as follows directly from the fact [Smi92, P5] that any solution fulfilling both the SDE and the functional Ward identity must be the exact solution. Additionally, we explained how to numerically *construct* the 2PI vertex I_t'—different from I_t—which is equivalent to a functional derivative of the parquet self-energy. This provides a fully conserving solution originating from the parquet self-energy, which fulfills the functional Ward identity but violates the SDE. According to the discussion in Sec. 2.3.1.4, it is not surprising that the vertex $I_t' = -\delta\Sigma/\delta G$, is more complicated than the original parquet vertices I_t and Γ, related to Σ through the SDE.

To summarize, the main insights of [P5] are:

- The mfRG flow can be derived on a purely algebraic basis from the self-consistent parquet equations with an underlying, scale-independent totally irreducible vertex, R. Multiloop flows beyond the PA can be constructed using $R \neq \Gamma_0$. Importantly, R does not appear explicitly if the flow has a nontrivial starting point $G_0^{\Lambda_i} \neq 0$.
- This makes multiloop DMF^{2}RG an ideal tool for diagrammatic extensions of DMFT. The self-energy and full vertex smoothly evolve from the self-consistent impurity model to the lattice problem in a flow along self-consistent solutions to the parquet equations, without reliance on (potentially divergent) 2PI vertices.
- The parquet equations are self-consistent at the one- and two-particle level. Yet, their differential form reveals that the PA fulfills conservation laws on the one- but not on the two-particle level. The 2PI vertex of the PA *cannot* be derived from an LW functional. However, a fully conserving solution, with the original parquet self-energy but a different vertex, can be constructed at cost $O(N_k^6)$.

7.1.2 Differential treatment of the parquet equations

The results of [P5] lead to the additional interpretation of mfRG as a differential form of the parquet equations. Initially, the parquet formalism provides an efficient organization of diagrams and enables approximations that fulfill a variety of essential properties, but it does *not* include the important notion of scale dependence and successive mode elimination, inherent to the RG (see Sec. 2.2).

---

[3] For instance, while [BS92] states that the PA is not guaranteed to satisfy conservation laws, [YFL$^+$09, Jan98] write in their abstract that the PA is conserving. Possibly, the confusion arose because there are functionals from which the PA can be derived [DDM64a, DDM64b, Jan98, AP16]. However, these do *not* have the form of an LW functional $\Phi[G, \Gamma_0]$ [LW60, Bay62] but further depend on two-particle propagators. In [P5], we show that there is *no* $\Phi[G, \Gamma_0]$ from which the parquet vertex can be derived as $I_t = \delta^2\Phi/\delta G^2$.

Instead, each equation contains an integration over all energy-momenta, which is numerically hard to perform accurately. Particularly in divergent perturbation series, the self-consistent equations lack any infrared regulator to numerically detect the leading instabilities in a controlled fashion. To treat such systems, it is vital to include a scale parameter Λ into the whole framework.

Replacing the bare propagator G_0 appearing in the self-consistent equations by a scale-dependent G_0^Λ allows us to organize their solution by energy scales. This results in a family of Λ-dependent diagrams and a family of self-consistent solutions to the Λ-dependent parquet equations. The RG strategy then starts from the observation that the parquet equations are easily solved for only the high-energy degrees of freedom. For instance, with $G_0^\Lambda(i\nu,\boldsymbol{k}) = \Theta(|\nu|-\Lambda)G_0(i\nu,\boldsymbol{k})$, this is trivially the case since $G_0^{\Lambda_i=\infty}=0$. Now, if the parquet algorithm is initialized with a converged, self-consistent solution at energy scales $|\nu|>\Lambda$ (defined by G_0^Λ), it will again be easy to find a solution at scales $|\nu|>\Lambda+\mathrm{d}\Lambda$ (defined by $G_0^{\Lambda+\mathrm{d}\Lambda}$) with small $\mathrm{d}\Lambda<0$. In this way, we can approach the full solution at $G_0^{\Lambda_f=0}=G_0$ in a controlled fashion. The transition between solutions at different scales becomes seamless for infinitesimal $\mathrm{d}\Lambda$. Then, one actually solves a flow, along the trajectory of self-consistent solutions to the parquet equations [cf. Fig. 7.3(a)].

Formally, we describe the parquet equations with fixed input R as a set of equations $\boldsymbol{F}$, which becomes scale-dependent upon promoting $G_0 \to G_0^\Lambda$ in all equations:

$$\begin{pmatrix}\Sigma\\ \gamma_r\end{pmatrix} = \boldsymbol{F}(\Sigma,\gamma_r,R,G_0) \qquad \to \qquad \begin{pmatrix}\Sigma^\Lambda\\ \gamma_r^\Lambda\end{pmatrix} = \boldsymbol{F}(\Sigma^\Lambda,\gamma_r^\Lambda,R,G_0^\Lambda). \tag{7.1}$$

By taking the Λ derivative on both sides, we can directly cast the family of self-consistent equations into a "self-consistent" differential equation

$$\partial_\Lambda \begin{pmatrix}\Sigma^\Lambda\\ \gamma_r^\Lambda\end{pmatrix} = \boldsymbol{f}_1\Big(\Sigma^\Lambda,\gamma_r^\Lambda,G_0^\Lambda,R,\dot{\Sigma}^\Lambda,\dot{\gamma}_r^\Lambda,\dot{G}_0^\Lambda\Big). \tag{7.2}$$

The striking outcome of [P5] is that, to a *very* good approximation, this differential equation can be rephrased as an ordinary differential (or flow) equation of the form

$$\partial_\Lambda \begin{pmatrix}\Sigma^\Lambda\\ \gamma_r^\Lambda\end{pmatrix} = \boldsymbol{f}_2\Big(\Sigma^\Lambda,\Gamma^\Lambda,G_0^\Lambda,\dot{G}_0^\Lambda\Big), \tag{7.3}$$

which is solved for $\dot{\Sigma}^\Lambda$ and $\dot{\Gamma}^\Lambda = \sum_r \dot{\gamma}_r$ and where γ_r^Λ and R appear on the r.h.s. *only* through the full vertex, Γ^Λ. The approximations are: (i) R is excluded from the flow, already in Eq. (7.1), as it is precisely the vertex part that lacks an efficient flow equation; (ii) Eq. (7.3) contains the multiloop iteration, which however is found to converge fast in practice; (iii) the self-energy flow involves a subtle mismatch between Eq. (7.2) and (7.3) when $R \neq \Gamma_0$—perfect agreement for the self-energy is only obtained within the PA, when the bare vertex of the SDE (that appears alien from an RG point of view) matches the totally irreducible vertex in the parquet framework.

A minimal example for an mfRG flow with a nonperturbative starting point (and limiting case of DMF^{2}RG without hybridization) initializes the self-energy and vertex in the atomic limit [KOBH13]. Two realizations for the Λ dependence could be

$$G_0^\Lambda(k) = \frac{1}{i\nu+\mu-(1-\Lambda)\epsilon_{\boldsymbol{k}}} \quad \text{or} \quad G_0^\Lambda(k) = \frac{1}{i\nu+\mu-\Theta(|\xi_{\boldsymbol{k}}|/B-\Lambda)\epsilon_{\boldsymbol{k}}}, \quad \Lambda_i=1,\ \Lambda_f=0, \tag{7.4}$$

where $B=\max_{\boldsymbol{k}}|\xi_{\boldsymbol{k}}|$ (with $\xi_{\boldsymbol{k}}=\epsilon_{\boldsymbol{k}}-\mu$) marks the half-bandwidth. The flow, starting from the atomic limit, smoothly turns on the dispersion, either in a plain fashion or at decreasing momentum shells towards the Fermi surface. It goes beyond strong-coupling perturbation theory [Met91] as it incorporates the dispersion in the two-particle self-consistent form of the parquet equations. Reminiscent of the advantages of DMF^{2}RG over parquet DΓA, a direct application of the parquet equations starting from the atomic limit is impossible since the totally irreducible vertex, entering the parquet algorithm, has a highly complicated expression (not explicitly given in the literature) and is interspersed with the divergence lines of 2PI vertices [TGCR18]. By contrast, the mfRG flow via (7.4) can be directly performed: The self-energy and full vertex in the atomic limit have compact analytical expressions [HJB$^+$09, RVT12, WLT$^+$16, TGCR18], which are regular at any finite temperature.

Finally, we recall from Sec. 2.5 that, when using a *single* BSE to compute nonlocal vertices, the 2PI vertex could be eliminated with the "ladder DΓA trick" (2.52). The same elimination of the 2PI vertex occurs naturally in the corresponding RG flow. There, it is known [Kat04, P5] that a ladder construction for a fixed 2PI vertex translates into a single-channel one-loop flow of full renormalized vertices, see Figs. 7.3(b) and (c). Put simply, the scale-differentiated bubble in the flow equation makes propagators on its left and right distinguishable, such that one need not use 2PI vertices to avoid double counting. Hence, by using G_0^Λ to interpolate between impurity and lattice, the momentum-space ladder construction (in the a channel) with 2PI vertex from DMFT is directly rephrased as

$$\dot{\Gamma}^\Lambda_{\text{lad}} = \Gamma^\Lambda_{\text{lad}} \circ \dot{\Pi}^\Lambda_a \circ \Gamma^\Lambda_{\text{lad}}, \qquad \dot{\Pi}_{a;k,k',q} = \partial_\Lambda \big(G^\Lambda_k G^\Lambda_{k+q} \big) \delta_{k,k'}, \qquad \Gamma^{\Lambda_i}_{\text{lad}} = \Gamma^{\text{DMFT}}. \tag{7.5}$$

It is *not* known how to extend the "ladder DΓA trick" to parquet DΓA. However, mfRG extends the "full-vertex RG" (7.5) from a BSE in single channel to the coupled BSEs of the parquet formalism. It replaces the reliance on 2PI vertices by *differential* diagrammatics, and thus sets a new paradigm for diagrammatic resummations on the two-particle level.

7.2 Counting of Feynman diagrams

Originating from our comparison of truncated fRG flows and the PA, we developed in Chapter 4 a general strategy to count Feynman diagrams from the set of many-body relations that generate the result. Usually, the number of Feynman diagrams is obtained in one of two possible ways. On the one hand, one can consider a zero-dimensional field theory, which is trivially solvable by explicit computation of the "functional" integral, collapsing to a simple, one-dimensional integral. At the same time, any quantity X as function of the (dimensionless) interaction u has a formal expansion $X(u) = \sum_n \mathcal{N}_X(n) u^n$ [CLP78]. This can be used to extract $\mathcal{N}_X(n)$, the number of Feynman diagrams at interaction order n (the bare propagator is set to unity without loss of generality). On the other hand, one can pursue a combinatorial strategy for an arbitrary theory and count the number of all possible contractions to find the number of connected or disconnected Green's-function diagrams [Jis13]. By contrast, our approach is based on many-body relations, applicable to the exact solution and to diverse approximations, and gives the number of (bare or skeleton) diagrams for all the involved objects, such as m-point 1PI vertices as well as 2PR and 2PI four-point vertices (see Sec. 2.3). Here, we recall some results on the asymptotic number of Feynman diagrams and explain why approximate diagrammatic resummations are likely to have a finite radius of convergence, as opposed to the vanishing radius of convergence expected from general grounds [NO98].

In [P6], we extracted the asymptotic number of diagrams of an m-point 1PI vertex (recall $\Sigma = \Gamma^{(2)}$) for large orders n as $\mathcal{N}_{\Gamma^{(m)}}(n) \sim n! n^{(m-1)/2} 2^{(m-2)/2}$. A striking outcome is that the totally irreducible vertex, R—thought to have a very compact diagrammatic structure—asymptotically contains *all* diagrams of the full four-point vertex, $\Gamma^{(4)}$. Whereas $\mathcal{N}_{\Gamma^{(4)}} = \mathcal{N}_R + \sum_r \mathcal{N}_{\gamma_r}$ is dominated by contributions from the 2PR vertices γ_r at low orders, we find $\mathcal{N}_R(n) > \mathcal{N}_{\gamma_r}(n)$ for orders $n > 8$. For large interaction orders, R is responsible for the factorial growth, $\mathcal{N}_R(n) \sim \mathcal{N}_{\Gamma^{(4)}}(n)$, and the contributions from the 2PR vertices to the total number of diagrams in the full vertex become negligible, $\mathcal{N}_{\gamma_r}(n)/\mathcal{N}_R(n) \sim 1/n \to 0$ as $n \to \infty$. For any application (except the zero-dimensional field theory), the sheer number of Feynman diagrams has only limited impact on the final results, as different diagrams can cancel or contribute with largely different magnitudes. Nevertheless, we can use these results to draw two general conclusions.

First, any type of parquet approximation sets $\mathcal{N}_R(n) = 0$ for $n > n_p$ (i.e., R is approximated by a finite number of diagrams), while the reducible vertices and the self-energy still extend to arbitrarily large orders through the self-consistent parquet equations. The standard parquet approximation with $R = \Gamma_0$ is often motivated by the fact that corrections to R start only at fourth order with the "nongeneric" envelope diagrams. However, taking into account that $\mathcal{N}_R(n) \sim \mathcal{N}_{\Gamma^{(4)}}(n)$ for large n, parquet-type approximations cannot be justified by the (inadvertently assumed small) *number* of Feynman diagrams in the totally irreducible vertex. Instead, one needs to estimate the *weight* of all contributions to R, depending on the internal integrations represented by the Feynman diagrams (except for zero space-time dimensions). Often, one argues that the topological structure of totally irreducible diagrams implies a limited phase space for internal integrations, but more precise estimates of R are certainly needed.

Second, from the structure of the BSEs, we derived in [P6] the statement

$$\mathcal{N}_{\Gamma^{(4)}}(n) \sim n! \qquad \Rightarrow \qquad \mathcal{N}_R(n) \sim \mathcal{N}_{\Gamma^{(4)}}(n), \qquad n \to \infty. \tag{7.6}$$

Evidently, this conflicts with the premise $\mathcal{N}_R(n > n_p) = 0$ of parquet-type approximations. Hence, we concluded that the number of diagrams in any type of parquet approximation can at most grow exponentially. Such asymptotic behavior is interesting because the factorial growth in the number of diagrams (of the exact solution) is often linked to an asymptotic perturbation series with vanishing radius of convergence [NO98]. The trivial example $\sum_n n!\, u^n$ surely is an asymptotic series with radius of convergence in u equal to zero. However, regarding the fermionic perturbation series, general convergence properties are less clear due to the fermionic anticommutation rules that produce alternating signs and cancellations between different diagrams (dubbed "sign blessing" in the diagrammatic Monte Carlo community). In certain lattice models at finite temperature, it was actually found to be convergent [vHKPS10, KvHG$^+$10, BGM06]. Now, the exponential growth in the number of diagrams of a parquet-type resummation, $\mathcal{N}_X^{\mathrm{PA}}(n) \sim b^n$ with $b > 1$, likely renders its radius of convergence finite. If we assume a maximal weight $w_{\max}$ for all involved diagrams, then there exist a number n_1 and constants c_1, c_2 such that a quantity X has the formal expansion

$$|X^{\mathrm{PA}}| \;=\; \Big|\sum_{n=0}^{\infty} u^n \sum_{i=1}^{\mathcal{N}_X^{\mathrm{PA}}(n)} w_{n,i}\Big| \;\leq\; c_1 + c_2\, w_{\max} \sum_{n=n_1}^{\infty} b^n\, |u|^n. \tag{7.7}$$

According to the Cauchy–Hadamard theorem, the series providing the upper bound converges for $|u| \leq 1/b$. Hence, X in a parquet-type approximation indeed has a finite radius of convergence. The same applies to any of the typical diagrammatic resummations, which contain at most a subset of the diagrams of a parquet-type approximation of sufficiently high order n_p.

7.3 Transport through multilevel quantum dots

As a test ground for the iNRG approach, later applied to three-orbital Hubbard models, we considered in Chapter 5 three-level quantum dots. First, we focused on the Coulomb-blockade regime, characterized by a singly occupied dot and large Coulomb repulsion. With the charge on the dot fixed, the remaining spin and orbital fluctuations can be described by effective Kondo models. The analytical considerations of [P7], using poor man's scaling and Fermi's golden rule, provide an important insight: While the equilibrium three-level quantum dot hosts an SU(3)-symmetric fixed point, this is not the case in nonequilibrium. The finite bias voltage does *not* act as a simple RG cutoff scale but drives the system towards an SU(3)-nonsymmetric nonequilibrium fixed point. In equilibrium, the analytical weak-coupling analysis is corroborated by numerically exact NRG results. Using NRG, we computed the linear conductance through the quantum dot, given proportional coupling matrices between the dot and both leads, directly from discrete data of the dot spectral function [P7]. Going beyond previous studies [MAvDZ12, LRMZ13] describing the presence and destruction of the SU(3) symmetry, we showed for general tunneling matrices that the SU(3) symmetry can be dynamically restored for suitably tuned level spacings on the dot. We analyzed the dependence of the SU(3) Kondo temperature on the tunneling matrix and identified SU(2) and SU(3) fixed points via their universal conductance G at zero temperature: Applying the Friedel sum rule [Hew93] with $G = \sum_l \sin^2(\pi n_l) \cdot e^2/h$ to a singly occupied ($\sum_l n_l = 1$) multilevel quantum dot, the SU(2) and SU(3) fixed points fulfill $G = 2\, e^2/h$ and $G = 2.25\, e^2/h$, as determined by $n_l = 1/2$ and $n_l = 1/3$, respectively.

The NRG setup developed for [P7] was used in a second article [P8] as a benchmark for two numerical approaches which are further able to describe the stationary-state current through multilevel quantum dots in nonequilibrium: the real-time renormalization group (RTRG) and a simplified implementation of Keldysh fRG. We found that, in the regime of strong charge fluctuations, Kondo-type correlations (as in the Coulomb-blockade regime studied in [P7]) are suppressed, and the dominant effects in the conduction as a function of the gate voltage are single-particle resonances (i.e. points of coinciding *effective* level position and gate voltage). Then, the linear conductance of fRG in a static approximation, which neglects the renormalization of higher-order vertices, agrees well with NRG data for weak to intermediate Coulomb interaction. The method is assumed to remain valid for moderate interaction *at finite bias* and can hence be used to test RTRG in this regime. The RTRG approach, which is perturbative in the hybridization between dot and leads, yields equilibrium results that match the NRG data surprisingly well. Still, the neglect of cotunneling processes in RTRG is reflected in deviations from the NRG linear conductance at large Coulomb interaction close to the single-particle resonances. Moreover, RTRG agrees very well with fRG in nonequilibrium for moderate Coulomb interaction. It thus appears as a promising and versatile tool to describe charge fluctuations in general quantum dots in and out of equilibrium.

7.4 Hund metals with nondegenerate orbitals

In 2015, it was shown [SYvD+15] that NRG is a viable three-orbital impurity solver for DMFT. However, there, the calculations had been restricted to the full, orbital SU(3) symmetry of an idealized Hubbard model. Employing the interleaved NRG (iNRG) [MGWF+14, SMvDW16], we were then able to significantly extend the range of applications, underlining the continued relevance of DMFT+NRG in cutting-edge computational condensed-matter physics: In [P9], we performed the first DMFT+iNRG analysis of a three-orbital system with reduced orbital symmetry; in [P10], NRG was used for the first time as impurity solver for a material analysis in the DFT+DMFT framework [KSH+06]. Below, we summarize the main insights from both of these works. Finally, we discuss the limitations of using DMFT+NRG for an even larger number of orbitals.

7.4.1 Summary

Orbital differentiation, disparate (low-energy) behavior among nondegenerate orbitals, is ubiquitous in the study of Hund metals [dM17]. However, due to the complexity and numerical challenges of the corresponding models, a complete understanding had been lacking so far. In [P9], we achieved a significant step forward by combining a *minimal model* for orbital differentiation in Hund metals with a *highly accurate* method. As explained in Sec. 2.4.3, a minimal setup for Hund metals can be constructed with three orbitals at filling $N = 2$ and an SU(3) orbitally symmetric local interaction. Orbital differentiation can then be incorporated by only a single parameter Δ, which acts as a crystal-field splitting and shifts the energy level of one orbital w.r.t. two degenerate ones. This symmetry configuration is indeed found in the t_{2g} orbitals of layered transition metal oxides, where the xy orbital is different from the symmetric xz and yz orbitals. Tuning Δ changes the polarization of the system, i.e., the difference in the occupation of the individual orbitals, and leads to several phase transitions. In particular, one finds, as an extreme form of orbital differentiation, the orbital-selective Mott transition (OSMT), where some orbitals become insulating while others remain metallic.

To accurately resolve the intricate low-energy physics of Hund metals, NRG is the unrivaled impurity solver for DMFT (see Chapter 6). Systems with nondegenerate orbitals are tractable with iNRG. However, close to phase transitions, it is crucial to maintain the symmetry of the degenerate doublet. Hence, we employed in [P9] a “two-step” iNRG approach, which interleaves the Wilson chains of the separate orbital and the *degenerate* doublet, thus exactly preserving the SU(2) orbital symmetry (as well as the overall SU(2) spin symmetry).

The main impact of [P9] is that we answered a list of controversial and long-standing questions on orbital differentiation in Hund metals in a unified picture and with conceptual arguments, supported by highly accurate numerical results. The questions, raised in the introduction of [P9], and the short versions of their respective answers (see [P9] for details and references) are:

- *For a given sign of crystal-field splitting, which orbitals localize?*

  The polarization induced by Δ has the strongest effect when some orbitals are pushed towards integer occupation. In particular, if an individual orbital approaches half filling (i.e. occupation unity), it shows the strongest correlations and can become Mott-insulating at sufficiently strong interaction.

- *Is the OSMT of first or second order?*

The transition between the metal and the band+Mott insulator shows a clear hysteresis region. However, for the OSMT, we did not find any hysteresis. Additionally, the polarization, which jumps at the former phase transition, appears to change in a differentiable way at the latter. While it is numerically hard to exclude a (possibly weak) first-order transition, the OSMT looks much more second-order-like than the transition between metal and band+Mott insulator.

- *Do correlations enhance or reduce orbital polarization as one approaches the OSMT?*

  Judging from the Hartree term of the self-energy, the gross interaction increases the orbital polarization. The same is found when looking at the self-energy difference at zero frequency for small Δ. However, curiously, we observed that close to the OSMT both the self-energy difference at zero frequency and the difference of the quasiparticle energies change their slope w.r.t. Δ and thereby counteract the splitting.

- *Is it true that quenching of orbital fluctuations makes the orbitals behave independently?*

  As a major conceptual conclusion, our analysis shows that this is *not* true. Weak, static interorbital correlators lead to the impression that orbital screening, facilitated by Hund J, makes the orbitals behave independently. However, this does *not* carry over to dynamical correlation functions. Instead, (i) the crystal field, which splits the ground-state manifold and suppresses the hybridization in orbitals pushed towards half filling, reduces the spin Kondo temperature of *all* orbitals due to the locking of spins by Hund J. (ii) The persistent charge fluctuations in the metallic orbitals enable interband doublon-holon excitations. These become visible in the spectral functions of orbitals with reduced quasiparticle weight. As gap-filling states, they cause the insulating spectral function in the OSM phase (OSMP) to differ from the familiar single-orbital Mott insulator. (iii) Localized spins in the insulating phase also affect the itinerant electrons. If the insulating orbital does not hybridize at low energies, the combined spin of all orbitals experiences an underscreened Kondo effect, implying singular Fermi-liquid behavior of the metallic orbitals.

- *Do the itinerant electrons in the OSMP form a Fermi liquid?*

  The itinerant electrons in the OSMP show singular instead of regular Fermi-liquid behavior. This is directly observable in logarithmic divergences of the self-energy and the divergent spin susceptibility of the underscreened Kondo effect. Intriguingly, we found that a restricted energy window for the Matsubara self-energy, as typically analyzed in Monte Carlo approaches, might falsely indicate low-energy power-law behavior.

- *Finally, how are the precursors of the OSMT related to the physics of Hund metals?*

  Precursors of the OSMT can already be seen in the Hund-metal phase. First, the spin Kondo temperature, T_{sp}, is very low in Hund metals due to the slowly fluctuating, large local spins. If the spin screening at very low energies cannot be resolved, this resembles the underscreened Kondo effect of the OSMP with a divergent spin response. Second, the Hund-metal spectral function has a typical shoulder in the quasiparticle peak, related to an orbital Kondo resonance. For nondegenerate orbitals, this orbital resonance gets destroyed by sizable $|\Delta| \gtrsim T_{\mathrm{orb}}(\Delta = 0)/2$ and changes into interband doublon-holon resonances, most prominently seen in the OSMP. Third, the real part of the self-energy of Hund metals has attracted attention due to a kink and an inverted slope at small frequencies on either side of $\omega = 0$. In the orbital approaching the Mott transition, these features become increasingly pronounced and ultimately give rise to a divergent self-energy in the OSMP.

Turning from models to materials, $\mathrm{Sr_2RuO_4}$ is an archetypal Hund metal. It can be synthesized with excellent quality and has been studied extensively [MM03]. It continues to attract interest as, on the one hand, a puzzling unconventional superconductor below $\sim 1.5\,\mathrm{K}$, which is structurally similar to the cuprate high-temperature superconductor $\mathrm{(La, Sr)_2CuO_4}$ [MRS01, MSHM17]. On the other hand, it shows exceptionally clean Fermi-liquid behavior below $T_{\mathrm{FL}} \approx 25\mathrm{K}$ [MHY+94, SMB+14]. However, previously, no method had allowed one to reliably tune temperature through the Fermi-liquid scale: State-of-the-art Quantum Monte Carlo impurity solvers can only access temperatures $\geq 29\,\mathrm{K}$ (see [TZR+19] and further references in [P10]) and tensor-network impurity solvers are confined to ground-state properties with limited resolution for dynamic properties

[BZT$^+$17, BTZ$^+$18, LZH$^+$19]. In a novel DFT+DMFT+NRG approach, we were able to perform an *ab initio* real-frequency analysis of the temperature-dependent Hund-metal properties of $\mathrm{Sr_2RuO_4}$.

In [P10], we first resolved zero-temperature dynamic correlation functions down to the lowest energy scales and detected susceptibilities with linear-in-frequency behavior below a scale of $T_{\mathrm{FL}} \approx 25\mathrm{K}$. Access to real-frequency correlation functions also revealed that the van Hove singularity in the xy orbital close to the Fermi level drives strong orbital differentiation in $\mathrm{Sr_2RuO_4}$ [MAM$^+$11]. Second, we computed characteristic quantities (like the quasiparticle weight or the static spin susceptibility) as a function of decreasing temperature and established their convergence below T_{FL}. Finally, using NRG as impurity solver in a real-materials setting elucidates the inherent DMFT idea as a flow from atomic constituents at high energies to a collective state at low energies. In $\mathrm{Sr_2RuO_4}$, we could then follow the RG flow from atomic spin and orbital fluctuations at high temperatures and energies, through a two-stage Kondo screening process, to a spin-coherent Fermi-liquid state below $T_{\mathrm{FL}} \approx 25\,\mathrm{K}$.

Technically, the DFT+DMFT+NRG approach is demanding both from the perspective of the impurity problem and of the self-consistent mapping. Even though the xz and yz orbitals are degenerate, the SO(3)-symmetric form of the local interaction leaves only a small (one-dimensional) SO(2) symmetry in this doublet. Hence, it is computationally preferential to artificially break the symmetry of the xz and yz orbitals by interleaving the Wilson chains of all three orbitals and to restore the symmetry by averaging over the results at each DMFT iteration. Additionally, the explicit momentum summation in the self-consistency cycle takes the impurity self-energy as input.[4] High accuracy, in the form of a small relative error, is most challenging for the self-energy, whose imaginary part vanishes in the Fermi-liquid regime. Finally, performing the self-consistency iteration entirely on the real-frequency axis, with the self-energy resolved to low energies where $\mathrm{Im}\Sigma = 0$, requires an extremely large number of $\boldsymbol{k}$ points (and ideally an adaptive integration routine) to numerically obtain smooth results.

In [P10], we extended the practice of extracting quasiparticle parameters directly from the NRG low-energy spectrum, as pioneered by Hewson and coworkers [HOM04, BH07, NCH10], to the nondegenerate multiorbital DMFT+NRG context. This technique is a very efficient and accurate alternative for computing the quasiparticle weight and quasiparticle energy [HOM04], compared to the typical fitting procedure in the dynamic self-energy $\Sigma(\omega)$. The agreement we found between both methods corroborates the accuracy of the self-energy computation. Moreover, by extracting the quasiparticle interaction, we got unique insight into a crucial two-particle quantity, the zero-energy real-frequency vertex [HOM04]. We detected a weak orbital but a strong spin dependence in the vertex, with an effective attraction in the spin-triplet sector. Presumably, this has the same origin as the Hund-metal s-wave spin-triplet pairing instability previously found in model studies [HW15, HW16].

In summary, the key points of [P10] are:

- Methodological advances have made NRG ready to be used in a real-materials setting, where it retains its advantages of providing real-frequency correlations at arbitrarily low temperatures and of revealing the key effects through analysis of the RG flow.
- $\mathrm{Sr_2RuO_4}$ undergoes a two-stage screening process where orbital fluctuations are screened at high energies and Fermi-liquid behavior emerges concomitant with spin coherence below a scale of $T_{\mathrm{FL}} \approx 25\,\mathrm{K}$. Orbital differentiation is mostly induced by the van Hove singularity in the xy orbital close to the Fermi level, and the quasiparticle parameters reveal an effective attraction in the spin-triplet sector.

7.4.2 Interleaved NRG for more than three orbitals

Our DMFT+NRG results for three-orbital systems with reduced orbital symmetry heavily rely on iNRG. Using iNRG, the local Hilbert space can be factorized between all orbitals, such that adding one (spinful) orbital degree of freedom between successive truncations increases its dimension only by a factor of 4. One might then be tempted to use iNRG for an arbitrarily large number of orbitals, M. However, there are three hurdles to overcome:

---

[4] By contrast, using a semicircular lattice density of states as in [P9], the hybridization function can be directly obtained from the spectral function [GKKR96].

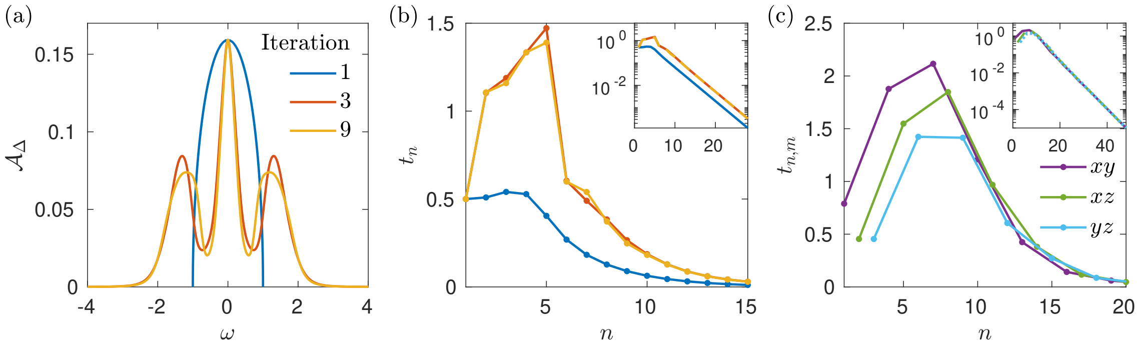

Figure 7.4 (a) The hybridization $\mathcal{A}_\Delta$ at different iterations during a DMFT+NRG computation of the single-orbital Hubbard model (semicircular lattice density of states, half-bandwidth 1, $U = 2$, $T = 0$). (b) For the initial, almost structureless hybridization, the hopping amplitudes t_n are well-behaved and almost decay monotonously. However, at later iterations, when $\mathcal{A}_\Delta$ reflects the different energy scales of the impurity itself, the t_n first rise notably. With a discretization parameter $\Lambda = 2$, energy-scale separation only applies after the first five bath sites have been added. Hence, one must fully diagonalize a system of six sites. With a local dimension of 4, this corresponds to a manageable matrix size of $4^6 = 4096$. (c) Hopping amplitudes for each orbital from a self-consistent hybridization in an iNRG run for $\mathrm{Sr_2RuO_4}$ in [P10]. With $\Lambda = 6$, energy-scale separation applies after the first two or three super sites (the first 6 or 9 interleaved sites) have been added. With a local dimension of $4^3 = 64$, this yields a matrix of size 4^9–4^{12}, i.e., $2.6 \cdot 10^5$–$1.7 \cdot 10^7$. The lower number is still feasible, but the upper one exceeds the numerical resources.

1. The hybridization function is discretized logarithmically on a grid $\xi_n^\pm \propto \pm\Lambda^{-n}$, set by the NRG discretization parameter $\Lambda > 1$ [BCP08]. The (impractical) continuum limit corresponds to $\Lambda = 1$; single-orbital calculations often use $\Lambda = 1.7 \ldots 2$. The hopping amplitudes along the Wilson chain, t_n, ultimately decay as $\Lambda^{-n/2}$, and—when interleaving M orbitals—as $\Lambda^{-n/(2M)}$ [SMvDW16]. Hence, justifying the truncation of high-lying states by energy-scale separation ($t_{n+1} \ll t_n$), requires sufficiently large $\sqrt[M]{\Lambda}$. In the three-orbital studies [P9, P10], we used $\Lambda = 6$. For more orbitals, Λ must increase and the discretization becomes cruder.

2. The many-body spectrum typically becomes denser with an increasing number of orbitals. Even if, in iNRG, the Hilbert space grows only by an M-independent factor, more orbitals require an exceedingly large number of kept states in order to sufficiently resolve the (rescaled) low-energy spectrum at each iteration.

3. Using NRG as impurity solver for DMFT comes with the additional challenge that the hybridization incorporates the energy scales of the impurity itself [HPT13], affecting the t_n, and delays the onset of energy-scale separation ($t_{n+1} \ll t_n$). At the first iterations, the nontrivial shape of the hybridization function is resolved, and the t_n might not decay at all. In fact, in the early days of DMFT, it was concluded that "NRG . . . does not work for the impurity models arising in the context of . . . [DMFT] applications" because of the mixing of energy scales between impurity and hybridization [GKKR96]. Yet later, NRG turned out to be very successful for that purpose [BCP08]. One reason for this are the increased numerical resources that allow the system to be diagonalized exactly for a sufficient number of initial Wilson-chain sites. Then, at lower energy scales (later iterations), the hybridization function is basically structureless and energy-scale separation applies. However, for a large number of orbitals, irrespective of using interleaved or standard NRG, fully diagonalizing the initial part of the Wilson chain prior to energy-scale separation becomes numerically unfeasible. This general problem is illustrated in Fig. 7.4.

Due to these obstacles, we believe that DMFT+NRG for more than three orbitals calls for further methodological innovations. Already in three-orbital applications with reduced orbital symmetry, NRG must be considered as an approximate impurity solver, with non-negligible errors for intricate quantities like the quasiparticle weight. Nonetheless, NRG can access arbitrarily low temperatures, and its errors apply *directly* to the real-frequency results, for which moderate uncertainties are highly competitive. Hence, even in these challenging situations, NRG can provide benchmark-quality data and unravel physical mechanisms invisible to other methods.

8 Conclusion and outlook

This thesis demonstrates that the renormalization group (RG) framework not only is pivotal to understand physical mechanisms at their respective energy scales but also pervades the most accurate techniques in condensed-matter physics. Specifically, we investigated two RG approaches to strongly correlated electron systems: (i) the functional RG (fRG) and (ii) the numerical RG (NRG) in conjunction with dynamical mean-field theory (DMFT). The two schemes are very different in their nature as well as their validity: The former is targeted towards long-range correlations at weak to intermediate coupling strength, the latter can describe arbitrarily strong but purely local correlations.

Regarding fRG, we achieved a methodological breakthrough with the invention of multiloop fRG (mfRG). It resolves many of the drawbacks from which fRG results suffered hitherto, establishes a rigorous relation to parquet theory, and, altogether, elevates the fRG approach to a *quantitative* method. We contributed to a first test-bed study of the two-dimensional (2D) Hubbard model, and many further applications are expected to follow. In the context of DMFT+NRG, we exploited recent methodological advances to treat more *realistic* multiorbital systems. In a model study, we explored orbital differentiation in Hund metals and unraveled key effects of the orbital-selective Mott transition. In a pioneering combination of DMFT+NRG with density-functional theory (DFT), we were able to analyze the archetypal Hund-metal material $\mathrm{Sr_2RuO_4}$ down to the lowest temperature and energy scales and revealed how its Fermi-liquid state emerges below $25\,\mathrm{K}$.

In the following, we first give a general conclusion of our results in the context of the employed method. We close with an outlook that suggests a combination of both approaches in order to overcome their respective limitations.

mfRG

The mfRG framework achieves a two-fold goal. On the one hand, it improves the truncation of the fRG hierarchy of flow equations while keeping its versatile structure. Instead of simply neglecting effective three-particle interactions in the form of the six-point vertex, it incorporates all contributions of the contracted six-point vertex that are of the same diagrammatic complexity as those terms retained in the rest of the flow. In view of the standard fRG hierarchy of flow equations, such terms would require n-point vertices of arbitrarily large n. From a two-particle diagrammatic perspective, they complete the *differentiated* parquet diagrams.

On the other hand, we incorporated the RG notion of successive mode elimination into traditional many-body frameworks and showed that mfRG emerges as a differential solution to the self-consistent parquet equations. Replacing self-consistent with differential equations comes with numerical benefits and promises unique, physical solutions. Moreover, our results demonstrate that it is possible to perform diagrammatic resummations at the two-particle level without using two-particle-irreducible (2PI) vertices. The importance of this can hardly be overstated, given the recent findings that 2PI vertices exhibit (likely unphysical) divergences and must be considered ill-defined objects when used in nonperturbative approaches, such as DMFT. Accordingly, an mfRG flow started from DMFT, dubbed multiloop DMF^{2}RG in reference to [TAB$^+$14], is formulated exclusively in terms of the regular full vertex. It continuously evolves the vertex functions from the self-consistent impurity towards the actual lattice model along the trajectory of solutions to the self-consistent parquet equations and is thus perfectly suited for the most accurate diagrammatic extensions of DMFT.

Since fRG is such a versatile method, with applications ranging from high-energy physics over effective theories for critical phenomena to microscopic models in condensed-matter physics, a broad use of mfRG is possible. In the rapidly developing field of quantum magnetism analyzed by means of the pseudo-fermion fRG [RW10], first mfRG flows are currently being implemented. Of prime interest to us is the 2D Hubbard model, where previous fRG studies of competing instabilities can now be brought under quantitative control, and calculations analogous to [P4] at finite doping promise insight into the enigmatic pseudo-gap phase of the cuprates.

DMFT+NRG

After the seminal real-frequency analysis of an SU(3) orbitally symmetric model of Hund metals by Stadler et al. [SYvD$^+$15], we reached the next milestones of DMFT+NRG by incorporating, first, orbital differentiation in a minimal model and, then, the specific bandstructure of the archetypal material Sr_2RuO_4. By exploiting recent algorithmic developments, particularly the interleaved Wilson-chain geometry [MGWF$^+$14, SMvDW16], we showed that low-symmetry three-orbital models can be treated and the large arena of t_{2g} physics explored. Still, including even more orbitals, such as the five orbitals that dominate electronic properties of the iron-based superconductors, remains challenging, due to the exceedingly large Hamiltonian that must be diagonalized before the energy-scale separation, vital to NRG, sets in.

Nevertheless, NRG, as a real-frequency impurity solver for DMFT, is a unique and indispensable tool to study Hund metals. Its access to arbitrarily small temperature and energy scales enabled unraveling the characteristic phenomenon of spin–orbital scale separation [SYvD$^+$15, SKWvD19], whose influence we further exposed in Hund metals with orbital differentiation. It is also crucial to understand the intricate low-energy physics of the orbital-selective Mott transition. We emphasized that spin dynamics keep the orbitals locked and explained controversial spectral features by the logarithmic, singular Fermi-liquid divergence in the metallic band and gap-filling, interband doublon-holon states in the insulating one.

Retaining all of its key properties, NRG now adds to the understanding of strongly correlated materials, too. The famous Sr_2RuO_4, superconducting below $\sim 1.5\,\mathrm{K}$ and a textbook Fermi liquid below $T_{\mathrm{FL}} \approx 25\,\mathrm{K}$, is extensively studied both experimentally and theoretically; however, no theoretical method had previously allowed one to tune temperature through T_{FL}. With DFT+DMFT+NRG, we were able to reveal the emergence of the Fermi-liquid state of Sr_2RuO_4 in an RG flow down to the lowest energies, characterized Fermi-liquid properties with zero-temperature real-frequency correlation functions, and provided *ab initio* theoretical evidence for a Fermi-liquid scale in accord with the experimentally observed 25 K. By extracting quasiparticle parameters from the low-energy spectrum, we even accessed the zero-energy real-frequency vertex and found an effective attraction in the spin-triplet sector. Extending the quasiparticle description to the lattice might help to understand the puzzling superconductivity of Sr_2RuO_4.

Outlook: Keldysh multiloop DMF^{2}RG

With mfRG, we developed a highly refined approach to study competing instabilities in strongly correlated electron systems and already demonstrated feasibility for the 2D Hubbard model. Like most other methods, the treatment of [P4] operated in the imaginary-frequency, Matsubara formalism. However, to characterize the pseudo-gap phase, with reduced spectral weight in specific parts of the Brillouin zone (Fermi arcs)—an effect properly seen only from the spectral function $\mathcal{A}(\omega, \boldsymbol{k})$—an equally accurate real-frequency approach would be invaluable. Building on previous Keldysh one-loop fRG works, albeit implemented with only a simplified parametrization of the vertices (see e.g. [Jak09, JPS10, SBvD17]), a full-grown Keldysh mfRG could provide exactly that. Furthermore, we highlighted the benefits of NRG as real-frequency impurity solver for DMFT. So far, NRG has only been used for two-point retarded Green's functions, and merely a glimpse beyond this is possible through quasiparticle interactions. In an ongoing collaboration with S.-S. B. Lee, we aim for a leap beyond the status quo by using NRG to compute real-frequency, Keldysh four-point correlation functions.

In the beginning of this section—and even in the introduction of this thesis—we emphasized the complementary nature of the field-theoretical fRG and the state-based NRG approach to strongly correlated electron systems. However, by aiming for a Keldysh mfRG program and four-point correlations obtained from DMFT+NRG, the best of both worlds can be combined, and the nonperturbative character of DMFT+NRG can be paired with the systematic account of long-range correlations provided by fRG. Indeed, a Keldysh mfRG flow started from the Keldysh vertices of DMFT+NRG will put the first real-frequency diagrammatic extension of DMFT, and thus a method with unprecedented frequency and momentum resolution and access to even the strong-coupling regime of correlated electron systems, within reach.

9 Appendix

9.1 Schwinger–Dyson equation with reversed order

The Schwinger–Dyson equation (SDE) for the self-energy, $\Sigma_{x',x}$, can be written in two ways, where either Γ_0 is attached to x' and Γ to x or vice versa. In Sec. 2.3, we derived the former form by varying the field $\bar{c}$. The latter can be obtained analogously, by varying c:

$$\begin{aligned} S[\bar{c}, c] &= -\bar{c}_{x'}(G_0^{-1})_{x',x} c_x - \tfrac{1}{4}\Gamma_{0;x',y';x,y}\bar{c}_{x'}\bar{c}_{y'}c_y c_x, \\ \zeta\frac{\delta S}{\delta c_x} &= -\bar{c}_{x'}(G_0^{-1})_{x',x} - \tfrac{1}{2}\Gamma_{0;x',y';x,y}\bar{c}_{x'}\bar{c}_{y'}c_y. \end{aligned}$$

The invariance of the partition function upon finite and infinitesimal shifts of c implies

$$\begin{aligned} Z[\bar{\jmath}, j] &= \int \mathcal{D}[\bar{c}, c] e^{-S[\bar{c},c]+\bar{\jmath}_x c_x + \bar{c}_x j_x} = \int \mathcal{D}[\bar{c}, c] e^{-S[\bar{c},c+\Delta]+\bar{\jmath}_x (c+\Delta)_x + \bar{c}_x j_x}, \\ 0 &= \int \mathcal{D}[\bar{c}, c]\Big(\bar{\jmath}_x - \zeta\frac{\delta S}{\delta c_x}\Big) e^{-S[\bar{c},c]+\bar{\jmath}_x c_x + \bar{c}_x j_x}. \end{aligned}$$

By differentiating w.r.t. $\bar{\jmath}_v$, setting the sources to zero, and insertion, we get

$$0 = \int \mathcal{D}[\bar{c}, c]\Big(\delta_{x,v} + \zeta\bar{c}_{y'}(G_0^{-1})_{y',x}c_v + \zeta\tfrac{1}{2}\Gamma_{0;z',w';x,y}\bar{c}_{z'}\bar{c}_{w'}c_y c_v\Big)e^{-S}.$$

Multiplying by $1/Z$, inserting Eq. (2.7), and using the (anti)symmetry of Γ_0 yields

$$\begin{aligned} 0 &= \delta_{x,v} - (G_0^{-1})_{y',x}G_{v,y'} + \zeta\tfrac{1}{2}\Gamma_{0;z',w';x,y}\langle c_v c_y \bar{c}_{w'}\bar{c}_{z'}\rangle \\ &= \delta_{x,v} - (G_0^{-1})_{y',x}G_{v,y'} + \zeta\tfrac{1}{2}\Gamma_{0;z',w';x,y}\big(2G_{v,z'}G_{y,w'} + G_{v,v'}G_{y,y'}\Gamma_{v',y';z,w}G_{z,z'}G_{w,w'}\big). \end{aligned}$$

The corresponding SDE is obtained after multiplying by $(G^{-1})_{x',v}$:

$$\Sigma_{x',x} = (G^{-1})_{x',x} - (G_0^{-1})_{x',x} = \zeta\Gamma_{0;x',y';x,y}G_{y,y'} + \tfrac{1}{2}\zeta\Gamma_{x',y';z,w}G_{y,y'}G_{w,w'}G_{z,z'}\Gamma_{0;z',w';x,y}.$$

9.2 Bethe–Salpeter equation in the parallel channel

The Bethe–Salpeter equation (BSE) in the *parallel* or p channel can be derived from the partition function Z with sources $\bar{J}$, J coupled to two c and two $\bar{c}$ fields, respectively,

$$Z[\bar{J}, J] = \int \mathcal{D}[\bar{c}, c]\, e^{-S[\bar{c},c]+\bar{J}_{x,y}c_x c_y + J_{x',y'}\bar{c}_{x'}\bar{c}_{y'}}.$$

Similar to the steps performed in Sec. 2.3, we take functional derivatives of the generating functional, $\mathcal{G}[\bar{J}, J] = \ln Z[\bar{J}, J]$, to obtain the propagator and the generalized susceptibility as

$$\begin{aligned} G^J_{x,y} &\equiv -\frac{\delta\mathcal{G}}{\delta\bar{J}_{x,y}} = -\langle c_x c_y\rangle_J, \\ \chi_{p;x,y;x',y'} &\equiv \zeta\frac{\delta^2\mathcal{G}}{\delta J_{x',y'}\delta\bar{J}_{x,y}}\Big|_{\bar{J},J=0} = \langle\bar{c}_{x'}\bar{c}_{y'}c_y c_x\rangle. \end{aligned}$$

Compared to $G_c^{(4)}$ in Eq. (2.10), no disconnected contribution is subtracted for χ_p. We have

$$\chi_{p;x',y';x,y} = -\zeta\frac{\delta G^J_{x,y}}{\delta J_{x',y'}}\Big|_{J=0}, \tag{9.1}$$

and can relate this to the self-energy similarly as in Sec. 2.3.

At finite sources $\bar{J}$, J, the propagator has anomalous components to be summed over:

$$G^J_{x,\alpha}(G^{-1})^J_{\alpha,\beta} = \delta_{x,\beta} \quad \Rightarrow \quad \frac{\delta G^J_{x,\alpha}}{\delta J_{x',y'}}(G^{-1})^J_{\alpha,\beta} + G^J_{x,\alpha}\frac{\delta (G^{-1})^J_{\alpha,\beta}}{\delta J_{x',y'}} = 0.$$

Multiplying by $G^J_{\beta,y}$, and evaluating at $\bar{J}, J = 0$, we then get

$$\frac{\delta G^J_{x,y}}{\delta J_{x',y'}}\big|_{\bar{J},J=0} = -\zeta G_{x,z'} G_{y,w'} \frac{\delta (G^{-1})^J_{z',w'}}{\delta J_{x',y'}}\big|_{\bar{J},J=0}. \tag{9.2}$$

The bold perturbation series of the self-energy implies

$$\Sigma^J = \Sigma[G^J, \Gamma_0] \quad \Rightarrow \quad \frac{\delta \Sigma^J_{x',y'}}{\delta J_{z',w'}} = \frac{\delta \Sigma^J_{x',y'}}{\delta G^J_{x,y}} \frac{\delta G^J_{x,y}}{\delta J_{z',w'}},$$

and allows us to obtain the vertex I_p, 2PI in the p channel, as

$$I_{p;x',y';x,y} \equiv \zeta \frac{\delta \Sigma^J_{x,y}}{\delta G^J_{x',y'}}\big|_{\bar{J},J=0} + \zeta \frac{\delta \Sigma^J_{x',y'}}{\delta G^J_{x,y}}\big|_{\bar{J},J=0} \quad \Rightarrow \quad \tfrac{1}{2} I_{p;x',y';x,y} = \zeta \frac{\delta \Sigma^J_{x',y'}}{\delta G^J_{x,y}}\big|_{\bar{J},J=0}. \tag{9.3}$$

Next, we employ Dyson's equation, $(G^{-1})^J = (G_0^{-1})^J - \Sigma^J = G_0^{-1} + J - \Sigma^J$, where the derivative of the anomalous bare propagator, $(G_0^{-1})^J$ w.r.t. J gives two trivial terms, and

$$\frac{\delta (G^{-1})^J_{z',w'}}{\delta J_{x',y'}}\big|_{\bar{J},J=0} = \delta_{z',x'}\delta_{w',y'} + \zeta \delta_{z',y'}\delta_{w',x'} - \frac{\delta \Sigma^J_{z',w'}}{\delta J_{x',y'}}\big|_{\bar{J},J=0}.$$

Further inserting the self-energy derivative (9.3) yields

$$\frac{\delta (G^{-1})^J_{z',w'}}{\delta J_{x',y'}}\big|_{\bar{J},J=0} = \delta_{z',x'}\delta_{w',y'} + \zeta \delta_{z',y'}\delta_{w',x'} + \tfrac{1}{2} I_{p;z',w';z,w} \frac{\delta G^J_{z,w}}{\delta J_{x',y'}}\big|_{\bar{J},J=0}. \tag{9.4}$$

Thus, by combining Eqs. (9.1), (9.2), and (9.4), we find the BSE

$$\chi_{p;x',y';x,y} = G_{x,x'}G_{y,y'} + \zeta G_{x,y'}G_{y,x'} + \tfrac{1}{2} G_{x,z'}G_{y,w'} I_{p;z',w';z,w} \chi_{p;x',y';z,w}. \tag{9.5}$$

We can translate this equation to the vertex level by inserting Eq. (2.7) for $\chi_p = G^{(4)}$ to get

$$\begin{aligned} G_{x,z'}G_{y,v'}\Gamma_{z',v';z,v}G_{z,x'}G_{v,y'} &= G_{x,z'}G_{y,w'}\tfrac{1}{2}I_{p;z',w';z,w} \\ &\quad \times \big(G_{z,x'}G_{w,y'} + \zeta G_{z,y'}G_{w,x'} + G_{z,v'}G_{w,u'}\Gamma_{v',u';v,u}G_{v,x'}G_{u,y'}\big). \end{aligned}$$

Removing the external legs, i.e., multiplying by $(G^{-1})_{\tilde{x}',x}(G^{-1})_{x',\tilde{x}}(G^{-1})_{\tilde{y}',y}(G^{-1})_{y',\tilde{y}}$, we obtain

$$\Gamma_{\tilde{x}',\tilde{y}';\tilde{x},\tilde{y}} = I_{p;\tilde{x}',\tilde{y}';\tilde{x},\tilde{y}} + \tfrac{1}{2} I_{p;\tilde{x}',\tilde{y}';z,w} G_{z,v'} G_{w,u'} \Gamma_{v',u';\tilde{x},\tilde{y}}.$$

Finally, by using a generalized matrix multiplication similar to Eqs. (2.24) and (2.28), the BSE in p channel can be analogously written as $\Gamma = I_p + I_p \circ \Pi_p \circ \Gamma$.

9.3 Bethe–Salpeter equation (p channel) with reversed order

In Sec. 2.3, we derived the BSEs for the generalized susceptibilities in the t and a channel and mentioned that the order of I_r and χ_r can be reversed by interchanging the order of $\delta/\delta J_{y',y}$ and $\delta/\delta J_{x',x}$. This reduces to a mere change of indices $y^{(\prime)} \leftrightarrow x^{(\prime)}$. In the p channel, the same result is not obtained as easily because, in Eq. (9.5), *both* in-going legs x' and y' are attached to χ_p and cannot simply be interchanged with x and y. Hence, for the sake of completeness, we also derive the BSEs in the p channel with reversed order, when first differentiating w.r.t. J rather than $\bar{J}$. We start from

$$G^J_{x',y'} \equiv -\frac{\delta \mathcal{G}}{\delta J_{x',y'}} = -\langle \bar{c}_{x'} \bar{c}_{y'} \rangle_J, \qquad \chi_{p;x,y;x',y'} = -\zeta \frac{\delta G^J_{x',y'}}{\delta \bar{J}_{x,y}}\Big|_{J=0}.$$

Similarly as above, we use

$$G^J_{x',\alpha}(G^{-1})^J_{\alpha,\beta} = \delta_{x',\beta} \quad \Rightarrow \quad \frac{\delta G^J_{x',\alpha}}{\delta \bar{J}_{x,y}}(G^{-1})^J_{\alpha,\beta} + G^J_{x',\alpha}\frac{\delta (G^{-1})^J_{\alpha,\beta}}{\delta \bar{J}_{x,y}} = 0$$

and, after multiplying by $G^J_{\beta,y'}$,

$$\frac{\delta G^J_{x',y'}}{\delta \bar{J}_{x,y}}\Big|_{\bar{J},J=0} = -\zeta G_{z,x'} G_{w,y'} \frac{\delta (G^{-1})^J_{z,w}}{\delta \bar{J}_{x,y}}\Big|_{\bar{J},J=0}.$$

From the self-energy derivative

$$\Sigma^J = \Sigma[G^J, \Gamma_0] \quad \Rightarrow \quad \frac{\delta \Sigma^J_{x,y}}{\delta J_{z,w}} = \frac{\delta \Sigma^J_{x,y}}{\delta G^J_{x',y'}} \frac{\delta G^J_{x',y'}}{\delta J_{z,w}},$$

we get another, equivalent expression for the 2PI vertex I_p:

$$I_{p;x',y';x,y} \equiv \zeta \frac{\delta \Sigma^J_{x,y}}{\delta G^J_{x',y'}}\Big|_{\bar{J},J=0} + \zeta \frac{\delta \Sigma^J_{x',y'}}{\delta G^J_{x,y}}\Big|_{\bar{J},J=0} \quad \Rightarrow \quad \tfrac{1}{2} I_{p;x',y';x,y} = \zeta \frac{\delta \Sigma^J_{x,y}}{\delta G^J_{x',y'}}\Big|_{\bar{J},J=0}.$$

As before, Dyson's equation yields

$$\begin{aligned}
\frac{\delta (G^{-1})^J_{z,w}}{\delta \bar{J}_{x,y}}\Big|_{\bar{J},J=0} &= \delta_{z,x}\delta_{w,y} + \zeta \delta_{z,y}\delta_{w,x} - \frac{\delta \Sigma^J_{z,w}}{\delta \bar{J}_{x,y}}\Big|_{\bar{J},J=0} \\
&= \delta_{z,x}\delta_{w,y} + \zeta \delta_{z,y}\delta_{w,x} + \tfrac{1}{2} I_{p;z',w';z,w} \frac{\delta G^J_{z',w'}}{\delta \bar{J}_{x,y}}\Big|_{\bar{J},J=0}.
\end{aligned}$$

In combination, we thus get the BSE

$$\chi_{p;x,y;x',y'} = G_{x,x'} G_{y,y'} + \zeta G_{x,y'} G_{y,x'} + \tfrac{1}{2} G_{z,x'} G_{w,y'} I_{p;z',w';z,w} \chi_{p;z',w';x,y},$$

where χ_p on the r.h.s. has x and y as external arguments. Expressed through the vertex, this relation implies

$$\begin{aligned}
G_{x,z'} G_{y,v'} \Gamma_{z',v';z,v} G_{z,x'} G_{v,y'} &= G_{z,x'} G_{w,y'} \tfrac{1}{2} I_{p;z',w';z,w} \\
&\quad \times \big(G_{x,z'} G_{y,w'} + \zeta G_{x,w'} G_{y,z'} + G_{x,v'} G_{y,u'} \Gamma_{v',u';v,u} G_{v,z'} G_{u,w'} \big)
\end{aligned}$$

and, after multiplying by $(G^{-1})_{\tilde{x}',x}(G^{-1})_{x',\tilde{x}}(G^{-1})_{\tilde{y}',y}(G^{-1})_{y',\tilde{y}}$, we finally obtain

$$\Gamma_{\tilde{x}',\tilde{y}';\tilde{x},\tilde{y}} = I_{p;\tilde{x}',\tilde{y}';\tilde{x},\tilde{y}} + \tfrac{1}{2} \Gamma_{\tilde{x}',\tilde{y}';v,u} G_{v,z'} G_{u,w'} I_{p;z',w';\tilde{x},\tilde{y}}.$$

Bibliography

[P1] F. B. Kugler and J. von Delft, *Fermi-edge singularity and the functional renormalization group*, J. Phys.: Condens. Matter **30** (2018), no. 19, 195501. See pages: 27, 32, and 211

[P2] F. B. Kugler and J. von Delft, *Multiloop Functional Renormalization Group That Sums Up All Parquet Diagrams*, Phys. Rev. Lett. **120** (2018), 057403. See pages: 18, 30, 32, 140, 212, 214, and 215

[P3] F. B. Kugler and J. von Delft, *Multiloop functional renormalization group for general models*, Phys. Rev. B **97** (2018), 035162. See pages: 14, 32, 140, 212, 214, and 215

[P4] A. Tagliavini, C. Hille, F. B. Kugler, S. Andergassen, A. Toschi, and C. Honerkamp, *Multiloop functional renormalization group for the two-dimensional Hubbard model: Loop convergence of the response functions*, SciPost Phys. **6** (2019), 9. See pages: 32, 212, 213, 214, 223, and 224

[P5] F. B. Kugler and J. von Delft, *Derivation of exact flow equations from the self-consistent parquet relations*, New J. Phys. **20** (2018), no. 12, 123029. See pages: 4, 9, 10, 12, 14, 16, 19, 32, 214, 215, 216, and 217

[P6] F. B. Kugler, *Counting Feynman diagrams via many-body relations*, Phys. Rev. E **98** (2018), 023303. See pages: 10, 15, 140, 217, and 218

[P7] C. J. Lindner, F. B. Kugler, H. Schoeller, and J. von Delft, *Flavor fluctuations in three-level quantum dots: Generic* $SU(3)$ *Kondo fixed point in equilibrium and non-Kondo fixed points in nonequilibrium*, Phys. Rev. B **97** (2018), 235450. See pages: 150 and 218

[P8] C. J. Lindner, F. B. Kugler, V. Meden, and H. Schoeller, *Renormalization group transport theory for open quantum systems: Charge fluctuations in multilevel quantum dots in and out of equilibrium*, Phys. Rev. B **99** (2019), 205142. See pages: 150 and 218

[P9] F. B. Kugler, S.-S. B. Lee, A. Weichselbaum, G. Kotliar, and J. von Delft, *Orbital differentiation in Hund metals*, arXiv:1904.10774 (2019). See pages: 20, 22, 24, 189, 219, 221, and 222

[P10] F. B. Kugler, M. Zingl, H. U. R. Strand, S.-S. B. Lee, J. von Delft, and A. Georges, *Strongly correlated materials from a numerical renormalization group perspective: How the Fermi-liquid state of* $\mathrm{Sr_2RuO_4}$ *emerges*, arXiv:1909.02389 (2019). See pages: 20, 22, 24, 189, 219, 220, 221, and 222

[Abr65] A. A. Abrikosov, *Electron scattering on magnetic impurities in metals and anomalous resistivity effects*, Physics **2** (1965), no. 1, 5–20. See pages: 11 and 18

[AK15] C. Aron and G. Kotliar, *Analytic theory of Hund's metals: A renormalization group perspective*, Phys. Rev. B **91** (2015), 041110. See page: 25

[And61] P. W. Anderson, *Localized Magnetic States in Metals*, Phys. Rev. **124** (1961), 41–53. See page: 20

[AP15] T. Ayral and O. Parcollet, *Mott physics and spin fluctuations: A unified framework*, Phys. Rev. B **92** (2015), 115109. See page: 27

[AP16] T. Ayral and O. Parcollet, *Mott physics and collective modes: An atomic approximation of the four-particle irreducible functional*, Phys. Rev. B **94** (2016), 075159. See pages: 29 and 215

[AS05] F. B. Anders and A. Schiller, *Real-Time Dynamics in Quantum-Impurity Systems: A Time-Dependent Numerical Renormalization-Group Approach*, Phys. Rev. Lett. **95** (2005), 196801. See pages: 23 and 24

[Bay62] G. Baym, *Self-Consistent Approximations in Many-Body Systems*, Phys. Rev. **127** (1962), 1391–1401. See pages: 15, 16, 22, and 215

[BBW04] T. Baier, E. Bick, and C. Wetterich, *Temperature dependence of antiferromagnetic order in the Hubbard model*, Phys. Rev. B **70** (2004), 125111. See page: 211

[BCP08] R. Bulla, T. A. Costi, and T. Pruschke, *Numerical renormalization group method for quantum impurity systems*, Rev. Mod. Phys. **80** (2008), 395–450. See pages: 2, 23, 24, and 222

[BGM06] G. Benfatto, A. Giuliani, and V. Mastropietro, *Fermi Liquid Behavior in the 2D Hubbard Model at Low Temperatures*, Ann. Henri Poincaré **7** (2006), no. 5, 809–898. See page: 218

[BH07] J. Bauer and A. C. Hewson, *Field-dependent quasiparticles in the infinite-dimensional Hubbard model*, Phys. Rev. B **76** (2007), 035118. See page: 221

[Bic04] N. Bickers, *Self-Consistent Many-Body Theory for Condensed Matter Systems*, Theoretical Methods for Strongly Correlated Electrons (D. Sénéchal, A.-M. Tremblay, and C. Bourbonnais, eds.), CRM Series in Mathematical Physics, Springer New York, 2004, pp. 237–296. See pages: 2, 5, 11, and 17

[BK61] G. Baym and L. P. Kadanoff, *Conservation Laws and Correlation Functions*, Phys. Rev. **124** (1961), 287–299. See pages: 14, 16, and 22

[BS89] N. E. Bickers and D. J. Scalapino, *Conserving approximations for strongly fluctuating electron systems. I. Formalism and calculational approach*, Ann. Phys. **193** (1989), no. 1, 206–251. See page: 11

[BS92] N. E. Bickers and D. J. Scalapino, *Critical behavior of electronic parquet solutions*, Phys. Rev. B **46** (1992), 8050–8056. See pages: 18 and 215

[BSW89] N. E. Bickers, D. J. Scalapino, and S. R. White, *Conserving Approximations for Strongly Correlated Electron Systems: Bethe-Salpeter Equation and Dynamics for the Two-Dimensional Hubbard Model*, Phys. Rev. Lett. **62** (1989), 961–964. See page: 11

[BTZ$^+$18] D. Bauernfeind, R. Triebl, M. Zingl, M. Aichhorn, and H. G. Evertz, *Dynamical mean-field theory on the real-frequency axis: $p-d$ hybridization and atomic physics in* $\mathrm{SrMnO_3}$, Phys. Rev. B **97** (2018), 115156. See page: 221

[BW91] N. E. Bickers and S. R. White, *Conserving approximations for strongly fluctuating electron systems. II. Numerical results and parquet extension*, Phys. Rev. B **43** (1991), 8044–8064. See page: 11

[BZT$^+$17] D. Bauernfeind, M. Zingl, R. Triebl, M. Aichhorn, and H. G. Evertz, *Fork Tensor-Product States: Efficient Multiorbital Real-Time DMFT Solver*, Phys. Rev. X **7** (2017), 031013. See page: 221

[CFD$^+$18] Y. Cao, V. Fatemi, A. Demir, S. Fang, S. L. Tomarken, J. Y. Luo, J. D. Sanchez-Yamagishi, K. Watanabe, T. Taniguchi, E. Kaxiras, R. C. Ashoori, and P. Jarillo-Herrero, *Correlated insulator behaviour at half-filling in magic-angle graphene superlattices*, Nature **556** (2018), no. 7699, 80–84. See page: 1

[CFF$^+$18] Y. Cao, V. Fatemi, S. Fang, K. Watanabe, T. Taniguchi, E. Kaxiras, and P. Jarillo-Herrero, *Unconventional superconductivity in magic-angle graphene superlattices*, Nature **556** (2018), no. 7699, 43–50. See page: 1

[CGS+18] P. Chalupa, P. Gunacker, T. Schäfer, K. Held, and A. Toschi, *Divergences of the irreducible vertex functions in correlated metallic systems: Insights from the Anderson impurity model*, Phys. Rev. B **97** (2018), 245136. See pages: 27 and 214

[Cha19] P. Chalupa, 2019, private communication. See page: 18

[CLP78] P. Cvitanović, B. Lautrup, and R. B. Pearson, *Number and weights of Feynman diagrams*, Phys. Rev. D **18** (1978), 1939–1949. See page: 217

[DDM64a] C. De Dominicis and P. C. Martin, *Stationary Entropy Principle and Renormalization in Normal and Superfluid Systems. I. Algebraic Formulation*, J. Math. Phys. **5** (1964), no. 1, 14–30. See pages: 10 and 215

[DDM64b] C. De Dominicis and P. C. Martin, *Stationary Entropy Principle and Renormalization in Normal and Superfluid Systems. II. Diagrammatic Formulation*, J. Math. Phys. **5** (1964), no. 1, 31–59. See pages: 10, 17, and 215

[dM14] L. de' Medici, *Weak and Strong Correlations in Fe Superconductors*, Iron-Based Superconductivity, Springer International Publishing, 2014, pp. 409–441. See page: 26

[dM17] L. de' Medici, *Hund's metals explained*, The Physics of Correlated Insulators, Metals, and Superconductors (Jülich) (E. Pavarini, E. Koch, R. Scalettar, and R. Martin, eds.), Forschungszentrum Jülich, 2017. See pages: 189 and 219

[dMGC14] L. de' Medici, G. Giovannetti, and M. Capone, *Selective Mott Physics as a Key to Iron Superconductors*, Phys. Rev. Lett. **112** (2014), 177001. See page: 3

[DSK+19] X. Deng, K. M. Stadler, Haule K., A. Weichselbaum, J. von Delft, and G. Kotliar, *Signatures of Mottness and Hundness in archetypal correlated metals*, Nat. Comm. **10** (2019), no. 1, 2721. See pages: 2 and 25

[DSTM57] I. T. Diatlov, V. V. Sudakov, and K. A. Ter-Martirosian, *Asymptotic meson-meson scattering theory*, Soviet Phys. JETP **5** (1957), no. 4, 631–642. See page: 11

[Edi13] Editorial, *The Hubbard model at half a century*, Nature Phys. **9** (2013), no. 9, 523–523. See page: 1

[GB17] Christian Gross and Immanuel Bloch, *Quantum simulations with ultracold atoms in optical lattices*, Science **357** (2017), no. 6355, 995–1001. See page: 1

[GdMM13] A. Georges, L. de' Medici, and J. Mravlje, *Strong Correlations from Hund's Coupling*, Annu. Rev. Condens. Matter Phys. **4** (2013), no. 1, 137–178. See pages: 25, 26, and 189

[GK92] A. Georges and G. Kotliar, *Hubbard model in infinite dimensions*, Phys. Rev. B **45** (1992), 6479–6483. See page: 20

[GKH17] J. Gukelberger, E. Kozik, and H. Hafermann, *Diagrammatic Monte Carlo approach for diagrammatic extensions of dynamical mean-field theory: Convergence analysis of the dual fermion technique*, Phys. Rev. B **96** (2017), 035152. See page: 31

[GKKR96] A. Georges, G. Kotliar, W. Krauth, and M. J. Rozenberg, *Dynamical mean-field theory of strongly correlated fermion systems and the limit of infinite dimensions*, Rev. Mod. Phys. **68** (1996), 13–125. See pages: 2, 20, 27, 29, 221, and 222

[GRS+17] O. Gunnarsson, G. Rohringer, T. Schäfer, G. Sangiovanni, and A. Toschi, *Breakdown of Traditional Many-Body Theories for Correlated Electrons*, Phys. Rev. Lett. **119** (2017), 056402. See pages: 27, 32, and 214

[Hew93] A. C. Hewson, *The Kondo Problem to Heavy Fermions*, Cambridge Studies in Magnetism, Cambridge University Press, 1993. See page: 218

[HH19] C. Hille and Y.-Y. He, 2019, private communication. See page: 213

[HJB$^+$09] H. Hafermann, C. Jung, S. Brener, M. I. Katsnelson, A. N. Rubtsov, and A. I. Lichtenstein, *Superperturbation solver for quantum impurity models*, EPL **85** (2009), no. 2, 27007. See page: 216

[HKP$^+$07] R. Hanson, L. P. Kouwenhoven, J. R. Petta, S. Tarucha, and L. M. K. Vandersypen, *Spins in few-electron quantum dots*, Rev. Mod. Phys. **79** (2007), 1217–1265. See page: 150

[HKT08] K. Held, A. A. Katanin, and A. Toschi, *Dynamical Vertex ApproximationAn Introduction*, Prog. Theor. Phys. Supp. **176** (2008), 117. See pages: 27, 28, and 29

[HOM04] A. C. Hewson, A. Oguri, and D. Meyer, *Renormalized parameters for impurity models*, Eur. Phys. J. B **40** (2004), no. 2, 177–189. See page: 221

[HPT13] K. Held, R. Peters, and A. Toschi, *Poor Man's Understanding of Kinks Originating from Strong Electronic Correlations*, Phys. Rev. Lett. **110** (2013), 246402. See page: 222

[Hun25] F. Hund, *Zur Deutung verwickelter Spektren, insbesondere der Elemente Scandium bis Nickel*, Z. Phys. **33** (1925), no. 1, 345–371. See page: 26

[HW15] S. Hoshino and P. Werner, *Superconductivity from Emerging Magnetic Moments*, Phys. Rev. Lett. **115** (2015), 247001. See page: 221

[HW16] S. Hoshino and P. Werner, *Electronic orders in multiorbital Hubbard models with lifted orbital degeneracy*, Phys. Rev. B **93** (2016), 155161. See page: 221

[HZM16] A. Horvat, R. Žitko, and J. Mravlje, *Low-energy physics of three-orbital impurity model with Kanamori interaction*, Phys. Rev. B **94** (2016), 165140. See page: 25

[Jak09] S. G. Jakobs, *Functional renormalization group studies of quantum transport through mesoscopic systems*, Ph.D. thesis, RWTH Aachen, 2009. See page: 224

[Jan98] V. Janiš, *Generating functional for the full parquet approximation*, arXiv:cond-mat/9806118 (1998). See page: 215

[Jis13] R. A. Jishi, *Feynman Diagram Techniques in Condensed Matter Physics*, Cambridge University Press, 2013. See page: 217

[JPS10] S. G. Jakobs, M. Pletyukhov, and H. Schoeller, *Nonequilibrium functional renormalization group with frequency-dependent vertex function: A study of the single-impurity Anderson model*, Phys. Rev. B **81** (2010), 195109. See page: 224

[Kai05] D. Kaiser, *Physics and Feynman's Diagrams: In the hands of a postwar generation, a tool intended to lead quantum electrodynamics out of a decades-long morass helped transform physics*, American Scientist **93** (2005), no. 2, 156–165. See page: 140

[Kat04] A. A. Katanin, *Fulfillment of Ward identities in the functional renormalization group approach*, Phys. Rev. B **70** (2004), 115109. See page: 217

[Kat13] A. A. Katanin, *The effect of six-point one-particle reducible local interactions in the dual fermion approach*, J. Phys. A **46** (2013), no. 4, 045002. See page: 31

[KBS10] P. Kopietz, L. Bartosch, and F. Schütz, *Introduction to the Functional Renormalization Group (Lecture Notes in Physics)*, Springer, Berlin, 2010. See pages: 5, 6, 7, 9, and 11

[KFG15] E. Kozik, M. Ferrero, and A. Georges, *Nonexistence of the Luttinger-Ward Functional and Misleading Convergence of Skeleton Diagrammatic Series for Hubbard-Like Models*, Phys. Rev. Lett. **114** (2015), 156402. See page: 32

[KKN$^+$15] B. Keimer, S. A. Kivelson, M. R. Norman, S. Uchida, and J. Zaanen, *From quantum matter to high-temperature superconductivity in copper oxides*, Nature **518** (2015), no. 7538, 179–186. See page: 5

[KOBH13] M. Kinza, J. Ortloff, J. Bauer, and C. Honerkamp, *Alternative functional renormalization group approach to the single impurity Anderson model*, Phys. Rev. B **87** (2013), 035111. See page: 216

[KSH+06] G. Kotliar, S. Y. Savrasov, K. Haule, V. S. Oudovenko, O. Parcollet, and C. A. Marianetti, *Electronic structure calculations with dynamical mean-field theory*, Rev. Mod. Phys. **78** (2006), 865–951. See pages: 20 and 219

[Kug16] F. B. Kugler, *Fermi edge singularity and the functional renormalization group*, Master's thesis, LMU Munich, 2016. See page: 9

[KvHG+10] E. Kozik, K. van Houcke, E. Gull, L. Pollet, N. Prokof'ev, B. Svistunov, and M. Troyer, *Diagrammatic Monte Carlo for correlated fermions*, EPL **90** (2010), no. 1, 10004. See page: 218

[LAK54] L. D. Landau, A. A. Abrikosov, and I. M. Khalatnikov, Dokl. Akad. Nauk. **95**, 497 (1954); **95**, 773 (1954); **95**, 1177 (1954). See page: 10

[LDSK15] P. Lange, C. Drukier, A. Sharma, and P. Kopietz, *Summing parquet diagrams using the functional renormalization group: X-ray problem revisited*, J. Phys. A **48** (2015), no. 39, 395001. See pages: 32 and 211

[Lee19] S.-S. B. Lee, 2019, private communication. See page: 26

[LKPH19] G. Li, A. Kauch, P. Pudleiner, and K. Held, *The victory project v1.0: An efficient parquet equations solver*, Comput. Phys. Commun. **241** (2019), 146–154. See page: 11

[LRMZ13] R. López, T. Rejec, J. Martinek, and R. Žitko, *SU(3) Kondo effect in spinless triple quantum dots*, Phys. Rev. B **87** (2013), 035135. See page: 218

[LSdlPR+17] J. Lichtenstein, D. Sánchez de la Peña, D. Rohe, E. Di Napoli, C. Honerkamp, and S. A. Maier, *High-performance functional Renormalization Group calculations for interacting fermions*, Comput. Phys. Commun. **213** (2017), 100 – 110. See page: 29

[LvDW17] S.-S. B. Lee, J. von Delft, and A. Weichselbaum, *Doublon-Holon Origin of the Subpeaks at the Hubbard Band Edges*, Phys. Rev. Lett. **119** (2017), 236402. See page: 2

[LW60] J. M. Luttinger and J. C. Ward, *Ground-State Energy of a Many-Fermion System. II*, Phys. Rev. **118** (1960), 1417–1427. See pages: 14, 16, and 215

[LW16] S.-S. B. Lee and A. Weichselbaum, *Adaptive broadening to improve spectral resolution in the numerical renormalization group*, Phys. Rev. B **94** (2016), 235127. See pages: 2 and 24

[LWP+16] G. Li, N. Wentzell, P. Pudleiner, P. Thunström, and K. Held, *Efficient implementation of the parquet equations: Role of the reducible vertex function and its kernel approximation*, Phys. Rev. B **93** (2016), 165103. See page: 11

[LZH+19] N.-O. Linden, M. Zingl, C. Hubig, O. Parcollet, and U. Schollwöck, *Imaginary-time matrix product state impurity solver in a real material calculation: Spin-orbit coupling in* Sr_2RuO_4, arXiv:1909.02503 (2019). See pages: 26 and 221

[MAM+11] J. Mravlje, M. Aichhorn, T. Miyake, K. Haule, G. Kotliar, and A. Georges, *Coherence-Incoherence Crossover and the Mass-Renormalization Puzzles in* $\mathrm{Sr_2RuO_4}$, Phys. Rev. Lett. **106** (2011), 096401. See page: 221

[MAvDZ12] C. Moca, A. Alex, J. von Delft, and G. Zaránd, *SU(3) Anderson impurity model: A numerical renormalization group approach exploiting non-Abelian symmetries*, Phys. Rev. B **86** (2012), 195128. See page: 218

[Met91] W. Metzner, *Linked-cluster expansion around the atomic limit of the Hubbard model*, Phys. Rev. B **43** (1991), 8549–8563. See page: 216

[MGWF$^+$14] A. K. Mitchell, M. R. Galpin, S. Wilson-Fletcher, D. E. Logan, and R. Bulla, *Generalized Wilson chain for solving multichannel quantum impurity problems*, Phys. Rev. B **89** (2014), 121105. See pages: 24, 219, and 224

[MHY$^+$94] Y. Maeno, H. Hashimoto, K. Yoshida, S. Nishizaki, T. Fujita, J. G. Bednorz, and F. Lichtenberg, *Superconductivity in a layered perovskite without copper*, Nature **372** (1994), 532. See page: 220

[MJPH05] T. Maier, M. Jarrell, T. Pruschke, and M. H. Hettler, *Quantum cluster theories*, Rev. Mod. Phys. **77** (2005), 1027–1080. See page: 26

[MJS06] T. A. Maier, M. S. Jarrell, and D. J. Scalapino, *Structure of the Pairing Interaction in the Two-Dimensional Hubbard Model*, Phys. Rev. Lett. **96** (2006), 047005. See page: 29

[MM03] A. P. Mackenzie and Y. Maeno, *The superconductivity of* $\mathrm{Sr_2RuO_4}$ *and the physics of spin-triplet pairing*, Rev. Mod. Phys. **75** (2003), 657–712. See page: 220

[Mor94] T. R. Morris, *The exact renormalization group and approximate solutions*, Int. J. Mod. Phys. A **09** (1994), no. 14, 2411–2449. See pages: 6 and 9

[MRS01] Y. Maeno, T. M. Rice, and M. Sigrist, *The Intriguing Superconductivity of Strontium Ruthenate*, Phys. Today **54** (2001), no. 1, 42–47. See pages: 3, 5, 189, and 220

[MSH$^+$12] W. Metzner, M. Salmhofer, C. Honerkamp, V. Meden, and K. Schönhammer, *Functional renormalization group approach to correlated fermion systems*, Rev. Mod. Phys. **84** (2012), no. 1, 299–352. See pages: 2, 6, and 9

[MSHM17] A. P. Mackenzie, T. Scaffidi, C. W. Hicks, and Y. Maeno, *Even odder after twenty-three years: the superconducting order parameter puzzle of Sr2RuO4*, npj Quant. Mater. **2** (2017), 40. See pages: 3, 189, and 220

[MV89] W. Metzner and D. Vollhardt, *Correlated Lattice Fermions in* $d = \infty$ *Dimensions*, Phys. Rev. Lett. **62** (1989), 324–327. See page: 20

[MW66] N. D. Mermin and H. Wagner, *Absence of Ferromagnetism or Antiferromagnetism in One- or Two-Dimensional Isotropic Heisenberg Models*, Phys. Rev. Lett. **17** (1966), 1133–1136. See page: 18

[NCH10] Y. Nishikawa, D. J. G. Crow, and A. C. Hewson, *Renormalized parameters and perturbation theory for an* n*-channel Anderson model with Hund's rule coupling: Symmetric case*, Phys. Rev. B **82** (2010), 115123. See page: 221

[NO98] J. W. Negele and H. Orland, *Quantum Many-particle Systems*, Advanced Books Classics, Perseus Books, New York, 1998. See pages: 4, 5, 10, 11, 140, 217, and 218

[OO94] W. C. Oliveira and L. N. Oliveira, *Generalized numerical renormalization-group method to calculate the thermodynamical properties of impurities in metals*, Phys. Rev. B **49** (1994), 11986–11994. See page: 24

[PKHL19] P. Pudleiner, Anna K., K. Held, and G. Li, *Competition between antiferromagnetic and charge density wave fluctuations in the extended Hubbard model*, Phys. Rev. B **100** (2019), 075108. See page: 11

[PTV$^+$19] P. Pudleiner, P. Thunström, A. Valli, A. Kauch, G. Li, and K. Held, *Parquet approximation for molecules: Spectrum and optical conductivity of the Pariser-Parr-Pople model*, Phys. Rev. B **99** (2019), 125111. See page: 11

[RGI$^+$17] T. Ribic, P. Gunacker, S. Iskakov, M. Wallerberger, G. Rohringer, A. N. Rubtsov, E. Gull, and K. Held, *Role of three-particle vertex within dual fermion calculations*, Phys. Rev. B **96** (2017), 235127. See page: 31

[RGN69] B. Roulet, J. Gavoret, and P. Nozières, *Singularities in the X-Ray Absorption and Emission of Metals. I. First-Order Parquet Calculation*, Phys. Rev. **178** (1969), 1072–1083. See pages: 11, 17, and 18

[RHT+18] G. Rohringer, H. Hafermann, A. Toschi, A. A. Katanin, A. E. Antipov, M. I. Katsnelson, A. I. Lichtenstein, A. N. Rubtsov, and K. Held, *Diagrammatic routes to nonlocal correlations beyond dynamical mean field theory*, Rev. Mod. Phys. **90** (2018), 025003. See pages: 3, 13, 18, 27, 28, 29, 30, and 31

[Rib18] T. Ribic, 2018, private communication. See page: 31

[RJM15] J. F. Rentrop, S. G. Jakobs, and V. Meden, *Two-particle irreducible functional renormalization group schemes—a comparative study*, J. Phys. A **48** (2015), no. 14, 145002. See page: 13

[RKL08] A. N. Rubtsov, M. I. Katsnelson, and A. I. Lichtenstein, *Dual fermion approach to nonlocal correlations in the Hubbard model*, Phys. Rev. B **77** (2008), 033101. See pages: 27 and 30

[RKL12] A. N. Rubtsov, M. I. Katsnelson, and A. I. Lichtenstein, *Dual boson approach to collective excitations in correlated fermionic systems*, Ann. Phys. **327** (2012), no. 5, 1320 – 1335. See page: 27

[RRH17] T. Ribic, G. Rohringer, and K. Held, *Local correlation functions of arbitrary order for the Falicov-Kimball model*, Phys. Rev. B **95** (2017), 155130. See page: 31

[RVT12] G. Rohringer, A. Valli, and A. Toschi, *Local electronic correlation at the two-particle level*, Phys. Rev. B **86** (2012), 125114. See pages: 11, 17, 19, and 216

[RW10] J. Reuther and P. Wölfle, *J_1-J_2 frustrated two-dimensional Heisenberg model: Random phase approximation and functional renormalization group*, Phys. Rev. B **81** (2010), 144410. See page: 223

[SBvD17] D. H. Schimmel, B. Bruognolo, and J. von Delft, *Spin Fluctuations in the 0.7 Anomaly in Quantum Point Contacts*, Phys. Rev. Lett. **119** (2017), 196401. See page: 224

[Sca12] D. J. Scalapino, *A common thread: The pairing interaction for unconventional superconductors*, Rev. Mod. Phys. **84** (2012), 1383–1417. See page: 2

[SCW+16] T. Schäfer, S. Ciuchi, M. Wallerberger, P. Thunström, O. Gunnarsson, G. Sangiovanni, G. Rohringer, and A. Toschi, *Nonperturbative landscape of the Mott-Hubbard transition: Multiple divergence lines around the critical endpoint*, Phys. Rev. B **94** (2016), 235108. See pages: 27 and 214

[Sha94] R. Shankar, *Renormalization-group approach to interacting fermions*, Rev. Mod. Phys. **66** (1994), no. 1, 129–192. See pages: 3, 6, 7, and 8

[SKWvD19] K. M. Stadler, G. Kotliar, A. Weichselbaum, and J. von Delft, *Hundness versus Mottness in a three-band Hubbard–Hund model: On the origin of strong correlations in Hund metals*, Ann. Phys. **405** (2019), 365 – 409. See pages: 2, 25, 189, and 224

[SMB+14] D. Stricker, J. Mravlje, C. Berthod, R. Fittipaldi, A. Vecchione, A. Georges, and D. van der Marel, *Optical Response of* Sr_2RuO_4 *Reveals Universal Fermi-Liquid Scaling and Quasiparticles Beyond Landau Theory*, Phys. Rev. Lett. **113** (2014), 087404. See page: 220

[Smi92] R. A. Smith, *Planar version of Baym-Kadanoff theory*, Phys. Rev. A **46** (1992), 4586–4597. See pages: 16, 19, and 215

[SMvDW16] K. M. Stadler, A. K. Mitchell, J. von Delft, and A. Weichselbaum, *Interleaved numerical renormalization group as an efficient multiband impurity solver*, Phys. Rev. B **93** (2016), 235101. See pages: 2, 24, 219, 222, and 224

[SRG+13] T. Schäfer, G. Rohringer, O. Gunnarsson, S. Ciuchi, G. Sangiovanni, and A. Toschi, *Divergent Precursors of the Mott-Hubbard Transition at the Two-Particle Level*, Phys. Rev. Lett. **110** (2013), 246405. See pages: 27 and 214

[Sta19] K. M. Stadler, *A model study of strong correlations in hund metals: The numerical renormalization group as efficient multi-band impurity solver for dynamical mean-field theory*, Ph.D. thesis, LMU Munich, 2019. See page: 24

[SYvD+15] K. M. Stadler, Z. P. Yin, J. von Delft, G. Kotliar, and A. Weichselbaum, *Dynamical Mean-Field Theory Plus Numerical Renormalization-Group Study of Spin-Orbital Separation in a Three-Band Hund Metal*, Phys. Rev. Lett. **115** (2015), 136401. See pages: 2, 25, 219, and 224

[TAB+14] C. Taranto, S. Andergassen, J. Bauer, K. Held, A. Katanin, W. Metzner, G. Rohringer, and A. Toschi, *From Infinite to Two Dimensions through the Functional Renormalization Group*, Phys. Rev. Lett. **112** (2014), 196402. See pages: 27, 29, 214, and 223

[TFY+13] K.-M. Tam, H. Fotso, S.-X. Yang, T.-W. Lee, J. Moreno, J. Ramanujam, and M. Jarrell, *Solving the parquet equations for the Hubbard model beyond weak coupling*, Phys. Rev. E **87** (2013), 013311. See page: 11

[TGCR18] P. Thunström, O. Gunnarsson, Sergio Ciuchi, and G. Rohringer, *Analytical investigation of singularities in two-particle irreducible vertex functions of the Hubbard atom*, Phys. Rev. B **98** (2018), 235107. See pages: 27, 214, and 216

[TKH07] A. Toschi, A. A. Katanin, and K. Held, *Dynamical vertex approximation: A step beyond dynamical mean-field theory*, Phys. Rev. B **75** (2007), 045118. See pages: 27, 28, and 29

[TZR+19] A. Tamai, M. Zingl, E. Rozbicki, E. Cappelli, S. Riccò, A. de la Torre, S. McKeown Walker, F. Y. Bruno, P. D. C. King, W. Meevasana, M. Shi, M. Radović, N. C. Plumb, A. S. Gibbs, A. P. Mackenzie, C. Berthod, H. U. R. Strand, M. Kim, A. Georges, and F. Baumberger, *High-Resolution Photoemission on* $\mathrm{Sr_2RuO_4}$ *Reveals Correlation-Enhanced Effective Spin-Orbit Coupling and Dominantly Local Self-Energies*, Phys. Rev. X **9** (2019), 021048. See page: 220

[vHKPS10] K. van Houcke, E. Kozik, N. Prokof'ev, and B. Svistunov, *Diagrammatic Monte Carlo*, Phys. Procedia **6** (2010), 95–105, Computer Simulations Studies in Condensed Matter Physics XXI. See page: 218

[VST+15] A. Valli, T. Schäfer, P. Thunström, G. Rohringer, S. Andergassen, G. Sangiovanni, K. Held, and A. Toschi, *Dynamical vertex approximation in its parquet implementation: Application to Hubbard nanorings*, Phys. Rev. B **91** (2015), 115115. See page: 11

[VT97] Y. M. Vilk and A.-M. S. Tremblay, *Non-Perturbative Many-Body Approach to the Hubbard Model and Single-Particle Pseudogap*, J. Phys. I France **7** (1997), no. 11, 1309–1368. See page: 18

[VTM19] D. Vilardi, C. Taranto, and W. Metzner, *Antiferromagnetic and d-wave pairing correlations in the strongly interacting two-dimensional Hubbard model from the functional renormalization group*, Phys. Rev. B **99** (2019), 104501. See pages: 29 and 214

[VWFP18] J. Vučičević, N. Wentzell, M. Ferrero, and O. Parcollet, *Practical consequences of the Luttinger-Ward functional multivaluedness for cluster DMFT methods*, Phys. Rev. B **97** (2018), 125141. See page: 32

[Wei12a] A. Weichselbaum, *Non-abelian symmetries in tensor networks: A quantum symmetry space approach*, Ann. Phys. **327** (2012), no. 12, 2972–3047. See pages: 2 and 24

[Wei12b] A. Weichselbaum, *Tensor networks and the numerical renormalization group*, Phys. Rev. B **86** (2012), 245124. See pages: 2 and 24

[Wet93] C. Wetterich, *Exact evolution equation for the effective potential*, Phys. Lett. B **301** (1993), no. 1, 90–94. See pages: 6 and 9

[Wil75] K. G. Wilson, *The renormalization group: Critical phenomena and the Kondo problem*, Rev. Mod. Phys. **47** (1975), 773–840. See pages: 3, 6, 7, and 23

[WLT$^+$16] N. Wentzell, G. Li, A. Tagliavini, C. Taranto, G. Rohringer, K. Held, A. Toschi, and S. Andergassen, *High-frequency asymptotics of the vertex function: diagrammatic parametrization and algorithmic implementation*, arXiv:1610.06520 (2016). See pages: 11, 18, 29, 30, 211, and 216

[WvD07] A. Weichselbaum and J. von Delft, *Sum-Rule Conserving Spectral Functions from the Numerical Renormalization Group*, Phys. Rev. Lett. **99** (2007), 076402. See pages: 2, 23, and 24

[YFL$^+$09] S. X. Yang, H. Fotso, J. Liu, T. A. Maier, K. Tomko, E. F. D'Azevedo, R. T. Scalettar, T. Pruschke, and M. Jarrell, *Parquet approximation for the* 4×4 *Hubbard cluster*, Phys. Rev. E **80** (2009), 046706. See pages: 11 and 215

[YHK11] Z. P. Yin, K. Haule, and G. Kotliar, *Kinetic frustration and the nature of the magnetic and paramagnetic states in iron pnictides and iron chalcogenides*, Nat. Mater. **10** (2011), no. 12, 932–935. See pages: 25 and 189

[ZP09] R. Žitko and T. Pruschke, *Energy resolution and discretization artifacts in the numerical renormalization group*, Phys. Rev. B **79** (2009), 085106. See page: 24